World Meteorological Organization
WWRP/Working Group on Tropical Meteorology Research
WWRP/Joint Working Group on Forecast Verification Research
Tropical Cyclone Programme

3rd WMO International Conference on Quantitative Precipitation Estimation and Quantitative Precipitation Forecasting and Hydrology

Extended Abstract Volume

Hosted by
Nanjing University of Information Science and Technology
MOST 973 Typhoon Program (2009CB421500) of China
NSF Key Research Program (40730948) of China
CMA/CAMS NMC

Nanjing China

18-22 October 2010

TABLE OF CONTENTS

Foreword iii

Conference Framework iv

Conference Programme v

EXTENDED ABSTRACTS 1

SESSION A1
High impact Precipitation Events (tropical cyclones, monsoons, and severe storms) 3

SESSION A2
High impact Precipitation Events (tropical cyclones, monsoons, and severe storms) 25

SESSION A3
High impact Precipitation Events (tropical cyclones, monsoons, and severe storms) 59

SESSION B1
Quantitative Precipitation Estimates, *in-situ*, remote sensing observations 79

SESSION B2
Quantitative Precipitation Estimates, *in-situ*, remote sensing observations 107

SESSION B3
Quantitative Precipitation Estimates, *in-situ*, remote sensing observations 125

SESSION C
Hydrologic prediction and coupled hydrology-atmosphere-land models 153

SESSION D1
Verification of precipitation forecasts 183

SESSION D2
Verification of precipitation forecasts 200

SESSION E
Data assimilation for precipitation forecasting systems 229

SESSION F
Precipitation variability and climate change 255

SESSION G1
Quantitative Precipitation Forecasts 287

SESSION G2
Quantitative Precipitation Forecasts 312

SESSION G3
Quantitative Precipitation Forecasts 331

SESSION G4
Quantitative Precipitation Forecasts 357

Session P
Posters 381

Foreword

Weather disasters often arise from heavy precipitation, especially the rainfall resulting from tropical cyclones (typhoon, hurricane, super cyclonic storm, etc.) and monsoons around the world. These disasters include but are not limited to river bank crumble, huge reservoir collapse, flash flooding inundation, and landslide and mud-stone (debris) flows which often swallow up villages and devastate societies and human lives. Accurate quantitative precipitation estimation (QPE), quantitative precipitation forecasting (QPF), and hydrological prediction play an important role in disaster prevention and mitigation.

The WMO International Conferences on QPE/QPF and Hydrology are quadrennial events organized by the World Meteorological Organization. The first of these meetings was held in Reading, UK, in September 2002. The second meeting was held in Boulder, Colorado, USA, in June 2006. The third meeting – represented by the abstracts included in this volume – will be held in Nanjing, China, in October 2010.

The overall objective of this conference is to improve the science and technology of QPE/QPF and hydrological prediction with an emphasis on rainfall caused by tropical cyclones and monsoons. The conference will bring together researchers and forecasters from around the world to review the progress of research in this area during the four years since the last conference. Research achievements and operational forecasting needs will be discussed and exchanged across the conference to help integrate research accomplishments and operational needs. We hope and expect that some of the mature research achievements can be transferred to operational use in relevant National Meteorological and Hydrological Services (NMHSs$_S$).

Progress has been made in the area of QPE as a consequence of the swift development and exploration of the utility of remotely sensed data from satellite, Doppler radar, and other sorts of remote sensing devices. Recent improvements in limited area model capabilities and data assimilation techniques using different and new data sources have greatly advanced QPF capabilities. We expect

that some major achievements in these areas will be demonstrated in the conference.

Seven topics have been selected as focus areas that are relevant for the conference objectives. The brief titles of these topics are:

- High impact precipitation events, related to tropical cyclones, monsoons, and severe storms;
- Quantitative Precipitation Estimation (QPE), *in situ* and remote sensing observations;
- Hydrologic prediction and coupled hydrology-atmosphere-land models;
- Verification of Quantitative Precipitation Forecasts (QPFs);
- Data assimilation for precipitation forecasting systems;
- Precipitation variability and climate change;
- Quantitative Precipitation Forecasting (QPF).

The major issues and relevant topics in QPE/QPF and hydrologic prediction are included in these topics, which will be the focus of presentations, discussions, and summaries in the meeting.

This extended abstract volume includes invited lectures, contributed papers, and posters. We would like to extend our genuine gratitude to all of the authors and the IOC members (abstract reviewers) for their great efforts toward the success of the conference, and would especially like to thank Ms. Nanette Lomarda, senior scientific officer from WMO, who offered major contributions to the conference. Staff at the National Center for Atmospheric Research, in particular Ms. Carol Makowski and Ms. Pam Johnson, also contributed greatly to these efforts. We also would like to express our sincere appreciation to NUIST and the local organizing committee for their efficient assistance in organizing the conference. Our genuine thanks also go to the MOST national 973 Typhoon Program (2009CB421500) and the Chinese NSF typhoon key research program (40730948) for their generous support of this event. Our appreciation is also extended to CMA/CAMS and NMC for their valuable help in organizing the meeting.

Lianshou Chen **(**Chinese Academy of Meteorological Sciences)
Chair, International Organizing Committee (IOC)

Barbara Brown (NCAR, USA)
Yihong Duan (CMA, China)
Chungu Lu (NSF, USA)
Co-chairs, IOC

CONFERENCE SCHEDULE

Third WMO International Conference on Quantitative Precipitation Estimation, Quantitative Precipitation Forecasting and Hydrology

Nanjing. China 18-22 October 2010

Date / Time	18 Oct (Mon)	19 Oct (Tue)	20 Oct (Wed)	21 Oct (Thu)		22 Oct (Fri)
09:00 09:50	Opening	Session B1	Session D1	Session G1		Session G3
	Photo					
10:05 10:30	Break					
	Session A1	Break				
10:50 12:15		Session B2	Session D2	TC Panel	Session G2	Session G4
Lunch (12:15 --- 13:45)						
13:45 15:40	Session A2	Session B3	Proposed Monsoon Rainfall RDP	Session E	Excursion	14:40 Summary 16:40
Break						Break
16:00 17:45	Session A3	Session C	Session F			17:00 Closing 17:30
18:15 20:30	Ice-breaker and Reception	Dinner 19:15 Poster			Banquet	

Topic areas A-G denote the 7 key topics for the workshop. A – High impact rain events for TC and monsoon; B – QPE; C - Hydrologic prediction; D – QPF verification; E - Data assimilation for QPF; F - Precipitation variability and climate change; G – QPF.

Conference program for the third WMO International Conference on QPE and QPF and hydrology

(Nanjing, China 2010)

List of topics:

A. **High impact precipitation events, related to tropical cyclones, monsoons, and severe storms**

B. **Quantitative Precipitation Estimates, *in situ* and remote sensing observations**

C. **Hydrologic prediction and coupled hydrology-atmosphere-land models**

D. **Verification of precipitation forecasts**

E. **Data assimilation for precipitation forecasting systems**

F. **Precipitation variability and climate change**

G. **Quantitative Precipitation Forecasts**

List of conveners and session chairs:

A. **Conveners:**
Russ Elsberry, C. -P. Chang

Session Chairs:
Lianshou Chen (A1)
Russ Elsberry (A2)
C. -P. Chang (A3)

B. **Conveners:**
Paul Joe, Richard Johnson

Session Chairs:
Chungu Lu (B1)
Paul Joe (B2)
Richard Johnson (B3

C. Conveners:
Jinping Liu, Zhiyu Liu

Session Chairs:
Zhiyu Liu (C)
Jinping Liu (C)

D. Conveners:
Anna Ghelli, George Craig

Session Chairs:
Anna Ghelli (D1)
George Craig (D2)

E. Conveners:
Volker Wulfmeyer, Susan Ballard

Session Chairs:
Volker Wulfmeyer (E)
Susan Ballard (E)

F. Conveners:
Bodo Ahrens

Session Chairs:
Bodo Ahrens (F)

G. Conveners:
Yihong Duan, Jian Lin

Session Chairs:
Jian Lin (G1)
Tiziana Paccagnella (G2)
Yihong Duan (G3)
Susan Ballard (G4)

P. Poster Session
Convener: Volker Wulfmeyer

H. Conference summary
Convener: Chungu Lu

Conference program:

A. High impact precipitation events, related to tropical cyclones, monsoons, and severe storms

Convener: Russ Elsberry, C. -P. Chang

A1. 10:50-12:15 Session Chair: Lianshou Chen

10:30-11:55 Richard Johnson (Invited): **Synoptic and Mesoscale Processes Associated with Extreme Convective Rainfall**

10:55-11:10 Christoph Brendel: **Convection over the Taunus Mountains: Distribution, Tracks, and Life Cycle** (Co-author: B. Ahrens)

11:10-11:25 Ben Jong-Dao Jou: **Monsoon Rainfall Characteristics: Precipitation Types and Associated Environment Regimes observed during SoWMEX/TiMREX** (Co-author: C. Tong, and W. Lee)

11:25-11:40 Yong Wang: **Spatial and Temporal Variations of Extreme Precipitation Events in the Huaihe River Basin, China** (Co-author: Q. Miao, Y. Ding)

11:40-11:55 Taoyong Peng: **Some TC forecasting issues related to TCP/WMO**

11:55-12:10 Lorena Ferreira: **Land-atmosphere interactions during a Northwestern Argentina Low event: impacts on precipitation fields** (Co-author: C. Sailo, and J. Ruiz)

A2. 13:45-15:40 Session Chair: Russ Elsberry

13:45-14:10 Lianshou Chen (Invited): **On the Study of Tropical Cyclone Rainfall Mechanism**

14:10-14:25 Yuqing Wang: **Influence of Typhoon Songda (2004) in Producing Distantly-Located Heavy Rainfall in Japan** (Co-author: Y. Wang, and H. Fudeyasu)

14:25-14:40 Ying Li: **On the Study of Rainfall Rate and Distribution Associated with the Typhoon Winnie (9711) during Its ET Process** (Co-author: X. Lei, and L. Chen)

14:40-14:55 Tong Xu: **The estimation of TC quantitative precipitation forecast affecting Shanghai in 2009** (Co-author: J. Li, X. Wang, H. Yu, B. Chen, and Y. Yang)

14:55-15:10 Mei-ying Dong: **Numerical Study of Topographic Effect on Rainfall Reinforcement Associated with Tropical Cyclone Talim (2005)** (Co-author: L. Chen, Y. Li)

15:10-15:25 Fumin Ren: **Changes in tropical cyclone precipitation over China** (Co-author: G. Wu, X. Wang, and Y. Wang)

15:25-15:40 Yu Wang: **The Verification of Tropical Cyclone Rainfall Prediction with global models of CMA and JMA** (Co-author: X. Shen, and D. Chen)

A3. 16:00-17:45 Session Chair: C. -P. Chang

16:00-16:25 Russ Elsberry (Invited): **Advances in Understanding the "Perfect Monsoon-influenced Typhoon"** (Co-author: C.-S. Lee, C.C. Wu, and T.-C. Wang)

16:25-16:40 Jinhai He: **The mechanism analysis of cloud and moisture sources/sinks in the formation of torrential rainfall** (Co-author: S. Gao, and L. Xu)

16:40-16:55 Shakeel Asharaf: **The Indian summer monsoon: precipitation – soil moisture feedback/recycling** (Co-author: A Dobler, and B. Ahrens)

16:55-17:10 Yuchun Zhao: **An Idealized Numerical Study on the Effects of Meiyu Front upon the Initiation and Development of MCSs Producing Rainstorms**

17:10-17:25 Andreas Dobler: **Regional climate projections of trends and variability in the Indian summer monsoon** (Co-author: B. Ahrens)

17:25-17:40 Soi Kun Fong: **The Effect of ENSO on the Summer Monsoon Rainfall in Macao** (Co-author: S. W. Chang, and I. H. Liu)

B. Quantitative Precipitation Estimate, in-situ, remote sensing observations

Convener: Paul Joe, Richard Johnson

B1. 09:00-10:30 Session Chair: Chungu Lu

09:00-09:25 Paul Joe (Invited): **Observations of Precipitation Processes at the Vancouver 2010 Winter Olympic Games** (Co-author: Multiple people)

09:25-09:40 Ping-ping Xie: **A High-Resolution Gauge-Satellite Merged Global Precipitation Analysis And its Applications for Model Verifications** (Co-author: R. Joyce, S. Yoo, and Y. Yarosh)

09:40-09:55 Dan Qi: **Analyses of Quantitative Precipitation Estimation (QPE) Based on Merging Satellite and Rain Gauge** (Co-author: F. Tian, H. Wu, L. Zhao, F. Xu, and H. Bao)

09:55-10:10 Philippe Chambon: **The Megha-Tropiques accumulated rainfall algorithm TAPEER (Tropical Amount of Precipitation with Estimation of ERrors): investigating the error budget of satellite quantitative precipitation estimations** (Co-author: I. Jobard, and R. Roca)

10:10-10:25 Rajendra P. Shrestha: **Performance and Applicability of Satellite-Rainfall Estimation in Nepal**

B2. 10:50-12:15 Session Chair: Paul Joe

10:50-11:15 Kazuhiko Nagata (Invited): **QPE and QPF of Japan Meteorological Agency**

11:15-11:30 Yan Shen: **A new gauge-based precipitation analysis over mainland China and its evaluation** (Co-author: Q. Li, and Y. Pan)

11:30-11:45 Zifeng Yu: **Verification of Tropical Cyclone-Related Satellite Precipitation Estimates in Mainland China** (Co-author: H. Yu, P. Chen, C. Qian, and C. Yue)

11:45-12:00 Anyuan Xiong: **Establishment of Real-time System for Daily Precipitation Analysis over China** (Co-author: Y. Shen, and M. Feng)

12:00-12:15 Jiuke Wang: **The representation of the rain gauges in estimating the strength of rainfall during the "plum rain" in Anhui province, China**

B3. 13:45-15:40 Session Chair: Richard Johnson

13:45-14:10 Yihong Duan (invited): **Recent Progresses on TC Precipitation QPE/QPF** (Co-author: L. Chen, Y. Li, H. Yu, J. Lin, and J. Callaghan)

14:10-14:25 Bin Wang: **Comparative Study on QPE Methods of X-band Polarimetric Radar in a Typhoon Event in South China** (Co-author: Y. Xiao)

14:25-14:40 P. Shucksmith: **A Multiscale Observation Error Estimation Scheme for QPE Using Local High Resolution Radar** (Co-author: G. Austin, and L.S.utherland-Stacey)

14:40-14:55 Minghu Cheng: **A Radar-based Technique for the Identification of Convective and Stratiform Precipitation using the FLNN with Its Application to Estimation of Precipitation** (Co-author: L. Zhang)

14:55-15:10 Hongli Li: **Mesoscale Analysis of a Severe Convective Event in Chongqing by LAPS** (Co-author: J. Peng)

15:10-15:25 Jianhong Wang: **CINRAD Warning Index of Local Extreme Torrential Rain in Huaihe Valley** (Co-author: C. Miao, S. Sun, Q. Wang, X. Wang)

15:25-15:40 Rui Wang: **Research of Rainfall Estimation using X-Band Polarimetric Radar** (Co-author: S. Gu, and Y. He)

C. Hydrologic prediction and coupled hydrology-atmosphere-land models

Convener: Jinping Liu and Zhiyu Liu

C. 16:00-17:45 Session Chair: Zhiyu Liu, Jinping Liu

16:00-16:20 Jinping Liu (Invited): **Hydrological Perspective on QPE/QPF**

16:20-16:40 Zhiyu Liu (Invited): **NWP models' Application in Flood Forecasting and Reservoir Operation of the Three Gorges Project**

16:40-16:55 Thomas Pagano: **NWP-forced short-term streamflow forecasts for Australia** (Co-authors**:** L. Cao, QJ Wang**)**

16:55-17:10 Fuyou Tian: **Probabilistic flood prediction using TIGGE on upriver of Huaihe catchment** (Co-author: D. Qi, L. Zhao, H. Wu, and Z. Wang)

17:10-17:25 Bongkiyung Ennanuel Byuki: **Extreme precipitation events in Cameroon**

17:25-17:40 Chunguang Cui: **The Flood Forecast Test on Quantitative Precipitation Forecast (QPF) Coupling with Hydrological Model** (Co-author: T. Peng, T. Shen, and Z. Yin)

D. Verification of precipitation forecasts

Convener: Anna Ghelli, George Craig

D1. 09:00-10:30 Session Chair: Anna Ghelli

09:00-09:25 Barbara Brown (Invited): **Intercomparison of verification methods for spatial quantitative precipitation forecasts** (Co-author: E. Ebert, E. Gilleand, and T. Fowler)

09:25-09:40 Kadarsah: **Verification of Quantitative Precipitation Forecasts with In Situ Measurements for Flood Forecasting and Warning in Jakarta**

09:40-09:55 Tressa Fowler: **New Model Evaluation Tools (MET) Software Capabilities for QPF Verification** (Co-author: T. Jensen, E. Tollerud, J. Halley Gotway, P. Oldnburg, and R. Bullock)

09:55-10:10 Qiuzhen Yang: **A Quantitative Hazard Assessing Method for Heavy Rainfall Events** (Co-author: M. Xu, and J. Li)

10:10-10:25 Chunze Lin: **Performance Evaluation of the AREM Prediction System for the Successive Heavy Rain Forecast of May 2010 in South China** (Co-author: Y. Gong,, J. Li, and M. Xu)

D2. 10:50-12:15 Session Chair: George Craig

10:50-11:10 Anna Ghelli (Invited): **Accounting for observational uncertainty when verifying precipitation forecasts**

11:10-11:30 Georg Craig (Invited): **A new field verification score based on optical flow technique** (Co-author: C. Keil)

11:30-11:45 Jamie Wolff: **Quantitative Precipitation Forecast (QPF) Verification Comparison Between the Global Forecast System and North American Mesoscale (NAM) Operational Models** (Co-author: B. Brown, J. Halley Gotway, M. Harrold, Z. Trabold, L. Nance, and P. Oldenburg)

11:45-12:00 Edward Tollerud: **Scale-related Issues Involving Verification of QPF: Results from a DTC Assessment of WRF Ensemble Forecasts during the HMT-West Winter Exercise** (Co-author: T. Jensen, J. Halley Gotway, P. Oldenburg, H. Yuan, I. Jankov)

12:00-12:15 Pertti Nurmi: **Experimentation with new verification measures for categorized QPFs in the verification of high impact precipitation events**

E. Data assimilation for precipitation forecasting systems

Convener: Volker Wulfmeyer, Susan Ballard

E. 13:45-15:40 Session Chair: Volker Wulfmeyer

13:45-14:10 Susan Ballard (Invited): **Progress in data assimilation for NWP based Nowcasting of Precipitation using radar and remote sensing data at the UK Met Office** (Co-author: Z. Li, D. Simonin, H. Buttery, C. Charlton-Perez, N. Gaussiat, L. Smith, G. Kelly, and R. Tubbs)

14:10-14:35 Hendrik Reich (Invited): **LETKF for the nonhydrostatic regional model COSMO-DE** (Co-author: A. Rhodin, and C. Schraff)

14:35-14:50 Xunlai Chen: **Impacts of multiple radar data assimilation on short-range quantitative precipitation forecasts of a squall line in South China** (Co-author: H. Lan, F. Kong, and F. Cai)

14:50-15:05 Pascal Horton: **Optimization of the Analogs method in the framework of statistical weather forecasting in the Swiss Alps** (Co-author: C. Obled, M. Jaboyedoff, and R. Metzger)

15:05-15:20 L. Sutherland-Stacey: **High resolution radar accumulation maps for verification of WRF+VAR (National Radar Network)** (Co-author: G. Austin, and P. Shucksmith)

15:10-15:25 Lei Zhang: **Application Test of Doppler Radar Data in Numerical Model ARPS** (Co-author: Z. Wang)

15:25-15:40 Yehong Wang: **Development of Rapid Update Cycle Forecasting System Based on AREM Model and Its Real-Time Rainfall Forecasts during Flooding-Season of 2009 in China** (Co-author: Y. Zhao, J. Peng, and H. Li)

F. Precipitation variability and climate change

Convener: Bodo Ahrens

F. 16:00-17:45 Session Chair: Bodo Ahrens, Yihong Duan

16:00-16:25 Bodo Ahrens (Invited): **Representation of Monsoon Systems in Regional Climate Models** (Co-author: A. Dobler, and S. Kothe)

16:25-16:40 Yanyu Lu: **Spatial and Temporal Variability Characteristics of Precipitation in Huai River Basin during 1961-2005** (Co-author: B. Wu, H. Tian, and S. Wei)

16:40-16:55 K.H.M.S. Premalal: **Variability of Rainfall, Increasing trend of One Day Heavy Rainfalls in Sri Lanka in the Context of Climate Change**

16:55-17:10 Jong-Pil Kim: **Regional Impact of Climate Change in Korea Rainfall Extremes** (Co-author: G. Kim, and J. Park)

17:10-17:25 Oleg Pokrovsky: **Implementation of the wind, NAO, AO and ENSO data in prediction of therain rate in the Mediterranean area by fuzzy-neural model**

17:25-17:40 Zablone Owiti: **Variability of Equatorial East African Rainfall based on Empirical Mode Decomposition derived variability components** (Co-author: W. Zhu)

G. Quantitative Precipitation Forecasts

Convener: Yihong Duan, Jian Lin

G1. 09:00-10:30 Session Chair: Jian Lin

09:00-09:25 Tiziana Paccagnella (Invited): **Ongoing developments on limited area ensemble forecasting And the coordination role of TIGGE LAM**

09:25-09:40 Jing Chen: **The Regional Ensemble Prediction System (REPS) at CMA and its application to heavy rainfall forecast in monsoon season in** (Co-author: G. Deng, Y. Li, X. Li, J. Gong, X. Wang, and J. Hu)

09:40-09:55 Tran Tan Tien: **Ensemble forecast of tropical cyclone motion using RAMS model and Breeding of Growing Modes method** (Co-author: C. Thanh)

09:55-10:10 Kirstin Kober: **Blending a probabilistic nowcasting method with a high resolution ensemble for convective precipitation** (Co-author: G. Craig, and C. Keil)

10:10-10:25 Fanyou Kong: **Probabilistic QPF from a realtime multi-model storm-scale ensemble forecasting system** (Co-author: M. Xue, and X. Wang)

G2. 10:50-12:15 Session Chair: Tiziana Paccagnella

10:50-11:15 Jian Lin (Invited): **Development of QPF approaches in NMC/CMA** (Co-author: X. Jiang, and K. Dai)

11:15-11:30 Thaejin Kim: **Research and Operation on Quantitative Precipitation Forecast (QPF) in DPR of Korea**

11:30-11:45 Huiling Yuan: **Quantitative Precipitation Forecasts during the HMT-West campaign** (Co-author: I. Jankov, S. Albers, and Z. Toth)

11:45-12:00 Yan Yin: **A numerical study of aerosol effectss on regional precipitation** (Co-author: H. Xiao)

12:00-12:15 Yong Wang: **The Challenge of LAMEPS on Quantitative Precipitation Forecast** (Co-authors: S. Tascu)

G3. 09:00-10:30 Session Chair: Yihong Duan

09:00-09:25 Chungu Lu (Invited): **Global QPF/QPE: Where do we have trouble to achieve them?** (Co-authors: H. Yuan, E. Tollerud, and N. Wang)

09:25-09:40 Hsiao-ming Hsu: **Multiscale Spectral Structures of Tropical Rainfall over Maritime Continent Simulated by NRCM and Observed by Satellites** (Co-authors: J. Tribbia, and M. Moncrieff)

09:40-09:55 Christian Keil: **Regime-dependent forecast uncertainty of convective precipitation** (Co-author: G. Craig)

09:55-10:10 Yongming Tang: **Rainfall forecasts from the Met Office variable resolution convective scale NWP model over the UK** (Co-author: H. Lean and J. Bornemann)

10:10-10:25 Martina Suaya: **Value of high resolution forecasts: convective climatology point of view**

G4. 10:50-12:15 Session Chair: Susan Ballard

10:50-11:05 Laurence Wilson: **Can Multi-model ensemble forecasts improve probability of precipitation forecasts compared to single model ensemble forecasts?** (Co-author: A. Ghelli)

11:05-11:20 Jingru Dai: **Improvement of Poor Man's Ensemble Precipitation Forecast in Mountainous Regions of Australia** (Co-author: M. Manton, and S. Siems)

11:20-11:35 Juan Ruiz: **How sensitive are probabilistic precipitation forecasts to the choice of ensemble generation method** (Co-author: C. Saulo)

11:35-11:50 Subramaniam Moten: **Quantitative Precipitation Forecast of Heavy Rainfall Episodes During the Northeast Monsoon Season over the Malaysian Region using the MM5 Model**

11:50-12:05 Xiefei Zhi: **Multimodel Consensus Forecasts of the Precipitation Using TIGGE Data** (Co-author: L. Zhang)

12:05-12:20 Jun Li: **The Development of Ensemble Prediction System in WHIHR** (Co-author: M. Wang, and C. Lin)

P. 19:15-20:30 19-20 Oct. 2010 Poster session

Convener: Volker Wulfmeyer

Hongjun Bao: **Coupling Ensemble weather predictions with Xinanjiang model for flood forecast** (Co-author: L. Zhao, Y. He, Z. Li, and P. Florian)

Christoph Brendel: **Convection over the Taunus Mountains: Distribution, Tracks, and Life Cycle** (Co-author: B. Ahrens)

Yangbo Chen: **Flash flood forecasting by coupling radar-based precipitation and distributed hydrological model** (Co-author: H. Zhou, Q. Ren)

Xingang Dai: **Statistical Prediction of China Summer rainfall Using Regression** (Co-author: Z. Cheng, and P. Wang)

Tommaso Diomede: **Comparison of calibration techniques for a limited-area ensemble precipitation forecast using reforecasts** (Co-author: C. Marsigli, A. Montani, and T. Paccagnella)

Sohyun Cho: **Quantitative Precipitation Estimation Using Neural Networks and Multi-sensor Data** (Co-author: G. Kim)

Shicheng Huang: **Analysis for Turbulence and Wind Gust Factor in Surface Layer Affected by Typhoon** (Co-authors: J. Zhou, W. Wang, B. Zhang, and B. Zhang)

Shicheng Huang: **Research and Application of Typhoon Gale Disaster Evaluation Methods --Taking Sutong Bridge as Example** (Co-authors: J. Zhou, W. Wang, B. Zhang, and B. Zhang)

Wei Jiang: **Study on Spatial-Temporal Distribution and Variation of Jiangsu Summer Precipitation** (Co-author: J. Lu)

Thaejin Kim: **The characteristic change and analysis of its cause of recent precipitation in DPR of Korea** (Co-author: C. Song)

Fanyou Kong: **An Hourly Updated Convection-Allowing Forecast System in Shenzhen region** (Co-author: H. Lan, W. Wang, F. Cai, X. Sun, X. Chen, Y. Wang, M. Xue, and J. Gao)

Anwei Lai: **Downscaling precipitation for weather forecast using high resolution terrain data and multi-model predictions** (Co-author: C. Lin, C. Cui, and J. Li)

Hongping Lan: **A Kalman Filter based QPF calibration system** (Co-author: F. Kong, J. He, and X. Chen)

Liang Li: **Probability Distribution of Daily Precipitation in the Huaihe Basin of China** (Co-author: L. Zhao, Y. Gong, F. Tian, and Z. Wang)

Yi Li: **The Impact of North Pacific subtropical highs upon ENSO on the interannual timescale** (Co-authors: X. Yang, and S. Huang)

Jian Lin: **Establishment and Verification of Multi-model Ensemble Forecast System** (Co-author: X. Jiang, and Y. Jiang)

Mu Xiao: **Multi-model Ensemble QPF for Southeastern China Using Bayesian Model Averaging** (Co-author: Y. Tao, Q. Duan, G. Zhang, and L. Zhao)

Pertti Nurmi: **Verification of QPFs in hydrological catchments applying the novelty SAL technique utilizing QPEs based on a local analysis system and radar data** (Co-author: S. Nasman, and E. Gregow)

Meijuan Pu: **Analysis on a permanent elongate convective system of rainfall** (Co-authors: D. Qin, Y. Xia, X. Zhang, L. Xie, and B. Zhang)

Youcun Qi: **Radar-based Quantitative Precipitation Estimation for the Cool Season in Mountainous** Regions (Co-author: J. Min, J. Zhang, D. Kingsmill, **and** K. Howard)

Youcun Qi: **Correction of Radar QPE Errors Associated with Partial Bright Band Observations Near the Ground** (Co-author: J. Zhang, K. Howard, and D. Kingsmill)

Carlos Santos: **QPF verification using object-oriented methods to investigate the benefits of higher resolution models** (Co-author: A. Ghelli, I. Guerrero, and L. Ferranti)

Mingdong Sun: **Quantitative Precipitation Forecasting using CSEOF-CCA in Korea** (Co-author: G. Kim, and J. H. Park)

Tchinda Tazo Simplice: **Probabilistic prediction of July-August-September rainfall in Cameroon**

Zhen-hui Wang: **Application of TCFM cloud motion wind in the analysis of Typhoon case study** (Co-author: L. Zhang, Y. Yang, Y. Zhan, and Z. Zhang)

Volker Wulfmeyer: **Methodological and experimental studies of data assimilation techniques on the convection-permitting scale**

Mingyi Xu: **Analysis of Convective Precipitation and Lightning Based on Multi-scale Wavelet Edge Detection** (Co-author: Z. Wang, and J. Pan)

Teng Xu: **Research on the Relationship between Attenuation Coefficient and Radar Reflectivity Factor for Spherical Particles in Clouds at mm Wavelengths (**Co-authors: Z. Wang, L. Ji, and F. Zhao)

Qiuming Yang: **Relationship between the interannual variation of the intensity of low-frequency oscillation for rainfall and the number of the heavy precipitation process over the lower reaches of the Yangtze River valley** (Co-authors: S. Huang and Y. Li)

Dongping Yin: **Study on Mechanism of an Extra Rainfall Process Caused by Remainder of Typhoon FUNGWONG** (Co-authors: H. Zeng, and M. Zang)

Hon-yin Yeung: **Development of a Localized Radar-Rain Gauge Co-Kriging QPE Scheme for Potential Use in Quality Control of Real-time Rainfall Data** (Co-author: C. Man, A. Seed, and S. Chan)

Yan Yin: **The Impact of Parameterization of Cloud Microphysical Processes on Convective Precipitation Forecasting** (Co-author: Q. Chen, and H. Xiao)

Linna Zhao: **Evaluation of Probabilistic Precipitation Forecast Using TIGGE data over Huaihe Basin** (Co-author: H. Wu, F. Tian, D. Qi, J. Di, Q. Duan, and Z. Wang)

Bing Zhang: **Impact of Different Boundary Layer Parameterization Schemes on the Numerical Simulation for a Rainstorm** (Co-author: M. Zhong)

Lifeng Zhang: **The dynamics and energetic of error-growth in heavy rainfall prediction** (Co-author: Y. Luo)

Shengjun Zhang: **The Estimation of Rainstorm Forecast Skill along Yangtze Valley through Atmospheric "Strong Signal" Area Data Assimilation in Key Area on Tibetan Plateau** (Co-authors: X. Xu, and S. Peng)

Haiguang Zhou: **Study on the 3D Structure of Typhoon Krosa (0716) Rainband with Dual-Doppler Radar**

Hong Zhuo: **Research of Mesoscale Convective Systems over Jinan on 18 July 2007** (Co-author: P. Zhao, J. Ren, Z. Pu,, and F. Yang) (A1 back-up)

H. Conference summary

Convener: Chungu Lu

14:40-14:55 Russ Elsberry
14:55-15:10 C.-P. Chang
15:10-15:30 Paul Joe, Richard Johnson
15:30-15:40 Jinping Liu, Zhiyu Liu
15:40-15:50 Anna Ghelli, George Craig
15:50-16:00 Susan Ballard, Volker Wulfmeyer
16:00-16:10 Bodo Ahrens
16:10-16:30 Yihong Duan, Jian Lin

Session A

High impact Precipitation Events (tropical cyclones, monsoons, and severe storms)

Synoptic and Mesoscale Processes Associated with Extreme Convective Rainfall

Richard H. Johnson

Department of Atmospheric Science
Colorado State University
Fort Collins, CO 80523
Johnson@atmos.colostate.edu

1. Introduction

Extreme convective rainfall accounts for substantial property damage and loss of life worldwide, both in monsoon/tropical regions and at midlatitudes. Such storms often cause flash floods, especially in regions with mountainous terrain. Just this summer, devastating floods hit many areas of China, Pakistan, and other parts of Asia. The primary environmental factors contributing to heavy rainfall are abundant moisture, instability, and a lifting mechanism. However, in order for extreme rainfall to occur, something other than just favorable environmental conditions must exist. In some cases a critical factor may be a low-level jet impinging on steep orography. However, in other cases, particularly in regions where the terrain is relatively flat, a unique pattern of mesoscale organization and behavior of convection has been identified to be associated with extreme rainfall. Heavy rainfall has also been observed to occur in connection with mesoscale convective vortices (MCVs), which are often observed downstream of major mountain barriers such as the Rocky Mountains and Tibetan Plateau. This paper reviews synoptic and mesoscale processes associated with extreme rainfall based on studies of such events during the warm season over the United States.

2. Synoptic and mesoscale settings associated with extreme convective rainfall

In a study of over 150 flash flood episodes in the United States, Maddox et al. (1979) identified four distinct types of heavy rain events. The two most common synoptic and mesoscale patterns, labeled *mesohigh* and *frontal*, had similar characteristics with respect to the behavior of convective cells that led to the extreme rainfall. In particular, these storms, aided by lifting along a frontal boundary or previous thunderstorm outflow boundary, repeatedly developed and moved over the same area. This pattern of behavior is often referred to as *back-building* or *training* convective cells.

Over East Asia, heavy rainfall often occurs along the Meiyu-Baiu rainband, which extends from southeast China to Japan (Ninomiya and Murakami 1987; Tao and Chen 1987) or the Chagma front across Korea. The Meiyu-Baiu rainband has

characteristics of a frontal zone, i.e., a strong moisture gradient and a horizontal wind shear line, but with a temperature gradient that is weak over China but somewhat stronger over Japan. From a large-scale perspective, the Meiyu-Baiu rainband represents a zone of convergence between the southwest monsoon flow and northerly flow associated with the passage of midlatitude disturbances around the Tibetan Plateau (Fig. 1)

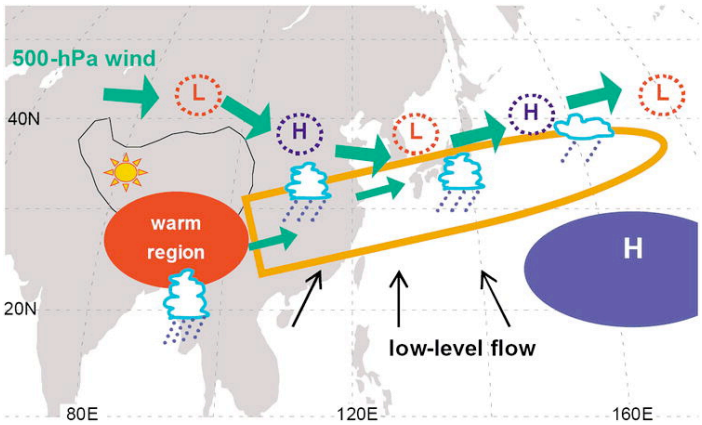

Fig. 1. Schematic diagram illustrating the factors that bring Meiyu-Baiu rainfall in early summer East Asia (Sampe and Xie 2010).

Within the Meiyu-Baiu-Chagma rainband, mesoscale disturbances develop accompanied by intense convection and heavy rainfall (Ninomiya 2004). The fact that this convergence boundary is often quasi-stationary leads to the frequent occurrence of extended periods of heavy rain and floods.

3. Mesoscale organization of extreme-rain-producing storms

In a study of extreme[1] rainfall events in the eastern two-thirds of the United States during a 5-year period, Schumacher and Johnson (2005, 2006) found that 66% of the cases were associated with mesoscale convective systems (MCSs). The others were of synoptic or tropical origin. Given that MCSs are dominant factors in extreme rainfall and flash floods, it is important to understand the organizational characteristics of MCSs. The most common organizational pattern for linear MCSs is that found in many squall lines, referred to as *trailing stratiform* precipitation systems (Smull and Houze 1985; Houze et al. 1989).

However, other organizational structures of MCSs have been found to exist. In a study of 88 linear, warm-sector MCSs over the United States, Parker and Johnson (2000) found three dominant modes of organization of convective lines and attendant stratiform precipitation (Fig. 2). The three modes are convective lines with trailing (TS), leading (LS), and parallel (PS) stratiform precipitation. TS systems were the most common, accounting for ~60% of the cases, with the LS

[1] Defined as rainfall that surpasses the 50-year recurrence interval.

and PS each accounting for about 20%. The key factor determining the organizational structure was the vertical wind shear. TS systems exhibited front-to-rear storm-relative flow throughout the troposphere, LS systems rear-to-front storm-relative flow aloft, and PS systems contained primarily line-parallel storm-relative flow aloft. Many systems did not retain one mode of organization throughout their life cycles, but rather transitioned between modes, the TS mode being the most-frequent final state.

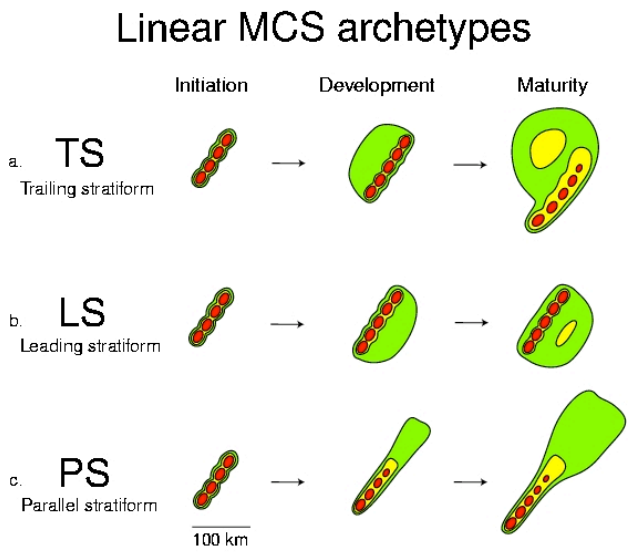

Fig. 2. Three modes of organization of MCSs in the central United States: trailing, leading, and parallel stratiform precipitation systems (Parker and Johnson 2000).

Not all of the modes of convective organization shown in Fig. 2 lead to heavy rainfall. Unique patterns of convective organization and cell propagation are necessary to produce extreme rainfall (Doswell et al. 1996). Such patterns have recently been documented by Schumacher and Johnson (2005).

A study of 184 heavy-rainfall cases for the period 1999-2003 reveals three dominant modes of MCS organization associated with extreme-rain-producing storms (Schumacher and Johnson 2005, 2006). These modes (Fig. 3) are referred to at training line/adjoining stratiform (TL/AS), back-building (BB), and trailing stratiform (TS). The first type, comprising 34% of the MCSs, is characterized by a typically east-west convective line along a quasi-stationary frontal boundary with west-to-east training convective cells on the cool side of the boundary and an area of stratiform precipitation displaced to the north. The second type, comprising 20% of the cases, is typically smaller in overall size and features back-building cells along an outflow boundary, with repeated cell formation over the same location and an area of stratiform precipitation typically downstream. The third type, also comprising 20% of the cases, has the overall structure of commonly occurring trailing-stratiform (TS) MCSs, but in the heavy-rain cases, the southern end of the line becomes oriented in an east-west

direction, approximately aligned with the overall motion vector of the MCS, leading to training convective cells (and heavy rainfall) on the southern end.

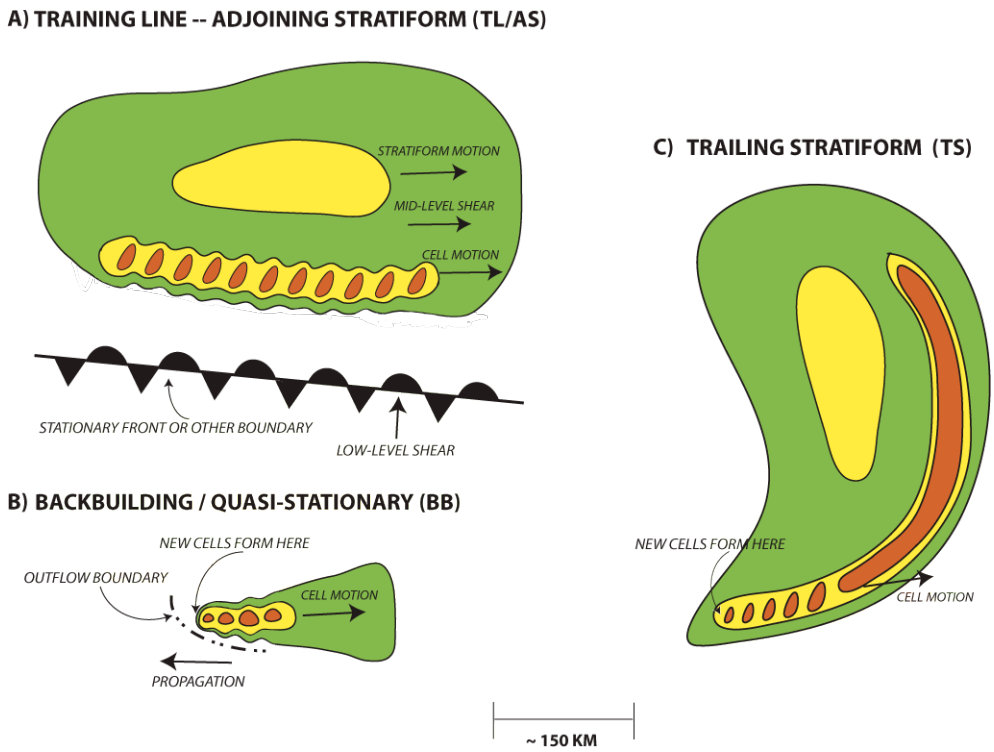

Fig. 3. Three extreme-rain-producing storm mature-stage archetypes, (a) training-line, adjoining-stratiform (TL/AS) organization, (b) back-building (BB) organization, and trailing-stratiform (TS) organizaton. TL/AS and TS systems are generally larger in horizontal scale than BB systems. From Schumacher and Johnson (2005, 2006).

The extreme rain events (all modes) were found to be a maximum during the nighttime hours, consistent with the earlier findings of Maddox et al. (1979). Similar findings of a nocturnal maximum in precipitation in general (not necessarily extreme events) along the Meiyu-Baiu frontal zone have been found (e.g., Kato et al. 1995; Asai et al. 1998; Geng and Yamada 2007), although recent studies show a diurnal phase of precipitation systems having a coherent eastward transition from a midnight maximum over the eastern Tibetan Plateau to an afternoon maximum over the lower Yangtze River valley (Wang et al. 2005; Yu et al. 2007). The nocturnal low-level jet has been implicated in the nighttime maximum of extreme rainfall over the United States, although the details of mechanisms are still under investigation.

4. Role of mesoscale convective vortices (MCVs)

Investigation flash floods associated with Midwestern United States MCVs has revealed a common pattern of behavior contributing to slow-moving, extreme-

rain-producing storms (Schumacher and Johnson 2008). Observations and simulations using the NCAR WRF model show that slow system motion arises from the interaction of a low-level jet and the MCV circulation. In a broad-scale sense, deep convection is favored on the downshear side of the MCV as a result of dynamic lifting (e.g., Raymond and Jiang 1990; Trier and Davis 2002). Locally, the reverse shear associated with the low-level jet in the presence of deep convective heating produces a low-level gravity wave that organizes convection into a line and contributes to back-building and heavy rainfall (Schumacher and Johnson 2008).

A study of a number of flash-flood cases has revealed a recurring pattern of heavy rainfall associated with MCVs that supports early findings for a single event – the May 7, 2000 St. Louis flash flood. A conceptual model for MCVs and heavy rainfall that brings together these results is shown in Fig. 5 (Schumacher and Johnson 2009).

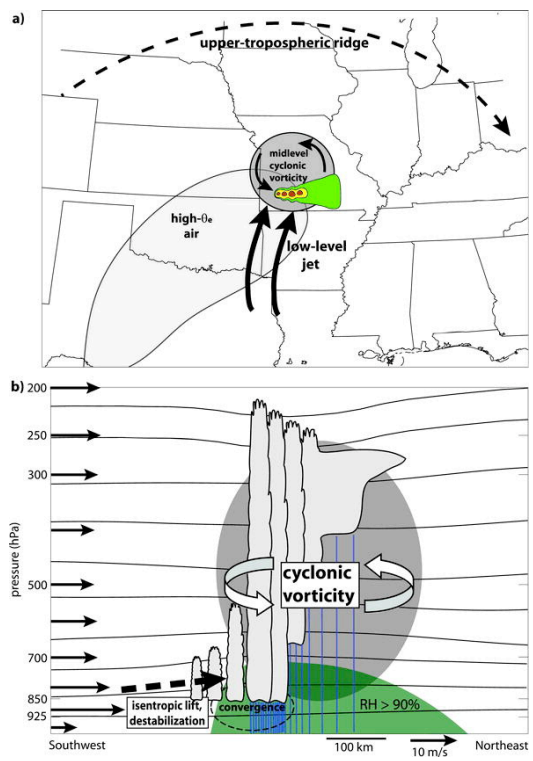

Fig. 5. Schematic diagrams showing important processes in the development and maintenance of extreme-rain-producing convective systems associated with midlevel circulations. (a) Plan view. A schematic representation of the radar reflectivity structure of an MCS is shown in color, in relation to the location of a midlevel vorticity maximum (dark gray shading and curved arrows). (b) Southwest-to-northeast cross section. Representative isentropes (every 5 K) are shown by the thin black lines; the wind profile (including LLJ) is shown by the vectors on the left. Green shading indicates areas with relative humidity > 90%; gray shading indicates high values of absolute cyclonic vorticity. From Schumacher and Johnson (2009).

MCVs are known to be important circulation features associated with heavy precipitation features downstream of the Tibetan Plateau. Recent studies suggest that MCVs can generate secondary convection (Fritsch et al. 1994) that can produce heavy rainfall and flooding over the Yangtze River valley and the Huaihe River Basin (e.g., Sun et al. 2010). The mechanisms occurring in United States extreme-rain events illustrated in Fig. 5 may be similar to those occurring over China. Moreover, the MCVs contributing to the heavy rainfall may be linked to potential vorticity anomalies generated by upstream mountain barriers: the Rocky Mountains in the United States and the Tibetan Plateau in China (Li and Smith 2010).

5. Summary and conclusions

This paper reviews synoptic and mesoscale mechanisms associated with extreme convective rainfall, with specific attention to the modes of organization of convective systems that are responsible for heavy precipitation. While synoptic conditions that provide abundant moisture and instability are critical for setting the stage for heavy rainfall, it is the existence of mesoscale processes – a lifting mechanism and favorable convective organization and cell propagation – that is necessary for extreme rainfall to occur. A study of United States extreme-rainfall, flash-flooding convective episodes indicates that two-thirds are associated with mesoscale convective systems (MCSs). Three recurring patterns of mesoscale organization were found in such MCSs: trailing-line/adjoining stratiform, back-building, and trailing stratiform structures. Mesoscale convective vortices (MCVs) are also frequently implicated in extreme rainfall, where dynamical lifting on the downshear side of the vortices coupled with a low-level jet conspires to generate intense, quasi-stationary convection.

Acknowledgments. This research has been supported under NSF Grant Nos. ATM-0639461 and ATM-0966758, NASA Grant Nos. NNX07AD35G and NNX10AG81G, and NOAA Office of Global Programs Grant No. NA07OAR4310263. Much of the work reported herein involves the graduate research of Matt Parker and Russ Schumacher, to whom the author is greatly indebted.

References

Asai, T., S. Ke, and Y. Kodama, 1998: Diurnal variability of cloudiness over East Asia and the Western Pacific Ocean as revealed by GMS during the warm season. *J. Meteor. Soc. Japan*, **76**, 675–684.

Doswell, C. A., III, H. E. Brooks, and R. A. Maddox, 1996: Flash flood forecasting: An ingredients-based methodology. *Wea. Forecasting*, **11**, 560–581.

Fritsch, J. M., J. D. Murphy, and J. S. Kain, 1994: Warm core vortex amplification over land. *J. Atmos. Sci.*, **51**, 1780–1807.

Geng., B, and H. Yamada, 2007; Diurnal variations of the Meiyu/Baiu rain belt, *SOLA*, **3**, 61-64.

Houze, R. A., Jr., S. A. Rutledge, M. I. Biggerstaff, and B. F. Smull, 1989: Interpretation of Doppler weather radar displays in midlatitude mesoscale convective systems. *Bull. Amer. Meteor. Soc.,* **70**, 608-619.

Kato, K., J. Matsumoto, and H. Iwasaki, 1995: Diurnal variation of Cb-Clusters over China and its relation to large-scale conditions in the summer of 1979. *J. Meteor. Soc. Japan*, 73, 1219–1234.

Li, Y., and R. B. Smith, 2010: The detection and significance of diurnal pressure and Potential Vorticity anomalies east of the Rockies. *J. Atmos. Sci.* (in press)

Maddox, R. A., C. F. Chappell, L. R. Hoxit, 1979: Synoptic and Meso-α scale aspects of flash flood events. *Bull. Amer. Meteor. Soc.*, **60**, 115–123.

Ninomiya, K., 2004: Large-and mesoscale features of Meiyu-Baiu front associated with intense rainfalls. *East Asian Monsoon*, C.-P. Chang, Ed., World Scientific, 404-435.

Ninomiya, K., and T. Murakami, 1987: The early summer rainy season (Baiu) over Japan. *Monsoon Meteorology*, C.-P. Chang, and T. N. Krishnamurti, Eds., Oxford University Press, 93–121.

Parker, M. D., and R.H. Johnson, 2000: Organizational modes of midlatitude mesoscale convective systems. *Mon. Wea. Rev.*, **128**, 3413-3436.

Raymond, D. J., H. Jiang, 1990: A theory for long-lived mesoscale convective systems. *J. Atmos. Sci.*, **47**, 3067–3077.

Sampe, T., and S.-P. Xie, 2010: Large-scale dynamics of the Meiyu-Baiu rain band: Environmental forcing by the westerly jet. *J. Climate*, **23**, 113-134.

Schumacher, R. S., and R. H. Johnson, 2005: Organization and environmental properties of extreme-rain-producing mesoscale convective systems. *Mon. Wea. Rev.*, **133**, 961-976.

Schumacher, R. S., and R. H. Johnson, 2006: Characteristics of United States extreme rain events during 1999-2003. *Wea. Forecasting*, **21**, 69-85.

Schumacher, R. S., and R. H. Johnson, 2008: Mesoscale processes contributing to extreme rainfall in a midlatitude warm-season flash flood. *Mon. Wea. Rev.*, **135**, 3964-3986.

Schumacher, R. S., and R. H. Johnson, 2009: Quasi-stationary, extreme-rain-producing convective systems associated with midlevel cyclonic circulations. *Wea. Forecasting*, **24**, 555-574.

Smull, B. F., and R. A. Houze, 1985: A midlatitude squall line with a trailing region of stratiform rain: Radar and satellite observations. *Mon. Wea. Rev.*, **113**, 117–133.

Sun, J., S. Zhao, G. Xu, and Q. Meng, 2010: Study on a mesoscale convective vortex causing heavy rainfall during the Mei-yu season in 2003. *Adv. Atmos. Sci*., **27**, 1193-1209.

Tao, S.Y., and L.-X. Chen, 1987: A review of East Asian summer monsoon research in China. *Monsoon Meteorology*, C.-P. Chang and T. N. Krishnamurti, eds. Oxford University Press, 60-92.

Trier, S. B., and C. A. Davis, 2002: Influence of balanced motions on heavy precipitation within a long-lived convectively generated vortex. *Mon. Wea. Rev.*, **130**, 877-899.

Wang, C.-C., G. T.-J. Chen, R. E. Carbone, 2004: A climatology of warm-season cloud patterns over East Asia based on GMS infrared brightness temperature observations. *Mon. Wea. Rev.*, **132**, 1606–1629.

Yu, R., T. Zhou, A. Xiong, Y. Zhu, and J. Li (2007), Diurnal variations of summer precipitation over contiguous China, *Geophys. Res. Lett.*, **34**, L01704, doi:10.1029/2006GL028129.

Convection over the Taunus Mountains: Distribution, Tracks and Life Cycle

Christoph Brendel and Bodo Ahrens
Institute for Atmospheric and Environmental Sciences, University of Frankfurt
christoph.brendel@iau.uni-frankfurt.de

1. Introduction

Deep convection belongs to one of the most intensive atmospheric processes on earth. Deep convection is often associated with heavy rainfalls, wind gusts, hail and lightning. In some cases, strongly depending on favourable meteorological key parameters, the development of tornados is possible (DOSWELL 2001). These natural hazards can result in high damages, insurance costs and sometimes loss of human lives. Convective processes occur on the local- and mesoscale, and are highly variable in space and time in their occurrence and intensity. For this reason forecasting of convection in detail is difficult. Especially the areas of formation, the tracks of single convective cells and their behaviour are not predictable. Rain gauge networks are also not able to detect convective precipitation in its totality and therefore a high-resolution long-term climatology of deep convection does not exist. Regarding these problems there was a motivation to find out how convective cells occur and trace over complex terrain, e.g. low mountain ranges. There are some examinations about the influence of mountainous areas on convection done in the USA. On the one hand the aim was to identify regions, which initiate convection depending on different stream directions (BANTA and SCHAAF 1987) and on the other hand the suggestion was to investigate the influence of the Colorado Rocky Mountain Range on the diurnal cycle of convective precipitation for two summer seasons (KARR and WOOTEN 1976).

2. Area of Investigation

The area of investigation is located in the German low mountain ranges with focus on the Taunus Mountains (Fig. 1). The Taunus Mountains consist of three parts: a main ridge (a) that is orientated from southwest to northeast; a northern part with some side ridges orientated from southeast to northwest, separated by a large valley/basin (b) into a western (c) and an eastern part (d); and a southern narrow zone (e) dropping off steeply to the Rhein-Main-Basin.

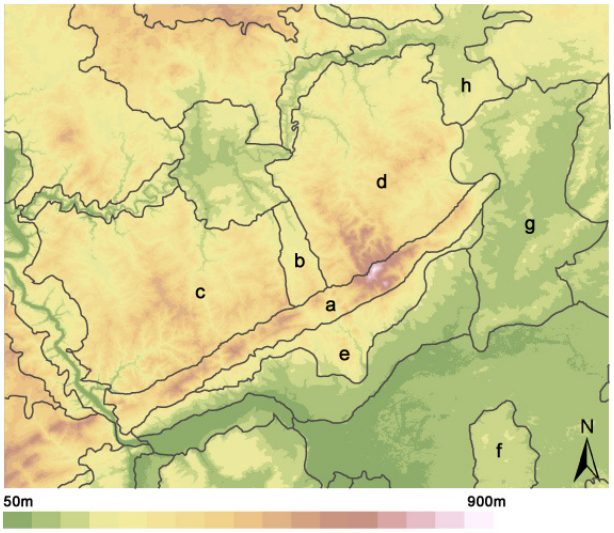

Figure 1: Area of investigation, digital elevation model (shaded), area borders of unspoiled nature (grey lines), dimension of the whole area (80km north-south and 100km west-east)

3. Data

For the investigation the weather radar data for the time period March 2000 – December 2007, provided by the German Weather Service (DWD), were taken into account. The advantage of this radar product is the high temporal (5 min) and spatial (1 km) resolution. Disadvantages are some shadowing effects caused by the highest mountain peaks due to the precipitation scan of the radar, which allows only the scan of the lowest layer. For further investigations, the output of convective cells and tracks has been subdivided into different stream directions, based on the objective weather classification of the DWD.

4. Method

Based on an existing tracking algorithm (STEINACKER et al. 2001) a simple algorithm was created to filter radar images, to identify convective cell cores, and to determine the tracks for every single cell core.

A 2-dimensional Gauss filter was used to smooth the radar images with a standard deviation σ of 0.85. The filter matrix consists of 7 x 7 grid points. The necessity of the filter is explained by remaining clutter and the precipitation structure in general, which can have weak secondary cell cores. After filtering they merge with primary cell cores and this make the identification of convective cell cores more clearly for the automatic algorithm.

To identify convective cell cores, two basic conditions have been defined to distinguish between convective and stratiform precipitation. On the one hand an intensity threshold for convective cell cores has to be considered, which was set to 8.12 mm/h. On the other hand the spatial variability of convective precipitation has to be considered. To check these conditions a 7 x 7 grid point matrix was again taken into account. The algorithm checks the differences in precipitation from the central grid point to the surroundings. Potential cell cores must have a larger precipitation intensity than its direct surrounding grid cells, and grid cells in larger distance to the central grid point of the matrix must have a certain precipitation difference to them.

For tracing convective cell cores from one time step to the next time step, additional data were needed. Thus, six hourly means of NCEP/NCAR reanalysis data for u- and v- wind vectors have been used (HARRIS 2008). To recover a cell core in the next time step from a radar image, a displacement vector, based on the reanalysis wind data, will indicate the expected position of the cell core. From the end of this displacement vector a searching area is defined to look for cell cores. In the case the algorithm finds a cell core within this area an identical ID number is assigned, otherwise the cell core is dissolved or a cell core beyond the area is assigned with a new ID number. A shortcoming of the algorithm is that merging and splitting of convective cells cannot be considered and the assumption that convective cell cores always shift with the mean stream direction of the troposphere.

5. Results

The whole dataset consists of 89671 cell cores, which mostly occur under southwesterly flow direction (59.6%). The second most frequently-occuring weather type for convective cells is the northwesterly flow (18.1%), followed by the undefined flow direction (17.3%) and the southeast (3.9%) and northeast (1.1%) flows. To get an overview of the large dataset of convective cells and their tracks, a line density per km^2 was calculated within a radius of 1.5km. Figure 2 shows the most interesting stream directions for the whole period of investigation. First of all the results show different regions for the highest densities of convection, highly depending on the stream direction. Southwesterly flows show a very high density of convective tracks caused by the eastern side ridge of the Taunus Mountains (c), which moves to the Wetterau Basin (g) and Lahn Valley (h) east of the Taunus Mountains (Fig. 2). The western part of the Taunus Mountains (d) shows significantly lower densities. Northwesterly flows show a significant high density of convective tracks at the Odenwald Foothills (f)

in the southeast of the investigated area (Fig. 2). Much less densities are located across the whole Taunus Mountains, but with a slightly higher density north of the Main Taunus Ridge (b,c,d). The comparison between summer and winter shows a more homogenous distribution of convection during the summer period than for winter times (not shown).

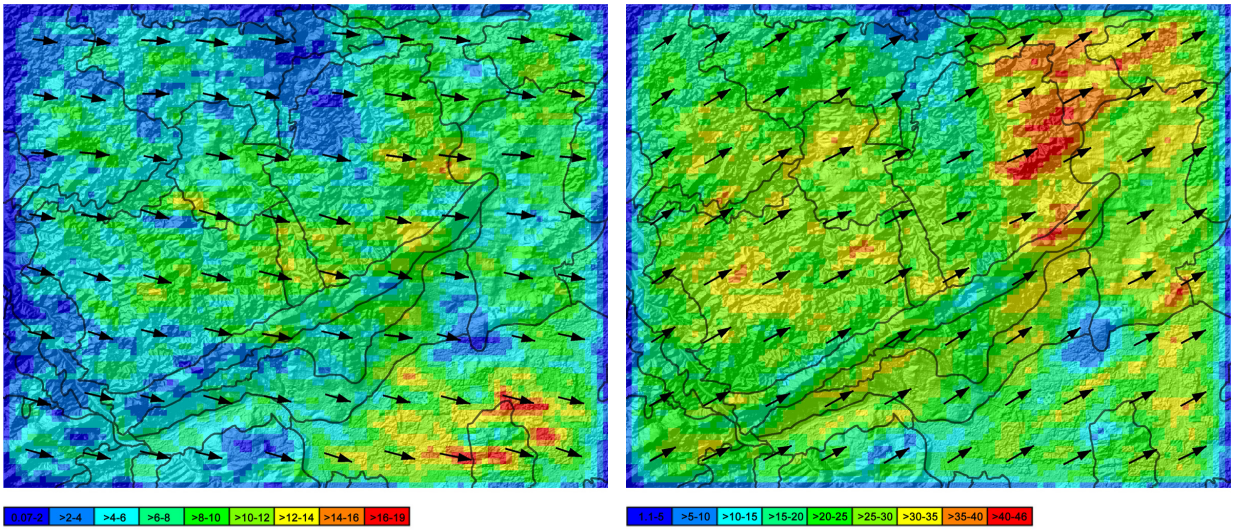

Figure 2: Density of convective tracks (shaded) for northwesterly flow (left) and southwesterly flow (right), mean track direction of convective cell cores (arrows), area borders of unspoiled nature (grey lines)

6. Conclusion

The distribution of convection is highly heterogeneous over the area of investigation. The number of convective cell cores does not much correlate with elevation but some specific elevated areas have a large influence on convection. Considering the shadowing effect at the highest mountains, it is still a little bit surprising that there seems to be only a small influence by the Main Taunus Ridge to the occurrence and initiation of convection. Especially southwesterly flows show an enhanced initiation of convection due to mountain ridge perpendicular to the flow, and additionally, a further development of the cells downwind the mountains.

Acknowledgments

The PF-Radar data were obtained from Elmar Weigl, DWD

References

BANTA, R. M. and SCHAAF, C. B. (1987): Thunderstorm Genesis Zones in the Colorado Rocky Mountains as Determined by Traceback of Geosynchronous Satellite Images. Monthly Weather Review 115 (2). 463-467.

DOSWELL, C. A. III (ed.) (2001): Severe Convective Storms. Meteorological Monographs 50. American Meteorological Society. Boston. 570.

HARRIS, I. (2008): NCEP/NCAR Reanalysis: http://www.cru.uea.ac.uk/cru/data/ncep/ (03/01/2009)

KARR, T. W. and WOOTEN, R. L. (1976): Summer Radar Echos Distribution Around Limon, Colorado. Monthly Weather Review 104 (6). 728-734.

STEINACKER R., DORNINGER, M., WÖLFELMAIER, F. and KRENNERT, T. (2000): Automatic Tracking of Convective Cells and Cell Complexes from Lightning and Radar Data. Meteorology and Atmospheric Physics 72 (2-4). 101-110.

Monsoon Rainfall Characteristics: Precipitation Types and Associated Environment Regimes observed during SoWMEX/TiMREX

Ben Jong-Dao Jou[1], Chong-Chi Tong[1], and Wen-Chau Lee[2]

1. Department of Atmospheric Sciences, National Taiwan University, Taipei, Taiwan

2. National Center for Atmospheric Research, Boulder, CO

Jouben@ntu.edu.tw

In this study, the composited hybrid scan radar reflectivity data of the Central Weather Bureau (CWB)'s Quantitative Precipitation Estimation Segregation Using Multiple Sensors (QPESUMS) system and the lightning data of the Taiwan Power Company (Taipower)'s Total Lightning Detection System (TLDS) are used to characterize the significant continuous rainfall periods in southwestern Taiwan during the 2008 Mei-Yu season. High temporal resolution sounding data taken during SoWMEX/TiMREX are used to describe the environment conditions.

A total of 40 rainfall events are identified in the 2008 Mei-Yu season. The results indicate that, based on the initiation location, the precipitation events can be classified into three types: land, oceanic, and mixed. The former two types are evenly distributed (18:17) and occupy most of the cases. For the time of development, the land events usually begin in the daytime with shorter durations. In contrast, the oceanic events have their initiations in the nighttime and persist longer. Most of the land events are related to the afternoon thunderstorms and reveal pronounced diurnal cycle signal. In terms of spatial distribution, on the average, the land-type (oceanic-type) precipitating systems are more concentrated (widespread) with higher fraction of convective (stratiform) precipitation and higher (lower) lightning density.

For the environmental conditions, the land (oceanic) events are associated with larger (smaller) convective available potential energy (CAPE) and smaller (larger) convective inhibition (CIN). Otherwise, the composited soundings show that the oceanic-type has a much stronger and moister southwesterly flow over the lower troposphere than the land-type.

Using dropsondes and shipsondes, it is found the upstream southwesterly possesses quite different characteristics from the one over the plain area in the southwestern Taiwan. The influence of terrain is indicated.

Spatial and Temporal Variations of Extreme Precipitation Events in the Huaihe River Basin,China

Yong WANG[1], Qilong MIAO[2], Yuanyuan DING[1]

[1]School of Remote Sensing, Nanjing Unversity of Information Science & Technology.
[2]College of Applied Meterology, Nanjing Unversity of Information Science & Technology. Email: wyong0210@163.com

1. Introduction

The spatial and temporal variations of extreme precipitation events are the direct source of flood and drought hazards. One of the major concerns related to anthropogenic climate change is an increase in extreme events that could have a profound impact on both human society and the natural environment. The fourth assessment report (AR4) of the Intergovernmental Panel on Climate Change (IPCC) pointed out extreme precipitation events in many mid-latitude regions were likely to increase, and the total area affected by drought since the 1970s has been likely to increase (Alexander et al., 2006; IPCC, 2007). These results described the general trends in extreme precipitation events at a large spatial scale, but the changes in particular regions were not conclusive (Kunkel, 2003; Wang et al., 2008) and need to be assessed.

Regional differences in extreme climate events can be great. In general, increasing temperatures speed up the water cycling process, which can possibly result in increases in precipitation amount and intensity.However, no trend or significant downward trends in extreme precipitation events have also been found in some areas due to variabilities such as topography and local circulation.

The objectives of this study were to analyze the temporal trends and their spatial distribution for each extreme precipitation indicator. Based on the daily observational data of 26 stations in the Huaihe River Basin (HRB), spatial and temporal variations of extreme precipitation in the last 48 years are analysed in the present study. The detailed analysis on trends of the extreme precipitation events at a regional scale is important to forecast and reduce the climate induced flood risks and provide information for rational countermeasures.

2. Data and Methods

2.1 Study area

In this paper, the study area is that the HRB is located in the eastern China (Fig. 1). It rises of the Tongbo and Funiu Mountains in west, and faces to the Yellow Sea in east. HRB totally covers 270,000km^2 area. The Huaihe River originates from the Tongbo Mountain of Henan province and flows through four provinces (Henan, Hubei, Anhui and Jiangsu province).

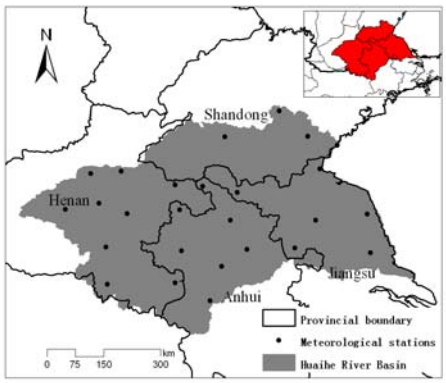

Fig.1 Location of the Huaihe River basin and meteorological stations.

2.2 Data

The time series of daily precipitation records at 26 meteorological stations on the HRB (Fig. 1) were collected for this study from 1st January 1960 to 31st December 2007. The data were provided by the National Climatic Center (NCC) of the China Meteorological Administration (CMA).

2.3 Indicators of extreme precipitation events

Six indicators (Tab.1) used in the STARDEX (STAtistical and Regional dynamical Downscaling of EXtremes for European regions) project were chosen to analyze the characteristics of extremes. R10mm and R20mm are two indicators of the frequency of significant precipitation days for a given year, while Rx1day, Rx5day, R95T and R99T measure the magnitude of the more intense precipitation events.

Tab.1 Extreme precipitation indicators.

Indicators	Definition	Unit
Maximum 1-day precipitation total (Rx1day)	Maximum rainfall during the continuous one days	mm
Maximum 5-day precipitation total (Rx5day)	Maximum rainfall during the continuous five days	mm
Heavy precipitation days (R10mm)	Number of days with precipitation≥10 mm day^{-1}	d
Very heavy precipitation days (R20mm)	Number of days with precipitation≥20 mm day^{-1}	d
Very wet days (R95T)	Annual total precipitation due to events exceeding the 1961–90 95th percentile	mm
Extremely wet day (R99T)	Annual total precipitation due to events exceeding the 1961–90 99th percentile	mm

2.4 Methodology

a. Trend analysis

Trend analysis methods used linear regression. Linear trend analysis indicated the tendency rate (slope) using least squares at the 95% confidence level. Linear trend analysis was used to quantify the change magnitude of all indicators.

b. Probability distribution functions

Probability distribution functions (PDFs) were calculated for extreme precipitation indicators for two different time periods. This was done by binning annual values across their range for the 1960-83 and 1984-2007 intervals. The results

were normalized to sum 1 to give the probability distribution.

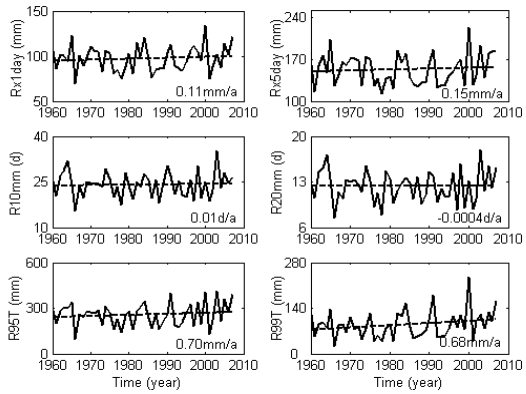

Fig.2 Temporal changes of extreme precipitation indicators on the Huaihe River Basin during 1960-2007.

3. Results

3.1 Temporal variations in extreme precipitation events

Fig.2 showed the trend in changes and the temporal evolution for six extreme precipitation indicators on the HRB from 1960 to 2007. Although the RX1day, Rx5day, R10mm, R95T and R99T showed upward trends and R20mm showed downward trends in their annual anomalies (Fig. 2), these were not significant.

Fig.3a-d show the PDFs for four annual extreme precipitation indicators on the HRB. From these figures it is evident that there has been an increase in the three wetness indicators and a litter decrease in the dryness indicator over the period. Figure 3ab show a marked increase in the rainfall of Rx1day and Rx5day over the 1984-2007 period. There has also been a little increase in the number of heavy precipitation days (R10mm) (Fig.3c). Figure 3d shows a little reduction in very heavy precipitation days (R20mm) over the latter interval. The probability distribution of R95T and R99T show also a little increase over the 1984-2007 period (Tab.2).

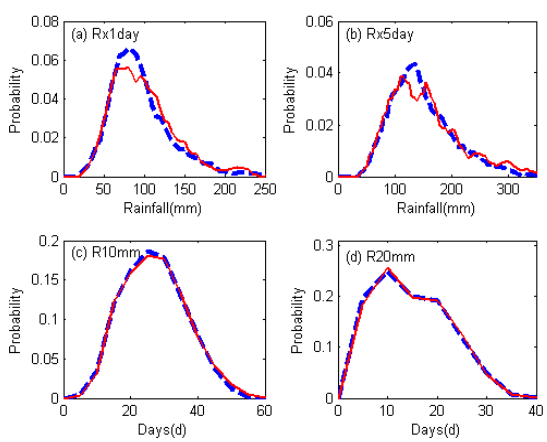

Fig.3 Annual probability distribution functions for (a) Rx1day, (b) Rx5day, (c) R10mm, and (d) R20mm between 1960 and 2007 for the two time periods: 1960-83 (Dotted line) and 1984-2007 (Solid line).

For all the indicators, except very heavy precipitation days (R20mm), the PDF for the most recent time interval (i.e., 1984-2007) is different from the former interval.

This indicates a shift in the distribution toward wetter conditions over the past two decades.

Tab.2 The probability distribution of R95T and R99T on the Huaihe River Basin.

Extreme precipitation indicators		Probability						
		0mm	40-70mm	71-140 mm	141-210 mm	211-280 mm	281-350 mm	≥350 mm
R95T	1960-1983	0.058	0.083	0.181	0.23	0.205	0.157	0.086
	1984-2007	0.06	0.094	0.188	0.196	0.212	0.152	0.098
R99T	1960-1983	0.523	0	0.279	0.093	0.063	0.023	0.019
	1984-2007	0.481	0	0.284	0.091	0.078	0.037	0.029

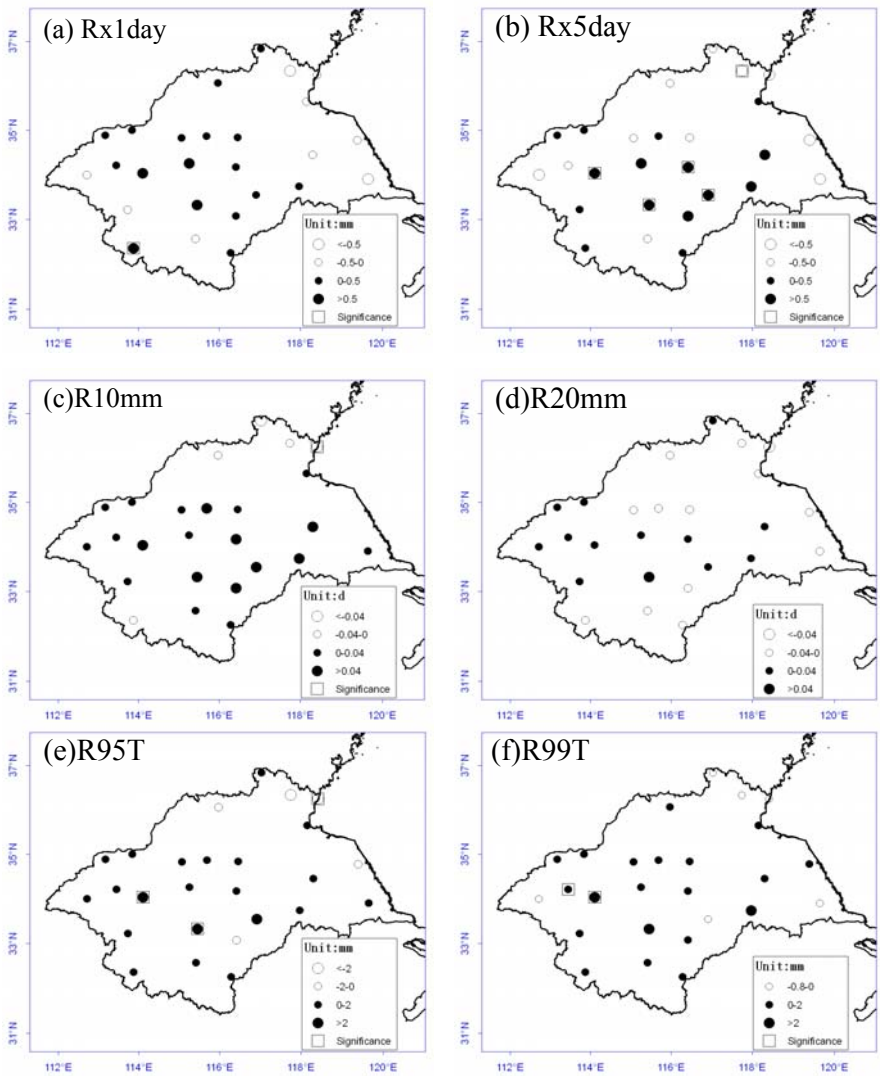

Fig.4 Spatial trends for six extreme precipitation indicators, for the 1960-2007 period. Squares indicate where significance was reached at the 5% level.

3.2 Spatial variations for extreme precipitation events

From the spatial trends of extreme precipitation indicators, extreme precipitation indicators have different change situations in various regions. The maximum rainfall

during the continuous one day (Rx1day) shows an increasing trend in middle part of HRB, and it is decreasing trend in the coastal areas of Jiangsu (Fig.4a). The maximum rainfall during the continuous five days (Rx5day) shows an increasing trend in middle part of HRB, but it is opposite in the coastal and north areas of HRB (Fig.4b).

For heavy precipitation days (R10mm), the trend shows a general positive trend toward wetter conditions, with the exception of some stations located in the northeast part (Fig.4c). The increasing and decreasing trend of very heavy precipitation days (R20mm) have half each (Fig.4d). The increasing trends are located in locates on the middle part of HRB.

Except northeast part of HRB, the rainfall of very wet day (R95T) and extremely wet day (R99T) in other regions all show an increasing trend (Fig.4ef). They decrease from the southwest to the northeast, with the highest value in the west of HRB (>0-0.04mm/a) and the lowest in the northeast of HRB (<-0.04 mm/a).

4. Conclusions

Total daily precipitation at 26 weather stations on the HRB during 1960-2007 was used to analyze the spatial distribution and temporal trends of extreme precipitation events.Some general conclusions can be reached: Except R20mm, other extreme precipitation indicators all showed the rising trend. All indicators were not significant. From the spatial distribution of extreme precipitation indicators, extreme precipitation indicators had different change situations in various regions. Rx1day shows an increasing trend in middle part of HRB, and it is decreasing trend in the coastal areas of Jiangsu. Rx5day shows an increasing trend in middle part of HRB, but it is opposite in the coastal and north areas of HRB. For R10mm, the trend shows a general positive trend toward wetter conditions, with the exception of some stations located in the northeast part. The increasing and decreasing trend of R20mm have half each. Except northeast part of HRB, the rainfall of R95T and R99T in other regions all show an increasing trend. A future study, which will address the projection of extreme precipitation indicators in the HRB, based on climatic models, is also planned.

References

Alexander, L.V., Zhang X., Peterson T.C. et al., 2006: Global observed changes in daily climate extremes of temperature and precipitation. *Journal of Geophysical Research,* 111 (D05109). doi:10.1029/2005JD006290.

IPCC, 2007. Climate Change 2007: The Physical Science Basis. Contribution of Working Group I to the Fourth Assessment Report of the Intergovernmental Panel on Climate Change. *Cambridge University Press*, Cambridge, United Kingdom and New York, NY, USA.

Kunkel, K.E., 2003: North American trends in extreme precipitation. *Natural Hazards,* 29 (2), 291-305.

Wang, W., Chen X., Shi P., van Gelder P.H.A.J.M., 2008: Detecting changes in extreme precipitation and extreme stream flow in the Dongjiang River Basin in southern China. *Hydrology and Earth System Sciences,* 12 (1), 207-221.

Land-atmosphere interactions during a Northwestern Argentina Low event: impacts on precipitation fields

Lorena Ferreira[1], Celeste Saulo[2,3] and Juan Ruiz[2,3]
[1] Servicio Meteorológico Nacional, Buenos Aires, Argentina. [2] Departamento de Ciencias de la Atmósfera y los Océanos, Universidad de Buenos Aires, Argentina. [3] Centro de Investigaciones del Mar y la Atmósfera (CONICET-UBA), Buenos Aires, Argentina. ferreira@smn.gov.ar

Abstract

The impact of changes in soil moisture in subtropical Argentina in rainfall amounts and distribution, and low level circulation is studied with a state-of-the art regional model in a downscaling mode, with different scenarios of soil moisture for a 10 day period. Four tests were conducted at 40 km horizontal resolution with 31 sigma levels, decreasing and increasing the soil moisture initial condition by 50% over the entire domain, and imposing a 50 % reduction over northwest Argentina and 50% increase over South East South America. In all cases, the WRF-NOAH model is used to represent the meteorological variables and the surface processes.

It was found that land-surface interactions are stronger when soil moisture is decreased, with a coherent reduction of precipitation over southern South America. Enhanced northerly winds result form an increase in the zonal gradient of pressure at low levels. In contrast, when soil moisture is increased, smaller circulation changes are found, though there appears to be a local feedback effect between the land and precipitation The combined effects of changes in the circulation and in local stratification induced by soil moisture modifications, through variations in evaporation and CAPE, are in agreement with what has been found by other studies. Finally, this sensitivity study shows the need to gain insight into the uncertainties in the initial condition, and in the interaction between the precipitation, one of the main forcing of the soil model, and the soil moisture in this region.

1. Introduction

There are very few studies addressing the issue of land-atmosphere coupling over South America, and most of these analyze impact of surface conditions on precipitation at monthly or seasonal time scales (Collini et al. 2008; Grimm et al. 2007; among others). These studies suggest that soil moisture has an important role on precipitation variability and in the monsoon development. However, if soil memory is indeed bounded by a 15 day period –as shown by Dirmeyer et al. (2009)-, monthly means may provide weak representations of land-atmosphere coupling over large areas in South America and actual feedbacks may be hidden. Consequently, inferences obtained from climate studies could be complemented by individual case examinations. This hypothesis constitutes our rationale to select a particular case study in order to analyze in more detail the pathways for land-atmosphere coupling over our region of concern, which covers southern and southeastern South America. We selected a Northwestern Argentina Low (NAL) event, characterized by an enhanced South American low level jet (SALLJ), rather persistent synoptic circulation, and high frequency of occurrence during summer time (Ferreira 2008). This kind of events are particularly sensitive to surface heating as well as enhanced soil moisture/surface temperature gradient, and are associated with heavy rainfall that is mostly concentrated over Southeastern South America (SESA), at the exit region of the LLJ.

In order to show how soil moisture-precipitation-circulation interaction takes place, and to see the impact of soil moisture changes on this interaction, we designed a series of sensitivity studies which are described in section 2. Sections 3 examine the impacts on precipitation and circulation, while the conclusions are presented in section 4.

2. Numerical Experiments

The Weather Research and Forecasting model (WRF) version 2.0 (Skamarock et. al. 2005) is used to perform all experiments in a domain centered over the area affected by the NAL and the SALLJ shown in Figure 1. The model was run in non-hydrostatic mode with 40 km grid spacing in the horizontal and 31 vertical levels. We utilize the Eta Grid-scale Cloud and Precipitation microphysics scheme, (Ferrier et al. 2002); convection was parameterized using the Kain-Fritsch method (Kain 2004).The NOAH Land Surface Model was used to represent surface processes (Chen and Dudhia 2000).

All simulations were initialized on 29 January 2003 at 1200 UTC and run for 10 days. Initial and boundary conditions with 6 hr intervals are derived from the NCEP-GDAS analysis. Land use categories employed by the WRF are those generated by the US Geological Survey Land Use/Land Cover System.

The experiment design is conceived to address the following questions: Is SESA precipitation modified by changes in soil moisture at regional scales? What kind of feedbacks, due to these changes, can be identified in the circulation at synoptic time scales? Experiments **E1** and **E3** should help to answer these issues, since they correspond to 50% decrease/increase –respectively- of soil moisture over the model domain. We also wish to evaluate the impact of enhanced soil moisture gradients on the LLJ and related precipitation. This goal motivates experiments **E2** and **E4** which are similar to E1 and E3 but with moisture changes bounded by two specific areas: drier conditions (E2) are limited to northwestern Argentina area while moister ones (E4) affect SESA (see the subareas in Figure 1b).

3. Results

Figure 1 shows the differences between the experiment E1 and E3, and the CTRL run. E1 and E3 lead to the expected results: decreased soil moisture produces less precipitation and vice versa. Differences take place over the areas where precipitation was simulated, with major changes over central and eastern Argentina, Uruguay, southern Brazil, a band north of 15°S and along the frontal area. In terms of relative importance (changes normalized by total simulated precipitation in the CTRL run, not shown) it can be noticed that larger impacts occur south of 20°S, regardless of whether soil moisture has been decreased or increased with respect to the CTRL run. Our difference fields for E1 and E3 look rather similar to Collini et al. (2008) results reinforcing our idea that this particular case is highly representative of an important component of the summertime variability.

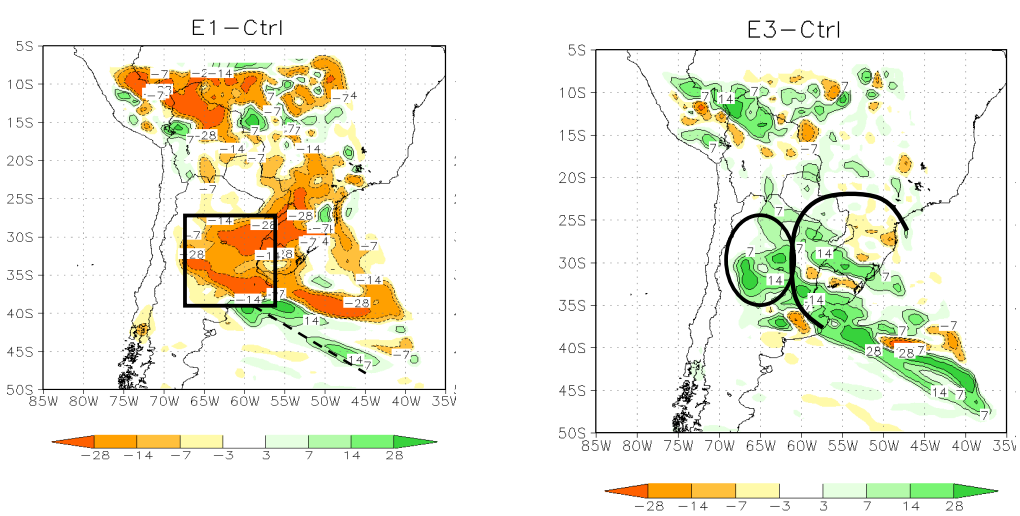

Figure 1: Accumulated precipitation differences (in mm) between each experiment and the control run. The box in the left panel indicates the area where averages have been performed. The circles in the right panel indicate the E2 and E4 experiments.

A southward shift of the frontal evident at the maritime portion of the front precipitation (the broken line in left panel of the Figure 1 denote the frontal position), is observed in the E1 and this is associated with the stronger northerlies denoted in Figure 2 and the enhanced convergence at the exit region of the LLJ –which is displaced towards the south. The wind response in E3 (not shown) is weaker, compatible with reduced northerlies over central Argentina (i.e associated with weaker NAL) and at the frontal area that can be related with the northward location of the precipitation maximum associated with the front.

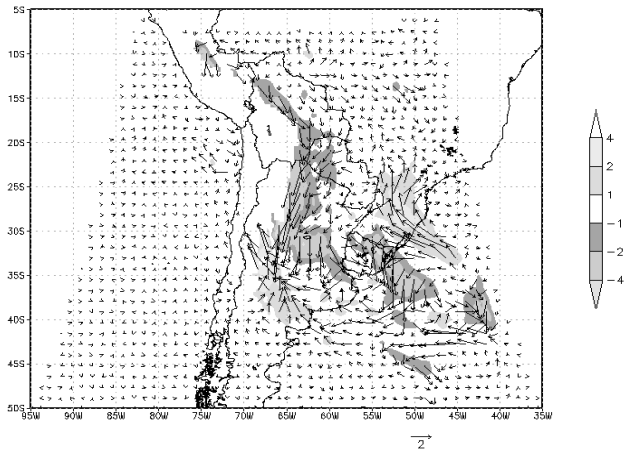

Figure 2: Mean 850 hPa wind anomalies in m s-1 at 0600 UTC for E1-CTRL.

To identify the pathways for land-atmosphere interactions it is useful to analyze the day-by-day evolution of soil moisture, precipitation and Convective Available Potential Energy (CAPE). We compute the areal average over a selected box located in the south portion of SESA indicated in Figure 1a. The results are depicted in Figure 3 and 4.

Changes in soil moisture (Figure 3a) affect the precipitation, where the stronger impacts are associated with the convective portion of precipitation.

If we compare E3 with E1, it is clear that convective precipitation starts earlier when soil moisture is higher over the area.

Besides the marginal precipitation in the first few days, the most important differences appear by February 2. This helps to explain soil moisture behavior from the beginning of the model run: before rainfall occurrence (i.e before February 2) soil moisture evaporates, especially in experiments with increased soil moisture (E3 and E4 values decrease substantially). Just after this time, all the experiments except E1 show the start of heavier precipitation, and soil moisture recovers rapidly, with larger increases in close correspondence to larger rainfall rates. There is a sustained recuperation of soil moisture amounts from February 3rd which is more evident in the drier runs.

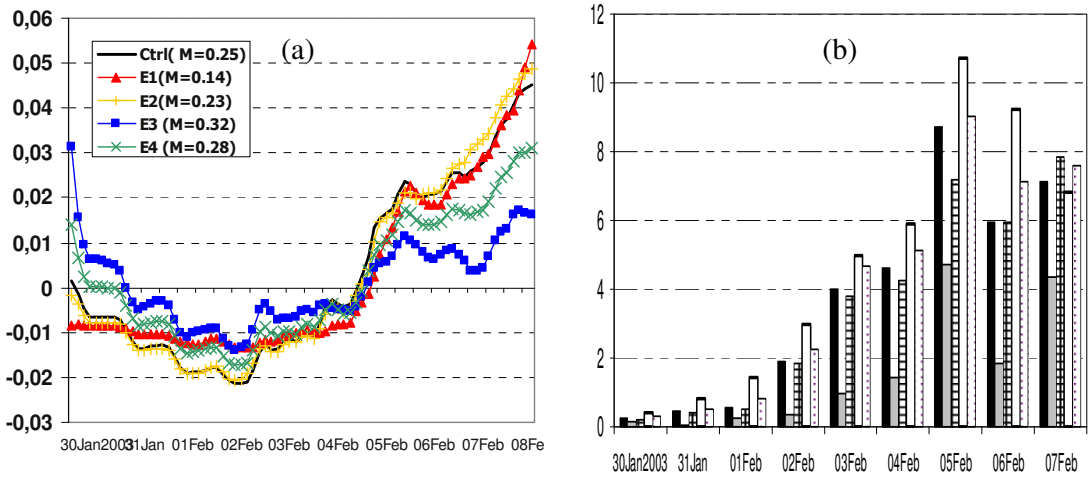

Figure 3: a) soil moisture anomalies (m^3m^{-3}), b) Daily accumulated convective precipitation (mm), area averaged over the box indicated in Figure 1.

Convective rainfall in wet runs is facilitated due to two positive effects: lower cloud base and CAPE increases through low level moistening. In contrast, dry runs, though warmer, result in very deep boundary layers (PBL) and lower CAPE. This response of the PBL to soil moisture has been confirmed in the present simulations, which exhibit the deepest PBL in E1, reaching almost twice the height of E3 on particular days (not shown).

The results for a reduction of soil moisture over northwestern Argentina (E2) and soil moisture (E4) increase over SESA perturb the associated precipitation in a similar way (both regarding the area and the type of modification), with a slight preference for the latter to increase it. This result leaves a warning on possible impacts of enhanced irrigation over SESA agricultural area.

With regard to CAPE variability (Figure 4) it can be seen that the experiments with higher CAPE have more convective rainfall. However, given similar CAPE amounts from the beginning of the experiment until February 3rd, significant precipitation does not start until February 2nd. This indicates that changes in the circulation may have occurred between these dates. The diurnal cycle of CAPE –increasing between 1200 UTC and 0000 UTC, and decreasing afterwards- is very similar for all the experiments except for E1. The particular diurnal cycle of CAPE in E1 is mostly explained by 2-m specific humidity variability that tends to maximize between 1200 and 1500 UTC –not shown-.

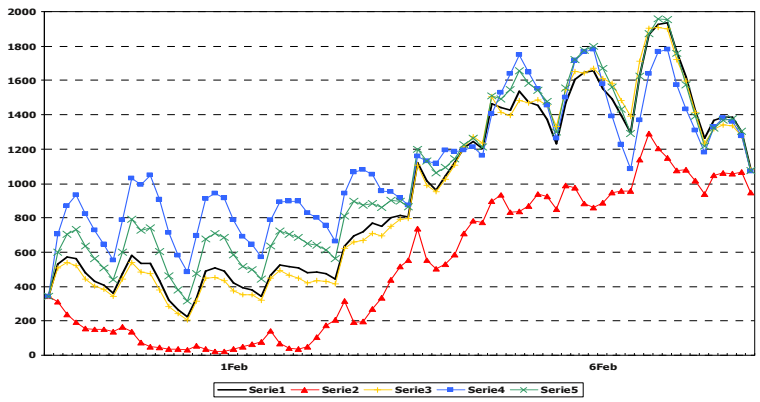

Figure 4: Maximum CAPE (J kg^{-1}) area averaged over the box indicated in Figure 1.

There is a strong similarity between CTRL, E2, E3 and E4 from 1200 UTC, February 3 to the end of the simulation (i.e. from the second cycle). CAPE in E1 does not reach 400J kg^{-1} until February 3: this increase is accompanied by light but sustained convective precipitation which explains the important recuperation of soil moisture between February 4 and the end of the model run. This is denoted by the increase of soil moisture rate during this last period. However CAPE in E1 remains lower than that of the other experiments during the entire integration. A clear delay between CAPE and precipitation maximum is not evident, showing that this region is affected by different mechanisms, as discussed by Nicolini and Saulo, 2006.

4. Concluding Remark

From this case study it can be inferred that soil moisture has a significant impact on precipitation, and this impact becomes evident when the areas where precipitation is occurring are clearly identified. This denotes the value added by analyzing individual cases. Most of the changes in precipitation are due to changes in the availability of moisture at low levels in the region.

The pathways relating soil-atmosphere interactions can be more easily tracked with the aid of E1 and E3: less (/more) soil moisture reduces (/enhances) CAPE so that precipitation -particularly its convective portion- is decreased (/increased). This positive feedback is maintained during the first five days of simulation. The second phase is characterized by a stronger synoptic forcing where the circulation is strong enough to initiate

precipitation in E1, even under less favorable CAPE preconditioning, and to recover soil moisture deficits by the end of the simulation.

Modifications in the circulation are less evident and need even a more careful analysis in order to be recognized. Nevertheless, we can distingue a low level circulation more reactive to a reduction in soil moisture than to an increase of this parameter.

Soil memory over the area of study is weak (compared with other regions) but enough to alter precipitation in a persistent way. For this reason, it is considered that this study further supports the importance of precise initial soil conditions in achieving maximum predictability at short and medium ranges.

Acknowledgments:

This study has been supported by The following projects: ANPCyT PICT 2004 25269, UBACyT X204, CONICET PIP 112-200801-00399, 490225/2008-0 (Prosul), 305302/2006-0 from CNPq. The research leading to these results has received partial funding from the European Community's Seventh Framework Programme (FP7/2007-2013) under Grant Agreement N° 212492 (CLARIS LPB. A Europe-South America Network for Climate Change Assessment and Impact Studies in La Plata Basin).

5. References

Collini E. A., E. H. Berbery and Barros V., 2008: How Does Soil Moisture Influence the Early Stages of the South American Monsoon?. J. Climate; 21, 2,195-213.

Chen, S.-H., and J. Dudhia, 2000: Annual report: WRF physics, Air Force Weather Agency, 38pp.

Dirmeyer, P.A., C.A. Schlosser, and K.L. Brubaker, 2009: Precipitation, Recycling, and Land Memory: An Integrated Analysis. *J. Hydrometeor.*, **10**, 278–288.

Ferreira, 2008: Causas y variabilidad de la Depresión del Noroeste Argentino e Impactos sobre los Patrones Regionales de Circulación (Causes and variability of the Northwestern Argentina Low and its impact over the regional circulations patterns). Ph.D. Dissertation. 177 pp. [Available from Departamento de Ciencias de la Atmosfera, Ciudad Universitaria (1428) Buenos Aires, Argentina].

Ferrier, B. S., Y. Jin, Y. Lin, T. Black, E. Rogers, and G. DiMego, 2002: Implementation of a new grid-scale cloud and precipitation scheme in the NCEP Eta model. 15th Conf. on Numerical Weather Prediction. San Antonio, Amer. Meteor. Soc., 280-283.

Grimm, A., J. S. Pal, and F. Giorgi, 2007: Connection between Spring Conditions and Peak Summer Monsoon Rainfall in South America: Role of Soil Moisture, Surface Temperature, and Topography in Eastern Brazil. J. Climate, 20, 5929–5945.

Kain J. S., 2004: The Kain-Fritsch Convective Parameterization: An Update. J. Appl. Meteor.. 43, 170-181.

Nicolini, M. and A. C. Saulo, 2006: Modeled Chaco low-level jets and related precipitation patterns during the 1997-1998 warm season. Meteor. nd Atmos. Phys. 94, 1-4, 129-143. doi: 10.1007/s00703-006-0186-7

Pal, J.S., and E. A. B. Eltahir, 2001: Pathways Relating Soil Moisture Conditions to Future Summer Rainfall within a Model of the Land–Atmosphere System. *J. Climate*, **14**, 1227–1242.

Skamarock, W. C., J. B. Klemp, J. Dudhia, D. O. Gill, D. M. Barker, W. Wang, and J. G. Powers, 2005: A description of the Advanced Research WRF Version 2. NCAR Tech Notes-468+STR . 100pp

On the Study of Tropical Cyclone Rainfall Mechanism

Lianshou Chen
Chinese Academy of Meteorological sciences

Extended Abstract

1. Introduction

Very heavy rainfalls are always caused by tropical cyclones (TCs). Extreme disastrous events would be occurred under TC heavy rainfall, such as river embankment crumble down, huge reservoir collapsed, flash flooding inundation, landslide and debris flow etc. That would devastate societies and human lives. To improve TC rainfall understanding is benefitial for disaster prevention and preparedness.

Sustainment and stagnancy of TC or its remnant would contribute towards the very heavy rains. Some rainfall over 1000 mm/24h occurs in a time period when TC is stagnant or looping in certain local area.

Environmental forcing is one of the factors to affect the TC rainfall. Water vapour supply with strong fluxes corresponding low layer jet stream is a basic condition for very heavy rainfall. Composite data analysis shows the distinct difference in moisture fluxes between two groups of TCs with and without heavy rainfall. Especially when TC encounters the monsoon onset, very heavy rainfall would be produced by the interaction between TC and monsoon surge. Cold air intrusion would play an important role to increase the unstable stratification which would help increasing rainfall. This process could be happened when a TC interact with a mid-latitude westerly trough.

Inner mesoscale structure of TC is a direct factor of the TC rainfall. Eye wall and spiral rain band is a major mesoscale strong convective systems to produce heavy rainfall. The other mesoscale vortices, wind shear and inverted trough in the TC

(Liying et al 2010) would enhance corresponding rainfall.

Underlying surface will influences the TC rain fall dra matically. Thes e inc lude the effects of coastal land, mountainous range topography. Huge inland water surface, saturated so il gro und an d boundary l ayer moisture t ransfer etc. Some mesoscale vortices within TC could be induced by land topographic effects (Duan et al, 20 05) which would increase the TC rainfall.

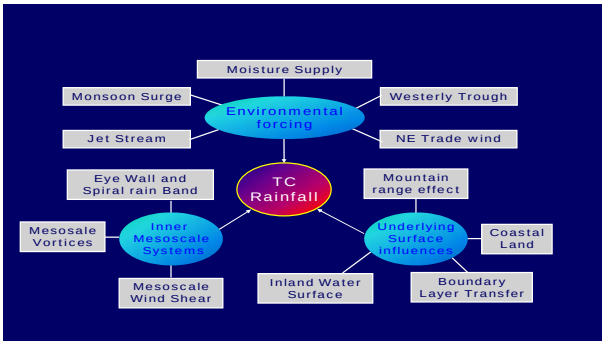

Fig.1 Factors affect tropical cyclone rainfall

The to tal T C rainf all is the results fro m t he interaction among environ mental forcing, inner mesoscale convective systems and underlying surface influences.(Fig.1). TC rainfall research usually focus on those physical processes.

2. TC Rainfall Revival

Landfalling tropical cy clones (L TCs) alwa ys bri ng about heavy rai nfall when they make landfall. Mo st of them would gradually be dissipat ed ow ing to that th e energy would be consu med by land surface friction. How ever, a few of rainfalls associated with th e remnant of L TC wou ld reinvigorate again. The reviv al precipitation rat e of th e re mnant could exceed it in l andfall s tage. This is a s mall probability event that is difficult to predict.

Remnant d epression o f L TC ov er la nd must absorb n ew en ergy for its reinvigoration. Diagnostic an alysis sh ows that there are two kind of ener gies would help th e r emnant revival to increase the rainfall, thos e are the pot ential en ergy from mid-latitude and the latent neat energy from the lower latitude.

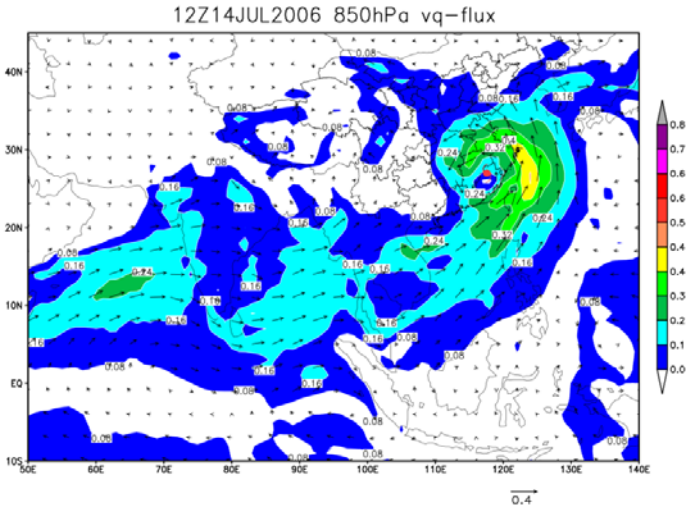

Fig.2 Severe tropical storm Bilis (0604) interact with south west monsoon flow

Remnant vortex would obtain baroclinic potential energy from the interaction between the remnant and mid-latitude trough, The potential energy it obtained would convert into kinetic energy to reinvigorate the remnant and increase the rainfall. On the other hand, when monsoon surge and its south west stream flow with wet cloud cluster merge and embroil into a LTC or its remnant which would obtain water vapour and latent heat. It would help remnant sustaining longer period over land to increase TC rainfall (Dong et al, 2010). Severe tropical storm Bilis (0604) is one of those typical cases (Fig.2) Which sustained five days over land and bring about very heavy rainfall in south China. Bilis interact with the humid south west monsoon flow and strong moisture flux which played a major role for this very heavy rainfall.

Some studies (Zeng et al, 2002) also showed that the heat island effect, land surface topography, cod air intrusion and jet stream coupling in upper level and lower layer play an important role in TC heavy rainfall.

Most of the LTCs with rain resuscitation made landfall in south east coastal area of China. Those LTCs have two motion trends after their landfall, namely move toward north and west respectively. LTCs with northward motion trend may interact with mid-latitude trough to gain baroclinic potential energy. Some of them have a

moisture channel connected with, it's more favorable to increase the rainfall of LTC. Some of the LTC in this group would undergo a process of extratropical transition. On the other hand, LTCs with westward motion trend may interact with monsoon surge and humid cloud cluster to gain latent heat energy if there is the occasion of monsoon onset. Some of them have a colder air intrusion in northern periphery of the remnant to increase unstable stratification.

Statistical study shows that LTC rainfall reinvigoration often appear in a weak depression remnant even in their slow down or stagnant stage and it happen frequently in the time of third day after it made landfall。

3. Remote rainfall with tropical cyclones

Tropical cyclone could produce a distant rainfall out of its periphery in addition to rainfall region covered by TC circulation. When tropical cyclone encounter a mid-latitude westerly trough and interact with it, large area rainfall could be distributed in front of the westerly trough away from the TC circulation (Fig.3). The appearance of this rainfall is closely related to the existence of TC in lower latitude. Water vapour is transported by south east low layer jet flow in eastern periphery of the TC. The moisture flow stretch out to the region in front of the trough. Humid unstable stratification with cyclonic vorticity are more favorable to increase the rain rate and expand its distribution.

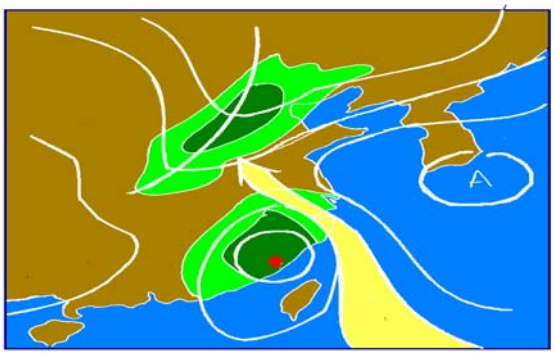

Fig.3 Schematic diagram of typhoon remote rainfall

Numerical simulation (Zhu H.Y, et al, 2000) showed that the remote rain rate is sensitive to tropical cyclone intensity and the strength of the westerly trough.

Heavy rain usually occur in north China when a typhoon make landfall in south east coast of China. This is also related to moisture transport from a typhoon in lower latitude around the coast.

This remote rainfall phenomenon is not only appear in China but also in Japan. Study (Yongqing Wang, Yuqing Wang, H. Fudeyasu 2009) shows that expanded distribution rainfall cover Japan from 2-4 sep 2004 when there is a typhoon Songda(0419) appeared in far away ocean from Japan (1300Km south away from southern coast of Japan). Their sensitive numerical simulation indicate that typhoon Songda(0419) play an important role for this remote rainfall over Japan far away from Songda. On the other hand, the topography of Honshu Japan also contribute positive effect to this remote rainfall.

Another remote rainfall was related to typhoon Meari(0422) which arosed from the topographic effect. Akihiko(2006) studied the three rain lumps occurring over the kii peninsula far away (500Km east) from Kyushu Japan where Meari made landfall. His sensitive simulation shows that one of three rain lumps corresponding to a mountain is disappeared when the topography is removed in the model while other two still remain. Obviously, the result of the numerical simulation implies that the mountain topography could contribute to the remote rainfall of tropical cyclone as well.

4. Summary

Tropical cyclone heavy rainfall is a integrated result from the interaction among TC and environmental forcing, inner mesoscale structure and underlying surface influences.

Sustentation and stagnation of LTCs is an important condition for heavy rainfall of remnant vortex. Vary heavy rainfall usually occurred in a period of LTC moving slow down, stagnant or looping.

Rainfall reinvigoration is a small probabilistic event which is hard to forecast.

Two kind of energies will help remnant of LTC revival to reinvigorate the rainfall of remnant. Those are the potential energy and latent heat energy. Those different kind of energy could be acquired when TC interact with westerly trough or monsoon surge respectively.

Remote heavy rainfall of TC is also an unusual phenomenon. Water vapour transport form a typhoon play a major role. Plenty of water vapour could be transported by the TC right side stream flow. Both of westerly trough and land topography have a positive effect to produce a remote rainfall of a TC.

Bibliography

Akihiko. M 2006: A cloud resolving numerical simulation for characteristic rainfall induced by typhoon Meari (2004). Team member report on topic 0.3 of sixth WMO IWTC.

Dong Meiying, et al, 2010: Rainfall Reinforcement Associated with Landfalling Tropical Cyclone. Journal of Atmospheric Sciences(waiting list).

Duan L et al 2005: Diagnostic analysis and numerical study of torrential rain associated with tropical storm Fitow (0114). Chinese J. Atmos SCI., Vol 29, No.3.

Liying et al, 2010: Study on formation and development of a mesoscale convergence line in typhoon Rananim. Acta meteorologica Sinica, Vol 24, No.4.

Yongqing Wang., Yuqing Wang, H Fudeyasu, 2009: The role of typhoon songda (2004) in producing distantly located heavy rainfall in Japan. Monthly Weather Review, Vol 137, PP3699-3716.

Zeng Z.H et al, 2002: Simulation of influence of “urban heat island” on torrential rain in Shanghai on 5Aug, 2001 Acta Meteorologica Sinica Vol 60, PP58-64..

Zhu H. Y., L.S.Chen., X. D. Xu 2000: A numerical Study of the interaction between typhoon and mid-latitude circulation and its rainfall Characteristics. Chinese Journal of Atmos. SCI., Vol. 24, No. 5.

Influence of Typhoon Songda (2004) in Producing Distantly-Located Heavy Rainfall in Japan

Yuqing WANG[1,2], Yongqing WANG[2], and Hironori FUDEYASU[1]

[1]International Pacific Research Center and Department of Meteorology, University of Hawaii at Manoa, Honolulu, Hawaii, USA
[2]Pacific Typhoon Research Center, KLME, Nanjing University of Information Science and Technology, Nanjing, China

When Typhoon Songda (2004) was located southeast of Okinawa over the western North Pacific during 2–4 September 2004, a heavy rainfall event occurred over southern central Japan and its adjacent seas, more than 1200 km from the typhoon center. The Advanced Research version of the Weather Research and Forecast (WRF-ARW) model was used to investigate the possible remote effects of Typhoon Songda on this heavy precipitation event in Japan. The National Centers for Environmental Prediction (NCEP) global final (FNL) analysis was used to provide both the initial and lateral boundary conditions for the WRF model. The model was initialized at 1800 UTC 2 September and integrated until 1800 UTC 6 September 2004, during which Songda was a supertyphoon. Two primary numerical experiments were performed. In the control experiment, a bogus vortex was inserted into the FNL analysis to enhance the initial storm intensity such that the model typhoon had an intensity that was similar to that observed at the initial time. In the no-typhoon experiment, the vortex associated with Typhoon Songda in the FNL analysis was removed by a smoothing algorithm such that the typhoon signal did not appear at the initial time. As verified against various observations, the control experiment captured reasonably well the evolution of the storm and the spatial distribution and evolution of the precipitation, whereas the remote precipitation in Japan was largely suppressed in the no-typhoon experiment, indicting the significant far-reaching effects of Typhoon Songda. Songda enhanced the remote precipitation in Japan mainly through northward moisture transport into the preconditioned precipitation region by its outer circulation. The orographic forcing of the central mountains in Japan played a small role compared with Typhoon Songda in this extreme precipitation event.

On the Study of Rainfall Rate and Distribution Associated with the Typhoon Winnie (9711) during Its ET Process

LI Ying[1] LEI Xiaotu[2] CHEN Lianshou[1]
1 Chinese Academy of Meteorological Sciences/LaSW, Beijing, 100081
2 Shanghai Typhoon Institute, Shanghai, 200030

1. Introduction

Typhoon may frequently encounter the cold air associated with a westerly trough. Typhoon extratropical transition (ET) could occur in this period. The structure of the typhoon remnant will appear a prominent change in the ET process (Harr et al ,2000; Klein etal, 2000). The baroclinic potential energy from the ET process could be converted into kinetic energy, reviving the remnant and increasing its rainfall(Chen et al, 2002). Numerical experiments by Niu et al. (2005) showed that the cold air which invaded into the periphery of the typhoon increased the rainfall amount there. However, when cold air penetrated into the vicinity of the typhoon center, it decreased the typhoon intensity dramatically and resulted in a remarkable decrease of rainfall. ET process of tropical cyclones will lead to variation of its rain rate and distribution, it has long been a challenge to forecasters.

Typhoon Winnie made landfall in Zhejiang province of China on 18 Aug. 1997. It moved northward and caused heavy rainfall in the next 3 days in its ET process. Zhu et al (2002) displayed the change of Winnie's cloud system successfully based on MM5. Study from Li et al. (2006) shows that Winnie coupled with a mid-latitude upper trough during its ET. The slantwise vorticity development caused by the increase of moist baroclinicity is a main factor responsible for Winnie re-intensification.

In this study, the change of rainfall rate and distribution related to the typhoon Winnie during its ET process was explored based CMA T106 data, TBB data issued by JMA and PSU/NCAR numerical model MM5 outputs.

2. Overview of Typhoon Winnie

Typhoon Winnie made landfall at 1300 UTC 18 August 1997 in Wenling City of Zhejiang, with a minimum sea level pressure of 960 hPa. Then it decayed and moved northwardly, and split into two centers of 994 hPa at 0000 UTC 20 August in Shandong. Then the vice center moved northeastwardly while the main center dissipated, and stagnated in the northeastern China at 0000 22 August. It eventually re-intensified as a extratropical cyclone with a minimum sea level pressure of 985 hPa. The change feature of typhoon precipitation in its re-intensification stage from 0000 UTC 20 August to 1200 22 August is investigated in this study.

Fig.1 displays TBB distribution and 850-hPa wind vectors with 6 hour interval from 0000 UTC 18 August to 1800 UTC 22 August 1997. Before landfall, the main cloud system of typhoon Winnie is symmetric in circular form, and there is a westerly trough cloud system developing in the region of 40ºN(Fig.1a,b). Then the trough and Winnie approached each other, both cloud systems blent together, resulting the development of convection in the northern part of typhoon circulation(Fig.1 c,d). The blent cloud system continually developed into a strong cloud band stretching in west-east direction (Fig.1 e-i). When the vice center of Winnie moved to the northeast, the cloud band curved to the south with the severe cloud area occurring in the northeastern part of typhoon circulation. A strong curving cloud band had been formed at 1200 UTC 21 Aug. 1997 as Winnie reached its strongest stage (Fig.1 o). After that, the curvature of the cloud band increased, making for ring from, and evolved into a mature extratropical cyclone at 0600 UTC 22 Aug (Fig.1 p-r). The cloud system weakened afterwards (Fig.1 s,f). In this process, strong cloud band moved to the

southeastern part of typhoon circulation.

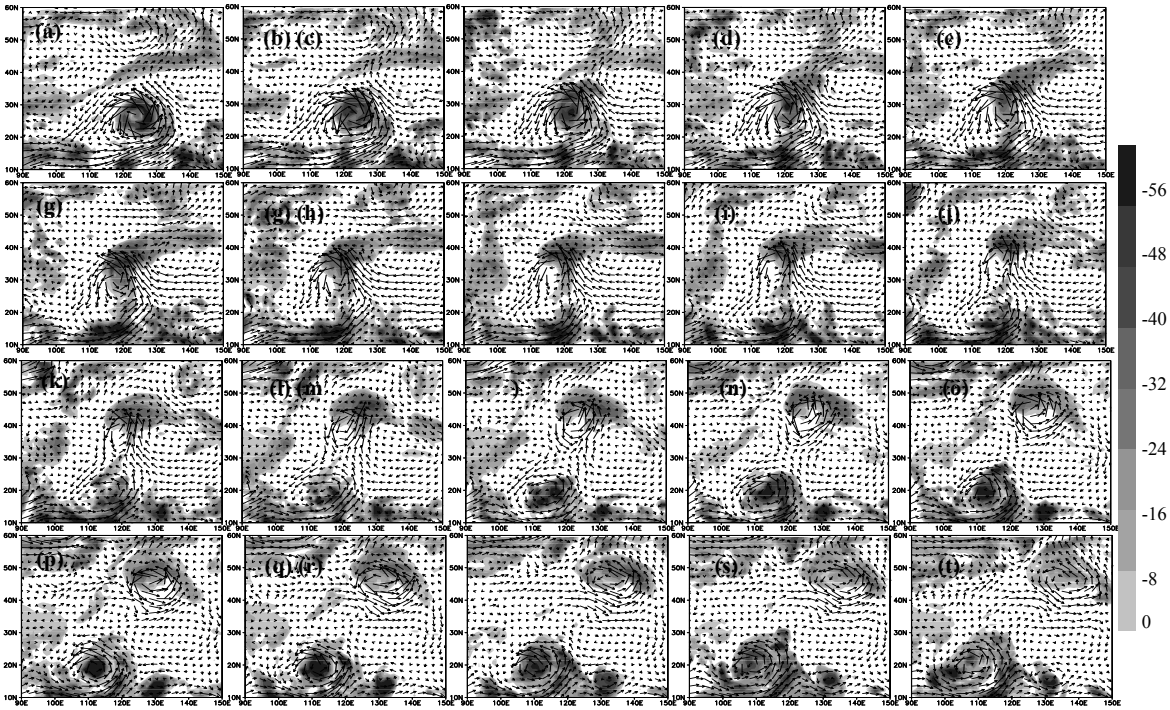

Fig.1 TBB distribution(shaded ,°C) and 800-hPa wind vectors with 6 hour interval from 0000 UTC 18 August to 1800 UTC 22 August 1997.

TBB distribution shows that Winnie's cloud system changes remarkably with asymmetric structure during its ET process. The strong cloud band occurs in the north, northeast and southeast in turn, going round typhoon center clockwise.

3. Numerical simulation

The PSU/NCAR non-hydrostatic model MM5v3 is used. It is configured in dual-way feedback and two-domain nesting, with grid lengths of 45 km and 15 km, respectively. The resolutions of orography inserted are 30 and 10 minutes, respectively. The center point of the two model domains is set at 41ºN , 123ºE, and 23 σ levels in vertical. The Kain-Fritsch convective parameterization scheme is applied for both model domains. CMA T106 data, with 1.125º horizontal resolution is applied to form original fields and and lateral boundary conditions in the model. It is integrated for 60 h from 0000 UTC 20 Aug. to 1200 22 Aug. 1997.

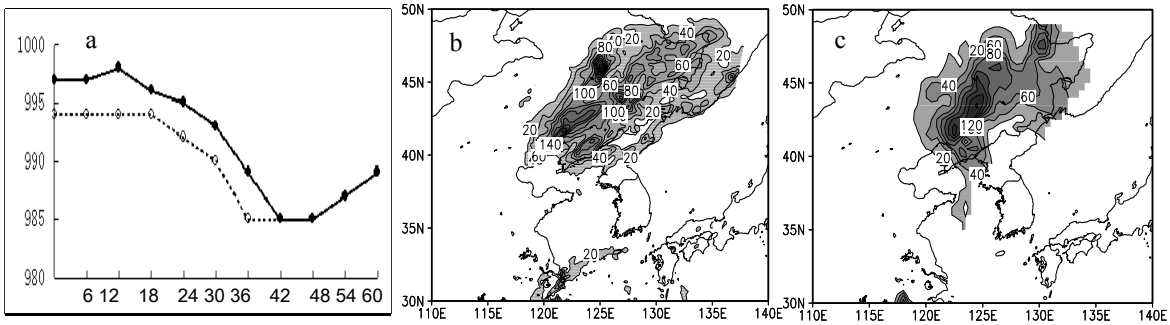

Fig.2 A comparison of the minimum sea level pressure(hPa) of the control simulation (solid curve) from the observation (broken curve) (a) and accumulative rainfall (mm,only ≥ 20 mm) from 1200 UTC Aug. 20

to 1200 UTC Aug. 22 1997(b、c). (b)simulation；(c)observation

Fig.2a compares the minimum central pressure of Typhoon Winnie between model outputs (solid curve) and CMA best analysis (broken curve). The simulation is weaker than the best analysis, with 2-4 hPa differences, however, their trends is similar. The model has exhibited the re-intensification of typhoon Winnie in its ET process. Fig.2b shows the comparison of accumulative rainfall from 1200 UTC Aug. 20 to 1200 UTC Aug. 22 1997. It also conforms well to the observed. In general, the model can reproduces well the change of typhoon intensity and the rainfall rate and distribution. In the following text, we will use the model outputs to analyze the change of rainfall associated with typhoon Winnie.

4. Results

4.1 Environmental wind vertical shear

Studies(Frank et al, 1999; Chen et al, 2006) show that typhoon rainfall distribution is related to the vertical shear of horizontal winds in the surrounding environment . Fig3 shows that the environmental vertical shear becomes very strong under the interaction between the typhoon remnant and high level southwesterly jet(figure omitted), and its direction turns in clockwise style from 216° to 279°. It is found that the rainfall mainly occurs on the left side of downstream of the shear. The rainfall center occurs in the north, northeast and southeast in turn(Fig.4), that is corresponding to the change of vertical shear direction .

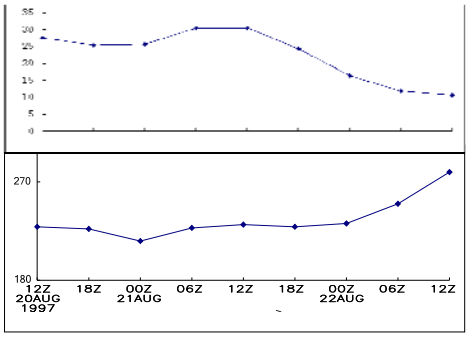

Fig.3 The vertical-time variation of wind vertical shear averaged on typhoon area (10°×10° latitude and longitude area) and upper panel shows the magnitude in unit of m/s and bottom panel the direction in degree.

4.2 Structure change

4.2.1 Slantwise vortex

The wind vectors, potential height and equivalent potential temperature distributions at 850 hPa, 700 hPa, 500 hPa and 300 hPa during 1200 UTC 20 Aug. To 1200 UTC 22 Aug. 1997 is examined (Figures omitted). It is found that the vertical structure of typhoon vortex is slantwise against height, inclined to the north at its transformation stage, then tend to perpendicularity in its reintensifying stage, and inclined to the southeast afterward. Thus the ascending motion of warm airflow also is slantwise, that is favorable for heavy rainfall occurring in the slanting direction of typhoon vortex.

4.2.2 Thermal advection

Shuanzhu et al.(2009) demonstrates that the diagnosis of thermal advection and associated ascent and descent behaviour are valid for extreme rainfall associated with typhoon Bilis (2006). Fig.4 shows 700hPa wind vectors(arrows), 850 to 500hPa thickness (contours, gpm) and 6 h accumulated rainfall(shading, only ≥ 5 mm). It is found that the warm advection (solid long arrow) is favorable for rainfall, however the cold advection (broken long arrow) is unfavorable for rainfall, it decreases or dissipates rainfall. The cold advection interacts with warm advections in typhoon circulation during its ET process. Thus

the thermal structure is asymmetric, resulting in the change of rainfall distribution.

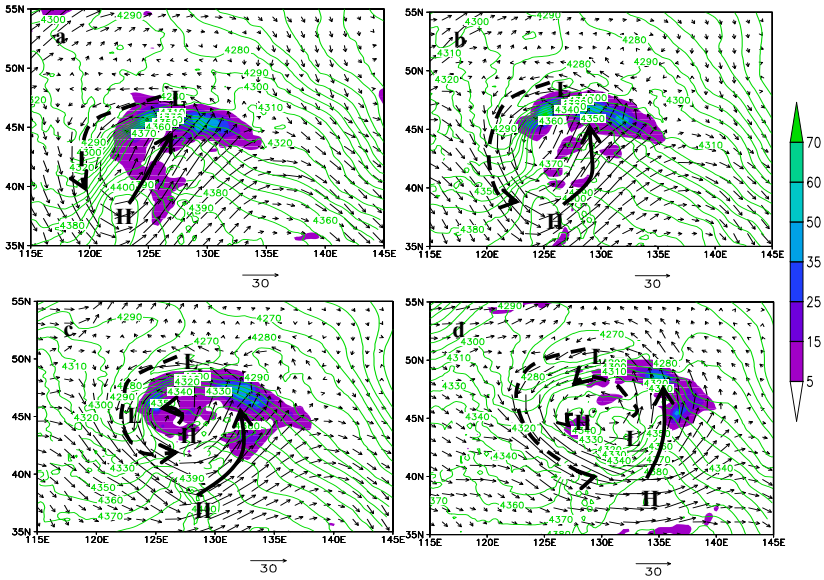

Fig.4 700 hPa wind vectors(arrows), 850 to 500hPa thickness (contours,gpm) and 6 h accumulated rainfall(shading,only ≥ 5 mm) (a) 0600 UTC 21 Aug. (b)1200 UTC 21 Aug. (c)1800 UTC 21 Aug. (d) 0600 UTC 22 Aug.

4.2.3 Convective Vorticity Vector

Convective Vorticity Vectors ($C = \frac{\omega_a \times \nabla \theta}{\rho}$) was put forward by Gao et al (2004a) to diagnosed the deep convection. Their study shows that the vertical component of convective vorticity vector has a good relationship with rainfall. It can be expressed as:

$$C_z = \frac{1}{\overline{\rho}}(\xi \frac{\partial \theta_e}{\partial y} - \eta \frac{\partial \theta_e}{\partial x})$$

Where, $\xi = \frac{\partial w}{\partial y} - \frac{\partial v}{\partial z}$, $\eta = \frac{\partial u}{\partial z} - \frac{\partial w}{\partial x}$ and $\overline{\rho} = \overline{\rho}(z)$ is the basic density of atmosphere.

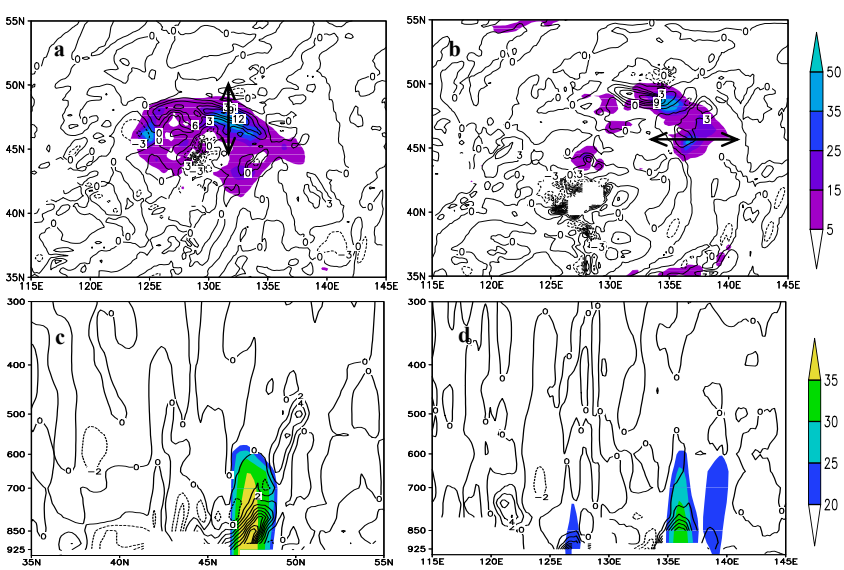

Fig.5 Distributions of $\overline{\rho} C_z$ (10^{-7} K $M^{-1}s^{-1}$) and 6 h accumulated rainfall (shading, only ≥ 5 mm) on

800 hPa (a,b, arrow indicates position for vertical section) , vertical sections of $\overline{\rho C}_z$ and simulated radar reflectivity (shading, only ≥10 dBz). (a)(c) 1800 UTC 21 Aug. (b)(d) 0600 UTC 22 Aug.

Fig.5 displays distributions of $\overline{\rho C}_z$ and 6 h accumulated rainfall on 800 hPa and vertical sections of $\overline{\rho C}_z$ and simulated radar reflectivity. It is found that the high value area of $\overline{\rho C}_z$ on lower layer is a good index to strong convection and heavy rainfall region in typhoon circulation.

5. Conclusion

The mechanism of rainfall change associated typhoon Winnie has been discussed based on satellite data and MM5 outputs in its ET process.

The results indicate that the rainfall distribution displays remarkable asymmetry. The heavy rainfall mainly occurs in the north at first, then the northeast and southeast part of typhoon circulation, going around typhoon center clockwise during ET process.

It is found that the environmental vertical shear becomes stronger under the interaction between the remnant and upper westerly trough during ET process, and results in the rainfall concentrated in the left side of downstream of the shear. Meanwhile, the vertical structure of typhoon vortex is slantwise against height, and the heavy rainfall occurs in the slanting direction. On the other hand, the rainfall variation also is related to the thermal advection activity in the remnant of typhoon circulation. The heavy rainfall is associated with warm air advection at 700hPa. Moreover, the vertical component of convective vorticity vector can reflect the impacts of wind vertical shear and front in ET typhoon circulation. Its high value area has a good relationship with heavy rainfall on lower layer .

Acknowledgments. This work was financed by the National Grand Fundamental Research 973 Program of China (Grant nos. 2009CB421504), and the National Natural Science Foundation of China (Grant nos. 40730948, 40975032).

References

Chen Lianshou, Xu Xiangde, Luo Zhexian and Wang Jizhi. Introduction to Tropical Cyclone Dynamics，Beijing：Meteorological Press. 2002.317pp

CHEN S Y S, KNAFF J A and MARKS F D Jr. Effect of vertical wind shear and storm motion on tropical cyclone rainfall asymmetries deduced from TRMM. Mon Wea Rev, 2006, 134:3190-3208.

FRANK W M and RITCHIE E A. Effects of environmental flow upon tropical cyclone structure. Mon Wea Rev, 1999, 127:2044-2061

Gao S, Wang X and Zhou Y. 2004a: Generation of generalized moist potential vorticity in a frictionless and moist adiabatic flow. Geophys. Res. Lett., 31, L12113,1-4

Harr P A, Elsberry E L. Extratropical transition of tropical cyclones over the western North Pacific. Part I: Evolution of structural characteristics during the transition process. Mon. Wea. Rev., 2000, 128: 2613-2633

Klein P M, Harr P A, Elsberry R L. Extratropical transition of western North Pacific tropical cyclones: An overview and conceptual model of the transformation stage. Wea. Forecasting, 2000, 15: 373-395

Li Ying, Chen Lianshou, Lei Xiaotu. Numerical study of impacts of upper-level westerly trough on the extratropical transition process of Typhoon Winnie (1997). Acta Meteorologica Sinica, 2006,64(5):552-563

Niu Xuexin, Du Huiliang, Liu Jianyong. 2005. The numerical simulation of rainfall and precipitation mechanism associated with typhoon Sinlaku (0216) . Acta Meteor Sinica, 63(1):57-63

SHUANZHU GAO, ZHIYONG MENG, FUQING ZHANG and LANCE F. BOSART. Observational Analysis of Heavy Rainfall Mechanisms Associated with Severe Tropical Storm Bilis (2006) after Its Landfall. Mon Wea Rev, 2009, 137: 1881-1897.

Zhu Peijun, Chen Min, Tao Zuyu, et al. Numerical simulation of typhoon Winnie(1997) after landfall. Part II: Structure evolution analysis. Acta Meteorologica Sinica (in Chinese), 2002, 60(5)：560-567

The estimation of TC quantitative precipitation forecast affecting Shanghai in 2009

Tong Xu, Jia Li, Xiaofeng Wang, Hui Yu, Baode Chen, Yuhua Yang
Shanghai Typhoon Institute of China Meteorological Administration
xut@mail.typhoon.gov.cn

1 Introduction

The estimation of TC quantitative precipitation forecast affecting Shanghai in 2009 was introduced in this paper. Besides the traditional verification measures [e.g., Mean Absolute Error(MSE), Mean Error(ME),etc], the Method for object-based Diagnostic Evaluation (MODE) was applied to estimate the precipitation forecast of Shanghai regional mesoscale model(STI-WARMS) which was based on WRF.

2 Data and Methods

The observation precipitation data in this paper is MICAPS format and the traditional verification measures and spatial verification method (MODE) were applied In this paper. The TC case which we choose is typhoon MORAKOT.

The Mean Error (ME) is defined as

$$ME = \frac{1}{n}\sum_{i=1}^{n}(f_i - o_i)$$

The Absolute Error (MAE)

$$MAE = \frac{1}{n}\sum_{i=1}^{n}|f_i - o_i|$$

The methods used by the MODE tool to identify and match forecast and observed objects are briefly described in this section.

Mode is based on a multi-step automated process, which includes the following stages:

(a) Object identification;
(b) Measurement of object attributes;
(c) Merging of objects from the forecast and observed fields;
(d) Matching of objects from the observed object attributes;
(e) Comparison of forecast and observed object attributes;
(f) Summarization and comparison across many cases.

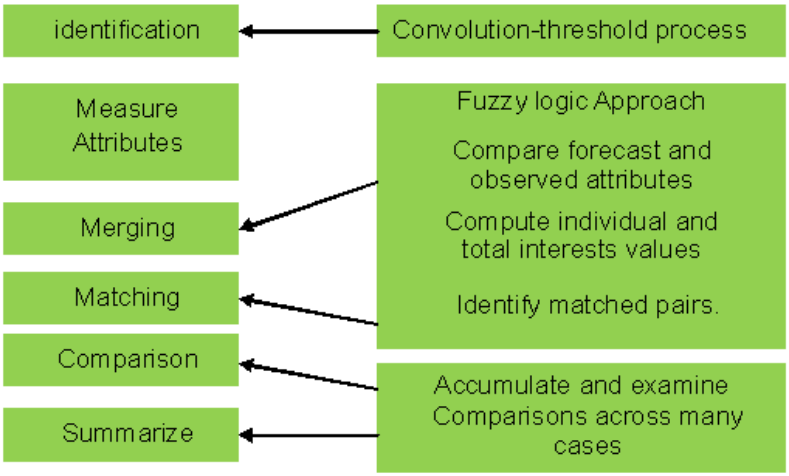

Figure1. Summary of steps involved in application of the Mode approach

3 Result of traditional verification methods

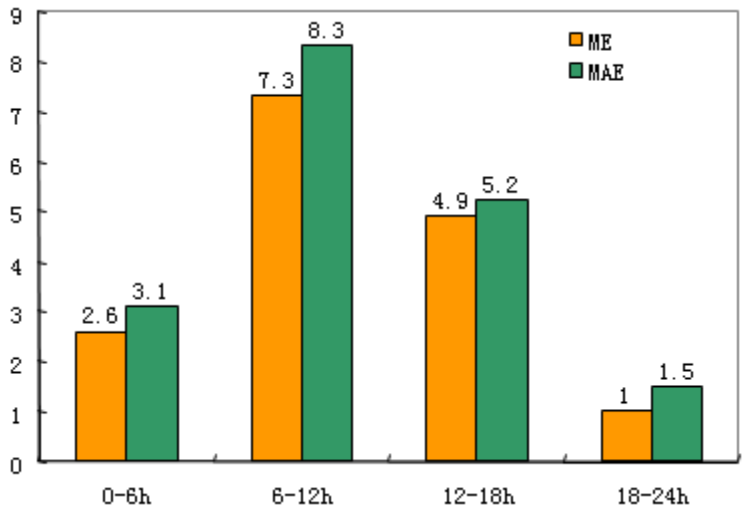

Figure2. Precipitation forecast error of STI-WARMS in Shanghai region during the affection of MORAKOT

Figure2 indicates the precipitation forecast error by 6 hour in Shanghai region during the affection of MORAKOT. The ME between forecast and observation is 2.6mm, 7.3mm, 4.9mm and1.0mm in 0-6h, 6-12h, 12-18h and 18-24h. It indicates that the forecast precipitation is mostly stronger than observed ones, especially in 6-12h. The MAE between forecast and observation is 1mm, 8.3mm, 5.2mm and 1.5mm. It also confirm that the forecast error in 6-12h is bigger than other intervals.

4 Result of MODE

The example presented in this section is based on STI-WARMS output

from 0000 UTC on 8 August 2009 to 0012UTC on 10 August 2009 during the affection of MORAKOT and in particular precipitation fields from the Advanced Research WRF(ARW) run at a 9-km horizontal resolution.

Figure 3 shows the WRF and MICAPS precipitation for a case valid at 0012UTC on 9 August 2009. The values shown are 24-h precipitation accumulations; the WRF output is based on a 24-h forecast initialized at 0012UTC. Figure 4 shows the precipitation objects created using a convolution radius of 15 grid squares and a threshold of 10mm. Color coding indicates which objects were merged and matched. Dark blue objects were unmatched.

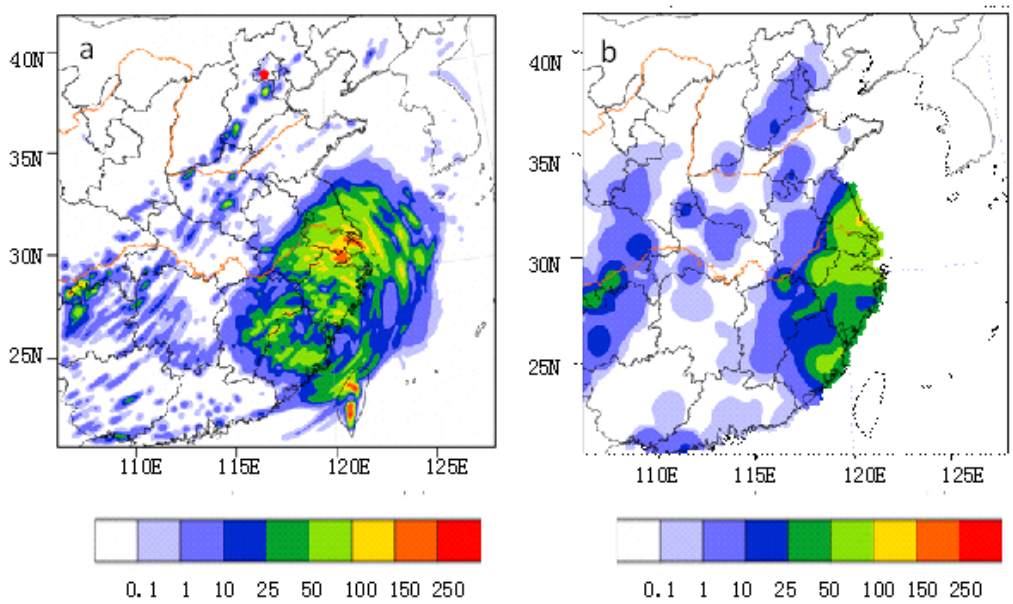

Figure3. (a)STI-WARMS (b) MICAPS precipitation values for 0012UTC 9 August 2009

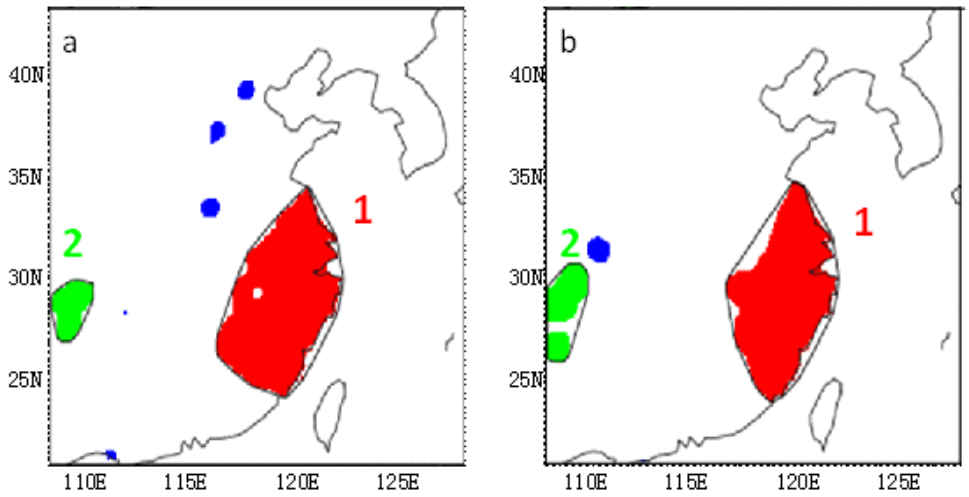

Figure4. Single and composite objects identified for the case shown in Fig.3 for (a) STI-WARMS and (b) MICAPS observation. Colors identify objects that are matched and merged. Dark blue objects are not matched.

In this case, a total of two composite objects were matched between the Forecast and observed fields. Some attributes of the composite objects shown in Figure4 are listed in Table 1. These attributes include area, distance and intensity measures. As shown in table 1, the first composite forecast object was somewhat larger than observed ones, but the second composite forecast is smaller than observed ones. The STI-WARMS tended to overforecast precipitation intensity, for both the median and the 0.90th intensity.

Attributes or comparison of objects	**Composite objects number**	
	1	**2**
STI-WARMS area	5762	684
MICAPS area	5165	951
Area ratio	1.12	0.72
Centroid distance	40	15
Median intensity ratio	1.22	0.97
0.90th intensity ratio	1.19	2.13

Table1.Example attributes and attributes comparisons for 9 August 2009 case shown in Fiugre3 and Figure4.

Table2 showed the averaged attribute comparison for multiple forecast times of STI-WARMS during the affection of MORAKOT. Results indicated that the averaged area ratio between composite forecast objects and observed ones is 1.23, the averaged centroid distance is 66.3, averaged median intensity ratio and 0.90th intensity ratio is 1.38 and 1.39.

Area ratio	1.23
Centroid distance	66.3
Median intensity ratio	1.38
0.90th intensity ratio	1.39

Table2. Averaged attribute comparison for multiple forecast times during the affection of MORAKOT.

5 Summary and Conclusions

From the comparison of forecast and observed object attributes, the results showed that:

(1) The area ratio between forecast and observed objects is 1.27:1 in 6h

and 1.23:1 in 24h, indicates that the forecast precipitation area is somewhat large than observed ones.

(2) The angle difference between forecast and observed objects is 6.48 degree in 6h and 7.21 degree in 24h.

(3) The median intensity ratio and 0.90th intensity ratio between forecast and observed objects is 0.945 and 1.22 in 6h and 1.38 and 1.39 in 24h, indicates that the forecast precipitation intensity is mostly stronger than observed precipitation intensity, especially in the center of precipitation area.

(4) The traditional verification between forecast and observed grid points Indicates that the model forecast precipitation intensity is stronger than observed precipitation intensity, the Mean Error between forecast and observed precipitation in Shanghai is 2.6mm, 7.3mm, 4.9mm and 1.0mm by 6 hour during 24 forecast lead time.

References

Ebert EE., 2008. Fuzzy verification of high resolution gridded forecasts: a review and proposed framework. Meterological Applications 15:53-66.

Grams JS., Gallus WA., Koch SE., Wharton LS., Loughe A., Ebert EE.2006. The use of a modified Ebert-McBride technique to evaluate mesoscale model QPF as a function of convective system morphology during IHOP 2002. Weather and Forecasting 21:288-306.

Davis, C.A., B.G. Brown, and R.G. Bullock, 2006b: Object-based verification of precipitation forecasts, Part Ⅱ : Application to convective rain systems.

Davis, C.A., B.G. Brown, and R.G. Bullock, 2006a: Object-based verification of precipitation forecasts, Part Ⅰ :Methodology and application to mesoscale rain areas. Monthly Weather Review, 134, 1772-1784.

Numerical Study of Topographic Effect on Rainfall Reinforcement Associated with Tropical Cyclone Talim (2005)

Mei-ying DONG[1], Lian-shou CHEN[2] , Ying LI[2]

Zhejiang Institute of Meteorological Sciences, China[1]; Chinese Academy of Meteorological Sciences, China[2];

dmy312@yahoo.com.cn

Extended Abstract

1. Introduction

Observational evidence (Chen and Ding, 1979; Tao et al., 1980; Chen, 2007) has shown that tropical cyclones (TC) often bring about torrential rains when they make landfall. When a TC weakens into a remnant, rainfall would be decreased correspondingly. However, in some cases, the remnant will be reviviscent and produce even heavier rainfall than it in landfall time. Such a phenomenon is known as Rainfall Reinforcement associated with Landfalling Tropical Cyclones (RRLTC; Fan et al., 1996). Because of the occurrence of RRLTC often under complex atmospheric environments, the prediction of RRLTC has always been a challenge to forecasters. As a result, it may induce tremendous disasters. Statistical research reveals that rainfall centers have a close relation with topography as mainly locating in coastal lines vicinity, the eastern and southern slopes of the Mountains (Dong et al., 2010). Typhoon Talim (2005) is a good case to investigate topographic effect on the rainfall reinforcement, which induced the strongest rainfall reinforcement so far in China and the rainfall center just situates in the east slope of Da-bie Mountains. In this paper, we will present results from simulation to understand the terrain impact.

2. Model description and experiment design

This study makes use of Weather Research and Forecasting Model (WRFV2.2). One control experiment and three sensitivity experiments are designed as the following: control experiment (CON), without the Da-bie Mountains experiment (T0.0), reducing the Da-bie Mountains elevation to 50% experiment (T0.5) and increasing the Da-bie Mountains elevation to 150% experiment (T1.5).

3. Control experiment results

1) Track and intensity

The comparison of the simulation track with the China Meteorological Administration (CMA) best-track analyses from 1200 UTC 1 September to 1200 UTC 3 September shows that the simulation can forecast Talim northwestward motion inland as well as the stagnation

in the latter 24-h, on average, the 48-h error is 58km. For the intensity simulation, the simulated minimum sea-level pressure agrees well with the estimated from CMA, which revives the slowly weakening trend of Talim over land. Meanly, the absolute error is 2.7 hPa during the 48-h. That is to say, the model does capture the evolution of Talim's intensity.

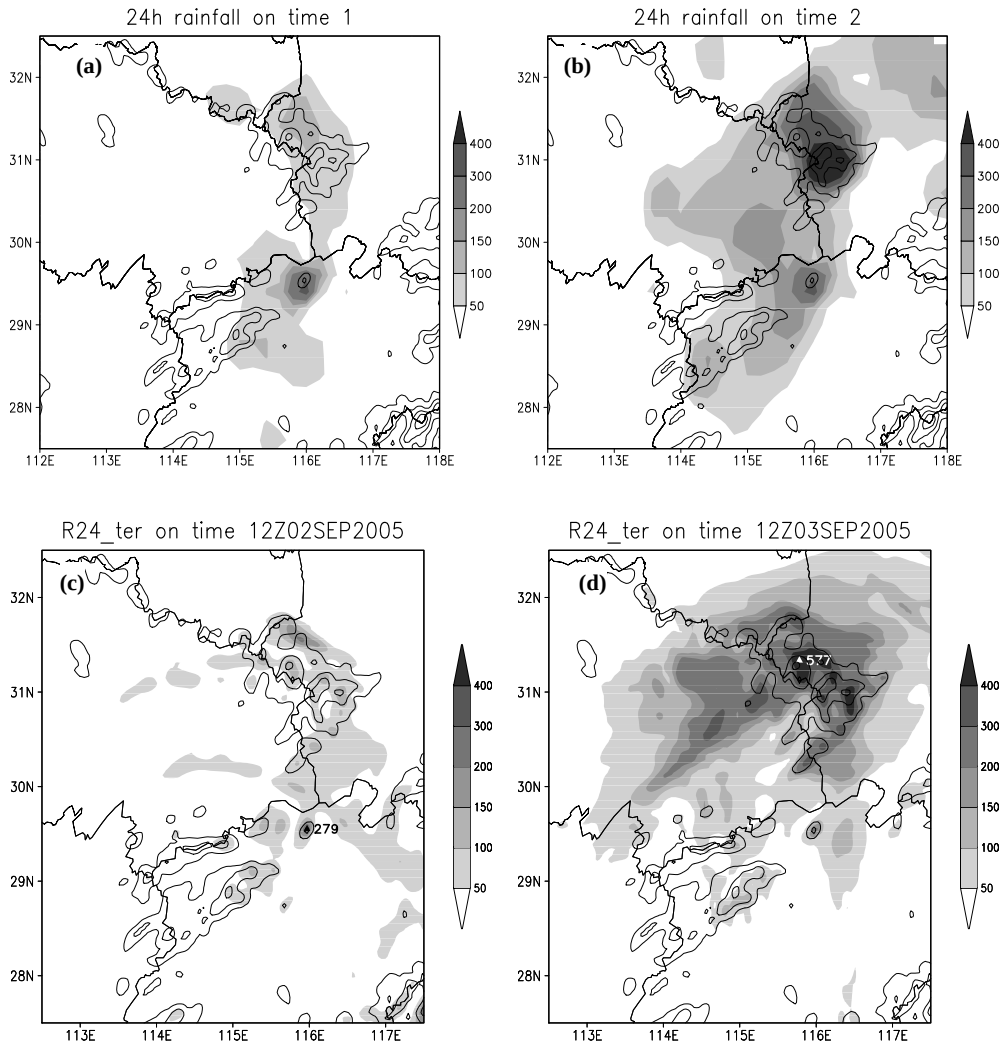

Fig.1. The observed (a,b) and simulated (c,d) 24-h accumulated rainfall with terrain at 1200 UTC 2 Sep (a,c) and 1200 UTC 3 Sep 2005

2) Precipitation

Figure 1a and 1b show the observation of the 24-h accumulated precipitation with the terrain at 1200 UTC 2 September and 1200 UTC 3 September 2005. The corresponding simulations are displayed in Fig.1c and Fig.1d. Their comparisons indicate that the rainfall distribution is alike and the rainfall intensity is equivalent. On 1200 UTC 2 Sep, the rainfall band with north-to-south orientation is simulated as well as the maximum in the Lu Mountains, but the simulated intensity 277 mm is less than the observation 351 mm. On 1200 UTC 3 Sep, the rainfall region of observation is enlarged obviously and rain-band

orientation shift to northeast-to-southwest. The heavy rainfall mainly focuses in the Da-bie Mountains with the maximum at 495 mm. Similarly, the simulated rainfall region is extended and has a northeast-to-southwest axis, the heavy rainfall also distribute in the Da-bie Mountains with the highest as 577 mm. In general, the simulated rainfall is stronger than the observation and its location is slightly shifts to north. As you know, rainfall is the product of complicated physics processes and thus its simulation is always a big challenge. The control experiment has basically described the main rainfall feature and such simulation is encouraging.

Above all, control experiment performed a successful simulation for the process of rainfall reinforcement associated with Talim (2005). Based on this, we further analyze the sensitivity experiments results in the next text.

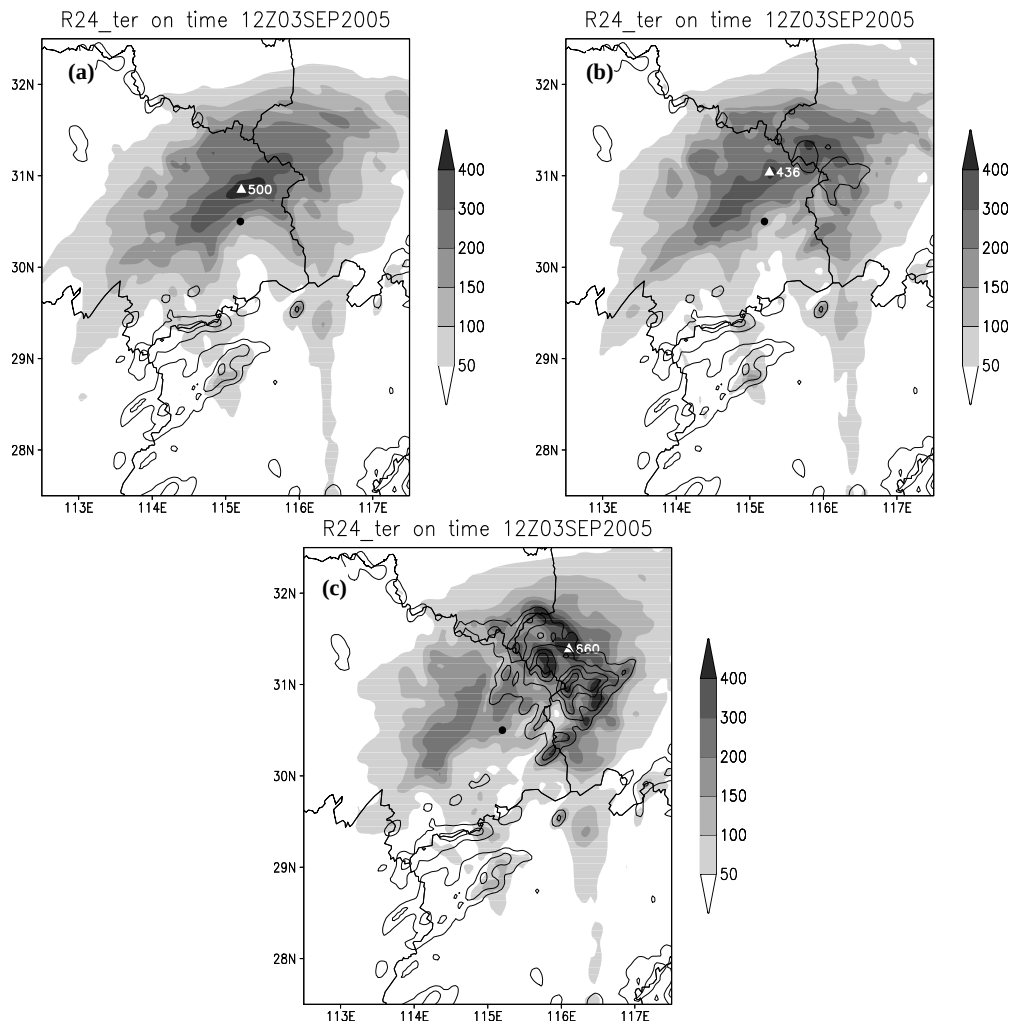

Fig.2. The 24-h accumulated rainfall from experiment T0.0(a), T0.5(b) and T1.5(c) with terrain at 1200 UTC 3 Sep 2005

4. Sensitivity experiment results

1) Precipitation

Rainfall precipitation from sensitivity experiments indicate that during the 24-h integration the intensity and range of rainfall are enhanced with the increase of terrain, the maxima in Lu Mountains are respectively 264, 271, 279 and 285 mm for T0.0, T0.5, CON and T1.5 experiment. From the 24 to 48-h integration (Fig.2a-c), the heavy rainfall mainly moves to Da-bie Mountains and terrain modulated the rainfall obviously. The higher the terrain is, the rainfall distribution is more uneven. Comparison of the T0.5, CON and T1.5 displays heavy rainfall can be blocked to the upslope of Da-bie Mountains, where the amount of rainfall center enhance from 436 to 660 mm with the increase of terrain. It is notable that terrain has minor impact on the total rain band distribution, the rainfall reinforced significantly even when Da-bie terrain is removed. In other word, in this case, there has no relationship between the occurrence of rainfall reinforcement and Da-bie Mountains. The terrain just strengthens the intensity of rainfall reinforcement and makes the rainfall distribution uneven. Moreover, Da-bie Mountains always situate in the northeast azimuth of Talim, warm and wet southeast flow from Talim maintain vapor and energy transfer to mountainous region, which are favorable for rainfall increase. Specifically, the intensity of rainfall center with Da-bie Mountains is larger about 15% than that without topography.

2) Topography impact analysis

a) Convergent line and meso-scale vortex

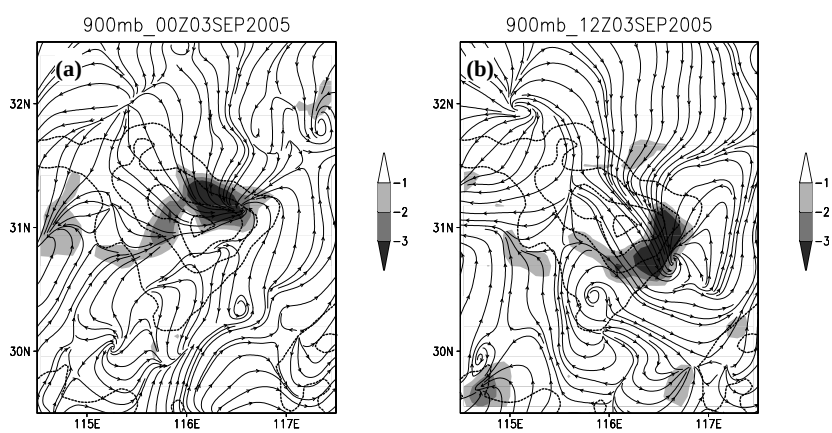

Fig.3. The difference of stream and divergence with terrain (dashed line) at 900 hPa between CON and T0.0 at (a) 0000 UTC 3 Sep and (b)1200 UTC 3 Sep 2005

To highlight the topography effect, figure 3 shows the difference wind field at 900hPa (CON minus T0.0). On 1800 UTC 2 Sep，a meso-scale convergent line between northward flow and southward flow is formed in the Mountains. After 6-h, the convergent move southward slowly and its convergence is larger than $3\times10^{-4}s^{-1}$ (Fig.3a). Interestingly, a meso-β vortex develops in the convergent line and intensifies, consequently, a strong

convergence occurs in the southeastern of Da-bie Mountains (Fig.3b). These results indicate that the topographic effect trigger the formation of convergent line and meso-scale vortex as well as the strong convergence, which are favorable factors to convection and rainfall.

b) Vertical motion

To understand how the terrain affects the rainfall, we calculate the vertical profiles of mean vertical velocity near rainfall center during the rainfall enhancing period from all experiments (see Fig.4a). Comparison of the average profiles shows that terrain mainly impacts the vertical velocity below 450hPa level and the peak increases with the terrain. The peak upward motion with true terrain is about 0.5 m s^{-1}, while that of without terrain is near 0.3m s^{-1}, the former is around 170% of the latter.

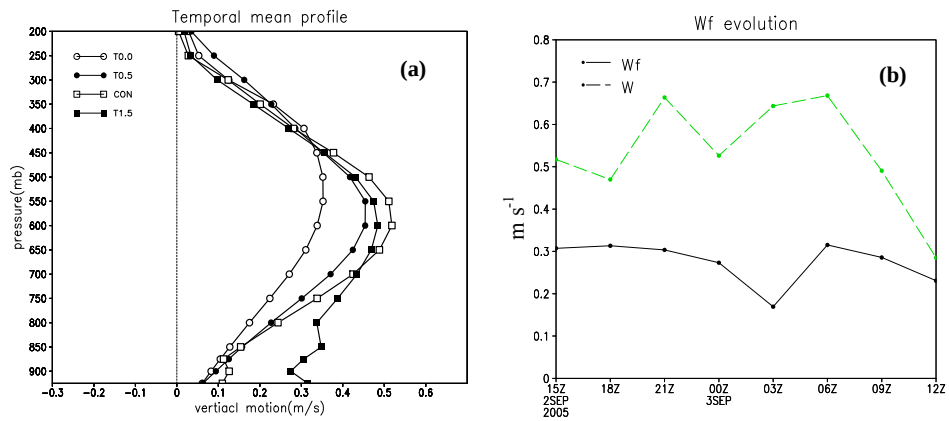

Fig.4. (a)Vertical profiles of mean vertical velocity near rainfall center from 1200 UTC 2 Sep to 1200 UTC 3 Sep 2005 and (b) Time series of the terrain-induced vertical velocity (w_f , solid line, m s^{-1}) near rainfall center and the vertical velocity (w , dashed line, m s^{-1}) at the lowest model level σ =0. 995 in CON experiment.

It has been shown (Tao et al. 1980; Lin et al. 2001; Smith et al., 2009) that the terrain-induced upward motion is favorable for enhancing the ascent and thus the rainfall strengthening. Here, we calculated the terrain-induced upward motion w_f for CON experiment. As indicated in the Fig.4b, the w_f near rainfall center in the Da-bie Mountains accounts for from 40% to 60% of the vertical motion w at the lowest model level (σ= 0.995)in that period, on average, the rate is about 50%. That is to say, the terrain plays important role in enhancing the vertical motion, which will be helpful to rainfall increase.

References

Chen, L., and Y. Ding, 1979: *Introduction to Tropical Cyclones in the Western Pacific.* Science Press, Beijing, 440-473.

Tao, S., et al., 1980: *Rainstorms in China*. Science Press, Beijing, 147-204.

Chen, L., 2007: On Research and Forecasting of heavy rainfall induced by landfalling tropical cyclones. Extended abstracts of the 14th National Workshop on Tropical Cyclones, Shanghai, China, 2007, 3-7.

Fan et al., 1996: *Study on sciences, operational experiments and dynamic theories of typhoons*. Series 4, China Meteorological Press, Beijing, 244pp.

Dong, M., L. Chen, and Y. Li et al., 2010: Rainfall reinforcement associated with landfalling tropical cyclones. *Journal of Atmospheric Sciences*, 2010 (in press).

Wu C. C., T. H. Yen and Y. H. Kuo, 2002: Rainfall simulation associated with typhoon Herb (1996) near Taiwan. Part I: The topographic effect. *Weather and Forecasting*, **17**: 1001-1015.

Smith, R. B., P. Schafer, D. J. Kirshbaum, and E. Regina, 2009a: Orographic enhancement of precipitation inside Hurricane Dean. *J. Hydrometeor.*, **10**, 820–831.

Lin, Y., C. Sen, T. Wang, et al. Some common ingredients of heavy orographic rainfall. *Weather and Forecasting*, 2001, 16(6): 633–660

Changes in tropical cyclone precipitation over China

Fumin Ren[1], Guoxiong Wu[2], Xiaoling Wang[1] ,Yongmei Wang[3]

[1]*Lab for Climate Studies, National Climate Center, China Meteorological Administration, Beijing 100081, China*

[2]*State Key Laboratory of Numerical Modeling for Atmospheric Sciences and Geophysical Fluid Dynamics (LASG), Institute of Atmospheric Physics, Chinese Academy of Sciences, Beijing 100029, China*

[3]*Yuncheng Weather Bureau, Yuncheng, 044000 , China*

1. Introduction

For more than a decade, the importance of analyzing changes in temperature and precipitation extremes has been realized and extensive analyses were carried out [IPCC, 2001]. Recently, an effort was made to design a realistic global distribution of extreme indices [Alexander et al, 2005]. While changes in tropical cyclone (TC) activity have drawn more and more attention, a few studies have addressed the precipitation associated with TCs (IPCC 2002) either in climate models or in observations. Harr et al.[2001] analyzed TC structural characteristics during extratropical transition as they related to expansion of torrential precipitation regions. Shuman et al.[2001] studied torrential precipitation events from TC remnants in the eastern United States. Laing[2001] carried out satellite estimates of TC precipitation (TCP) using Tropical Rainfall Measuring Mission(TRMM), Geostationary Operational Environmental Satellites(GOES), and Special Sensor Microwave Imager (SSM/I) datasets. Meanwhile, by simply defining TCP as that within a radius of 1000 km from the center of a TC, Hasegawa[2005] studied TC and TC torrential precipitation over the western North Pacific (WNP) in present and doubled CO_2 climates simulated by climate models. Englehart et al.[2001] explored the role of tropical storms over the eastern North Pacific in the rainfall climatology of western Mexico by defining TCP as that within a radius of 550 km from the center of a TC . Using an objective analysis technique, Ren et al.[2002] and Gleason et al.[2000] analyzed the climate characteristics of TCP in China and the United States, respectively.

Some studies indicate that there was no statistically significant long-term trend in both the number and the intensity of TCs in WNP over the past 4-5 decades [IPCC, 2001; Yeung et al., 2005; Chan et al., 1996]. However, two recent studies argued that TC intensity has increased markedly in recent decades [Emanuel, 2005; Webster et al., 2005]. In addition, Wu et al. [2005] found that the TC influence on the South China Sea has considerably decreased and the two prevailing typhoon tracks in the WNP have shifted westward over the past four decades, leading to increasing typhoon influence over the subtropical East Asia. However, little is known about the influence

of the documented intensity and track changes on TCP.

Several discontinuous spiral rainbelts often occur in a TC, which are generally asymmetric around the TC center (Elsberry et al., 1987). Therefore, simply using the distance between station location and TC center location, namely a circle around the TC center, cannot accurately catch TCP. Recently, an advanced technique named the Objective Synoptic Analysis Technique (OSAT), which is capable of partitioning TCP in China, has been proposed [Ren et al., 2005].

In the present study, we use the TC track dataset and a station precipitation dataset to examine the climatological characteristics of TCP, with special focus on its long-term changes and TC-induced torrential precipitation events in China.

2. Data

The information about the WNP TC positions used in this study is from Shanghai Typhoon Institute of China Meteorological Administration(CMA). The dataset ranges from 1949 to 2004 and is believed to be more accurate for those TCs that affected China because the positions have been carefully validated. The daily precipitation dataset used in this study includes 677 China stations that represented the spatial distribution of precipitation in China, in which 659 stations are over the mainland of China and the Hainan Island from National Meteorological Information Center/CMA and the other 18 stations are in the Taiwan Island. A close inspection of the dataset reveals that time coverage of the daily precipitation for the 659 stations ranged from 0UTC to 24UTC, and the number of stations increased sharply from about 170 in 1951 to about 570 in 1957. Since the number of stations can affect the results of the estimated TCP, the period 1957~2004 is selected as the period for analyzing long-term trend in TCP.

3. Analysis Method

The TCP can result from the TC eyewall and spiral rainbands, and from the interactions between the TC circulation and other weather systems. The spiral rainbands are generally asymmetric with respect to the TC center. The OSAT imitates the analysis procedure taken by an operational weather forecaster. There are two steps: First, based on the spatial structure of the observed station precipitation, all the precipitation observations can be grouped into different rainbelts. Then, given the distances between a station and the TC center, between the precipitation center of the rainbelt which includes the station and the TC center, and the distance function between the TC center and the distribution of the rainbelt, one can identify whether the station precipitation is TCP by comparing these distances with the specified TC maximum size (D_1) and mininum size (D_0) [Ren, et al., 2005]. In this study, D_0 and D_1 vary with TC intensity. The typical values for D_0 and D_1 are 500 km, which is the maximum distance between a TC center and the associated squall lines, and 1100 km, which is usually given as the maximum radius for a TC outlet (Brand, 1972, Elsberry, et al., 1987), respectively.

In this study, a TC is defined as an influencing TC when its rainbelt is over the mainland of China or any of the two biggest islands of China, Taiwan and Hainan. The

influencing TCs include landfall TCs and those passing offshore around China.

The rainfall data are interpolated on 0.5°×0.5° latitude-longitude grids to calculate the rainfall volume for a TC. Inverse-distance interpolation was applied to transform the TC rainfall data. To limit the possible expansion of the TC rainbelt, the gridding procedure is limited to the rainbelt region. The area represented by a given grid can be calculated as,

$$A_{grid}=(\pi r/360)^2\times\cos(\varphi), \quad (1)$$

where r is the radius of the Earth, φ is the latitude of the grid, and A_{grid} is in km^2.

The rainfall volume for a given grid can be

$$V_{grid}= A_{grid}\times P_{grid}\times 10^{-6} \quad (2)$$

where P_{grid} is the grid precipitation in mm, V_{grid} is in km^3. The TCP volume is the total of the grid rainfall volume (V_{grid}) in the TC rainbelt.

4. Results and Discussion

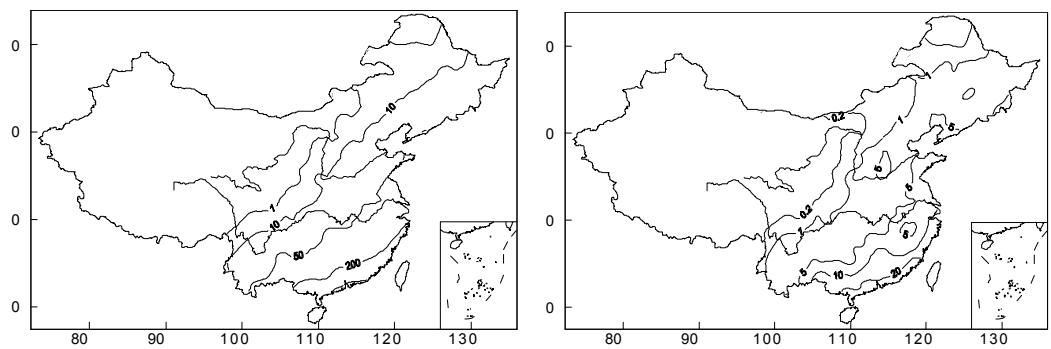

a b

Fig.1 Climatology of station TC precipitation during 1971-2000.
a. Spatial distribution of average annual TC precipitation(unit: mm);
b. Spatial distribution of ratio of average annual TC precipitation to average total rainfall

Figure 1a presents the distribution of the annual mean TCP averaged over 1957-2004. TCs mainly influenced central and eastern China, roughly east of 98°E. Generally, annual TCP above 200 mm is observed in the southeastern coastal regions including the Taiwan and Hainan Islands. Significant TCP usually occurred in the mountainous regions, which is not shown in Figure 1a. The annual TCP exceeds 500 mm in central-eastern Taiwan, central-eastern Hainan and along the eastern coastline in South China. Some Taiwan stations received 1000~1350mm annual TCP. The TCP decreased northwestward quickly, with values less than 10mm in northern and western parts of the TC influenced region, while the annual TCP was 50~200mm in the lower valley of the Yangtze River, most regions south of the middle and lower valleys of the Yangtze River.

Figure 1b shows the distribution of the ratio of annual TCP to total annual rainfall averaged over the period 1957-2004. In Taiwan, Hainan, the southeastern coastal regions, and the easternmost Shandong Peninsula, TCP contributes more than 10% precipitation, with 20~30% in most of Taiwan, the coastline south of 25°N, and 30~40% in most of Hainan and locations of Taiwan and the coastline. In southernmost Taiwan and westernmost Hainan, TCP accounts for 40-45% of the total precipitation. Meanwhile, the ratios decrease northwestward quickly, with values less than 1% in northern and western parts of the TC influenced region.

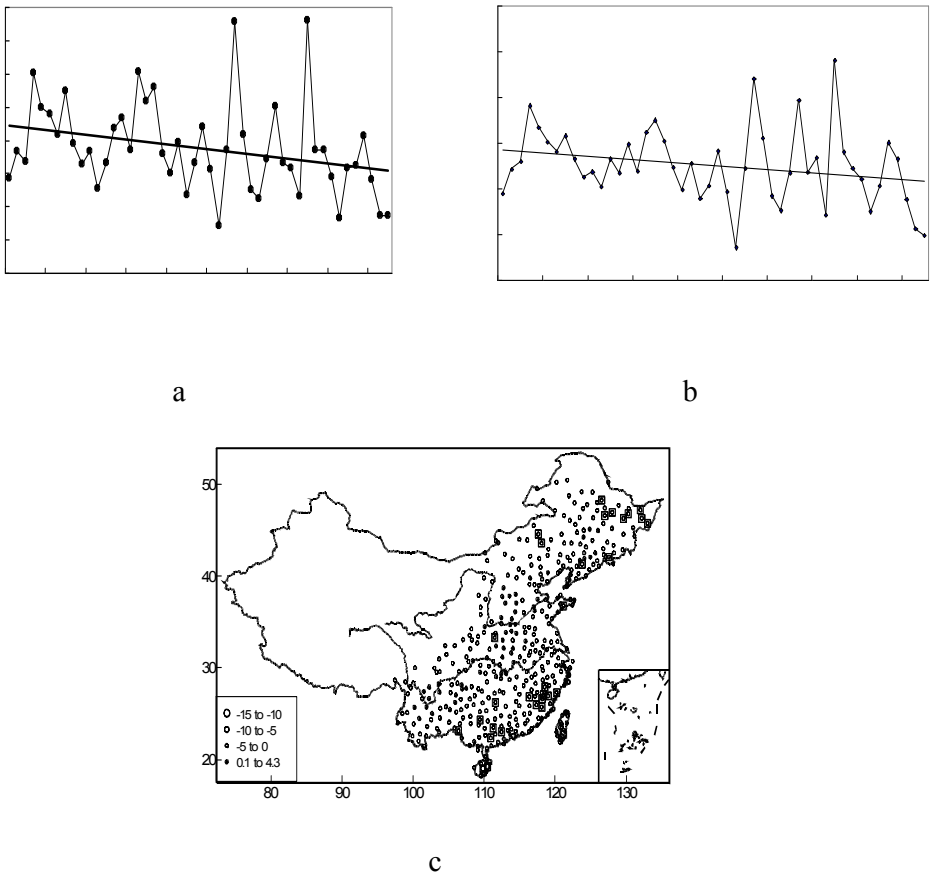

Fig.2 Variations of TC precipitation

a. Variations of total annual volume of TC precipitation for China(unit: km^3)

b. Variations of accumulated number of times with torrential TCP(≥50mm/day) of individual station

c. Spatial distribution of trends of annual typhoon precipitation(unit: mm/yr) (square boxes indicating statistically significant at 0.05 level by Kendall test)

Figure 2a displays time series of the total annual TCP volume for China. First, a downward linear trend can be found during 1957~2004, with a rate of -3.0 km^3/yr. A Kendall test indicates that the trend is statistically significant at 0.01 significance level.

Second, the TCP includes interdecadal variation and prominent year-to-year fluctuations. In the early 1960s, early 1970s, 1985 and 1994, China received much above-normal TCP, with maximums of 761.3 km^3 and 759.2 km^3 in 1994 and 1985, respectively. Meanwhile, in the late 1960s, 1983 and 1998, much below-normal TCPs were observed in China, with minimum of 141.8 km^3 in 1983.

Figure 2b presents variations of the total annual frequency of the torrential TCP events (≥50mm/day) for individual stations. A significant (at 0.05 level) decreasing trend can be clearly seen with similar interdecadal variations and year-to-year fluctuations as shown in Figure 2a for the annual TCP volume. The most frequency of the torrential TCP events occurred in 1994 and 1985, with least frequency in 1983. Further examination shows that the total annual frequency of the torrential TCP events is well correlated with the annual TCP, with a correlation coefficient being 0.94.

The time series of annual TCP at each station were also examined for the long-term trends. Results displayed in Fig.2c show that decreasing trends exist in most of the stations, with less than -5 mm/yr in southern Taiwan, central-eastern Hainan. The decreasing trends reached -10~ -15 mm/yr in southeastern Taiwan. The increasing trends primarily occurred along two belts extending from southwest to northeast. One is from the middle valleys of the Yangtze and Yellow Rivers to northeastern China. Further inspection reveals that, while decreasing trends are statistically significant at the 0.05 level by a Kendall test, the increasing trends are very small (between 0.05~0.5mm/yr) and no increase trend is statistically significant during the period 1957-2004.

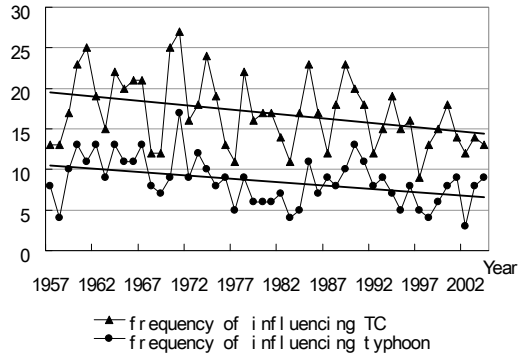

Fig.3 Variations of frequency of influencing TC and influencing typhoon(MSWS ≥32.7m/s) for China

Figure 3 shows time series of the frequency of TCs and typhoons that affected China from 1957 to 2004. The frequencies of the influencing TCs and typhoons also display significant decreasing trends during the period, with 0.05 and 0.01 significant levels, respectively. Both of them also show obvious year-to-year fluctuations, with maximums of 27 and 17 both in 1971.The variations in frequency of influencing TCs and TCP imply that, during the past 48 years, China experienced decreasing typhoon

influence.

In order to explain the variations in TCP, the relationships between the TCP and the influencing TCs and typhoons were calculated. The two correlation coefficients are 0.62 and 0.47, which are both statistically significant. Therefore, the decrease in influencing TCs may be the main reason for the decrease in TCP. For year-to-year fluctuation, TC tracks were inspected for three years of 1971, 1985 and 1994, which show most significant year-to-year fluctuations. It suggests that the most important factor for annual variation in TCP in China is the tracks of landfall TCs and the length of their lifetimes over the land, rather than the number of influencing TCs.

5. Summary

In this study, the TCP of the China 677 weather stations from 1957 to 2004 was analyzed with a special focus on its long-term changes because some recent studies have argued that tropical cyclone activity over the WNP has been changed in response to the ongoing global warming. We examined the TCP spatial distribution, its ratio to total annual rainfall, and the changes in the TCP volume and the total annual frequency of the torrential TCP events.

As expected, tropical cyclones significantly contribute to the annual rainfall in southern, southeastern, and eastern China, primarily Taiwan, Hainan, and most of the southeastern coastal regions received more than 500mm annual TCP, contributing about 20~40% of the total annual precipitation. The TCP and its contribution to annual precipitation generally decrease with the increase of latitude.

Despite interdecadal and interannual variations, a significant downward trend is found in both the TCP volume and the total annual frequency of the torrential TCP events over the past 48 years. Both influencing TCs and typhoons also show significant decreasing trends during the period 1957-2004. These changes strongly suggest that the TC influence has been decreased over the past 48 years. We also examined the time series of the TCP ratio to the annual precipitation averaged over the southern and southeastern China, where TCP contributes significantly to the annual precipitation. A decreasing trend is also found in the ratio, further indicating that China has experienced decreasing TCP over the past 48 years.

Although further study is needed for the exact cause of the decreasing trends found in this study, correlation analysis indicates that the decrease in number of the influencing TCs may be the main reason for the decreasing trend in the annul TCP. Recently, Wu et al. (2005) examined the changes in the prevailing tropical cyclone tracks in the WNP basin and found that more and more tropical cyclones took the two recurving prevailing tracks over the WNP while decreasing tropical cyclones moved westward and northwestward. As a result, the influence of tropical cyclones on South China Sea and southern China decreased over the past 40 years. Their results are consistent with decreasing TCP in China. Note that the decreasing TCP trend is dominated by the TCP changes in southern China.

The Verification of Tropical Cyclone Rainfall Predictions with Global Models of CMA and JMA

WANG Yu SHEN Xuesun CHEN Dehui
(Numerical Prediction Center, Beijing, 100081)
wangyu@cma.gov.cn

1 Introduction

The occurrence num bers of TC (T ropical Cyclone) in 2009 were significantly decreased in com parison to the climatology over the South China Sea and the W est Pacific. However, the more number and the earlier time of TC which landed on China were observed. And it was showed the hea vy precipitation zones were located along with the southeast coast line of China with a U shape in 200 9. As the intensity of the most of landing TC in China m ainland was weaker, it was more dif ficult to forecast precipitation caused by the landing TC . Meanwhile T yphoon Morakot caused the unprecedented disastrous flooding within past 50 years in Taiwan Island: at least 491 dead and several hundreds m issing. The dist ributions of rainfa ll were uneven and complicated.

The archiving data sets in NMC included the tropical cyclones which occurred in Western North Pacific and the South China Sea and the 24h accumulated precipitation (from 00UTC to 00UTC) from 2510 observatio n stations in China m ainland in 2009. These data sets were used for the analysis study in this paper. It observed that the TC landfall started with a typhoon on June 22, and ended with a tropical depression on October 23 2009. During the TC season of four months (July, August, September and October) in 2009, 9 tropical storm s and 2 tropi cal low pressures, causing the heavier precipitation, were observed. In order to well understand the behaviors of the NW P models, a typhoon torrential rain day was defined: when th e tropical weather systems were dominant and the am ount of a bove 50mm precipitation accumulated over 24 h (from 00UTC to 00UTC) was obs erved in m ore than 3 weather statio ns at least. In total, a number of 32 typhoon torrential rain days was identified during the TC season of four months. The m ean rainfall distri bution for the 32 typhoon to rrential rain days was calculated in this paper, and was intercompared to those predicted for the same 32 typhoon torrential rain days by CMA 'T639 m odel and JMA 's T959 m odel, respectively. Certainly, the forecasts were st ill verified with the statistical methods to understand well the performance of the NWP models in comparison to the forecasters. In order to give m ore details of typhoon rainfall process forecast in the dif ferent provinces which were more af fected by th e typhoon landfalls, the evolution of rain process was verified. The resu lts showed th at th e typh oon rainfall forecasts in Guangdong province were better than those in Hainan and other provinces.

2 Distributions of observationed precipitation for the specified TC period in 2009

Figure 1 illustrated the m ean observe d rainfall distribution for the 32 typhoon

torrential rain days in 2009. The distribution of the typhoon rainfall was mainly along the southeast coastal of China. The stronger rain zones covered Leizhou Peninsula of Guangdong province and the north of Hainan province. In this year, Hainan province typhoon rainfall was dominant in all 32 typhoon torrential rain days. Except for the southern area, daily rain rate exceeded only 20 mm/d, and the yearly amount of precipitation exceeded 600 mm. In addition, the typhoon rainfall spatial distribution was in U shape: less precipitations were observed in the central part of China mainland. The precipitation of the southeast coastal and the east of southwest of China is much more than other regions. In the most parts of Hubei, Hunan and Jiangxi provinces, the rainfall was less relatively. The distribution shape is due to blowing northeast wind in 110 E and leading to less rainfall when the typhoons landed in the southeast coastal. Why were there more rainfall in the southwest? It needs further research on it.

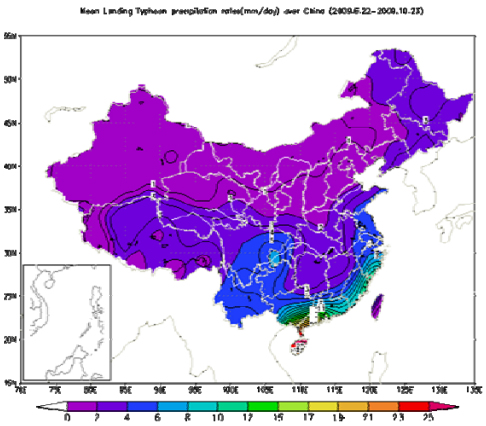

Fig.1 Mean observed rainfall distribution for the 32 typhoon torrential rain days in 2009

3 Mean predicted rainfall distribution by CMA's T639 and JMA's T959

Figure 2 and figure 3 depicted the mean predicted rainfall distribution by CMA's T639 and JMA's T959, respectively. The predicted rain zones were similar to the observation for all 1.5 to 4.5 days forecasts. The 60 h forecast was better in agreement with observation for both the general distribution and the heaviest rainfall locations. But the both models under-estimated the intensity of typhoon precipitation in comparison to the observation, the intensity predictions by T639 model was better than those by T959 model.

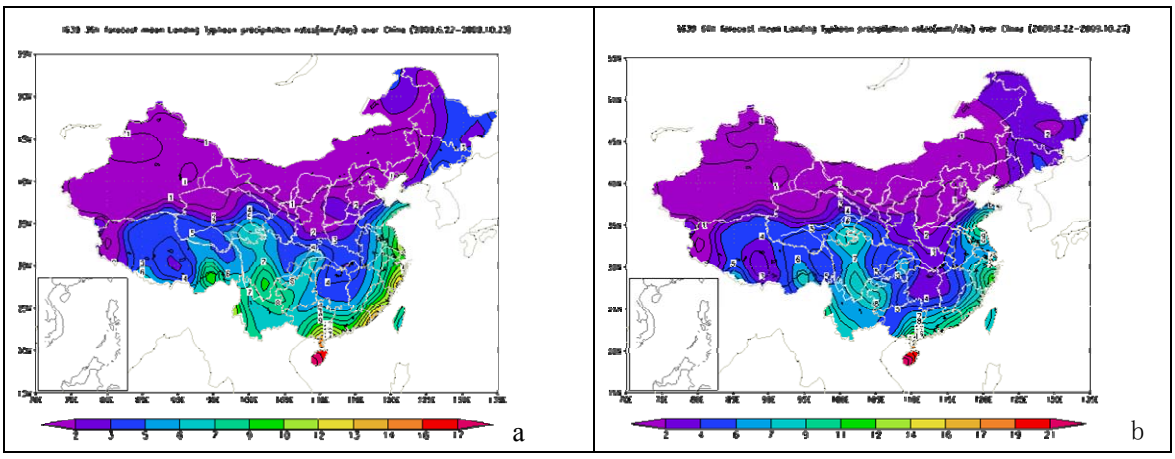

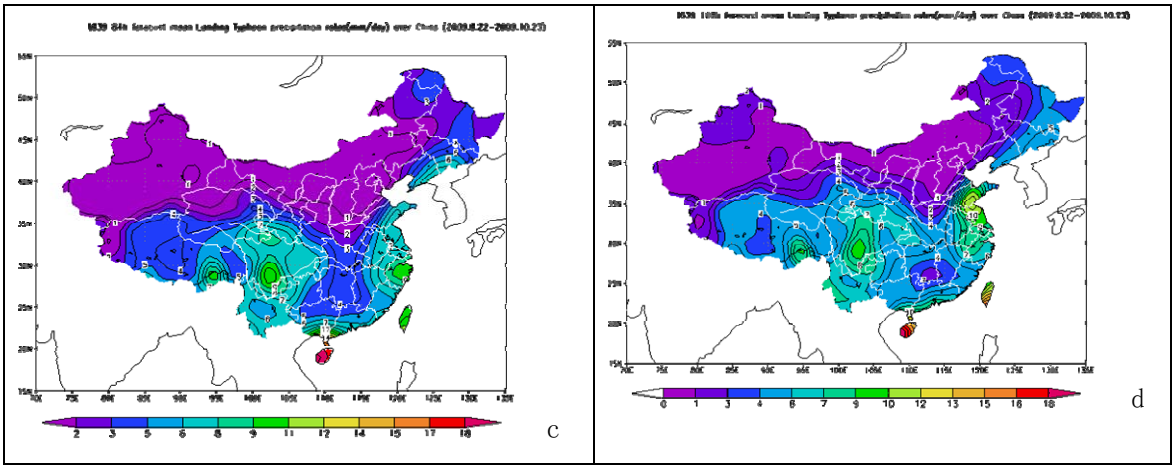

Figure 2 as Fig.1, but predicted by CMA's T639 model (a,36h, b, 60h, c,84h, d,108h)

The parttern in U-shape of the rainfall spatial distribution of 84 h forecasts was still easily identified for both T639 and T 959 models, but with over-estimations of precipitation in East, South and West parts of China mainland. For 108h forecasts, the rainfall amount decreased in general with a relatively indistinct parttern in U-shape of the rainfall spatial distributi on. After 132h forecast the rain belts do not display any clear consistent with observation.

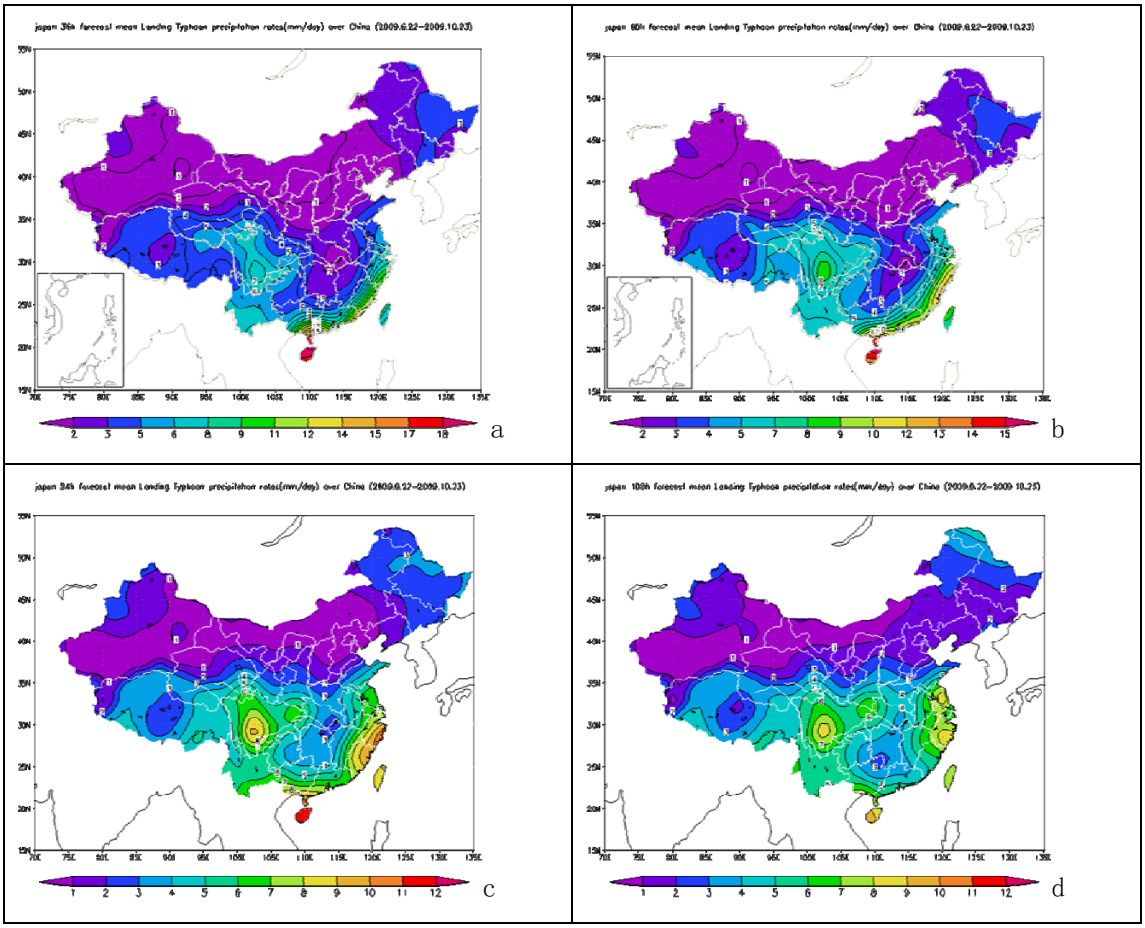

Figure 3 as Fig.1, but predicted by JMA's T959 model (a,36h, b, 60h, c,84h, d,108h,)

4 Verification of precipitation forecasts by CMA'sT639 and JMA's T959 models

over China mainland for the 32 typhoon torrential rain days

The traditional statis tic m ethods TS(Threat Score) and Bias were used for the verification of precipitation forecast s by CMA 's T639, JMA 's T959 and the forecasters. Figure-a showed that in general, TS by forecasters were higher than those by both NWP m odels nearly for all thresh olds, except for the threshold of above 10mm/d of 24h forecasts. This m ean that the forecasters could well "ingest" all most recently available information of predictions and observations to give better forecasts than the model. However, bias by forecasters was also higher than those by both NWP models for the higher thresholds of above 10mm/d - 50mm/d for 24h – 108h forecasts. Beyond of 120h, the bias by T639 was highe st. In other word, T639 m ostly over-estimated the precipitation beyond of 120h of forecast length.

Meanwhile, for the cases of Goni and Morakot of which the typhoon tracks were complicated, the NW P m odels gave better predictions of pr ecipitation than the forecasters.

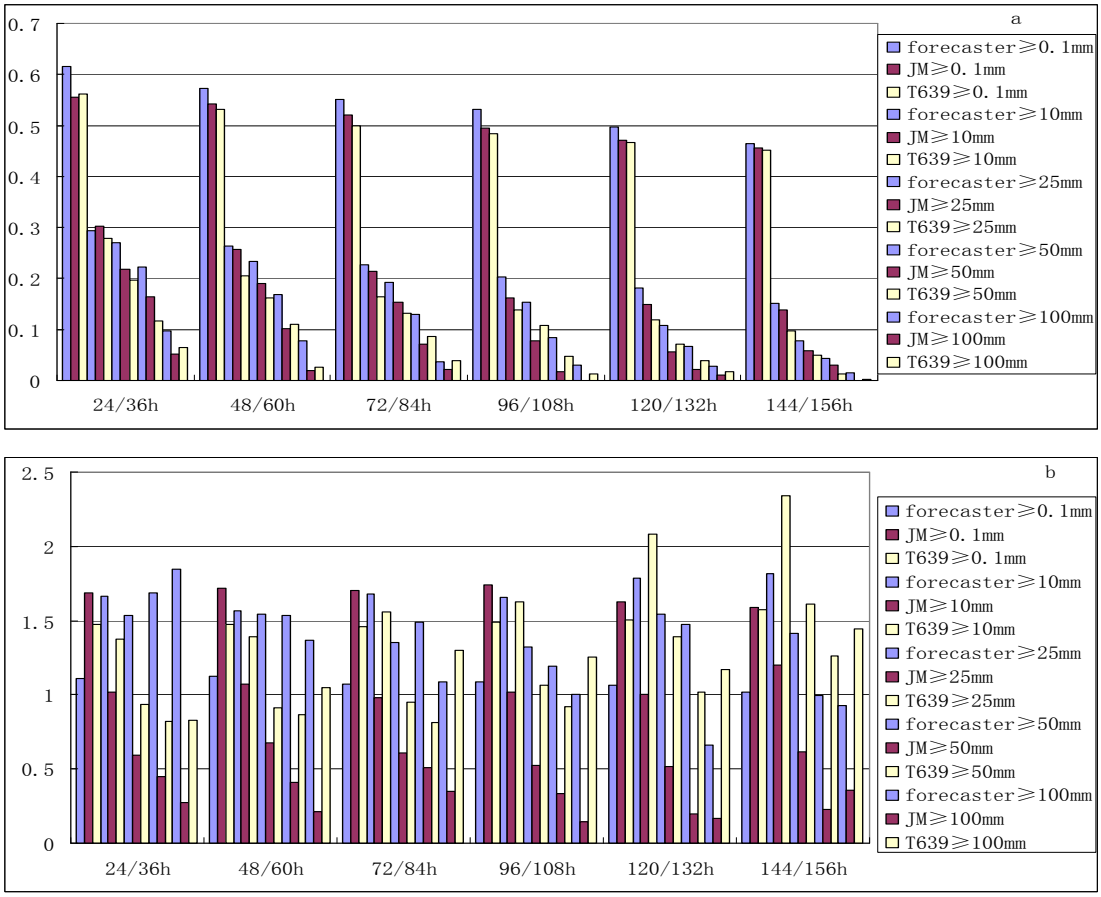

Figure 4 The mean TS and Bias of precipitation forecasts by CMA's T639, JMA 's T959 models and the forecaster s over China mainland for all 32 t yphoon t orrential rain da ys in 2009: (a) TS ; (b) Bias. Th e five thresholds of 24h accumulated rainfall were chosen for the verification: above 0.1mm/d, above 10mm/d, above 25mm/d, above 50mm/d and 100mm/d.

5 The processes (or cases) verification of precipitation forecasts

Because the TC landfall mainly affected Hainan, Guangdong, Guangxi and Fujian

provinces in 2009, the TC rainfall processes verification were specifically conducted in this paper for these four provinces. The results showed that the evolution of process rainfall was not well predicted beyond 3 days ahead. From the daily mean rain rate of typhoon rainfall processes over Hainan province where typhoon affected most frequently in 2009, it showed that the forecasts of JMA's T959 model were slightly more skilful than those of CMA's T639 model. But for over 20 mm/d rainfall it underestimates the amount of rain. Moreover the forecast extremes of most typhoon rainfall processes exit ahead or behind of observation. Only is over 50mm torrential rain the time of extremes forecast accurately for 0917 typhoon – Parma. The typhoon rain amount of T639 60h forecast is near to observation, particularly for Goni, Mujigae and the tropical depression in October over 50mm torrential rain. In addition the extreme date of 0917 typhoon is consistent with the observation for t639 forecast, but the amount is less than real rain.

The typhoon precipitation processes forecast for Guangdong is better than for Hainan for NWP models. The changing tendency of rainfall processes of two models is insistent with the real rain observation, and the intensity is near to the observation, particularly the for 36h and 60h forecast.

Moreover for the Guangxi tropical cyclones rain the tendency of processes changing is insistent with real rain, meanwhile the 36h forecast for Molave and Koppu is accurate, and the tendency and the intensity is near to the real rain. While the precipitation prediction of Morakot typhoon in Fujian province by T639 is better than by Japanese model in short term,

6 Summary

The analysis results showed the rain belts of 60h forecasts by both models (T639 and JMA) were similar to the observations. The location of rain belts and maximum rainfall center were also well in agreement with the observations. But the rain belts of 3 day forecast were oriented towards the north of the observed area, and the models under-estimated the amounts of precipitation in comparison to observation.

The statistical verification showed the forecasters of NMC made the better forecast than the NWP models. TS by forecasters were higher than those by the NWP models and the bias by forecasters were still higher than those by the NWP models for the higher thresholds of above 10mm/d - 50mm/d for 24h – 108h forecasts.

The verifications of precipitation forecasts were conducted specifically process by process in the Southern and South-eastern coast line of China, such as Guangdong, Guangxi, Fujian and Hainan provinces where TC affected more frequently than in other regions of China. The verification results showed that the predictions of NWP models were more skillful in the precipitation forecasts for Guangdong and Guangxi provinces than for Hainan province.

7 References:

1 钱传海，路秀娟，陈涛，2009:引起“碧利斯”强降水的MCS 数值模拟研究，气象，4，11-19

2 王咏梅，任福民，李维京等，2008:中国台风降水的气候特征， 热带气象学报，3，233-238

3 王雨 闫之辉，2007:降水检验方案变化对降水检验评估效果的影响分析，气象，12，53-61

Advances in Understanding the "Perfect Monsoon-influenced Typhoon"

Russell L. Elsberry[1], Cheng-Shang Lee[2], Chun-Chieh Wu[2], and Tai-Chi Chen Wang[3]
[1]Department of Meteorology, Naval Postgraduate School
[2]Department of Atmospheric Sciences, National Taiwan University
[3]Department of Atmospheric Sciences, National Center University
elsberry@nps.edu

1. Introduction

In the book and movie "The Perfect Storm," a special set of circumstances (including a human element) led to a disaster because a ship encountered extreme winds and waves. By analogy, the disaster in which at least 500 people in the mountain village of Shiaolin died when a landslide was triggered by extreme precipitation in Typhoon Morakot may justify it to be labeled as "The Perfect Monsoon-influenced Typhoon." Typhoon Morakot was the deadliest typhoon to impact Taiwan in recorded history with 619 confirmed deaths, 76 missing persons, and roughly NT $16.4 billion (USD 547 million) agricultural losses. This typhoon produced 2 855 mm of rain, which greatly surpassed the previous record of 1994 mm set in Typhoon Herb (1996). This slow moving storm also caused widespread damage in China with nearly 6000 homes destroyed and 136,000 homes that were damaged at a cost of USD 1.3 billion.

In the case of Morakot and other extreme rain events over Taiwan, the monsoon influence that led to the long duration and intense rainfall (Fig. 1) then triggered the landslide that wiped out the entire village. In these cases, the southwest monsoon flow provides water vapor flux to a heavy rain area well to the south of the center (Fig. 1). Large moisture convergence between the monsoon flow and the equatorward moisture flux on the west side of the typhoon then leads to an east-west oriented rainband over the Taiwan Strait to the west of the CMR. However, this rainband only occurs when the typhoon is in a limited range of positions relative to the CMR. Furthermore, a long duration of the heavy rain in a concentrated region of the CMR will only occur if the typhoon is slowly moving. If the typhoon is moving at typical translation speeds, the heavy rain at a point will be relatively transient.

In summary, the perfect monsoon-influenced typhoon that leads to extreme precipitation and associated flooding and potential landslides such as in Morakot requires a special combination of factors: (i) Strong southwesterly monsoon winds; (ii) convergence between the typhoon circulation and monsoon flow to form an east-west oriented convective band over the Taiwan Strait that is quasi-stationary and long-lasting; (iii) typhoon in specific locations relative to the CMR and moving slowly; and (iv) steep topography that provides rapid lifting of the moist air stream over a limited horizontal area such that the heavy precipitation is highly concentrated.

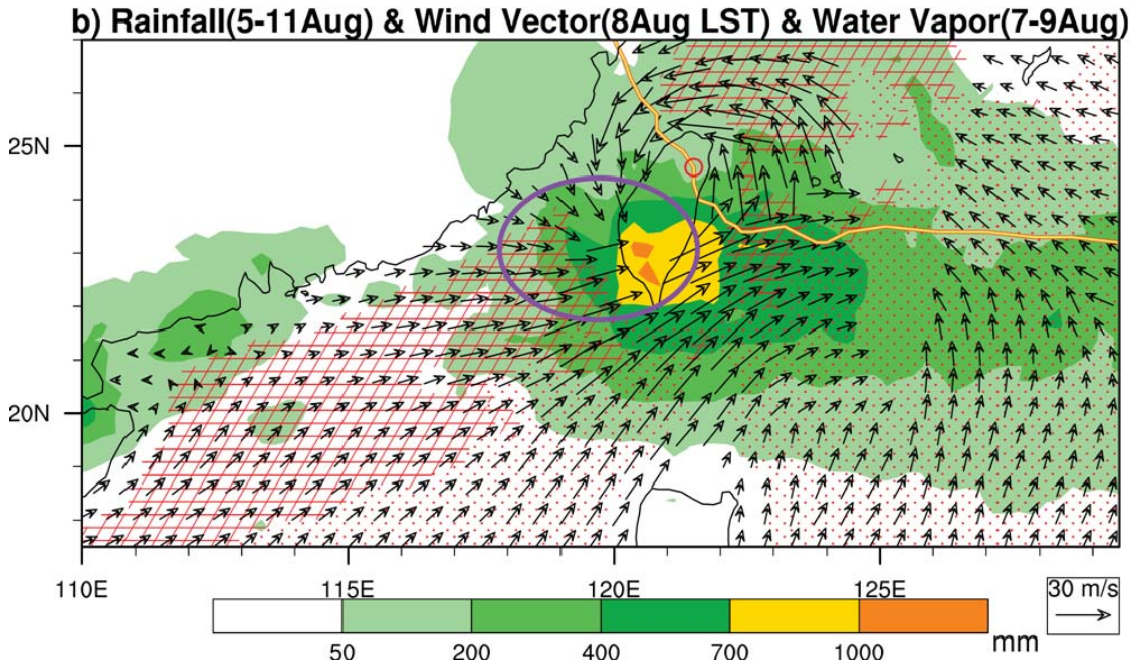

Fig. 1. b) Wind vectors on 9 August 2009 and water vapor transport averaged over 7-9 August with arrows indicating the convergence between the southwesterly monsoon flow and the outer circulation of Typhoon Morakot (Hong *et. al.* 2010).

The first objective of this review is to use presentations at the *International Workshop on Typhoon Morakot (2009)* in Taipei, Taiwan during 25-26 March 2009 to describe extensive research with historical data sets, new radar observations, and numerical modeling that have advanced understanding, and that this research is then leading to modifications of existing, and development of new, forecasting tools to improve forecast guidance. The second objective is to describe gaps in understanding and the advanced forecast guidance tools that are considered to be required to improve warnings of these extreme precipitation and flooding events in monsoon-influenced typhoons.

2. Contributions of the monsoon flow

Even if it is uncertain as to whether Morakot originated from a monsoon gyre or a monsoon depression, the southwesterly monsoon flow and the associated southwesterly water vapor flux played a key role in the extreme precipitation over southern Taiwan. Chien et. al. (2006) had previously studied the heavy rain over southern and central Taiwan associated with northward-moving Typhoon Mindulle (2004) that also featured a convergence line between the typhoon circulation and the southwesterly flow of the monsoon. They examined 56 y of the Joint Typhoon Warning Center northward-moving tracks near Taiwan and found that 33 of the 59 cases were associated with a southwesterly monsoon flow. However, the remaining 26 cases did not have southwesterlies, so a sizeable fraction of these cases did not interact with the monsoon flow.

3. Contributions of the east-west oriented convective band

Chuang and Wei (2010) used the C-band dual-polarization radar in Makung, Taiwan and the S-band Doppler weather radar in Qigu to analyze the kinematic structure of the convective cells in Typhoon Morakot during 2200 UTC 8 August to 0600 UTC 9 August. A linear rainband oriented east-west existed in the vicinity of the Taiwan west coast with a significant confluence between the westerly flow and the southwesterly flow. The dual-Doppler radar wind analysis documented a jet-like westerly flow between 2 km and 5 km with a maximum exceeding 24 m s $^{-1}$ that was associated with the east-west rainband. New cells developed upstream of the confluence line and propagated westward inland toward the CMR.

Wang et. al. (2010) utilized the entire Taiwan weather radar network of six Doppler radars and four dual polarization radars during five stages of the Morakot passage: (1) Approach to Taiwan; (2) Slow movement; (3) Landfall; (4) Typhoon center in Taiwan Strait; and (5) Approach to Fujian Province. From the radar analyses of Tang (2010), strong east-west oriented rainbands repeatedly formed during stage (4) near southwestern Taiwan along the convergence zone between the typhoon circulation and the southwesterly monsoon flow (Fig. 2). Notice the east-west band designated D3 in Fig. 2a that extends from over the Taiwan Strait at the edge of the radar coverage to the region of the southern CMR where the landslide occurred. Individual convective cells in the bands are shown in the horizontal radar reflectivity depiction at 4 km at 1600 LST 8 August 2009 (Fig. 2b). The curvature of the rainband suggests it is related to the outer circulation of Typhoon Morakot and that deep convective cells are beginning at the western end and grow as they propagate along the band toward the coast. These deep convective towers persisted for about two hours and moved rapidly toward the island. A north-south cross-section through one of the convective cells (not shown) indicates a strong updraft on the north side (side toward typhoon center) with a strong downdraft in the mid-troposphere on the south side. At this time, the strongest low-level relative inflow to the band was from the south. The corresponding vertical cross-section of the wind speeds indicates the deep convective cell was on the southern boundary of a low-level jet with speeds of 35-45 m s $^{-1}$. Clearly, this low-level jet was transporting large amounts of water vapor toward the west coast of Taiwan and the southern CMR, and this was contributing to the extreme precipitation.

Although these rainbands generally propagated southward, the major devastating rainband oscillated between 22.5°N and 23.5°N, as indicated in the Hovmoller diagram in Fig. 3. This oscillatory motion of the rainband appeared to be related to a reversal in the relative strength of the low-level inflow from the south and then from the north. These radar studies provide conclusive evidence of the convective cells that build in the convergence line between the typhoon circulation and the southwesterly monsoon winds, and that the east-west orientation of this rainband directed the convective cells toward the CMR.

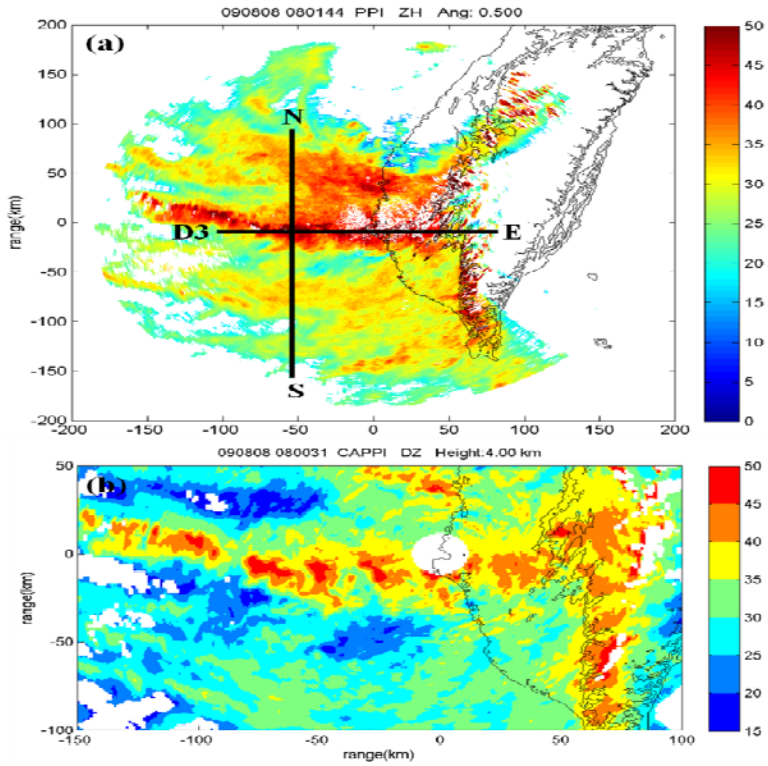

Fig. 2. (a) Plan-position indicator of the radar reflectivity (dBZ, scale on right) at 0801 LT 8 August 2009 as the principal rainband designated D3 extended from over the Taiwan Strait to the CMR. (b) Radar reflectivity at 4 km at 0800 LT 8 August indicating individual convective cells along the rainbands (Wang *et. al*. 2010).

4. Contributions due to typhoon location and slow translation

Yeh and Chang (2009) updated a previous climatological study of the average rainfall amounts when a typhoon existed within various 1° latitude by 1° longitude boxes around Taiwan. This new study utilizing the 400 automated surface observation sites did not fundamentally change the distribution in various regions of Taiwan. However, this study re-affirms that large rain accumulations are to be expected in the southern CMR region where the disastrous landslide occurred during Morakot when the typhoon is near the northern tip of Taiwan. However, these are average rainfall amounts, and do not take into account topographic irregularities. Furthermore, the climatological study does not take into account the typhoon translation speed (or direction).

Kuo et. al. (2010) demonstrated that large variability exists in translation speed of typhoons near Taiwan. They defined the translation speed of a typhoon crossing Taiwan as the distance between the landfall and departure points divided by the crossing time. Many of the largest rainfall events associated with tropical cyclones have occurred when this storm translation speed was small. Indeed, Typhoon Morakot had one of the slowest translation speeds while it was in the Taiwan Strait and this is clearly an important factor in the duration of the heavy rainfall amounts both in Taiwan and in mainland China region.

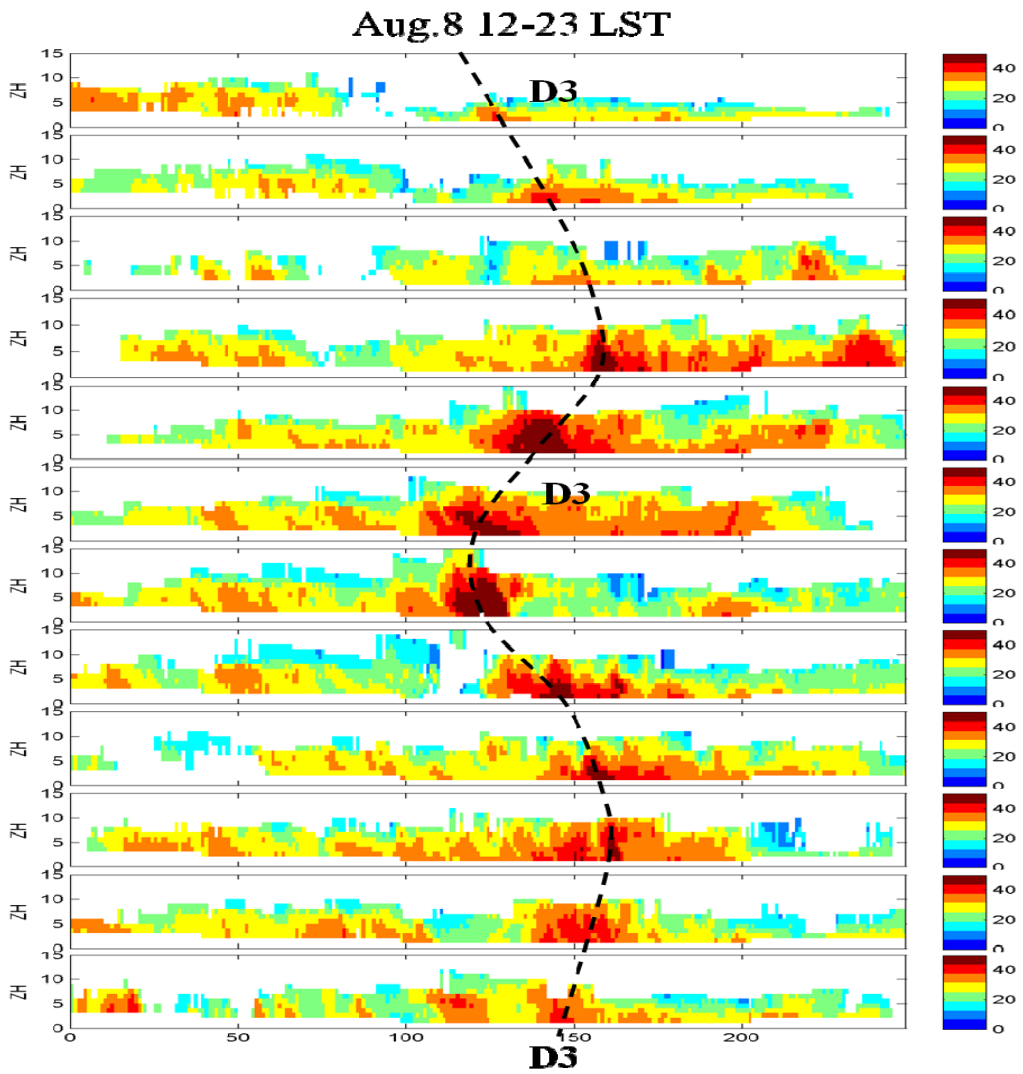

Fig. 3. Hovmoller diagram of the radar reflectivity associated with rainband D3 in Fig. 2a as a function of distance from the radar during 12-23 LT August 2009, which indicates the presence of very deep convective towers while the rainband oscillates between 22.5N and 23.5N (Wang *et. al.* 2010).

5. Gaps in understanding and forecast guidance products

A number of scientific, predictability, and forecast guidance product deficiencies became evident at the *International Conference on Typhoon Morakot (2009)*. These deficiencies will be discussed in the same order as the four contributions to monsoon-influenced typhoon extreme precipitation events described in the previous sections.

a. *Monsoon influence*

Whereas it is generally accepted that typhoon prediction is a multi-scale problem with scales ranging from synoptic scale to the convective scales, the monsoon-influenced typhoon introduces a need for observing and predicting on a still larger scale. One positive factor is that these typhoons occur at the downstream portion of the Asian summer monsoon, and the Asian observational network provides reasonably accurate

initial conditions. However, important Asian summer monsoon variability on intraseasonal time scales is not always well predicted. Such variability includes the 10-15 day monsoon trough variability that in turn affects the formation and initial structure of the pre-typhoon seedlings. The variable that is least well observed and predicted is the moisture field, which affects the convective heating distribution that then feeds back to the circulation changes. The particular challenge for the monsoon-influenced typhoon prediction is to predict the horizontal and vertical structure of the water vapor flux toward the typhoon. More accurate observations of the moisture distribution and representation of the moist processes in the numerical weather prediction models are required. However, it is considered that the monsoon-influence contribution is the most predictable of the factors affecting the monsoon-influenced typhoon extreme precipitation events.

b. *East-west oriented convective band*

The east-west oriented convective band over the Taiwan Strait and its associated low-level jet have an essential contribution in initiating, growing, and propagating deep convective cells with heavy rain toward the CMR. As indicated by Kuo et al. (2010), analyses of past events indicate such a mesoscale convective band is a common feature of the ten most damaging monsoon-influenced typhoon precipitation events in Taiwan. This convective band forms in a confluence zone between the southwesterly monsoon flow and the outer circulation of the typhoon. Depending on the relative strength of these two circulations, the confluence zone will occur at several different latitudes over the Taiwan Strait. Thus, the outer wind structure of the typhoon must be known accurately in addition to the southwesterly monsoon flow structure.

This mesoscale region of confluence, deep convective cell growth and propagation, and the dynamical processes associated with the low-level jet, are the most interesting and challenging of the multi-scale interactions leading to the heavy precipitation and flooding in a Morakot-type scenario. A key issue is why and how the mesoscale convective band remains quasi-stationary so that deep convective cells move onshore and are focused in the same region of the CMR, and thus a heavy rain occurs for a longer period of time than if the band was moving. The dynamical and thermodynamical processes leading to such intense (> 40 m s^{-1}) low-level jets in association with the convective band are not understood or well predicted, and yet this low-level jet is a major contributor to the horizontal vapor flux across the west coast of Taiwan and toward the CMR.

Even if the outer wind structure and the southwesterly monsoon flow were known perfectly, it seems likely that the mesoscale and convective scale processes must have a significant role in maintaining a quasi-stationary east-west convective band. Thus, the predictability of such an event is likely to be considerably shorter than if it was only controlled by the typhoon circulation and the monsoon flow. In addition to a requirement for high horizontal resolution in the numerical weather prediction model, advances in the representation of mesoscale, convective scale, and boundary layer processes will be required to predict the initiation and evolution of the east-west

convective band over the Taiwan Strait that then contributes to the extreme precipitation events on the slopes of the CMR.

c. *Typhoon location and slow movement*

Although dramatic progress has been made during the last decade in tropical cyclone track forecasting, special aspects of track prediction exist when a typhoon is interacting with the CMR. As indicated in section 4, the modifications of the typhoon outer wind structure, as well as changes in the convective heating distribution, may lead to track deflections from the environmental steering. If this environmental steering is relatively weak (e.g., near the subtropical ridge line, a midlatitude trough passage imposing an equatorward steering component, etc.), the typhoon-topography interaction effect will be more significant. In some cases, the low-level circulation is so modified by the interaction with the orography that it is difficult to determine where the center is. Indeed, a new low-level center may form over the Taiwan Strait so that the movement appears discontinuous.

When a typhoon is approaching northern Taiwan, the movement may be slow because the steering flow is being affected by the subtropical anticyclone, a midlatitude trough, the self-propagation associated with the beta gyres, and the typhoon-topography interaction described above. If a slow movement is anticipated, the forecast errors may be quite small, but the situation may have low predictability because of these four influences on the steering flow. Depending on which of the four influences becomes the dominant factor, the direction and speed of the typhoon motion may be quite different. Few conventional observations are available to the east of Taiwan in the subtropical anticyclone, which may not be well predicted due to the physical process representations in the model. Since large typhoons may also modify the subtropical anticyclone and thus "break through the ridge," the outer wind structure of the typhoon must be observed and forecast. While the midlatitude trough influence on tropical cyclone recurvature is well understood in principle, the amplitude and translation of the trough must be predicted as it interacts with the typhoon circulation. When the typhoon circulation is also interacting with the CMR orography, the prediction of the location and movement of the typhoon near northern Taiwan is not a well-defined forecast problem. Huang et. al. (2010) indicate great sensitivity to the typhoon track prediction in their numerical prediction where a relatively small northward deflection reduced the maximum accumulated rainfall by several hundred millimeters.

d. *Taiwan topography*

Some early numerical model simulations of typhoons interacting with the Taiwan topography utilized highly smoothed representations of the CMR. The high resolution radar studies of Morakot have indicated that the detailed topographical features of ridges and valleys in the foothills and canyons in the CMR affect the rain distribution. For example, Yu and Cheng (2010) documented that the local terrain features in the foothills must be considered to explain the precipitation maximum near the valley exit. They also emphasized that the low-level jet associated with the convergence zone can

lead to flash flooding in the CMR canyons when the orientation is "optimum." This sensitivity to the detailed features of the Taiwan topography suggest a limited predictability of the rainfall at specific sites in the CMR.

Acknowledgments. This workshop was hosted by TTRFI and sponsored by the Taiwan National Science Council and National Applied Research Laboratories. Additional support was provided by the Central Weather Bureau, Institut Francias de Taipei, and the National Center for High-Performance Computing. The permission of various people for permission to publish their research and for providing figures is gratefully acknowledged. The participation of Russell Elsberry is funded by the U.S. Office of Naval Research Marine Meteorology section. Mrs. Penny Jones skillfully prepared the manuscript.

REFERENCES*

Hong, C.-C., M.-Y. Lee, H.-H. Hsu, and J.-L. Kuo, 2010: Role of submonthly disturbance and 40–50 day ISO on the extreme rainfall event associated with Typhoon Morakot (2009) in Southern Taiwan. *Geophys. Res. Lett.,* **37**, L08805, doi:10.1029/2010GL042761.

Maddox, R. A. 1980: Mesoscale convective complexes. *Bull. Amer. Meteor. Soc.*, **61**, 1374-1387.

Tang, Y.-S., 2010: The mesoscale characteristics of rainband from radar analyses: Typhoon Morakot (2009). *Masters thesis, Department of Atmospheric Sciences*, National Central University, 82 pp (In Chinese).

Wang, T.- C., Y.-S. Tang, C.-H. Wei, P.-L. Lin, Y.-C. Liou, W.-Y. Chang, C. B. Chou, B.-T. Ji, and C.-Y. Lin, 2010: Precipitation characteristics of Typhoon Morakot (2009) from radar analyses. *Science report of Typhoon Morakot*, National Science Council, Taipei, Taiwan, 192 pp (In Chinese).

Yeh, T.-C., and C.-P. Chang, 2009: Terrain effects on the tropical cyclone rainfall over Taiwan. Presentation, *Second International Workshop on Tropical Cyclone Landfall Processes*, Shanghai, China, 19-23 October 2009.

* All references not shown are from *International Conference on Typhoon Morakot (2009)* and the powerpoints are available at www.ttfri.narl.org.tw/workshop/morakot/index.php

The mechanism analysis of cloud and moisture sources/sinks in the formation of torrential rainfall

Jinhai HE[1], Shouting GAO[2], and Luan XU[3]

Key Laboratory of Meteorological Disaster of Ministry of Education, Nanjing University of Information Science &Technology[1]*, Laboratory of Cloud-Precipitation Physics and Severe Storms, Institute of Atmospheric Physics, Chinese Academy of Sciences*[2]*, Department of Atmospheric Sciences, Nanjing University of Information Science &Technology*[3]

Moisture and cloud sources/sinks are the two main aspects that contribute to torrential rainfalls. While moisture process is most important associated with precipitation, cloud sources/sinks should not be neglected. During rainfall, there are intense convective activities in the clouds. Convergence in the lower layer forces the ascending motion, and divergence occurs on top of clouds. This outward divergent flow can generate downdrafts all around. The downdrafts encounter the warm moist air at the bottom of the clouds, unstable stratification forms, then triggers new convections. All the convective clouds may join together, resulting in more intense rainfall. Thus, more attention should be paid on cloud process.

In this study, surface rain rate formulation with cloud sources/sinks is applied. By use of the data based on Japan regional spectral model, the cloud sources/sinks are analyzed in rainfall events during Meiyu period. This term can modify the surface rain rate calculated based on the moisture sink, especially when during the light rainfall events. The inclusion of cloud sources/sinks favors quantitative calculation of the surface rain rate, and this formulation has considerable potential in the quantitative precipitation estimation.

The Indian summer monsoon: precipitation - soil moisture feedback/recycling

Shakeel Asharaf[1], Andreas Dobler[1], and Bodo Ahrens[1]
Institute of Atmospheric and Environmental Sciences, Goethe-University Frankfurt am Main, Germany[1]
Asharaf@iau.uni-frankfurt.de

1 Introduction

The importance of land surface processes arises because of the large energy and water exchange between the continental surface and the overlying atmosphere (Zhang et al., 2004). It involves how radiation energy (short wave and long wave) arriving at the land surface is partitioned into latent and sensible heat fluxes, and how water reaching the land surface becomes soil water storage, runoff, drainage, and how much water is recycled into the atmosphere. The exchange of radiation, sensible heat, latent heat, and momentum has direct impact on wind vector, precipitation, and surface soil (Sellers, 1991). All aforesaid components are intimately linked to each other, such that changes in one may involve compensatory changes throughout the entire climate system. These changes may amplify the initial disturbance (anomaly) or damp it. Disturbance amplifying interactions are termed a positive feedback mechanism, and the ones vice-versa are called negative feedback processes.

The present work focuses on the investigation of the soil moisture precipitation (S-P) feedback and recycling process (contribution of locally evapotranspirated water to precipitation) over the Indian region, using the state of the art model COSMOCLM. The importance of soil-moisture-climate relationship and impacts of land-surface processes to overlying atmosphere with details are as follows. Section 2 presents the model setup, experimental design, and a description of methods and assumptions are given in Sec. 3. The results and discussion are addressed in Sec. 4 and followed by conclusions (Sec. 5).

2 Model and experimental design

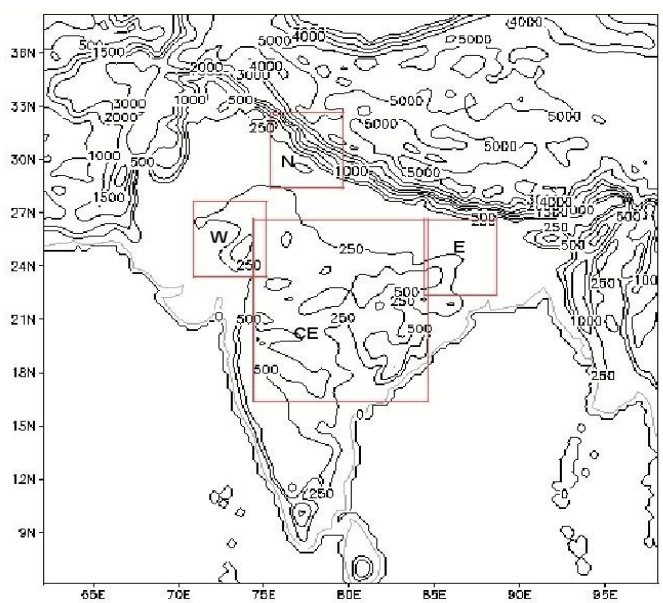

Figure 1: Simulation and analysis (N, W, CE, and E) domains

The simulations were performed with the non-hydrostatic limited-area climate model COSMO-CLM (Steppeler et al. 2003; Dobler and Ahrens, 2008). As model input, the initial and lateral boundary conditions were taken from the ERA-Interim reanalysis. In the present study, the horizontal resolution was set to 0.25° with 32 vertical layers. The simulation domain encompassed the entire Indian region (Fig. 1). More details about the model are given at the community website (www.clm-community.eu).

In order to assess the influence of soil moisture, we have performed several simulations: a reference simulation (CTL) for the period 1989-2008 and perturbed simulations. These latter simulations are initialized each year at 2nd April with CTL, but with perturbed soil moisture. For each year there are DRY runs with an initialized soil 50% drier and WET runs 50% wetter relative to CTL (with perturbations limited by plant wilting point and field capacity). This setup is motivated by Schär et al. (1999) and Pielke Sr. et al. (1999).

3 Theory

Here the S-P feedback/recycling analysis were based by Schär et al (1999), in which they formulated two bulk characteristics: the recycling ratio β and the precipitation efficiency χ. The recycling model makes four basic assumptions: (1) atmospheric flow across the region is approximately unidirectional; (2) water vapor transported across the boundary or evapotranspirated within the region is well mixed; (3) vertical fluxes precipitation *P* and evapotranspiration *ET* have minimal spatial variability; and (4) at long time scales within the investigation period, the changes in atmospheric moisture storage over the region are neglectable.

With the flux integral approach, we can calculate the incoming (*IN*) and outgoing (*OUT*) flux across any arbitrary boundary line. Also, the three-dimensional problem can be reduced to a two-dimensional problem through vertical integration of the vapor flux. The recycling ratio is given by $\beta = ET/(ET+IN)$ and the precipitation efficiency can be defined as $\chi = P/(ET+IN)$.

The precipitation changes in the sensitivity experiment (WET and DRY) are estimated by the following equation (see Schär et al 1999):

$$\Delta P = \chi'(\Delta ET + \Delta IN) + \Delta\chi(ET + IN) \qquad (1)$$

Where χ' is the efficiency in the perturbed simulation and the Δ-terms indicate differences between the perturbed and the control simulations. The first term on the right hand side of the eq. (1) reflects the precipitation change through direct (recycling) processes and the second term depicts the indirect (feedback) contribution. The results for the different analysis domains (Fig. 1) were made comparable by normalization following Zangvil et al. (2010).

4 Results

Figure 2 depicts inter-annual variation of the recycling ratio β and precipitation efficiency χ of CTL and the soil moisture sensitivity simulations for the analysis domain E and W. The precipitation recycling ratios are generally in the range of 0.1 to 0.25 with larger values for the northern region (N, the Himalayan region with high precipitation values, but relatively small influx). The recycling strength increases with larger evapotranspiration and precipitation, and smaller moisture influx.

The bulk characteristics χ is of moderate sensitivity to soil moisture initialization (Fig. 2) in most of the years with small positive feedback (except for in region W, see Tab. 1). However, some years (1992 in E, 1993 in W, 1995 in N) experience a negative feedback to soil moisture initialization perturbation. This result is opposite to the results in Schär et al. (1999), where χ always increased

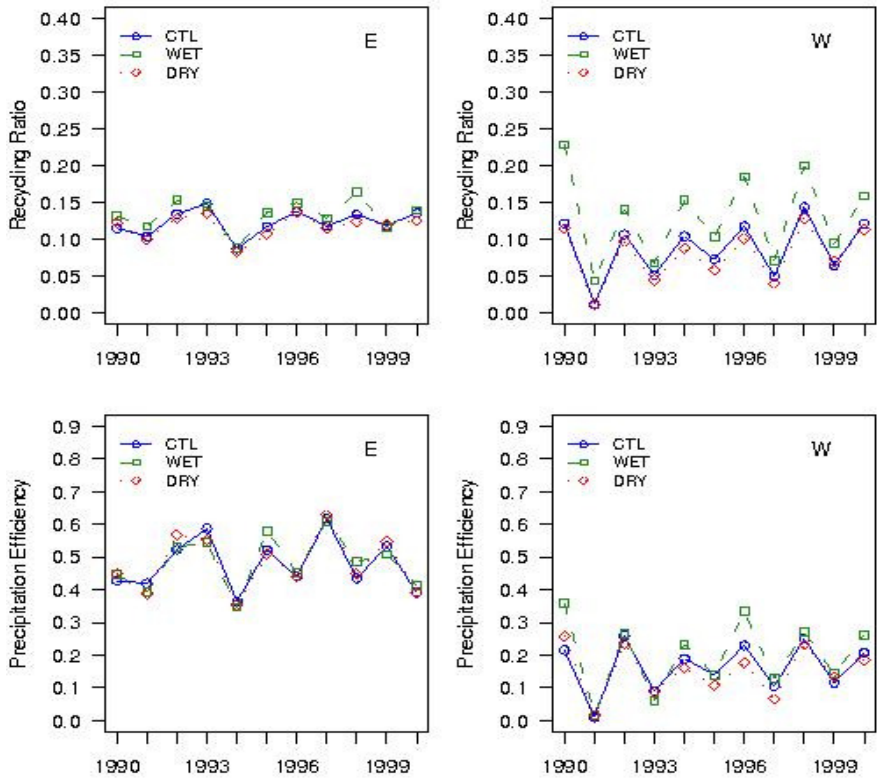

Figure 2: Recycling ratio and precipitation efficiency in the analysis domains W and E

with increase in initial soil moisture.

The sensitivity of monsoonal precipitation to changes in initial soil moisture is well drawn in Fig. 3. Often wet soils enhance precipitation. This follows the positive feedback concept. But, negative feedback is also present in all domains. In this case drier soil moisture condition lead to higher sensible heat flux and deepening of the boundary layer height, which may yield rainfall (Collini et al., 2008), whereas moist conditions stabilize the atmosphere, inhibiting vertical movement of air parcels and as a result decreases rainfall (Cook et al., 2006).

The inter-annual variability of the bulk characteristics recycling ratio and precipitation efficiency (Fig. 2, Tab. 1) are very difficult to interpret in their nature. Is the leading impact through recycling or feedback? Is the impact on precipitation locally driven (direct: through evapotranspiration over the same region) or remotely (indirect: through advection of water vapor) yet locally modified, driven from the outside advected atmospheric transport of water vapor (indirect). For this region, Fig. 3 shows the contribution to precipitation change through the direct and indirect terms in eq. (1). The indirect processes dominate most of the years in the western domain W, but the direct recycling processes dominate in the eastern domain E.

A small change in precipitation efficiency can have significant influence. For example, in the year 1998 for the WET case in the analysis domain E the efficiency changes by 0.06 yielding to enhance precipitation by more than 30 mm/month through indirect/feedback processes. Moreover, negative values for the indirect and direct terms reflect change in precipitation contrary to the change in initial soil moisture. In the DRY case the negative feedback even dominates in the western domain W.

5 Conclusions

In this paper, precipitation recycling and feedback process were investigated through perturbation simulations with the COSMO-CLM over India. The results suggest that soil moisture has significant impact on the precipitation formation. Furthermore, the moisture budget has been examined for

different sub-regions to interpret the leading factor as precipitation originating from local evapotranspiration (direct process) or advected from external sources (indirect). As a first result, the Indian summer monsoon contains both processes, where the dominant one varies spatially and temporally as well. In general, recycling ratio increases with increasing soil moistures. For example, in the eastern analysis domain, the main reason for increasing recycling ratio with soil moisture is evaporation. But, in the northern and western parts of the Indian region, the high recycling rates are likely due to a combination of low moisture influx and moderately high evaporation rate. Additionally, low moisture influx with increasing soil moisture is related to a negative feedback processes in these regions.

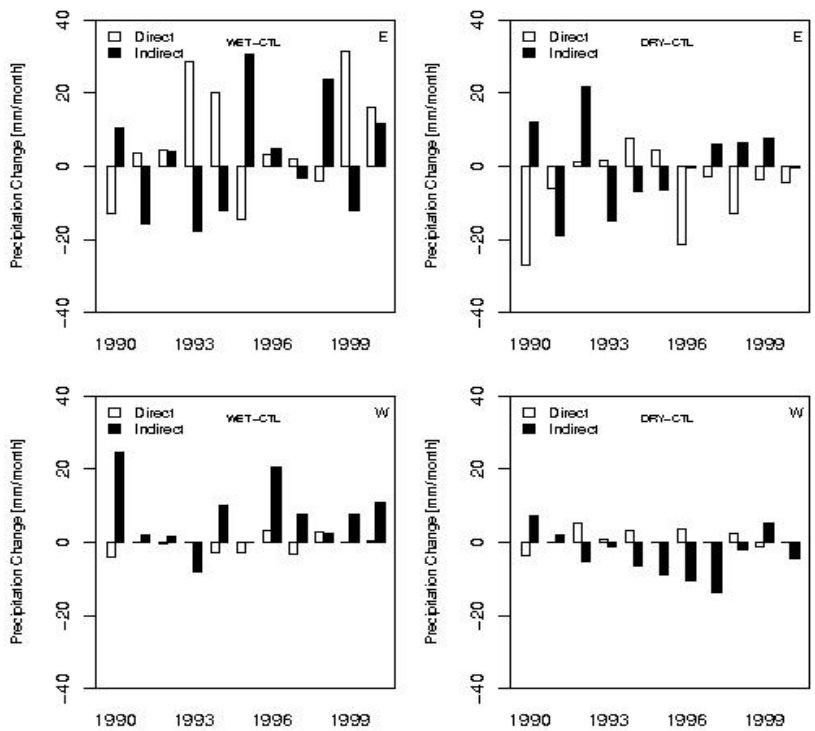

Figure 3: Changes in monsoonal rainfall for WET-CTL (left) and DRY-CTL (right) in the analysis domains E and W

Region	χ			β			***IN*** (mm/month)			$P_{\mathbf{WET\text{-}CTL}}$ (mm/month)		$P_{\mathbf{DRY\text{-}CTL}}$ (mm/month)	
	WET	CTL	DRY	WET	CTL	DRY	WET	CTL	DRY	Direct	Indirect	Direct	Indirect
E	0.48	0.48	0.48	0.13	0.12	0.12	465.7	457.2	448.4	7.05	2.14	-5.8	0.58
W	0.2	0.16	0.15	0.13	0.09	0.08	200	213.5	220.7	-0.67	7.23	0.95	-3.4
N	0.51	0.48	0.48	0.29	0.22	0.2	148.7	160.8	161.5	1.09	6.7	-1.42	1.86
CE	0.29	0.28	0.28	0.1	0.09	0.09	490.2	490.2	485	1.19	4.14	-1.85	-0.7

Table 1: Mean values of recycling ratio and precipitation efficiency, moisture influx, and changes in precipitation

5 References

Collini, E. A., Berbery, E. H., Barros, V. R., and Pyle, M.E., 2008. How does soil moisture influence the early stages of the south American Monsson?, *J of Climate,* 21, 195-213.

Cook, B.I., Bonan, G.B., and Levis, S., 2006. Soil moisture feedback to precipitation in southern Africa, *J. of Climate,* 19, 4198-4206.

Dobler, A., and Ahrens, B., 2008. Precipitation by a regional climate model and bias correction in Europe and South Asia, *Meteorolgische Zeitschrift,* 17(4), 499-509.

Pielke Sr., R. A., Listan, G. E., Eastman, J. L., and Lu, L., 1999. Seasonal weather prediction as an initial value problem, *J. Geophys. Res.*, 104, 19463-19479.

Schär, C., Lüthi, D., and Beyerle, U., 1999. The soil -precipitation feedback: A processes study with a regional climate model, *J. of Climate*, 12, 722-741.

Sellers, P., 1991. Modeling and observing land-surface-atmosphere interactions on large scales, Survey in Geophysics, 12, pp. 85-114.

Steppeler, J., Dom, G., Schattler, U., Bitzer, H. W., Gassmann, A., Damrath, U., and Gregoric, G., 2003. Meso-gamma scale forecasts using the non-hydrostatic model LM, *Meteorol. Atnm. Phy.*, 82, 75-96.

Zangvil, A., Lamb, P. J., Portis, D. H:, Jin, F., and Malka, S., 2010. Comparative study of atmospheric water vapor budget associated with precipitation in central US and eastern Mediterranean, *Adv. Geosci.,* 23,3-9

Zhang, H., McGregor, J. L., Seller, A. H., and Katzfey, J. J., 2004. Impacts of land surface model complexity on a regional simulation of a typical synoptic event, *J. of Hydrometeorol.,*5, 190-198.

An Idealized Numerical Study on the Effects of Meiyu Front upon the Initiation and Development of MCSs Producing Rainstorms

ZHAO Yuchun
Institute of Heavy Rain, Wuhan, CMA
zhaoych@cma.gov.cn

Aimed at the fact that the mesoscale convective systems (MCSs) usually develop on the Meiyu front, lasting a long time and producing rainstorms along the valleys of Yangtze river, a series of three-dimensional idealized numerical experiments are carried out to investigate the effect of moisture difference between the two sides of Meiyu front, the impacts of basic flow, wind vertical shear upon the MCSs' development along the Meiyu front, and the convection organization by the Meiyu front.

The mass imbalance resulting from the Meiyu front can generate small-amplitude gravity waves, which may organize upward motions in the low-level and trigger convection when coupled with diabatic heating, leading to a convective rain-band forming along the Meiyu front. The scale of the convective systems is usually 20~60km. The convection rain band moves southward after its formation.

The Meiyu front plays a role in the convection organization. The convective perturbations near the Meiyu front may develop into MCSs with a scale of 100~200km. When convective perturbation effected by low-level northerly winds organized by Meiyu front, a convergence band forms in its low level and its flow structure tilts in the vertical direction, which is beneficial to the maintenance and development of MCSs.

The basic flow's advection impacts the Meiyu front's movement, which can offset the southward movement of Meiyu frontal convection rain-band. The moisture and energy transportation by it is very important in the initiation and development of MCSs. The wind vertical shear resulting from wind direction variations is beneficial to convection initiation and MCSs' organization along the Meiyu front and impacts the moving direction of convective systems, while that from wind velocity variations seems to be not favorable for the convection initiation on the Meiyu front and the long-time maintenance of MCSs.

Regional climate projections of trends and variability in the Indian summer monsoon

Andreas DOBLER, Bodo AHRENS
Biodiversity and Climate Research Centre & IAU, Goethe-University Frankfurt am Main, Germany dobler@iau.uni-frankfurt.de

The Indian summer monsoon (ISM) influences daily lives and economies in many countries in the South Asian region, and a wide range of indices have been defined to measure and predict the strength of the ISM. The most obvious impact is on rainfall in the monsoon season (June to September), which accounts for about 75% of the annual precipitation in India. Thus, the all-India monsoon rainfall (AIMR) index has been defined as the total rainfall amount from June to September averaged over whole India. Although the observed interannual standard deviation in the AIMR is only about 10% of the long-term mean, the extremes lead to floods and droughts. Other indices for the ISM are based on the vertical shear over certain pressure levels of zonal or meridional winds or on the use of outgoing longwave radiation as a measure of convection. Also, there is a well documented relationship between the nino3.4 index and the ISM. However, the question which index best estimates the ISM strength remains controversial. This study gives an overview on projections of different ISM indices by the regional climate model COSMO-CLM and its driving GCM ECHAM5 for the time period 1960-2100. To generate a small ensemble of possible future developments, the scenarios A1B, B1, A2, and the commitment scenario have been used. Trends and temporal variabilities of the indices are investigated as well as the pairwise correlations between the indices over different time spans.

The Effect of ENSO on the Summer Monsoon Rainfall in Macao

Soi Kun FONG, **Sau Wa CHANG**, and I Hang LIU
The Macao Meteorological and Geophysical Bureau

Abstract

The characteristic of rainfall in Macao has a two dominant peak in annual, the primary rainfall peak during the first flood period of May-June and the secondary peak during the typhoon season of July-September. Numerous studies have been revealed it have a relation between El Nino-Southern Oscillation (ENSO) phenomenon and the rainfall in different area.

The main purpose of this study is to review the characteristics of the summer monsoon and the associated rainfall in Macao during different ENSO conditions from 1952 to 2009. The synoptic scale patterns associated with El Niño and La Niña summer will also be studied.

Session B

Quantitative Precipitation Estimates, *in-situ*, remote sensing observations

Observations of Precipitation Processes at the Vancouver 2010 Winter Olympic Games

Paul Joe[1], George Isaac[1], Stewart Cober[1], Jocelyn Mailhot[1], Jason Milbrandt[1], Chris Doyle[1], Ismail Gultepe[1], Edwin Campos[1], Ron Stewart[2] and Teresa Fisico[2]

[1]Environment Canada, [2]University of Manitoba
Email: paul.joe@ec.gc.ca

Introduction

The Vancouver 2010 Winter Olympic Games were conducted in February and March 2010. The Nowcasting Working Group (NWG) of the World Weather Research Program (WWRP) of the World Meteorological Organization (WMO) promoted the Science of Nowcasting of Olympic Weather (SNOW-V10) Research Development Project (RDP). The main goal of SNOW-V10 was to accelerate the development of winter nowcasting in complex terrain. Nowcasting weather elements included precipitation type, intensity, wind, visibility and low cloud which are all critical to support the forecasting/nowcasting for safety and security of the public, athletes and organizers but also for fair conditions for the competitions. There is both an operational and research component to the forecasting and to monitoring network (Joe et al, 2010). The focus of this paper is the precipitation processes revealed by remote sensing observations. In-situ and model observation are or will be discussed elsewhere.

The Domain and the Observation Network

There are five distinct areas of interest (see Fig. 1). The Vancouver urban area has many indoor venues and is therefore of minor concern. Cypress Mountain is on the North Shore of the Fraser Valley and site of many of the freestyle events. It is on the edge of the ocean (actually Georgia Strait) and the terrain rises sharply creating strong weather gradients. The Creekside of Whistler Mountain is the location of the Alpine events. It is about 100km from the ocean and is of prime concern. The sliding events are conducted on the west side of Blackcomb Mountain. The fifth site is the Callaghan Valley which is the site of the Nordic events. Each site has its own micro-climate, its own forecast and nowcast issues.

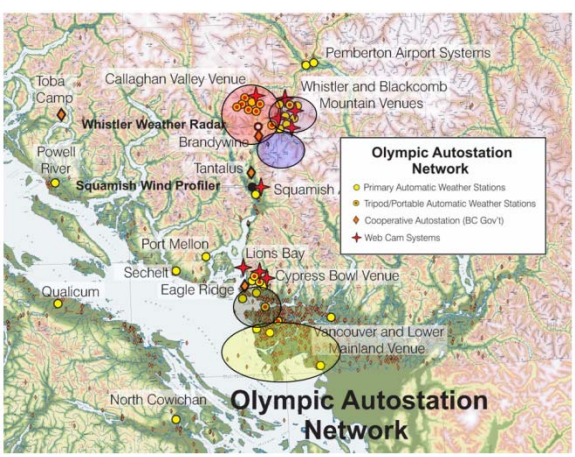

Figure 1: *Location of the main forecast areas for the Vancouver Olympic Games. From top to bottom and left to right, they are the Callaghan Valley (Nordic), Blackcomb (Sliding Centre), Whistler (Creekside), Cypress Mountain (Freestyle), Vancouver (Indoor Venues).*

Fig. 2 shows in visual detail the research instruments deployed to support the SNOW-V10 project which focuses on research in precipitation, wind and

visibility/low cloud. There is another separate surface bases observation network deployed to support operational forecasting. It is not described here. Output from both observation networks were available to all.

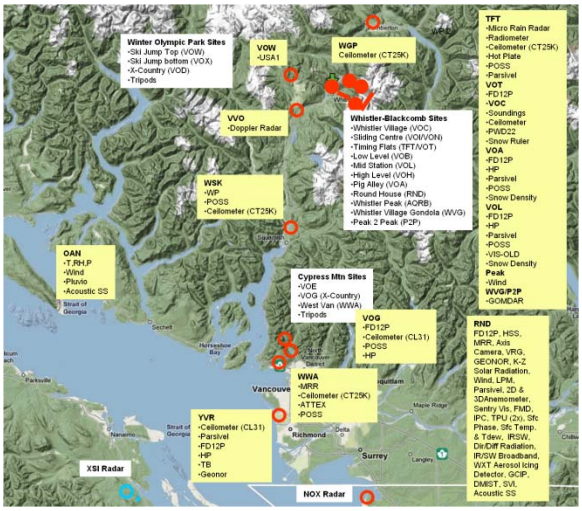

Figure 2: *Location and instrumentation list for the Science of Nowcasting of Olympic Weather (SNOW-V10) research component of the project***.**

Of particular importance to this discussion, a C Band Doppler radar was located in the valley (about 557m ASL) at the confluence of three key valleys (Fig. 3). The mountain peaks (about 2000m) are very near (Fig. 4) and a 12° elevation scan is required to scan above the mountains. This a unique setup and is designed to meet the low level scanning nowcasting and science requirements of nearby venues. Surveillance scanning is provided by the normal operating radars. Observations from a vertically pointing 24 GHz radars, (MRR) located at the base of Cypress Mountain will also be presented.

Survey of Precipitation Processes

In this section, a preliminary surveys of the precipitation processes are illustrated primarily via radar examples. The winter of 2010 was an el nino year and the temperatures were much warmer than normal.

Melting: Freezing levels were above the surface and below mountain top. Fig. 3 shows a plane position indicator (PPI) image of the 12° elevation angle data. The transition from snow to rain was a critical and common forecast issue since this affected athletic performance and athlete safety. Identification of the bright band was one technique used by the forecasters to identify the melting process and level. Precision of about 100 m was required.

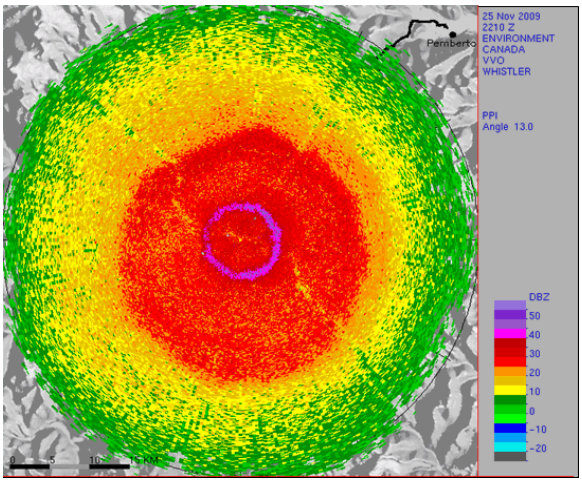

Figure 3: A 12° PPI of reflectivity. The purple (40 dBZ) ring indicates the bright band which is interpreted as the freezing/melting level

Virga: Winter precipitation processes are efficient and sensitive to environmental conditions. Evaporation/sublimation at low or mid levels resulted in a lack of precipitation. In the example provided (Fig. 4), the echo at the outer edge of the outer ring represents the height of the origin of the precipitation since this is radar data collected at a constant

elevation angle. It grows and then evaporates creating the inner edge of the outer ring. The gap represents a precipitation free layer. The precipitation then begins again below mountain top and evolves all the way to the valley height (origin or radar location). This also indicates layering (strata of air of different characteristics) which is very evident in winter. The radial velocity image showing different air flow directions also indicates that there is a separation of the air mass above mountain top and in the valley. So that there is a discontinuity in the air masses that impact precipitation formation. If the air is unstable, evaporation and mixing processes below the virga was used to forecast gusty winds.

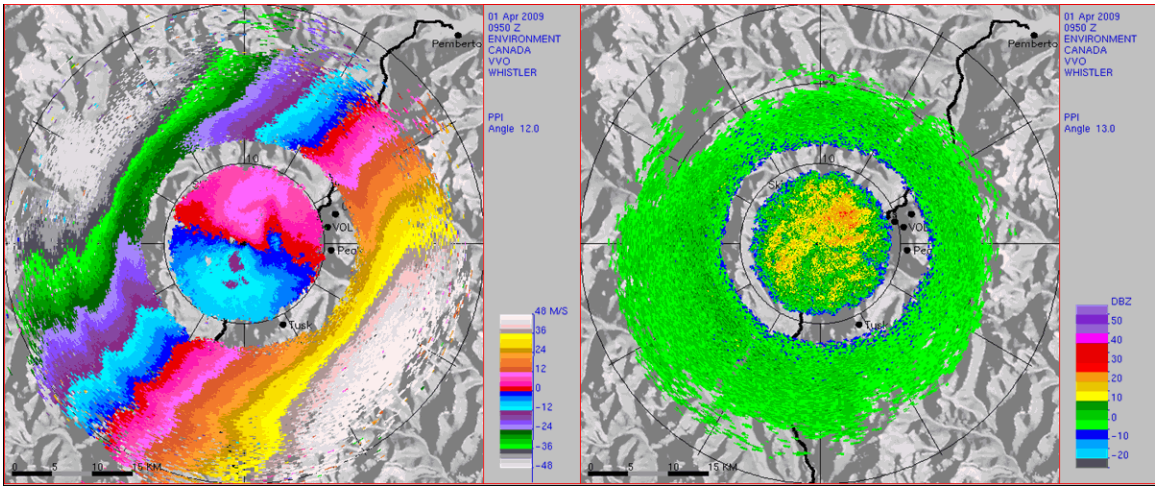

Figure 4: *Radial velocity (left) and reflectivity PPI of virga (outside ring of echo) with precipitation development below.*

Blocked Flow: An example of a radial velocity and reflectivity Range Height Indicator (RHI) displays are shown indicating a blocked flow or flow reversal (Moist Froude Number < 1). The orographic precipitation occurs on the slope and not the crest of the mountains. A surveillance radar located on the mountain top would not see such an important feature for precipitation nowcasting in complex terrain.

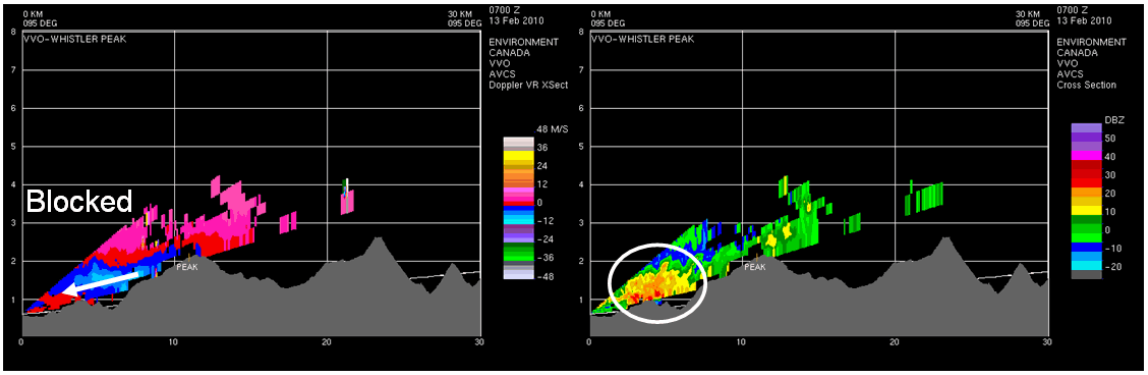

Figure 5: *RHI of radial velocity and reflectivity showing downslope winds indicating a blocked flow situation which results in precipitation on the slope of the mountain.*

Unblocked Flow: An example of a unblocked flow (Moist Froude Number > 1) where the precipitation is on the crest of the mountain. These vertical sections are not normally used in forecasting, particularly the radial velocity RHI's, but for the Olympics they were

used extensively and were intuitive to the forecaster and they conceptualized weather in the vertical.

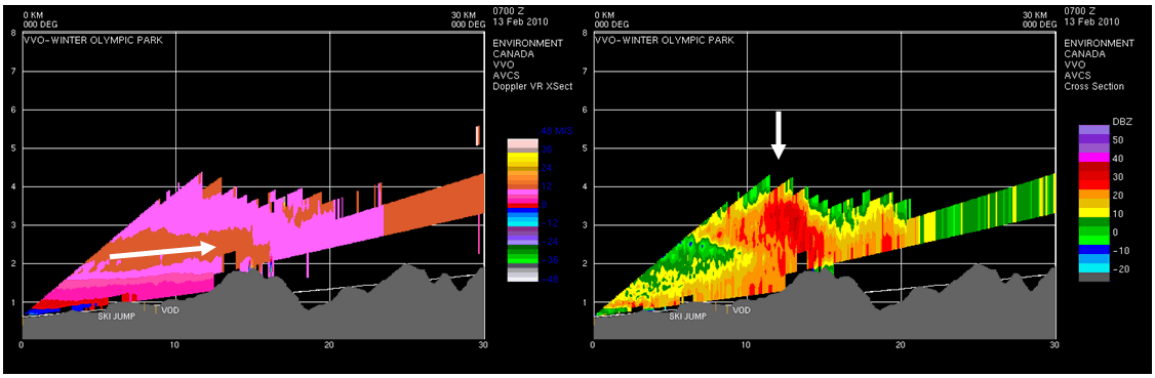

Figure 6: *In this unblocked flow situation, the radial velocity image shows away velocities from the radar which results in heavy precipitation on the crest of the mountain.*

Hybrid Flow: There is a continuum of flow regimes. In the following example, a "deep" downslope situation is shown where the precipitation is both on the slope, on the crest and to the lee of the mountains. The downslope flow has extended above the mountain top and precipitation occurs on the crest as well as on the slope.

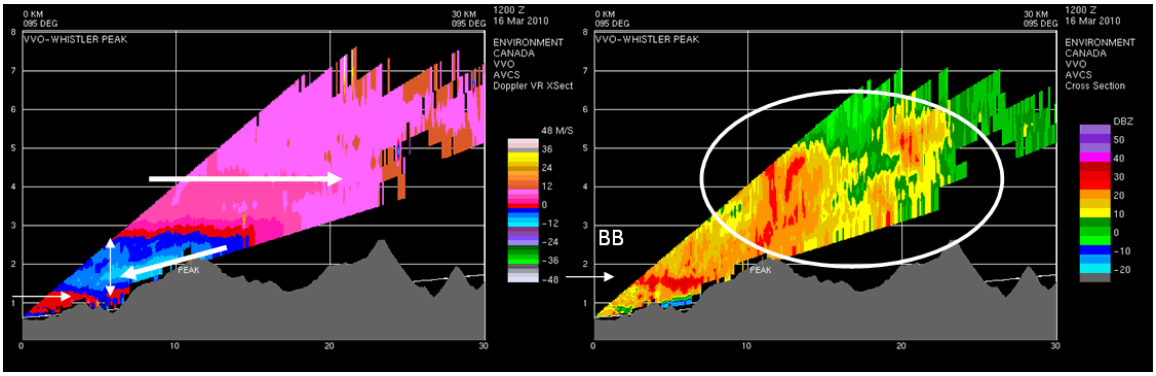

Figure 7: *A deep downslope situation where the downslope winds extend above the mountain top and the precipitation is both on the crest and on the slope.*

Inflow and Outflow winds: Inflow/outflow are valley scale flows (from coast to Squamish) and generally indicate moist/dry and warm/cold conditions from the coast to the interior and vice versa. Warm moist inflows are key factors in the forecasting of low cloud advection or very localized cloud formation on the wind ward (south) side of Whistler mountain. This cloud has often been the cause of downhill races being postponed or cancelled, in the past (Fig. 8a).

The height of the outflows were also used to forecast the advection of terrain locked cloud and precipitation at Cypress mountain (Fig. 8b).

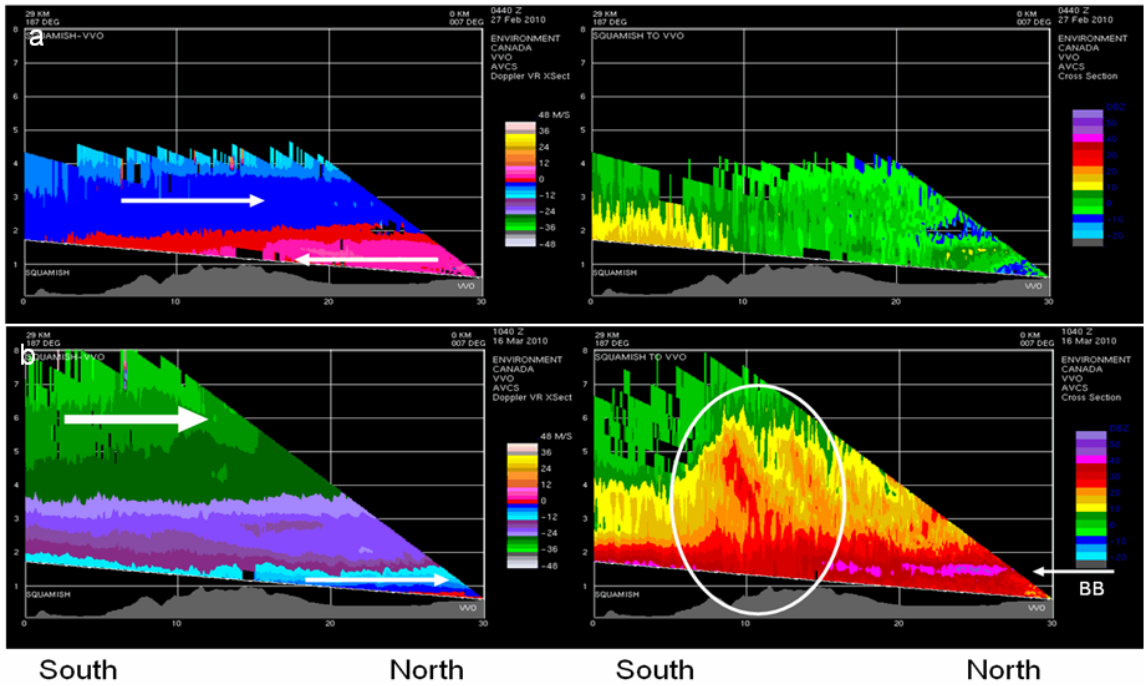

Figure 8: *Outflow (above) and inflow (below) along Howe Sound. The RHI's are created from Squamish (left) to Whistler (right). The radial velocity images show how the atmosphere is layered. The outflow winds are evident by the red away velocities in 8(a, left) but are more subtle in the inflow situation (8b, left) where there are strong winds aloft.*

Snow and Riming Processes: A vertically pointing radar was deployed at the base of Cypress Mountain. Fig. 9 shows two vertical profiles of Doppler spectra. The image indicate the intensity of the reflecitivity at different velocities (abscissa) and different heights (ordinate). Snow is identified as reflectivities falling around 1-2 m/s, whereas rain is identified as reflectivities falling around 5-8 m/s). On the left, snow is melting into rain. On the right, snow is riming, becoming more dense and falling faster and then melting into rain. It appears that evaporation is also occurring since the intensities are decreasing in intensity with height and the fall velocities are not as large as in the figure on the left. The noisy background is the system noise.

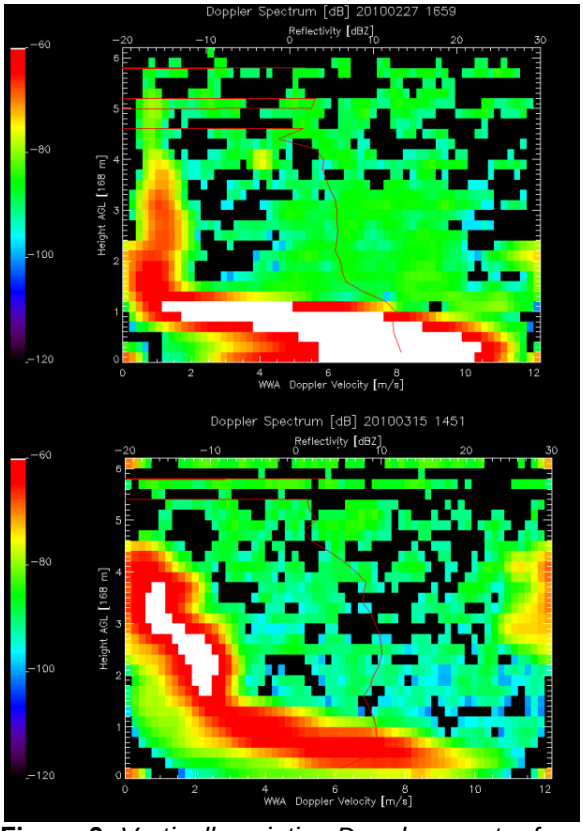

Figure 9: *Vertically pointing Doppler spectra from a Micro Rain Radar (MRR). See text for explanation.*

Precipitation Forecasting

A 1km with a double moment scheme with 6 categories (snow, graupel, ice crystal, rain, drizzle, freezing rain, ice pellets) was used for forecasting (Mailhot et al, 2010). The 1km model was initiated through a nesting with lower resolution models (2.5 and 15 km) and was often able to capture the details of the precipitation. It is still being evaluated.

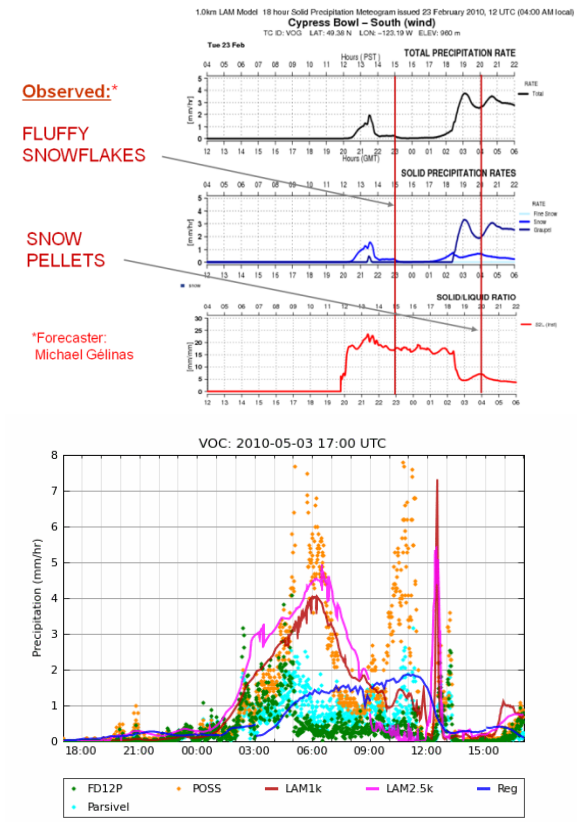

Figure 10: *Model forecasts of various precipitation types presented as meteograms. On the left, verification observations are provided by a forecaster on-site and on the right, the high resolution SNOW-V10 instrumentation provided the observations, some of which do not agree with each other.*

In-situ Observations

Fig. 10 (right) show some of the observations made with automated precipitation intensity and type instruments. Using different sensing technologies, there are differences in the measurements and this is an active area of investigation. Fig. 11 shows measurements by in-situ snow micro-photographers overlaid on a vertical profile of liquid water produced by a microwave profiling radiometer. The sequence of photos show a sequence of snow crystals, some of which are more rimed than others over the period of observation which appear to be consistent with the liquid water observations. These latter observations are still in the process of development. This figure shows the complexity of the environment and the impact on the precipitation processes.

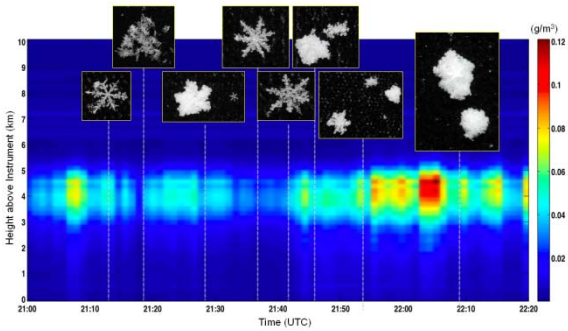

Figure 11: *Micro snow photographs taken at ~1800 m level overlaid on liquid water content vertical profiles from a microwave profiling radiometer. These latter measurements need to be confirmed.*

Summary

A research component was developed to take advantage of the operational monitoring network that was being established to support the forecasting for the Vancouver 2010 Winter Olympic Games. Only the precipitation component to study processes in complex terrain is described here.

Winter precipitation processes are already complicated since particle shapes, density, riming and aggregation must be considered. The complex terrain and associated flows and thermodynamic structures (not discussed here) add another level of detail. Since the analysis is still underway, a preliminary survey of the observations of precipitation processes mainly revealed by remote sensing, were presented. This included melting, evaporation, precipitation initiation, blocked and unblocked flows, inflows and outflows, riming and aggregation.

A double moment precipitation scheme was developed for the Olympics and the impression is that it showed excellent results though the analysis is ongoing. High resolution temporal measurements (1 minute data) using state of the art automated sensors were also made and indicate highly variable meteorological phenomena. The analysis of these measurements are also ongoing.

In summary, the SNOW-V10 project has already produced many qualitative insights and understanding into precipitation processes in complex terrain and it is expected that detailed analyses of the observations and model outputs will greatly advanced our quantitative knowledge.

Acknowledgements:

Special thanks to the technicians and support staff who deployed the network and processed the data in trying conditions. These include Rob Reed, Michael Harwood, Steve Bacic, Ivan Heckman, Brian Clark, Mike Virdi, Quinton Jansen, Ron Ruff, Bogdan Rasti, Frank Mirecki and Bill Scott and the staff of the Pacific and Yukon Region of Environment Canada.

References

Paul Joe, Chris Doyle, Al Wallace, Stewart G. Cober, Bill Scott, George A. Isaac, Trevor Smith, Jocelyn Mailhot, Brad Snyder, Stephane Belair, Quinton Jansen, Bertrand Denis, 2010: Weather Services, Science Advances, and the Vancouver 2010 Olympic and Paralympic Winter Games, *Bulletin of the American Meteorological Society,* Volume 91, Issue 1 (January 2010) pp. 31-36

J. Mailhot, S. Bélair, M. Charron, C. Doyle, P. Joe, M. Abrahamowicz, N. B. Bernier, B. Denis, A. Erfani, R. Frenette, A. Giguère, G. A. Isaac, N. McLennan, R. McTaggart-Cowan, J. Milbrandt, L. Tong, 2010: Environment Canada's Experimental Numerical Weather Prediction Systems for the Vancouver 2010 Winter Olympic and Paralympic Games, *Bulletin of the American Meteorological Society,* Volume 91, Issue 8 (August 2010) pp. 1073-1085

A High-Resolution Gauge-Satellite Merged Global Precipitation Analysis
And its Applications for Model Verifications

Pingping Xi, Robert Joyce, Soo-Hyun Yoo, and Yelena Yarosh

NOAA Climate Prediction Center

1. INTRODUCTION

Over the past decade, systematic efforts have been made at the NOAA Climate Prediction Center (CPC) to construct high quality, high-resolution global precipitation analyses through integrating information from multi-sensor, multi-platform satellite observations. Called CPC Morphing technique (CMORPH, Joyce et al. 2004 [1]), an innovative algorithm was developed that combines estimates of instantaneous precipitation rates derived from passive microwave (PMW) observations of all available LEO satellites through propagating and morphing them via the cloud advection vectors derived from consecutive infrared (IR) images from geostationary platforms. The CMORPH satellite precipitation analysis has been produced on an 8kmx8km resolution over the globe (60°S-60°N) for an 11-year period from November 1998 to the present [2]. Intercomparison and validation studies illustrated excellent performance of the CMORPH estimates in capturing precipitation variations of various time / space scales [3].

The second generation CMORPH is under development to further improve the performance through a) adopting the Kalman Filter (KF) technique for refined accuracy and enhanced flexibility in incorporating additional inputs, and b) adjusting the all-satellite combined estimates against gauge observations to remove biases. The objective of this paper is to report the progress of the development of this new blending technique.

2. THE KALMAN FILTER BASED CMORPH

Under the Kalman Filter framework, precipitation analysis defined at step (k+1) Z_{k+1} is computed from the analysis at the previous step (Z_k) and the additional observations (O_k) through the following equation:

$$Z_{k+1} = Z_k + K_k \cdot (O_k - Z_k)$$

where K_k is the Kalman gain defined from error for the previous analysis (σ_k) and the observations (σ_o):

$$K_k = \sigma_k^2 / (\sigma_k^2 + \sigma_o^2)$$

In our application, PMW estimates from multiple LEO platforms are first propagated backward and forward to

produce the 'predicted' analysis at the target analysis time. The prediction is then refined by incorporating information from IR-based estimates at the target time to form the final analysis.

The PMW precipitation estimates used in this study include those from TRMM/TMI, AQUA/AMSR-E, SSM/I aboard DMSP satellites and NOAA/AMSU-B. The IR-based estimates used here are from the IRFREQ developed at CPC through PDF matching of the IR cloud top temperatures against that of the collocated PMW estimates and are available globally at 30-min intervals.

Key to the development of the KF CMORPH is the definition of error structure for the propagated PMW and IR-based estimates as a function of instrument type, propagation time, location, and season. A preliminary test is first performed to define the error (expressed as correlation) through comparing the IR-based precipitation estimates and the PMW estimates propagated through various length of time against the Stage-II radar observations over CONUS for summer 2007.

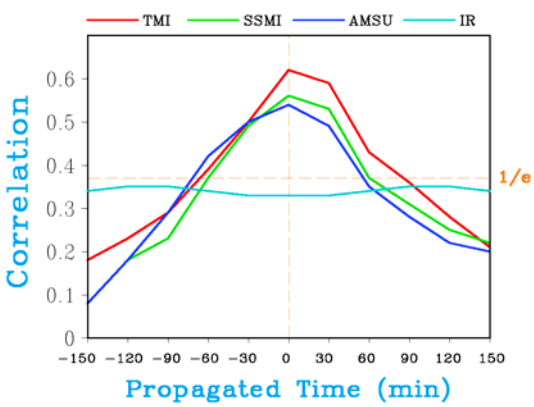

Figure 1:
Correlation for the IR-based and PMW propagated precipitation estimates as a function of instrument type and propagation time computed by comparisons with Stage-II radar data over CONUS for JJAS 2007. Positive and negative propagation times indicate forward and backward propagation, respectively.

Correlation for the PMW estimates degrades shapely as they are propagated from their observation time (figure 1). The magnitude and the degradation rate of the correlation, however, differ for different instruments, indicating the importance of defining the error separately for estimates from different platforms. The IR-based precipitation estimates outperform the PMW estimates when the propagation time is longer than 90 minutes or so, suggesting potential improvements in the final analysis through the inclusion of IR estimates to fill in PMW observation gaps.

Using these error statistics, a conceptual model for KF-CMORPH is developed to construct high-resolution precipitation estimates over CONUS. The precipitation analysis produced by the KF-CMORPH is re-calibrated through PDF matching against the original PMW and IRFREQ precipitation estimates to reduce the damping in high precipitation intensity caused by linear processing of the Kalman Filter. The final analysis is compared

against the radar observations to examine their quantitative accuracy. Precipitation estimates generated by the KF-CMORPH present consistently improved accuracy compared to those from the original CMORPH (figure 2).

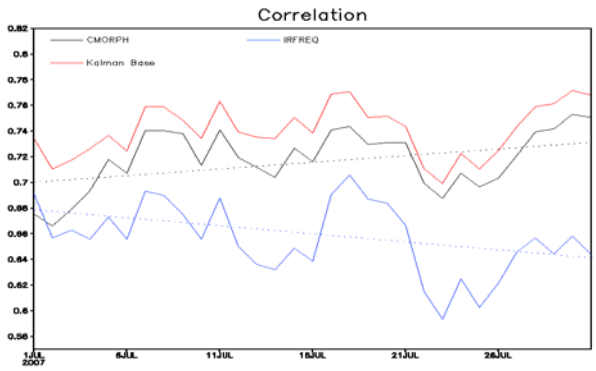

Figure 2:
Time series of correlation between radar-estimated precipitation and satellite precipitation estimates derived from a) IR observations (blue); b) the original CMORPH (black); and c) the prototype Kalman Filter (KF) CMORPH over CONUS (red).

This conceptual model is further modified and implemented for constructing the precipitation estimates over the global domain from 60°S to 60°N. Error statistics for PMW and IR-based precipitation estimates are defined for individual instruments as a function of region and season through comparisons with the concurrent estimates from the TRMM/TMI. Evolution of estimation error over the propagation period presents strong regional variations, indicating differences in the time scales of the target precipitation systems.

The prototype Kalman Filter based CMORPH is applied to generate high-resolution precipitation analysis for a 6-month period from April – September, 2009 for further tests and examinations.

3. REMOVING BIAS IN SATELLITE ESTIMATES

As shown in many validation studies, CMORPH and all other satellite-based precipitation estimates contain regionally dependent and seasonably changing biases. One way to remove the bias is to combine information from gauge observations. To this end, we have developed a prototype algorithm to remove the CMORPH bias through matching the probability density function (PDF) of the daily CMORPH with that of a daily gauge analysis produced routinely at NOAA/CPC [4].

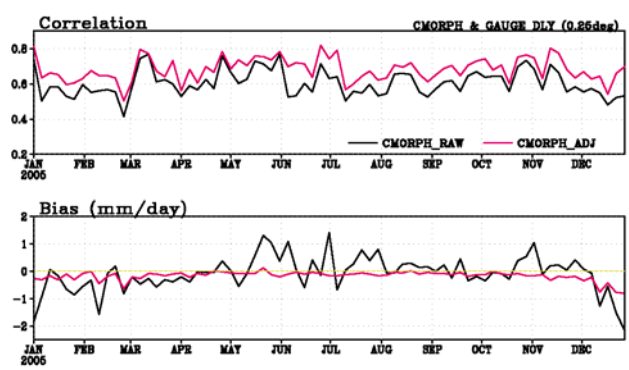

Figure 3:
Time series of correlation between the daily gauge-based analysis of precipitation and the daily estimates from a) the CMORPH (black), and b) the bias-corrected CMORPH over the global land.

This bias correction is performed for each 0.25°lat/lon grid box over the global land and updated daily on a real-time

basis. First, co-located daily CMORPH and gauge analysis data are collected over grid boxes with at least one gauge over a spatial domain centering at the target grid box and a 30-day time period ending at the target date. The PDF for the CMORPH is then created and matched against that of the gauge analysis to correct the biases. To examine the effects of this procedure, the bias corrected CMORPH estimates are compared against gauge analyses over the entire global land. As shown in figure 3, seasonally changing biases in the original CMORPH are removed substantially after the correction, and the correlation for the bias-corrected CMORPH is improved by ~0.05 upon that for the original CMORPH.

4. SUMMARY AND FUTUREWORK

A prototype algorithm has been developed for the second generation CMORPH. First, the Kalman Filter technique is adopted to integrate the PMW and IR precipitation estimates using error statistics computed as a function of instrument type, propagation type, location and season. The blended satellite precipitation estimates are then adjusted against a gauge-based analysis through PDF matching to remove the bias. The prototype algorithm is applied to produce 30-min precipitation analysis on an 8kmx8km resolution over the globe for a six months period from April – September 2009. The results showed substantial improvements of the new analysis compared to the previous version. Further work is underway to fine tune the error statistics, include information from additional sources (e.g. radar observations and model simulations), and to extend the domain to the entire global domain from pole to pole. Detailed results will be reported at the conference.

5. REFERENCES

[1] R.J. Joyce, J.E. Janowiak, P.A. Arkin, and P. Xie, "CMORPH: A Method That Produces Global Precipitation Estimates From Passive Microwave and Infrared Data at High Spatial and Temporal Resolution," *Journal of Hydrometeor.*, AMS, Vol.5, pp. 487-503, June 2004.

[2] P. Xie, S.-H. Yoo, R.J. Joyce, and Y. Yarosh, "CPC Unified Gauge – Satellite Merged Precipitation Analysis for Improved Monitoring and Assessment of Global Climate", 34th Annual Climate Diag. & Pred., Monterey, CA, October 2009..

[3] E. Ebert, J. E. Janowiak, and C. Kidd, "Comparison of Near Real Time Precipitation Estimates from Satellite Observations and Numerical Models", *Bull. Amer. Meteor. Soc.*, AMS, Vol.88, pp. 47 – 64, January 2007.

[4] P. Xie, M. Chen, and W. Shi, "CPC Unified Gauge-Based Analysis of Global Daily Precipitation," 24th AMS Conference on Hydrology., AMS, Atlanta, GA, January 2010.

Analyses of Quantitative Precipitation Estimation(QPE)Based on Merging Satellite and Rain Gauge

QI Dan[1], TIAN Fuyou[1], WU Hao[2], ZHAO Linna[2], XU fengwen[2], and BAO Hongjun[2]
1. National Meteorological Center, China Meteorological Administration, Beijing 100081, China
2. Public Weather Service Center, China Meteorological Administration, Beijing 100081, China
qidan@cma.gov.cn;qidan@126.com

1. Introduction

Satellite precipitation estimates are widely used to measure global rainfall on monthly, daily, and hourly timescales for studies. Near real-time satellite precipitation estimates are becoming increasingly available to the wider community. These precipitation estimates are potentially very useful for applications such as numerical weather prediction (NWP) data assimilation, now casting and flash flood warning, tropical rainfall potential, and water resources monitoring, etc. As with any observational data, it is important to understand their accuracy and limitations. This is done by verifying the satellite precipitation estimates against independent data from rain gauges. The terms evaluate and verify are used here to mean "to determine or test the truth or accuracy of the QPE (Quantitative Precipitation Estimation) product" (John E.1999)

High resolution rainfall distribution map can be derived from satellite observation, and rain gauges data can give us accurate rainfall measurements at a fixed location .Combined them together, the merging of satellite precipitation estimates and rain gauge measurement is to "calibrate" satellite precipitation estimation with ground observation, so that a more accurate rainfall field can be drawn. In this paper, we use a intellective objective analysis scheme which is brought forward by LU nai-meng (2004) to accomplish the merging or called "fusing".

In this study, the satellite precipitation estimation data we used to fusing is from the National Satellite Meteorological Center (NSMC) which resolution is 0.1 degree. The rain gauge data is from the National Meteorological Information Center (NMIC). Based on the hourly and daily rain gauge precipitation observations of over 30000 rain gauges and the satellite precipitation estimation products, a real-time merging system to get the QPE product is established. At last we have done a series of evaluate and verify job to test the accuracy of the QPE products.

2. Data and method description

2.1 Data description

There are mainly two kinds of original data sources. The satellite precipitation estimation data we

used in this paper were obtained from the "FY-2E" weather satellite provided by the National Satellite Meteorological Center (NSMC) which horizontal resolution of 0.1 by 0.1 degree. The station rainfall observation we used in this study is obtained from the National Meteorological Information Center (NMIC) as shown in the Fig1.a.

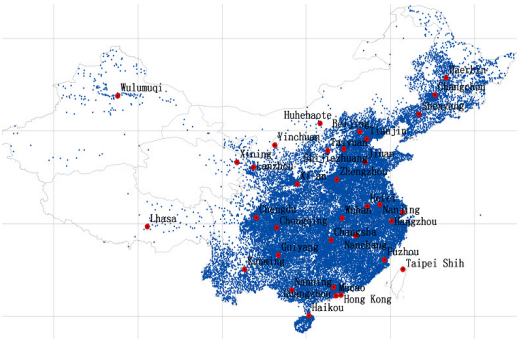

Fig.1.Illustration of automatic weather stations location

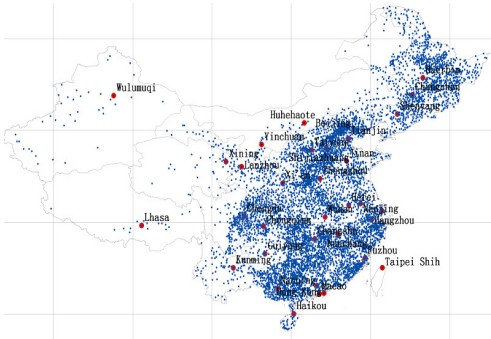

Fig.1.b Distribution of hydrological observation stations

The evaluation precipitation data we used is the observed precipitation in the hydrological stations. The location of the hydrological stations was given in Fig2.b, which is obtained from the sharing data system between the China Meteorological Administration (CMA) and the Bureau of Hydrology, the Ministry of Water Resources of P.R.China (Bureau of Hydrology, MWR).

2.2 "Fusing" technique description (combine satellite result with rain gauge data)

The satellite precipitation estimation product we used is based on the "split window channel technique" by NSMC. As well known, there are many kinds of typical algorithms of satellite precipitation estimation in the world , for example ,Barrett Method, Arkin Method, Life History Method, Stout Method, Griffith Method, Scofield Method, etc (Arnold Gruber,2000). But what we concerned technique is how to combine or "fusing" the satellite precipitation estimation product and the rain gauges data together. In this paper, we use a intellective objective analysis scheme which is brought forward by LU mai-meng (2004) to accomplish the fusing, which method is not only considered distance between the grid and rain gauges, but also consider the orientation of the rain gauges.

The R represents precipitation , superscibe O to refers to observation,a refers to analysis and s refers to satellite estimate,the suffix i is for the ith grid-point and k is the k_{th} raingauge location .the p_k is weights and n is the tatal number of raingauges.The $W\theta j$ is a distance factor ,Wr is a function of distance ,the Π is the orientation factor ,in which

$$R_i^a = R_i^s + \sum_{k=1}^{N} P_k (R_k^o - R_k^s)$$

$$P_k = (W_{rk} / \sum_{j=1}^{N} W_{rj}) \cdot \prod_{j=1}^{N} W_{\theta f}$$

$$W_{\theta j} = \begin{cases} 1 - \cos\theta_j & \theta_j < \pi / 2 \quad , r_j < r_k \quad , j \neq k \\ 1 & else \end{cases}$$

$$W_{rj} = \begin{cases} 1 & r_j \leq 0.33 D \\ 1 + (r_j / D - 0.33)^{-3} & r_j > 0.33 D \end{cases}$$

Where W_θ is a function of orientation. r is the distance between station j and grid point i, D is the average station distance θj is the angle from the connection line between station j and grid i to the connection line between grid i and station k.

2.3 The test scheme description

In this study, the period from 20th May, 2010 to 10th Sep, 2010 in China were tested. First of all, the Satellite precipitation estimates data were downloaded, decoded, at the same time, the rain gauges precipitation data obtained, then the 2 steps was done:

①: Quality control. By a simple quality control method, we eliminated the irrationality rain gauges, then a relative immobile station list got.

②: Data supplement. Based on the step ① and the daily and hourly rain gauges precipitation ,we supply the "zero" to the record in the station list in the step① .That means if the rain gauge doesn't observed precipitation, we considered the precipitation in the rain gauge is "zero".

In the fusing arithmetic, we selected 0.6° as the adjusting radius, which is the best adjusting radius after we have done a series of test from 0.1° to 2°(table ignoring).At last we have done a series of evaluation test by using the hydrological stations to examining the performance of the QPE products.

3. Evaluation of the QPE products

3.1 Evaluation methodology description

Evaluation was made with the threat score (TS), false alarm rate and missing alarm rate between the observations and the QPE products, and with the brier score to evaluate the performance. The precipitation was divided into four categories with the consistency of operational forecasts at the National Meteorological Center (NMC) of CMA as no rain, little rain, moderate rain and heavy rain

with thresholds of 0.1mm (including), 9.9mm (including), 24.9mm (including) and 49.9mm (including), respectively. (Zhao et al 2010).

3.2 A case study and the Evaluation results

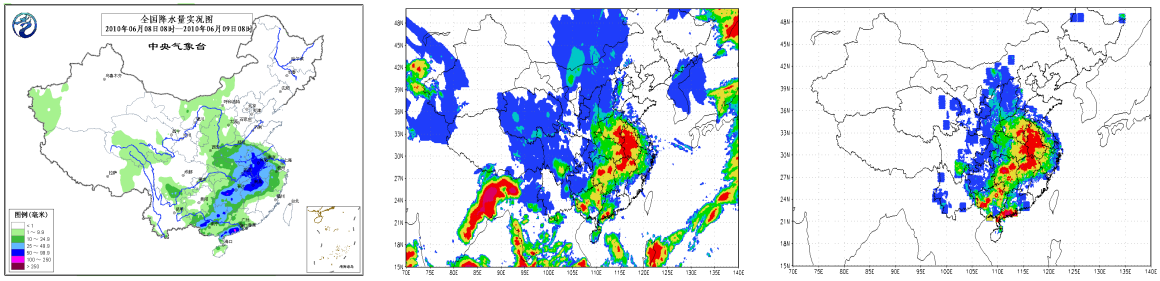

Fig.2. A case of quantitative precipitation estimation(QPE) in the 6th, Jun,2010
(a. Observational precipitation in the rain gauges(from (NMIC);
b.The satellite precipitation estimates product (from NSMC);
c. The quantitative precipitation estimation(QPE) product by fusing the satellite precipitation estimates and the rain gauges precipitation.(unit:mm)

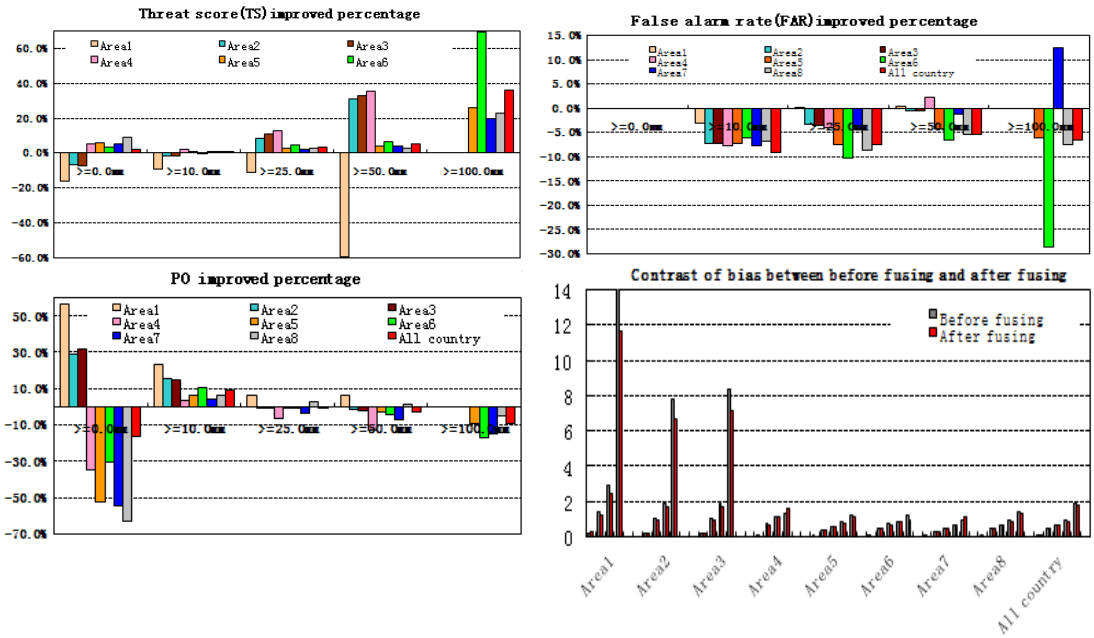

Fig.3 The improved performance between before fusing and after fusing

We find that the satellite precipitation estimates product would highly estimate the magnitude of precipitation in some area where the regional automatic weather stations is sparse, such as in Xinjiang province, Qinghai province and Inner Mongolia, etc, in 9th Jun, 2010 (Fig.2).

During the period of 20th May to 10th Sep. 2010, the threat score shows that precipitation accuracy was

improved in all 8 regions and the whole china, the heavier the rainfall intensity, the more significant the improvement with the percentage between 20% and 60%. Meanwhile, bias score reveals decrease in all 9 regions; False alarm rate indicates obvious decrease for all 9 regions with a rate of 5% to 10%, for some region it is high up to 30%. Meanwhile, evident improvement was displayed by the missing alarm rate, especially for the shower and little rain, with a percentage of 30% for some regions (Fig.3).

4. Results and discussion

In this study, we find that the test results show that the optimal result was given with an adjusting radius of 0.6-0.8 based on the "fusing" technique. The evaluation results show that the performance of QPE product based on the "fusing" technique is well improved than the satellite precipitation estimates product before fusing while the case study results explained it also.

As well known, there are obvious difference between satellite precipitation estimate and other remote technique as radar measurement, etc. But the results of satellite precipitation estimate can be widely used because the resolution of both spatial and temporal is good enough for the use of precipitation estimation .So, better results could be expected when the satellite precipitation estimate result fusing with rain gauges data and other data by multiple observed data.

Acknowledgements: This work was supported by the China Meteorological Administration under Grant No. GYHY200706001, GYHY200906007, GYHY2010 and CMATG2010Y23. The authors would thank You Ran of NSMC for her guidance and help on the fusing arithmetic and providing the satellite data.

References

John E. JANOWIAK, PINGPING XIE, 1999: CAMS–OPI: A Global Satellite–Rain Gauge Merged Product for Real-Time Precipitation Monitoring Applications. *Journal of climate.*12:3335-3342

Arnold Gruber, Xiujuan Su, M. Kanamitsu, et al., 2000: The Comparison of Two Merged Rain Gauge–Satellite Precipitation Datasets. *Bulletin of the American Meteorological Society,* 18 (11), 2631-2644

Lu Nai-meng, You Ran, Zhang Wen-jian.2004: A Fusing Technique with satellite precipitation estimate and rain gauge data. *ACTA Meteorological Sinica* (in Chinese), 18 (2), 141-146.

Zhao Lin-na, Wu Hao, Tian Fu-you, Qi Dan, et al., 2010: Assessment of probabilistic precipitation forecasts for the Huaihe basin using TIGGE data. *Meteorological Monthly* (in Chinese), 36 (7), 133-142.

The Megha-Tropiques accumulated rainfall algorithm TAPEER (Tropical Amount of Precipitation with Estimation of ERrors): investigating the error budget of satellite quantitative precipitation estimations

CHAMBON Philippe[1], Isabelle JOBARD[1] and Rémy ROCA[2]
[1]Laboratoire de Météorologie Dynamique, IPSL/CNRS, Palaiseau, France
[2]Laboratoire de Météorologie Dynamique, IPSL/CNRS, Paris, France
philippe.chambon@lmd.polytechnique.fr

1. Introduction

Precipitation estimation algorithms based on satellite observations have shown an increase of their overall quality, especially at the meteorologically relevant scales, over the recent decade. The need for a comprehensive error estimate along with the basic rain amount has become a key issue for quantitative precipitation estimation.

The TAPEER (Tropical Amount of Precipitation with Estimation of ERrors) algorithm is based on a merging approach of Passive Microwave (PM) instantaneous rain retrievals together with observations from geostationary cloud top sensitive Infrared (IR) channels. This technique relies on the Universally Adjusted GOES Precipitation Index (Xu et al., 1999) and on the PMIR algorithm (Kidd et al., 2003). It is developed for the Megha-Tropiques mission as a tool for a better understanding of the error budget on accumulated rain estimations. TAPEER will provide daily rain accumulations at one-degree resolution over the whole Tropical belt and their associated errors.

Roca et al. (2010) developed a sampling error model for satellite accumulated rainfall estimation. It was then adapted to provide global sampling error maps for the TAPEER algorithm. While sampling errors are often assumed to have the most significant contribution to the error budget (Bell et al., 1990), algorithmic issues can also lead to significant bias and random errors (Xu et al., 1999). Therefore they need to be quantified. This study shows a methodology developed as a first step to derive algorithmic errors for satellite precipitation estimation algorithms. A novel approach to quantitative precipitation verification, taking into account the errors on both satellite and surface rain datasets when comparing the estimates, is then used as a tool to infer the importance of each component of the budget to the total error.

2. Data

The satellite datasets used for this study are time series of Meteosat Second Generation 10.8μm images and Passive-Microwave (PM) derived instantaneous rain rates retrieved from several instruments over the 2006's monsoon season: the TRMM Microwave Imager (TMI), the Advanced Microwave Scanning Radiometer-Earth Observing System (AMSR-E) aboard Aqua and the Special Sensor Microwave Imager (SSMI) aboard Defense Meteorological Satellite Program (DMSP) satellites. The rain rate estimates are derived from microwave brightness temperatures using the BRAIN algorithm (Viltard et al., 2006). This algorithm is developed in the framework of the Megha-Tropiques mission as the instantaneous rainfall product derived from its MADRAS PM imager data.

A validation dataset of block-kriged (Journel and Huijbregts, 1978) rain gauge measurements from two dense networks, implemented for the AMMA experiment over Niamey (Niger) and Ouémé (Benin), is also used as a ground reference in this study.

3. Method

The errors related to the estimation of precipitation can be attributed to several sources. If we assume variance separation between the sources, a general error budget can be written as:

$$S^2 = S^2_{CALIBRATION} + S^2_{ALGORITHM} + S^2_{SAMPLING}$$

The calibration term is related to the instruments themselves but is known to be the less critical issue in precipitation estimation. The algorithmic term addresses both the error of the instantaneous rain retrievals but also the error related to the merging methodology. The sampling term addresses the error related to the discrete nature of measurements.

The error modeled by Roca et al. (2010) gives an estimation of the error, which is a mixture of pure sampling and merging methodology (Huffman, 1997). Eventually, in the algorithmic term of the budget, the error of instantaneous rain estimations remains and possibly is magnified at the accumulated scale.

Therefore, an error propagation approach was chosen to evaluate this algorithmic error. Algorithms providing instantaneous rain estimates are subject to systematic and random errors that depend on rain regimes and intensities (e.g. Viltard et al., 2006). Different scenarios of error propagation are considered in this study, assuming random and systematic biases of different magnitudes, on regimes of low, medium and high rain rates (respectively 0-2mm.h^{-1}, 2-10mm.h^{-1} and above 10mm.h^{-1}). Distributions of the resulting anomalies on TAPEER rain accumulations are then analyzed in order to infer statistical properties of the algorithmic errors.

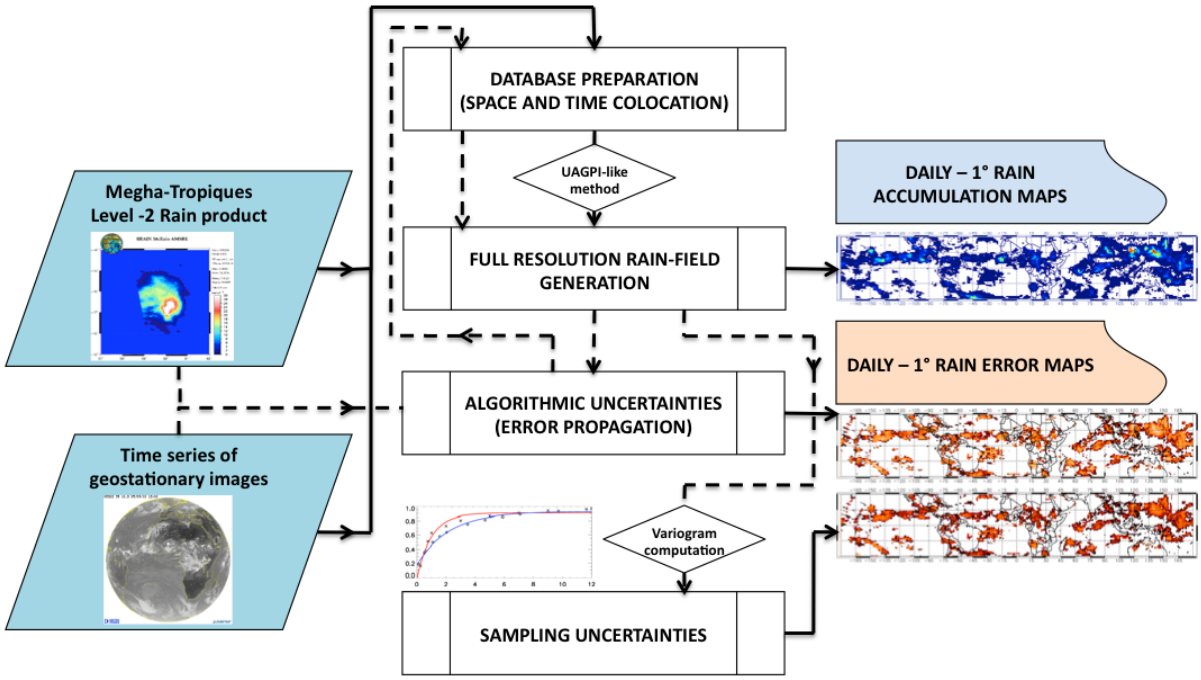

Fig 1. Flow chart of the TAPEER algorithm. Full arrows show the flow to produce rain accumulation maps, dashed arrows show the flow to produce error maps.

Figure 1 shows the flow chart of the TAPEER algorithm. Daily rain accumulation maps are derived from high-resolution rain fields that are produced through a process involving space and time collocation of the two inputs. They are also used to perform variogram calculations in order to deduce sampling error maps. Propagating disturbances on the instantaneous rain input data in the TAPEER framework performs the algorithmic error analysis.

4. Results

4.1 Anomalies analysis

The distributions of relative anomalies computed between the reference TAPEER time series and the TAPEER time series with biased inputs, show common characteristics. Random and systematic disturbances on the instantaneous rain inputs demonstrate a similar behavior with bias on rain accumulations increasing with disturbance magnitudes. Figure 2 shows an example of the distributions of relative anomalies for systematically biased high rain rates. While the magnitude of the bias on the input is increasing from 20 % to 100 %, the distribution becomes less peaky, and the standard deviation and the mean are increasing.

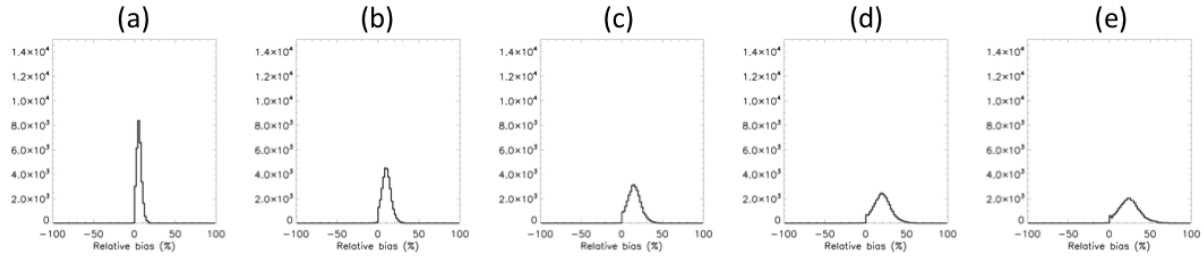

Fig 2. Distributions of relative anomalies between reference degree-daily rain accumulations and degree-daily rain accumulations built with a systematic error on instantaneous high rain rates of 20% (Fig. a), 40% (Fig. b), 60% (Fig. c), 80% (Fig. d) and 100% (Fig. e). The samples (more than 30 000) are land-only pixels over Western Africa during the 2006 rainy season.

A comparison of the distribution statistical moments in the different cases of errors (random error, systematic on low, medium and high rain rates) showed that:

- None of the distributions being close to a Gaussian distribution or conserving the properties of the error on the input, the errors propagate strongly non linearly in the TAPEER algorithm
- Random errors have less impact on TAPEER estimations than systematic errors
- The impact of a systematic bias depends on the rain rate regime, which is biased. This impact is strongly related to the percentage of population considered

4.2 An approach to the total error budget analysis

Depending on the bias characteristics of the rain rates produced by the PM-based algorithm and used as input in the TAPEER framework, the characteristics of algorithmic errors on the rain accumulations will be different. For instance, if the errors are only dominant in the rain regime that is not much represented in the population of rain rates, algorithmic errors might be negligible and the sampling errors will have therefore the most significant contribution to the total error.

A novel approach to quantitative precipitation verification is then used as a tool to infer the importance of each component of the error budget in the different scenarios envisioned. This

approach was developed by Roca et al. (2010) to compare satellite and ground rain datasets, taking into account their respective uncertainties. Using a dedicated regression technique (Kelly, 2007), Roca et al. showed that classical comparison scores such as the coefficient of determination or the bias of the regression can be computed in this error context.

Taking into account the sampling errors of TAPEER rain estimates and an additional algorithmic error issued from the different distributions computed above, the scores of comparison with rain gauge data over the two sites of Niamey and Ouémé are computed. Figure 3 shows the evolution of the coefficient of determination depending on the applied disturbance magnitude. For the scenario in which the instantaneous rain estimations have no systematic bias but only a random bias, Figure 3a shows that the algorithmic error has no impact in the comparison with the gauge, R^2 being stable until approximately 80 % of relative error magnitude. Figure 3b shows that algorithmic errors related to systematic bias on low rain rates are negligible with respect to the sampling errors for magnitudes of at least 50%. Figure 3c and 3d show that even small systematic biases on medium and high rain rates induce errors on rain accumulations that are not negligible with respect to the sampling errors and require to be handled carefully.

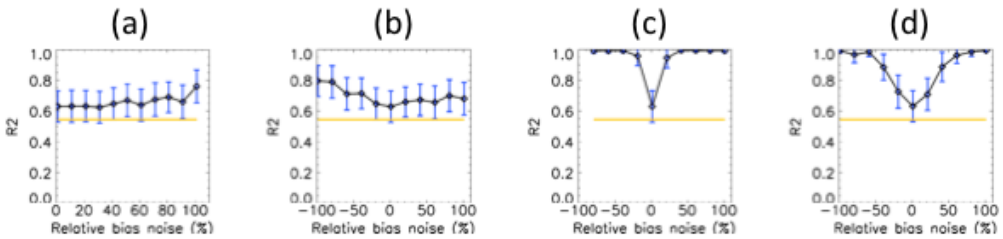

Fig 3. Evolution of the coefficient of determination R^2 of TAPEER rain estimates versus rain gauge estimates over Niamey for the 2006 monsoon season. These scores were computed, taking into account sampling errors and algorithmic errors, as a function of the error magnitude propagated on (a) random rain rates and systematically on (b) low rain rates (c) medium rain rates (d) high rain rates. In each case where the scores are computed from a distribution of scores, the blue bars correspond to the standard deviation of the distribution. The scores computed without errors are over plotted in yellow for each case.

Figure 4 shows the evolution of the biases of the regressions, confirming the different impacts highlighted in the evolution of the coefficient of determination. Figures 4a and 4b demonstrate a stable behavior of the bias, whereas Figures 4c and 4d show the increase of the bias on accumulated rain with increasing magnitude of bias on instantaneous rain.

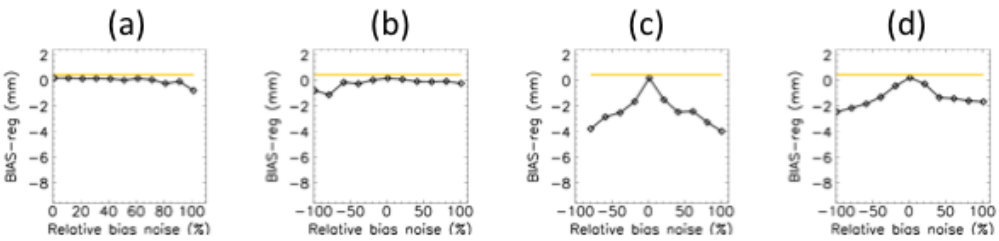

Fig 4. Evolution of the Bias of the regression of TAPEER rain estimates versus rain gauge estimates, taking into account sampling errors and algorithmic errors, as a function of the error magnitude propagated on (a) random rain rates and systematically on (b) low rain rates (c) medium rain rates (d) high rain rates.

Over the Ouémé site, the evolution of comparison scores (not shown) presents a similar behavior with negligible impact of random errors and systematic errors on low rain rates. The main difference between the two sites is that: where algorithmic errors issued from systematic errors on high rain rates are not negligible with respect to sampling errors over Niamey, the higher importance of medium rain rates is stronger over Ouémé.

5. Conclusion

User's needs in terms of precision and accuracy on accumulated rain datasets vary with the application. The error propagation methodology developed here allows performing an analysis of the algorithmic errors with respect to the bias characteristics of the instantaneous rain product used. Moreover, this kind of method allows a backward estimation of the requirements on instantaneous rain retrievals, which are necessary to reach these user's needs on the rain accumulation. Indeed, for instance knowing that the PM-derived rain estimator is only biased in the medium rain rates regime, a maximum bias tolerated by users of the final rain accumulation product can be backward propagated to a constraint on the developments of the PM instantaneous rain algorithm.

In this study, a simple technique was used to spread the distribution of algorithmic errors on time series of TAPEER degree-daily rain accumulation to compare them to sampling errors. A more detailed modeling and in-depth analysis of the space and time variability of these distributions is planned in order to deduce a precise knowledge of these algorithmic errors and producing algorithmic error maps that will be provided with TAPEER precipitation estimations. The approach developed here is general and consequently applicable to estimate the algorithmic errors of other precipitation algorithms.

References

Bell, TL., Abdullah, A., Martin, RL., North GR., 1990: Sampling errors for satellite-derived tropical rainfall: Monte Carlo study using a space–time stochastic model. *J. Geophys. Res.* **95** (D3), 2195 - 2205.

Huffman, GJ., 1997: Estimates of root-mean-square random error for finite samples of estimated precipitation. *J. Appl. Meteor.* 36: 1191 - 1201.

Journel, A., Huijbregts, C., 1978: Mining Geostatistics. London, Academic Press, pp. 600.

Kelly, BC., 2007: Some aspects of measurement error in linear regression of astronomical data. *Astrophys. J.* **665**: 1489–1506.

Kidd, C., Kniveton, DR., Todd, MC., Bellerby, TJ., 2003: Satellite Rainfall Estimation using a Combined Passive Microwave and Infrared Algorithm. *J. Hydrometeor.* **4**: 1088 - 1104.

Roca, R., Chambon, P., Jobard, I., Kirstetter, PE., Gosset, M., Bergès, JC., 2010: Comparing Satellite and Surface Rainfall Products over West Africa at Meteorologically Relevant Scales during the AMMA Campaign Using Error Estimates. *J. Appl. Met. and Clim.* **49**:4. 715-731.

Xu, L., Gao, X., Sorooshian, S., Arkin, PA., Imam, B., 1999: A microwave infrared threshold technique to improve the GOES precipitation index. *J. Appl. Meteor.* **38**: 569 - 579.

Performance and Applicability of Satellite Rainfall Estimation in Nepal

Rajendra Prasad Shrestha
Meteorological Forecasting Division, Department of Hydrology and Meteorology
rp_shrestha@hotmail.com

1. Introduction

Owing to the monsoon precipitation, diverse geological settings and rugged terrain, Nepal is prone to flood and landslides. Many lives and properties worth millions of dollars are destroyed. The monsoon season in Nepal occurs between June and September; monsoon is the dominant rainfall season, with 80% of the annual rainfall occurring in that period. Based on 20 years of data (1980-2000), Nepal is found to have high vulnerability of flood disasters as reported in the UNDP global report on reducing disaster risk (UNDP 2004). Between 1983 and 2005, on average 309 people lost their lives in Nepal, due to floods and landslides that accounting for over 60% of those who died due to different types of disasters in the country. (Khanal et al, 2007) The high level of poverty and rate of population growth has further increased the vulnerability to flood and landslides.

Reliable weather forecasting systems are one of the most effective ways to minimize the loss of life property. Accurate rainfall estimations are essential for reliable and timely weather forecasting and warning. In many countries weather forecasting has been relied upon by a dense network of rain gauge or ground based rainfall measuring radars that report in real time. In Nepal, like many other developing countries, the hydrometeorological station networks are sparse and rainfall data are available only after a significant delay. According to the Department of Hydrology and Meteorology (DHM) of Nepal, the country average density is one gauge for about 331 km^2 and is especially very sparse in mountainous areas. Owing to the limited spatial coverage of ground base gauges, unavailability of real-time rainfall data and constraint in technical and financial resources operational flood forecasting is yet to be initiated. Precipitation is highly variable in both space and time and is an important input in rainfall-runoff modeling. The availability of global coverage of satellite data offers effective and economical means of calculating areal rainfall estimates in sparsely gauged areas (Artan et al., 2007b). Thus, satellite rainfall estimates (RFEs) may be one of the best and appropriate approaches for Nepal to predict and forecast rainfall-induced runoff that may produce flooding.

2. Operational System and Products

National Oceanic and Atmospheric Administration (NOAA) has developed several satellite-based techniques and an algorithm for rainfall estimation to support weather and flood monitoring activities of USAID. Among them is the system developed at the Climate Prediction Center for Rainfall Estimates known as the CPC-RFE, which was tested and applied in the African region. The CPC-RFE is a combined satellite- and surface-based rainfall estimation technique. The CPC-RFE product has been available since 2001 on an operational basis for South-East Asia. The CPCRFE2.0 uses a merging technique that increases the accuracy of the rainfall estimates by reducing significant bias and random error compared with individual precipitation data sources (Xie and Arkin, 1996), thereby adding value to rain gauge interpolations.

Starting from June 15, 2001, the system has been put into operation at the Climate Prediction Center of NOAA and its products are available on a quasi real time basis

3. Flood Forecasting

The flood forecasting project of the Department of Hydrology and Meteorology has been working on establishing an operational flood forecasting and warning system in major rivers of Nepal. Data acquisition system is being modernized with real time telemetry. Flood forecasting models are being developed in collaboration with International Centre for Integrated Mountain Development (ICIMOD). Application of satellite rainfall estimation (SRE) for flood forecasting has been successfully tested for Narayani basin and GeoSMF model has been customized for Narayani basin with modified SRE as input. The model will be soon used for operational flood forecasting.

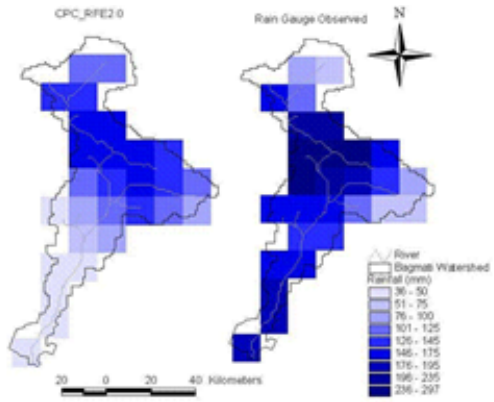

Figure 1 Comparison of rain gauge observed and satellite rain fall estimates for the Bagmati Basin on 23 July 2002.

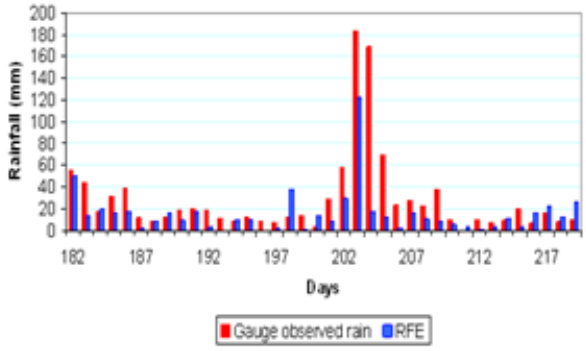

Figure 2 Comparison of rain gauge observed and satellite rain fall estimates for the Bagmati Basin (1 July to 7 August 2002).

The rainfall observed at the rain gauge stations was higher than the concurrent RFE. Figure 1 shows an example of a rainfall event on 23 July 2002 along with the details of the statistical analysis. The probability of detection is 1 and the false alarm ratio is 0, showing that the RFE is capturing the rainfall event quite well qualitatively in terms of occurrence. However, the estimated rainfall is lower than the observed amount, indicating a negative bias. Figure 2 shows the comparison of the observed gauge rainfall and CPC rainfall for the 38-day period from 1 July to 7 August 2002. The RFE captures the rainfall trends well but underestimates the amount. However, the RFE almost completely misses to register any significant rainfall on day 204, a day when the rain gauge network showed the second highest rainfall amount of the period. This is consistent with the findings of Yatagai et al. (2007) that satellite-based precipitation underestimates heavy precipitation compared with rain gauge-based observations.

4. Performance of the analysis system during monsoon 2008 (July-August)

2008 monsoon had normal monsoon, as discussed in report from Department of Hydrology and Meteorology. Rainfall for the country as a whole was 90% of its long period average. During this period, the rainfall was more or less evenly distributed compared to the previous years. Monthly total rainfall analyzed maps were prepared for four different months (June, July, August and

September). At the depart ment's climate section, monthly rainfall m aps for Nepal are prepared and published regularly by subjectively analyzing the good quality monthly rainfall data. These color map of monthly analyzed rainfall depict distribution of monsoon rainfall during each month Here only July and August which are two pick monsoon month are considered (Fig 3a, 3b). Fig. 4a and 4b shows objectively analyzed monthly total rainfall prepared by NOAA CPC for Asia Flood Network.

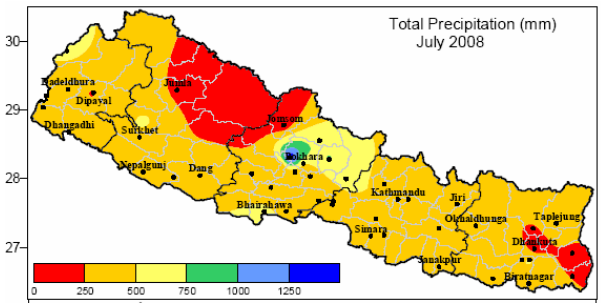

Fig 3 a

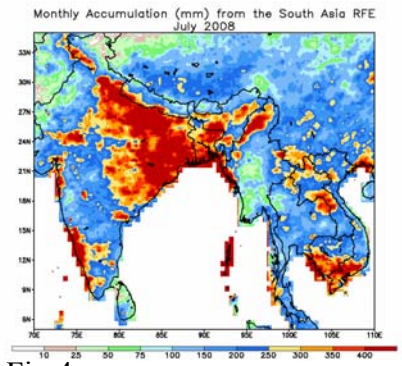

Fig 4 a

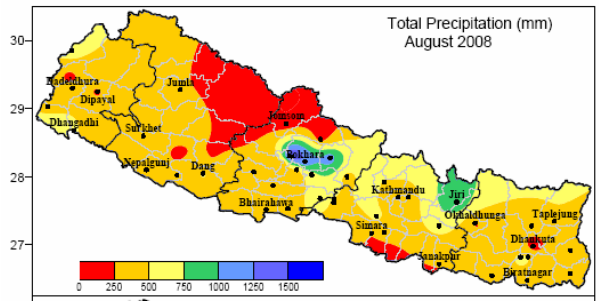

Fig 3 b

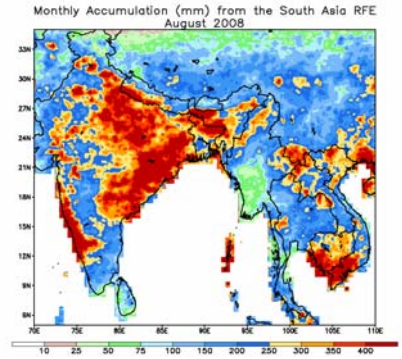

Fig 4 b

Figure 4a indicates that most of the country had around 250 mm to 500 mm of rainfall. The north central of the country shows rainfall amount from 500mm to 1250mm. Compare to this analysis, satellite analysis (Fig 4a) underestimates the rainfall over almost all the country except some parts of the northwest. The rainfall distribution pattern over the country does not agree well. The areas with rainfall amounts less than 100 mm match almost well with the RFE. The sharp gradient of rainfall between central middle mountain (Pokha ra) and rain shadow reg ion to nort h high mountains brought out realistically in the REF analysis.

During the month of Aug ust, generally the steady monsoon fl ow is well established and whole country receives more rainfall. In the department's analysis (Fig 3b), contours of 500 mm or more cover the m ost of the cou ntry. In this chart we find two maxim a of 16 44 mm and 98 1 mm of rainfall in central mountainous region. In the south west part of the country, rainfall amount in the REF charts (Fig 4b) is a lmost match with observed analyzed chart whereas the REF analy sis produces realistically low value of rainfall in the rest. There are no significant pockets of high and low rainfall area in the REF analy sis whereas two di stinctly high rainfall areas are located in the observed analyzed chart.

5. Year and Season-wise Comparison of Rainfall Estimate with Observed Rainfall.

Before analy zing the results, first all Nepal rain fall anomaly chart wa s prep ared to see i f the validating years fall in extreme rainfall years. It is seen from the figure that 2003 is a wet year and all other years fall into normal catego ry i.e. w ithin the 1 standard deviation. Analy ses were performed on an annuall y, seasonally and m onthly basis for the year 2002-2005, t he results for 2002 and 2003 are presented as a map for seasonal and annual. .

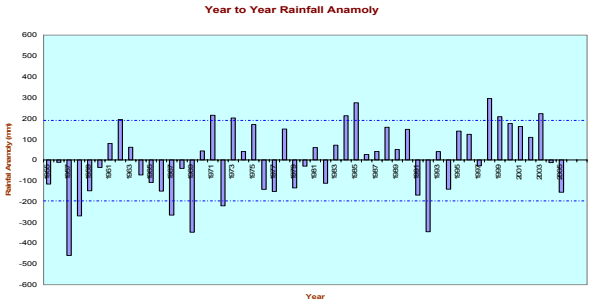

Fig. 5 Year to year variation of Rainfall (ano maly)

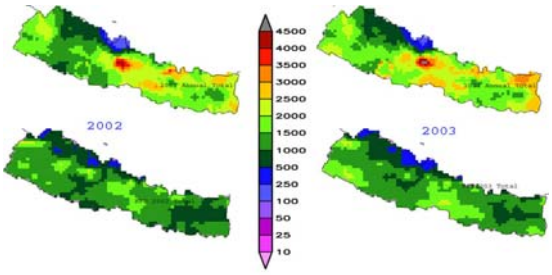

Fig. 6 Year to year comparison between observed rainfall and SRE

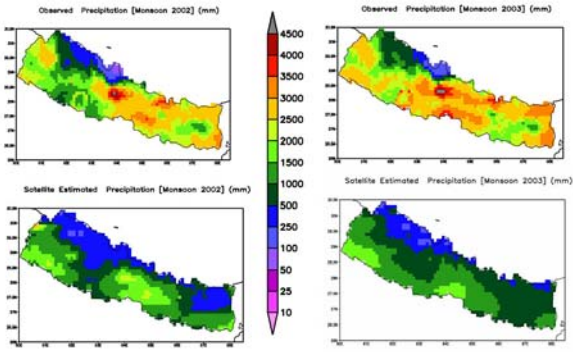

Fig. 7 Comparison between observed rainfall and SRE for the monsoon season

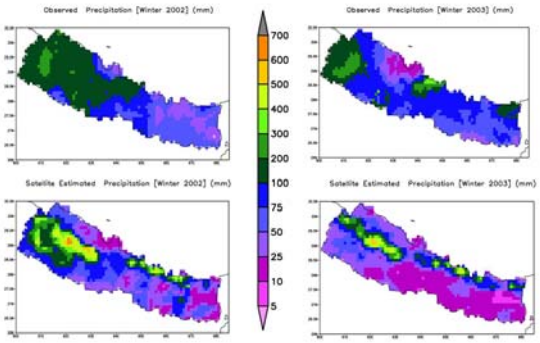

Fig. 8 Comparison between observed rainfall and SRE for the winter season

Year to year comparison between observed rainfall and SRE as shown in the figure 6 that there is a big difference in rainfall along the p ockets of hi gh rainfall area. This is also true in case of monsoon season (figure 7). But during winter season, for som e r eason, SRE is overesti mating over some area in central western region and northern part of the central Nepal (figure 8).

Bias map shows no definite pattern but band of ma xima can be seen in both the y ears in annual and monsoon season. In an annual map, along th e southern port ion of west Nepal, SRE shows higher values. There is no definite relationship between values. (Maps are not shown here).

Scattered plot show for the both the year with slope less than 45º. Since X-axis is observed value, it can be deduced that SRE underestimates.

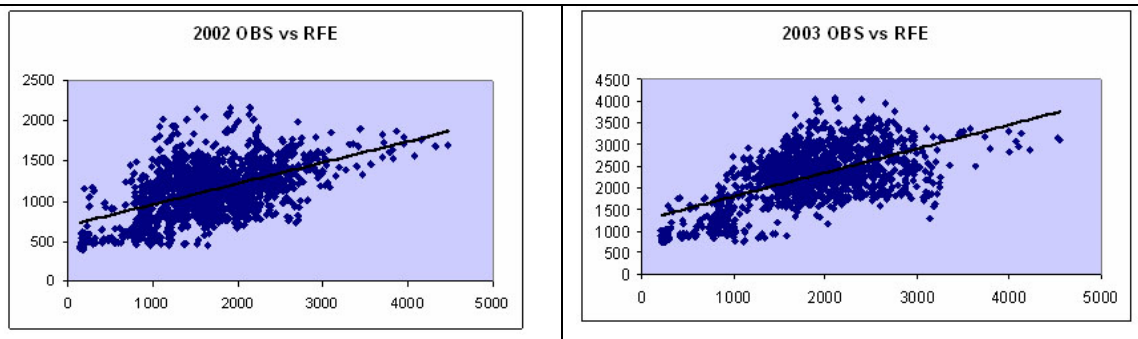

Figure 9 : Scatter plot 2002, 2003

5. Summary

With the advancement of technology REFs are becoming available with greater accuracy and coverage. The NOAA CPC-REF-2.0 rainfall estimates have been applied to the Bagmati Basin in Nepal to stimulate flow. The satellite based rainfall products are capable of detecting a particular rainfall event within the Bagmati Basin. The magnitude of the rainfall is much lower in the RFE compared with gauge observed rainfall. More accurate (quantitatively) and high-resolution data are necessary for reasonable flood prediction. It is difficult to predict the floods quantitatively using current satellite data. We can only provide an indication of probability of occurrence. With longer term rainfall and stream flow data and improved REF, GeoSFM rainfall runoff model could be tested for applicability of real time flood forecasting and flood risk management in the basin.

Satellite rainfall estimates mostly underestimate over region. SRE failed to capture heavy rainfall. From the experience flood forecasting and weather forecasting, it is evident that rainfall detection and prediction accuracy by NOAA are more sophisticated than India Meteorological Department .Limitation of SRE is delay of product by more than 24 hours.

Acknowledgement

The author is grateful to Department of Hydrology and Meteorology for supply of data and record of events to carry out the work. The author also thanks Mr. Rupak R. Rajbhandhari Head of Meteorology Department of Tric handra Campus for his valuable guidance. The author also thanks to ICIMOD to provide valuable information.

References

Department of Hydrology and Meteorology (DHM) 2008: Monthly Climatological Reports

Mitra A.K., Gupta M.D, Singh S.V. & Krishna T.N 2003: Daily Rainfall for the Indian Monsoon Region from Merged Satellite and Rain gauge Values: Large Scale Analysis from Real-Time Data: Journal of Hydrometerology 4, 769-780

Shrestha M.S., Artan G.A., Bajrachary a S.R. & Sharma R.R. 2008: Using satellite based rainfall estimation for stream flow modeling: Bagmati Basin Journal Flood risk Management1 (89-99

Workshop SRE Phase-II 15-19 Dec 2008: Application of Satellite Rainfall Estimates in the HKH Region – Phase II

QPE and QPF of Japan Meteorological Agency

Kazuhiko NAGATA
Forecast Division, Japan Meteorological Agency

1 INTRODUCTION

The Japan Meteorological Agency (JMA) has been producing analyzed hourly precipitation called "Radar/Raingauge-Analyzed Precipitation (here after call "R/A") since 1983, and precipitation nowcasting (Very-Short-Range Forecast of precipitation, here after call "VSRF") since 1988, in order to mitigate disasters caused by heavy rainfall, such as landslides, flash floods, and debris flows.

R/A and VSRF are disseminated to local meteorological offices, local governments, TV stations, as well as private weather companies. When disasters caused by heavy rain are likely to occur, JMA issues warnings and advisories based on R/A and VSRF and indices of possibilities of landslides and flood produced with them.

2 DATA

R/A and VSRF are produced with rain gauge data, radar data, and NWP outputs. Raingauge data are collected, every ten minutes or every one hour, from 10000-raingauge network operated by JMA, Ministry of Land, Infrastructure, Transport and Tourism (here after call "MLIT") and local governments (raingauges are located every 7km grid square on average). 46 C-band radars data with a spatial resolution of 1 km are collected, every five minutes, from the radar network operated by JMA and MLIT. A radar of the network covers a 500km×500 km square domain. Mesoscale model (here after call "MSM") outputs used for VSRF are wind from surface to 700hPa, temperature and relative humidity from surface to 850hPa, and hourly precipitation. MSM produces 15 or 33-hour forecast at 5km of spatial resolution every 3hours.

3 ALGORITHM AND ACCURACY OF R/A

3.1 ACCUMURATION OF RADAR INTENSITY DATA

In this section, we introduce the procedure for calculating one hour accumulated echo intensity. One hour accumulated echo intensity is calculated as sum of echo intensities obtained every five minutes. However, if some echo intensities move fast, one hour accumulated echo intensities sometimes show unnatural stripe pattern (See the left image of Fig.1). To avoid such unnatural patterns, the accumulation must be conducted taking the movement of the echoes into consideration (See the right image of Fig.1). In this process, we first divide observed echo intensities into some pieces and trace them every five minutes. Then, by summing up the echo intensities passing a grid, the one hour accumulated echo intensity of the grid is estimated. Here, quality

check of echo intensity data is also conducted.

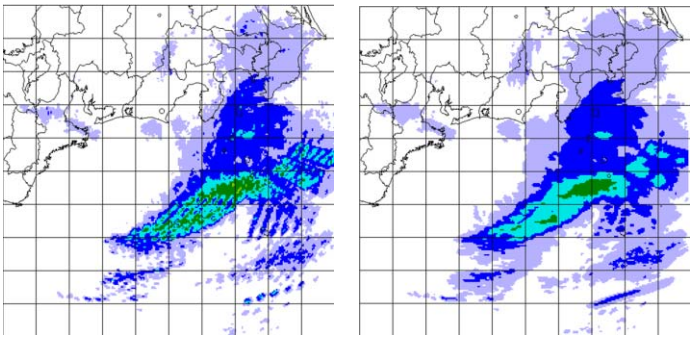

Fig. 1 Accumulation of radar intensity data.
(Left) one hour averaged echo
(Right) same as the left except for consideration of movements of echoes.

3.2 CALIBRATION OF RADAR DATA

In this section, we describe the procedures for calibrating one hour accumulated echo intensities with raingauge measurements to estimate precipitation.

3.2.1 CALIBRATION OVER ALL RADAR OBSERVATIONAL RANGE

One hour accumulated echo intensities at the grids of raingauges are generally different from those raingauge values. Because raingauge measurement is more reliable, we calibrate the echo intensities of a radar with raingauge observations within the observational range of the radar under the following two conditions.

(1) an average of calibrated echo intensities of a radar over a domain should be equal to those of other radars observing the same domain.
(2) an average of the calibrated echo intensities at the grids of raingauges should be equal to the average of the raingauge values.

3.2.2 CALIBRATION OVER LAND

The calibrated echo intensities as above are further calibrated to be equal to raingauge data at local scales (Makihara, 2000). For example, the calibrated echo intensities at a grid *g* derived in 3.2.1 is calibrated again with raingauges within about 40km from the grid *g*. A calibration factor at the grid *g* is calculated with weighted interpolation of the calibration factors of the grids of above raingauges. Here, a calibration factor of a raingauge grid is defined as a ratio of a raingauge value to the calibrated echo intensity at the grid of raingauge derived in 3.2.1. The weight for the interpolation takes into account following items.

(1) distances between the grid *g* and raingauges
(2) differences between the echo intensity at the grid *g* and those at the grids of raingauges
(3) beam attenuation rate by precipitation
(4) uniformity of raingauge distribution

By multiplying calibrated echo intensities by the calibration factor as determined above, an estimated precipitation at the grid g is obtained.

3.3 COMPOSITION OF CALIBRATED DATA ON EACH RADAR FIELD

After the above calibration, we produce a composite precipitation map using the calibrated echo intensities from 46 radars by transforming the coordination from zenithal projection into latitude-longitude grid with equidistant cylindrical projection. If multiple radars observe the same grid, the largest value is selected.

3.4 ACCURACY OF R/A

To assess the accuracy of R/A, about 200 raingauge data were excluded for verification. Then, R/A data were produced without these raingauge data. R/A data were compared with excluded raingauge data. Here we compared a raingauge value with the R/A values at 9 grids including 8 neighboring grids, considering location errors about by one grid (i.e. 1 km) due to advection of raindrops by wind before reaching the ground, and/or ones resulting from the coordinate transform.

Fig. 2 shows a scatter plot for comparisons between hourly R/A values and corresponding raingauge measurements for 4 months in a warm season (from August to November in 2009). Here, only best R/A values among ones at the 9 grids are plotted. This figure shows a good agreement between raingauge data and R/A values.

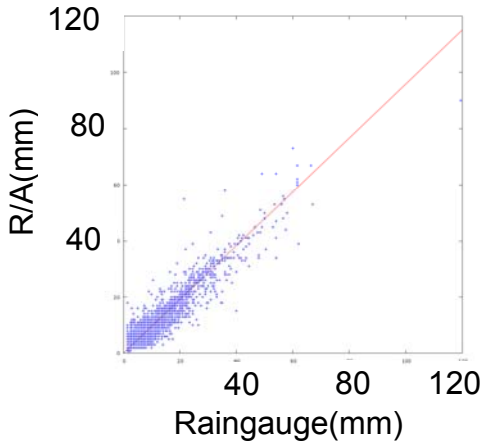

Fig. 2 Scatter plot of R/A and raingage with a regressed line(red) (R/A=0.96 x Raingauge)

4 ALGORITHMS AND ACCURACY OF VSRF

VSRF is a 6-hour forecast of precipitation with a spatial resolution of 1km. VSRF is made up to 6 hours ahead by merging the forecast precipitation with MSM and those with the extrapolation method. Here, we introduce details of the procedures for producing VSRF

4.1 EXTRAPOLATION METHOD

4.1.1 MOVEMENT VECTORS

We first divide the region over Japan into 50 km grid squares. Then, a movement vector of the precipitation systems at a grid is estimated with a pattern matching method. In order to avoid the adverse influence due to orographic effects on this estimation, time subtractions of R/A are used. 30 candidates for movement vector at the grid with highest matching scores are obtained using differences between R/A(t=0h), R/A(t=-1h), R/A(t=-2), and R/A(t=-3h) accordingly. After that, the most suitable candidate vector at the grid is selected considering time-space smoothness. Movement vectors gradually approach 700hPa winds of MSM as forecast time increases.

4.1.2 OROGRAPHIC EFFECT

Precipitation by orographic enhancement is considered as the stationary parts of precipitation over windward side of mountains. The algorithm follows the concept of seeder-feeder model (Browning & Hill,1981). A rainfall passing through the feeder cloud, which is generated by orographic effect, is enhanced due to the cloud droplet in the feeder cloud. Precipitable water, which is estimated with the data of temperature, relative humidity and wind from surface to 850hPa of MSM, is used to judge whether the feeder cloud is generated or not. If the feeder cloud is generated, the precipitation is enhanced depending on the amount of the rainfall from the seeder cloud.

Dissipation of echo in a lee side of mountain is also considered. It occurs when the echo top is low, the angle between the directions of mid level and low level wind is small, and no echoes exist at the dissipation area. The stronger the echo intensity is and the longer the traveling time from mountain top to dissipation area is, the more effective the dissipation is. Dissipation of echo is estimated statistically from 700hPa wind, 900hPa wind and relative humidity of MSM.

4.1.3 ACCUMULATION OF FORECAST INTENSITY

Initial field used for forecast is a composite echo intensity field obtained in the derivation process of R/A. The echo intensity field is moved along the movement vector derived in 4.1.1 with the time step of 2 or 5 minutes. 1-hour precipitation at a point is calculated as a sum of echo intensities passing the point. In the process, enhancement and dissipation of precipitation due to orographic effect are considered.

4.2 MERGING OF EXTRAPOLATION METHOD AND MSM

The performance of the conventional extrapolation method is good up to 3 to 4 forecast hours. And for the forecast time of more than 6 hours, MSM is supposed to be better than extrapolation method. Then we can improve the 4 to 6-hour forecast by merging the results of extrapolation method and those of MSM at their blending ratio. Blending ratios are estimated based on accuracies of extrapolation method and MSM respectively for the last few hours (Araki, 2000). VSRF is the output of this merging process.

4.3 ACCURACY OF VSRF

Critical Success Index (CSI) of VSRF, extrapolation method (EXT), MSM, and persistent forecast (PST) for the averaged hourly precipitation from June to August 2010 are shown in Fig. 3. Here the region over Japan was divided into 20 km grid square. The threshold of rainfall is 1mm/hour. It shows that VSRF distinctly has best performance.

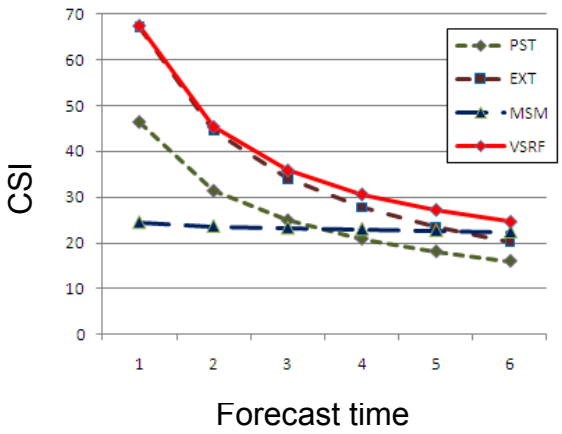

Fig. 3 CSI of VSRF, extrapolation method (EXT), MSM and persistent forecast (PST) from June to August 2010.

References

Araki, K, 2000: 6-hour forecast of precipitation. Reports of Numerical Prediction Division, **47**, 36-41(in Japanese).

Browning, K.A., F. F. Hill, 1981: Orographic Rain. Weather, **35**, 326-329.

Makihara, Y., 2000: Algorithms for precipitation nowcasting focused on detailed analysis using radar and raingauge data, Study on the Objective Forecasting Techniques, Technical Reports of the Meteorological Research Institute,**39**,63-111.

A new gauge-based precipitation analysis over mainland China and its evaluation

Yan SHEN, Qingxiang LI, Yang Pan Affiliations: Y Shen, Li, Pan
National Meteorological Information Center, China Meteorological Administration, Beijing, China, 100081

Daily gauge-based precipitation analysis over Mainland China has been constructed from about 2000 gauge reports on a 0.25°lat-long grid for the 57-yr period from 1953 to 2009 following the interpolation method named as climatology-based Optimal Interpolation proposed by XIE (Xie et al., 2007). Investigation showed no apparent systematic differences in annual mean spatial distribution or discontinuities in time series in the 57-yr CPAP dataset used for the different periods. Comparisons with three widely used only-gauge-based analyses including PREC, CRU2.1 and GPCC_V4 presented close agreements for the annual and seasonal mean precipitation for the period of 1953-2002 over most areas in Mainland China, while large differences were found along the northern slope of the Tianshan mountain range over the northwest China, because of the orographic correction in our analysis. On the other hand, CPAP captured many more extreme events and light events, while the other products showed a much smaller number of these events. This highlights the advantage of CPAP and, in turn, the use of the many more gauge reports than other products. Therefore we believe CPAP is a more reliable estimate of the precipitation over mainland China than other existing products, and should be used as a drop-in replacement for applications such as numerical model or satellite validation, flood monitoring as well as climatological studies. Based on the evaluation, we recommend CPAP should be used as a drop-in replacement over mainland China for other global analysis, whenever possible. The work reported in this paper is an integral part of our efforts to construct an analysis of hourly merged precipitation analysis in the future (Shen et al., 2010). Further work is to extend its temporal coverage and to improve the quality of the CPAP. The dataset for the period of 1900-1952 with only ～100 gauge reports available over mainland China is under consideration for development. Gauge network is an important element to determine the quality of the dataset, while the gauge distribution is very sparse over the northwestern China and the Tibetan Plateau, the effective tool to improve the quality of the dataset over these areas is to merge the gauge observations with the satellite precipitation products which is under way.

Verification of Tropical Cyclones-Related Satellite Precipitation Estimates in Mainland China

Zifeng Yu[1*], Hui Yu[1], Peiyan Chen[1], Chuanhai Qian[2], Caijun Yue[1]
[1] Shanghai Typhoon Institute, China Meteorological Administration, Shanghai, China
[2] National Meteorological Center, China Meteorological Administration, Beijing, China

1. Introduction

Accurate estimates of precipitation at both high temporal and spatial resolutions are required for many applications. Whereas rain gauge data are routinely available, they are sparse in many important regions even over land. Many gauge stations report only 6 hourly or even daily rainfall amounts. The weather radar network could provide good spatial and temporal coverage, but problems associated with inter-radar calibration and blockage by mountains still limit its accuracy and capability. Retrievals of precipitation from satellite measurements become the major products widely used to document precipitation characteristics and verification of model predictions/simulations.

There have been several global satellite rain rate products available, including Tropical Rainfall Measuring Mission (TRMM) 3B42 (Huffman et al. 2007), NOAA Climate Prediction Center's morphing method (CMORPH) (Joyce et al. 2004) and the Precipitation Estimation from Remotely Sensed Information Using Artificial Neural Networks (PERSIANN) (Sorooshian et al. 2000). In addition, the Geostationary Meteorological Satellite-5 (GMS-5) infrared brightness temperature (TBB) estimated rainfall dataset (hereafter the "GMS5-TBB data") developed by Yue et al. (2006a, b) is used operationally in Shanghai Typhoon Institute (STI) since 2008. A number of efforts have been made to compare the satellite estimated rainfall products with other direct rainfall measurements (Zhou et al. 2008). However, these studies are usually limited to compare the monthly mean products.

Recent studies have shown that satellite estimated rain rate can resolve the tropical precipitation systems reasonably well. However, the evaluation of satellite rain estimates for landfalling TCs on daily and multi-hours scales has not been carried out over China. Since inland flooding caused by heavy rainfall from landfalling TCs is a significant threat to life and property. It is necessary to provide a quantitative evaluation of the precipitation products from different datasets. Such an evaluation would give the confidence for their use in TC rainfall forecast and research.

The objective of this study is to provide an initial evaluation of the satellite precipitation estimates for TCs affecting mainland China during 2003-2006. Both 6 hourly and 24 hourly precipitation products from TRMM V6 3B42, CMORPH, and GMS5-TBB data are compared with the corresponding rain gauge data.

2. Verification Method

The 3B42, CMORPH and GMS5-TBB data are verified directly against the gauge observations because this study is focusing on the TCs-related rainfall and heavy precipitation is very important to be truly represented as referred observations.

* This work is supported by the State 973 Program (2009CB421505).

Corresponding author: Zifeng Yu, Shanghai Typhoon Institute, 166 Puxi Road, Xujiahui, Shanghai 200030, China. **Email: yuzf@mail.typhoon.gov.cn.**

A number of categorical statistics such as threat score (TS) and equitable threat score (ETS) are then applied. The term "categorical" refers to the "yes"/"no" nature of the verification at each station. Some thresholds (i.e., 1, 10, 25, 50, 100 mm) are considered to define the transition between a rain versus no-rain event. Then at each gauge station, each verification time is scored as falling under one of the four categories of correct no-rain estimate, false alarms, misses, or hits (Z, F, M, or H).

In addition, the correlation coefficient (CC) is calculated as below:

$$CC = \sum[(Y-\overline{Y})(X-\overline{X})] \ / \ \sqrt{\sum(Y-\overline{Y})^2 \sum(X-\overline{X})^2}\ , \qquad (1)$$

where X represents the observation, and Y represents the estimate, $\overline{X}, \overline{Y}$ are the area mean of X and Y, respectively.

Finally, hit, bias and root mean squared error (RMSE) are also used in comparisons.

3. Comparison results of 24h rainfall

A typhoon may affect rainfall in China when its center is either over the ocean or after its landfall. In this section, we first analyze all cases that affected mainland China regardless their centers were over the ocean or after landed and then those cases after landfall over mainland China during 2003-2006. All available 24-h gauge rain data for the four years of CMORPH operation are used. There are a total of 50 TC cases which affected mainland China with 27216 rain gauge data records, while there are 25 TCs landed over mainland China during the 4 year period. The 24-hr rainfall estimates from 3B42, CMORPH, GMS5-TBB data for the 25 landed TCs are compared with the corresponding 24-h gauge rainfall. For landfall TCs, the skills of 3B42 and CMORPH are similar to that for all cases (see Table 1). However, GMS5-TBB retrieved rainfall product has a much higher skill in TS and ETS in general, especially for rainfall greater than 25 mm, than either 3B42 or CMORPH although its CC is slightly lower than both 3B42 and CMORPH. Importantly, the GMS5 TBB shows high skill in estimating the heavy rainfall (50 and 100 mm per day) with TS of 0.27 and 0.17, respectively, while the TS are near zero for both 3B42 and CMORPH. This indicates that GMS5-TBB data product can be a good reference for heavy rainfall associated with landfall TCs.

Table 2 shows averaged performances for the 5 categories of rainfall amount (namely, 0-1, 1-10, 10-25, 25-50, ≥50 mm) for 3B42, CMORPH, and GMS5-TBB data respectively. For 3B42 and CMORPH, their hits, bias and RMSE are still similar but 3B42 has relatively higher hits, lower bias and smaller RMSE generally for all rainfall amount categories. For light rain (0-1 mm), both 3B42 and CMORPH overestimate the gauge rain with a positive bias of 1.1 and 1.0 mm, while they underestimate the non-light rainfall, especially the heavy rain (≥50 mm), with negative biases. For GMS5-TBB data, its hits are quite higher than that of 3B42 and CMORPH, especially when the rainfall is over 50 mm, and it still has somewhat skill with a hit rate of 5.1% for the heavy rainfall events. However, it overestimates light and moderate rainfall (0-25 mm) with a relatively larger bias than both 3B42 and CMORPH. For moderate and heavy rain (≥25 mm), the GMS5-TBB based rain data could do a better job, with a hit rate of 0.9%, a bias of -29.7, and a RMSE of 63.2 for 100 mm rain. The bias is about half of that from either 3B42 or CMORPH.

To compare the abilities of 3B42, CMORPH, and GMS5-TBB products in different regions of China, the area of 90ºE-150ºE, 10ºN-50ºN are divided to 5o × 5o grid boxes, and then TS and ETS are averaged in each grid box (Fig. 1).

4. Comparison results of 6h rainfall

Although GMS5-TBB based rain dataset has higher TS and ETS scores than 3B42 and CMORPH for rainfall of 10, 25 and 50 mm/6h, the 6-h rainfall is not as good as that for the 24-h rainfall. Its TS, ETS, and CC for 6-h rainfall become almost half of that for 24-h rainfall too (Table 3). The TBB retrieved 6-hourly rainfall has no skill for heavy rainfall.

5. Conclusions

The results show that compared with rain data from both the 3B42 and CMORPH, the GMS5-TBB data show much higher skill in representing the heavy rainfall events. All three satellite-retrieved rainfall datasets seem to give quite reasonable 6-h and 24-h rainfall distributions and their skills decrease with the increase in both the latitude and the rainfall amount in general. But they have different performance skills in reflecting rainfall of different amounts. The TSs for the 24-h rainfall retrievals for landfall TCs are 0.62, 0.47, 0.35, 0.27, 0.17 for GMS5-TBB data, respectively, for 1, 10, 25, 50 and 100 mm/day while they are 0.59, 0.33, 0.13, 0.03, and 0.0 for the 3B42, and 0.56, 0.25, 0.07, 0.01, and 0.0 for CMORPH. It indicates that 3B42 and CMORPH have a similar performance skill in reflecting the TCs-related rainfall but the 3B42 show a little better performance in general, which would be likely related to its gauge rain adjustment.

The datasets of 3B42 and CMORPH have overestimated the light rainfall (0-1 mm/day) and underestimated the non-light rain (over 1 mm/day). Large differences between the 3B42 or CMORPH and GMS5-TBB products are found mainly for the heavy rainfall. Even though the GMS5-TBB data overestimate the light and moderate rainfall and underestimate the heavy rain like 3B42 and CMORPH, it gives much improved heavy rain estimates with almost halved bias of that from 3B42 and CMORPH products. We also find that the three satellite products evaluated in this study are more accurate for the 24-h rainfall estimates than for the 6-h rainfall estimates.

Main references:

Huffman G. J., R. F. Adler, D. T. Bolvin, G. Gu, E. J. Nelkin, K. P. Bowman, Y. Hong, E. F. Stocker, and D. B. Wolff, 2007: The TRMM Multisatellite Precipitation Analysis (TMPA): Quasi-Global, Multiyear, Combined-Sensor Precipitation Estimates at Fine Scales. *J. Hydromet.*, **8**, 38–55.

Joyce R. J., J. E. Janowiak, P. A. Arkin, and P. Xie, 2004: CMORPH: A method that produces global precipitation estimates from passive microwave and infrared data at high spatial and temporal resolution. *J. Hydromet.*, **5**, 487-503.

Sorooshian S., K. Hsu, X. Gao, H. V. Gupta, B. Imam, and D. Braithwaite, 2000: Evaluation of PERSIANN System Satellite–Based Estimates of Tropical Rainfall. *Bull. Am. Meteor. Soc.*, **81**, 2035–2046.

Yue C., P. Chen, X. Lei, and Y. Yang, 2006a: A preliminary study on method of quantitative precipitation estimation (QPE) for landfall typhoon. *Scientia Meteorologica Sinica*, **26**, 17-23. (in Chinese)

——, 2006b: Preliminary study of short-term quantitative precipitation forecast method for landfalling typhoon. *Scientia Meteorologica Sinica*, **34**, 7-11. (in Chinese)

Zhou T., R. Yu, H. Chen, A. Dai, and Y. Pan, 2008: Summer precipitation frequency, intensity, and diurnal cycle over China: A comparison of satellite data with raingauge observations. *J. Climate*, **16**, 3997–4010.

Table 1. TS, ETS, and CC of 3B42, CMORPH and GMS5-TBB data for 24-h rainfall

			1mm	10mm	25mm	50mm	100mm
All cases	3B42	TS	0.59	0.31	0.13	0.03	0.0
		ETS	0.31	0.21	0.11	0.03	0.0
		CC	0.62				
	CMORPH	TS	0.55	0.23	0.06	0.01	0.0
		ETS	0.28	0.15	0.05	0.01	0.0
		CC	0.57				
Landfall TCs	3B42	TS	0.59	0.33	0.13	0.03	0
		ETS	0.33	0.23	0.11	0.03	0
		CC	0.66				
	CMORPH	TS	0.56	0.25	0.07	0.01	0
		ETS	0.29	0.16	0.06	0.01	0
		CC	0.60				
	TBB	TS	0.62	0.47	**0.35**	**0.27**	**0.17**
		ETS	0.24	0.24	**0.23**	**0.21**	**0.15**
		CC	0.51				

Table 2 Average of hits, bias and RMSE for 5-category 24-h rainfall for 3B42, CMORPH and GMS5-TBB data

	3B42			CMORPH			TBB		
	Hits	Bias	RMSE	Hits	Bias	RMSE	Hits	Bias	RMSE
0-1 mm	8221 (39.2%)	1.1	3.3	7720 (34.3%)	1.0	2.9	10795 (47.9%)	8.3	20.8
1-10 mm	2464 (10.9%)	-1.3	4.8	1826 (8.1%)	-1.9	4.3	6029 (26.8%)	12.3	25.9
10-25 mm	504 (2.2%)	-10.6	12.7	259 (1.2%)	-11.7	13.2	2934 (13.0%)	10.5	31.1
25-50 mm	58 (0.26%)	-25.7	27.4	14 (0.06%)	-27.7	29.0	1147 (5.1%)	3.6	35.2
> 50 mm	1 (0.004%)	-74.2	86.5	0 (0%)	-79.2	91.6	213 (0.9%)	-29.7	63.2

Table 3. TS, ETS, and CC of 3B42, CMORPH and GMS5-TBB data for 6-h rainfall

			1mm	10mm	25mm	50mm	100mm
All cases	3B42	TS	0.33	0.11	0.03	0.01	0
		ETS	0.29	0.11	0.03	0.01	0
		CC	0.40				
	CMORPH	TS	0.27	0.05	0.01	0	0
		ETS	0.23	0.05	0.01	0	0
		CC	0.42				
Landfall TCs	3B42	TS	0.35	0.12	0.03	0.01	0
		ETS	0.30	0.11	0.03	0.01	0
		CC	0.38				
	CMORPH	TS	0.30	0.06	0.01	0	0
		ETS	0.24	0.06	0.01	0	0
		CC	0.43				
	TBB	TS	0.27	0.18	**0.12**	**0.07**	**0**
		ETS	0.19	0.15	**0.12**	**0.07**	**0**
		CC	0.37				

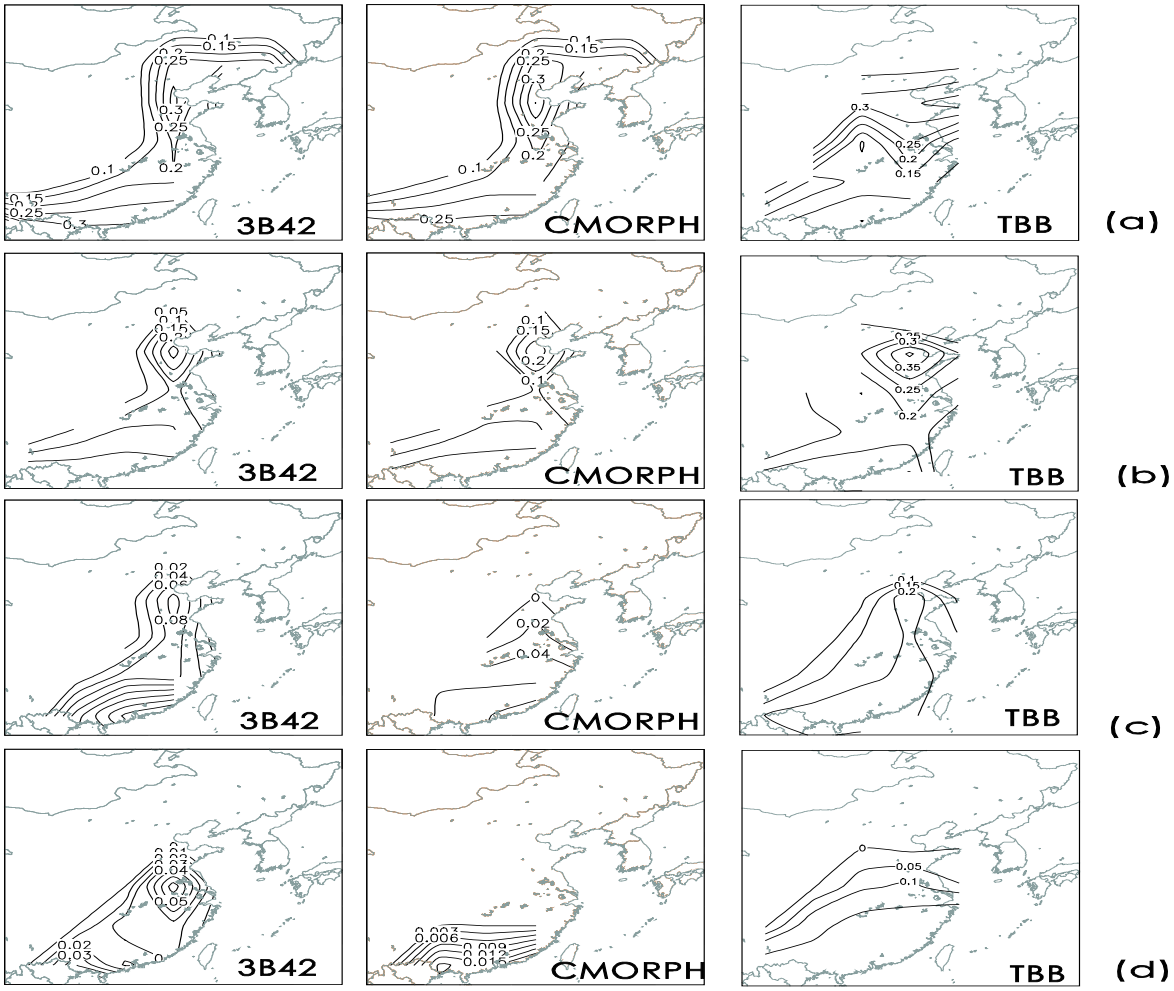

Fig.1. ETS for 3B42, CMORPH and GMS5-TBB 24-h rain data. (a) for 1 mm, (b) for 10 mm, (c) for 25 mm, and (d) for 50 mm.

Establishment of Real-time System for Daily Precipitation Analysis over China

Anyuan Xiong, Yan SHEN, Mingnong Feng
Affiliations: A Y Xiong, Shen, Feng — National Meteorological Information Center, China Meteorological Administration, Beijing, China, 100081

Under the cooperation with the Climate Prediction Center (CPC) affiliated to National Oceanic and Atmospheric Administration (NOAA), the real-time operational system of daily precipitation analysis over China is established in the National Meteorological Information Center (NMIC). This system is developed based on the daily precipitation observations over 2400 gauges which are used to produce its analysis at the 0.25°lat/lon grid. Four modules are contained in this system including data's obtainment, quality control, data analysis and service. The kernel interpolation algorithm of this system is introduced from the CPC called as the climatological Optimal Interpolation (OI) method which can reduce the analysis error substantially arising from the large spatial incontinuity of precipitation. Firstly, daily climatology is defined for each station as the summation of the first 6 harmonics for the 365-calendar-day time series of the mean daily precipitation climatology are then created by interpolating the truncated station climatology through the algorithm of Shepard. Secondly, to account for the orographic effects, these fields are then adjusted by the PRISM (Parameter-elevation Regressions on Independent Slopes Model) monthly precipitation climatology data so that the monthly precipitation accumulation of the daily climatology meets that of the PRISM while temporal variation patterns in the original daily climatology time series are retained. Thirdly, analyzed fields of ratio of daily precipitation to daily climatology are created by interpolating the corresponding station values through the OI technique. Analyses of total daily precipitation are finally calculated by multiplying the daily climatology with the daily ratio. The users can get the products in three formats after 9:20 Local Time (1:20 UTC) through CDC website (http://cdc.cma.gov.cn). This system runs stable with reasonable products. This dataset can be used in the field of climate diagnostics, numerical models verifications and satellite products checking. The work reported here is an integral part of our long-term effort to construct real-time and fine-resolution precipitation analyses over China domain. Further improvements of the gauge-based analysis are underway to add in bias correction for the wind effects through employment of published correction coefficients. We welcome collaborations in improving this system by refining the algorithm and merging with the satellite-based precipitation products.

The representation of the rain gauges in estimating the strength of rainfall during the "plum rain" in Anhui province

Jiuke Wang, Xiaoyang Liu

Department of Atmospheric and Oceanic Science, Peking University

wangjiuke@gmail.com

Key word: Rainfall, Rain gage, Representation

1 Introduction

It is widely known that the precipitation has a great influence on human lives, for example, water resource arrangement, flood forecast and agricultures, Therefore, the quantitative evaluation of the spatial distribution of rainfall is of great impotence (Manel Ellouze, 2008). Since a weather surveillance radar could cover a huge area with high spatial and temporal resolution, using radar for precipitation estimation is always the best choice (Lisbeth Pedersen, 2008).

However, not all of the river basins or interested areas are under the monitoring of radar, the most common way to estimate rainfall is still the use of rain gages. Many hydrologists consider the rain gauge data to be the "ground truth", filled the data of rain gauge into the hydrological model as mean depth of the rainfall of a given area, assuming that a single gauge is representative of the entire given area. In some cases, this very assumption leads to a huge error (Lisbeth Pedersen, 2008).

The flood probability, one of the results of the hydrological model, is sensitive to the spatial distribution of rainfall, the uncertainty of the spatial distribution of rainfall has important impact not only on the properties of floods, such as runoff volumes, but also on the estimations of hydrological model parameters (Patrick Arnaud, 2001). Therefore, the errors of the data of the rain gages, due to the lack of representation, must be determined before further usage.

The "plum rain" is a set of processes of precipitation in southeast of China, usually from June to July, which always contains floods or other hydrologic disasters. In order to provide accurately hydrological information, a dense network of rain gages is set up. In general, denser the network is, more accurate the spatial distribution of rainfall is. However, maintaining one more hydrological station or weather station operational is always need good financial support while the accuracy of estimations is not equally improved.

Supported by a CINRAD-98D radar located in Hefei, provincial capital of Hefei province, spatial distribution of rainfall with high spatial and temporal resolution can be acquired through the joint estimation of radar and network of rain gages. In this research, the relationship between the number of the rain gages and the accuracy of the estimation of rainfall will be analyzed.

2 Data and Methodology

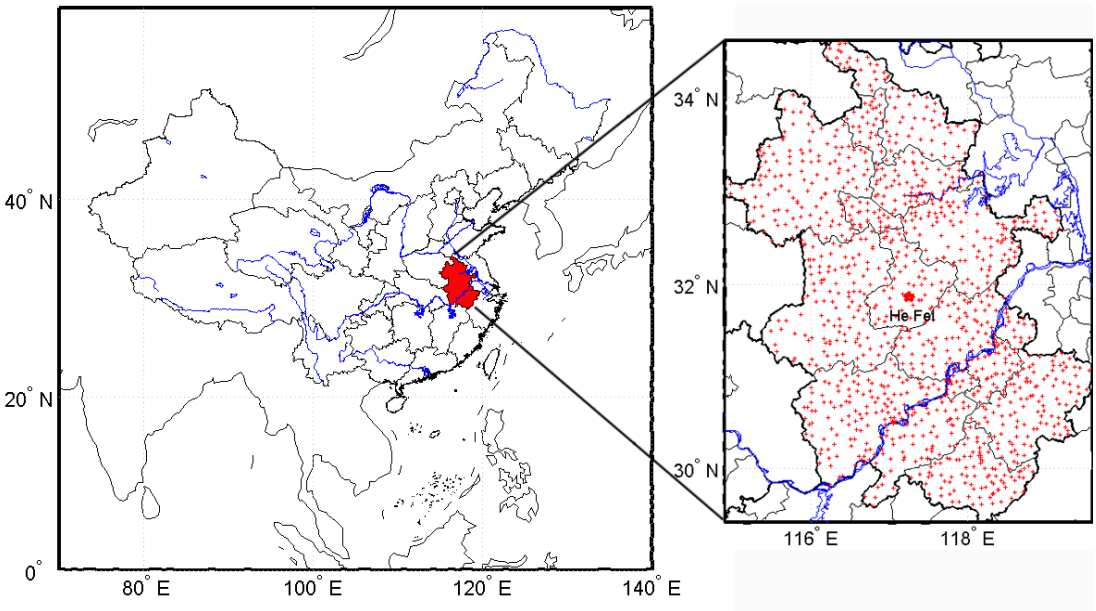

Fig 1. location of the research area

The CINRAD-98D radar located in Hefei, the red dot in the right figure of *Fig 1*, covers the area with the radius of 230km, calibrated by total1165 rain gages, marked as red cross in *Fig 1*. The estimation of the spatial distribution of rainfall is computed based on one rain gauge adjustment techniques (Xiaoyang LIU, 2009). With the spatial resolution 1Km*1Km, the hourly accumulated precipitation data during the "plum rain" was acquired from the joint estimation of radar and a dense network, made up of 1165 rain gauges, with the average interval of 14km, deployed in Anhui province. The data include the major process of "plum rain" from year 2005 to 2008.

Former research pointed out, the Gamma distribution was found fitted well to the rainfall data.(S.C. Michaelides, 2008), the spatial variability of the rainfall has been expressed by use of the standard error of rainfall fields.(Rycroft, 1947). And the accuracy of the rainfall estimation is highly affected by the mean depth and the standard deviation of the rainfall, therefore, the estimation of the mean depth and the standard deviation is somehow a key factor affecting the results of hydrologic applications (Sharon, 1972).

In order to evaluate the representation of the rain gauges, the relationship between the number of rain gages and the mean depth and the standard deviation of the strength of rainfall will be investigated first. Data of all rain gages were used to obtain a mean depth and mean standard deviation of the rainfall, which was treaded as "true value", at least this was the best mean value that was able to be acquired. Then take one random rain gage out, compute the mean value and standard deviation, figure out the difference between the "true value" and the new computed result. Repeat the process above until only one gauge remains. Since the area if fixed, a connection between the mean depth and the standard deviation and the number/ representative area is set up.

Using the high resolute radar-rain gages joint estimation, the representation of the rain gages could also be expressed by a more direct method, that is, for one rain gage, increase the area/radius that this rain gage represented, calculate the difference each time the area/radius changed.

3 Results

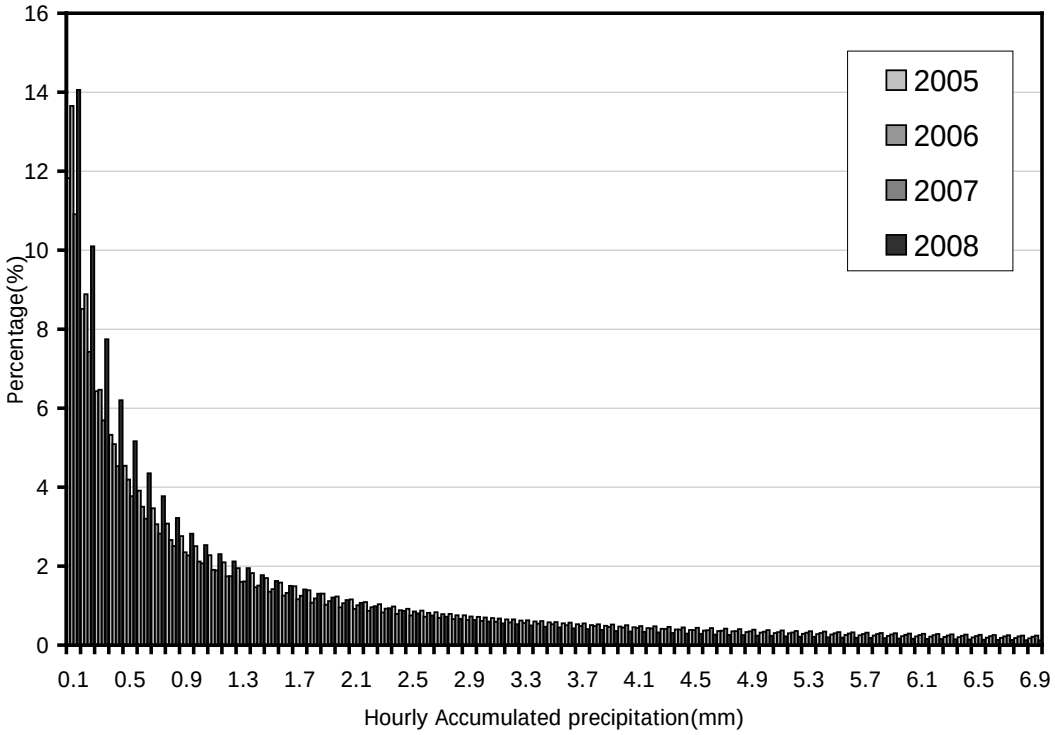

Fig 2. distribution of the strength of rainfall

The distribution of the strength of rainfall was shown in Fig 2, the shape of the distribution curve fitted the Gamma distribution form, there was no obvious difference among the shapes of the distribution curves based on the rainfall data of 4 years, and the "plum rain" was always from prevailing cloud, which conduced lower standard devotion (5.4mm) compared to convectional precipitation.

The relationship between the number of rain gages and the mean depth and the standard deviation of the strength of rainfall was shown in *Fig 3*, the number of the rain gages come to calculate was drawn on X axis, the relative error was implied on Y axis. From the *Fig 3*, if only one rain gage was used to describe the mean depth and the standard deviation of the strength of rainfall of the whole area, the relative error of both average depth and standard deviation could reached up to 66%, while more rain gages come to calculate, the relative error rapidly decrease below 30%, however, the trend of the decrease is not stable. When the number of the rain gages reached 100, which is 10% of the total number of the rain gages network, the relative error between the computed value and "true value" arrived at a low level that is lower than 4%, and the increase of the number of rain gages didn't lead to obvious increase in accuracy, which implicated 10% of the total rain gages would describe the character of the mean depth and the standard deviation of the strength of "plum rain".

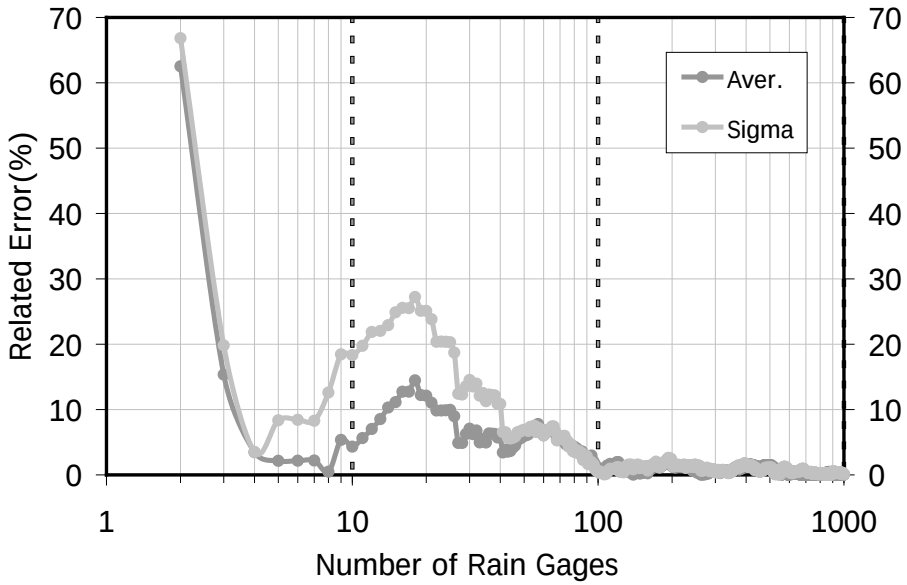

Fig 4 The relationship between the number of rain gages and the mean depth and the standard deviation of the strength of rainfall

The representation of the single rain gage is indicated in Fig 4 and Fig 5. in Fig 4, X axis represents the distance between two adjacent rain gages, Y axis represents the relative error between calculated result and the "true value", and error bar is the standard devotion of each distribution of relative error. Shown in *Fig 5*, the number of the rain gages is marked on X axis while the relative error is still marked on Y axis. From the *Fig 5*, for the purpose of the improvement of 3%, from relative error 18% to 15%, the number of rain gages needs to increase from 26 to 76, however, from relative error 15 to 11%, the number of rain gages needs to increase from 76 to 316! In other words, along with the increasing number of rain gages, the efficiency of improvement of the accuracy decreases.

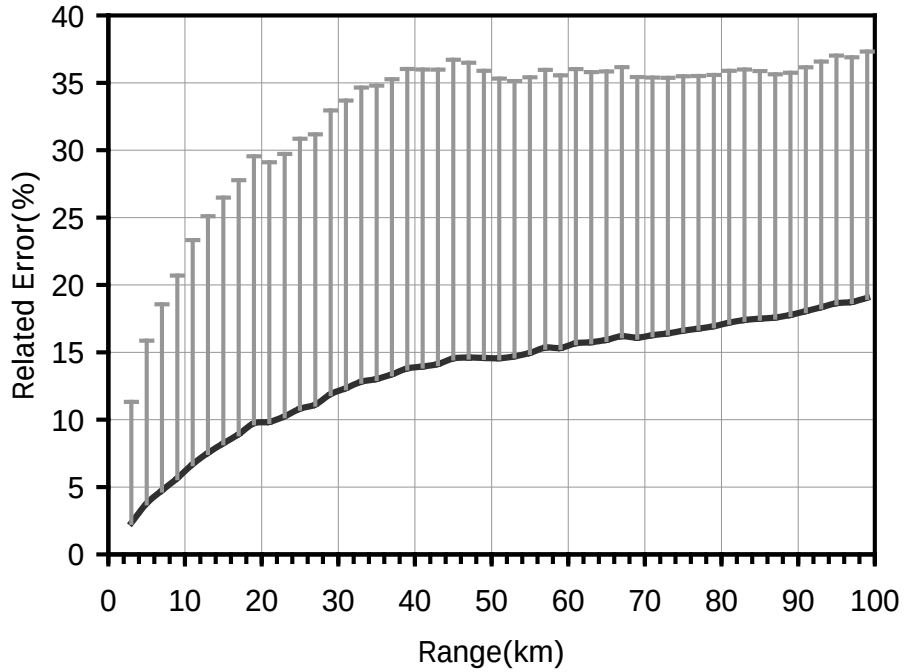

Fig 4. the relationship between range of rain gages and the relative error

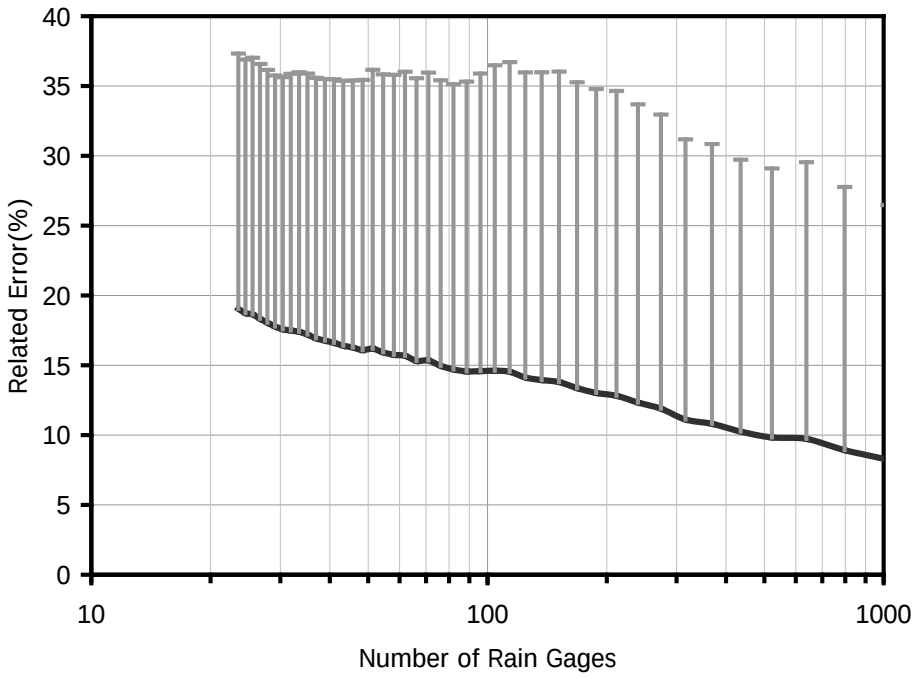

Fig 5. the relationship between number of rain gages and the relative error

4 Conclusions

Since the distribution of the precipitation was not uniform and was a long with high variability, the accurate estimation of the rainfall was difficult and of great importance. The most common and traditional way to acquire distribution of the rainfall was the use of rain gages, however, the uncertainties or errors introduced by the representation of the gages could cause bigger uncertainties or errors in further hydrological or other applications.

From the analysis on Anhui, China, during the process of "plum rain", due to the stable shape of the distribution of precipitation strength, good representation was found, using only 10% number of the rain gauges(average distance 48km) could give a mean depth and standard deviation over Anhui province with relative error less than 2%, in other words, for estimating mean depth and standard deviation during the "plum rain", the current density of network is far exceed necessary.

In order to lower the uncertainties in estimating the distribution of the precipitation, dense network of rain gages was set up and the number of rain gages increased rapidly, however, the calculation shows that, the efficiency of improvement in accuracy by adding new rain gages was lower when reached a higher level of accuracy.

Therefore, the estimation of that uncertainties or errors introduced by the representation of the gages was necessary not only to estimate the uncertainties or errors in further applications, but also to save budget under an acceptable accuracy.

References

RYCROFT, H.B. (1947) Random sampling of rainfall. J. S. Afr. For. Ass., 18, 71-81.

SHARON, DAVID(1972), SPATIAL ANALYSIS OF RAINFALL DATA FROM DENSE NETWORKS, Hydrological Sciences Journal, 17: 3, 291—300.

LIU Xiaoyang, YANG Hongping, LI Jiantong, LI Bai, ZHAO Kun, ZHENG Yuanyuan,

CINRAD R adar Quantitative P recipitation E stimation G roup S ystem, M eteorological Monthly, April 2010, Vol. 36, No 4

S.C.Michaelides, F.S.Tymvios, T.Michaelidou,Spatial and temporal characteristics of the annual rainfall f requency distribution i n Cyprus, Atmospheric R esearch, V olume 94, I ssue 4, December 2009, Pages 606-615.

Lisbeth P edersen, L isbeth P edersen, N iels E inar Jensen, L asse E ngbo C hristensen, H enrik Madsen, Quantification of the spatial variability of rainfall based on a dense network of rain gauges, Atmospheric Research, Volume 95, Issue 4, March 2010, Pages 441-454.

Manel Ellouze, Chafai Azri, Habib Abida, Spatial variability of monthly and annual rainfall data over S outhern Tunisia, A tmospheric R esearch, Volume 93, I ssue 4, A ugust 2009, P ages 832-839.

Patrick A rnaud, C hristophe B ouvier, L eonardo C isneros, R amon D ominguez, I nfluence o f rainfall spatial variability on flood prediction, Journal of Hydrology, Volume 260, Issues 1-4, 15 March 2002, Pages 216-230.

Recent Progresses on TC Precipitation (QPE/QPF)

Yihong DUAN, Lianshou CHEN, Ying LI, Hui YU, Jian LIN, Jeffrey CALLAGHAN

National Meteorological Center/CMA
Chinese Academy Meteorological Sciences/CMA
Shanghai Typhoon Institute/CMA

1. Introduction

In recent years, extreme weather events and calamities occurring in both Pacific and Atlantic coastal regions have been generated by landfalling tropical cyclones (LTCs), such as the super typhoons Rananim (2004), Haitang (2005), Saomai (2006) and Morakot (2009) in the Pacific, and the super hurricanes Ivan (2004), Rita (2005) and Katrina (2005) in the Atlantic. Additionally, super cyclonic storm Gonu (2007) in the Arabian sea and super cyclonic storm Nargis (2008) in Bay of Bengal. Consequently, the top priority for scientists working in this field should be the improvement of forecasting techniques and early warning systems for LTCs (Chen et al, 2010).

TC rainfall forecasting techniques are lagging behind those of the track forecast. However, significant progress has been made in recent years due to the advance in remote sensing observations and the improvement of mesoscale models and data assimilation techniques. Until relatively recently, TC rainfall prediction was carried out mainly using empirical speculation and subjective experience on the part of the forecaster. However, advanced techniques for quantitative precipitation estimation (QPE) and quantitative precipitation forecasting (QPF) are currently employed in operational applications in some major forecasting centers, which already have greatly improve the forecasting for LTC-related rainfall. Nevertheless, further improvements in QPF based on a better understanding of TC rainfall mechanisms are still required.

2. Progress of TC QPE/QPF in past four years

2.1 QPE

Radar reflectivities have been widely used to estimate the rainfall rate and distribution of TCs. Some techniques have been developed to find the relationships between radar rainfall and true rainfall (Ji et al., 2008).

Satellite measurements at microwave frequencies are key elements of present and future observing systems. Passive microwave data have been used to estimate TC precipitation. The 10.7-GHz frequency of the NASA Advanced Microwave Precipitation Radiometer (AMPR) has demonstrated high-resolution detection of anomalous surface water and flooding in numerous situations (Buckley et al, 2009）. Although limited for operational use by their dimensional sampling, the dual-frequency capability makes altimeters a unique satellite-borne sensor to perform measurements of key surface parameters in a consistent way (Quilfen et al, 2009）. The response of the precipitation field for tropical cyclones in relation to the surrounding environmental vertical wind shear has been investigated using 20000 snapshots of passive-microwave satellite rain rates (Wingo et al, 2010）. Available for more than 20 years, passive microwave measurements are very valuable but still suffer from insufficient resolution and poor wind vector retrievals in the rainy conditions encountered in and around tropical cyclones.

On the other hand, active sensors data has been used widely to estimate TC rainfall since Tropical Rainfall Measuring Mission (TRMM) satellite with Precipitation Radar on board launched on Nov. 1997. Chen et al (2006) researched the effects of vertical wind shear and storm motion on TC rainfall asymmetries deduced from TRMM. Study results from

Yokoyama et al (2008） show that three-dimensional rain characteristics of tropical cyclones (TCs) are statistically quantified, using TRMM data from December 1997 to December 2003. Launched in April 2006, the National Aeronautics and Space Administration Earth System Science Pathfinder (ESSP) *CloudSat* mission began making significant contributions toward broadening the understanding of detailed cloud vertical structures around the earth. The CloudSat's sensitivity to cloud droplets has proven very useful in profiling TC inner-core cloud and precipitation structure, thus has potential capability to estimate TC rainfall (L'Ecuyer et al, 2007; L'Ecuyer et al, 2008）.

However, the vast majority of methods developed for deriving cloud and precipitation information from satellite measurements is highly sensitive to model parameters, which merely reflects the underconstrained nature of the problem and the need for other information in deriving solutions (Stephens and Kummerow, 2007）. To mix together data from different sources with certain data processing technique may reduce model error. The combination of active and passive measurements offers much hope for improving cloud and precipitation retrievals.

Ebert et al.（2007）have been performing daily validation and intercomparisons of several operational satellite rainfall retrieval algorithms over Australia, the United States, and northwestern Europe since late 2002. Short-range quantitative precipitation forecasts from four numerical weather prediction (NWP) models are also included for comparison. Results shows that the satellite-derived estimates of precipitation occurrence, amount, and intensity are most accurate during the warm season and at lower latitudes, where the rainfall is primarily convective in nature. In contrast, the NWP models perform better than the satellite estimates during the cool season when nonconvective precipitation is dominant. An optimal rain-monitoring strategy for remote regions might therefore judiciously combine information from both satellite and NWP models.

2.2 QPF

2.2.1 Statistical models

a. The TC QPF based on climatology

In the R-CLIPER model, a climatological rainfall rate is determined and then integrated along the storm track. The sample including nearly all U.S. landfalling tropical storms and hurricanes from 1948 to 2000 was used to construct the model. Based on the relationship, an accurate estimate of the storm rainfall rate can be considered a function of radius from the storm center and of the time from when the storm center moved inland (Tuleya et al, 2007). Additionally, to include the tendency for higher rain rates for stronger storms (e.g., Lonfat et al. 2004), a comprehensive satellite climatology of tropical cyclone rainfall rates determined from the Tropical Rainfall Measuring Mission (TRMM) was used. To further improve the model, particularly to represent hurricane rainfall asymmetries, Lonfat et al. (2007) developed a Parametric Hurricane Rainfall Model (PHRaM) which builds on the original R-CLIPER algorithm and includes parametric representations of the shear and topography effects.

A climatology model for QPF during typhoon periods was developed by Lee et al. (2006). Verification indicated that this climatology model could provide reasonable cumulative rainfall estimate for each river basin and around the whole Taiwan, if a well forecasted typhoon track was given. However, it was noted that the climatology model could only give the average condition, thus any deviations from the average condition inherent in the individual cases would appear as errors when the climatology model was applied during real-time operation.

b. The TC QPF based on a Dynamic Similarity Scheme

Zhong et al. (2009) developed a dynamic similarity scheme for TC QPFs. This model statistically considered the dynamic evolution of TC features and associated environmental

fields, particularly taking account for the corresponding similarity after forecast time. The 6-12 h change of TC parameters before the forecast time, and the numerically predicted environmental fields at 12, 24, 36, and 48 h after the forecast time are chosen to conduct the QPF.

2.2.2 TC QPFs based on satellite and radar detection

a. eTRaP

To address the need for cyclone-related heavy rainfall, the National Oceanic and Atmospheric Administration's (NOAA) Satellite Data and Information Service (NESDIS) has been producing operational areal Tropical Rainfall Potential (TRaP) forecasts for landfalling tropical cyclones since the early 2000's. TRaP forecasts (called TRaPs herein) are essentially 24h extrapolation forecasts of satellite-estimated rain rates that give the expected location and intensity of the rain maximum as well as the spatial rainfall pattern (Kidder et al. 2005).

Results from both validation studies (Ebert et al. 2005) suggest that the errors in TRaP forecasts are more likely to be related to errors in satellite rain rates and the assumption of steady state rainfall than to errors in operational track predictions. One way to reduce the random error is to average several forecasts together in an ensemble. In principle an ensemble TRaP (abbreviated eTRaP) can be made up of forecasts using observations from several microwave sensors, initialized at several observation times, using several different track forecasts. Kusselson et al. (2010) further improved the eTRaP, mainly including new sensor weights of 1.0 for AMSU and TRMM, and new weights for forecast latency.

Liu et al (2008) included estimates of storm rotation from geostationary cloud drift winds in past TRaP extrapolation forecasts and found that this one enhancement alone reduced the mean absolute errors by 40% compared to original TRaP forecasts for tropical cyclone rainfall over Taiwan.

b. SWIRLS

The Hong Kong Observatory developed a rainstorm nowcasting system SWIRLS (Short-range Warning of Intense Rainstorms in Localized Systems) to monitor and predict local rainfall distribution trends within the next couple of hours. In SWIRLS, the motion vectors of rain echoes between successive radar reflectivity images at 6-min interval are determined by the TREC (Tracking Radar Echoes by Correlations) technique (Tuttle and Foote 1990). To reduce pattern deformation during the integration period, a modified semi-Lagrangian advection scheme has been introduced in SWIRLS. The scheme is based on Robert's 3-step iterative, bi-cubic interpolation integration algorithm (Robert 1982) with flux limiters employed (Bermejo and Staniforth 1992).

2.2.3 TC QPFs based on numerical weather prediction models

Xiao et al. (2006) introduced a radar reflectivity data assimilation scheme within the fifth-generation Pennsylvania State University–National Center for Atmospheric Research Mesoscale Model (MM5) three-dimensional variational data assimilation (3DVAR) system. The model total water mixing ratio was used as a control variable. A warm-rain process, its linear, and its adjoint were incorporated into the system to partition the moisture and hydrometeor increments.

Zhao and Jin (2008) also investigated the role of radar data assimilation in the QPF for hurricane Isabel (2003). Radar observations of reflectivity and Doppler radial velocity from five WSR-88D radars in the landfall area during the hurricane landfall period were collected and assimilated into COAMPS using a variational approach. Zhao and Xue (2009) assimilated the Z and Vr data from two coastal operational WSR-88D radars to investigate the QPF for the landfalling Hurricane Ike (2008), using the ARPS 3DVAR and cloud analysis package through 30-min assimilation cycles. The prediction with both the Z and Vr data

assimilated also represented highest equitable threat scores of rainfall in the first 10 h.

Additionally, airborne Doppler radar data were also used in assimilation to improve TC QPFs. Pu et al. (2009) used airborne Doppler radar data collected during the NASA Tropical Cloud Systems and Processes (TCSP) field experiment in July 2005 to examine the impact of airborne radar observations on the short-range numerical simulation of hurricane track, intensity changes, as well as rainfall.

2.2.4 Superensemble QPFs for TCs

Cartwright and Krishnamurti (2007) introduced a regional superensemble consisting of 12–60-h daily quantitative precipitation forecasts from six models. The computation of the superensemble forecast required a training and a forecast phase with all member models and observations available. The superensemble technique used a regular multiple regression method to obtain the regression coefficients for each ensemble forecast at each grid point for each forecast time. The superensemble seemingly pinpointed the locations of the most intense precipitation, which improved the ETS values.

2.2.5 Forecasters technique for diagnosing areas of extreme rainfall

The turning of winds with height, mostly between the 850hPa and 500hPa levels, has been used by forecasters for decades to diagnose likely regions of thermal advection and thus ascent and descent, but due to its roots in geostrophic theory, the diagnostic is generally not applied in the tropics. An exception is staff at the Severe Weather Section in the Brisbane office of the Australian Bureau of Meteorology. After more than ten years of use, they have found the anti-cyclonic turning of winds with height to be an important indicator for extreme tropical and sub-tropical rainfall (Bonell and Callaghan 2008; Callaghan and Bonell 2005; see also the numerous rainfall event reports at, http://www.bom.gov.au/hydro/flood/qld/fld_reports/reports.shtml).

The diagnostic technique have been used to investigated several extreme rainfall events associated with tropical cyclones around the globe such as typhoon Bilis (2006）, Hurricane Mitch (1998), and Tropical Storm Chataan (2002) etc. Results show that the heavy rainfall area was associated with warm air advection at 700hPa.

2.3 QPF/QPE operational development

2.3.1 QPF/QPE systems

Based on FY2C stationary satelite data, TBB gradient, offset of cloud body and its moving speed etc. are selected to build regression equation to estimate TC rainfall in China. Blending the estimated rainfall rate and rain gauges, TC rainfall distribution products at 0.1 º×0.1º resolution over China are made in 1 hr, 3 hr and 24 hr intervals. Besides, a Multimodel Ensemble QPF System has been developed to estimate TC rainfall by National Meteorological Center. Similar disparity parameter and gradual classification method are used to analyze the outputs from different operational models such as CMA, ECMWF, JMA and NCEP etc, provide QPF products of TC rainfall within 24 hr.

In USA, Tropical Rainfall Potential (TRaP) system takes the latest microwave rain rate data from DMSP, SSM/I, AMSU, or TRMM/TMI and performs an extrapolation of the rain rate values based on the latest forecast track and speed of the storm. Ensemble Tropical Rainfall Potential Product (eTRaP) is a simple ensemble of 6-hourly TRaP, in which a satellite “member” is included when its path passes over the TC, and “members” are weighted according to age of pass and past performance of sensor. It provides products 4 times a day at 0315, 0915, 1515, and 2115 UTC.

JMA Ensemble Prediction System (EPS) includes Weekly EPS and Typhoon EPS, and the main differences between the two are singular vector (SV) target area and operational

form. The initial conditions of ensemble member are defined by adding (subtracting) initial perturbation, which is generated by SVs to the control analysis field.

Hong Kong Observatory develops a nowcasting rainstorm forecasting system called RAPIDS (Rainstorm Analysis & Prediction Integrated Data-processing System) to blend or merge the SWIRLS with NWP. SWIRLS makes use of raingauge data over Hong Kong to calibrate radar reflectivity in real time, however, it becomes less skillful with time when the rainstorm motion is erratic or when echoes develop or dissipate rapidly.

2.3.2 Verification for TC QPFs

It is generally accepted that QPSs must first be validated against observations to identify model limitations and biases and possible areas for improvement in the forecasts. Standard QPF validation techniques, such as bias and equitable threat scores (ETSs), can be used to assess some aspects of TC QPFs. However, an additional set of QPF validation techniques specific to TCs is needed in order to evaluate the ability of the models to predict rainfall attributes unique to TCs, such as the extreme rain amounts so often responsible for the death and damage accompanying landfall (Marchok et al. 2007).

3 Recommendations

To meet the needs of TC-related disaster mitigation, observational and forecasting techniques relating to heavy rainfall caused by LTCs still require urgent improvements and significant development.

Heavy rainfall and flooding caused by LTCs are recognized as extreme weather events, but the science behind the behaviors of LTC rainfall is not currently understood to a great enough extent.

For numerical modeling, differences in the resolution and microphysical parameterization likely cause distinct QPFs. Further improvements in microphysical and boundary layer parameterization are required to obtain successful TC QPFs.

For data assimilation, more realistic microphysics scheme needs to be included in the radar data assimilation.

One of the major reasons for the slow pace of improvement in TC QPFs may be deficiencies in the collection and assimilation of real-time inner core data into numerical weather prediction models. Due to cloud and rain effect, satellite retrieved products usually have large uncertainties under cloudy and precipitating areas, thus most of the cloudy and rain-effected data are rejected during the quality control procedures in data assimilation.

Bibliography

Buckley C. D., Hood R. E. and LaFontaine F. J., 2009: Application of Airborne Passive Microwave Observations for Monitoring Inland Flooding Caused by Tropical Cyclones. J. Atmos. Oceanic Technol., 26, 2051-2070.

Bermejo, R. and A. Staniforth, 1992: The conversion of Semi-Lagrangian advection scheme to quasi-monotone schemes, Mon. Wea. Rev., 120, 2622-2632.

Bonell, M. and J. Callaghan, 2008: The synoptic meteorology of high rainfalls and the storm runoff response in the Wet Tropics. Living in a Dynamic Tropical Forest Landscape, N. Stork and S. Turton, Eds. Blackwell Press, 448 pp.

Callaghan, J. and M. Bonell 2005. Synoptic and mesoscale rain producing systems in the humid tropics. Forests, Water and People in the Humid Tropics International Hydrological Series, M. Bonell, and L. A. Bruijnzeel, Eds., Cambridge University Press, 925 pp.

Callaghan, J. and M. Bonell 2005. An overview of the Meteorology and climatology of the humid tropics. Forests, Water and People in the Humid Tropics International Hydrological Series, M.Bonell, and L. A. Bruijnzeel, Eds., Cambridge University Press, 925 pp.

Cartwright, T. J., and T. N. Krishnamurti, 2007: Warm season mesoscale superensemble precipitation forecasts in the southeastern United States. Wea. Forecasting, 22, 873–886.

Chen, L. S., Y. Li, and Z. Q. Cheng, 2010: An overview of research and forecasting on rainfall associated with landfalling tropical cyclones. Adv. Atmos. Sci., 27(5), 967-976, doi: 0.1007/s00376-010-8171-y.
Chen S. S., Knaf J. A., Marks JR. F. D., 2006, Effects of Vertical Wind Shear and Storm Motion on Tropical Cyclone Rainfall Asymmetries Deduced from TRMM. Mon. Wea. Rev., 134, 3191-3208.
Ebert, E., S. Kusselson and M. Turk, 2005: Validation of NESDIS operational tropical rainfall potential (TRaP) forecasts for Australian tropical cyclones. Aust. Meteorol. Mag., 54, 121-135.
Ebert, E.E., Janowiak, J. and Kidd, C. 2007: Comparison of Near-Real-Time Precipitation Estimates from Satellite Observations and Numerical Models. Bulletin of the American Meteorological Society, 88,1,47-64.
Ji, C. X., L. S. Chen, X. D. Xu, and F. Zhao, M. C. Wu , 2008: A study on variable quantitative precipitation estimation using Doppler radar data. Journal of Tropical Meteorology , 24(2), 147-155. (in Chinese)
Kusselson, S. J., M. Turk, M. Seybold, E. E. Ebert, and S. Q. Kidder, 2010: Satellite derived ensemble tropical rainfall potential (eTRaP): 2008-2009 results. 24th Conference on Hydrology, AMS 90th Annual Meeting.
Lee, C.-S., L.-R. Huang, H.-S. Shen, and S.-T. Wang, 2006: A climatology model for forecasting typhoon rainfall in Taiwan. Natural Hazards, 37, 87-105.
L'Ecuyer T, Miller S, Mitrescu C, Haynes J, Kummerow C, Turk FJ (2007) A first look at the CloudSat precipitation dataset. In: Proceedings 3rd IPWG Workshop. 23–27 October 2006, Melbourne [http://www.isac. cnr.it/~ipwg/]
L'Ecuyer T, Turk J., Partrain P., Stephens G., 2008: Near-Real-Time Applications of CloudSat Data. J. Appl. Meteor., 47, 1982-1994.
Liu, G.-R., C.-C. Chao, and C.-Y. Ho, 2008: Applying satellite-Estimated storm rotation speed to improve typhoon rainfall potential technique. Wea. Forecasting, 22, 259-269.
Lonfat, M., F. D. Marks, and S. Chen, 2004: Precipitation distribution in tropical cyclones using the Tropical Rainfall Measuring Mission (TRMM) Microwave Imager: A global perspective. Mon. Wea. Rev., 132, 1645–1660.
Lonfat, M., R. Rogers, T. Marchok, and F. D. Marks Jr., 2007: A parametric model for predicting hurricane rainfall. Mon. Wea. Rev., 135, 3086–3097.
Marchok, T., R. Rogers, and R. Tuleya, 2007: Validation schemes for tropical cyclone quantitative precipitation forecasts: evaluation of operational models for U.S. landfalling cases. Wea. Forecasting, 22, 726-746.
Quilfen Y., Charpon B., and Trounadre J., 2009: Satellite Microwave Surface Observations in Tropical Cyclones. Mon. Wea. Rev., 138, 421-437.
Pu, Z., X. Li, and J. Sun, 2009: Impact of airborne Doppler radar data assimilation on the numerical simulation of intensity changes of Hurricane Dennis near a landfall. J. Atmos. Sci., 66, 3351–3365.
Robert, A., 1982: A semi-Lagrangian and semi-implicit numerical integration scheme for the primitive meteorological equations. J. Meteorol. Soc. Japan, 60, 319-325.
Stephens GL, Kummerow CD (2007) The remote sensing of clouds and precipitation from space: A review. J Atmos Sci 64:3742–3765
Tuleya, R. E., M. DeMaria, and R. J. Kuligowski, 2007: Evalution of GFDL and simple statistical model rainfall forecasts for U.S. landfalling tropical storms. Wea. Forecasting, 22, 56-69.
Tuttle, J. D. and G. B. Foote, 1990: Determination of the boundary layer airflow from a single Doppler radar. J. Atmos. Ocean. Technol., 7, 218-232.
Wingo M. T., Cecil D. J., 2010: Effects of Vertical Wind Shear on Tropical Cyclone Precipitation. Mon. Wea. Rev., 2010, 138, 645-662.
Xiao, Q., Y.-H. Guo, J. Sun, W.-C. Lee, D. M. Barker, and E. Lim, 2006: An Approach of Radar Reflectivity Data Assimilation and Its Assessment with the Inland QPF of Typhoon Rusa (2002) at Landfall. J. Appl. Meteoro. Clim., 46, 14-22.
Yokoyama C., Takayabu Y. N., 2008: A Statistical Study on Rain Characteristics of Tropical Cyclones Using TRMM Satellite Data. Mon. Wea. Rev., 136, 3848-3862.
Zhao, K., and M. Xue, 2009: Assimilation of coastal Doppler radar data with the ARPS 3DVAR and cloud analysis for the prediction of Hurricane Ike (2008), Geophys. Res. Lett., 36, L12803
Zhao, Q., and Y. Jin, 2008: High-resolution radar data assimilation for Hurricane Isabel (2003) at landfall. Bull. Amer. Meteor. Soc., 89, 1355–1372.
Zhong, Y., H. Yu, W. Teng, and P. Chen, 2009: A dynamic similitude scheme for tropical cyclone quantitative precipitation forecast. J. Appl. Meteoro. Sci., 20, 17-27. (In Chinese)

Comparative Study on QPE Methods of X-band Polarimetric Radar in a Typhoon Event in South China

Bin WANG, Yanjiao XIAO

Institute of Heavy Rain, China Meteorological Administration, Wuhan

In this paper, several QPE methods based on X-band polarimetric radar measurements are evaluated by comparing retrieved rainfall rate with rain gauges data in a typhoon event in South China on 5 August, 2009. The first QPE approach is built based on Gamma drop size distribution (DSD) from polarimetric radar measurements. Other algorithms are to compute precipitation amount by using relationships between rainfall rate and polarimetric radar measurements with three empirical equations R (Z_H), R (Z_H, Z_{DR}) and R (K_{DP}, Z_{DR}, Z_H), respectively. Comparing retrieved results from these QPE methods with one hour rainfall amounts from rain gauges, their performances are evaluated and error effects on QPE are qualitatively analyzed. And, a preliminary discussion of Gamma DSD retrieval method is conducted.

A Multiscale Observation Error Estimation Scheme for QPE Using Local High Resolution Radar

P E SHUCKSMITH[1], G L AUSTIN[1], L SUTHERLAND-STACEY[1]
[1]University of Auckland, Auckland, New Zealand, pshucksmith@orcon.net.nz

1. Introduction

It is well known that there are myriad sources of error associated with the retrieval of surface rainfall rate from radar reflectivity measurements made aloft (for example, see Villarini and Krajewski, 2010). Some of these sources of error, such as the uncertainty in the observed rainfall's drop size distribution and the resulting effect on the Z-R relationship, have been researched extensively over the past several decades. Fewer studies have focussed on the fundamental sampling error associated with the measurement of precipitation at spatial resolutions and at sampling intervals that are coarse compared to precipitation systems' decorrelation length and time.

From the studies that have been undertaken it is evident that this source of error is very significant and could dominate over other sources of error in many cases. For instance, Fabry et al. (1994) studied one hour of high resolution data, downgrading it to a range of spatial and temporal resolutions. For this case, they found that a 39% error was introduced into a 5 minute rainfall accumulation solely from downgrading a radar's spatial and temporal resolution to 2 km and 5 minutes respectively. Similar results were observed by Piccolo and Chirico (2005) who looked at error due to temporal sampling at three different accumulation spatial scales and by Jordan et al. (2000) who found that among other results, the error due to decreasing sampling resolution to 5 km was of the order of 100% of the mean rainfall rate.

Lack of attention to this error source could perhaps be because there is little which can be done to improve the spatial sampling of existing fixed radar networks without increasing the density of the network or changing the fundamental parameters of the radars. Decreasing the sampling interval of the same radars may be impractical for operational reasons, particularly if a slow Doppler scan is incorporated in the scan cycle.

As well as affecting a radar's ability to measure fine scale structure in precipitation systems, the spatial resolution of a radar, if it is coarser than the observed rain field, can also lead to an overestimation of precipitation area and intensity. These latter effects are due to non-uniform beam filling and incomplete beam filling problems. The temporal resolution, dependent upon the radar's sampling rate, determines a radar's ability to observe a rain field's evolution as well as to better track its movement. Fabry et al. (1994) found this to be particularly important regarding 5 minute rainfall accumulations.

The ability to estimate the magnitude of this error using only the low resolution data, along with supplementary data such as that from rain gauges, would allow, after combination with estimates of other error sources, the creation of an ensemble of

possible rain states that could be used to evaluate a quantitative precipitation forecast or be input into a hydrological model.

2. Dataset

The data used for the analysis presented here was collected using the University of Auckland Trailer Radar over a three month deployment in the central North Island of New Zealand during the winter of 2009. Over this period 48 rainfall events were selected as being significant. The radar was operated to observe precipitation out to 20 km so that a comprehensive multiple elevation scan regime was not required, reducing the radar's sampling period to around 50 s. At these near ranges, the radar's 1.8° beam stays relatively narrow over the data domain, expanding to 800 m at 20 km (when an adjustment for the rotation of the dish is included). The data from a single scan elevation of 6° were processed onto a Cartesian grid with a pixel length of 200 m. Across the whole domain, an average pixel length of around 400–500 m would be a more conservative estimate of the radar's spatial resolution.

Figure 1: University of Auckland Trailer Radar deployed at a farm near Mangakino, New Zealand.

3. Method

To investigate quantifiably how sampling errors can affect the estimation of rainfall accumulation, spatial temporal sampling error plots of 10 minute rainfall accumulations were generated for the 48 selected events in the dataset. This type of plot was originally suggested by Fabry et al. (1994).

Spatial temporal sampling error plots are generated by progressively downgrading the spatial and temporal resolution of the high resolution radar images and comparing them to the original image. The spatial resolution is downgraded by averaging radar reflectivity, *Z*, in space in a manner physically analogous to increasing the sampling volume (assuming reflectivity is uniform with height). Temporal resolution is downgraded by sampling only every nth (for n = 2,3,…) radar frame when constructing the 10 minute accumulation, simulating an increase in the sampling period of n times the original interval. The accumulation is then determined using an advection based interpolation scheme similar to that of Method 1 from Fabry et al. (1994). The rainfall accumulation between consecutive radar scans is generated by translating the earlier frame in the direction of diagnosed echo motion for half of the sampling period whilst accumulating at each one second step of the translation while the latter frame is translated in the opposite direction for the second half of the period in the same manner.

The comparison between the downgraded accumulation and the original high resolution accumulation is made by

$$\mathrm{NMAE} = \frac{\langle |L_i - H_i| \rangle_{H>T \vee L>T}}{\langle H_i \rangle_{H>T}}$$

Where L_i and H_i represent rainfall depth (in mm) in a single pixel from the downgraded and original resolution accumulations respectively, $\langle \ldots \rangle_{H>T \vee L>T}$ indicates calculating the mean over all pixels with intensities greater than T mm in either the downgraded or original resolution accumulations. This gives the per pixel mean absolute error (MAE) as a fraction of the mean per pixel rainfall accumulation for all pixels with intensities over a certain threshold. This is termed normalized mean absolute error (NMAE) in the following analysis.

3. Results

A typical spatial temporal sampling error diagram is shown in Figure 2. The diagram shows that the magnitude of the error due to sampling is very significant. We see that for 2000 m and 5 minute sampling, the sampling error is of a magnitude of 40% of the mean rainfall accumulation.

It is evident that when observing with lower spatial resolutions, the temporal resolution is not as important as it is with higher spatial resolution observations. It is also the case that with low temporal resolutions it is not very beneficial in terms of the error in rainfall accumulation to increase the spatial resolution of the measurement.

It is apparent that the sampling errors are greatest for rainfall with shorter length scales. This is because the overestimation in precipitation area seen with a low spatial resolution observation is more severe for rainfall with length scales closer to or smaller than the size of the low resolution pixel. Also, small scale precipitation possesses much shorter temporal evolution times (Venugopal et al., 1999) so that the radar sampling rate is much more important for capturing evolution of the rainfall field at these scales.

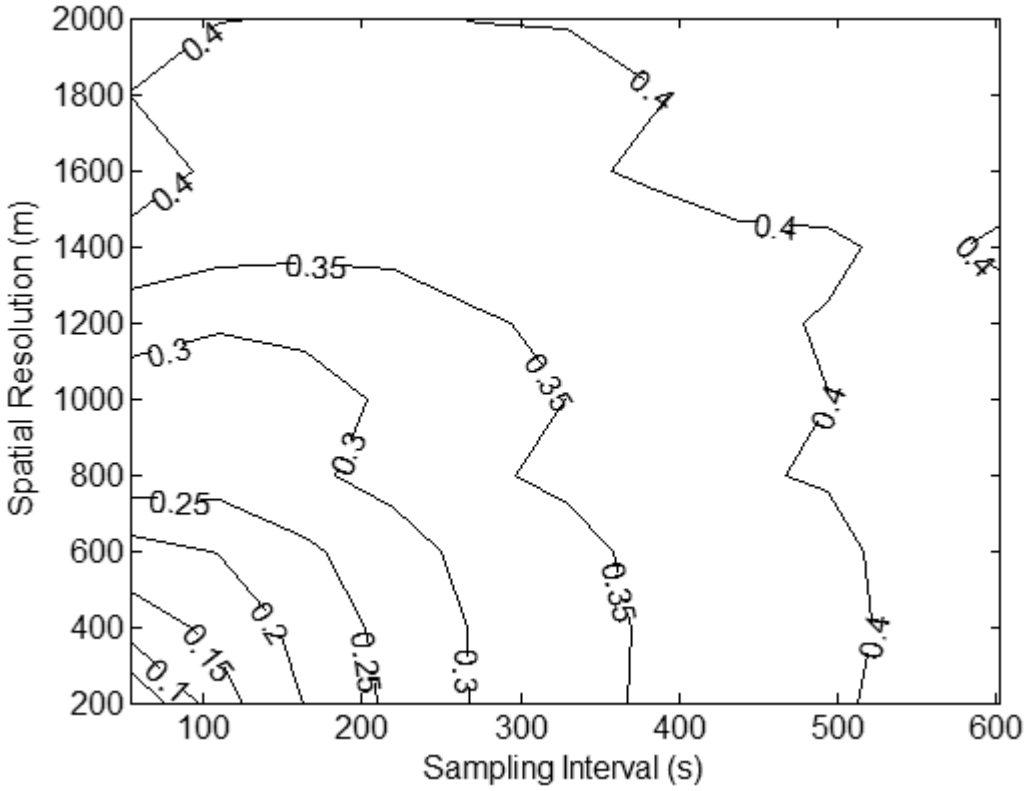

Figure 2: Spatial temporal sampling error diagram for a mixed convective/stratiform event on 4th August 2009. Contours show normalized mean absolute error.

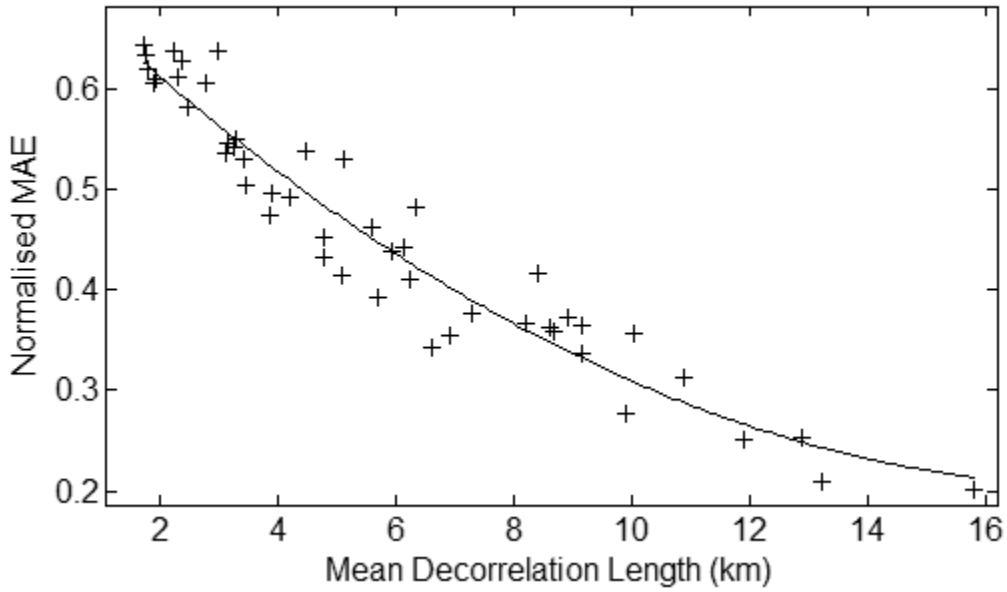

Figure 3: Normalized mean absolute error, due to spatially averaging radar data to 2000 m, as a function of an event's mean spatial decorrelation length. A curve has been fitted returning an R^2 value of 0.92.

The relationship between sampling error and precipitation systems' spatial scales is evident in Figure 3 which plots the mean NMAE over an event that is introduced by downgrading spatial resolution to 2000 m as a function of the mean decorrelation length of the event. The mean decorrelation length is able to account for 92% of the variance in the mean error with a threshold in the rainfall accumulation amount corresponding to rainfall rates of greater than 1 mm/hr. If a higher threshold is used, such as for accumulations corresponding to 10 mm/hr the strength of this relationship decreases so that the decorrelation length explains only 55% of the variance in the error.

The shape of this diagram, indicating the relative importance of temporal resolution to sampling resolution also varies between events. A much weaker relationship with decorrelation length is found however. Similarly, its dependence upon the mean rainfall intensity is also weak.

4. Conclusion

Spatial temporal sampling error diagrams have been created for 48 rainfall events showing normalized mean absolute error due to sampling effects for 10 minute rainfall accumulations. These errors were of significant magnitudes, varying from 20% to 70% of the mean accumulated rainfall. A strong relationship was discovered between the magnitude of the sampling error and the mean decorrelation length of an event, with longer decorrelation lengths resulting in lower error. This relationship is weaker when considering only more intense rainfall, such as for mean 10 minute rainfall rates of 10 mm/hr and above. An estimate of this sampling error could be included in a more comprehensive radar error model to improve the estimation of the total measurement error so that more representative ensembles could be generated for use with probabilistic quantitative precipitation forecasting and hydrology.

References

FABRY, F., BELLON, A., DUNCAN, M. R. & AUSTIN, G. L. (1994) High resolution rainfall measurements by radar for very small basins: the sampling problem reexamined. *Journal of Hydrology,* 161**,** 415-428.

JORDAN, P., SEED, A. & AUSTIN, G. (2000) Sampling errors in radar estimates of rainfall. *Journal of Geophysical Research D: Atmospheres,* 105**,** 2247-2257.

PICCOLO, F. & CHIRICO, G. B. (2005) Sampling errors in rainfall measurements by weather radar. *Advances in Geosciences,* 2**,** 151-155.

VENUGOPAL, V., FOUFOULA-GEORGIOU, E. & SAPOZHNIKOV, V. (1999) Evidence of dynamic scaling in space-time rainfall. *Journal of Geophysical Research D: Atmospheres,* 104**,** 31599-31610.

VILLARINI, G. & KRAJEWSKI, W. F. (2010) Review of the different sources of uncertainty in single polarization radar-based estimates of rainfall. *Surveys in Geophysics,* 31**,** 107-129.

A Radar-based Technique for the Identification of Convective and Stratiform Precipitation using the FLNN with Its Application to Estimation of Precipitation

CHENG Minghu and ZHANG Lejian
Meteorological Observation Center, China Meteorological Administration,
Beijing 100081, P.R. China, chengmh@cma.gov.cn

1. Introduction

The improvement for radar data derived quantitative precipitation estimation (QPE) has been a challenge task in radar meteorology since the first weather radar was used to measure precipitation in 1940s (Cheng,1994). This is due to many factors affecting the accuracy for radar derived precipitation. One of most important factors is the variation of the relationship (Z-I) between radar observed reflectivity (Z) and precipitation intensity (I). It is generally accepted that the Z-I relationships may be much different for different precipitation types. Therefore, there have been many methods presented to classify the convective and stratiform precipitation echo of radar, which were use to estimate precipitation using different *Z-I* relationships (Steiner et al., 1995, Rosenfeld et al. ,1995, Houze 1997, Biggerstaff et al. , 2000). Following this methodology in this paper, fuzzy neural network (FNN) was presented to identify precipitation types from radar echoes, which were applied to QPE using different Z-I relationships.

2. Data used

Data used in this study were radar reflectivity data obtained from an S-band Doppler radar located at Heifei (31°52′1″N, 117°15′28″E), Anhui, China, and precipitation data from the raingauge network associated with the Heifei radar. The radar was operated with 1° beamwidth. The scan strategy for the radar was VCP11 or VCP 21, which completed a volume scan in five or six minutes. The VCP11 scan strategy had 14 elevations (0.5°, 1.45°, 2.4°, 3.35°, 4.3°, 5.25°, 6.2°, 7.5°, 8.7°, 10.0°, 12.0°, 14.0°, 16.7° and 19.5°) and the VCP21 scan strategy had 9 elevations (0.5°, 1.45°, 2.4°, 3.35°, 4.3°, 6.0°, 9.9°, 14.6° and 19.5°). The radar data were interpolated form polar coordinates to Cartesian coordinates using interpolation method. The horizontal domain of the grid was 301×301 with 1km×1km resolution, and the vertical domain of the grid was 15 with 1km resolution.

3. Fuzzy neural network used

Artificial neural network has been theoretically proved to have capability to solve many complex non-linear problems, and actually already applied to many different fields, such as time serial forecast, pattern recognition and

process control etc. The key for neural network application is to select the right type of network and how to train the network with samples. Actually there are neural network types, such as perception, error back propagation neural network, radial basis function neural network, compete neural network self-organization map neural network, Hopfield neural network and support vector machine etc (Principe et al., 2006; Simon, 2006; Martin T, 2006; Wang, 1998). Training method of neural networks includes supervised learning and unsupervised learning etc.

It is generally accepted that the FNN, composed of fuzzy logic and artificial neural network, is suitable for classification and pattern recognition. Therefore, in this study, Co-Active Neuro-Fuzzy Inference System (CANFIS) (Wang, 1998; Principe, 2000; http://www.neurosolutions.com/) was used to classify the radar echoes as convective or stratiform. The CANFIS is shown in Fig. 1, which is composed of input layer, middle layer with upper layer (fuzzy logical layer) and lower layer (feedforward neural network layer), composed layer and output layer.

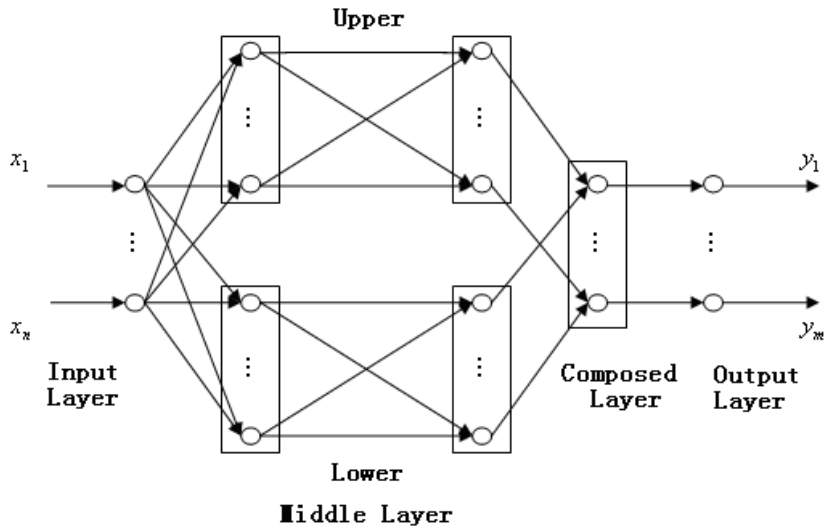

Fig. 1 The schematic for FNN

In this study, linear functions are used in the layers of input, output and the lower layer of the middle layer, bell fuzzy function and normalized distribution function are used for the upper layer of the middle layer, and a combined function is applied to composed layer. Mean squared error (MSE), normalized mean squared error (NMSE) and percentage error (%Error) are applied as criterion functions. Four classification parameters are radar reflectivity (Z_c), horizontal reflectivity gradient (G_h), vertical reflectivity lapse rate (V_d), and echo-top height (H).

4. The identification of convective and stratiform based on CANFIS

(a) Choice for training samples

Before networks were trained, the samples were identified through human experiment method (HEM) and mathematical algorithm (MA). Based on Xiao

et al. (2007), the HEM obtained examples from suitable data sets. The identification of convective and stratiform was derived from the conceptual model presented by Houze (1997) in which convective is associated with one or more cores while stratiform includes bright band or weak echoes. The MA is based on improved SHY95 (ISHY95) (Steiner et al., 1995).

(b) Cross estimation of identification

We used four cases in the cross estimation listed in Table 1, in which data a was used to train the networks and data b was used to estimate the result of classification, vice versa. Fig. 2 shows examples for these identifications for a squall line case at 0114 BJT on 18 July 2003. From the figure, it can be seen that the patterns derived from the two algorithms are nearly the same. But weak reflectivity echoes for stratiform were incorrectly classified as convective by SHY95, which was successfully avoided by CANFIS. Therefore, CANFIS achieved better results than SHY95, which were also observed in all cases in this study.

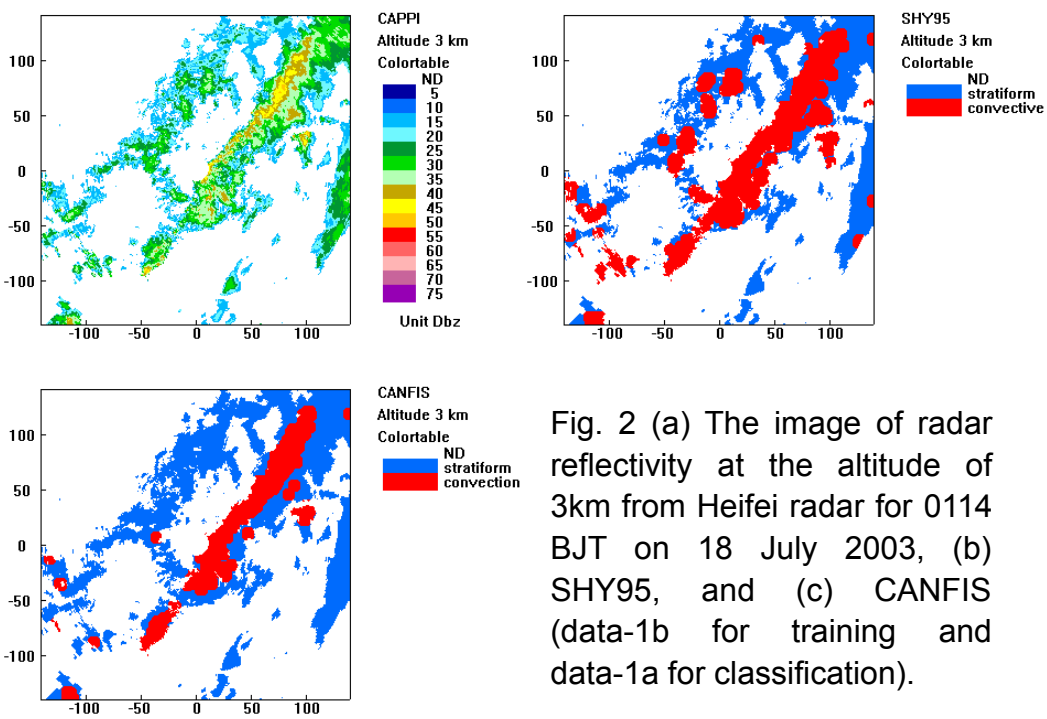

Fig. 2 (a) The image of radar reflectivity at the altitude of 3km from Heifei radar for 0114 BJT on 18 July 2003, (b) SHY95, and (c) CANFIS (data-1b for training and data-1a for classification).

Table 1 Radar Data Used for Cross Estimation of Identification

Data Pair	Flag	Time	Images
1	a	0000-0200 BJT on 18 July 2003	4
	b	0500-0700 BJT on 06 July 2003	5
2	a	0700-0900 BJT on 09 July 2007	6
	b	1100-1300 BJT on 08 July 2007	7

6. Quantitative precipitation estimation

In 2003, floods occurred in the Huaihe River basin. Huaihe River water

level reached the highest record since the founding of People's Republic of China in 1949, which was caused by heavy precipitation events frequently occurred from June to October 2003. In this study, three heavy precipitation events, listed in Table 2, were used to investigate the quantitative precipitation estimation from radar data.

Table 2 Heavy precipitation events occurred in Huaihe regions in 2003

Cases	Last Time (hour)
0000 BJT 29 June to 2300 BJT 3 July	120
0000 BJT 4 July to 2300 BJT 7 July	96
0000 BJT 8 July to 2300 BJT 11 July	96

Table 3 The CC and RMSE derived from the radar obtained QPE using Z-Is for the stratiform , convective, and mixture of stratiform and convective respectively with and without rain gauge calibration for the cases in 2003

Cases (No. used)	Z-I	No Gauge Calibration		Gauge Calibration	
		CC	RMSE	CC	RMSE
0000 BJT 29 June to 2300 BJT 3 July (534)	$Z=200R^{1.6}$	0.85	3.88	0.96	1.48
	$Z=300R^{1.4}$	0.85	3.88	0.95	1.59
	MCS	0.84	3.72	0.97	1.29
0000 BJT 4 July to 2300 BJT 7 July (189)	$Z=200R^{1.6}$	0.91	7.86	0.99	1.77
	$Z=300R^{1.4}$	0.90	7.08	0.99	2.02
	MCS	0.90	7.01	0.99	1.67
0000 BJT 8 July to 2300 BJT 11 July 2 (814)	$Z=200R^{1.6}$	0.76	4.13	0.98	1.09
	$Z=300R^{1.4}$	0.76	4.17	0.97	1.26
	MCS	0.76	4.02	0.98	1.07

In order to achieve the better QPE, $Z=200R^{1.6}$ and $Z=300R^{1.4}$ were used to estimate precipitation for stratiform and convective respectively identified by FNN technique described in the previous section, which is named mixture for convective and stratiform (MCS) in this paper. $Z=200R^{1.6}$ and $Z=300R^{1.4}$ were also applied to the QPE for the comparison with the MCS. The calibration algorithms using hourly rain gauge data were also applied to above investigations. Table 3 summarizes these investigations.

From Table 3, it can be seen that the CC and RMSE significantly vary from case to case for the QPE algorithms without calibration. And the three algorithms nearly achieve the same CC but the MCS has the smallest RMSE. The MSC only obtains slightly better results than other algorithms, which may suggest two Z-I relations selected cannot represent actual Z-I relations. The similar results can also be observed for the calibration algorithms. However, it can be seen that the calibration algorithms achieve much better scores than the algorithms without calibration. These arise from the fact that the same rain gauge data were used for both calibration and validation in this study. Therefore, the better scores shown only indicate the improved upper limits for

these calibration algorithms.

7. Conclusion

Based on three-dimensional characteristics of S-band Doppler radar observed reflectivity including reflectivity, horizontal gradient, vertical integrated liquid water content and echo-top height, an algorithm was presented to automatically classify the radar observed echoes as convective and stratiform precipitation using fuzzy logical neural network (FLNN). And the convective and stratiform *Z-I* relationships were used to estimate precipitation for the identified convective and stratiform echoes respectively for both algorithms with and without rain-gauge calibration in this paper. In order to examine the above algorithms, the case studies were carried out in this investigation using the data observed by the S-band radar located in Hefei, Anhui with the associated rain-gauges from 2002 to 2007. The results show the FLNN classification algorithm can achieve better performance of echo classification than the algorithm of Steiner et al. (1995). And the presented c pitation algorithm can improve the d nation of precipitation obtained by se of the single Z-I relationship o r both algorithms with and without rain-gauge calibration.

Acknowledgements. The radar and rain gauge data were provided by the Information Office of Atmospheric Sciences, Chinese Academy of Meteorological Sciences.

REFERENCES

Biggerstaff, M. I., A. Listenmaa, 2000: An improved scheme for convective/stratiform echo classification using radar reflectivity. J. Appl. Meteor., 39, 2129-2150

Cheng, M., 1994: Estimation of precipitation using satellite, radar and rain gauge data, Ph.D Thesis, University of Bristol, 1-400

Houze, R. A. Jr, 1997: Stratiform precipitation in regions of convection: a e eteorological paradox? Bull. Amer f eor. Soc., 78 (10), 2179-2196

/www.neurosolutions.com/

Martin, T. H., B. D. Howard, H. B. Mark, 2005: Neural Network Design. China Machine Press. 1-463

Principe, J. C., R. E. Neil, Lefebvre, W. C., 2000: Neural and Adaptive Systems: Fundamentals Through Simulations. John Wiley & Sons, Inc. 1-656

Rosenfeld, D., E. Amitai, and D. B. Wolff, 1995: Classification of rain regimes by the three-dimensional properties of reflectivity fields. J. Appl. Meteor., 34, 198-211

Simon, H., 2006: Neural Networks. Artificial Intelligence. 1-633

Steiner, M., R. A. Jr. Houze, S. E. Yuter, 1995: Climatological characterization of three-dimensional storm structure from operational radar and rain gauge data. J. Appl. Meteor., 34, 1978-2007

Wang, S. T., 1998: Neural Fuzzy System and Application. Beihang University Press. 1-315

Mesoscale Analysis of A Severe Convective Event in Chongqing by LAPS

LI Hongli PENG Juxiang
Institute of Heavy Rain, CMA, Wuhan

Abstract

Mesoscale reanalysis fields are built to accurately describe the mesoscale system by LAPS ingesting sev eral types of dat a such as satellite, dopplar radar, radiosonde, surface and automatic observations. We use these fields to study the local strong convective event in Chongqing from 5 to 6 June 2010. The results show that the supercell sto rm is the main i mpact system, which is triggered by convective cloud moving east from Chuanxi plat eau. In the first period of the strong convective event Chongqing surface is heating rapidly by solar radiation. The instability energy is very strong. It is dry in the middle and high levels and wet in the low lev el. A dry and warm cover occurs at 800hPa, which limits the inst ability in the low level. T riggered by the convective cloud, the inst ability energy releases violently , which causes the strong convectiv e event with high wind, hail and heavy rain.

CINRAD Warning Index of Local Extremely Torrential Rain in Huaihe Valley

Jianhong Wang [1], Chunsheng Miao [1], Shuqin Sun [1],

Qun Wang [2], Xiaocheng Wang [2]

1 Jiangsu Key Lab of Meteorological Disaster and College of Atmospheric Sciences, Nanjing University of Information Science & Technology , Najing 210044,China, jhwang@nuist.edu.cn

2 Yancheng Meteorological Bureau,Yancheng 224001,China

With the products of Doppler weather radar at Yancheng City in lower Huaihe River Valley during early summer, including the radar echo and the radial velocity, and based on analysis of the half hourly rainfall data from Jianhu, the precipitation intensity, the precipitation periods, and the general circulation background, two classified indexes of extremely precipitation warning are established. (1) The combined Perison-III warning index of radar echo intensity and rainfall process. (2) The joint probability warning index of the radar echo intensity, the radial velocity and precipitation system vertical dynamic structure. The main conclusions are as follows:

(1) According to historical precipitation data, P-III statistic method can provide seasonal climate extremes of the local precipitation. But its predicting capability of extreme value is relatively low.

(2) The combined P-III index established relationship between the radar echo classification and the dynamic features of rainfall events. The warning index combined the statistic probability of the radar echo classification and dynamics of precipitation process, it improves the pure statistic calculation and supports the extremely precipitation warning with more reasonability.

(3) To extract the precipitation system vertical dynamic structures from the radar radial velocity distributions, the joint probability warning index of extremely precipitation adds another reference of rainfall vertical environment than the combined P-III index. The joint probability index used more powerful monitoring information of radar products, and provides a comprehensive dynamic statistics warning for the extremely precipitation.

(4) For better application of the two indexes, a practical interface of the

warning index is built, it provides a convenient platform of extremely prediction warning and prediction.

Key words: Huaihe river， the extreme rainfall events, the radar warning index, the combined P-III distribution，the Joint probability distribution

Sponsored by the SNSF of China，40776017, the HRRF20080170, the State 908 2654and the State 908， the meteorological funding of Huaihe River valley.

Research of Rainfall Estimation using X-Band Polarimetric Radar

WANG Rui[1], GU Songshan[1], and HE Yuxiang[2]
[1]Department of Atmospheric Physics, Nanjing University of Information & Technology, Nanjing,
[2]Institute of Atmospheric Physics, Chinese Academy of Sciences, Beijing,
milo118@126.com

1. Introduction

After several decades of research, polarimetric weather radar is now gradually used into operational observation to improve the measurement accuracy of rainfall as compared with the conventional Doppler weather radar. (Bringi and Chandrasekar 2001; Ryzhkov 2003). The three key parameters of polarimetric weather radar are horizontal polarization (Z_H), differential reflectivity (Z_{DR}) and specific differential phase (K_{DP}). With attenuation correction issues properly addressed, some advantages of X-band polarimetric radar have been increasingly evident over longer wavelength radar operating at C or S band. The sensitivity of K_{DP} is the one of the most significant advantages. For the same rain rate, K_{DP} at X-band wavelength is more than three times larger than that at S band, and about twice as large as that at C band. In addition, K_{DP} can be immune to radar miscalibration, microwave attenuation, and partial beam blockage. It is also less contaminated by hail and is less affected by drop size distribution (DSD) variations (Zrnic and Ryzhkov 1996). Combination of K_{DP} and Z_H can improve the rain rate estimation to some extent, which is frequently used for self-consistency of the calibration and retrieval process.

In this paper, we make use of self-consistent attenuation correction, which was modified by Park et al. in 2005 to correct Z_H and K_{DP}. Meanwhile, Time Weight Average method (TWA) is presented to average K_{DP} and Z_H in order to form the initial K_{DP} field and Z_H field, and also retrieve the intensity of regional rainfall to get a more accurate distribution of the precipitation. Section 2 describes TWA method and the attenuation correction method in detail. In Section 3, TWA method is tested in a field experiment by 714XD P-A Radar during the period of May 2007, in Yitong of Jilin Province, China, along with the high resolution rain-gauges. Summary and discussion is in Section 4.

2. Theory

2.1 Attenuation in atmosphere

Attenuation in atmosphere is always ignored during the signal processing of S-band, C-band, even X-band Radar. Oxygen and water vapor are main gas media which cause the attenuation of radar signal. As to Ulaby et al. (1981), the attenuation caused by atmosphere will increase linearly with the distance. So the signal attenuation at X-band could be corrected by the following algorithm:

$$\Delta Z_H^{(g)}(r)(dBZ) \approx 0.03 * r^{0.96} \qquad (1)$$

Where r is in kilometer, $\Delta Z_H^{(g)}(r)$ represents the attenuation which is caused by atmosphere by the distance of r.

2.2 K_{DP}-Z_H Correction

The quantitative use of the X-band power measurements requires use of attenuation-correction procedures. In this study, the self-consistent method of ZPHI by Bringi et al. (2001), the modified method by Park et al. (2005), and Hu zhiqun et al. (2008) are employed. We correct the Z_H and K_{DP} for the test in the nest section.

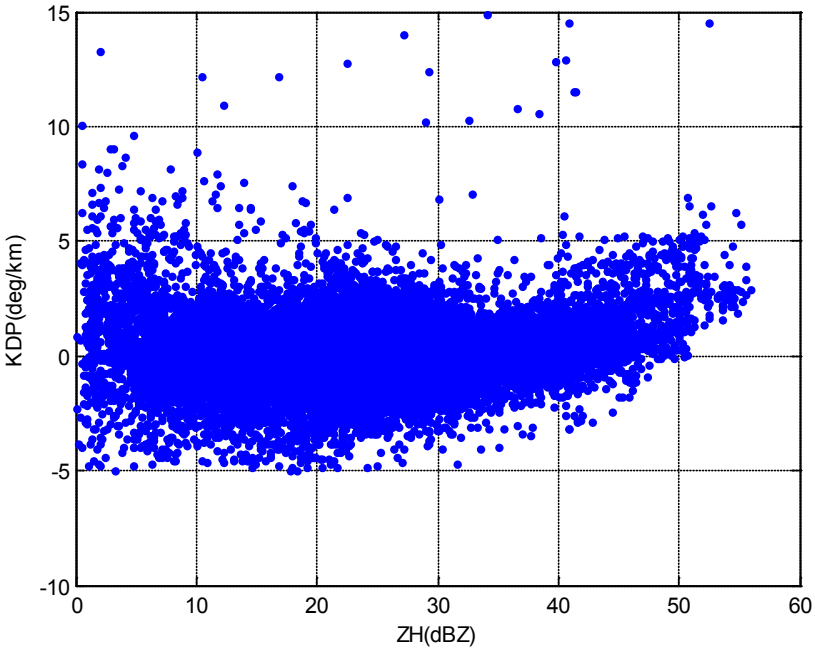

(a)

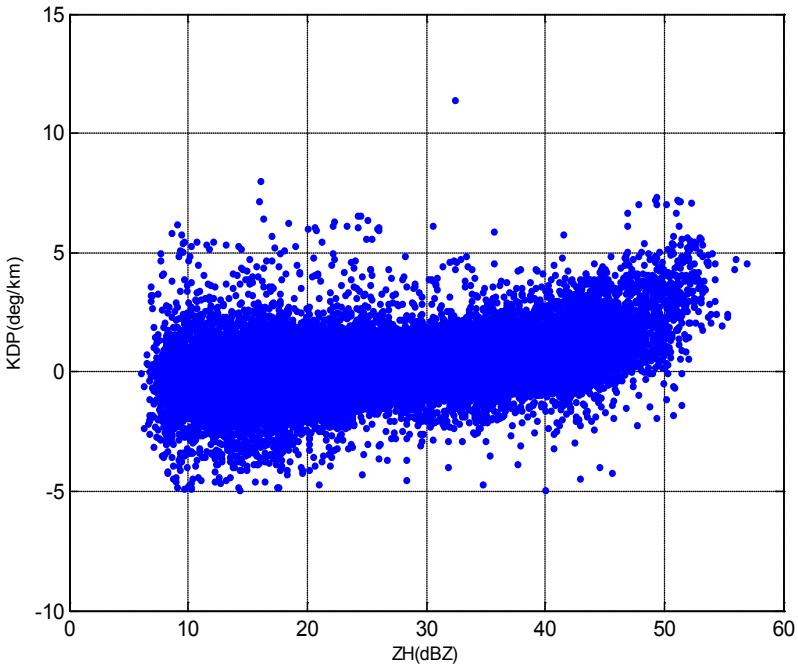

(b)

Fig. 1 the relationship between K_{DP} and Z_H, (a) is before attenuation, and (b) is after attenuation correction.

Figure 1 has shown the relationship between K_{DP} and Z_H before and after attenuation correction. Comparing Fig.1(a) with (b), it is shown that, for a given K_{DP}, the corrected Z_H values are much more assembling than the uncorrected. When the Z_H values are smaller than 30 dBZ, the values of K_{DP} are instable. Otherwise, K_{DP} values keeps increasing with Z_H. This fact is consistency with the conclusions of Ryzhkov et al. (2003) and Park et al. (2005)

2.3 Time Weight Average Method (TWA)

Time Weight Average Method, first proposed by Li Jiantong et al. (2005) was applied in precipitation estimation by conventional Doppler weather radar. In this paper, we use this method to average the polarimetric variables (K_{DP} and Z_H) in order to form a more accuracy radar initial field.TWA method makes a comprehensive consideration not only at spatial coherence, but time consistency as well.

In the method, select typical PPI images, which are at the same elevation angle and observed in the same hour. According to the interval of observation time between the adjacent images, we determine value of time weight coefficient.

Figure 2 is the schema of TWA method. Suppose there are three PPI images at the same elevation angle which were observed in the same hour, such as t1, t2, and t3. The amount of rainfall in this hour can be retrieved by the accumulated radar echoes observed in the time period of A, B and C. Point a and b are the midpoints of t2 and t1, t3 and t2, respectively.

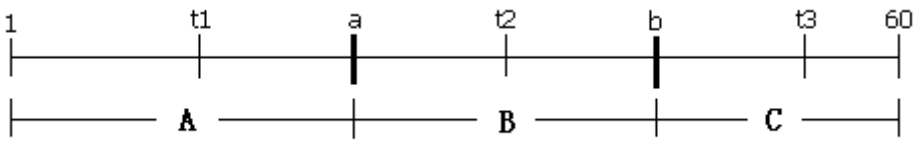

Fig. 2 The schema of TWA method

The equations are as follows, K_{DP} and Z_H are the radar initial fields of K_{DP} and Z_H.

$$K_{DP} = \frac{\frac{1}{2}(t_1 + t_2)K_{DP1}}{60} + \frac{\frac{1}{2}\sum_{n=3}^{N}\left[(t_n - t_{n-2})K_{DPn-1}\right]}{60} + \frac{\left[60 - \frac{1}{2}(t_{N-1} + t_N)\right]K_{DPN}}{60} \quad (2)$$

$$Z_H = \frac{\frac{1}{2}(t_1 + t_2)Z_{H1}}{60} + \frac{\frac{1}{2}\sum_{n=3}^{N}\left[(t_n - t_{n-2})Z_{Hn-1}\right]}{60} + \frac{\left[60 - \frac{1}{2}(t_{N-1} + t_N)\right]Z_{HN}}{60} \quad (3)$$

3. Observation and comparison

Supported by Institute of Atmospheric Physics, Chinese Academy of Sciences, 714XD P-A Radar is X-band dual polarimetric radar (XPOL), was operated at Yitong (43.16N, 125.5E) China, with the altitude of 342.5m. Figure 1 shows the location of the radar.

A significant period of convectional rainfall occurred during the period 15th -16th May, 2007. 714XD gathered plate scan data measuring the following polarimetric variables: Z_H, Z_{DR}, K_{DP} and correlation coefficient. We choose 8 PPI images during the hour of 20:00~21:00, 15th May to establish the radar initial fields.

The gauge rain rate data supplied by Jilin Weather Modification Office is as the standard to inspect and verify the initial field of polarimetric variables.

Table 2 the coefficients of the formula at polarimetric parameters

Formula	***a***	***b***	**Correlation coefficient**
$I = aZ_H^b$	0.03925	0.4032	0.78
$I = aZ_H^b$ (TWA)	0.01864	0.5546	0.914
$I = aK_{DP}^b$	5.515	0.766	0.865
$I = aK_{DP}^b$ **(TWA)**	11.04	0.7908	0.945

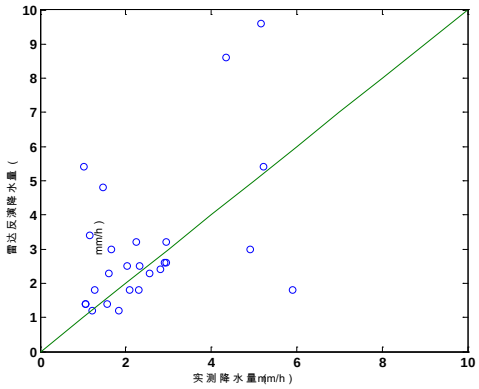

Fig.3 (a)

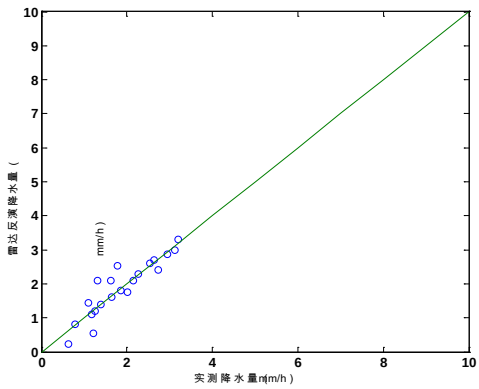

Fig.3 (b)

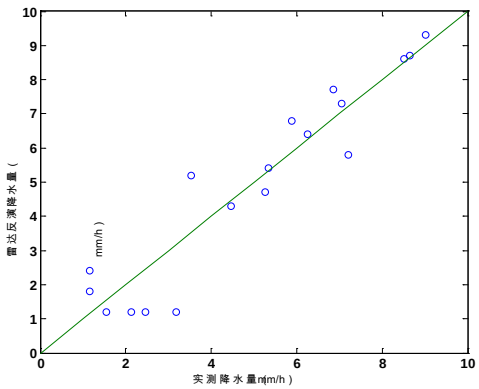

Fig.3 (c)

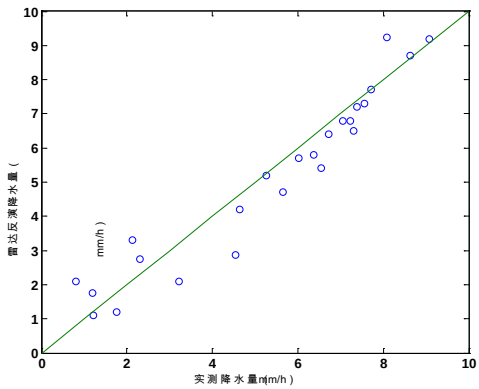

Fig.3 (d)

Fig.3 Comparisons between the rain rate retrieved by variables of Z_H and K_{DP}, and the rain rate observed by rain-gauges. (a) is the rain rate retrieved before the Z_H initial field; (b) is the rain rate retrieved after the Z_H initial field; (c) is the rain rate retrieved before the K_{DP} initial field; (d) is the rain rate retrieved after the K_{DP} initial field.

Comparing (a) with (b), the discrete points are more assembling after corrected by TWA method, and the correlation coefficient of (b) is better than (a). (c) and (d) are with the same feature. Meanwhile, Comparing (b) with (d), we find that the rain rate retrieved by Z_H is more consistency when the rain rate is lignter than 4 mm/h, while the rain rate retrieved by K_{DP} is more coherent when the rain rate is heavier than 5 mm/h.

4. Summary and discussion

(1) The TWA method comprehensively considers the time consistency between the radar detection and the observation of rain-gauge, so it can improve the capability of radar data to describe the strong center and spatial distribution of the rainfall. Thus, it meets the demands of regional rainfall estimation by radar and rain-gauge on the initial field of radar echo.

(2) The values of K_{DP} for light rain are too small, which results in instable quality and larger error. Therefore, reflectivity and specific differential phase should be combined together in the Z_H-K_{DP} method to correct the attenuation error.

(3) The correction of K_{DP}-Z_H needs a more profound calculation so as to improve the correlation coefficient, and also get a more accuracy rain rate distribution.

Acknowledgements

I would like to extend my appreciation to Institute of Atmospheric Physics, Chinese Academy of Sciences and Jilin Weather Modification Office for their supplement of the dataset of 714XD Radar and rain gauges.

Thanks to Professor Gu for his guidance and help.

I am grateful to Dr. He for readily sharing his knowledge and experiences. And in particular, thanks for his suggesting on attenuation correction.

References

V. N. Bringi, R. M. Rasmussen, J. Vivekanandan. Multiparameter Radar Measurements in Colorado Convective Storms. Part I: Graupel Melting Studies [J]. Journal of the Atmospheric Sciences 1986; 43: 2545-2563.

Li JianTong, Guo Lin, and Yang HongTing, A Study of the Formation of Initial Radar Field in Estimating Areal Rainfall Using Radar and Rain-gauge[J]. Chinese Journal of Atmospheric Sciences, 2005; 1010-1020

S.-G. Park, V. N. Bringi and V. Chandrasekar, M. Maki and K. Iwanami Correction of Radar Reflectivity and Differential Reflectivity for Rain Attenuation at X Band. Part I: Theoretical and Empirical Basis[J]. Journal of Atmospheric and Oceanic Technology, 2005; 1621-1632

S.-G. Park, M. Maki and K. Iwanami, V. N. Bringi and V. Chandrasekar, Correction of Radar Reflectivity and Differential Reflectivity for Rain Attenuation at X Band. Part II: Evaluation and Application[J]. Journal of Atmospheric and Oceanic Technology, 2005; 1633-1655

Hu Zhiqun, Liu Liping, Chu Rongzhong, Jin Ronghua. Comparison of different attenuation correction methods and their effects on estimated rainfall using X-band dual linear polarimetric radar[J]. Acta Meteorologica Sinica , 2008.66 (2) : 251 - 261

Session C

Hydrologic prediction and coupled hydrology-atmosphere-land models

Hydrological Perspective on QPE/QPF

Jinping Liu
UN ESCAP/WMO Typhoon Committee Secretariat
Avenida de 5 de Outubro, Coloane, Macao, China
jpliu@typhooncommittee.org

Abstract

The main purpose of hydrological service is to provide real-time decision-making support for flood-related disaster management and water resources management. Precipitation inputs are used in hydrologic runoff and snow-melt models to generate estimates of discharges and stages of streamflow, or used in flash flood prediction models to issue early warning of rainfall-triggered sediment disasters. Therefore, precipitation inputs, strongly influence real-time hydrologic forecasts. Precipitation inputs consist of quantitative precipitation estimations (QPEs), satellite-based precipitation measurements, and quantitative precipitation forecasts (QPFs). The accuracy of hydrologic products is largely dependent on the accuracy of QPE and skill of QPF.

This paper describes briefly the hydrological service and its input, hydrological modeling approaches and hydrological perspectives on QPE/QPF in aspects of catchment hydrological forecasting, sediment disaster and flash flood prediction, reservoir operation and etc. It analyses the possible reasons that QPE/QPF products have not been used very extensively in aspects of hydrological service and water-related disaster reduction. The paper finally points out that QPE/QPF for hydrologic forecasting and prediction could be strengthened through an end-to-end evaluation that assesses QPE/QPF quality and impacts on flood and streamflow products, and direct communications between meteorologists and hydrologists should be engaged in real time operational forecasting to understand each other.

1. Hydrological service and its inputs

Hydrologic services are products that provide technical information that can be used in water-related reduction, water resource management, water rights administration, water planning, and water environment protection. Hydrologic services enhance or complement the usefulness of weather forecasts with new hydrological service, hydrologic techniques developed for operational use and advanced hydrologic products (i.e., river stage forecasts, flood inundation maps) that meet user needs.

A broad set of users from various fields rely on hydrologic information to mitigate damage from floods and droughts and make decisions that save lives and property. Decisions for efficient water resource use are increasingly based on hydrologic forecasts across wide-ranging temporal (day-to-day, seasonal, inter-annual, decades and longer) and spatial (local, regional, continental) scales. This diversity of needs and services requires a variety of hydro-meteorological and hydro-climate forecasts.

Damages from droughts not withstanding, the needs for timely and accurate hydrologic predictions most strongly relate to floods and fast rising river levels. The

lead-time for mitigating flood damages is much shorter than that of mitigating and planning for circumstances of drought; for this reason, hydrologic services most often emphasize accurate hydrologic predictions for flooding scenarios.

The basic structure of a hydrological service system involves data inputs, model's response and product outputs (figure 1). For the outputs aiming to the especial purposes, the requirements to the data inputs may be variable on the spatial and temporal scale as mentioned above.

Precipitation inputs, including real time observation and whether forecasting, are used in hydrologic runoff and snow-melt models to generate estimates of rates and stages of streamflow or used in flash flood prediction models to issue early warning of rainfall-triggered sediment disasters. Therefore, hydrometeorological inputs, generally, and precipitation inputs, specifically, strongly influence real-time hydrologic forecasts. Hydrometeorological inputs consist of quantitative precipitation estimations (QPEs), satellite-based precipitation measurements, and quantitative precipitation forecasts (QPFs). The accuracy of hydrologic products is largely dependent on the accuracy of QPE and the skill of QPF.

Historically, precipitation analysis operations in hydrological models and methods have been based on interpolation of gage observations to mean areal precipitation (MAP) within individual hydrologic basins. Nowadays, with an abroad application of weather radars and satellite images, the radar-based precipitation processing system and satellite-based precipitation processing system are developed and applied. Accordingly, the finer spatial and temporal scales precipitation products (QPE/QPF) would be available and applicable for better hydrological service.

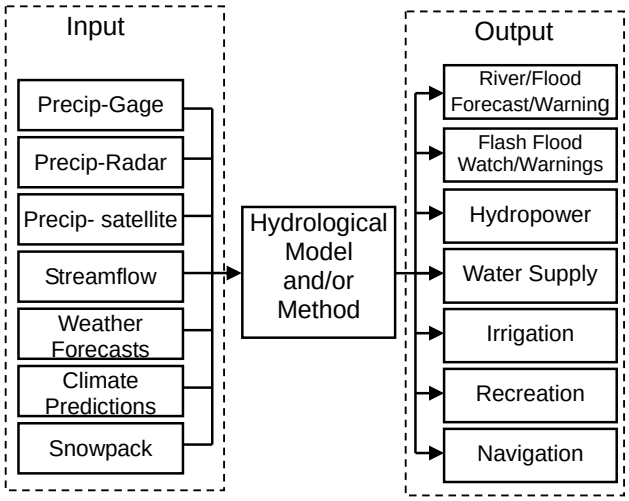

Fig. 1 Basic structure of hydrological service system

2. Hydrological modeling approaches

There are a number of hydrological models/methods available for hydrological service at present, including lumped modeling and distributed modeling.

As hydrological traditional model, the lumped modeling are commonly used as main approaches in the real time operational flood forecasting, in which where the catchment behaviour is described by catchment scale parameters as a unit. The spatial resolution is linked to the schematization of the basin, which can be considered as a single element or an ensemble of sub-basins. In order to get the appropriate model's parameters, a large river basin is usually divided into several or decades forecasting catchments based on the feature of topographic and geographic, type of soil, vegetation, the distribution of rainfall and hydrological observation stations, and

the river system in the basin. The magnitude of the catchment area is usually variable from 10^2 to 10^3 km^2. At present, the lumped models are dominative in hydrological service.

As a new approach of hydrological modeling developed with development of Digital Earth, the distributed modeling describes the hydrologic processes at small scale and then adding these up and routing the flows through the landscape by taking an explicit account of spatial variability of processes, input, boundary conditions, land use and wathershed characteristics provided by Digital Elevation Models (DEM). The scale of model grid can vary from 10^1m x 10^1m up to 10^3 m x 10^3m with the catchment area and the purpose of modeling. Considering the limitation of DEM and the computing speed, the solution of 1km x 1km ~ 4km x 4km is usually adopted in the real-time operational use.

Model resolution has been at the center of a debate in the hydrologic community about the advantages/disadvantages of lumped versus distributed models (Figure 2, Smith et al., 2004a.). One side of the debate notes that lumped models create coarse but accurate results, even though they do not effectively represent spatial variability of hydrologic processes, or intra-basin differences in elevation or terrain. Distributed models are designed to work at spatial and temporal scales finer than lumped models.

The other side of the debate, the argument in favor of distributed models, posits that because distributed models can account for differences in site specific characteristics, including basin size, topography, land cover. It has not been popularly used in hydrological service yet because the precipitation inputs (QPE/QPF) do not meet the needs of spatial and temporal resolution of hydrologic models.

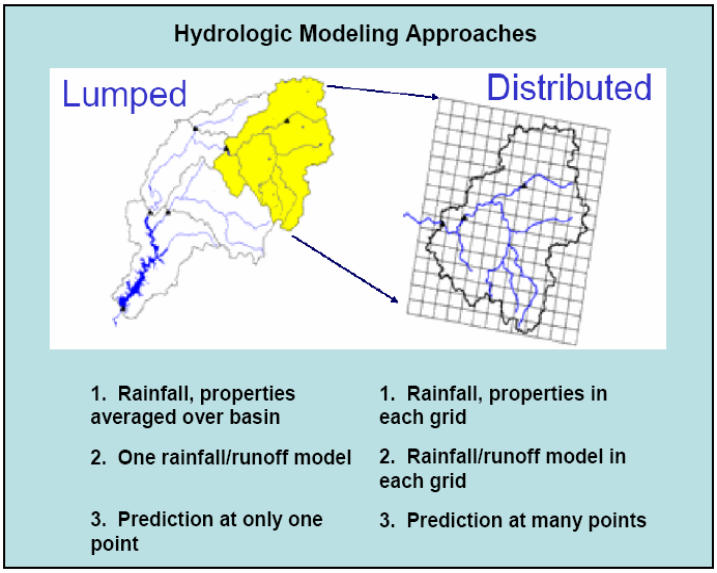

Fig. 2 Differences between lumped and distributed model approaches

3. Catchment hydrological forecasting

Catchment hydrological forecasting is one of main tasks in hydrological service system. Its functions include providing short-term flood forecasting and long-term

water resources prediction. The spatial scale depends on what kind of hydrological model/method used in the system. As mentioned above, the catchment can vary from 10^2 km^2 to 10^3 km^2 for lumped conceptual models and from 1km x 1km ~ 4km x 4km for distributed models in the real-time use.

The time resolution depends on the objective of the forecasting and the time scale of the catchment response. In the most cases, 6-hourly rainfall are sufficient for real-time flood forecasting, but in rapidly responding catchments where an accurate representation of the peak is required, rainfall input must have a finer resolution. Considering the rapid flow concentration in mountainous catchments, hourly rainfall is required. In the flat catchments daily rainfall might be sufficient. It is strongly suggested to use data in hourly resolution for hydrological distributed modeling.

The lead time of flood forecasting varies with the size of catchment and the availability of forecasted rainfall. Without the rainfall forecasting, theoretically, the maximum lead time is the concentration time of flow in the river basin after precipitation falls on the ground. The desired forecasting lead time may vary from several hours to several days according to the decision targets.

(1) Forecasting for early warning. hydrologists are required to provide river flood prediction products with lead time of 3 days at least to decision makers for flood disaster preparedness including warning issuing, dweller evacuation from flood prone area, material redeploying for flood defense and etc. In some main rivers, the lead time might be expected up to one week for some key points in downstream.

(2) Forecasting for real-time flood control. Based upon real-time observed rainfall and river stream flow and the operation of water projects, hydrologists are required to provide continual flood forecasting to the whole river system from upstream to downstream with lead time of 1 day at least or nowcasting for flood fighting, water dispatching and water projects operation.

(3) Forecasting for flood disaster rehabilitation. In order to meet the demands of promoting what is beneficial and abolishing what is harmful, hydrologists are required to provide the recession prediction up to 30 days in advance.

The basic meteorological inputs for catchment hydrological forecasting are rainfall and potential evapotranspiration (optional). If snow melt has to be represented, temperature and radiation (optional) data are required. The precipitation falling in different area (catchment) will cause the totally different flood situation and the totally different flood control response, rainfall forecasting products are strongly expected to aim at the given river basin or catchment for special purposes of hydrology and/or decision-making of flood control (it is usually issued by regions, like eastern or northwestern part of a country).

Based on the above discussion, the requirements on QPE and QPF for catchment hydrological forecasting may be described as following:

(1) As input of the hydrological lumped modeling, the 6 hourly QPEs/QPFs with the lead-time of 1-3 days are required to be downscaled to the desired catchment-scale (10^1~10^3 km^2).

(2) As input of the hydrological distributed modeling, the hourly QPEs/QPFs with the lead-time of 1-3 days are required to be downscaled to the desired gird (less than 10^1km x 10^1km).

The rainfall in the period of the lead-time of flood forecasting will become the most important factor for the decision-making at the emergency moment, even thought only several millimeters. Therefore, the accuracy of QPF is judged crazily sometimes.

4. Sediment disaster and flash flood forecasting and warning

4.1 Sediment Disaster Forecasting and Warning

The largest basic influences on the occurrence of sediment-related disasters are topography and geology, and heavy rain acts as the catalyst. At the present moment, the technique of properly and theoretical analyzing occurrences of rainfall-triggered sediment-related disasters is still in the experimental stage.

Typhoon committee (TC) Working Group on Hydrology (WGH) conducted a project named “Sediment Disaster (including debris flow and landslide) Forecasting and Warning System” led by Japan. This project provided a forecasting method (a kind of statistic method) of occurrence of rainfall-triggered sediment disaster.

It is considered that sediment disaster does not occur only due to rainfall but terrain, geology and forest are involved complicatedly and optimum rainfall index will vary from a region to another. In the method, Critical Line (CL), Warning Standard Line (WL) and Evacuation Standard Line (EL) are set up based on historical record (retrospective QPE). Figure 3 shows setting of sediment disaster CL and Figure 4 shows general expression for EL and WL.

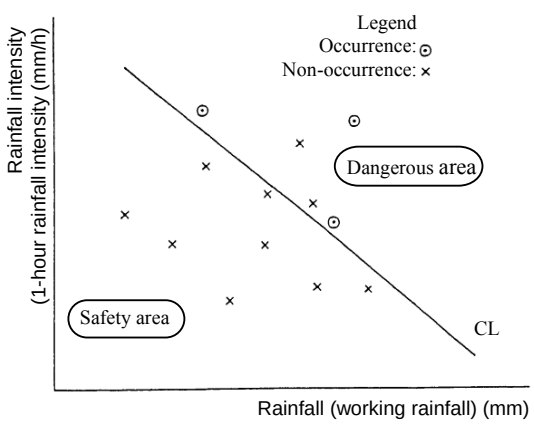

Fig. 3 Setting of sediment disaster CL

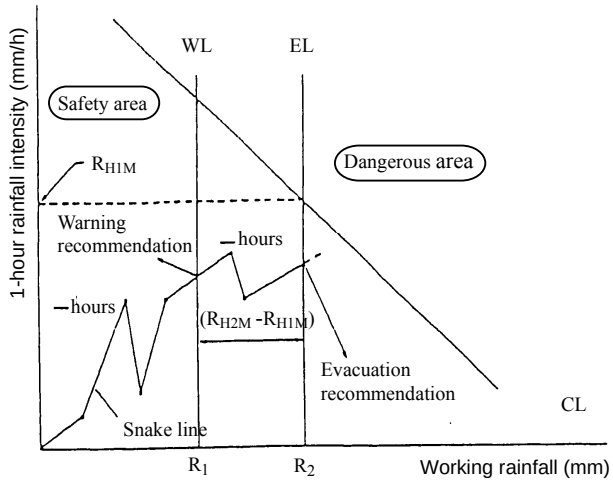

Fig .4 General expression for EL and WL

In this method, QPE, nowcasting and QPF with short time-interval (normally 10-minute, 30-minute, 1-hour rainfall, etc) are expected. Even though minutes lead-time (nowcasting products) would play very important role in sediment disaster reduction, especially mortality risk reduction.

4.2 Flash flood forecasting and warning

A flash flood can be defined as: “a flood that rises and falls quite rapidly with little or no advance warning, usually as a result of intense rainfall over a relatively small area”. Flash floods are distinguished from other types of flooding by the short timescales over which flood-producing rainfall occurs (generally less than 6 hours) and the small spatial scales (generally less than 1000 km^2) of drainage basins in which flooding occurs. Most flash floods occur at night and, as would be expected, produce the most damage in urban areas. Aside from intense rainfall and small net storm motion, factors that contribute strongly to flash flooding are low permeability or saturated soils, impervious ground surfaces, and steep slopes. Failure of small to medium-sized dams, including debris dams, contributes significantly to the fatalities and damage associated with flash floods.

The purposes of flash flood forecasting are to provide flash flood watch and warning. Flash flood watching is to (1) inform the public of hydro-meteorological conditions which may cause flooding when the flooding is neither certain nor imminent; (2) provide advance notice on flooding possible within 36 hours; and (3) enable decision makers to monitor conditions more closely and elevate flood mitigation resources to a higher state of readiness.

Flash flood warning is to (1) issue when flooding is imminent; (2) provide advance notification of short-fused flood events which require immediate action to protect lives and property; (3) allow customers and partners to take immediate mitigation actions such as evacuation to higher ground.

The physical processes causing flash floods and river floods are not much different; however, predictive uncertainties tend to be greater for flash floods than for river floods. This is partly due to errors in rainfall data which tend to average out over the larger spatial and temporal scales associated with river floods. In addition, predictive models for river floods can be calibrated using streamflow observations at forecast points. Most regions where flash flood predictions are required do not have streamflow gages, even rain gages. The historical sediments disaster and flash flood events and their corresponding rainfall record are also hard to collect.

Both lumped and distributed models can be used in hydrological modeling of flash flood. Due to averagely Mean Area Precipitation (MAP), the high peak is very hard to be predicted by lumped models. With increasing of availability of geographic data and radar rainfall data, distributed or semi-distributed hydrological models are adopted widely in practice. The statistical model would be based on developing the frequency distribution of flooding at ungaged locations based on retrospective QPE data.

The requirements on QPE/QPF for flash flood prediction could be described as (1)improved accurate high–resolution seamless hourly QPE; (2) hourly nowcasting; (3) hourly high quality seamless QPF.

QPE and nowcasting are very important for flash flood warning. They refer to the estimation of rainfall up to the current time using multiple sensors (radar, rain gauges,

satellite estimates) and the forecasting of rainfall out to 1-3 hours in the future based heavily on current observed data.

For flash flood forecasting and warning, it is expected that the precipitation analyses in a “basin world”, which means all calculations are done over the areas of small basins. The spatial scale of QPE/QPF is expected to be at 1km x 1km grid resolution. This gridded precipitation is then converted to Mean Area Precipitation (MAP) for a predefined set of watershed boundaries.

The coupled meteorological–hydrological nature of flash floods is becoming more and more evident. Prediction of flash flooding events will require interactive meteorological and hydrological models that introduce the new weather radar data and include feedbacks from the near-surface soil water to the atmosphere. Coupled hydrological–meteorological models should be constructed in a manner that permits prediction of the time and space distribution of both the rainfall and the resultant flooding.

5. Dam operation

Dams (or reservoirs) are necessary infrastructure and plays a vital role in water supply, flood control, power generation, navigation, recreation, and environmental requirements, etc. Some dams might serve for single purpose, but the most dams serves for multi-purposes. Dam operators would consider many factors simultaneously when making water release decisions to accommodate competing objectives. Dam regulation manuals provide the operator with guidance or “rules” for release decisions that are often based on conditions of reservoir inflow, pool elevation, and downstream flow rates, etc.

Reservoir regulation in flood season has to put the security of dam itself and flood security in downstream of the dam at the first priority, and then take into account the floodwater capture for water supply, power generation and agriculture irrigation, etc. The key variables governing the operation of flood control reservoirs are: (1) the available storage capacity, (2) the expected volume of inflow from an incoming flood, and (3) predicted precipitation in future. Although the residual storage is always known, the uncertainty regarding the expected inflow volumes and predicted precipitation makes dam operation a challenging task.

The estimation of the expected inflow volume is one of the major products of the methodologies. Ultimately, the regulation schedules are defined based on this volume, and thus, the adopted procedure for its estimation has great influence over the results. The stored water in reservoir may has to be pre-released if the inflow volume is predicted too much. The outflow process is decided by shape of forecasted inflow hydrograph.

The Consequently, hourly or 6-hourly QPE and QPF are essential and vital for the purpose of flood regulation, daily QPE and QPF would be enough for water resources regulation. One-day lead-time might be sufficient for small-scale reservoirs, However, 1~3 days, even one-week lead-time would be required for medium- and large-scale reservoirs which have to take charge of the objective of flood control for its downstream.

6. Conclusions

In hydrological modeling, there are three main sources of uncertainty: the input measurements; the precipitation forecast; and the hydrological modeling. The most significant improvements needed are without doubt to improve the spatial and temporal distribution of rainfall intensity which is one of the most crucial parts for successful hydrological modeling especially for basins characterized by a complex topography. The QPE/QPF with high spatial and temporal resolution which can meet the needs of hydrological modeling should be a very important factor to improve hydrological service.

QPE/QPF products have not been used very extensively at present in the aspects of hydrological service and water-related disaster reduction. One reason could be that the sensors (radar and/or satellite) and technology for QPE/QPF procedures is not available and applied easily in many countries and regions. Another reason could be that QPE/QPF products were developed for meteorological, not hydrologic purposes, so verification aspects of accuracy and performance are neither consistent nor calibrated with hydrologic models. Unfitted spatial and temporal resolution of QPE/QPF has fallen short of convincing many hydrologists of their operational value. For these and maybe other reasons, QPE and QPF remain underutilized in generating hydrologic forecasts.

QPE/QPF for hydrologic forecasting and prediction could be strengthened through an end-to-end evaluation that assesses QPE/QPF quality and impacts on flood and streamflow products for basins of diverse size and topography. Also the direct communications between meteorologists and hydrologists should be engaged in both research and real time operational forecasting to understand each other.

References

Toward a New Advanced Hydrologic Prediction Service (AHPS), Committee to Assess the National Weather Service Advanced Hydrologic Prediction Service Initiative, National Research Council. ISBN: 0-309-65847-0, 2006

Typhoon Committee, Guideline for Reservoirs Operation in Relation to Flood Forecasting, WMO/TD-No. 1471, 2008

Typhoon Committee, Report on UNESCAP/WMO Typhoon Committee Members Early Warning System, WMO/TD-No. 1475, 2009

Typhoon Committee, Sediment-related Disaster Forecasting Warning System Peoject, WMO/TD-No. 1520, 2010

UN ESCAP. Statistical Yearbook for Asia and the Pacific 2008, ST/ESCAP/2531

FFMPA User's Guide: http://www.weather.gov/mdl/ffmp/

Bull. Amer. Met.Soc. Prediction and Mitigation of Flash Floods. adopted by AMS Council, 2000.

NWP models' Application in Flood Forecasting and Reservoir Operation of the Three Gorges Project

LIU Zhiyu
Bureau of Hydrology, Ministry of Water Resources of China
2 No.2 Baiguang Road, Beijing 100053
Email: liuzy@mwr.gov.cn

Abstract

Traditional flood forecasting used observed rainfall as a model input thus limiting the forecast lead time to the natural flow concentration time of a basin. With the currently available computer capacity, numerical weather predictions (NWP) models are being introduced for operational meteorological and hydrological forecasts. The incorporation of NWP into a reservoir flood forecasting and operation system can increase forecast lead times from a few hours to a few days, and can provide significantly improved early flood warning.

The availability of multiple NWP models from various weather services such as China Meteorological Administration, Japan Meteorological Agency, European Centre for Medium-Range Weather Forecasts (ECMWF), offers a new opportunity for the development of hydro-meteorological coupling and flood forecasting & operation coupling systems in China. It aims to realize the combination between rainstorm forecast, flood prediction, and flood-control regulation for a reservoir.

This paper presents a case study using NWP models for flood forecasting and operation for the Three Gorges Project located on the Upper Yangtze River, which is one of the biggest hydropower-complex projects in the world.

The Three Gorges Dam experienced three major floods in the summer of 2010. In July, 2010, it reached a flood peak of 70,000 cubic meters per second exceeding the peak in 1998 Yangtze River Floods. During that time, national hydrological forecasting service issued a timely, accurate flood forecasting 2 days in advance, which was performed by combining NWPs with national flood forecasting system. It also demonstrated the feasibility of using NWP models for improvement of hydrological forecasting.

.

NWP-forced short-term streamflow forecasts for Australia

Thomas C Pagano[1], Lan Cuo[2], QJ Wang[1]
[1] Land and Water Division, Commonwealth Scientific and Industrial Research Organisation
[2] Institute of Tibetan Plateau Research, Chinese Academy of Sciences
Email: Thomas.Pagano@csiro.au

1. Introduction

For many catchments, the primary source of streamflow forecast uncertainty is unknown future precipitation. The accuracy of weather forecasts has steadily improved over the years, but it has been challenging to integrate quantitative precipitation forecasts (QPF) into flood forecasting operations. The Australian Bureau of Meteorology has recently expanded its role in providing water information services and is interested in extending the leadtimes and accuracy of its short-term flow forecasts. Therefore, a study is being done to inform the development of Numerical Weather Prediction (NWP)-based streamflow forecasts in Australia.

This article documents the preliminary findings of this study, including a review of the current situation of operational forecasting at the Bureau of Meteorology. It will document the expected NWP datasets that would be available for use. Finally, based on a survey of international practice and the research literature, it will identify expected barriers to more effective use of NWP in operational hydrology.

2. Operational streamflow forecasting in Australia

Australian operational streamflow forecasting practices have been discussed in more detail elsewhere (e.g. Pagano et al., 2009). Briefly, the Bureau of Meteorology has a data collection system for in-situ daily and sub-daily rainfall and streamflow measurements. In the face of a possible flood, the Bureau will use these data to force an event-based hydrologic model. Humans adjust the model parameters as the events unfold to keep simulated streamflow in line with the observed. Occasionally the Bureau will release quantitative forecasts (e.g. plots of the expected hydrograph) to an inner circle of decision-makers and other users, but the products to the public are largely categorical and/or qualitative (e.g. “This rain may cause strong rises in rivers and streams”).

Streamflow forecasters commonly seek out Bureau meteorologists to obtain an expert opinion on expected future rainfall. The meteorologist may provide a range of possibilities to indicate the uncertainty (e.g. “It could be as bad as 150 mm, but 50 mm is more likely”). The hydrologist may use this information in a crude sensitivity test to see if the heavier rainfall scenarios shift the event-based model’s guidance into a higher level of flood damage. Until recently, it was rare for hydrologists to use raw NWP quantitatively, instead relying on expert assessment of the output of a suite of many NWP models. Such reliance by hydrologists on human expert meteorologists is a common operational practice around the world (A. Wood, National Weather Service, Personal Communication, January 2010).

Recently, the Bureau has been evaluating new tools for producing short-term streamflow forecasts. The components of a future flood forecast system may include

Deltares' Flood Early Warning System (FEWS) and WIRADA's Short-term Water Information Forecasting Tools (SWIFT, Pagano et al., 2010). FEWS is a complete forecast production system and may ease some of the operational challenges of ingesting, preparing and using NWP output. SWIFT is a semi-distributed rainfall-runoff and river-routing modelling application that can be used by FEWS. The combined system is currently being run in an experimental pilot on the Ovens catchment in Victoria. The rainfall-runoff models are being forced by observed rainfall data and raw Australian NWP output (described in the following section).

3. Australian weather guidance

Kuzmin et al. (2007) provide a more detailed inventory of NWP products available for hydrological forecasting over Australia. The Bureau of Meteorology recently implemented the Australian Community Climate and Earth System Simulator (ACCESS) model for its weather forecasting. It is based on the Unified Model/Variational Assimilation (UM/VAR) system developed by the UK Met Office, and has been tested by research staff in the Centre for Australian Weather and Climate Research (CAWCR). The system recently underwent operational trials and configuration in the National Meteorological & Oceanographic Centre (NMOC). Parallel tests showed that ACCESS outperformed, by a significant margin, the previous generation of Australian NWP models.

NWP System	Domain	Type	Resolution	Duration (hours)	Runs (UTC)
ACCESS-G	Global	A+F*	N144 (80 km)	+240	00,12
ACCESS-R	Regional	A+F	0.375˚ (37.5 km)	+72	00,12
ACCESS-T	Tropical	A+F	0.375˚ (37.5 km)	+72	00,12
ACCESS-A	Australia	A+F	0.11˚ (12 km)	+48	00,06,12,18
ACCESS-C	Brisbane	Forc	0.05˚ (5 km)	+36	00,12
	Perth	Forc	0.05˚ (5 km)		
	Adelaide	Forc	0.05˚ (5 km)		
	VICTAS	Forc	0.05˚ (5 km)		
	Sydney	Forc	0.05˚ (5 km)		
ACCESS-TC	Tropical cyclone	A+F	0.11˚ (12 km)	+72	00,12

Table 1. Resolutions/domains of Australian NWP models. Type "A+F" indicates assimilation and forecasting ("Forc"). Adapted from NMOC (2010).

The ACCESS-Australia model (ACCESS-A) is run continent-wide at 12 km resolution while the City model (ACCESS-C) is run at 5 km over a limited domain (Table 1). WIRADA researchers will produce forecasts at a finer spatial scale (2-5 km) for selected study catchments to test the potential benefits of higher resolution runs.

Until recently, the Bureau used its now-defunct NWP models to generate 85-km resolution ensemble rainfall forecasts. These results were combined with model outputs from six other operational weather forecasting centers to form a 100 km "Poor Man's Ensemble" with leadtimes up to 7 days (Ebert, 2001). A similar multi-model consensus product is going to serve as the base layer for the Graphical Forecast Editor (GFE, a full graphical forecast that includes adjustments by human

forecasters and will serve as the official forecast). In the meantime, ACCESS ensembles are planned but not yet available.

The Bureau's Short-Term Ensemble Prediction System (STEPS) currently produces fine resolution short-leadtime forecasts over parts of Australia. It is a multi-source blended system, developed in collaboration with the United Kingdom Met office (Bowler et al., 2006). In STEPS, the rainfall distribution is separated into different sizes of rainfall features. Large events are more predictable and small events have a shorter lifetime. Information from an NWP model and/or radar field is used to extrapolate/propagate larger rainfall features, whereas the smaller events are filled using a statistical method. Many scenarios are generated to represent various moving speeds for large events and different random statistics for small events, hence, it is an ensemble system. Currently, STEPS is only run in Australia as an hours-ahead extrapolation of observed radar data and does not use NWP.

4. Limits to the use of NWP in hydrology

Cloke and Pappenberger (2009) discussed the problems and challenges in the short to medium range hydrological ensemble prediction practices. They identified 7 challenges in the hydrological ensemble forecast practice: 1) improving NWPs; 2) understanding the total uncertainty in the system; 3) data assimilation; 4) having enough case studies; 5) having enough computer power; 6) Ensemble prediction system operationalization; 7) communicating uncertainty and probabilistic forecasts. Nearly all of these challenges are relevant to the use of NWP and some are explored further in the following sections.

Despite steady progress, poor skill of NWP model output remains a perennial complaint of hydrologists. NWP model output can have conditional and systematic biases. For example, some NWP models perform better during winter than in summer (Buizza et al., 1999). The most skilful rainfall forecasts over Australia have strong synoptic forcing, such as tropical cyclones or mid-latitude systems (Ebert, 2004). For most situations, displacement (i.e. rainfall location) is the dominant source of QPF error (Ebert and McBride, 2000). Australian operational hydrologists sometimes develop a "worst case scenario" by relocating the maximum rainfall in a given NWP field to over the catchment of interest.

Although some may describe the skill of NWP as having "insufficient" accuracy for flood prediction, low discrimination (e.g. low probability of detecting events) is acceptable as long as reliability is high. Ideally, the forecasts should "do no harm" and at their worst be uninformative. Large systematic biases can affect reliability and should be corrected through the use of downscaling and/or bias correction, such as through the use of STEPS.

A long record of historical forecasts is necessary for effective correction of systematic biases. High resolution retrospective NWP forecasts are invaluable, but seemingly unattainable beyond isolated case studies. Interestingly, researchers have used retrospective NWP forecasts from a very coarse (250 km) model and post processed them to make them more reliable than the state of the art uncorrected forecasts (Whitaker et al., 2006).

A further challenge for hydrologic forecasting is the quantification of total uncertainty. Most hydrologic forecasting applications consider only future climate uncertainty, e.g. through the use of NWP ensembles, ignoring past input error and structural error. The latter can be addressed through the use of an ensemble of hydrologic parameter sets, multiple models and/or post-processing. It is unknown how hydrologic data assimilation (e.g. state updating, error correction) will interact with NWP forcing data, particularly if the hydrologic model was calibrated using observed rainfall data.

Finally, it is uncertain if NWP-forced hydrologic guidance could serve as a product for users. There is clear interest in having such guidance inform forecasters. However, there is a reluctance to expose users to raw guidance without the interpretive assistance of the forecaster. Furthermore, difficult situations arise when the NWP output is substantially different from the meteorologist's official forecast.

Acknowledgements

This work is part of the water information research and development alliance between CSIRO's Water for a Healthy Country Flagship and the Bureau of Meteorology.

References

Bowler, N., C. Pierce, and A.W. Seed, 2006: STEPS: A Probabilistic Precipitation Forecasting Scheme which Merges an Extrapolation Nowcast with Downscaled NWP. Q. J. R. Meteorol. Soc., 132, 2127-2155.

Buizza R., M. Miller, and T.N. Palmer, 1999: Stochastic Representation of Model Uncertainties in the ECMWF Ensemble Prediction System. Q. J. R. Meteorol. Soc., 125, 2887-2908.

Cloke H.I. and F. Pappenberger, 2009: Ensemble Flood Forecast: a Review. J. Hydrol., 375, 613-626.

Ebert, E.E., 2001. Ability of a Poor Man's Ensemble to Predict the Probability and Distribution of Precipitation. Mon. Wea. Rev., 129(10), 2461-2480.

Ebert, E. E., 2004: Accuracy of NWP Daily Rainfall Predictions for Hydrologic Basins, BMRC Research Report. Bureau of Meteorology, Melbourne, VIC, pp. 36.

Ebert E.E. and J.L. McBride, 2000: Verification of Precipitation in Weather Systems: Determination of Systematic Errors. J. Hydrol., 239, 179-202.

Kuzmin A. W., A. W. Seed, and J.P. Walker, 2007: Australian Government Bureau of Meteorology Forecast and Real-time Observational Hydrometeorological Data for Hydrologic Forecasting. eWater Technical Report, eWater Cooperative Research Centre, Canberra, ACT. 59 pp.

NMOC, 2010: NMOC Operations Bulletin no. 80. Australian Bureau of Meteorology National Meteorological & Oceanographic Centre, Docklands, VIC. 11 pp.

Pagano, T. C., H.A.P. Hapuarachchi and Q. J. Wang, 2009: Development and Testing of a Multi-Model Rainfall-Runoff Streamflow Forecasting Application. CSIRO, Melbourne, VIC. 40 pp.

Pagano, T.C., H.A.P. Hapuarachchi, and Q.J. Wang, 2010: Continuous Rainfall-Runoff Model Comparison and Short-Term Daily Streamflow Forecast Skill Evaluation. CSIRO, Melbourne, VIC, Australia. 70 pp.

Whitaker, J. S., X. Wei, and F. D. R. Vitart, 2006: Improving Week-2 Forecasts with Multimodel Reforecast Ensembles. Mon. Wea. Rev., 134(8), 2279-2284.

Probabilistic flood prediction by TIGGE on upriver of Huaihe catchment

Fuyou Tian[1], Dan Qi[1], Linna Zhao[2], Hao Wu[2], and Zhi Wang[2]
1. National Meteorological Center, China Meteorological Administration, Beijing 100081, China
2. Public Weather Service Center, China Meteorological Administration, Beijing 100081, China
tianfy@cma.gov.cn

1. Introduction

Flooding is one of the most challenging problems we facing. Meteorologists and hydrologists pay specially attention to this problem, especially in China. Numerical weather prediction system output precipitation and temperature could be used as driven of flood warning systems, and the forecast lead time be significantly increased (Krzysztofowicz 2002). The meteorological elements used as the forcing fields of hydrological model inputs and initial fields have many uncertainties. Atmospheric and hydrological models involving parameter uncertainties are a kind of approximation of the real meteorological and hydrological process. These complex factors lead to uncertainty of hydrological forecasting, and usually restraint the making of proper decisions.

Uncertainties of numerical prediction come mainly from the atmosphere initial state and the forecasting models, while the probability forecasting is effective in taking all the uncertainties into consideration. No matter how a collection of members was formed, each member represents one possibility of the future weather status. With integrating of all members the probability of weather phenomena can be obtained, and consequently the probability of hydrological processes with these probability elements as driven. Currently, integrating an EPS with flood forecasting and warning systems has been considered the future of hydrology. Regular forecasts have being provided to the public and well feedback have been received (Krzysztofowicz 1998). Recently, European Flood Alert System (EFAS) has also established its probabilistic forecasts system which providing a 3-10 day probabilistic flood forecast products (Thielen 2009).

2. The data and the test area

2.1 The data

The model output total precipitation and temperature data initialized at 0000 UTC provided by the TIGGE ECMWF, NCEP and CMA ensemble systems were used as driven in this study. Though all the forecast days are longer than 10 days, only 24, 48, and 72 hours' results were used on account of the present setting of VIC. A detailed description of the characteristics of the ensemble systems would be referred to Matsueda et al (2008) and Zhao et al (2010). As the spatial resolution of VIC is 15km × 15km, the bilinear interpolation method was employed. The test period lasts from July 23 to Aug 3, 2008. For other parameters, the operational waterlog settings were employed as VIC also runs over the test catchment for waterlog forecasts.

2.2 Test area

Huaihe Basin locates in the East China, and is the monsoon-humid areas and semi-humid climate transition region which leads to frequent drought and flood over the Huaihe river basin. The studied upriver of Dapoling-wangjiaba locates in the Dabie-mountain and Tongbai-mountains with a complex terrain conditions (Fig. 1), where the head source of Huaihe River lies. When heavy precipitation occurs in the upriver basin, the stream merges into the mainstream rapidly, usually leads to the rapid increase of water level and imposes tremendous pressure to the outlets of Xixian and Wangjiaba control station. However, the terrain of middle basin of Huaihe river basin is flat, where water flows slowly and frequently leads to the happening of water-logging and other disasters. Therefore, the hydrological characteristics of the main hydrological control stations on the up river have important demonstrative significance. Therefore, the Huaihe river basin was chosen as the test area, especially the upriver of the basin. The flood forecasting of Xixian and Wangjiaba hydrological point are investigated in this paper.

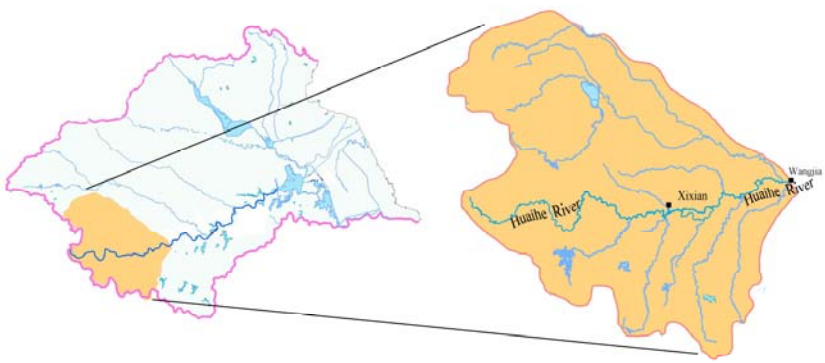

Fig. 1 Illustration of the test catchment

3. Model description and experimental design

The variable infiltration capacity (VIC) hydrological model is a co-developed large-scale semi-distributed hydrological mode. The inputs are time series of daily or sub-daily meteorological drivers such as precipitation and air temperature. This model was used as candidates in many projects such as the Inter comparison of Land-surface Parameterization Schemes (PILPS) to study the applications in different climatic conditions from small-scale river basin to large-scales and the global scale. It is good at simulating the land-atmosphere fluxes and the energy and water balance at the land surface, and also be used for the water balance calculations, which compensate the description lack of energy on the traditional process of hydrological model. VIC has been widely used as candidates in basins of the United States to test its performance and do flood forecast and runoff simulation. Some experiments have also been carried out by Xie et al (2007) and Liang et al (2001) over basins of China, and some good results been achieved. In this paper, a version developed by Liang et al (2001) and Xie et al (2007) with a new surface runoff parameterization scheme was used with the spatial resolution of 15km × 15km. Fig. 2 shows the designed flow chart.

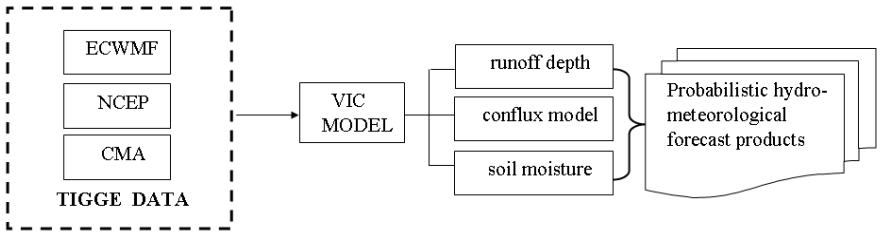

Fig.2 Designed flow chart of probabilistic hydro-meteorological Forecast with VIC

4. Results

3-day's forecasts obtained with ECMWF, NCEP, CMA output temperature and total precipitation data at Xixian station was shown in Fig. 3 with the 5th and 95th percentile distribution. ECMWF gives a better result compared to NCEP and CMA. The peak was not well forecasted by any of the EPS and the Grand ensemble shows no superiorities, though the tendency of the rising limb and the coming recession limb was well indicated. It is considered that the rapid merging of water into the mainstream and complex topography are main reasons.

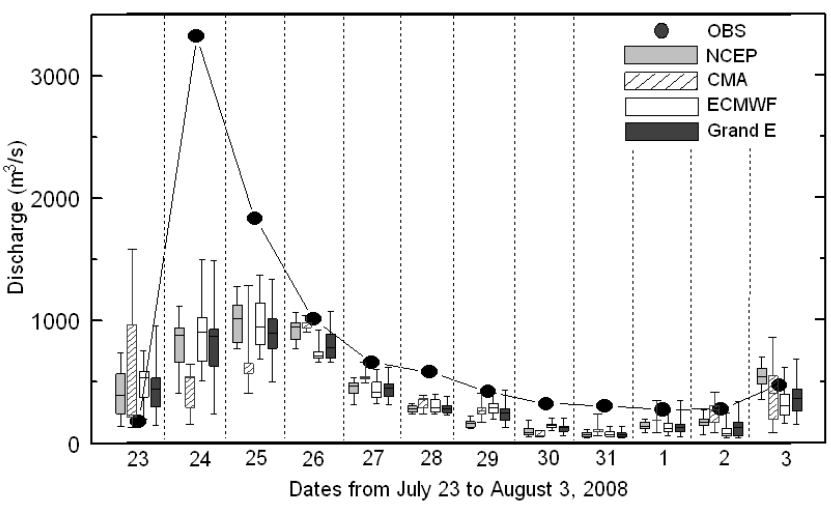

Fig. 3 Comparison of 5th and 95th percentile discharge of simulation with model output temperature and total precipitation of ECMWF (a), NCEP (b), CMA (c) and Grand ensemble (d) with the 3-day's lead time at Xixian

Wangjiaba is the outlet of the whole test area. Fig. 4 shows that all the EPS predicted the discharge well compared to Xixian station for which most of observation fall in the 5th-95th quantile though the NCEP has a severe underestimates. It is much different from Xixian that all ECMWF, CMA and Grand ensemble simulated the peak well, and twice of timing and discharge thresholds of rinsing limb were nicely captured (Fig. 4). It is a valuable reference for decision-making. But something still unsatisfactory is that the prediction in the recession limb is generally much quick than the observations.

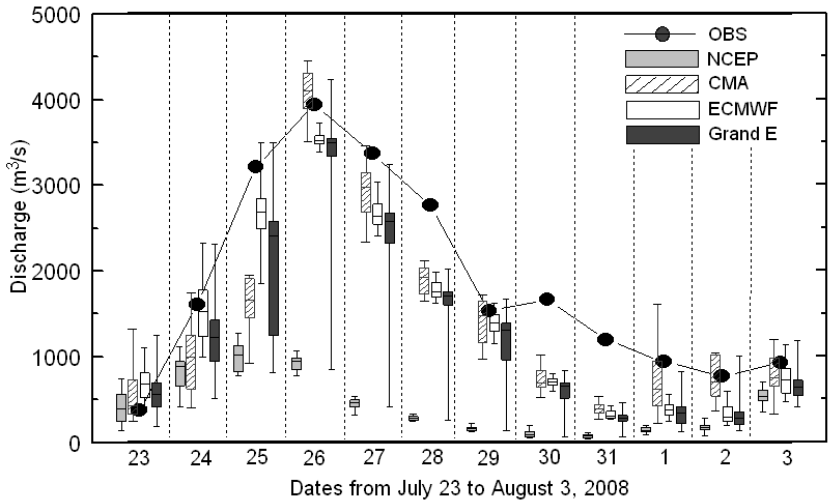

Fig. 4 The same as Fig.3, but at Wangjiaba.

The Nash-sutcliff efficiency coefficient was also obtained to assess the simulated discharge of three EPS at Xixian and Wangjiaba station. The Nash-sutcliff efficiency coefficient was written as:

$$E = 1.0 - \frac{\sum (Q_0 - Q_s)^2}{\sum (Q_0 - \overline{Q_0})^2} \qquad (1)$$

Where Q_0 and Q_s are observed and simulated discharge, and $\overline{Q_0}$ is the time average of observed discharge. A value of E close to 1.0 indicates the good agreement of observation and the prediction (Nash and Sutcliffe 1970). It is obviously seen from table 2 that the best E appeared with that driven by ECMWF which is 0.97 and 0.96 while the worst E appeared with NCEP. For Wangjiaba, the average of E with ECMWF is 0.68, which is much better than the other two EPS. The maximum, minimum and average E were also given in table 2. Something must be pointed out is that other references should also be taken into consideration when you must make decision with these results to make sure not be confused.

Table 2 Nash-Sutcliffe efficiency coefficient of Wangjiaba and Xixian

	Wangjiaba			Xixian		
	Max	Min	Ave	Max	Min	Ave
ECMWF	0.97	0.54	0.68	0.96	-0.15	0.26
NCEP	-1.22	-1.47	-1.36	0.41	-0.08	0.21
CMA	0.74	0.28	0.51	0.76	-0.45	-0.13

5. Conclusion and Discussions

Driving by the TIGGE provided ECMWF, NCEP and CMA EPS output total precipitation and temperature, discharges at Xixian and Wangjiaba control stations were simulated and compared to observation. It seems that the results are not in good consistence with the analysis of precipitation (Zhao et al 2010). The performance of all three EPS at Xixian is not so satisfied, especially on the first onset of rising limb, while the tendency of the recession limb was well performed, but is much lower than the observation. At Wangjiaba, the performance is better than at Xixian station. All captured the

onset of the rising limb correctly in terms of timing and river discharge thresholds for the first and the second rising limb. The reason may be that Xixian station locates at the upriver of the entire basin with a very complex terrain and small drainage area. Xixian drainage area was included in Wangjiaba drainage area, and there is sufficient time for it to respond to the flood. Though ensemble systems are designed to capture all possible weather probabilities, it is still possible that severe events be entirely missed. In contrast, Multi-Model EPS produces more reliable results and provides more valuable information.

Acknowledgments: This work was supported by the China Meteorological Administration under Grant No. GYHY200706001, GYHY200906007, GYHY 2010 and Huaihe River Meteorology Opening Research Fund(HRM200701). The authors thank Pro. Xie Zhenghui and his research team for help on running VIC.

References

Krzysztofowicz, R., 1998: Probabilistic hydro-meteorological Forecasts: Toward a New Era in Operational Forecasting. *Bull. Amer. Meteor. Soc.*, 79: 243-251.

Krzysztofowicz, R., 2002: Bayesian system for probabilistic river stage forecasting. *J. Hydrol.*, 268, 16-40.

Liang X., and Zheng-hui Xie, 2001: A new surface runoff parameterization with subgrid-scale soil heterogeneity for land surface models. *Adv. Water. Resource*, 24:1173–1193.

Matsueda, M., and Tanaka, H. L.: Can MCGE outperform the ECMWF ensemble? *SOLA*, 4: 77-80, 2008.

Nash, J. E., and J. V. Sutcliffe, 1970: River flow forecasting through conceptual models. Part I: A discussion of principles. *J. Hydrol.*, 10, 282-290.

Thielen, J., J. Bartholmes, M.-H. Ramos, and A. de Roo., 2009: The European Flood Alert System-Part I: concept and development. *Hydrol. Earth Syst. Sci.*, 13: 125-140.

Xie Zheng-hui, Fei Yuan and Qing-yun Duan, 2007: Regional Parameter Estimation of the VIC Land Surface Model: Methodology and Application to River Basins in China. *J. Hydrol,,* 8:447-468.

Zhao Lin-na, Wu Hao, Tian Fu-you, Qi Dan, et al., 2010: Assessment of probabilistic precipitation forecasts for the Huaihe basin using TIGGE data. *Meteorological Monthly* (in Chinese), 36(7), 133-142.

Third WMO International Conference On Quantitative Precipitation Estimation And Quantitative Precipitation Forecasting and Hydrology, (Nanjing China, 18-22 October 2010)

Paper Category: **Societal and economic assessments of high impact precipitation events**.

Title of Paper/Poster: **Extreme precipitation events in Cameroon.**

Extended Abstract

By

Bongkiyung Emmanuel Nyuyki
Department of National Meteorology
P.O Box 186, Douala, Cameroon
E-mail: bnyuyki@yahoo.co.uk

ABSTRACT

Cameroon is located in the junction between Central Africa and West Africa

* Latitudes 2°N – 13°N
* Longitudes 8°E – 17°E

Has a Humid Tropical climate in the south to a semi-arid and hot climate in the north

It has a surface area of 475,442km^2 with a population of about 19.4 million inhabitants and a coastline of about 402 km at the Gulf of Guinea.

Four geographical regions stand out

1. West/north west rolling hills and volcanic mountains.
2. Low coastal plains of the south
3. Central plateau up to the midlands of the Adamawa plateau
4. Northern plains from the midlands northward to lake Chad

It is bordered in the North east by Chad, East by Central Africa Republic, West by Nigeria, South west to South east by Equatorial Guinea, Congo Brazzaville and the Democratic Republic of Congo as can be seen from the map below

Cameroon like most of the countries in the equatorial region experiences cases of extreme precipitation and subsequent flooding.

The amount and frequency of extreme precipitation have tremendous socio-economic impacts in tropical countries in general and Cameroon in particular. The most recent and pertinent example is the cholera outbreak in the North of Cameroon in June 2010 after reported cases out flooding. More than 300 people are now known to have died from more 5 000 detected cases. The 7th August 2009 heavy down pour in Bamenda the North West region of Cameroon led to landslide which cut the main road linking the region with the South of the Country. Economic activities came to a standstill for some days. The 22th July heavy rains and strong winds in Pouss, village in the Far North region leading to flooding, 13 people died and more than 600 rendered homeless. The government had to intervene by dispatching emergency aid worth more than 100,000 000 CFA francs. Many cases of extreme rainfall abound in Cameroon with corresponding socio-economic consequences. Extreme rainfall events are usually observed during the peak periods in the climate calendar of Cameroon. The map below shows the peak for the various parts of the country.

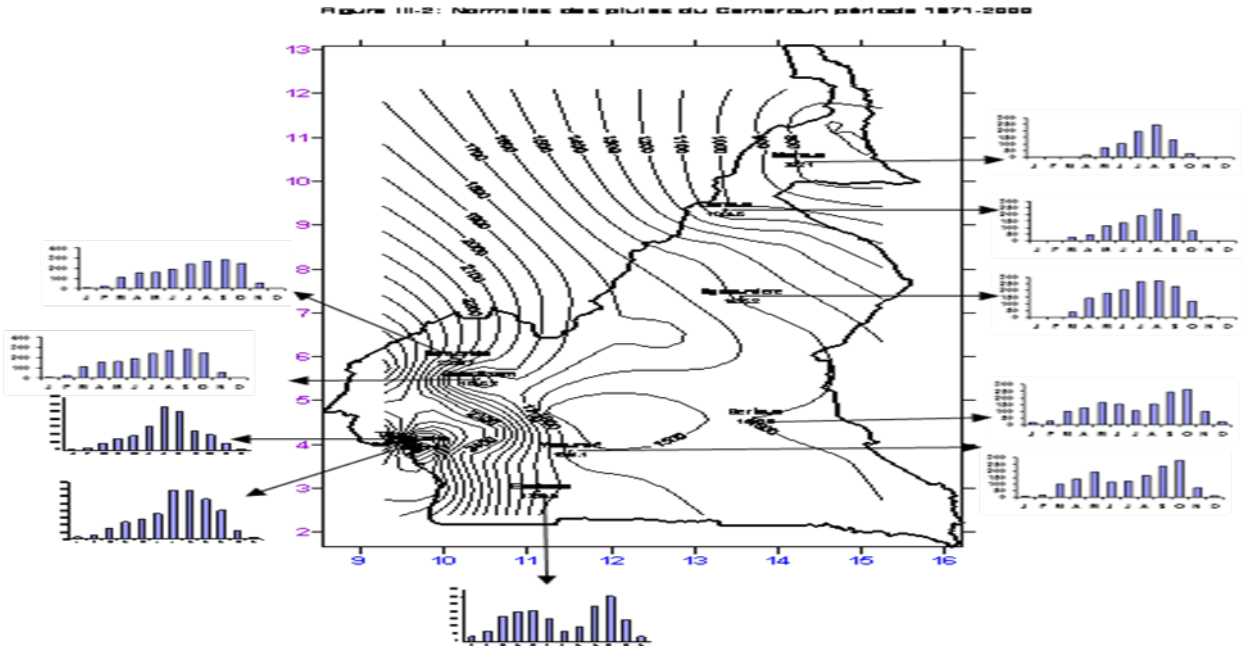

There is a unimodal pattern in the Western and in the northern part of the country with the peak in July-August-September period.
The only difference is that, in the northern part of Cameroon, we have four to five months completely dry.
The South experiences a bimodal rainfall pattern with one peak during March-April-May and the other one in September-October periods.
Considering that most of the rainfall in Cameroon are from convective clouds, though we have also orographic and advective, it means simply that heavy rains can occur at any time in the course of the rainy season leading to floods and landslides, essentially during the peak periods.
The global energy and water cycles are driven by heating and water vapor transport. The tropics in general are noted for sufficient solar energy and high relative humidity from water bodies, large equatorial forest and the ocean. These explore how moisture is distributed, vertically, horizontally, and temporally. The thermodynamic or static energy of the tropical atmosphere is used to distinguish between fair and stormy weather.
The accidental relief in Cameroon favours uplift and buoyancy of moisture laden are parcels. Mount Cameroon is the highest in the Central and West African sub-regions with a height of about 4,095m above sea level.
The geographic location of the Country also plays a very great role in its rainfall patterns. The country having a coastline of about 402km, often has onshore moisture laden winds from the Atlantic Ocean which in contact with the mountainous relief triggers large-scale mechanisms for lifting air to its condensation level adiabatically and subsequently showers.
Another very important parameter is the position of the ITCZ.
The above factors and other more made is possible for the NOAA/NCDC to come out with places of extreme rainfall on the globe. The map below clearly elucidates this;

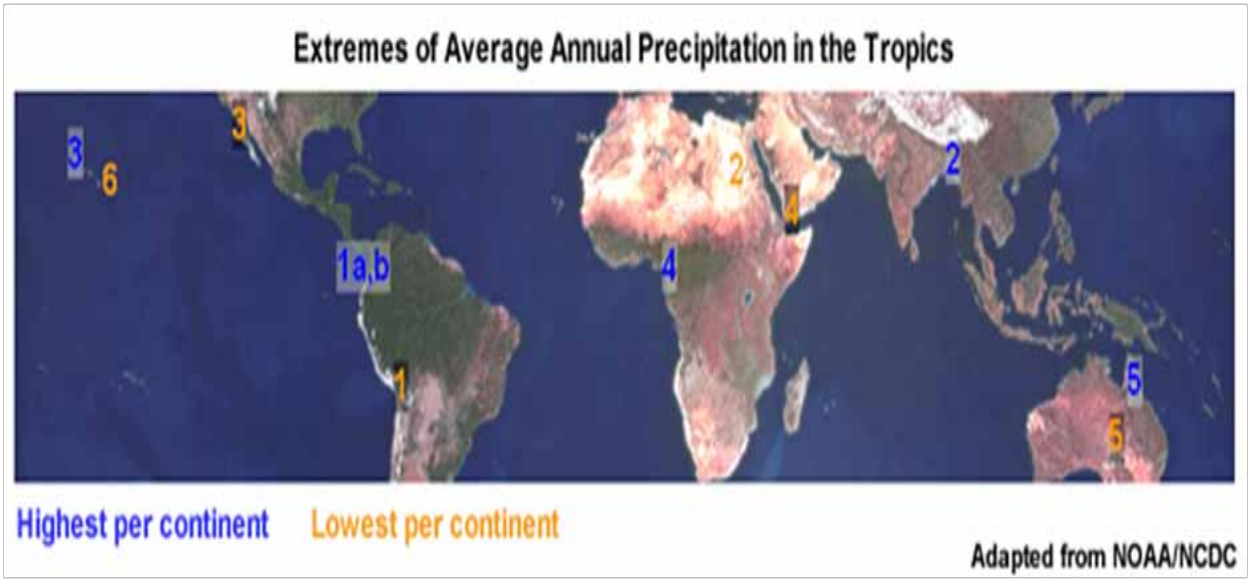

Cameroon is noted to be the continent's highest spot in Extreme Annual rainfall in the tropics. The table below t estifies t his w ith D ebundscha on t he w est end of m ount C ameroon r egistering on a verage 10,287mm of rainfall annually.

Highest Average Annual Precipitation Extremes in the Tropics

Continent	*Highest Avg. (mm)*	*Place*	*Elevation (m)*	*Years of Record*
1a South America	13299 ! ^	Lloro, Colombia	158.5*	29
2 Asia	11872 !	Mawsynram, India	1401.2	38
3 Oceania	11684 !	Mt. Waialeale, Kauai, HI	1569.1	30
4 Africa	10287	Debundscha, Cameroon	9.1	32
1b South America	8992 ^	Quibdo, Colombia	36.6	16
5 Australia	8636	Bellenden Ker, Queensland	1555.1	9

The Littoral region from statistics shows an all round rainfall scenario with highest of about 687.5mm on average in the month of August, and the lowest of about 27.5mm in the month of December. The chart below for July-August-September (JAS) peak season for Douala clearly elucidates the magnitude of the situation. Out of the 92 days of the JAS season, some years registered 92 on 92 days of rain, giving a proportion of 0.067 and a return period of about 15years with an exceedance probability of 6.7% in a year. The average for the period of study 1971-2000 is 75 days, the minimum being 54 days on 92.

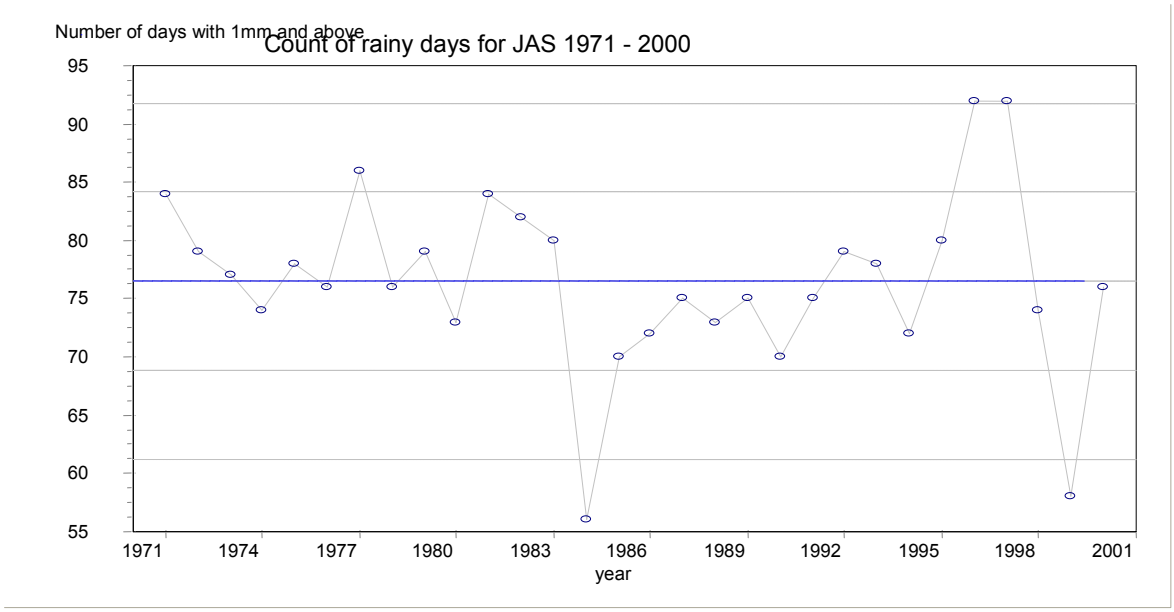

The government has not been indifferent to the situation. It has been mounting up efforts in order to avoid or minimize the socio-economic negative impacts of extreme rainfall in Cameroon.

There has been forceful eviction of inhabitants from flooding prone areas; improvement of the drainage systems in major towns by local governments by opening up of blocked sewerages; afforestation and reaforestation to improve on the land and conserve the soil; Widening of stream channels in cities like Yaoundé (Mfoundi river) to minimize if not avoid flooding after a heavy down pour.

Cameroon is exposed to a variety of hazards/disasters causing a high prevalence of risks; some of them are weather related.

Floods, landslides and other related events are major and permanent threats to the survival of populations and their goods from extreme rainfall; accurate national mapping is an urgent necessity, to determine the risky areas, and to define the sectors where the population could eventually be moved in to safety; appeal for civic responsibility and good citizenship is encouraged in order to report all (major) cases; providing the meteorological service with adequate tools (infrastructure and personnel) will very much enable the institution to play its role of informing and securing inhabitants and goods from the extreme rainfall and its related consequences.

The Flood Forecast Test on Quantitative Precipitation Forecast (QPF) Coupling with Hydrological Model

Cui Chun-guang , Peng Tao ,Shen Tie-yuan ,Yin Zhi-yuan
Institute of Heavy Rain, CMA, Wuhan Hubei, 430074 , China;
cgcui@whihr.com.cn

1 . Introduction

Rainstorm is the major catastrophic weather affect China. Floods come form torrential rains often brought huge losses to People's lives and property of the national economic construction. Precipitation in Foreseeable period has a direct impact on the accuracy of flood forecasting. The longer the period foreseen, the greater the impact on the forecast results. Therefore, the rainfall in foreseeable period and the flood forecasting coupling technology has gradually been concerned by majority of hydrologist and meteorologist in recent years (YANG Wen-fa,2003; WANG Qing-zai,2003; LI Chaoqun GUO Shenglian,2006). At present, with the rapid development of the numerical prediction‘s theory and methods, numerical prediction is now becoming an scientific method to achieve fixed, timing and quantitative rainstorm precipitation, and provide strong support for the estimates of rainfall in foreseeable period in Hydrological model. So under the support of mesoscale rainstorm numerical model forecasting technique, combined with flood process of the ZhangHe reservoir basin during the flood season in 2008, the paper made a pilot study of short-term flood forecasting considering the Precipitation in Foreseeable period.

2 . Summary of Research Area

ZhangHe originated from the southern foot of Jingshan, Nanzhang county, Hubei. It flows through counties and cities as Baokang, Yuan’an, Jingmen and Dangyang etc. In Dangyang city, the two embouchures and west extension JuHe confluence, full length of 202 km. The basin a long strip, from northwest to southeast tilt, with an average length of 100 km and a width of 30 km, a drainage area of 2 980km^2. ZhangHe reservoir located in Jingmen city, with catchment area 2212 km^2. The total storage capacity is 2.035 billion m^3.

(Fig. 1)

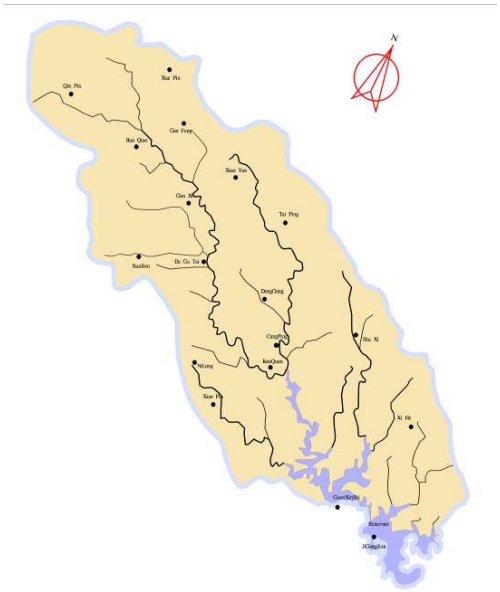

Fig1 The sketch map for ZhangHe Catchment

The basin belongs to the Middle Yangtze River subtropical monsoon area. The annual average rainfall is 1003.6mm with concentrating in the period from May to September . Rainstorms happen frequently with large rainfall intensity. Floods fluctuate greatly. Afflux time is short. The hydrological monitoring network in the basin is

homogeneous (Fig. 1). This area is also covered by the Wuhan radar. These may help the study of short-term flood forecast.

3 . AREM forecast model

Faced with the challenge of China's heavy rain numerical prediction, the majority of meteorologists make overall consideration of China region, topographical features and the complex evolution process of water vapor, in the process of developing numerical model with independent property rights, through the tireless efforts, five-layer fine-mesh primitive equation precipitation forecast model (Xiaoping Zhou) and REM patterns (Ru-Cong Yu, etc.) are successfully developed. Mesoscale numerical model AREM is developed by the Institute of Heavy Rain, CMA, Wuhan, it evolved based on the framework of the REM model (developed by Institute of atmospheric physics, Chinese Academy of Sciences), from the AremV2.1, AremV2.3 to the current AremV3.0, it improves and perfects in the model resolution, mode standardization, lateral boundary conditions, the physical parametric process, and dynamic initialization scheme, moreover, a complete set of three-dimensional variational assimilation program has been developed too, all of these form the Mesoscale numerical prediction model system for rain storm with high-resolution and three-dimensional variational assimilation system(Cui Chun-guang,2007).

Many years forecast results show that: AREM model has a strong ability for spatial and temporal distribution forecasting, it can more accurately given the distribution of the rain zone in rainy season in South China and rainy season of Yangtze River, the main precipitation Center and the intensity of precipitation are close to the actual situation, as regard to the occurrence, development and the end time it can also be a good prediction model, further more it can correctly reflect space-time evolution characteristics of summer precipitation in southern China(Li-jun,2007).

4 . Hydrological Forecast model and its forecast results

4.1 Hydrological Model Select

Based on the humid climate characteristics of research area, the paper select Xin'anjiang model as hydrological forecasting model, that is widely used at home and abroad(Zhao Ren-jun,1984,1988; Song Xing-yuan,2005; Pengtao,2010). The model adopts the concept of storage run-off and Muskingum afflux, and has the characteristics of unit, water sources and afflux phase, with simple structure, less parameters, which have a clear physical meaning, high accuracy. The model divide the whole catchment into unit catchment, and then the model make the run-off and afflux calculation after rain was consumed through evapotranspiration in each unit, and got the flux in the outlet of unit, and then calculate the flood in river, lastly make the sum of all afflux and get the whole flux of catchment.

4.2 Assessment Index for Flood Forecast

During the research, the Model effectivity, the percent of pass about flood peak and the hour rate for flood peak happening are selected to assess the model.

(1) Model Effectivity

$$DC_j = 1 - \frac{\sum_{i=1}^{M} \left[y_c(i) - y_0(i) \right]^2}{\sum_{i=1}^{M} \left[y_o(i) - y_0 \right]^2} \qquad (1)$$

In the formula, DCj is the certainty coefficient for a flood process; among them, the yC(i) is the forecasting

result; y0(i) is the observation flux of flood, y0 is the average of actual flux, M is the whole nodes in a flood process.

(2) The Percent of Pass about Flood Peak

$$DQ_m = \left|Q_{obv} - Q_{cal}\right| / Q_{obv} \times 100\% \qquad (2)$$

Among the formula, Qobv is the actual measured flow volume. Qcal is the simulated flow volume.

(3) The hour rate for flood peak happening

$$DT = \left|T_{Qc} - T_{Qa}\right| \leq 3 \qquad (3)$$

Among the formula, the T_{Qc} is forecasting occurrence time of the peak charge. The T_{Qa} is the occurrence time of peak charge.

4.3 Forecast scheme and Forecast results

Without considering precipitation in future, when we make the forecast, the precipitation of the forecast for each moment is set as zero; in some forecast with considering the precipitation in future, the rainfall after forecast time shall be precipitation which come form numerical model. During the test, we make the flood forecast, which consider the precipitation in future, with using the measured rainfall and AREM model predicted precipitation. In the forecasting process, we use ground rainfall stations or radar quantitative precipitation estimation technology to get the period measured rainfall before forecast time firstly, and then use AREM numerical models to obtain rainfall in future 12,24,36 hours, lastly make the flood process forecast considering precipitation prediction in advance.

In actual testing process, we carried out several studies combining with the flood process of basin in 2008, In view of the length and the actual effect of the results calculated, this article only analyzed and summarized one process of the flood process results (Tab1,Fig 2), the results showed that: under the conditions that the model forecast results are accurate, the forecast ,which consider rain in future, have obvious effect on flood forecast result, the relative error can be reduced by 50%, but when the time of prediction goes on, rainfall process tends to end, the impact of considering the future rain on flood forecasting results also will be reduced.

Table 1 flood process comparison considering expected flood flow of different phases

Prediction time	Future precipitation (h)	Actual peak discharge (m3/s)	Simulation peak discharge (m3/s)	Relative error (%)	Time difference (h)	deterministic coefficient
7-22 08:00	0 3	050	1496	50.95	30	-0.42
	12 3	050	1604	47.41	2	0.72
	24 3	050	2755	9.67	2	0.83
	36 3	050	2755	9.67	2	0.75

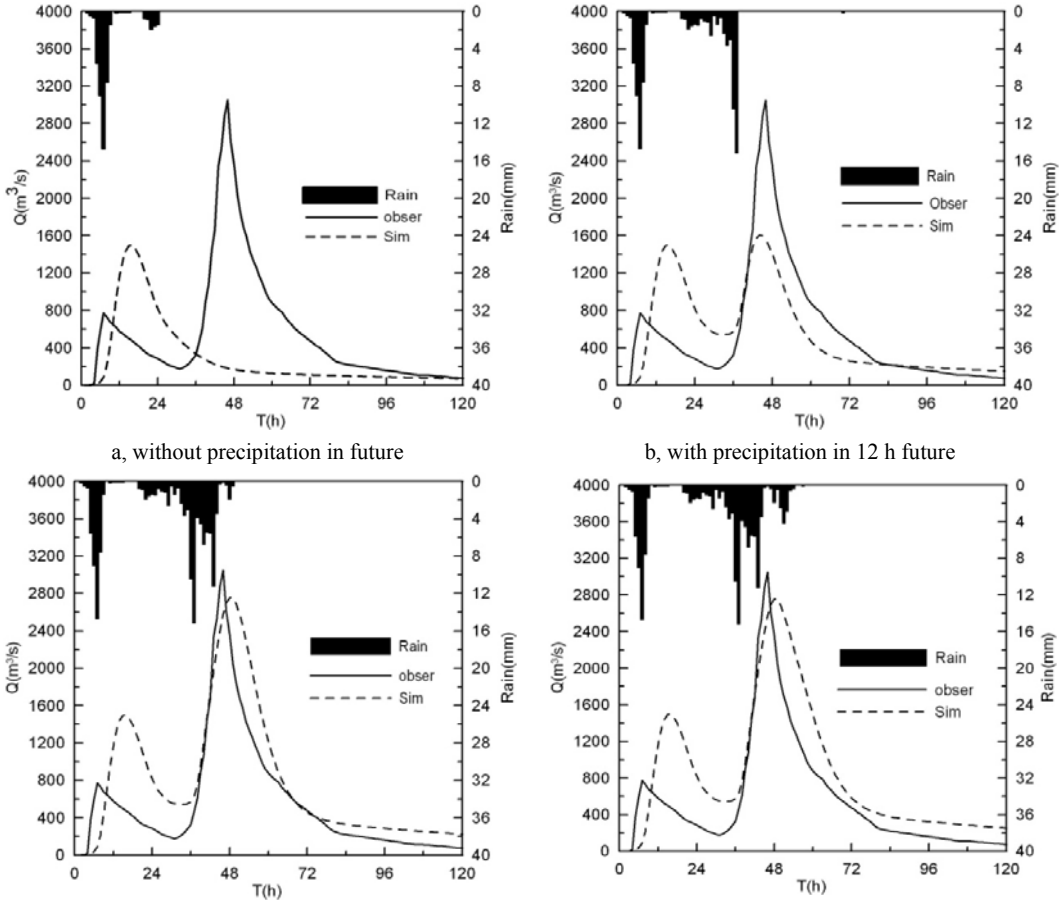

a, without precipitation in future

b, with precipitation in 12 h future

c, with precipitation in 24 h future

d, with precipitation in 36 h future

Figure2 flood discharge hydrograph considering expected flood flow of different phases

5. Conclusions

Precipitation is one of the most important information in flood forecasting, while precipitation in forecast period has a direct impact on the flood forecasting accuracy, the longer the foreseen period is, the greater the impact on the forecast result is. Therefore the article bases on previous human studies, takes the Zhang River Basin floods during the flood season in 2008 in Hubei for example, uses AREM model forecast results as precipitation in forecast period to input the hydrological model, and make the test on the impact of considering precipitation in forecast period on flood forecast results, its conclusions are as follows:

(1) During the flood forecast, under the conditions of rainfall occurring in the future, compared without considering precipitation in forecast period, the flood forecast result of considering precipitation in forecast period exist the obvious improvements, the max can get 50% improvements, and it can make forecast on flood process in advance during the whole rain process.

(2) Although that the precipitation in forecast period is considered, there still is the difference between the flood forecast result and actual condition, the differences shows that the forecast accuracy of the precipitation in forecast period need to be improved further.

(3) The impact of the precipitation in forecast period on the flood forecast accuracy have been noted by more and more hydrologist and meteorologist, modern weather forecast technology provides a good technical support to offer the precipitation in forecast period during the flood forecasting. With the development of modern operation system, especially is QPE and QPF, the high spatial and

temporal resolution weather forecast will provide the good technical support for flood forecasting.

Ackonwledgement

This work has been supported by the National Natural Science Foundation of China (50879061); the Special Research Project (meteorology) of the Ministry of Science and Technology of China (GYHY200806002, GYHY200906019);The Tackle Key Problem Plan of Science and Technology of HuBei Province in China (2007AA301B57); The Research Foundation of the Heavy Rain in IHR(IHR2009G07,IHR2009G08);The project of Research and Operation in IHR(1013,1014).

References

[1] YANG Wen-fa. The primary research on coupling application in precipitation and flood forecast[J].the investigation of water resource, 2003.24(1)：38-40

[2] WANG Qing-zai, LIU Xiao-wei, XU Ke-Yan. The research on coupling technology on rainstorm flood forecast in area of Xiao LAND Di and Hua YuanKou in Yellow River[J]. Yellow River, 2003. 25(2): 17-19

[3] LI Chaoqun GUO Shenglian ZHANG Honggang; Application of Short-term Quantitative Precipitation Forecasts in Flood Forecasting in Geheyan Reservoir Basin[J], Water Resources and Power, 2006.24(4):31-35

[4] Cui Chun-guang，Li Jun，Shi Yan. Development and application of the advanced regional eta-coordinate numerical heavy-rain prediction model system in china[J].Advances in Geosciences,2007(6):23-33

[5] LI Jun; SHEN Tieyuan; SONG Xingyuan; ZHANG Liping. Precipitation forecast experiments of a meso-scale numerical model AREM[J] Engineering Journal of Wuhan University,2007,40(1)13-16

[6] Zhao Ren-jun. Hydrological Simulation in Basins [M].WaterPower Press. BeiJing,1984

[7] Zhao Ren-jun, Wang Pei-lan. The analysis of Xinanjiang model parameter[J]. Hydrology,1988,8(6):2-9

[8] PengTao, Song Xing-yuan,Shen Tie-yuan The Application of Radar Quantitative Precipitation Estimation in Flood Forecasting during Flood Season[A],The Proceedings of the 4th International Yellow River Forum on Ecological Civilization and River Ethics [C].Zhengzhou:Yellow River Conservancy Press,2010,309-314

[9] Liyunjun ,Songxing-Yuan Research and Application of Flood Forecast to Longwangshan Reservoir in Huai'an City Journal of University of Hydraulic and Electric Engineering/yichang 2005,27(3):209-212.

Session D

Verification of Precipitation Forecasts

Intercomparison of verification methods for spatial quantitative precipitation forecasts

Barbara BROWN[1], Elizabeth EBERT[2], Eric GILLELAND[1], and **Tressa FOWLER[1]**

[1]*National Center for Atmospheric Research, Research Applications Laboratory, Boulder, CO USA*
[2]*Centre for Australian Weather and Climate Research (CAWCR), Bureau of Meteorology*
bgb@ucar.edu

1. Introduction

As model forecasts and observations have increased in resolution, new challenges in evaluating their quality and performance have arisen. Traditional grid-point comparisons break down because of small-scale errors and double penalty issues associated with possible positioning errors. These approaches often reward smoother (coarser scale) products without providing diagnostic information regarding the causes of performance issues, even if the higher resolution models actually provide more realistic and useful information. Many new methods for evaluating high-resolution gridded products have been developed in recent years. A major international intercomparison effort (the Spatial Forecast Verification Inter-Comparison Project: ICP) has improved understanding of the benefits and limitations of each method, and has clarified the types of information each provides about forecast performance. The ICP has focused on application of the new methods to evaluate precipitation products. Results of the ICP have identified specific categories of methods and have helped to characterize the attributes and capabilities of the new approaches.

2. The ICP

In the previous decade or so, with the onset of high-resolution weather forecast models, new challenges in forecast verification and product evaluation have become evident. Traditional forecast grid-point to observed grid-point verification typically rewards smoother (less resolved) forecasts because they are sensitive to small-scale errors and because of the double-penalty issue whereby the same position error will penalize a forecast for both misses and false alarms (e.g., Mass et al. 2002). Furthermore, traditional methods do not discriminate types of errors that may be of interest in terms of improving forecast models or interpreting their output.

These issues provided a focal point for the rapid development of newly proposed methods for verifying gridded forecasts against gridded observations in recent years. The brisk pace of development made it difficult to assess which methods were best to use and what diagnostic information each method provided. Subsequently, the Spatial Forecast Verification ICP was organized to compare the various approaches and to document the benefits and limitation of each method. Gilleland et al. (2009, 2010a) and Ahijevych et al. (2009) provide overviews of the project and a review of the methods that have been evaluated.

The cases considered in the ICP include 24-h forecasts of 1-h precipitation from three configurations of the Weather Research and Forecasting (WRF) model, known perturbations of one of these cases, and simple geometric cases with prescribed spatial displacement and/or spatial extent errors. The geometric cases are simple elliptical-shaped precipitation patterns with common forecast errors, which provide useful information about the output of each method. Perturbed "real" cases illustrate the capabilities of each method with more complex precipitation situations and similar errors to the geometric cases. For nine real WRF cases, a subjective evaluation was carried out to compare the human ranking to the spatial

verification methods, though subjective evaluations can be varied and even misleading. More detailed information about the test cases and the subjective evaluations can be found in Ahijevych et al. (2009).

3. Spatial verification methods

One important outcome of the ICP has been the categorization of the new verification methods into groupings that characterize the way they treat the spatial features and attributes. The four main categories of methods are depicted in Figure 1. Panel a) shows a test case from the ICP that is subsequently evaluated in the other panels by a representative from each of the method categories. It was found that the methods generally fall into one of two main categories: filter and displacement.

The filtering approach includes neighborhood methods and scale separation methods, both of which measure forecast quality as a function of scale. Neighborhood methods (Fig. 1b) relax the requirement for an exact match by allowing forecasts within spatial neighborhoods of the observation to be counted as (at least partly) correct. Statistics are computed for a sequence of neighborhood sizes starting from a single grid box (equivalent to traditional verification) and increasing to some much larger, but still meaningful, scale. Thus, this approach can provide forecast users with practical information on the scale at which an acceptable level of skill is attained. Ebert (2008) provides an excellent overview of these types of approaches, which include the Fractions Skill Score (FSS) described by Mittermaier and Roberts (2010). Scale separation methods (Fig. 1c) diagnose and estimate the errors at distinct scales. For example, performance at small, medium, and large scales may be examined separately using these approaches. Because different physical processes are associated with different spatial scales, this information can be very useful for model and forecast developers. Examples of these methods include the wavelet approach by Briggs and Levine (1997) and the intensity-scale approach of Casati (2010).

Forecast displacement approaches include feature-based methods (Fig. 1d) that identify and evaluate objects of interest in the spatial fields, and field deformation methods (Fig. 1e) that alter the forecast to better match the observations. Feature-based methods focus on the attributes of well-defined spatial objects such as rain areas or wind maxima. Matching of forecast and observed objects allows evaluation of errors in the location, size, shape, and other attributes of the forecast objects, which give useful information to both users and forecast developers. Even when matching is not possible, distributions of forecast and observed feature attributes can be compared to assess forecast realism. Field deformation methods use morphing techniques to stretch and squeeze the forecast to resemble the observations. In contrast to feature-based methods, field deformation methods yield an array of vector location errors for the field. Once the forecast has been aligned with the observations, errors in amplitude can be measured. These methods are ideally suited for diagnosing phase errors.

4. Comparison of types of methods

Table 1 briefly summarizes the methods by category in the context of several aspects of forecast quality. It should be noted that while the table gives yes or no answers for categories of methods, the answer shown may not apply to a particular method in the category. For example, while the displacement methods are not generally designed to inform about scales at which a forecast has skill, it is certainly possible to apply any of the methods to particular scales (e.g., an upscaled field). The method by which MODE, a features-based displacement method (Davis et al. 2010), creates objects involves a convolution of the field using a user-defined radius. The amount of convolution can be considered as a scale (similar to upscaling) so that skill at different scales can be obtained.

All of the methods supply information about intensity errors, but they do so in very different ways. A deformation approach, for example, typically computes traditional verification scores that pertain to

intensity for pre- and post-deformed fields. Neighborhood methods also typically provide traditional verification scores, but on filtered fields of different scales. In this way, information is obtained about the scales where a forecast has skill. Contingency table information (i.e., hits, misses, false alarms, and correct negatives) and binary scores are naturally summarized by neighborhood and scale-separation methods. Features-based methods provide a new way of determining such errors, where matched objects can be thought of as hits, and unmatched objects as misses or false alarms.

5. Summary

The verification methods outlined in this paper are described in much more detail in Gilleland et al. (2009, 2010 a), and in other papers that were produced as a result of the ICP (see http://www.ral.ucar.edu/projects/icp/index.html). Through the ICP, the capabilities of the various methods have been clearly delineated, and the advantages of each approach relative to traditional approaches have been characterized.

Although most of the methods were developed using gridded precipitation forecasts and observations, and the ICP focused on precipitation, it is reasonable to expect that most techniques will easily transfer to other spatial fields. Image warping, for example, has been applied successfully to numerous types of fields including binary fields, QPF, wind vector fields, and an air quality field (Lindström et al. 2011). MODE has been applied to simulated reflectivity fields during the HWT spring experiments (Kain et. al 2010). Methods such as the wavelet approach of Briggs and Levine (1997) that did not work as well for precipitation fields, should prove useful for smoother products.

The ICP website also provides links to software that can be used to apply some of the methods that have been described here. The Model Evaluation Tools (MET) also includes capabilities for applying MODE, the intensity-scale approach, and several of the neighborhood methods. MET is described in Fowler et al. (2010) and is a community-supported software available at http://www.dtcenter.org/met/users/.

In the future, the ICP is expected to continue but with a slightly different focus. For example, precipitation forecasts may continue to be of interest, but for regions with more complex terrain. How will the different members handle non-homogeneous terrain, and will some methods perform better than others? In addition, the ICP is likely to begin to consider verification methods for other variables, such as wind, which also are difficult to evaluate in a meaningful way.

Acknowledgements

The authors would like to thank the participants in the ICP for all of their contributions. NCAR is sponsored by the National Science Foundation.

References

Ahijevych, D., E. Gilleland, B.G. Brown, and E.E. Ebert, 2009: Application of spatial verification methods to idealized and NWP gridded precipitation forecasts. *Wea. Forecasting*, **24**, 1485-1497.

Briggs, W.M. and R.A. Levine, 1997: Wavelets and field forecast verification. *Mon. Wea. Rev.*, **125**, 1329-1341.

Casati, B., 2010: New Developments of the Intensity-Scale Technique within the Spatial Verification Methods Inter-Comparison Project. *Wea. Forecasting*, **25**, 113-143.

Davis, C.A., B.G. Brown, R.G. Bullock and J. Halley Gotway, 2009: The Method for Object-based Diagnostic Evaluation (MODE) Applied to Numerical Forecasts from the 2005 NSSL/SPC Spring Program. *Wea. Forecasting*, **24**, 1252-1267.

Ebert, E E, 2008. Fuzzy verification of high resolution gridded forecasts: A review and proposed framework. *Meteorol. Appl.*, **15**, 51-64.

Fowler, T.L., T. Jensen, E. I. Tollerud, J. Halley Gotway, P. Oldenburg, and R. Bullock, 2010: New Model Evaluation Tools (MET) Software Capabilities for QPF Verification. *Proceedings, Third WMO International Conference on QPE and QPF and Hydrology*.

Gilleland, E., D. Ahijevych, B.G. Brown, B. Casati, and E.E. Ebert, 2009: Intercomparison of spatial forecast verification methods. *Wea. Forecasting*, **24**, 1416-1430.

Gilleland, E., D.A. Ahijevych, B.G. Brown and E.E. Ebert, 2010a: Verifying Forecasts Spatially. *Bull. Amer. Meteor. Soc.*, in press.

Gilleland, E., J. Lindström, and F. Lindgren, 2010b: Analyzing the image warp forecast verification method on precipitation fields from the ICP. *Wea. Forecasting*, **25**, 1249-1262.

Kain, J.S., M. Xue, M.C. Coniglio, S.J. Weiss, F. Kong, T.L. Jensen, B.G. Brown, J. Gao, K. Brewster, K.W. Thomas, Y. Wang, C.S. Schwartz, and J.J. Levit, 2010: Assessing advances in the assimilation of radar data within a collaborative forecasting-research environment. *Weather and Forecasting*, in press.

Lindström, J., E. Gilleland, and F. Lindgren, 2011: Forecast verification using image warping. Manuscript in Preparation, available at: http://www.ral.ucar.edu/staff/ericg/LindstromEtAl2009.pdf).

Mass, C.F., D. Ovens, K. Westrick, and B.A. Colle, 2002: Does increasing horizontal resolution produce more skillful forecasts? The results of two years of real-time numerical weather prediction over the Pacific Northwest. *Bull. Amer. Meteorol. Soc.*, **83**, 407-430.

Mittermaier, M. P. and N. Roberts, 2010: Intercomparison of Spatial Forecast Verification Methods: Identifying skillful spatial scales using the Fractions Skill Score. *Wea. Forecasting*, **25**, 343-354.

Table 1: Summary of the types of information that the general categories of methods can provide. Entries represent general characteristic of the method type, and understood that there are exceptions among individual methods; see text for more information.

Method category	Scales with skill	Location errors	Intensity errors	Structure errors	Occurrence (hits, misses and false alarms)
Neighborhood	Yes	No	Yes	No	Yes
Scale-separation	Yes	No	Yes	No	Yes
Features-based	No	Yes	Yes	Yes	Yes
Deformation	No	Yes	Yes	No	No

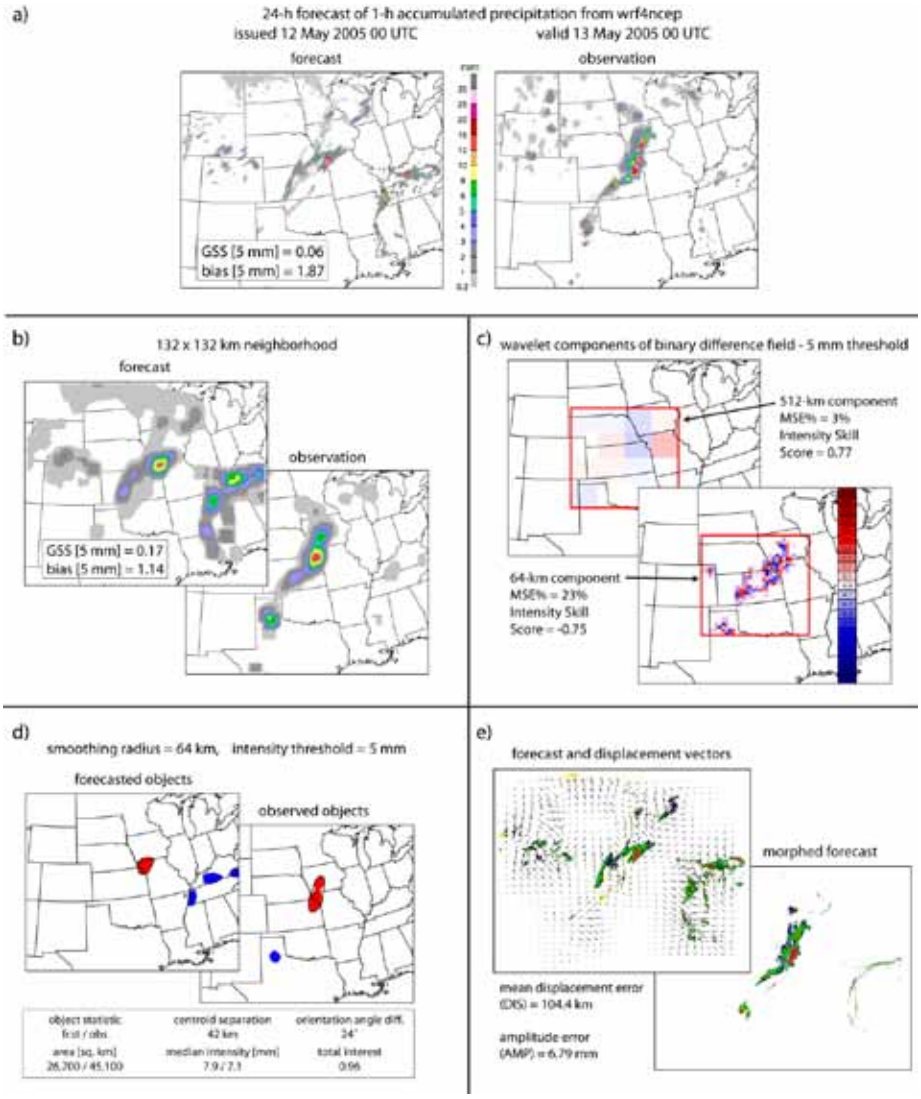

Figure 1: From Gilleland et al. (2010a, Fig. 3). Shows the 13 May 2005 ICP real test case, which is a 24-h accumulated precipitation forecast (in this case from the WRF 4-km NCEP model) along with the Stage II analysis field (panel a). Panel b depicts a simple neighborhood approach (upscaling) applied to the test case, panel c shows the scale separation wavelet decomposition to a binary difference field (i.e., part of the IS method) applied to the same test case. Panel d) is an example of MODE (a feature-based method) and panel e is an example of an optical flow (a deformation approach) also applied to this test case.

Verification of Quantitative Precipitation Forecasts with In Situ Measurements for Flood Forecasting and Warning in Jakarta

Kadarsah
Meteorological Climatological and Geophysical Agency
Jl.Angkasa I No.2 Kemayoran, Jakarta 10720
Telp.(021)4246321 ext 2322, 2425, Fax.(021)65866238

Abstract

Almost every rainy season in Indonesia, Jakarta experienced a flood disaster. The most significant reason of the disaster is the high rate of rain, since the rainy season in Indonesia starts in December until March. The rain intensity reached its peak in December-January-February, with the greatest intensity towards the end of the month. Eventually, water flowing into Jakarta overflows some of the city's flood control systems and causes devastation in these areas. Use of WRF model for process Quantitative Precipitation Forecasts have been used, the results were verified by using ROC curves by comparing the results of the In Situ measurements. Furthermore, the prediction model was built and flood warnings by using the results from radar, satellite and rain gauge as a source of observational data

Keyword: Quantitative Precipitation Forecasts, flood forecasting, ROC Curve

New Model Evaluation Tools (MET) Software Capabilities for QPF Verification

Tressa L. FOWLER, Tara JENSEN, Edward I. TOLLERUD, John HALLEY GOTWAY, Paul OLDENBURG, and Randy BULLOCK
National Center for Atmospheric Research (NCAR, Boulder, CO USA)
tressa@ucar.edu

1. Introduction

Verification plays a crucial role in improvement of precipitation forecasts The Model Evaluation Tools (MET) software was designed to provide the numerical weather prediction community with quality software incorporating the latest advances in forecast verification, including methods for verifying quantitative precipitation forecasts (QPF).

The recent addition of probabilistic and ensemble verification capabilities to the MET software has led to innovations demonstrated in the verification activities of two QPF projects in the United States. The Hydrometeorology Testbed (HMT) conducted an experiment examining heavy, prolonged winter precipitation. Prediction of convective precipitation was one focus of the Hazardous Weather Testbed (HWT) 2010 Spring Experiment. Examples from these projects demonstrating MET's spatial, object-based verification of ensemble relative frequency (e.g. probability) and ensemble mean will be presented and compared to traditional methods. In addition to verifying QPF, atmospheric river and radar reflectivity fields were evaluated using MET's object based spatial verification. These examples illustrate the enhanced diagnostic information available from spatial verification versus traditional metrics.

2. MET Software

The MET verification software is designed to provide the numerical weather prediction community with a consistent means to verify model forecasts. Traditional verification measures for precipitation are available in MET. For precipitation, traditional verification often utilizes skill scores, such as the Threat Score, computed for cases that exceed some minimum precipitation amount. Unfortunately, for this type of verification, a shift in time or space of the forecast precipitation area can lead to the so-called "double penalty", where the forecast is a false alarm and observation is missed event. Ensemble and probability forecasts contain more information than standard deterministic forecasts. Thus, though traditional methods and statistics can be applied, additional information is a benefit to the user.

Recent additions to the MET software have enhanced the precipitation verification capabilities to address these issues. Ensemble means and probability values can be produced from a set of forecasts by a new MET preprocessing tool. Probabilistic forecasts are verified using traditional statistics such as Brier score, while ensemble mean and spread can be used to calculate the continuous ranked probability score (CRPS). Additionally, both types of forecasts can be used in advanced spatial verification techniques.

MET's object based spatial verification software, MODE (Method for Object-based Diagnostic Evaluation; Davis *et al*, 2009), can use ensemble means or ensemble probabilities to define forecast objects then compare these to objects identified in gridded observation fields. This software was developed on precipitation fields. However, it has also been successfully applied to other spatially coherent fields, such as radar echo top, atmospheric rivers, cloud percent, and winds.

Although the software was created to work with the weather and research forecasting (WRF) model, MET can be used with any model in GRIB format. Users have reported success using MET with

both MM5 and GFS models. The most recent release of MET, version 3.0, also supports the netCDF format output from pinterp, the WRF ARW postprocessing tool.

3. Model Data

For the HWT spring experiment, the Center for the Analysis and Prediction of Storms (CAPS) produced ensemble forecasts from 26 unique 4-km WRF runs that utilize different cores and configurations (Jensen *et al*., 2010). Products include accumulated precipitation, probability of precipitation, radar reflectivity, and radar echo top.

The forecasts for the HMT effort come from the Division of Water Resources (DWR) 9-km nine member WRF-based ensemble (Jankov *et al*., 2007). The ensemble mean forecast is calculated by MET prior to evaluation.

4. Observational Precipitation Data

The accumulated precipitation, radar reflectivity, and radar echo top observations used during the HWT project come from the National Severe Storms Laboratory Q2 (second generation quantitative precipitation estimation, QPE) product (Zhang *et al*, 2009). This product incorporates data from rain gauges, radar, satellite, and numerical models.

For HMT, the gridded precipitation observations are from the Stage IV product, a multi-sensor (radar and rain gauges) composite rainfall estimate over the continental United States (CONUS). Precipitation analyses, including some manual quality control, are produced by the River Forecast Centers and merged together at National Center for Environmental Prediction within an hour of receipt (Lin and Mitchell, 2005).

For verifying forecasts of atmospheric rivers during HMT, the gridded atmospheric river observation field is satellite-derived integrated water vapor (IWV) from the microwave sensors on polar-orbiting satellites, of which most is located in the surface layer (0-2 km) above the Pacific. Land values of IWV are not as credible as marine values, hence are not shown (Ralph *et al*., 2006).

5. Results

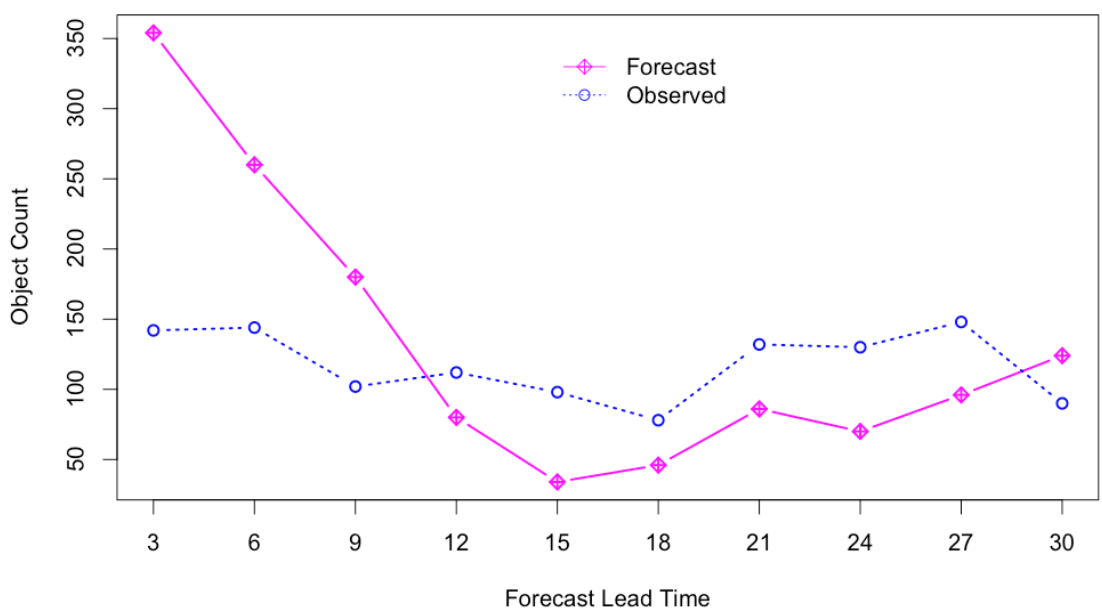

Figure 1: Total object count for HWT CAPS ensemble probability >50% for 3-hour precipitation exceeding 12.7mm by lead time.

During the HWT project, precipitation objects, i.e. cohesive areas of precipitation, based on ensemble probability (probability of precipitation > 50% for 12.7mm in a 3 hour period) were identified for the entire 6 weeks of the project. Then total counts of both forecast and observed objects were accumulated for 3 hourly lead times and are shown in Figure 1. Since the issue time of all forecasts is 0Z, the lead time also indicates the time of day. The model forecast too many objects in the earlier hours (3, 6, and 9), and too few objects in the remaining hours. A similar plot of the total object areas (not shown) shows that the objects cover more of the domain than the forecasts at all lead times except 3 hours, when the areas are similar. The Brier Scores for all lead times are quite small, ranging from 0.017 to 0.009. Since Brier Score is similar to mean squared error, these small values indicate a good forecast.

In addition to examining precipitation, the HWT experiment also examined radar reflectivity and radar echo top. The reflectivity is in dBz, while radar echo top is the height of the 18 dBz isopleths. Prior to this experiment, MODE had not been used directly on radar fields. This project confirmed that object based verification is appropriate for these fields. An example is shown in Figure 2. The location and orientation of the reflectivity and echo top forecasts match well with the observations, though the forecasts are shifted slightly too far to the southwest. Forecast areas are somewhat too small. This analysis is for a single case, but this type of information can also be derived for longer periods.

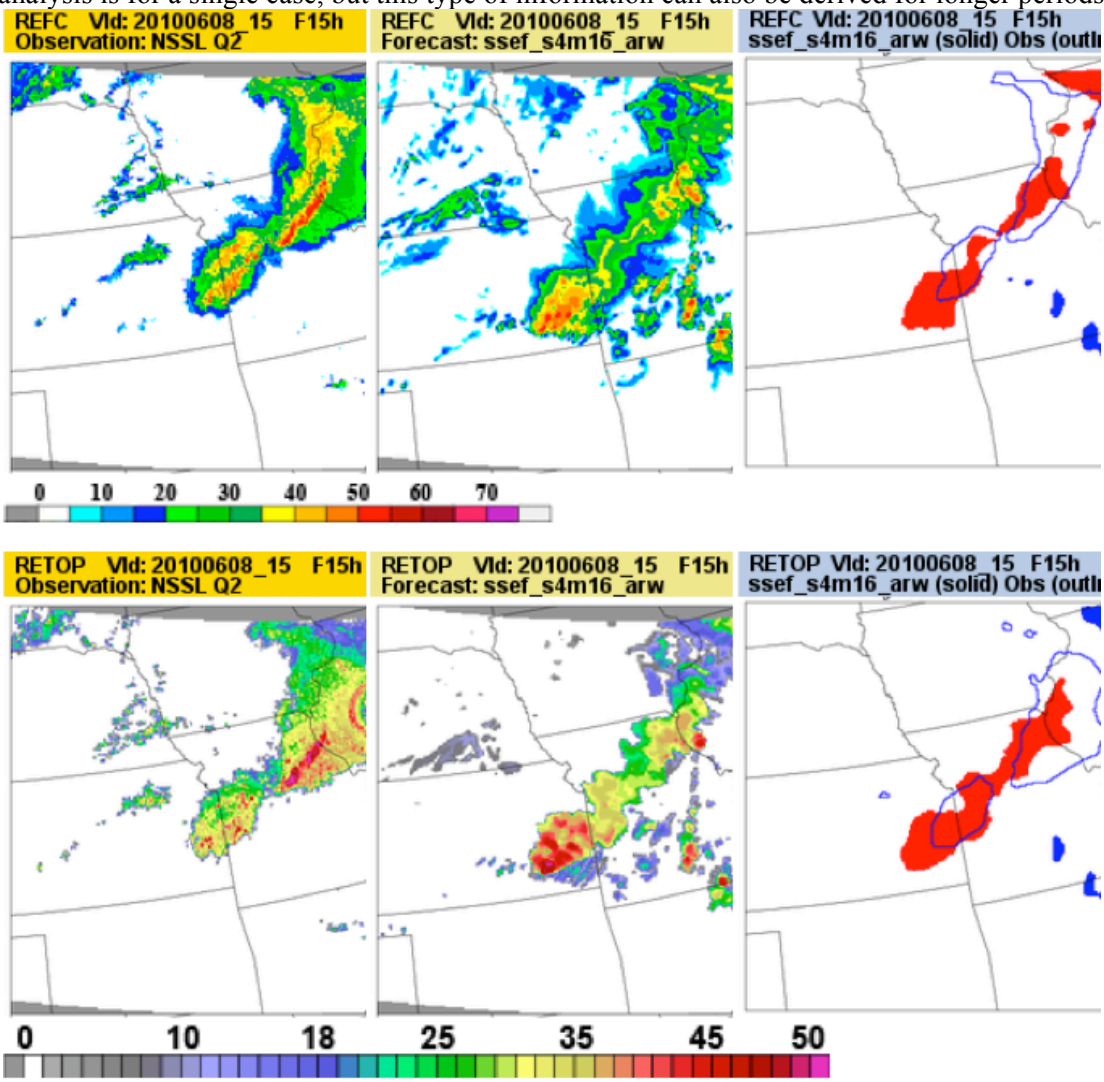

Figure 2: Top: Observed (left) and simulated (middle) composite reflectivity valid on June 8, 2010 at 15 UTC. Corresponding MODE objects (right) for observed field (blue line) and forecast field (red and blue solid objects). Bottom: Observed (left) and simulated (middle) height of 18dBZ reflectivity field, called Radar Echo Top, valid on

June 8, 2010 at 15 UTC. Corresponding MODE objects (right) for observed field (blue line) and forecast field (red and blue solid objects).

For the HMT West experiment, conducted during the winter of 2009-2010 in the western United States, the ensemble mean forecasts were analyzed by MODE for the whole season. A single case is shown in Figure 3. Although it is best to analyze several cases together, looking at MODE results for a single case can give the user a better feel for how object verification works. In this case, the forecast area is too small (497 grid squares) compared to the observed area (706 grid squares), but the overlap is very good (intersecting area = 429 grid squares). The median precipitation value within the forecast object is about 7.5 mm, while the median observed precipitation within the object is about 8mm. Thus, the typical amount of precipitation was well forecast. One benefit of using objects is that these amounts do not have to be forecast in the exact same locations to be compared. By comparison to traditional statistics, the probability of detection is 0.31 and the false alarm rate is 0.63, suggesting a not very good forecast. An alternate interpretation, confirmed by the object based method, is that this is a good forecast, with a low level overforecasting bias (common for ensemble mean forecasts).

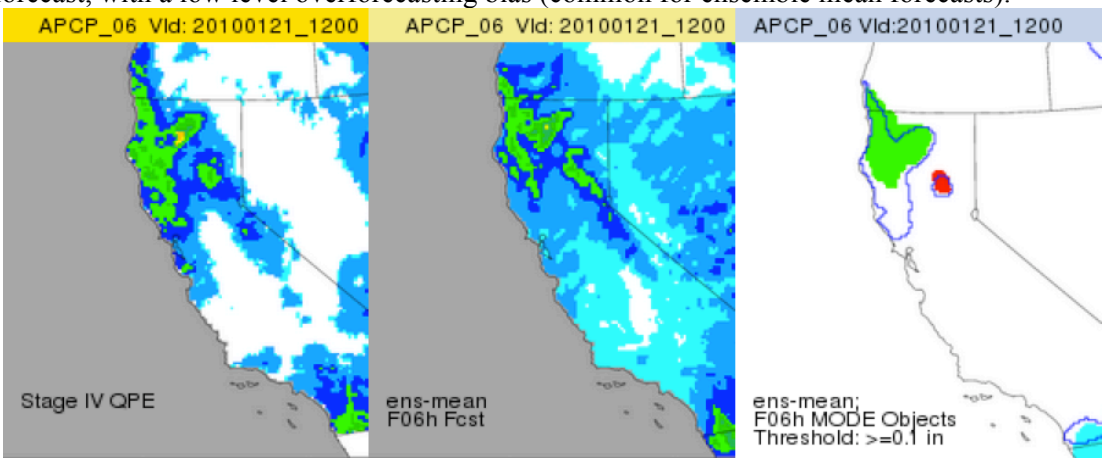

Figure 3: Panels show 6-hour observed precipitation, ensemble mean forecast precipitation, and MODE objects (solid=forecast, outline=observation) for a single case.

An example of object-based atmospheric river verification, completed as part of the HMT West experiment, is shown in Fig. 4 below. This case is from December 18, 2005. The forecast is for precipitable water, while the observation is integrated water vapor (Ralph *et al*, 2006). The area of the forecast object is nearly twice that of the observed object (244 vs. 126 grid squares). However, the observed object is almost nearly encompassed by the forecast object (intersection area: 114 grid squares).

6. Conclusions

MET provides a variety of methods for verifying precipitation forecasts, including diagnostic and spatial methods for ensemble and probability forecasts. The spatial verification in MODE seems to extend well to assessment of ensemble mean forecasts, probability forecasts, and other spatial fields related to precipitation, such as radar reflectivity, radar echo top, and atmospheric rivers. Object based verification compensates for many deficiencies in traditional verification measures, providing assessments of forecast size and intensity accuracy, even when displacement errors are present.

MET software simplifies and standardizes verification across projects while providing easy access to the most current verification capabilities. Short term updates to the software will include capability to read CloudSat data, use of MODE object verification on vertical rather than just horizontal surfaces, and capability to track MODE objects through time to better examine forecast timing errors.

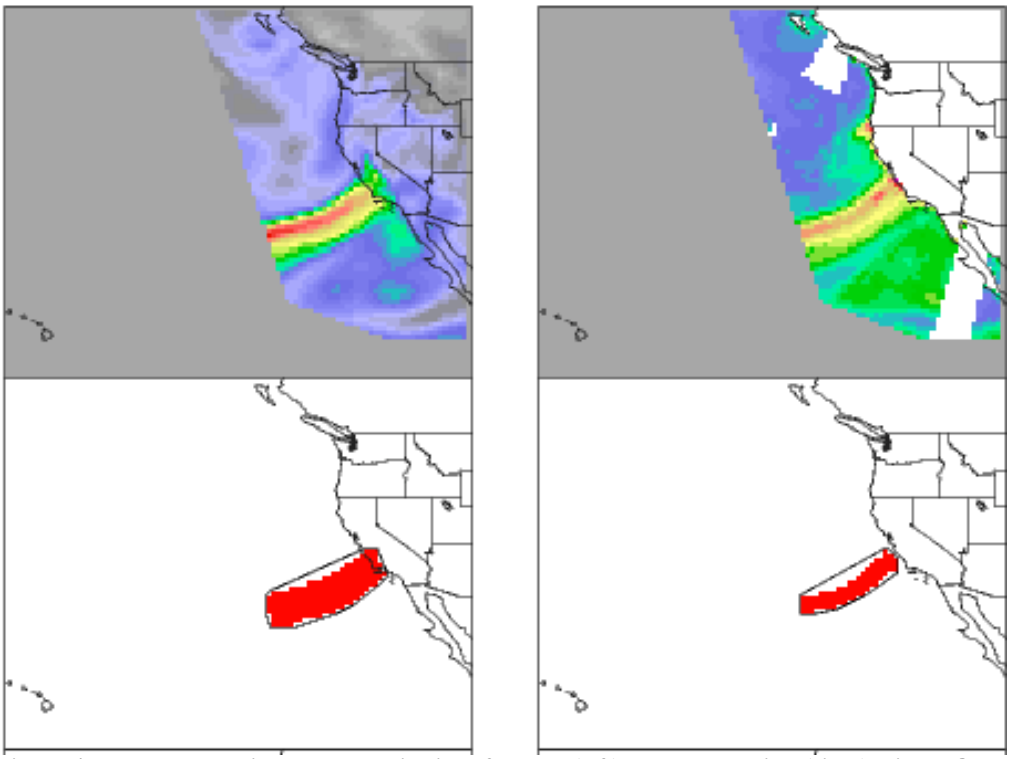

Figure 4: Example showing atmospheric river forecast (left) and observation (right) with MODE objects (bottom) for each.

Acknowledgements

The authors would like to thank the Air Force Weather Agency (AFWA), the National Oceanic and Atmospheric Administration (NOAA), and the Developmental Testbed Center (DTC) for their support of MET.

References

Davis, C. A., Brown, B. G., Bullock, R. G., Halley Gotway, J. E., 2009: The Method for Object-based Diagnostic Evaluation (MODE) applied to numerical forecasts from the 2005 NSSL/SPC Spring Program. *Weather and Forecasting*, 24, doi: 10.1175/2009WAF2222241.1, 1252-1267.

Jankov, I., P. J. Schultz, C. J. Anderson, and S. E. Koch, 2007: The Impact of Different Physical Parameterizations and Their Interactions on Cold Season QPF in the American River Basin. *Journal of Hydrometeorology*, **8**, pp. 1141–1151

Jensen T., S. Weiss, J. Kain, M. Harrold, M. Xue, F. Kong, B.G. Brown, P. Marsh, Adam Clark, K. Thomas, M. Coniglio, and R. Schneider, 2010: The Developmental Testbed Center (DTC) Objective Evaluation Performed During the Hazardous Weather Testbed (HWT) 2010 Spring Experiment. *The 11th WRF Users' Workshop,* June 21-25, Boulder, CO, P48.

Lin, Y., K.E. Mitchell, 2005: The NCEP Stage II/IV precipitation analyses: development and applications. *Preprints, 19th Conf. on Hydrology,* Amer. Meteor. Soc., San Diego, CA. Paper 1.2.

Ralph, M.F., P. J. Neiman, G. A. Wick, S. I. Gutman, M. D. Dettinger, D. R. Cayan, and A.B. White, 2006: Flooding on California's Russian River: Role of atmospheric rivers. Geophysical Research Letters, **33**, doi:10.1029/2006GL026689

Zhang, J., K. Howard, S. Vasiloff, C. Langston, B. Kaney, A. Arthur, S. Van Cooten, K. Kelleher, D. Kitzmiller, F. Ding, M. G. Mullusky, E. Wells, D. Seo, T. Schneider, and C. Dempsey: 2009: National Mosaic and Q2 (NMQ) system—description, results and future plans. *34th Conference on Radar Meteorology*. Amer. Meteor. Soc.,, Omaha, NE. Paper 7A.1

A Quantitative Hazard Assessing Method for Heavy Rainfall Events

Qiuzhen YANG [1,2], **Ming XU [1,2]**, Jun LI [3]

1. Shanghai Typhoon Institute of CMA, Shanghai 200030,China;,2. Laboratory of Typhoon Forecast Technique , Shanghai Typhoon Institute of CMA , Shanghai 200030,China,3. Shanghai Climate Center /SMB, Shanghai 200030, China

xum@mail.typhoon.gov.cn

Abstract : Heavy rainfall and its associated amounts of surface runoff and floods occur frequently in Shanghai during the rainy season. They usually result in tremendous negative impacts such as huge property and economic losses, damage of natural resources, as well as social problems. The spatial and temporal distribution patterns of heavy rainfall hazard intensity largely determine the place and evolving of disasters impacts. The accurate diagnosis of heavy rainfall hazard degree is the base for assessing their impacts on economy, society and ecology. In this paper, the definition of rainfall hazard and its categorizing criterion and assessing model for both local and regional areas were put forward. The distribution of rainfall hazards was described by using random variables' probability form, and the risk threshold field, which is composed of rainfall hazard threshold values at risk probability level, was also set up. The rainfall hazard degree was then defined as the integration of similarity and close degree of the observation values of an event to the threshold value in the risk field. Using a variety of proper random variable probability distribution model, the rainfall hazard threshold values under the specific risk probability levels in any given place and their threshold field were determined, the quantitative evaluating model of rainfall hazard degree were established for both single point and connected area. As a demonstration, the hazard degrees of heavy rainfall events in Shanghai have been assessed, and the surface runoff of annual maximum daily rainfall for 1-200 year return periods were estimated by the runoff models. The results show that the impact assessing method is applicable in evaluating hazard of high impact rainfall events. The method provides a reference for the rainfall disaster evaluation.

Key words: Heavy rainfall risk thresholds, Hazard degree assessing,, return periods ,Surface runoff

Foundation item: Shanghai Key Agricultural Projects (Hu Nong Ke 2006-4-10)

Performance Evaluation of the AREM Prediction System for the Successive Heavy Rain Forecast of May 2010 in South China

Chunze Lin[1], Ying Gong[1], Jun Li[1] and Ming Xu[1]
[1]Institute of Heavy Rain, CMA, Wuhan 430074.
E-mail:regularbus8@yahoo.com.cn

1 Introduction

AREM model is a heavy rainfall numerical prediction model with China's own intellectual property right which take into account our country's unique topography and climate characteristics, so it has comprehensive application basis in the field of meteorology, hydrology and environment. AREM operational version has been running in Wuhan Institute of Heavy Rain since 2003. Many aspects of the AREM model, including background fields, objective analysis method, boundary condition, the top height of model, and forecast period, was upgraded and improved to enhance heavy rain forecast accuracy in recent years. AREM improved version were developed in July 2007. Based on the AREM model platform the rapid update cycle (RUC) version and ensemble prediction model have been developed and put into operational use. So a complete AREM prediction system consist of operational model, improved model, RUC model and ensemble model was been constructed. Then the forecast effect and character of the member of the AREM prediction system was the focus for the forecaster and the model developer.

Five successive heavy rain courses caused by the interaction of the subtropical highs, the upper trough, the mesoscale shear and the mesoscale vortex hit the most regions of south China from 5 to 23 May. More than 200mm of rain has fallen on the most regions of south China. Especially the strong rain belt located at Hunan province, Jiangxi province, Guangdong province and coastal areas of the southern Zhejiang province. The center of the heavy rain focused on the areas from Hunan province to the middle part of Jiangxi province and the areas between Jiangxi province and Fujian province. In order to know the forecast effect and character of each member of AREM prediction system, in this study the precipitation forecast outcomes of AREM prediction system for five successive heavy rain courses in South China in May 2010 were verified and assesed. Section 2 discusses the results of skill score calculation for precipitation. Section 3 analyzes the daily precipitation forecast of the member of the AREM prediction system for the five heavy rain events. Section 4 is the summary of this study.

2 Results of skill score calculations for precipitation

The Threat Score(TS) and forecast bias are popular measures of the precipitation forecast's effect for the NWP. The values of the TS rang from 0 to 1, where a value of o indicates no skill. The forecast bias can represent the intensity of the model precipitation forecast. The values of bias range from o to +∞, where a perfect scoring forecast has a bias of 1. If the value of bias is greater than 1, the larger the value, the stronger the precipitation forecast. If the value is less than 1, the smaller the value, the weaker the forecast.

In Fig.1, the TS are shown for the 0-24h, 12-36h, 24-48h and 36-60h forecast of the AREM operational model, improved model, RUC model and ensemble model. For 0-24h forecast, ensemble model has the highest skill. For 12-36h forecast, at 0mm, 10mm and 25mm the operational performs better than the others. For 24-48h and 36-60h, at 0mm and 10mm ensemble model's TS is higher than the others, but at 25mm the operational model has better performance and at 50mm the operational model and improved model performs better than ensemble model.

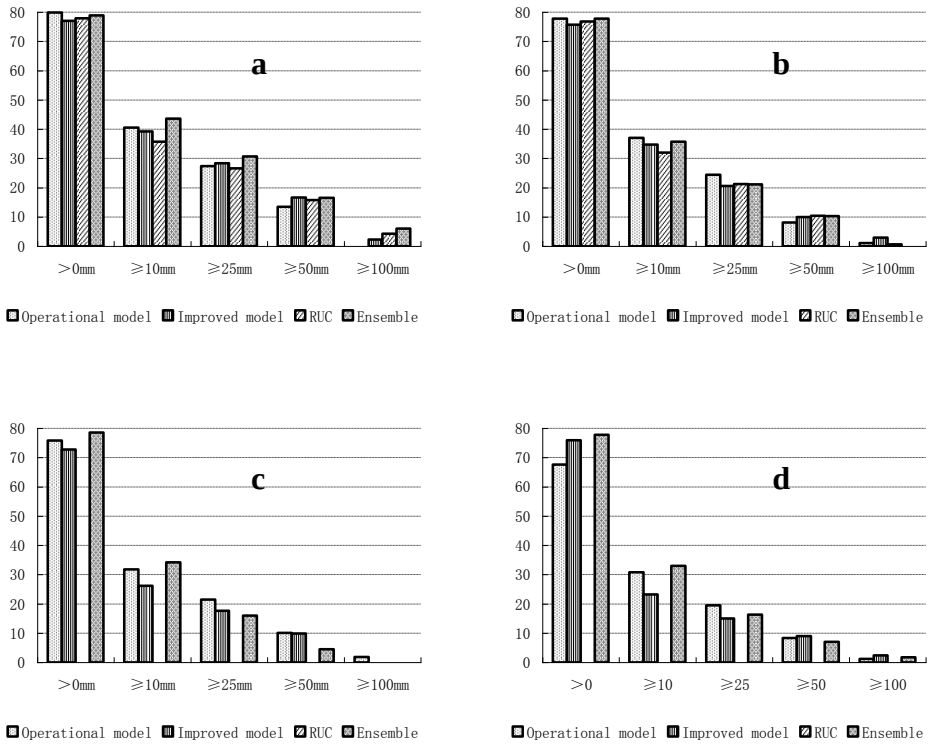

Fig.1 The TS of 0-24h(a), 12-36h(b), 24-48h(c),and 36-60h(d) accumulative precipitation forecast of every model from 5 to 23 May 2010

Fig.2 is same as the Fig.1, but for the forecast bias. The precipitation forecast intensity of the operational model is closer to the observation. The RUC model has stronger forecast, especially for the precipitation above 10mm. At 100mm, the value of the bias for the RUC forecast is higher than 5. For

0-24h and 24-48h, the improved model has good performance. For 12-36h, the improved model's precipitation forecast is stronger than observation overall. For 36-60, the value of bias of the improved model is closer to 1 at 0mm, 10mm and 25mm, but at 50mm and 100mm, the value is far ahead 1. The value of the bias for the ensemble model is higher than 1 at 0mm, 10mm, 25mm and 50mm, but lower than 1 at 100mm.

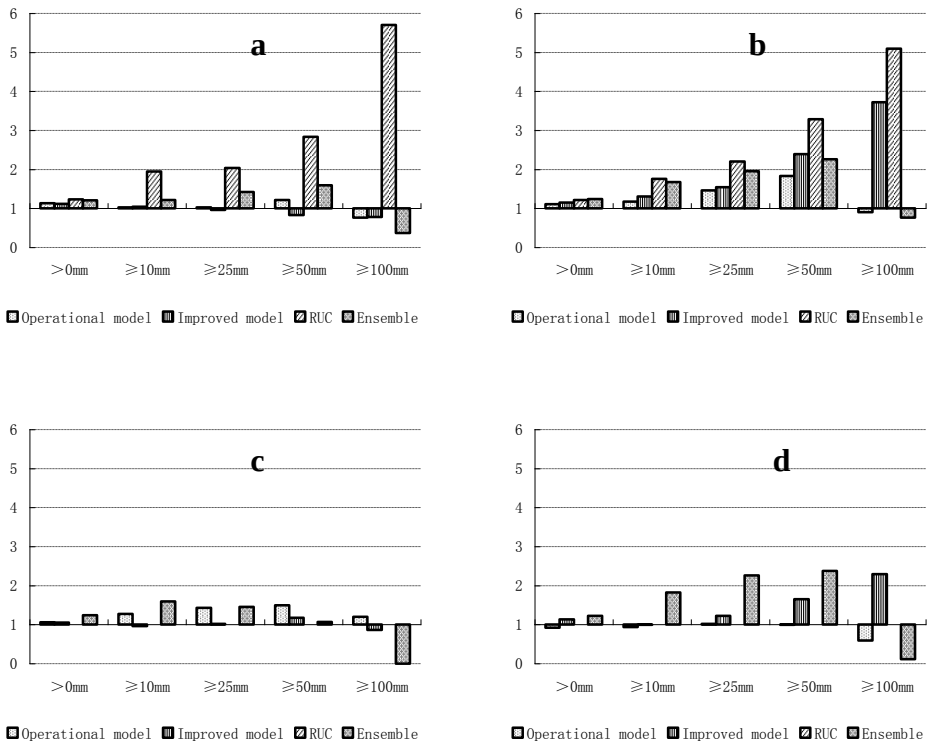

Fig.2 The same as fig.1, but for the precipitation forecast bias

3 Analysis of the daily precipitation forecast for the five heavy rain events

The AREM operational model, improved model and ensemble model is run twice daily with initialization times of 0000 and 1200 UTC. But the AREM Rapid Update Cycle (RUC) model is initialized every 3 hours beginning at 0000UTC. In the operational application, the forecast outcomes of eight times can be provided by RUC. In Fig.3, the 24h accumulative precipitation distribution of the observation and RUC forecast. The rain belt of 12-36h and 9-33h forecast lies much farther north. The location of strong precipitation of 6-30h forecast moved south. The rain belt of 3-27h forecast is closest to the observation.

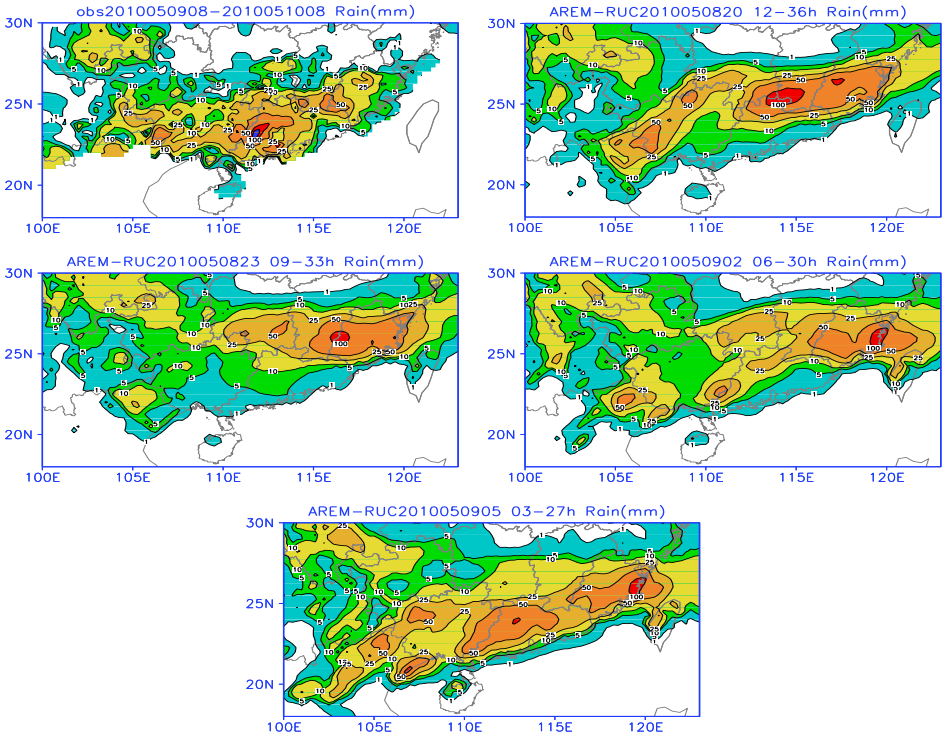

Fig.3 24h accumulative precipitation distribution of the observation and RUC model forecast at 0000 UTC 10 May 2010

In Fig.4 the 24h accumulative precipitation distribution of the observation, RUC model forecast and ensemble mean forecast, probability distribution of 50mm and 100mm of ensemble forecast at 0000 UTC 14 May 2010 is shown. The AREM improved model has good performance in the location and intensity of the main rain belt for 12-36h and 24-48h forecast, especially it gives stable forecast for the heavy rain in Jiangxi province. The precipitation distribution of ensemble mean's 0-24h forecast is much close to the observation. The high probability areas indicate the location where heavy rain happen.

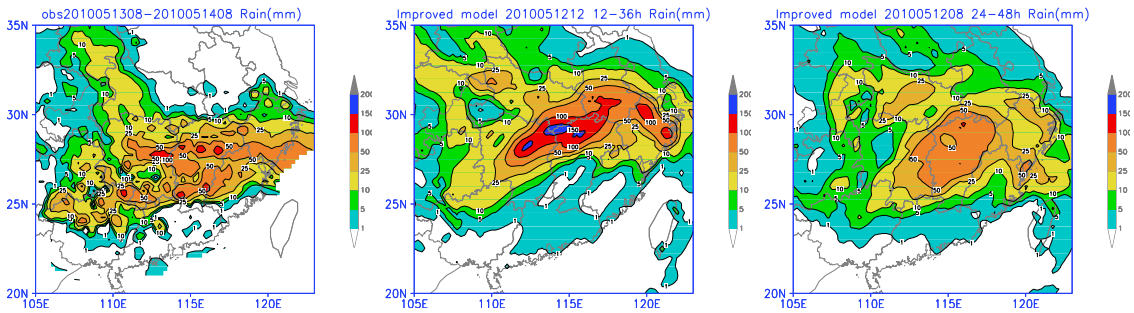

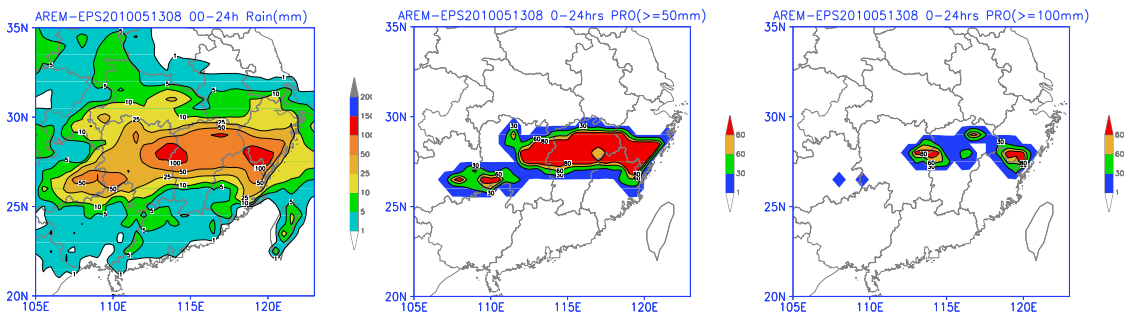

Fig.4 24h accumulative precipitation distribution of the observation, RUC model forecast and ensemble mean forecast, probability distribution of 50mm and 100mm of ensemble model forecast at 0000 UTC 14 May 2010

4 Conclusions

The results show that every member of the AREM prediction system had good performance in the successive heavy rain courses, and had their own forecast features. Operational model had better forecast effect for main rain belt in short prediction period. The advanced model had steady forecast effect for the location, range and amplitude of the main rain belt in longer prediction period. AREM-RUC had the advantage of providing the prediction of shorter period. Based on the organic combination of the average prediction and probable prediction, Ensemble model can provide important reference for the forecast of the main rain belt and the rain center.

Acknowledgments

This study has been supported by the following projiects: Meteorological research project of public sector of Ministry of Science and Technology (NO:GYHY200706012, GYHY200906010). Scientific research project of Wuhan Institute of Heavy Rain (NO:0903, 1008)

References

Yinggong., 2007: Evaluation and analysis of AREM prediction products in flood season of 2005. J. Meteorological Monthly., 33(1), 88-93.

Yinggong., 2007: Evaluation and analysis of the rainfall prediction of AREM in flood season of 2007. J. Torrential Rain and Disasters., 26(4), 372-380.

Junli, Minghuan Wang, etal., 2010: Precipitation verifications to an ensemble prediction system based on AREM. J. Torrential Rain and Disasters., 29(1), 30-37.

Qiuxia Wu etal., 2007: Verification for AREMS/973 real-time precipitation forecasts over China during the flood season in 2004. J. Chinese Journal of Atmospheric Sciences., 31(2), 298-310.

Accounting for observational uncertainty when verifying precipitation forecasts

Anna Ghelli [1] and Carlos Santos [2]
[1] European Centre for Medium Range Weather Forecast
[2] Agencia Estatal de METeorologia
anna.ghelli@ecmwf.int

Abstract

It is general practise when assessing the skills of either deterministic or ensemble forecasts to consider the observations with no uncertainty. Observation uncertainty may be associated to different causes and in the present talk the uncertainty derived by the mismatch between model generated and the locally measured precipitation is addressed. There{have?} been many attempts to add uncertainty in the verification process. Such uncertainty has been derived either splitting the error components of the observing system, or by adding a normally distributed noise to the model output, among others. The present talk will present some work done using the uncertainty obtained directly from the observed precipitation distribution within gridboxes. An extended? Brier Skill Score is calculated for the standard verification method and verification technique, which include uncertainty information. The results show a noticeable impact on the score when uncertainty is included and, though further research is needed, they encourage into effectively use in operational contexts.

1. Introduction

Verification of numerical weather prediction models plays a central role in the improvement of numerical weather prediction models both in the short and medium range forecasts. Deterministic and ensemble forecasts are assessed to ascertain their skill against observations and the latter are assumed to be exact. Even though this assumption is not in general true, it is widely accepted. In the last few years, many papers have been discussing the validity of such an assumption and concluded that it may be legitimate for longer forecast ranges, when the model error is much larger than the observation uncertainty, but there is an inconsistency when accepting that model can be uncertain while observations are exact.

Earlier attempts to take into consideration of observation uncertainties can be found in Ciach and Krajewski (1999). Their paper describes how uncertainties in the observations can alter the results of the estimation schemes to convert radar-measured reflectivity into radar-predicted rainfall intensity.

Bowler (2006) looks at the influence of observation error on the verification of categorical forecasts. The author states that the observation error is highly dependent on the type of observation, for example the principal source of error in precipitation observations is representativity due to the spatial variability of rainfall. The observed amounts at one location will not be a good estimate of rain at a close by location.

Candille and Talagrand (2008; hereafter CT08) validate an ensemble prediction system introducing observational error in the verification process. They find that reliability is degraded and resolution is improved, while discrimination is also degraded. The observation uncertainty is defined by the normal distribution whose expectation and standard deviation are obtained by random draws from a normal and lognormal distribution, which guarantees that the uncertainty is variable in both mean and spread.
In this paper, the effect of the observation uncertainty on a number of metrics used to assess the performance of an ensemble system is investigated for the case of precipitation. Section 2 contains the description of the observed database and of the forecasting system. Section 3 describes metrics and methodology, while results are discussed in section 4. Conclusions are drawn in section 5.

2. Observation dataset and models

Models and observation dataset will be briefly introduced in this section.

a. Observation dataset

European meteorological offices maintain high-density rain gauges networks, which comprise both synoptic and climatological stations. Precipitation data are collected at different temporal resolution and quality controlled. The analysis is computed on grid resolutions (1x1 degree and 0.25x0.25 degree) using a

simple upscaling technique whereby stations are assigned to model grid boxes and then averaged to produce one areal average value to be assigned to the relative gridpoint. The observation uncertainty is then defined by using the values of the 10,25,50,75, and 90 quantiles. The methodology is described in Ghelli and Lalaurette (2000) and Cherubini et al. (2002). The observation dataset was available for the period April 2007 to December 2008.

b. Models

Two forecasting systems have been used for this study: the Ensemble Prediction System (EPS) from the European Centre for Medium Range Weather Forecast (ECMWF) and the Short Range Ensemble Prediction System (SREPS) from the Spanish Meteorological Agency (AEMET). Both forecasting systems produce an ensemble of forecasts, which provide a description of a probability density function of forecast states of the atmosphere. This probabilistic approach to forecasting aims at alleviating the effects of uncertainties present in the initial conditions and the approximate simulation of atmospheric processes that numerical model can achieve. A more detailed description of the models and their performance in terms of precipitation can be found in Buizza and Palmer, (1995), Buizza et al. (2003), Ghelli and Primo (2009) and Garcia-Moya et al. (2009)

3. Metrics and methodology

In this talk an application of CT08 approach is described using observed accumulated precipitation data. This application is referred to as Observed Observational Probability (O-OP). The notation adopted by CT08 is used for consistency.
When unceratinty is taken into consideration, BSS can be written as:

$$BSS=1-BS/(E [p_0^2] - p_c^2)$$

where

$$BS = E [(p-p_0)^2] = E [(p-p'(p))^2] - E [(p'(p) - p_c)^2] + E [p_0^2] - (E [p_0])^2$$

and E represents the expectiation value, p is the forecast probability, p_0 is the observed probability, p'(p) gives the conditional observation distribution (given the forecasts) and p_c is the base rate.
The BSS decomposition can be written as BSS=1-BSS_rel-BSS_res, where now its components are given by:

$$BSS_rel = E [(p-p'(p))^2] / (E [p_0^2] - p_c^2)$$
$$BSS_res = 1 - E [(p'(p) - p_c)^2] / (E [p_0^2] - p_c^2)$$

Rainfall thresholds 1, 5, 10 and 20 mm have been selected to define the corresponding binary events of exceedence. For each binary event the joint distribution of forecasts and observations has been computed, for both the classical and O-OP approach.

4. Results

The effect of introducing the observation uncertainty into the verification process is evaluated looking at the BSS.

4.a ECMWF EPS

Figure 1 shows the timeseries of the BSS and its components for two different thresholds. The standard verification (black) and the O-OP method (grey) for the 1mm/24h (panel a) , 5mm/24h (panel b), 10mm/24h (panel c) and 20mm/24h (panel d) thresholds. The resolution (BSS_res, thin solid lines) and the reliability (BSS_rel, dashed lines), both negatively oriented, are displayed and show that BSS_rel is greatly degraded if the O-OP method (black) is used, while the BSS_res (thin solid line) is improved (black) when compared to the standard verification approach (grey). This behaviour can be observed for the other precipitation thresholds (panel b and c) and it is in agreement with the finding of CT08.
The degradation of BSS_rel is inversely proportional to the precipitation threshold in consideration

therefore, the O-OP methodology highlights the over-estimation of reliability when the standard verification procedure is adopted. The largest degradation can be found for the 1mm/24h threshold where the spring and summer reliability goes from values of around 0.05 to 0.3-0.4 (the reliability component is negatively oriented therefore, the smaller the reliability the better the system).

Moreover, the increase in BSS_res observed throughout the precipitation thresholds (fig.1 panel a, b, c and d) is linked to a systematic decrease in of the uncertainty term in the Brier Score decomposition. The uncertainty term is related solely to the observing system. The variance in probability space decreases when uncertainty is included because each observation has associated an "observed" probability of occurrence rather then just a yes/no option. The decrease of Brier uncertainty (panel a) and the increase of BSS_res (panel b) as function of time for three precipitation thresholds (1, 5 and 10mm/24h), show a strong seasonality: larger uncertainty in the summer and smaller in the winter, which coincides with an increased resolution in the winter and decreased in the summer months. The larger uncertainty during the summer months can be attributed to the predominant convective situation whereby within a grid box the precipitation variability may be larger as precipitations are very local in nature.
The BSS slightly improves when using the O-OP method for higher thresholds and this is in agreement with the findings of CT08, while for the 1mm/24h threshold the BSS deteriorates because of the large effect of the worsening of the BSS_rel has on the total skill score.

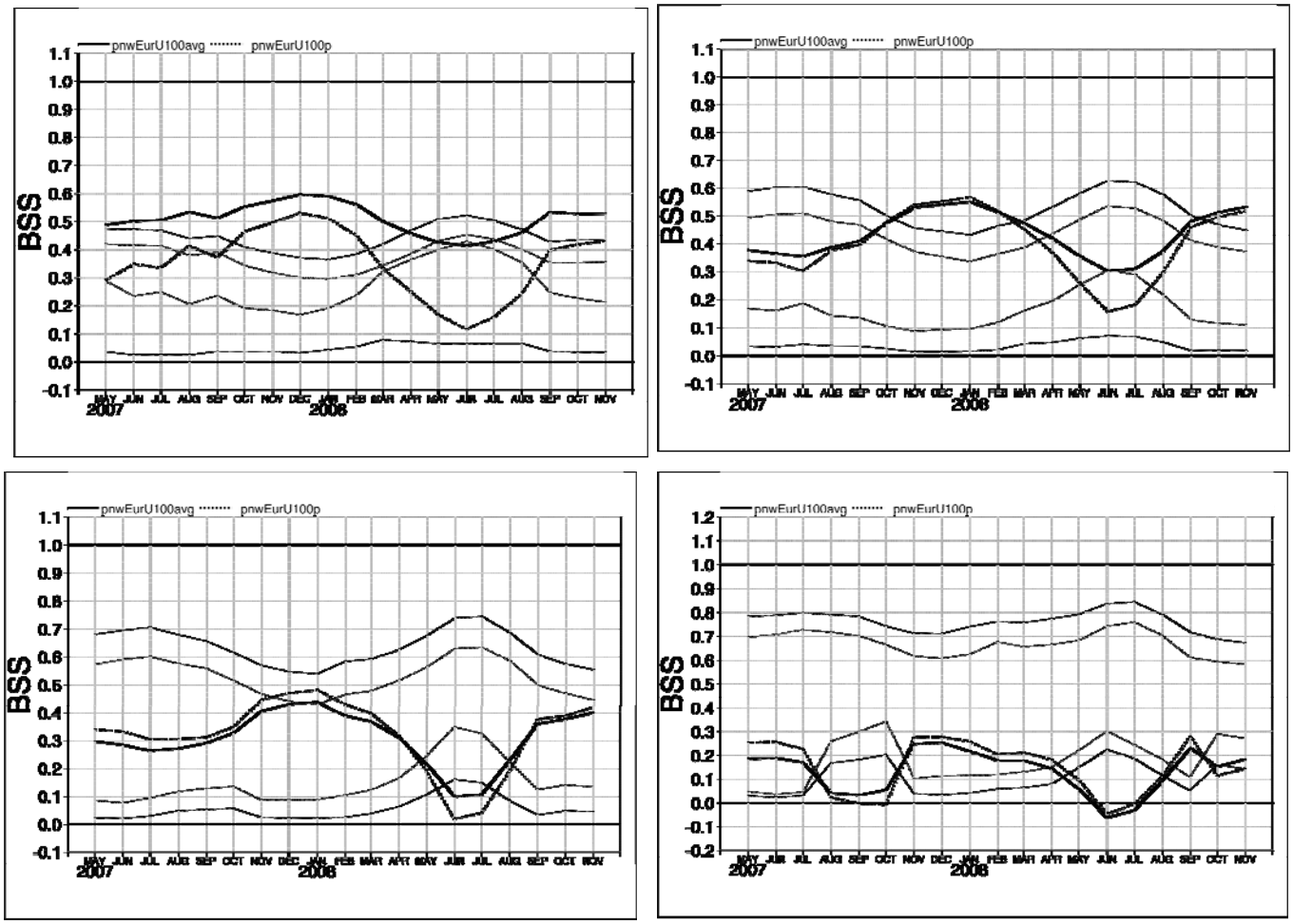

Figure 1: ECMWF EPS Standard verification (black lines) and the O-OP method (grey lines) for the 1mm/24h (panel a) , 5mm/24h (panel b), 10mm/24h (panel c) and 20mm/24h (panel d) thresholds. Also shown BSS resolution (solid lines) and BSS reliability (dashed lines)

4.b SREPS

Figure 2 shows the BSS and its components for 1mm/24h (panel a), 5mm/24h (panel b), 10mm/24h

(panel c) and 20mm/24h (panel d) for AEMET-SREPS. BSS slightly improves if the O-OP method is used for all the thresholds except the 1mm/24h. Like for the ECMWF EPS, the BSS_rel component increases, that is the reliability deteriorates when the observational uncertainty is taken into consideration and it is worse for the 1mm/24h. Even though a straight comparison between the ECMWF EPS and the SREPS is not fair, as the two systems have been scored at different resolutions, it seems appropriate to conclude that both systems suffer from the same overestimation of precipitation at small thresholds, and that the issue affects the limited area model to a lesser degree. The BSS_res increases by 10-12 percent with peaks of 16 percent during winter and spring periods. As the resolution increases, the observational uncertainty decreases, with the lower values in winter and spring. This is consistent with both CT08 and the results previously presented for the ECMWF EPS.

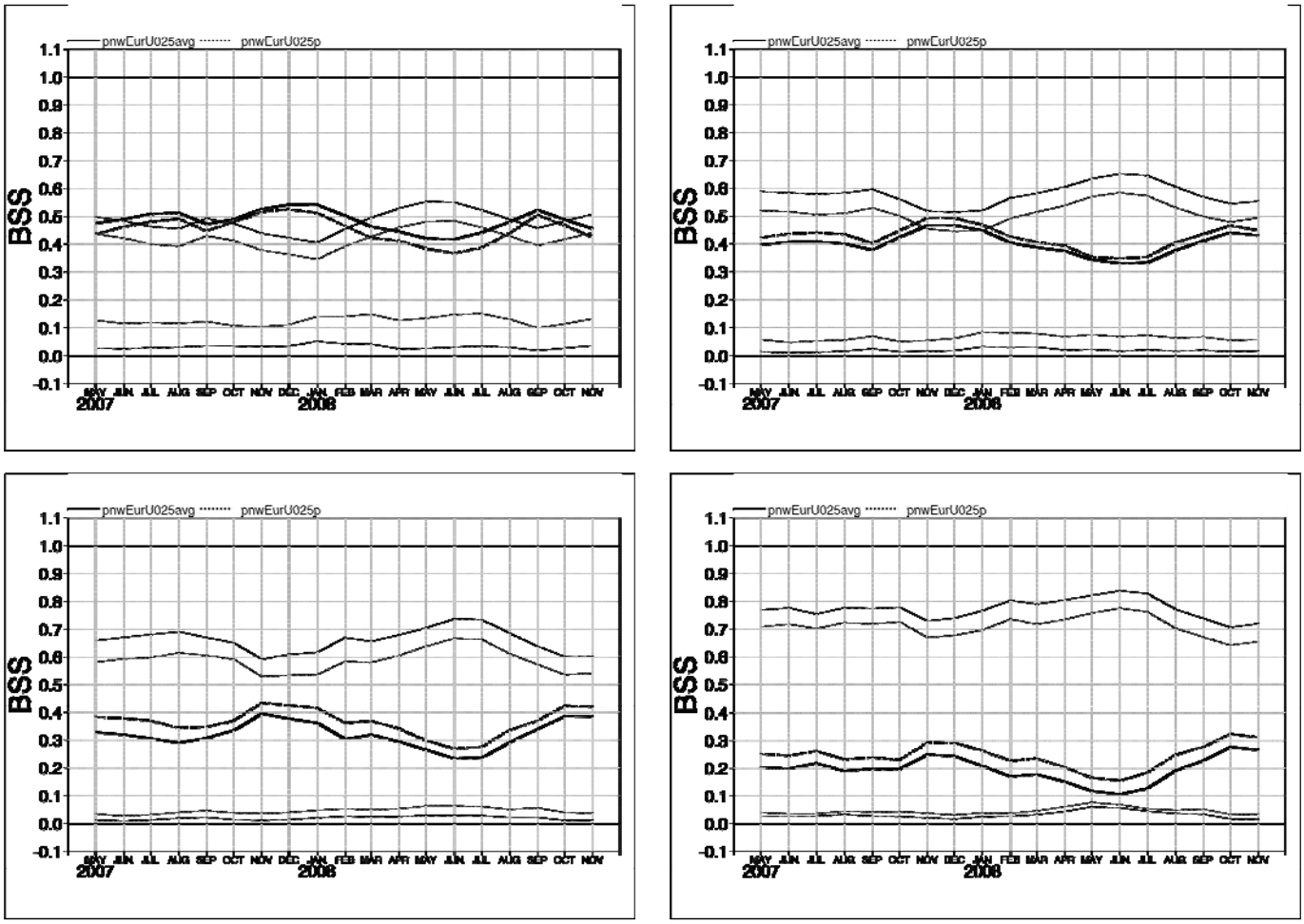

Figure 2: same as figure 1 but for SREPS

5. Conclusions

The effect of observation uncertainty in the forecast verification process has been investigated in several papers. The uncertainty has been mostly associated to the inability to ascertain the exact amplitude of observational error and as such the estimated error has been added to the observations used in the verification methodology. Another approach is to modify the scoring process to include the uncertainty and this has been done by introducing uncertainties in the contingency tables, scoring alternative scenarios to produce confidence intervals and using observational probabilities to score ensemble forecasts. The latter approach relies on an artificially produced observational probability constructed assuming that the observation noise is normally distributed. In the present paper, the uncertainty of the observations is not

due to errors in the measurements themselves but it is linked to representativeness issues due to the inability of a point observation to represent an averaged behaviour that can be fairly compared to a model field.

Precipitation forecasts for a period of about a year and a half and range up to t+54 are verified against a precipitation analysis built using the observed reports of 24 accumulated precipitation from the European high resolution network data. The precipitation analysis comprises of an areal value of the observed precipitation and information on the observed precipitation distribution for each grid point. The EPS ECMWF and the AEMET-SREPS (LAM) ensembles precipitation forecasts are scored against their own analysis

The BSS shows slight improvements when using O-OP for both ECMWF EPS and AEMET-SREPS for precipitation thresholds above 5mm/24h. This is in agreement with the findings of CT08. The improvements are due to an improvement in the BSS resolution component and a decrease in the BS uncertainty term, which are in excess of the degradation of the BSS reliability component. This degradation signals that the standard method over-estimates the reliability of the system.

The timeseries of the percent increase in BSS_res for both systems indicate a seasonal behaviour with winter being the period when the O-OP method is the most beneficial. The largest increase is for the ECMWF EPS pointing to the changes to the model convections in November 2007. Such changes have improved the ability of the EPS to produce conditional probabilities, given different forecasts that differ from the climatic average.

6. References

Bowler, N. E., 2006: Explicitly Accounting for Observation Error in Categorical Verification of Forecasts. *Mon. Wea. Rev.*, **134**, 1600-1606

Buizza, R. and Palmer, T., 1995: The singular vectors structure of the atmospheric general circulation. *J. Atmos. Sci.*, **52**, 1434-1456.

Buizza, R., Richardson, D. S., Palmer, T. N. 2003. Benefits of increased resolution in the ECMWF ensemble system and comparison with poor-man's ensembles. *Q. J. R. Meteorol. Soc.* **129**, 1269-1288.

Candille, G. and Talagrand, O., 2008. Impact of observational error on the validation of ensemble prediction systems. *Q. J. R. Meteorol. Soc.*, **134**: 959-971.

Cherubini, T., Ghelli, A., and Lalaurette, F., 2002: Verification of precipitation forecasts over the Alpine region using a high-density observing network. *Weather and Forecasting*, **17**, 238–248.

Ciach, G. J. and Witold F. Krajewski, 1999: Radar–Rain Gauge Comparisons under Observational Uncertainties. *J. Appl. Meteor.*, **38**, 1519-1525

García-Moya, J.A., Callado A., Santos C., Santos-Muñoz D. and Simarro J., 2009: Predictability of Short-range Forecasting: A Multi-Model Approach. *AEMET Technical Report* **NT SPPE-1**, pp. 30.

Ghelli, A. and Lalaurette, F., 2000: Verifying precipitation forecasts using up-scaled observations. *ECMWF Newsletter* **87**, ECMWF, Reading, United Kingdom, 9–17.

Ghelli, A., and Primo, C., 2009: On the use of the extreme dependency score to investigate the performance of a NWP model for rare events. *Meteorol. Apps.*, **16** , p 537-544

A new field verification score based on optical flow technique

Christian Keil and George C. Craig
Meteorologisches Institut der Ludwig-Maximilians-Universität München, Germany
Email: Christian.Keil@lmu.de

1. Introduction

Nowadays, high resolution numerical models forecast weather with great detail and we might find them useful because observed features are better reproduced. However, the value of these forecasts is difficult to prove using traditional grid-point based verification statistics. The classical 'double penalty problem' illustrates the limitations of the grid-point based error measures: a forecast of a precipitation feature that is correct in terms of intensity, size and timing, but incorrect concerning location, results in very poor categorical error scores (many misses and false alarms) and large root mean square errors. To address this problem spatial verification techniques are being developed that do not require the forecasts to exactly match the observations at fine scales (see e.g. Ahijevych et al. 2009 and Gilleland et al. 2009 and references therein).

2. The displacement and amplitude based error measure DAS

The error measure presented here attempts to quantify the difference between a forecast F(x,y) and an observation field O(x,y) in terms of how accurately features are predicted in position and amplitude. The problems of defining what constitutes a feature, and identifying which feature in one image is to be matched with a feature in the other image, are avoided by using an optical flow technique. This method computes a vector field that deforms, or "morphs", one image into a replica of another, simultaneously displacing all features in the image. The magnitude of these vectors provides a measure of the displacement error, while the difference between the images after morphing provides a measure of the residual amplitude error.

The optical flow method used here is based on a pyramidal matching algorithm and computes its vector field by seeking to minimize an amplitude-based quantity at successively finer scales within a fixed search environment. The image matching algorithm and its application to meteorological data are described in detail by Zinner at al. (2008) and Keil and Craig (2009, 2007), respectively, and will not be repeated in detail here. There are several parameters that must be specified in the pyramidal image matching algorithm, but only one has a decisive impact on the resulting vector field. This parameter is the radius of the search environment (maximum search distance), which defines the largest distance over which a feature in one field will be displaced to match a feature in the other field. It has been suggested that this should be based on a dynamical scale such as the radius of deformation that characterises the spatial separation between different synoptic weather conditions. It should be noted that, as with any verification measure, the results will also be influenced by properties of the fields being matched, such as an intensity threshold to remove background values.

For any feature in the observation field, we can ask how well it is forecast (if at all) in terms of amplitude and location. To do this, the image matching algorithm is

used to deform the forecast field to match the observations. Two fields are constructed: a displacement error field $DIS_{obs}(x,y)$ equal to the magnitude of the displacement vector, and an amplitude error field $AMP_{obs}(x,y)$ defined as the root mean square (RMS) difference between the observation field and the morphed forecast field. Both fields are set to zero wherever the observation field is zero, so that errors are only defined where an observed feature is present. A nonzero value of $DIS_{obs}(x,y)$ at the location of an observed feature implies that there was a forecast feature within the maximum search distance, while a zero value means either a perfect location forecast or that no feature was forecast within the maximum search distance. These two possibilities are distinguished by the amplitude error, which will be large for a missed feature.

Similarly, one can ask for each forecast feature how well it corresponds to the observations in amplitude and location. For this, displacement and amplitude error fields for the forecast space error, $DIS_{fct}(x,y)$ and $AMP_{fct}(x,y)$ can be constructed by morphing the observation field onto the forecast field. In this case a large amplitude error for a feature where the displacement error is zero indicates a false alarm, i.e. something was forecast, but nothing was observed within the maximum search distance. Note that false alarms were not treated correctly by the FQM defined in Keil and Craig (2007), which applied the image matcher only in observation space.

For many applications, it is not sufficient to have separate amplitude and displacement errors; a single measure of forecast quality is required. Before combining the two components, the displacement error field is normalised by the maximum search distance D_{max}, while the amplitude error field is normalised by a characteristic intensity I_0 chosen to be typical of the amplitude of the observed features. Analogously to the computation of the amplitude error the characteristic intensity I_0 is chosen to be the RMS amplitude of the observed field. However, the choice of I_0 depends on the application. For comparing forecast quality over large datasets the characteristic intensity I_0 could be specified by a climatological rain rate, for instance.

The normalisation is based on the principle that, for an observed feature with the characteristic amplitude, a forecast displaced by the distance D_{max} gives the same error as a miss plus a false alarm, i.e. no forecast feature is found within a distance D_{max}, but rather there are two unrelated errors in widely separated regions. The final displacement-amplitude score, DAS, is defined as the average of the two normalised components:

$$DAS = \frac{DIS}{D_{\max}} + \frac{AMP}{I_0}.$$

The DAS values are bounded from below by zero (for a perfect forecast), and will typically take values of order one, although there is no upper limit. A value of one would result from a forecast with the correct amplitude, but an average position error of D_{max}, or a forecast with the correct position with an RMS amplitude error of I_0, or a combination of both types of error.

3. DAS performance for geometric ICP cases

In the intercomparison project (ICP) of spatial verification measures there are three different sets of test cases (Ahijevych et al. 2009) on which DAS has been applied. For geometric case 5 (forecast feature much larger in size, displaced but

still overlapping the observed feature) results are presented here in detail to illustrate various properties of the DAS measure. These calculations use a maximum search distance D_{max} of 360 km, corresponding to 90 points at 4 km resolution. For the precipitation fields, an intensity threshold of 1 mm was applied, and a characteristic amplitude I_0 was determined by the RMS average of all observed precipitation values that exceeded the threshold.

A sequence of images is shown in forecast space (Fig. 1) and observation space (Fig. 2). In forecast space, the overestimated size of the forecast feature (Fig. 1a) results in a strongly divergent displacement vector field, so that the morphed observation field matches the left part of the huge ellipse seen in the forecast (Fig. 1c). The ability of the image matching algorithm to stretch the observed field is limited by the specified maximum search distance and thus only part of the forecast feature is regarded as displaced, while the rest is regarded as a forecast "false alarm". This is clearly seen in the components $DIS_{fct}(x,y)$ and $AMP_{fct}(x,y)$ (Fig. 1d,e).

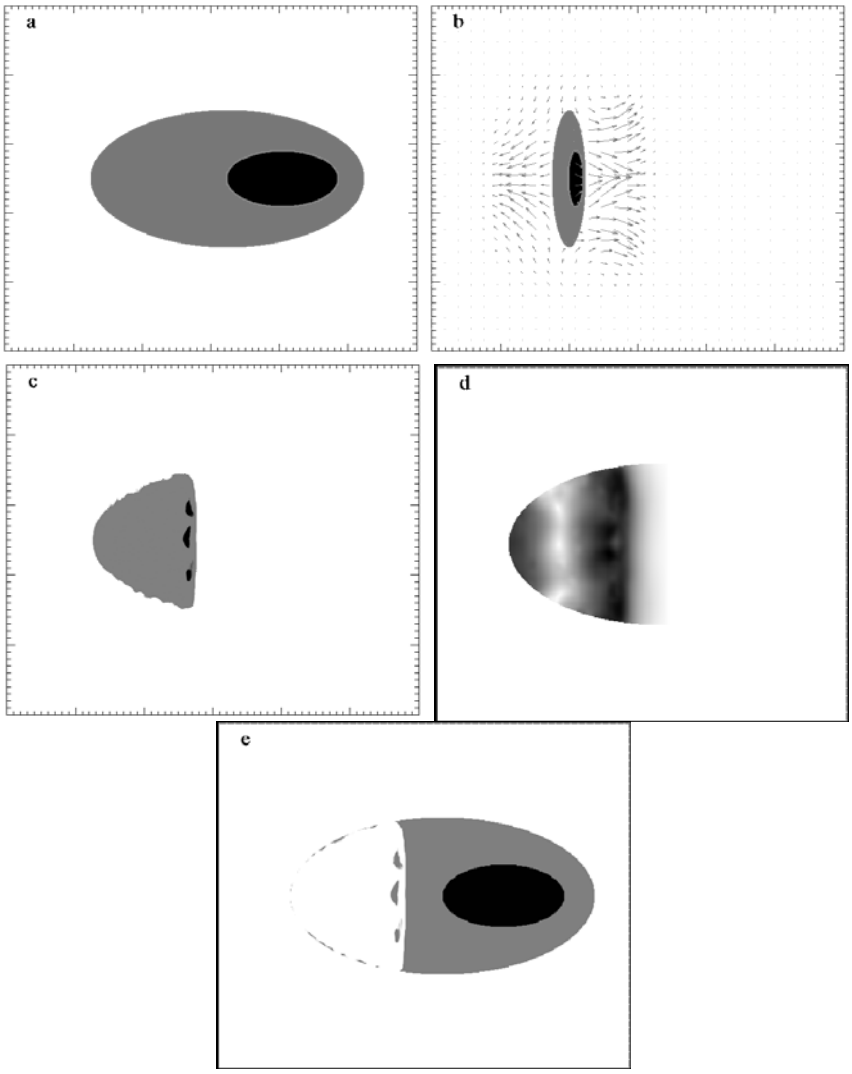

Figure 1: Sequence of different stages in the computation of DAS for geometric case 5 (forecast shifted 125 points to the right and huge) in forecast space: (a) forecast, (b) observation superimposed with displacement vector field, (c) morphed observation, (d) visual illustration of the $DIS_{fct}(x,y)$ field, and (e) the $AMP_{fct}(x,y)$ field.

In contrast, in observation space a convergent vector field is generated (Fig. 2b), morphing the left side of the forecast feature to match the observations, and shrinking the remaining part (Fig. 2c). Again due the limitation of the maximum search distance, the excess area of the forecast feature is not completely removed, but this does not contribute to the error amplitude of the observed feature $AMP_{obs}(x,y,)$ but represents a false alarm and is accounted for in forecast space (Fig. 1e). The amplitude error (Fig. 2e) in observation space is mainly due to the region of high intensities, which was too far away in the forecast to match to the observations.

The DAS values listed in Table 1 provide an objective ranking of forecast quality. Also listed are the normalised displacement and amplitude components DIS/D_{max} and AMP/I_0, to show the contribution of each component to the final DAS. In geometric case 1 the forecast feature is displaced by 50 points to the right that is corresponding to 55% of the maximum search distance. This is accurately captured by the DIS component. The small residual AMP error is caused by interpolation errors during morphing. In contrast, the large forecast feature displacement of 200 points in geometric case 2 is beyond the maximum search distance, thus no matching is possible and DIS = 0, while AMP equals 1 as expected for a false alarm

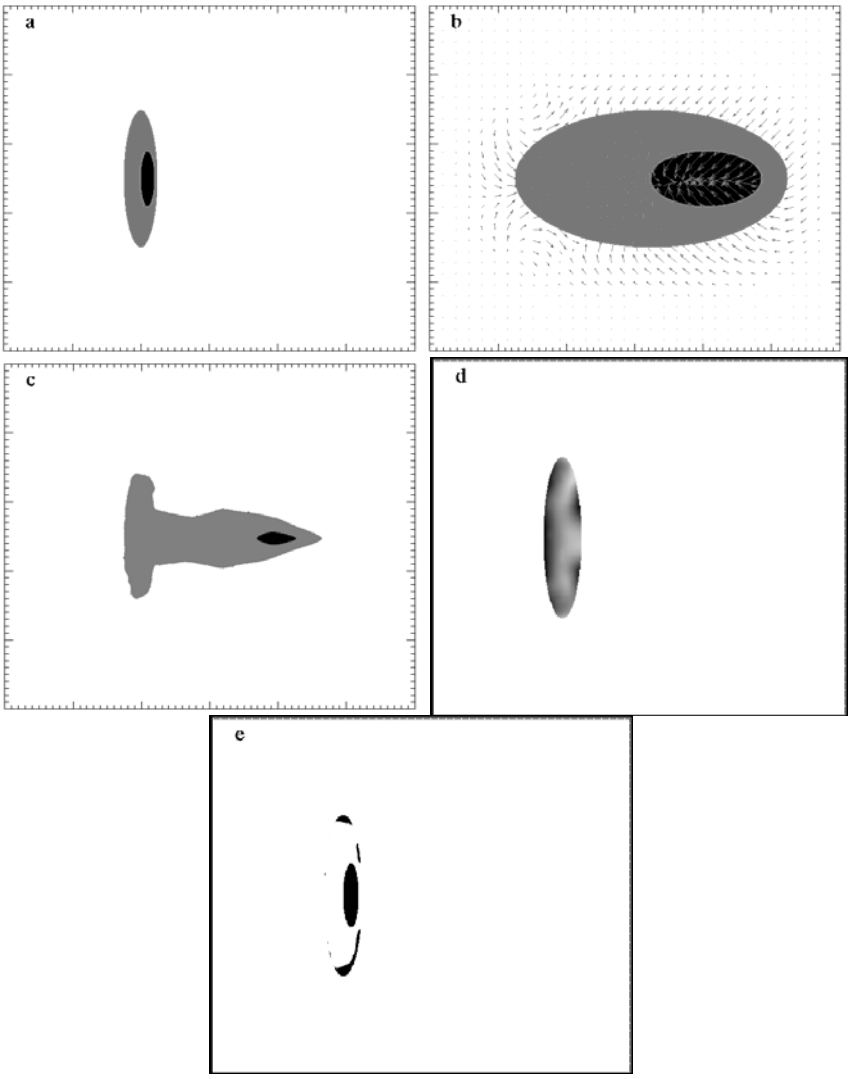

Figure 2: Same as Fig.1, but in observation space.

Case	Description of forecast feature	DAS	DIS/D_{max}	AMP/I_0	Rank
1	50 points displacement	0.62	0.55	0.07	1
2	200 points displacement	1.00	0.00	1.00	2
3	125 pts. displacement and biased high	1.11	0.21	0.91	5
4	125 pts. displacement and wrong aspect ratio	1.09	0.22	0.87	4
5	125 pts. displ. and biased very high, but overlapping	1.02	0.19	0.83	3

Table 1: Summary of geometric cases 1 to 5 depicting a brief description, the DAS, normalised DIS and AMP values (i.e. DIS/D_{max}, and AMP/I_0 with D_{max}=360km and I_0=15.4mm) and the corresponding rank.

plus a miss. For the other geometric cases, that are mixtures of displacement, bias and aspect ratio errors, both DIS and AMP make significant contributions, although in all cases the amplitude term AMP is larger, indicating large false alarms. The ranking of the geometric cases using DAS gives reasonable results agreeing with human expectation. Geometric case 1 scores best since the pure displacement within the maximum search distance is captured by the morphing process. Case 2 has the second best score, with the large displacement of the identical feature detected by the algorithm by a pure AMP error. The forecast of case 5 hugely overestimates the observation, but since there is an overlap it receives some credit and ranks third. Next in rank is case 4 with the wrong aspect ratio. Geometric case 3 scores worst. Note that traditional scores based on contingency tables indicate no skill (for cases 1 to 4) and rank case 5 as best because of the overlap (Ahijevych et al. 2009). This illustrates the potential for some of the traditional metrics to be misleading.

4. Discussion

Progress in weather forecast models has lead to substantially improved and more realistic-appearing forecast fields. However, traditional verification measures often indicate poor performance because of the increased small scale variability. As a result, the true value of high resolution forecasts is not always characterized well. To address this problem spatial verification techniques are being developed that do not require the forecasts to exactly match the observations at fine scales. One promising class of spatial verification methods makes use of optical flow techniques to quantify spatial differences between forecast and observation fields. The new displacement and amplitude score DAS, proposed in this paper, relies on a computationally efficient pyramidal image matching algorithm (~ 10 sec/image pair on a PC). To account for false alarms and misses the algorithm is applied first in observation space, morphing the forecast on to the observation, and then in forecast space, morphing the observation onto the forecast. Contributions from observation and forecast space are averaged to give scalar amplitude and displacement scores. For applications that require a single measure of forecast quality, the separate amplitude and displacement errors are combined. To do this, the displacement error field is normalised by the maximum search distance, while the amplitude error field is normalised by a characteristic intensity chosen to be typical of the amplitude of the observed features, and the two normalised errors are summed.

In the framework of ICP DAS has been applied on all common cases, including the geometric, the perturbed, and the nine cases of the SPC spring program 2005. The displacement error term accurately measured the distance between observed and forecast features. In the synthetic experiments with pure displacement errors, the amplitude error term was contaminated by a small residual error, probably a result of interpolation errors in the matching algorithm, however there was no evidence of such an error in cases where the displacement was combined with an actual amplitude difference. There is however an inherent ambiguity between displacement and amplitude errors in complex fields, where a forecast object might be regarded as a bad amplitude forecast of a nearby object, or as a better amplitude forecast of a more distant feature. Matching forecast and observations through optical flow avoids part of this ambiguity since there is no need to define criteria to identify individual objects in the two fields, and is found to provide consistent identification of displacement and amplitude errors in idealised cases where there is no ambiguity.

In the context of the ICP a wide array of possible forecast errors has been addressed. However, closeness in time has not explicitly been considered. Since the errors in high resolution forecasts are often related to, e.g., mis-timing of frontal passage or the onset of convection, it would be highly desirable to extend the application of DAS to multiple times. The application of DAS to rank and select individual realistic ensemble members to generate probabilistic forecasting products will be explored in future work.

Acknowledgments. CK acknowledges funding from the German Research Foundation (DFG) priority program on Quantitative Precipitation Forecasts (SPP1167). This work has been performed during the COST731 Action of the European Science Foundation.

References

Ahijevych D., E. Gilleland, B. Brown, and E. Ebert, 2009: Application of spatial forecast verification methods to idealized and NWP-gridded precipitation forecasts. *Wea. Forecasting*, **24**, 1485-1497.

Gilleland E., D. Ahijevych, B.G. Brown, B. Casati, and E.E. Ebert, 2009: Intercomparison of spatial forecast verification methods. *Wea. Forecasting*, **24**, 1416-1430.

Keil, C. and G. C. Craig, 2009: A displacement and amplitude score employing an optical flow technique. *Wea. Forecasting*, **24**, 1297–1308.

Keil, C. and G. C. Craig, 2007: A displacement-based error measure applied in a regional ensemble forecasting system. *Mon. Wea. Rev.*, **135**, 3248–3259.

Zinner, T., H. Mannstein, and A. Tafferner, 2008: Cb-TRAM: Tracking and monitoring severe convection from onset over rapid development to mature phase using multi-channel Meteosat-8 SEVIRI data. *Meteorol. Atmos. Phys.*, **101**, p. 191-210, DOI 10.1007/s00703-008-0290-y.

Quantitative Precipitation Forecast (QPF) Verification Comparison Between the Global Forecast System (GFS) and North American Mesoscale (NAM) Operational Models.

Authors: **Jamie WOLFF**, Barbara BROWN, John HALLEY GOTWAY, Michelle HARROLD, Zach TRABOLD, Louisa NANCE and Paul OLDENBURG

National Center for Atmospheric Research/Research Applications Laboratory (NCAR/RAL) and Developmental Testbed Center (DTC), Boulder, CO USA
jwolff@ucar.edu

1. Introduction

Numerical weather prediction models continue to move toward higher resolution, which, in turn, provides both a finer level of detail and a more realistic structure in the resulting forecast. It is widely acknowledged, however, that using traditional verification metrics for evaluation may unfairly penalize these high-resolution forecasts (e.g., Davis et al. 2006; Roberts and Lean 2008). Traditional verification requires near-perfect spatial and temporal placement for a forecast to be considered good; this approach favors smoother forecast fields of coarser resolution models and offers no meaningful insight regarding why a forecast is considered good or bad. In contrast, more advanced spatial verification techniques, such as object-based methods, can provide information on differences between forecast and observed objects in terms of displacement, orientation, intensity and coverage areas; neighborhood methods can provide information on the spatial scale at which a forecast becomes skillful.

The Developmental Testbed Center (DTC) performed an extensive evaluation of the Global Forecast System (GFS) and the North American Mesoscale (NAM) operational models to quantify the differences in the performance of Quantitative Precipitation Forecasts (QPF) produced by two modeling systems that vary significantly in horizontal resolution. Traditional verification metrics computed for this test included frequency bias and Gilbert Skill Score (GSS). Two advanced spatial techniques were also examined - the Method for Object-based Diagnostic Evaluation (MODE) and the Fraction Skill Score (FSS) - in an attempt to better associate precipitation forecast differences with different model horizontal scales.

2. Data

2.1 Model Data

QPF output at 3h intervals from the GFS and NAM models initialized at 00 UTC daily were retrieved from the U.S. National Centers for Environmental Prediction (NCEP) for 18 December 2008 through 15 December 2009. The NAM native output employs an E-grid domain with approximately 12-km grid spacing, while the GFS native output is a global Gaussian grid with 0.5 x 0.5 degree resolution. The ***copygb*** program, developed by NCEP, was used to regrid the native model output to a 15-km and a 60-km contiguous U.S. (CONUS) grid on a Lambert-Conformal map projection. The budget interpolation option in ***copygb*** was utilized (described in Accadia et al. 2003). This approach attempts to conserve the total area-average precipitation amounts.

2.2 Precipitation Analyses

For this evaluation, precipitation accumulation periods of 3 h and 24 h were assessed. The observational datasets included the 4-km NCEP Stage II analysis (Lin and Mitchell 2005) for the 3-h accumulations and the 1/8-degree NCEP Climate Prediction Center daily gauge analysis (Higgins et al. 2000) for the 24-h accumulations (valid at 12 UTC). Both observational datasets were also interpolated, using the budget

option, to the same 15-km and 60-km domains as the model output, prior to the comparison with the forecasts.

3. Verification Method

Objective model verification statistics were generated using version 3.0 of the Model Evaluation Tools (MET) software package, which offers a wide variety of state-of-the-art verification methods (Fowler et al. 2010). Grid-to-grid comparisons were performed to verify QPF using traditional metrics (Wilks 1995), including frequency bias, which measures the ratio of the frequency of forecast events to the frequency of observed events and indicates whether the forecast system has a tendency to under-forecast (<1) or over-forecast (>1) events, and GSS, which measures the fraction of observed and/or forecast events that were correctly predicted and is adjusted for hits associated with random chance; where zero indicates no skill and one is a perfect score. In addition, an object-based verification approach, MODE, and a neighborhood verification method, FSS, were applied. The process of identifying and verifying objects with MODE is fully described in Davis et al. (2006). Briefly, this approach consists of the following steps: (i) resolve objects within the raw forecast and observation fields, (ii) determine if objects within each field should be *merged*, (iii) determine which objects should be *matched* between the forecast and observation fields and determine if additional *merging* in either field should occur, (iv) calculate various quantities of interest (attributes) to assess forecast quality. For FSS, the purpose of the method is to obtain a measure of how forecast skill varies with spatial scale (Roberts and Lean 2008), and includes the steps: (i) convert all forecast and observed fields into binary fields, for each threshold of interest (ii) generate fractions within a square of length *n* that have exceeded the threshold, (iii) compute the mean squared error relative to a low-skill reference forecast (i.e., FSS).

For the NAM model output, precipitation forecasts were interpolated to both the 15-km (NAM15) and 60-km (NAM60) domains, while the GFS model output was interpolated to the 60-km (GFS60) domain only. Verification results were computed for select spatial (CONUS, CONUS-East) and temporal (all cases, seasonal) aggregations; however, only the CONUS domain over the entire set of cases will be discussed here. For the 3-h QPF, all verification scores were evaluated every 12 h out to 84 h. The 24-h QPF verification scores were evaluated at the 36-, 60- and 84-h lead times. A subset of these results will be discussed in Section 4.

Verification statistics generated by MET for each retrospective case were loaded into a MySQL database, from which data was then retrieved to compute and plot requested aggregated statistics using routines developed by the DTC in the statistical programming language, R. The traditional verification metrics are accompanied by confidence intervals (CIs), at the 99% level, computed using a bootstrapping technique. When comparing all three models, a conservative estimation of statistically significant (SS) differences was employed based solely on whether the aggregate statistics with the accompanying CIs overlapped between the models. If no overlap was noted for a particular threshold, the differences between the models were considered SS.

4. Results

4.1 Traditional Verification Metrics

4.1.1 Gilbert Skill Score

For the 3-h QPF, all three models show an exponential decrease in GSS values with increasing threshold, regardless of forecast lead time (Fig. 1a). Also, as expected, the base rate decreases with increasing threshold, with very few observations associated with the highest accumulation values. When examining lead times valid at 00 UTC (i.e., 24-h, 48-h, 72-h), the NAM15 has a SS lower GSS compared to the

GFS60 and NAM60 at the lowest threshold of 0.1″; at the 0.2″ threshold, the GSS for the NAM15 is only significantly smaller than the value for the GFS60. For all other thresholds valid at 00 UTC, and for all other lead times and thresholds valid at 12 UTC (not shown), there is no SS difference, in general, between the models interpolated to the 15-km and 60-km domains. The latter result also holds for the 24-h QPF (Fig. 1b).

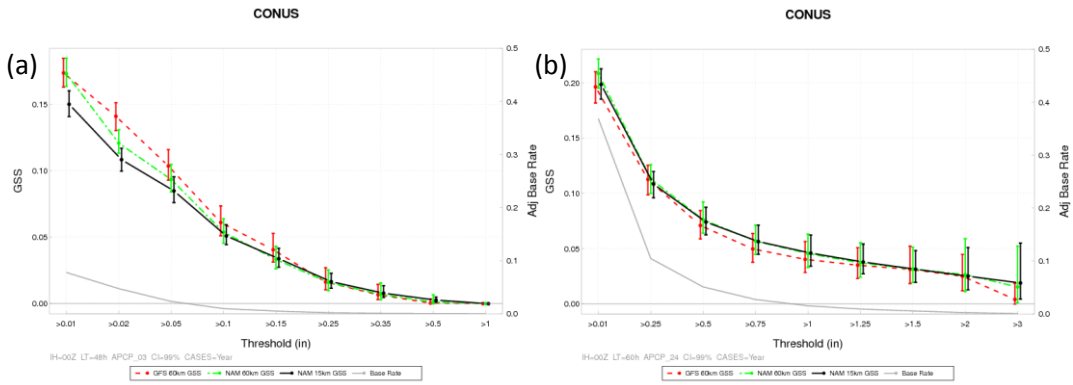

Figure 1. Threshold series plots of (a) 48-h lead time for 3-h QPF (in) and (b) 60-h lead time for 24-h QPF (in) for median GSS for all model initializations. The GFS60 is shown in red (dashed), NAM60 in green (dot-dashed) and NAM15 in black (solid). The vertical bars represent the 99% CIs. Associated with the second y-axis, the light grey line is the adjusted base rate, or the ratio of observed grid box events to the total number of grid boxes in the domain, by threshold.

4.1.2 Frequency Bias

A consistent SS high bias (bias SS larger than one) for the 3-h QPF is seen for all of the models at all lead times (Fig. 2a). As with GSS, the thresholds at which there is a SS difference between the models depends on valid time. For forecasts valid at 00 UTC (e.g., Fig. 2a), the NAM15 has a SS smaller over-prediction (i.e., high bias) for all thresholds above 0.25″ compared to the two models at 60-km. However, for forecasts valid at 12 UTC, this result is only seen for the 1″ threshold (not shown). For the 24-h QPF (Fig. 2b), the CIs associated with the NAM model, interpolated to both the 15-km and 60-km domain, encompass the value of one for all thresholds, indicating the estimated bias is not statistically different from the value for an unbiased forecast. However, the results for the GFS60 reveal a SS high bias for thresholds at and below 0.25″, while CIs for all other thresholds encompass a bias value of one. The widths of the CIs increase with increasing threshold for all models; however, the degree of inflation is considerably smaller for the NAM15 compared to the two models at 60-km for 3-h QPF.

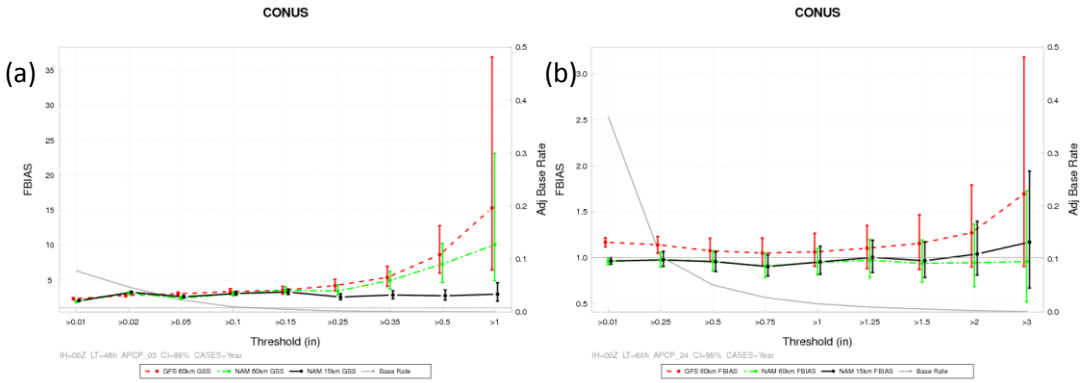

Figure 2. Threshold series plots of (a) 48-h lead time for 3-h QPF (in) and (b) 60-h lead time for 24-h QPF (in) for median frequency bias for all model initializations. The GFS60 is shown in red (dashed), NAM60 in green (dot-dashed) and NAM15 in black (solid). The vertical bars

represent the 99% CIs. Associated with the second y-axis, the light grey line is the adjusted base rate, or the ratio of observed grid box events to the total number of grid boxes in the domain, by threshold.

4.2 Spatial Verification Techniques

4.2.1 Method for Object-based Diagnostic Evaluation (MODE)

For this test, a convolving disk of 2 gridpoints for the 60-km domain and 8 gridpoints for the 15-km domain was used. A threshold of 0.01″ for the 3-h and 0.2″ for the 24-h precipitation accumulation fields was then applied to define discrete rain objects of the approximate size of interest for this study. A second, lower threshold was then applied to each individual field and merging of objects in the same field was allowed if the original objects defined became one object after the lower threshold was applied. Objects were matched between the forecast field and observed field if the total interest value between a forecast observation object pair (a weighted sum of interest values for centroid distance, boundary distance, angle difference, area ratio and intersection area ratio) was greater than 0.7. Additional merging was allowed if two or more objects in one field matched the same object in the other field. Many unique attributes can be examined when looking at MODE output; however, only a few will be shown here.

Box plots of the distributions of object size by lead time for the GFS and the observations at 60-km and the NAM and observations at 15-km are shown in Fig.3. The distribution of object sizes from the NAM15 more closely matches the distribution from the 15-km observation field than is the case for the GFS60 compared to the 60-km observation objects. In particular, the latter comparison indicates a large bias in the sizes of the 60-km GFS objects. Fig. 4 shows the results of the median of maximum interest (MMI) for the GFS60 and the NAM15 models. MMI is the median value of the maximum total interest values associated with each forecast and observed object, with larger values indicating a better match between all forecast and observed objects. In general, there is very little difference between the two models for this measure.

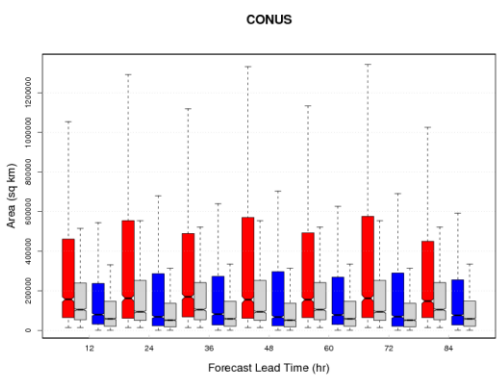

Figure 3. Box plots by lead time of the size distribution for objects defined within the GFS60 field (red), 60-km observation field (gray), NAM15 field (blue) and 15-km observation field (gray). The top and bottom of the box correspond to the 25th and 75th percentile, respectively; the black line at the "waist" is the median value.

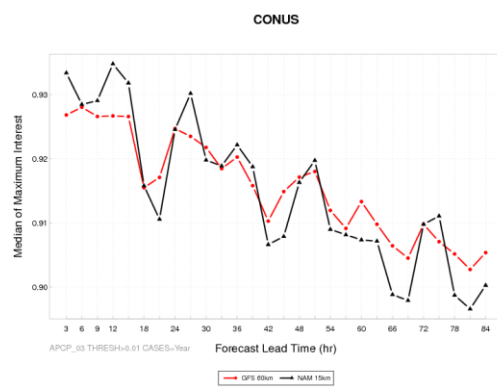

Figure 4. Time series plot of MMI for 3-h QPF values greater than 0.01" for all model initializations. The GFS60 is shown in red (circles) and the NAM 15-km in black (triangles).

4.2.2 Fractional Skill Score (FSS)

For this evaluation, neighborhood sizes (in terms of grid squares) of *n*=3, 5, 7, 9, 11, 13 were computed for each model. For the NAM15, additional neighborhood sizes of *n*=19, 21, 27, 29, 35, 37, 43, 45, 51, 53, 59, 61 were also examined to represent the similar horizontal scales as those used for the 60-km neighborhood sizes. Because the neighborhood size is required to be an odd integer and the resolution

difference between the two models is a factor of four, an exact match between the neighborhood sizes for the GFS60 and NAM15 was not possible. As expected, FSS increases with neighborhood size and decreases with lead time (Fig. 5). A diurnal cycle is also evident with the largest FSS values seen during the evening and overnight hours (00-12 UTC) and the smallest values during the daytime (15-21 UTC). For the 0.1″ threshold, the FSS for the NAM15 (e.g., 405-km neighborhood) is consistently larger than the corresponding value for the GFS60 (e.g., 420-km neighborhood). When examining multiple precipitation accumulation thresholds for a single lead time, it is clear that there is an increase in FSS with decreasing threshold (Fig. 6); however, the result holds that the NAM15 FSS is always higher than the GFS60 at similar neighborhood sizes.

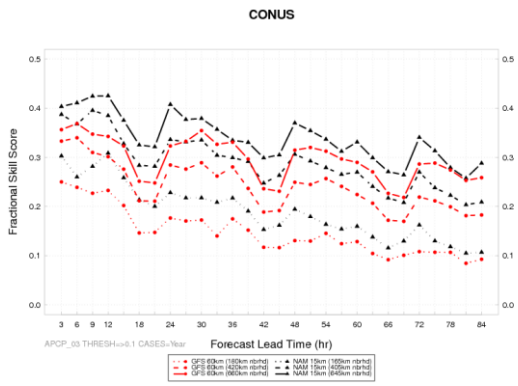

Figure 5. Time series plot of FSS using a threshold of 0.1″ for all model initializations. The GFS60 is shown in red (circles) for n=3 (dotted), 5 (dashed) and 7 (solid) and the NAM 15-km in black (triangles) for n=11 (dotted), 19 (dashed) and 27 (solid).

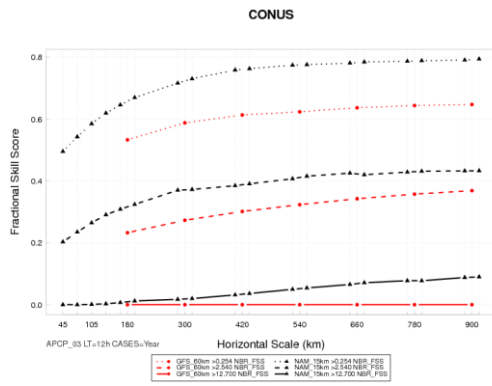

Figure 6. Neighborhood series plot of FSS for the 12-h lead time and all model initializations. The GFS60 is shown in red (circles) and the NAM 15-km in black (triangles) for thresholds of 0.01″ (dotted), 0.1″ (dashed) and 0.5″ (solid).

5. Summary

Results comparing two NWP models which vary significantly in horizontal resolution were described. Using traditional verification metrics, there is no notable, consistent forecast improvement with the higher resolution NAM model even though, subjectively, the finer detail more closely matches the observations in many cases. However, when looking at MODE and FSS, additional attributes can be examined that provide further information about the skill of the forecast. The objects created by MODE reveal additional information on the area and correspondence of objects, between the forecasts and observations. A clear high bias is noted for the GFS object areas, while the MMI values for these comparisons do not appear to be significantly different. The FSS evaluation clearly shows that the higher-resolution NAM has comparable skill to the GFS at considerably smaller neighborhood sizes and larger FSS values at comparable neighborhood sizes.

In order to perform a more direct comparison of the two models against similar observation objects defined in MODE, future work with this dataset will include upscaling both the NAM and GFS model output to the Stage II 4-km CONUS domain prior to examining the full suite of MODE attributes. The traditional metrics, along with the FSS will also be reexamined with the new, higher-resolution domain.

Acknowledgements

The authors would like to thank Ying Lin at NCEP/EMC for her assistance in acquiring the model and observation data used for this evaluation. This work was funded by the National Oceanic and Atmospheric Administration. NCAR is sponsored by the National Science Foundation.

References

Accadia, C., S. Mariani, M. Casaioli, and A. Lavagnini, 2003: Sensitivity of Precipitation Forecast Skill Scores to Bilinear Interpolation and a Simple Nearest-Neighbor Average Method on High-Resolution Verification Grids. *Wea. and Forecasting*, **18**, 918-932

Davis, C., B. Brown, R. Bullock, 2006: Object-Based Verification of Precipitation Forecasts. Part I: Methodology and Application to Mesoscale Rain Areas. *Mon. Wea. Rev.*, **134**, 1772-1784.

Fowler, T. L., T. Jensen, E. I. Tollerud, J. Halley Gotway, P. Oldenburg, R. Bullock, 2010: New Model Evaluation Tools (MET) Software Capabilities for QPF Verification. *Preprints*, 3rd Intl. Conf. on QPE, QPF and Hydrology, Nanjing, China, 18-22 October 2010.

Higgins, R. W., W. Shi, E. Yarosh, and R. Joyce, 2000: Improved United States precipitation quality control system and analysis. *NCEP/Climate Prediction Center Atlas 7,* National Weather Service, NOAA, U.S. Department of Commerce, 40 pp.

Lin, Y. and K. E. Mitchell, 2005: The NCEP Stage II/IV hourly precipitation analyses: development and applications. *Preprints*, 19th Conf. on Hydrology, American Meteorological Society, San Diego, CA, 9-13 January 2005.

Roberts, N. M., H. W. Lean, 2008: Scale-Selective Verification of Rainfall Accumulations from High-Resolution Forecasts of Convective Events. *Mon. Wea. Rev.*, **136**, 78-97.

Wilks, D. S., 1995: *Statistical Methods in the Atmospheric Sciences.* Academic Press, 467 pp.

Scale-related Issues involving verification of QPF: Results from a DTC assessment of WRF ensemble forecasts during the HMT-West winter exercise

Edward I. Tollerud[1], Tara Jensen[2], John Halley Gotway[2], Paul Oldenburg[2], **Huiling Yuan**[3], and Isidora Jankov[4]

[1]*NOAA Earth System Research Laboratory (ESRL), Global Systems Division, Boulder, Colorado*
[2]*Research Application Laboratory, National Center for Atmospheric Research, Boulder, Colorado*
[3] *School of Atmospheric Sciences Nanjing University, Nanjing, P.R.China*
[4]*Cooperative Institute for Research in the Atmosphere, Colorado State University, Fort Collins, Colorado USA, and Earth System Research Laboratory (ESRL), Global Systems Division, Boulder, Colorado*
Huiling.yuan@colorado.edu

1. Introduction

Since 2005-6, the United States National Oceanic and Atmospheric Administration (NOAA) has supported a winter exercise in California that seeks in part to improve quantitative precipitation forecasts (QPF) during severe winter storms. The United States National Weather Service, the California Division of Water Resources, and the Hydrometeorological Testbed (HMT) have each played important roles in this project. Part of the effort during the most recent winter (2009-2010) has been the production and assessment of high-resolution WRF forecasts that employ ARW/WRF and NMM/WRF cores with different physics packages and initial conditions to form a 9-member ensemble. To critically and quantitatively assess the performance of this ensemble, a real-time on-line verification system has been assembled and used for both real-time monitoring and retrospective diagnostic study. This effort has been funded by the United States Weather Research Program (USWRP) and has been primarily undertaken by the Developmental Testbed Center (DTC), a joint venture of NOAA and NCAR. We present here some initial verification results that serve to illustrate important features of the ensemble QPF, including strong apparent diurnal cycling related to actual heavy rainfall events. In particular, we describe some effects of scale on verification by comparing ensemble mean and individual member verification for the 9-km resolution WRF Forecasts with parallel forecasts produced by the Global Forecast System (GFS) deterministic run with an effective resolution of ~40 km. We also briefly illustrate the strong and complicating impact of verification dataset choices on interpretation of verification results.

2. The 2009-2010 HMT winter exercise

Domains were selected for the winter exercise that included a large domain covering most of California and Nevada and extending several hundred km westward into the Pacific Ocean (Fig. 1). Nine ensemble member forecasts were produced in the large domain using both ARW and NNM cores

of the WRF model initiated with several randomly-selected GFS ensemble members for boundary conditions. Forecasts were output every three hours up to 5 day lead times. The spatial resolution of this domain was approximately 9 km. An ensemble mean was produced from these members, and a coarser-resolution GFS forecast was included in the verification for base-lining. In addition, forecasts within a smaller nested domain were produced, and another domain with high temporal resolution (1 hr) was produced for shorter duration forecasts. Verification results presented here are for the full domain.

The results described in this paper are primarily representative of stormy periods during January 2010. During the week of 17-21, in particular, several storms moved on to the northern and central California coast resulting in heavy precipitation in most of the coastal mountains and the Sierra Nevada Mountains.

3. Equitable threat scores: Scale-related impacts and diurnal cycling

Fig. 2 displays equitable threat scores (ETS) for individual ensemble members, thae ensemble mean, and GFS forecasts, all initiated at 1200 UTC 17 January 2010 and run out to 114 h. The most remarkable feature on the figure is the clear diurnal pattern to the ETS scores. As the 6h fractional coverage values (shaded bars) suggest, the best scores closely reflect (but slightly lead) the maximain area precipitation frequency. The likely explanation for this correlation is that forecast verification scores like the ETS are relatively more easily attained under conditions of substantial areal coverage of precipitation, especially for lower thresholds. It is of interest to investigate the nature of this somewhat unexpected diurnal sequence, which persists for several days during the period. Fig. 3 reveals that along the coast north of San Francisco, there is also a very strong diurnal cycle to the mid- and low-level winds, with strongest westerlies (and presumably strongest upslope flow) centered around 0000 UTC and very strong southerlies at 1200 UTC. This pattern is also evident at many other sites in California, particularly in the western half of the state and along the coast. Further analyses are necessary to determine if it is simply the result of chance waves moving on shore or if a true diurnally-driven circulation is in evidence. The conclusion to that question has strong implications for the development of relevant verification strategies.

Concerning resolution-based verification differences, the results shown on Fig. 2 indicate a generally good performance of the ensemble mean compared with individual members during the full 4+ day period of the forecasts. Similarly good performance is also indicated by scores for the coarser-resolution GFS. However, it is possible that the GFS scores are simply an effect of coarser spatial resolution; some scores (including the ETS) are scale-sensitive in the sense that coarser resolution can result in better values. Conversely, several other scores (not shown; false alarm rates, for instance, and areal frequency bias) show superior performance for the WRF ensemble mean. As Fig. 4 clearly illustrates, there is also a clear deterioration

of scores for the GFS at heavier rainfall thresholds even for scores that show relatively good GFS forecasts at smaller thresholds.

4. Gages vs. Stage IV analyses: observational impacts

What impacts can the choice of verification datasets have in a real-life setting? One indication is given by Fig. 3, which demonstrates significant PODY differences that originate solely from the choice of 24h gages vs. that of 6h analysis from the Stage IV product as verification data. Two factors may be relevant to this difference: rainfall during 6h accumulation periods cannot reach given thresholds as easily, reducing sampling and negatively affecting ETS scores; and gages are predominantly located in California as opposed to Nevada whereas Stage IV analyses extend across the full domain (excluding Pacific Ocean grid points of course), resulting in verification in poorly-observed geographic regions.

5. Conclusions and Further Research

The extensive verification results obtained during the winter experiment in California represent a rich source for studies like those briefly introduced here. In addition to dataset options, the real-time and retrospective scores also offer opportunities for comparing verification within different regions and over various meteorological scenarios, and for directly examining scale-related scoring impacts.

Acknowledgments

We thank Paul Neiman, Seth Gutman, Allan White, Jian-Wen Bao, and Dan Gottas for supplying some of the graphics presented in this paper. The USWRP provided funding for the website development and other research shown here.

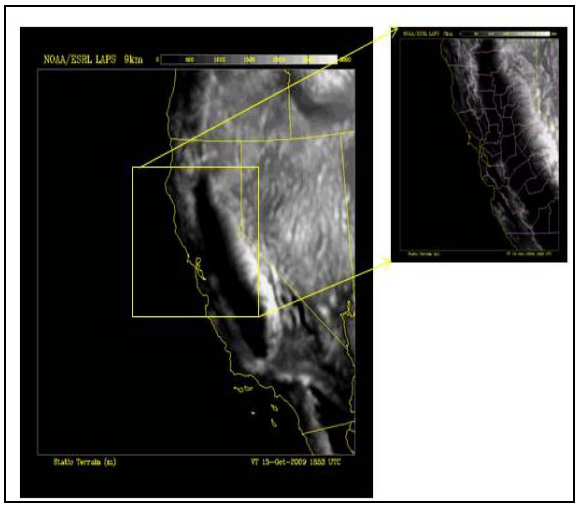

Fig. 1. Full (9 km resolution) domain and nested (3km resolution) domain during the 2009-2010 HMT West winter exercise.

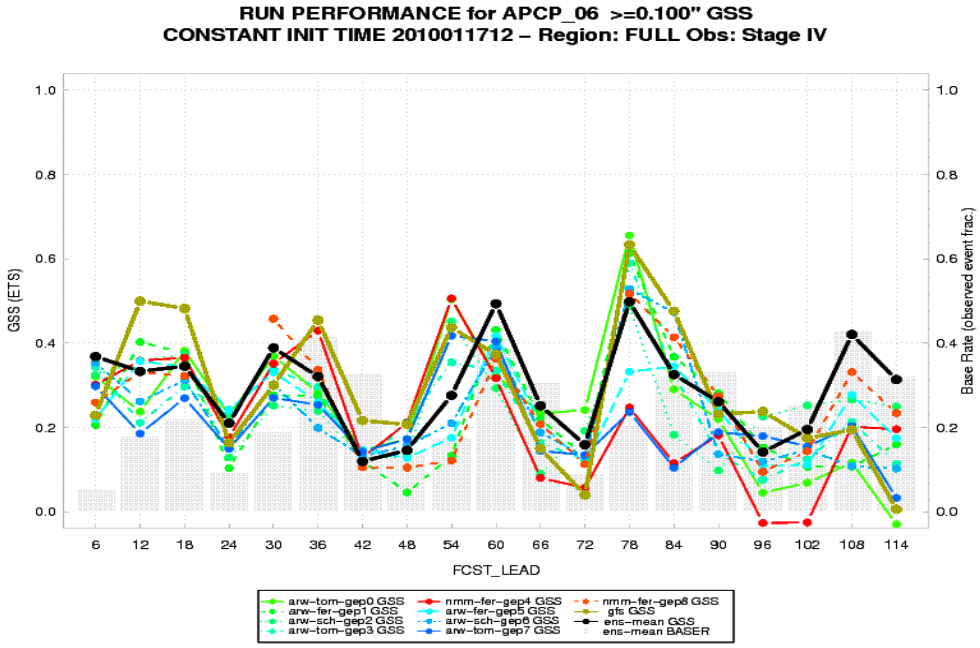

Fig. 2. Equitable Threat Scores (ETS) for ensemble model runs initiated at 1200 UTC 17 January in the HMT-West domain. Individual ensemble ARW and NNM core members are as shown in legend; black curve is for the ensemble mean; and brown curve is for the deterministic GFS forecast. Lead times are in hours. Verification was performed using Stage IV 6h analyzed precipitation. Shaded bars indicate areal frequency of observed precipitation for each 6h period.

Fig. 3. Time series of precipitation, winds, and other quantities as shown for the period 0000 UTC 19 January to 1200 UTC 20 January 2010. Stations BBY and CZC are located on the Pacific coastline and close by in the coastal mountain range, respectively, about 50 km N. of San Francisco. Plots are generated by the Physical Sciences and the Global Systems Divisions of the Earth System Research Laboratory and displayed at http://www.esrl.noaa.gov/psd/data/obs/ .

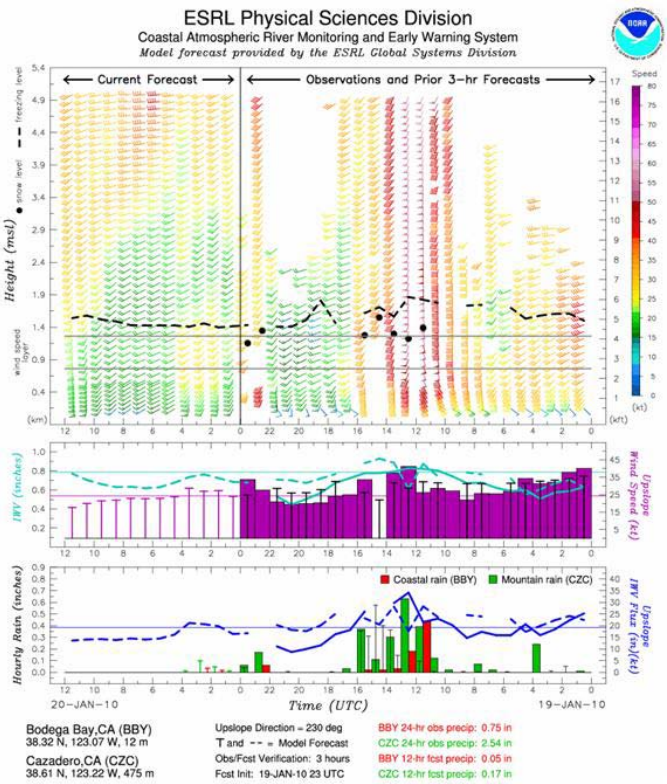

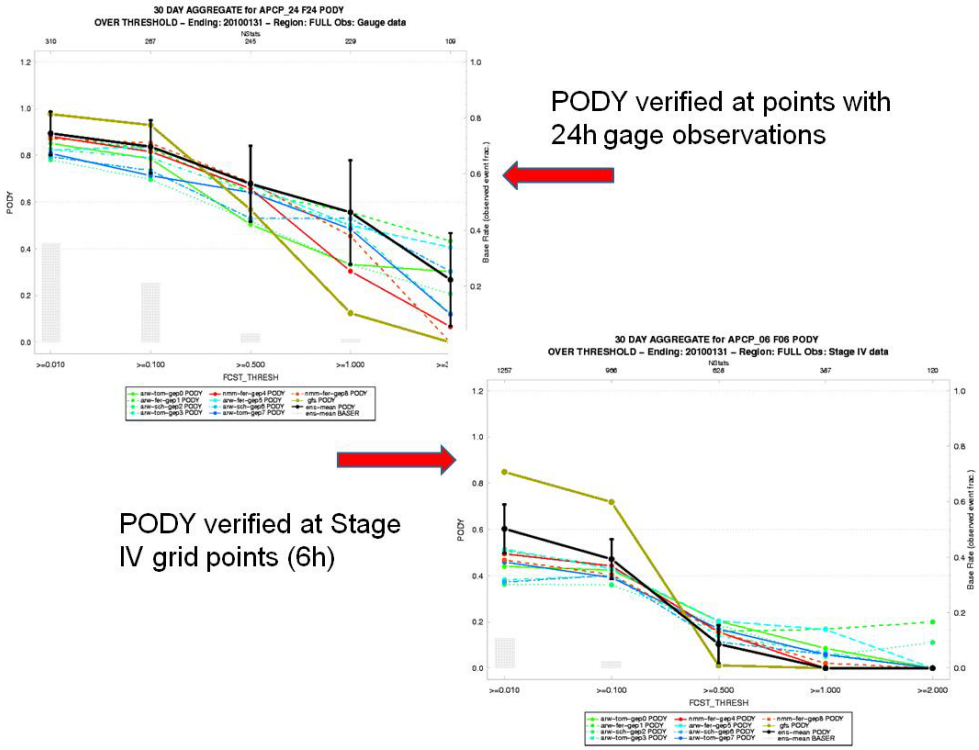

Fig. 4. Comparison of probability of detection yes (PODY) scores for January 2010 in the full HMT-West domain as verified using 24h gage totals (top) and 6h Stage IV estimates (bottom). Designation of individual ensemble members coded by color and line type is as in Fig. 2.

Experimentation with new verification measures for categorized QPFs in the verification of high impact precipitation events

Pertti NURMI

Finnish Meteorological Institute
P.O. Box 503, 00101 Helsinki, Finland
pertti.nurmi@fmi.fi

1. Introduction

General traditional methodology for the verification of deterministic Quantitative Precipitation Forecasts (QPF) is readily available in literature (e.g. Nurmi, 2003). However, sound and meaningful verification measures for rare and extreme weather events, like heavy precipitation, remain an open and unresolved issue, much because small data samples effectively hinder the computation of reliable verification statistics. Moreover, the traditional verification measures have a tendency to degenerate to trivial (zero) values when the rarity of the event increases.

Some of the novelty verification techniques potentially suitable and proper for heavy QPF verification include the Extreme Dependency Score, EDS (Stephenson et al., 2008) and its derivative, the Symmetric Extreme Dependency Score, SEDS (Hogan et al., 2009). Very recently, Ferro & Stephenson (2010) proposed two further modifications of them. Section 2 of this paper introduces briefly these new verification measures, and initial experimental verification results based on long-term precipitation forecast datasets available at the Finnish Meteorological Institute (FMI) are presented in Section 3.

2. The measures EDS, SEDS, EDI and SEDI

A set of binary (yes/no) forecasts is typically displayed as a two-by-two contingency table:

Event forecast	Event observed		
	Yes	No	Marginal total
Yes	a	b	a + b
No	c	d	c + d
Marginal total	a + c	b + d	a + b + c + d = n

from which some common verification quantities are defined as:

H = a / (a+c), hit rate

F = b / (b+d), false alarm rate

p = (a+c) / n, base rate

q = (a+b) / n, relative frequency of forecasted events

The EDS (Extreme Dependency Score) can be written in the form (Stephenson et al., 2008; Ferro & Stephenson, 2010):

$$\text{EDS} = (\log p - \log H) / (\log p + \log H)$$

and its symmetric version, SEDS (Hogan et al., 2009):

$$\text{SEDS} = (\log q - \log H) / (\log p + \log H).$$

From these equations one can see that the only difference is that the base rate p is replaced in the numerator of SEDS with q. By definition, SEDS > EDS only and if $p > q$. If the forecasts were to be re-calibrated by having $p = q$ then SEDS would equal EDS.

Ferro & Stephenson (2010) very recently proposed two new versions to the "extreme dependency score family", the Extremal Dependency Index EDI and the Symmetric Extremal Dependency Index SEDI:

$$\mathrm{EDI} = (\log F - \log H) / (\log F + \log H)$$

and

$$\mathrm{SEDI} = \frac{\log F - \log H - \log(1 - F) + \log(1 - H)}{\log F + \log H + \log(1 - F) + \log(1 - H)}.$$

In the former, p and q of EDS and SEDS, respectively, are replaced by the false alarm rate F and, in the latter, there are two additional terms log (1-F) and log (1-H). The role of these terms is negligible in rare event cases when both H and F would decay towards zero with the rarity of the event (when p approaches 0). These terms are included to make the score SEDI complement symmetric according to the authors. One reasoning behind these two new scores is to obtain a base rate independent measure, thus having the measures as functions of H and F only.

Primo & Ghelli (2009) and Ghelli & Primo (2009) have reported several undesirable properties of the EDS measure like being dependent on the base rate p and being easy to hedge (i.e. issuing a forecast which would be against one's judgement). These shortcomings were tried to be rectified by the SEDS measure, but the undesirable base rate dependency property still remained. The following table quoted from Ferro & Stephenson (2010) showcases properties related to all of these four measures (for more details, see the original paper):

	EDS	SEDS	EDI	SEDI	ETS
base-rate independent	×	×	✓	✓	×
non-trivial to hedge	×	✓	✓	✓	✓
regular	×	×	✓	✓	×
fixed range $[-1, 1]$	×	×	✓	✓	×
asymptotically equitable	×	✓	✓	✓	✓
meaningful origin	×	✓	✓	✓	✓
complement symmetric	×	×	×	✓	✓
transpose symmetric	×	✓	×	×	✓

Ferro & Stephenson (2010) elaborate extensively on various properties of the EDS and its derivative scores. They conclude that the new scores, EDI and SEDI, overcome the disadvantages of the EDS and SEDS. They further recommend that all forecasts should be re-calibrated before adopting and computing any of these scores and that the (frequency) bias should be examined separately. This, however, has not been done in the present study. We are merely showcasing results from initial experimentations utilizing real forecast data used as guidance in an operational environment.

3. Results

The data utilized in this study are seven years of NWP output of QPFs originating from the global ECMWF model and the limited area HIRLAM (high resolution) model operated by the Finnish Meteorological Institute. Some verification statistics are presented for the four verification measures, EDS, SEDS, EDI and SEDI, as well as, for comparison, for two traditional categorical verification measures, namely:

PSS = $H - F$ Peirce Skill Score

ETS = $(a - a_r) / (a+b+c - a_r)$ Equitable Threat Score

where a_r is the number of hits for random forecasts.

Figure 1 shows seven-year (2003-09) accumulated and averaged results of ECMWF QPFs for the forecast accumulation period of +18-42 hours, averaged over 100 rain gauge stations in Finland. Due to the large dataset there are quite many extreme heavy precipitation cases (in the Finnish climate), i.e. over 300 cases with 24-hour accumulated precipitation exceeding 30 mm. One can immediately note how the traditional verification scores degenerate towards zero beyond 5-10 mm of daily precipitation. On the other hand, the novelty scores defined in the previous section, behave remarkably different. At the lowest precipitation rates they are somewhat different to each other and qualitatively comparable to the PSS. When the precipitation events become more extreme they tend to converge to each other but not trivially towards zero. The EDS is somewhat lower compared to the others when daily precipitation amounts exceed 10 mm, and EDI and SEDI are almost identical at highest precipitation rates as can be interpreted from their definitions.

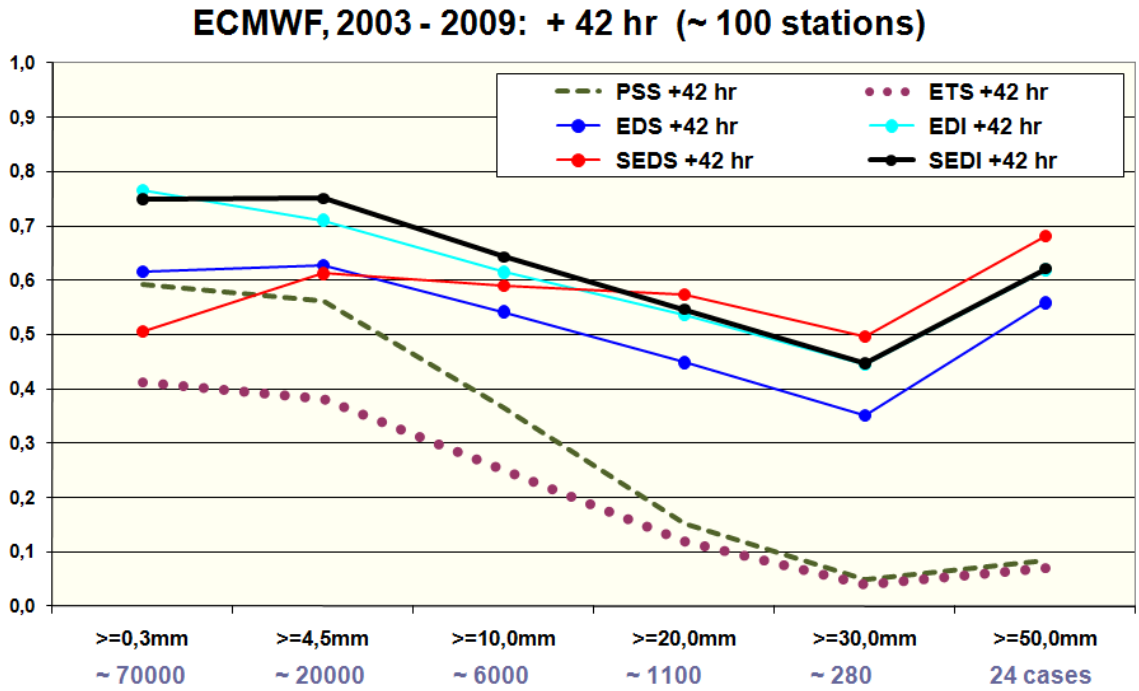

Figure 1. Verification scores as a function of precipitation threshold for 42 hour ECMWF 24-hour accumulated (+18-42 hrs) QPFs, averaged over seven years (2003-2009) and c. 100 rain gauge stations in Finland. The lowermost numbers indicate the number of cases in each category. See text for the explanation of acronyms.

Figure 2 presents a comparison between the EDS, SEDS and EDI scores at two different ECMWF QPF ranges, c. two days (+18-42 hour accumulation) and c. five days (+114-138 hour accumulation). (SEDI was not available at the longer forecast range). The two pairs of three curves behave qualitatively in a similar manner and as one would hope to expect the longer range forecasts produce the poorer verification results. Going to the most extreme (and rare) events of precipitation exceeding 50 mm per day all of the scores fall down to zero level at day D+5 forecast range.

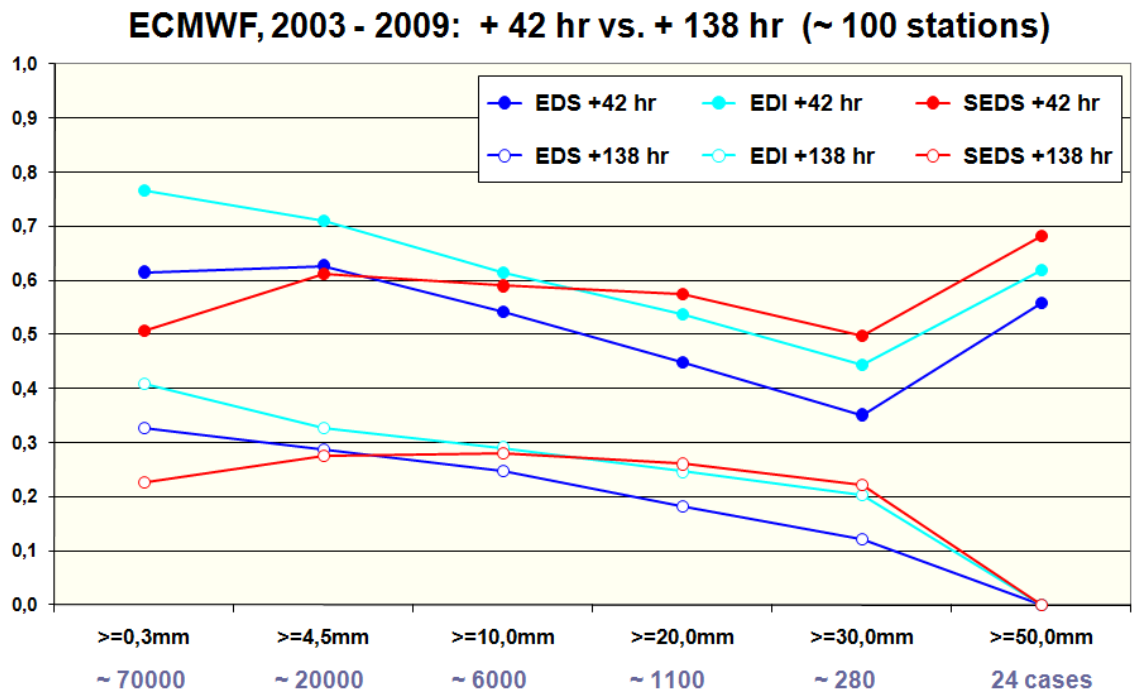

Figure 2. Verification scores as a function of precipitation threshold for 42 hour (+18-42 hr accumulations) (upper three curves with solid markers) and 138 hour (+114-138 hr accumulations) (lower three curves with open markers) ECMWF QPFs, averaged over seven years (2003-2009) and c. 100 rain gauge stations in Finland. The lowermost numbers indicate the number of cases in each category. See text for the explanation of acronyms.

The final Figure 3 shows a time-series comparison between the global ECMWF and limited area HIRLAM models during the past seven years, 2003 to 2009, looking at QPF accumulations exceeding 20 mm during 24 hours at the day D+2 range. The EDS produces generally somewhat lower values than the other novelty scores, and the traditional measures (PSS, ETS) remain at a much lower level as expected from what was shown already earlier. HIRLAM appears to have caught up the edge which ECMWF had in the early part of the study period.

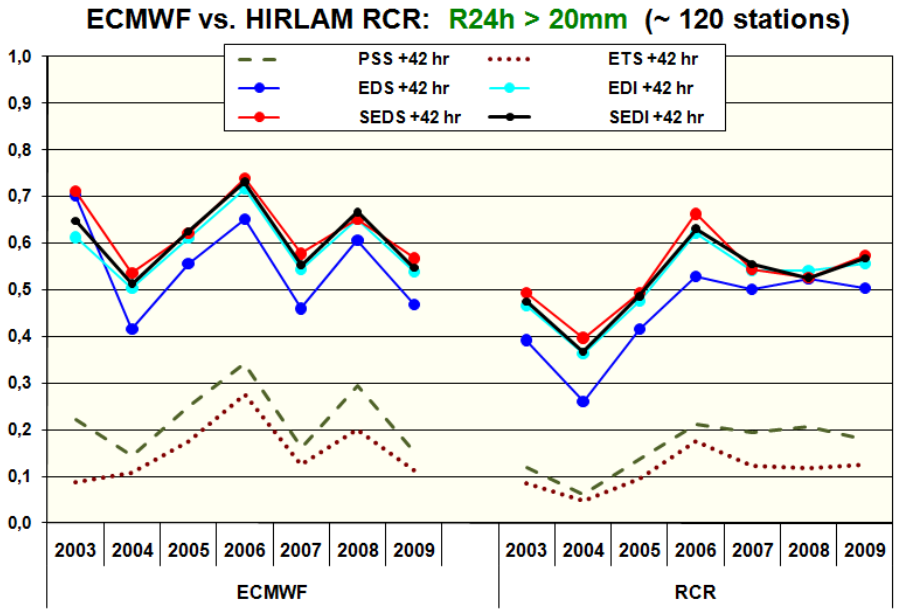

Figure 3. Time evolution of verification scores of 42 hour ECMWF (left-hand-side curves) and HIRLAM RCR (right-hand-side curves) accumulated (+18-42 hrs) QPFs for precipitation exceeding 20 mm dueing the 24 hours, averaged over c. 120 rain gauge stations in Finland (except for years 2008-09 c. 100 "better" stations). See text for the explanation of acronyms.

Acknowledgements

Contributions and feedback from the 12 members of the ECMWF Technical Advisory Committee Subgroup on Verification Measures and the WMO Joint Working Group on Forecast Verification Research (JWGFVR) are acknowledged.

References

Ferro, C.A.T. and D.B. Stephenson, 2010. Improved verification measures for deterministic forecasts of rare, binary events. *Wea. and Forecasting (submitted).*

Ghelli, A. and C. Primo, 2009. On the use of the Extreme Dependecy Score to investigate the performance of an NWP model for rare events. *Meteorol. Appl.*, **16**, 537-544.

Hogan, R.J., E.J. O'Connor and A.J. Illingworth, 2009. Verification of cloud-fraction forecasts. *Q. J. R. Meteorol. Soc.*, **135**, 643, 1494-1511.

Nurmi, P., 2003. Recommendations on the verification of local weather forecasts. *ECMWF Technical Memorandum*, **430**, 19 pp.

Primo, C. and A. Ghelli, 2009. The effect of the base rate on the Extreme Dependecy Score. *Meteorol. Appl.*, **16**, 533-535.

Stephenson, D.B., B. Casati, C.A.T. Ferro and C. Wilson, 2008. The extreme dependency score: a non-vanishing score for forecasts of rare events. *Meteorol. Appl.*, **15**, 41-50

Session E

Data assimilation for precipitation forecasting systems

Progress in data assimilation for NWP based Nowcasting of Precipitation using radar and remote sensing data at the UK Met Office

Susan P BALLARD, Zhihong LI, David SIMONIN, Helen BUTTERY, Cristina CHARLTON-PEREZ, Nicolas GAUSSIAT, Lee HAWKNESS-SMITH, Graeme KELLY, and Robert TUBBS

Met Office, Meteorology Building, University of Reading, Reading, RG6 6BB, UK
sue.ballard@metoffice.gov.uk

The Met Office now has an operational short range NWP prediction system for the UK using a variable resolution version of its Unified Model (UKV) with the main domain at 1.5km resolution stretching to 4km resolution in the boundary zone. This uses 3 hourly 3D-Var with conventional observations and 3D cloud cover on a fixed 3km resolution grid and then latent heat nudging using a radar derived precipitation analysis during the 3 hour assimilation window. This is nested in the regional NWP system at 12km resolution using 6 hourly 4D-Var (at 36km resolution) plus latent heat nudging.

We are developing an hourly cycling NWP based nowcasting system at 1.5km resolution. The test system covering Southern England and Wales is nested in the current UK 4km NWP system and will ultimately be nested in the UKV. A 3D-Var analysis at 1.5km resolution with humidity nudging using an hourly 3D- cloud analysis and latent heat nudging using 15min radar derived surface precipitation analyses has been tested as well as 4D-Var at 3km plus humidity and latent heat nudging. We are also undertaking work to directly assimilate radar Doppler winds and reflectivity data as well as geostationary satellite data and assessing the impact of high time frequency wind profiler and GPS data. Future use of cloud radar, ceilometer and microwave radiometer data is also being considered.

This paper will describe results from the operational and developmental Met Office systems for short-range and nowcasting predictions of precipitation and comparisons with the current nowcast system.

This work also contributes to working group 1 (Propagation of uncertainty from observing systems (radars) into NWP) of COST-731 - Propagation of uncertainty in advanced meteo-hydrological forecast systems - and will contrast the work with that of other European Met Services, institutions and universities.

LETKF for the nonhydrostatic regional model COSMO-DE

Hendrik Reich*, Andreas Rhodin*, Christoph Schraff*

*Deutscher Wetterdienst (DWD), Frankfurter Strasse 135, 63067 Offenbach, Germany, hendrik.reich@dwd.de

1 Introduction

Data assimilation for numerical weather prediction (NWP) at the convective scale meets with a number of challenges. They include: strongly flow dependent and unknown spatial balances between the different model variables, importance of nonlinear processes, non-Gaussian error statistics and large forecast errors in 'weather'-parameters due to imperfections in the physics, in particular in the cloud and boundary layer formulations.

The Local Ensemble Transform Kalman Filter (LETKF) (Hunt et al., 2007) offers some very attractive features: it is a simple algorithm, no tangent linear and adjoint versions of the prognostic model are required, and the forecast error covariance matrix is cycled and thus flow-dependent.

At Deutscher Wetterdienst (DWD) it is planned to use the LETKF on the global scale (in a hybrid approach together with 3dVar) as well as on the local scale. The LETKF analysis ensemble will also serve as initial conditions for COSMO-DE EPS, a convection permitting EPS system under development at DWD.

The outline is as follows: we will give a short overview on the LETKF and the NWP model COSMO-DE in sections 2 and 3. In section 4 we present the results of our LETKF experiments and we conclude in section 5.

2 LETKF theory

Our Implementation follows (Hunt et al., 2007). The basic idea of the LETKF is to do the analysis in the space of the *ensemble perturbations*. This is computationally efficient, but also restricts corrections to the subspace spanned by the ensemble. An explicit localization is necessary to confine the ensemble size; this means to compute a separate analysis at every grid point, where only certain observations are selected. Thus, the analysis ensemble members are a locally linear combination of first guess ensemble members.

The analysis mean $\bar{\mathbf{x}}^a$ is given by

$$\bar{\mathbf{x}}^a = \bar{\mathbf{x}}^b + \mathbf{X}^b \tilde{\mathbf{P}}^a (\mathbf{H}\mathbf{X}^b)^T \mathbf{R}^{-1} (\mathbf{y} - \bar{\mathbf{y}}^b) \tag{1}$$

where $\bar{\mathbf{x}}^b$ is the first guess mean; $\mathbf{H}$ is the (linearized) observation operator and $\mathbf{X}^b$ are the first guess ensemble perturbations. The analysis ensemble is obtained via

$$\mathbf{X}^a = \mathbf{X}^b [(k-1)\tilde{\mathbf{P}}^a]^{1/2} = \mathbf{X}^b \mathbf{W}^a. \tag{2}$$

Here, k is the number of ensemble members and $\tilde{\mathbf{P}}^a$ is the analysis error covariance matrix which is (in the ensemble space) given by

$$\tilde{\mathbf{P}}^a = [(k-1)\mathbf{I} + (\mathbf{H}\mathbf{X}^b)^T \mathbf{R}^{-1} \mathbf{H}\mathbf{X}^b]^{-1}. \tag{3}$$

3 The COSMO-DE model

COSMO-DE is a convective scale NWP model which provides very short range forecasts (up to 18 h), it has been running at DWD since 2007. The focus of interest is on severe weather events related on the one hand to deep moist convection leading e.g. to super- and multi-cell thunderstorms or squall lines and on the other hand to interactions with fine scale topography which can induce e.g. severe downslope winds or Föhn-storms. COSMO-DE has a horizontal mesh size of 2.8 km, 50 layers in the vertical and covers the area of Germany, parts of its neighbouring countries and also a large part of the Alpine region. The dynamical formulation of the COSMO-DE is based on the COSMO-Model (Baldauf et al., 2010). It is a non-hydrostatic, fully compressible model in advection form. COSMO-DE does no longer use a parameterisation of deep convection, but resolves at least the larger-scale elements of organized convection. For the smaller scales a parameterisation of shallow convection is retained. Currently, the intial conditions are provided by a nudging scheme including latent heat nudging for the assimilation of radar data (). The COSMO-DE EPS is a ensemble prediction system currently under development at DWD. The purpose is to produce probabilistic forecasts of severe weather events such as wind gusts, thunderstorms and heavy precipitation. It will run at the same resolution of 2.8 km as the deterministic COSMO-DE.

4 Experiments and results

We performed several preliminary experiments with successive LETKF assimilation cycles. In all experiments, 32 ensemble members were used. The initial ensemble members where drawn from the 3dVar B-Matrix of the global model GME. Conventional observations from the global network were assimilated. We have run a 3-hourly cycle up to 2 days (7-8 Aug. 2009: 1 quiet + 1 convective day) and used lateral boundary conditions (BC) from COSMO-SREPS () (3 * 4 members) or deterministic BC.

In our first experiments we concentrate on general topics, such as the rms/spread ratio of the ensemble, the noise (as measured by dps/dt) and the general behaviour of LETKF (analysis increments, spread structures). The effect of parameter variation (e.g. localization length scales) was tested, but fine tuning is left to be done with longer running experiments.

The set of analysed variables is given by $u, v, w, T, pp, qv, qcl, qci$ (wind components including vertical velocity w, temperature, pressure pertubation, humidity, cloud water and cloud ice content). Here, 'analysed' means that linear combination is applied to these variables; other variables are taken from first guess ensemble members or ensemble mean.

We verify the LETKF results (i.e. the analysis *mean*) against the nudging analysis and observations. When comparing with the nudging analysis one has to take into account that the nudging scheme uses a larger set of observations. A verification tool (deterministic/ensemble scores) is currently under development within the COSMO consortium.

Fig.1 shows the spread of the u-wind component of the first guess ensemble, obtained with deterministic and ensemble BC, respectively. In the case of deterministic BC we observe a lack of spread at the lateral boundaries, whereas "new" spread is coming in from the west with ensemble BC. This demonstrates the need to use ensemble BC's, and it can be seen that a large

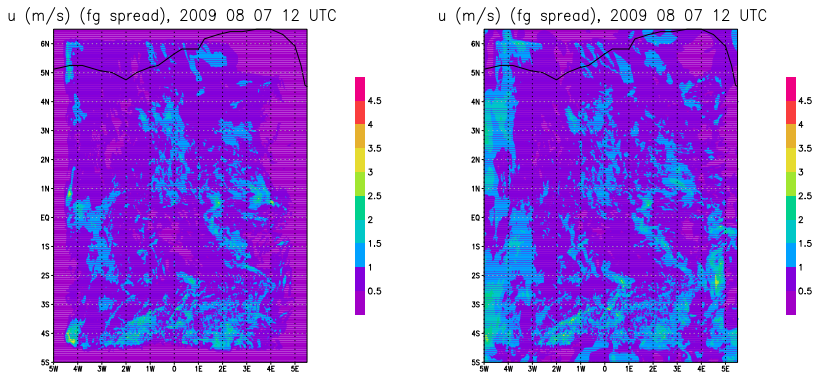

Fig.1: spread (wind component u in m/s) of first guess on 7 Aug. 2009 at 12 UTC (after 4 analysis cycles) for deterministic BC (left) and ensemble BC (right).

amount of the whole domain is influenced by the spread stemming from the BC. As we will see later, the use of ensemble BC leads to some difficulties.

In order to test the implementation of the LETKF and it's capability of making use of observations we compare the analysis produced by the LETKF with a free forecast which uses the same BC but no observations. Fig.2 shows the temporal development of the first guess and free forecast rmse of the u-component of wind velocity (as measured with respect to the nudging analysis) on the 500 hPa level. One can see that the LETKF performs better than the free forecast on all levels.

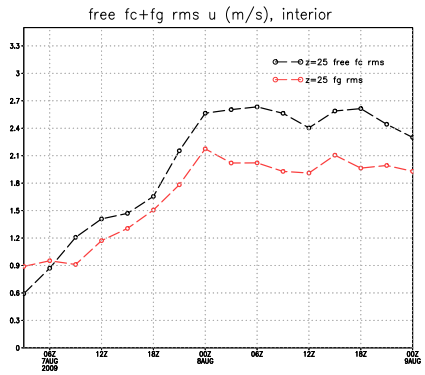

Fig.2: rms of u,(m/s) (interior) of first guess and free forecast; results for det BC.

Next we verify the LETKF analysis against observations; the results are shown in Fig. 3. The reduction of spread between first guess and analysis indicates that the LETKF makes use of the observations. As also the rmse of the analysis is smaller than that of the first guess we conclude that the LETKF is able to use the information contained in the observations. The spread of first guess and analysis is much smaller than the corresponding rmse; this means that the ensemble is underdispersive.

The lack of spread is (partly) due to model error which is not accounted for so far. One (simple) method to increase spread is multiplicative covariance inflation:

$$\mathbf{X}_b \rightarrow \rho \mathbf{X}_b \tag{4}$$

with $\mathbf{X}_b$ being the ensemble perturbations and $\rho > 1$. The tuning of the inflation factor ρ takes much time, and it is expected that the optimal value will change in time, depending e.g. on observation density. For this reason, an adaptive procedure is preferable. (Li et al., 2009) propose an online estimation of the inflation factor. The idea is to compare the "observed" obs minus first guess, given by $(\mathbf{y} - H(\mathbf{X}_b))$ with the "predicted" one, given by $(\mathbf{R} + \mathbf{H}\mathbf{P}_b\mathbf{H}^t)$. This

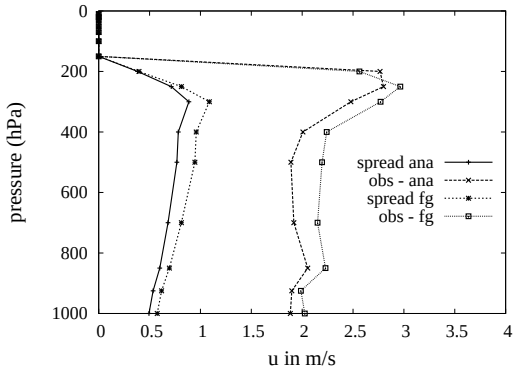

Fig.3: time average (20090807 15 UTC - 20090809 00 UTC)of obs-fg and spread of u,(m/s) (whole area), AIREP

method was applied in a LETKF environment by Bonavita et al. (2010), where ρ was time and space dependent. Here, in a first step, we tested a version with a space independent ρ.

It is also assumed that the observation errors and thus the **R**-matrix are specified incorrectly, and a correction is desirable. This can be achieved by comparing the observed observation covariance with the assumed one (in ensemble space) and correcting **R** automatically if necessary. Both methods (est. of inflation factor / **R** matrix) have been tested with reasonable numerical cost and success with a toy model, and have been implemented in the COSMO LETKF. For deterministic BC, a positive effect of the adaptive ρ inflation is visible, which is shown in Fig.4. In the case with ensemble BC the method was not succesful. Currently, an improved version with a space dependent ρ and doing the computation in ensemble space is tested.

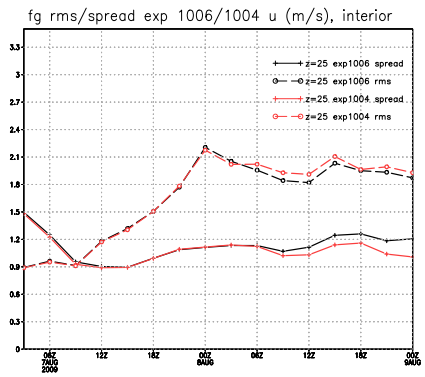

Fig.4: intercomparison of first guess rms and spread of u,(m/s) (interior); results for det BC and constant inflation factor ρ (exp1004) and adaptive covariance inflation (exp1006)

The LETKF produces an analysis ensemble as a (local) linear combination of the first guess ensemble. The analysis fields obtained are not necessarily balanced, and noise (e.g. external gravity waves, measured by dps/dt) might be present when starting the integration. Indeed we find an increased level of noise (as compared with the nudging scheme). Fig.5 (left plot) shows that noise is present in the whole domain.

We observed that the diagonal elements of weight matrices W are larger than the off diagonal elements; this means that the analysis ensemble member k gets the largest contribution from first guess ensemble member k plus (smaller) corrections from members $i \neq k$. Thus, the difference between analysis and first guess ensemble member k (the analysis increment) is small compared to the full fields, and hydrostatic balancing can be applied to this increment: this leaves the full fields nonhydrostatic as it should be in a nonhydrostatic model.

Applying this method reduces the noise in the interior of the domain (Fig.5, right plot); at

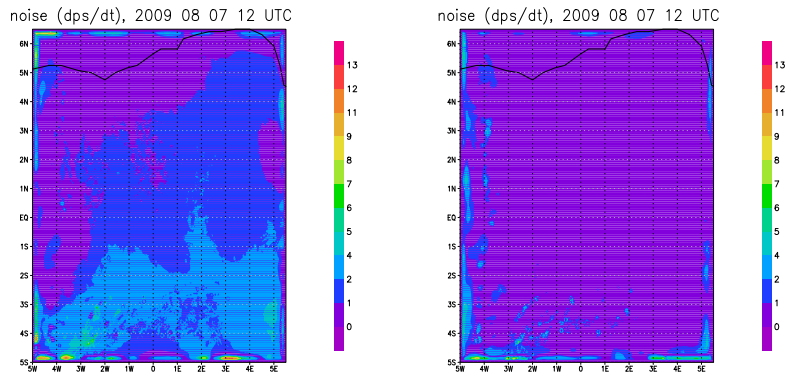

Fig.5: area plots of noise (dPs/dt) at the first time step; ens BC without hydrostatic balancing (left) and with hydrostatic balancing applied (right).

the boundaries, there is still noise present.

5 Conclusions

We have tested the LETKF in preliminary, short assimilation cycles. The LETKF demonstrated its capability of assimilating conventional observations correctly. Problems such as a lack of spread and noise introduced by the ensemble BC were identified. The latter could be alleviated by applying hydrostatic balancing to the analysis increments. The effect of this balancing on the rms/spread ratio will have to be investigated. Furthermore, we will study the effect of the remaining noise on e.g. precipitation at the beginning of the integration.

The adaptive covariance inflation, which was tested in a simple version, was successfully applied in the case of deterministic BC. For ensemble BC a more sophisticated version is currently tested. Within the COSMO consortium, alternative methods to account for model errors are developed and will also be implemented in the LETKF.

In the future we will run experiments over a period of weeks or months. In this experiments, we will use more observations (radar data in particular) and do the analysis more frequently ($\approx$ all 15 min). With this more realistic setup, parameters as the localization length scales will have to be tuned.

References

Baldauf M., Seifert A., Förstner J., Majewski D., Raschendorfer M., Reinhardt T., 2010: Operational convective-scale numerical weather prediction with the COSMO model. *submitted to MWR*

Bonavita M., Torrisi L., Marcucci F., 2010: Ensemble data assimilation with the CNMCA regional forecasting system. *Q.J.R.Meteorol.Soc.* **136**: 132-145

Hunt B.R., Kalnay E., Kostelich E.J., Szunyogh I., 2007: Efficient data assimilation for spatiotemporal chaos: A local ensemble transform Kalman filter. *Physica D* **230**: 112-126

Li H., Kalnay E., Miyoshi T., 2009: Simultaneous estimation of covariance inflation and observation errors within an ensemble Kalman filter. *Q.J.R.Meteorol.Soc.* **135**: 523-533

Stephan K., S. Klink, C. Schraff, 2008: Assimilation of radar derived rain rates into the convective scale model COSMO-DE at DWD. *Q.J.R.Meteorol.Soc.* **134**: 1315-1326

Impacts of multiple radar data assimilation on short-range Quantitative Precipitation Forecasts of a squall line in South China

CHEN Xunlai[1], LAN Hongping[1], Fanyou KONG[2] , CAI Fei[1]
Shenzhen National Climate Observatory/Shenzhen meteorological Bureau, Shenzhen, China[1]
Center for Analysis and Prediction of Storms, University of Oklahoma, USA[2]

cxlxun@163.com

The impact of multiple-Doppler radar data assimilation on quantitative precipitation forecasting (QPF) is examined in a case study of May 7, 2010 Guangzhou heavy precipitation. The Advanced Regional Prediction System (ARPS) and its three-dimensional variational data assimilation system (ARPS 3DVAR) and cloud analysis package are used to analyze radar radial wind and reflectivity into WRF (Weather Research and Forecasting) modelling system. In this study, multiple-Doppler radar assimilation in Guangdong province is applied to predict a squall line system on 7 May 2010 that caused heavy precipitation and flooding in Guangzhou. The QPF skills are evaluated. Numerical prediction experiments demonstrate that the ARPS 3DVAR can successfully assimilate Doppler radial velocity and reflectivity from 7 radar sites and extract useful flow and hydrometeor information from the radar data to initiate the squall line system. Radar data assimilation adjusts both the dynamical and thermodynamical fields for the initial condition. Assimilation of both radial velocity and reflectivity results in higher QPF skill scores than assimilation of either radial velocity or reflectivity only. In addition to the improvement of the QPF skill, the predicted structure of the squall line is also improved by the multiple Doppler radar data assimilation in the cycling experiment. To investigate the impact of different initial fields, three groups of sensitivity experiments are conducted with the initial fields and lateral boundaries from GFS and NCEP FNL data. Differences in sub-synoptic scale characteristics between the GFS and FNL initial fields are found to result in different simulation results. The influence remains throughout the forecast duration.

Optimization of the Analogs method in the framework of statistical weather forecasting in the Swiss Alps

Pascal HORTON[1], Charles OBLED[2], Michel JABOYEDOFF[1], Richard METZGER[1]
[1] *University of Lausanne, IGAR, Lausanne, Switzerland (pascal.horton@unil.ch),*
[2] *Grenoble Institute of Technology, LTHE, Grenoble, France*

In southwestern Switzerland, the MINERVE project aims at reducing the flood peaks of the Rhône river by means of water retention in dams. Their operation requires therefore precipitation forecasts for several days ahead. In parallel to physically based numerical weather prediction model (NWP) outputs processed by MeteoSwiss, probabilistic quantitative precipitation forecasts (PQPF) by means of an Analog method are being developed. The principle of this downscaling approach is to bypass the modeling of the precipitation generating processes by finding in a past meteorological archive situations that are similar to the target one and to use their concurrent rainfalls to build a conditional distribution.

The meteorological archive contains a large amount of candidate predictors. The goal is to find the best set of variables and of parameters (time and spatial windows, number of analogs, weightings, etc…) to connect synoptic information to local rainfall. This makes the model opened to improvements that are impossible to explore manually. Thus, an optimizer based on the Nelder–Mead method was implemented to perform an automatic parameter calibration. This allows to introduce new concepts and to remove some limitations that existed for the simplification of the manual calibration.

Since the different regions in the Swiss Alps are sensitive to distinct meteorological situations, the best predictors vary from a sub-region to another. This was observed for various parts of the alpine Rhône catchment that are characterized by strong orographic effects under specific circumstances.

The spatial windows of the selected predictors highlight the best location where predictors must be compared to downscale at best the precipitation of a given sub-region. It was found that those locations correspond to features in the patterns of situations giving severe rainfall, which differ from the average state. Results are in good agreement with known case studies and consistent with the underlying physics.

High Resolution Radar Accumulation Maps for Verification of WRF+VAR(National Radar Network)

L SUTHERLAND-STACEY, G L AUSTIN, P E SHUCKSMITH
University of Auckland, Auckland, New Zealand, l.sutherland-stacey@auckland.ac.nz

1. Introduction

A contemporary theme in numerical weather prediction (NWP) is the assimilation of radar observations of reflectivity and radial Doppler winds into convective scale models. As NWP is partly an initial value problem, there is some expectation that by assimilating high resolution observations the short term skill of model predictions should be increased.

However there remains some question about the best way to determine quantitative precipitation forecasts (QPF) skill. Direct comparison of model accumulations to gauge networks or remotely sensed satellite or C-band radar areal accumulations is problematic as each observation type suffers from scale problems (e.g. Fabry et al. 1994), particularly at the scales associated with convective rainfall. In this work we use a high resolution X-band radar accumulation product, which overcomes some scale problems, to estimate the total precipitation falling into the catchment. This observation can then be compared to model accumulation above the catchment.

2. Radar Data

There are two groups operating weather radars in New Zealand.

The New Zealand Meterological Service (MetService Ltd.) operates a national network of fixed C-band radars (for details see Crouch 2003). Usually the radars generate a volume scan every 7.5 minutes. The radars are Dopplerised and employ a dual pulse repetition frequency (PRF) strategy to expand the Nyquist velocity ambiguity to about 16 ms^{-1}. In this work we use a velocity unfolding techniques based on an estimate of the regional wind obtained from the echo motion vector (EMV), an estimate of the speed reflectivity is advected across the radar domain based on subsequent reflectivity images. The MetService radar data is further post-processed with a super-observation procedure similar to Salonen et. al. (2009) in preparation for NWP data assimilation.

The UoAAPG runs a variety of small 25 kW X-band radars. The radars are constructed from modified off the shelf components. The radars are mounted in different vehicles or structures depending on the application or logistical requirements, for example a trailer radar can be towed to sites near campus or a more robust sea-container based unit can be moved by commercial transport (Figure 1). UoAAPG radars have been involved in a variety of experiments including observations of orographic rain processes (Purdy et al. 2005) and a small tornado (Sutherland-Stacey, Shucksmith and Austin 2010).

Figure 1: University of Auckland Mobile radars Left: deployed at a farm near Mangakino, New Zealand and Right: In the Blue Calf mountains in Australia.

In the winters of 2008 and 2009 one radar was deployed, along with ancillary rain gauges and graduate students, to a site in the central North Island of New Zealand (NZ) overlooking a catchment of about 130 km^2. The radars were run with a low elevation scan pattern, completing one sweep about every 50 seconds. Reflectivity was then converted to areal accumulation over the catchment by applying the classic Marshal-Palmer Z-R relationship. Comparison of the radar accumulation to gauge point measurements suggests the radar retrieved rain rates agree with a mean absolute error of order 1 mm/hr at range less than 15 km and that the radar areal accumulation is more representative than comparable estimates that could be made with gauges alone. An example of an X-band observation is given from this study is Figure 2.

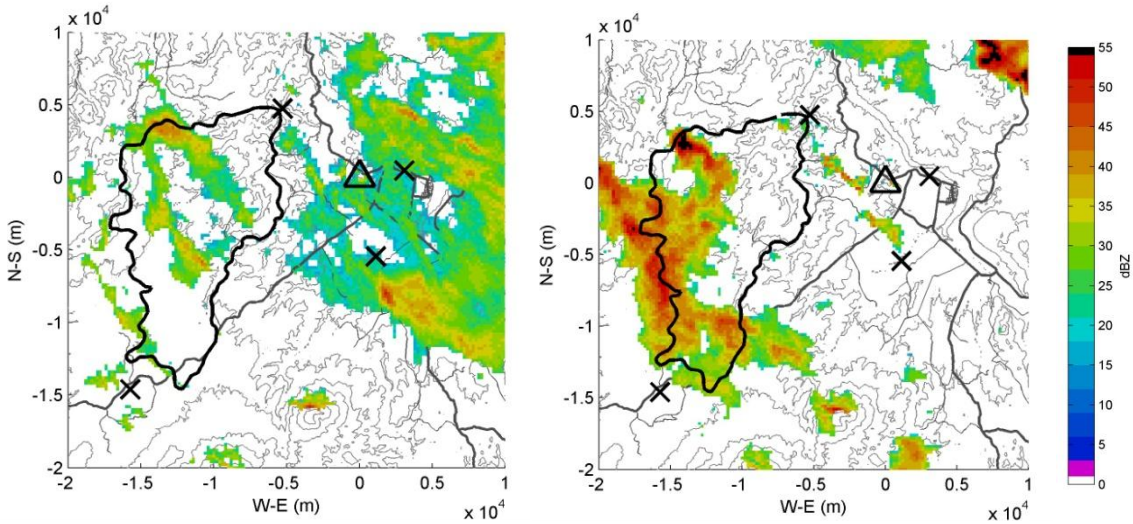

Figure 2: Characteristic X-band radar reflectivity observation over the Waipapa catchment (solid black). The radar location is indicated (Δ) along with rain gauges (×) surface roads (solid gray) and terrain (light gray).

3. Method

The non-hydrostatic version of the Weather Research and Forecast model (AWR-WRF) includes variational data assimilation (VAR) capabilities (Barker et al. 2004) including a facility for the assimilation of radar reflectivity (Xiao et al. 2007) and radial Doppler velocity observations (Xiao et al. 2005). The details of the variational assimilation scheme, which is not modified for this work, are not repeated here, but it is noted that the rain model used in the assimilation includes only warm rain processes, which may not be suitable for NZ winter situations. For this reason only Doppler radial velocity observations are assimilated in this example.

WRF is run in - outer nest with 15 km grid spacing covering NZ and the Tasman sea which feeds boundary conditions to a nest with 3 km grid spacing over the North Island of NZ (Figure 3). The nested domain is integrated without a cumulus parameterisation, as the grid spacing should be small enough to resolve some (but clearly not all) convective features. (The model is run on a modest custer of some 15 dual-core Intel nodes which is maintained as a learning and research resource by and for graduate students.)

Both nests are run as ensembles with 10 members. The outer nest receives boundary conditions from the NCEP global run with radiance and insitu observations assimilated with 3DVAR every 6 hours. Radar data from the 3 North Island MetService C-band weather radars that were operational during the 2008 and 2009 winter UoAAPG deployments is assimilated was the nested domain every 15 minutes, although due to computational limitations the model error statistics are not updated for every assimilation cycle. The inner nest is also integrated without assimilation as a control.

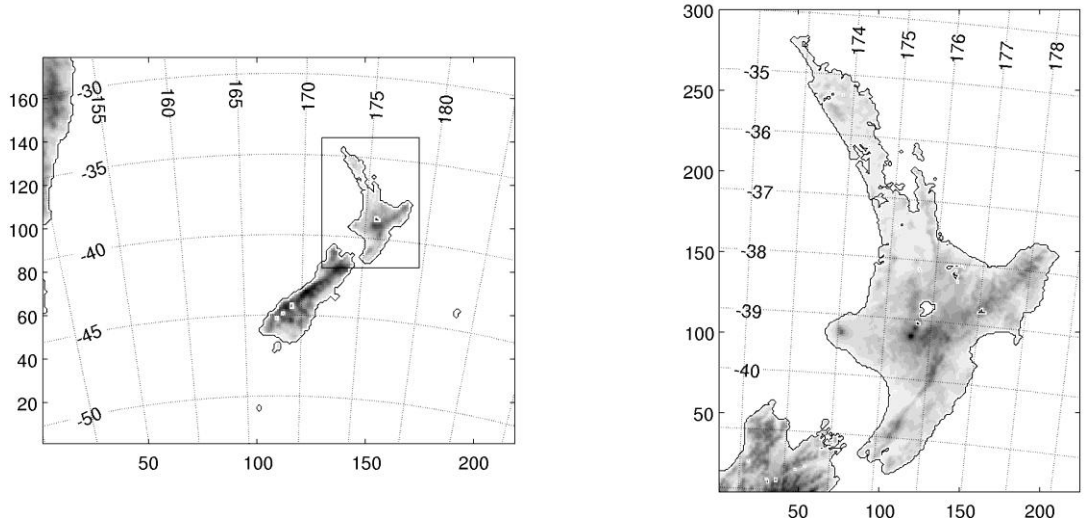

Figure 3: WRF domains. Left: 15km grid point spacing outer domain and Right: 3km grid point spacing nest.

An example of the proposed observation experiment is given for a case on 2009/09/27 18:00 to 2009/09/27 05:00 UTC, when a complex frontal system advanced over the country from the north west. The inner nest ensemble is run with Doppler radial velocity

data assimilation every 15 minutes for the first 6 hours and then for a further 5 hours with no additional data assimilation.

To qualitatively compare the model rain field with reflectivity observations the rainwater mixing ratio is converted to reflectivity after Sun and Crook (1997). For quantitative assessment of model skill the spatially averaged model accumulation over the study catchment can be extracted for comparison against the X-band radar accumulation.

4. Discussion

In the example images presented here (Figure 4) assimilation of Doppler winds every 15 minuites for 3.5 hours displaces the resolved frontal precipitation system to the west, compared to the control run, and increases its width in the north of the country. A rain band off the west of New Zealand is partially removed by the assimilation process but also relocated to the east around the southern end of the Island. The changes appear to be broadly consistent with reflectivity observations.

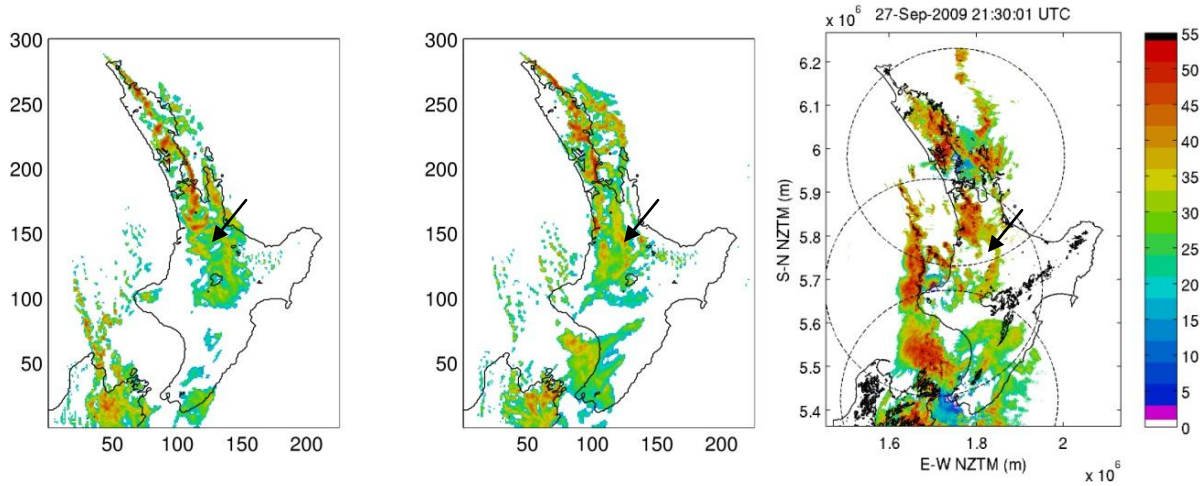

Figure 4: Reflectivity 2009/09/27 21:30 UTC Left: Model without Doppler wind assimilation, Middle: model with Doppler wind and Right: observation from the national radar network. The location of the Waipapa study catchment is indicated with an arrow.

A method to test the QPF skill of the model is to compare it against actually observations. In

Figure *5* the control and Doppler wind ensemble model accumulations are plotted alongside an estimate of the areal accumulation from the X-band radar observations. Both the control and Doppler wind ensemble spreads include the X-band radar estimates for most of the time period, however the Doppler wind ensemble overestimates the total accumulation while the control run underestimates the accumulation.

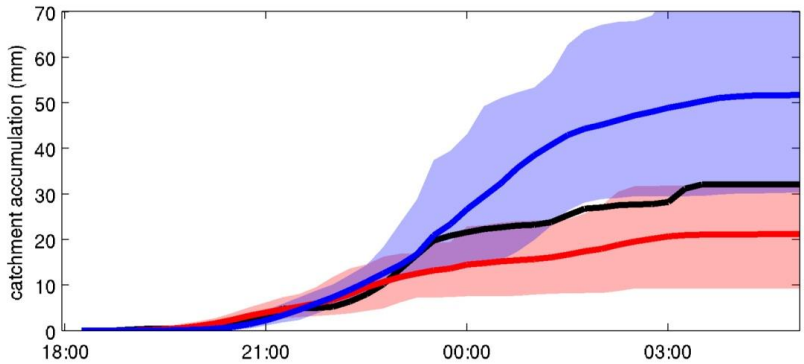

Figure 5: Accumulation in the Waipapa catchment for the same case study. Black line: X-band radar estimate, Blue line: Doppler wind model, Red: Control run. (shaded area model spread and solid lines the ensemble mean).

5. Concluding Remarks

In this work a system for comparison of model predictions to high resolution X- band radar measurements of areal accumulation is proposed and demonstrated by way of an example. Statistical analysis of a larger dataset of cases is presented in the associated talk.

6. Acknowledgments

C-band radar data was provided by the New Zealand Meterological Service Ltd.

7. References

Barker, D. M., W. Huang, Y. R. Guo, A. J. Bourgeois & Q. N. Xiao (2004) A three-dimensional variational data assimilation system for MM5: Implementation and initial results. *Monthly Weather Review,* 132**,** 897-914.

Crouch, J. (2003) Using Radar to Diagnose Weather Systems. *Tephar***,** 46-48.

Fabry, F., A. Bellon, M. R. Duncan & G. L. Austin (1994) HIGH-RESOLUTION RAINFALL MEASUREMENTS BY RADAR FOR VERY SMALL BASINS - THE SAMPLING PROBLEM REEXAMINED. *Journal of Hydrology,* 161**,** 415-428.

Purdy, J. C., G. L. Austin, A. W. Seed & I. D. Cluckie (2005) Radar evidence of orographic enhancement due to the seeder feeder mechanism. *Meteorological Applications,* 12**,** 199-206.

Salonen, K., H. Jarvinen, G. Haase, S. Niemela & R. Eresmaa (2009) Doppler radar radial winds in HIRLAM. Part II: optimizing the super-observation processing. *Tellus Series a-Dynamic Meteorology and Oceanography,* 61**,** 288-295.

Sun, J. Z. & N. A. Crook (1997) Dynamical and microphysical retrieval from Doppler radar observations using a cloud model and its adjoint .1. Model development and simulated data experiments. *Journal of the Atmospheric Sciences,* 54**,** 1642-1661.

Sutherland-Stacey, L., P. Shucksmith & G. Austin (2010) High Resolution Observation of a Small Tornado, Ardmore, New Zealand. *Weather and Climate,* 30**,** 46-53.

Xiao, Q. N., Y. H. Kuo, J. Z. Sun, W. C. Lee, D. M. Barker & E. Lim (2007) An approach of radar reflectivity data assimilation and its assessment with the inland QPF of Typhoon Rusa (2002) at landfall. *Journal of Applied Meteorology and Climatology,* 46**,** 14-22.

Xiao, Q. N., Y. H. Kuo, J. Z. Sun, W. C. Lee, E. Lim, Y. R. Guo & D. M. Barker (2005) Assimilation of Doppler radar observations with a regional 3DVAR system: Impact of Doppler velocities on forecasts of a heavy rainfall case. *Journal of Applied Meteorology,* 44**,** 768-788.

Applicitation Test of Doppler Radar Data in Numerical Model ARPS

ZHANG Lei[1,2] WANG Zheng-hui[1,2]

[1] Key Laboratory of Meteorological Disaster of Ministry of Education，Nanjing University of Information Science &Technology, Nanjing 210044, P. R. China
[2] School of Atmospheric Physics, Nanjing University of Information Science & Technology 210044, P. R. China, leizhang_zl@hotmail.com

1.Introduction

In Numerical weather forecast, whether the initial field is good have a direct impact on the forecast.In the traditional numerical prediction, we choose routine meteorological observation data as the initial field, which lack the macroscopic and microscopic physics features of cloud for precipitation forecast, and this caused the problem called spin-up.

Doppler weather radar can obtain the information within the cloud,such as radial wind speed and reflectivity, with high resolution that conventional observation data is incomparable. In recent years, there are more and more meteorologist at home and abroad studying the application of doppler radar radial velocity and reflectivity material into the high-resolution forecasting model.

By simulating one rainstorm process around Jiangsu Province, based on ARPS model and its Data Analysis System ADAS and three-dimensional variational assimilation 3DVAR, we analyzed the impact of improving the initial field and getting better forecast results which brought by the two kinds of radar data added in differernt combinations.

2. Assimilation of Doppler radar radial wind and reflectivity data

ARPS(The Advanced Regional Prediction System)model is developed by the Center for Analysis and Prediction of Storms established at the University of Oklahoma.Central to achieving this goal is an entirely new three-dimensional, nonhydrostatic model system known as the Advanced Regional Prediction System (ARPS).It is a entirely new and complete numerical prediction system designed for the explicit representation of convective and cold-season storms. It includes a data ingest, quality control, and objective analysis package known as ADAS (ARPS Data Analysis System), a single-Doppler radar parameter retrieval and assimilation system known as ARPSDAS (ARPS Data Assimilation System, of which ADAS is a component), the prediction model itself, which is the topic of this paper, and a post-processing package known as ARPSPLT. It is a model system that can be used effectively for both basic atmospheric research and operational numerical weather prediction, on scales ranging from regional to micro-scales. An iterative scheme used in ADAS can offer computational savings in that large matrix solutions need not be found, the Bratseth interpolation method accounts for the relative error between the background and the error in each observation source, and is relatively insensitive to large variations in data density. To deal with Doppler radar, it needs radial wind adjustment, microphysical adjustments, complex cloud analysis, quality control and incremental analysis updating.

2.1 Assimilation of Doppler radar radial wind data

ADAS is combined with ARPS3DVAR to adjust the radial wind, the cost function is：

$$J(X) = J_b + J_o + J_c$$
$$= \frac{1}{2}(X - X_b)^T B^{-1}(X - X_b) + \frac{1}{2}[H(x) - y_o]^T R^{-1}[H(X) - y_o] + J_c(X) \quad (1)$$

where, J_b represents the difference between analysis variables X and background X_b, B is the background error covariance matrix, X includes three-dimensional wind (u, v, w), potential temperature θ、pressure p and rain water ratio q_r。J_o is observation,which stands for the difference between analysis result $H(X)$ and observation variables y_o, R is the observation error covariance, H is observation operator。J_c is mass conservation constraint。Generally, observation error covariance matrix is the diagonalization matrix which not related to the observation error, and the diagonal elements is the observation error estimate. The observation of the radial velocity is interpolated into the analyze lattice point by 3DVAR system, in that the spatial interpolation for forward difference operator is not needed.

2.2 Assimilation of Doppler radar reflectivity data

ADAS complex cloud analysis method introduced water vapor and moisture based on radar data,with the ground observation of cloud and cloud height and radar data to analysis and microphysis adjustment,and the reflectivity values and threshold will be compared, on the grid points within the scope of radar observations, if the threshold value is high, we take it for clear sky, otherwise, the quantity of humidity such as humidity, landscare, rain, snow, ice, and hailstones on the grid point should be local adjusted in 3d space according to the radar reflectivity.

In the latter analysis, according to the relationship of rain mixing ratio and radar basic reflectivity factor Z:

$$Z = 43.1 + 17.5\log(\rho q_r) \quad (2)$$

where, ρ is air density. Visible, radar reflectivity values factor the water mix ratio.

3 Case Selection and Test Design

We selected a thunderstorm rainfall process as simulated case near jiangsu province at 22:00(UTC) in July 6th 2009 to 02:00 7th in jiangsu province.Control test is double one-way nested grid,and both the inner and outer layer grid center situated at (32.05°N, 118.16°E), the 6h interval NCEP/NCAR $1.0° \times 1.0°$ FNL reanalysis data is as background, and the output data of every 10 minutes of outer layer grid is offered as the inner layer grid lateral boundary condition, and the simulation schemes see table 1.

Figure of radar reflectivity factor at 22:00-02:00 in July 6, 2009(a 22:00,b 23:00,c 00:00,d 01:00,e 02:00),ellipsis

Table 1 Simulation scheme

	Outer layer	Inner layer

Horizontal grid distance	18km	6km
Horizontal grid number	102×102	83×83
The vertical resolution	500m	500m
Layer number	35	35
Cumulus clouds parameter schemes	Kain-Fritsch	none
radiative process	Atmospheric radiative transfer parameterization scheme	
microphysical process	Ice microphysical process	
Earth's surface scheme	double surface model	

We added the radar data in the inner layer initial field from 22 :00,and lasts for 6h. Contrast tests are divided into seven groups, see table 2.

Table 2 7 contrast experiments

Short title	Radar reflectivity data	Radar radial wind data
ref	Initial field assimilation	Not assimilation
vel	Not assimilation	Initial field assimilation
refvel	Initial field assimilation	Initial field assimilation
refs	Every hour assimilation	Not assimilation
vels	Not assimilation	Every hour assimilation
refvels	Every hour assimilation	Every hour assimilation
cntl	Not assimilation	Not assimilation

4 effect that radar reflectivity and radial wind to the initial humidity and wind field

4.1 humidity analysis after radar data added

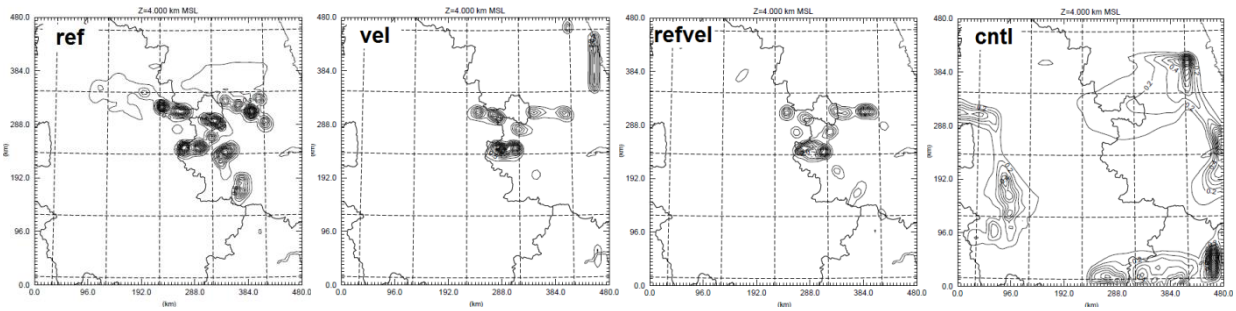

Fig.1 the rain water mixing ratio of ref、vel、refvel and cntl experiments at 23:00(4km height,unit: g/kg

Visible, reflectivity assimilation is better than radial wind assimilation for the moisture forecast, but with the integration, the test will gradually deviated from moisture position and more false liquid water appeared.

4.2 wind field analysis after radar data added

After the initial time that radar data added, the refvel and vel tests appeared wind convergence corresponded to the strong convective center,which means that radial wind data assimilation promoted the mesoscale activity but reflectivity didn't.

With the integration of assimilation, the initial assimilation effect will be weakened gradually. Therefore, the following experiments are designed: the output of an hour will be the initial field of next time for

prediction, and so forth, to observe how much influence for 2-4h forecasting after multiple time radar data assimilated.

4.3 Multiple time radar data assimilation, 1-3 hour moisture field analysis

After a long time continuous assimilation,we found that the tests which reflectivity assimilated—refvels and refs experiments show better liquid distribution than vels test.

The figure of 00:00-02:00 rain water mixing ratio at 4km height(unit:g/kg),ellipsis.

4.4 Multiple time radar data assimilation,wind field analysis

Refs and vels experiments have positive effect on wind field forecast,and refvels test,and refvels test has the advantages of the above two tests,which make the wind field structure and convection activities more apparent.

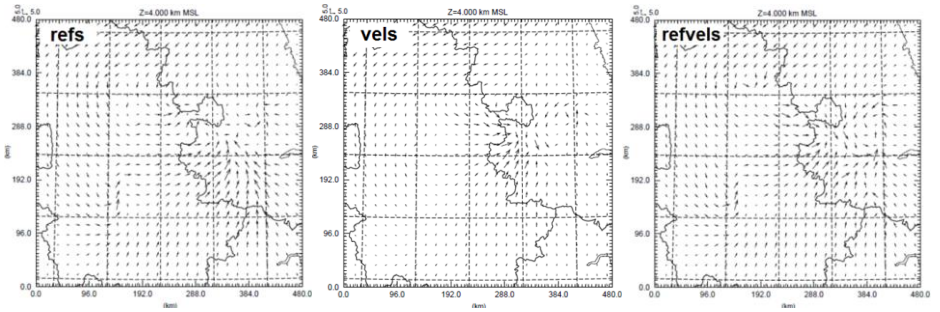

(a)

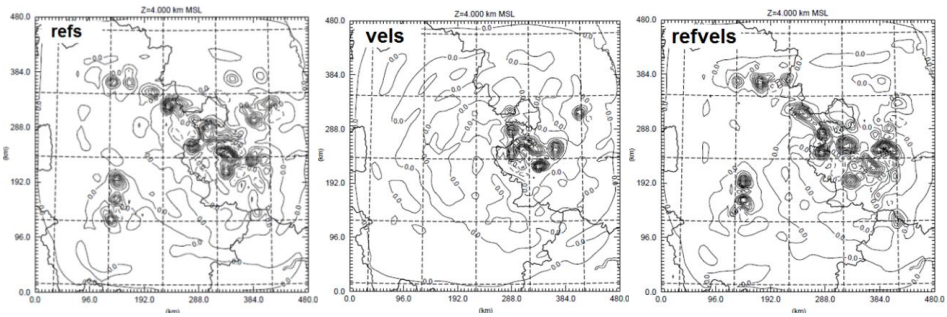

(b)

Fig.2 forcasted wind field at 4km height from refs、vels and refvels experiments (a)u-v wind field (b) w wind field

In order to quantitatively compared, we choose the forecasting wind speed from refvel test near sounding site(32.0 N °, 118.8 E °) at 00:00 to compare the sounding data at the same time.

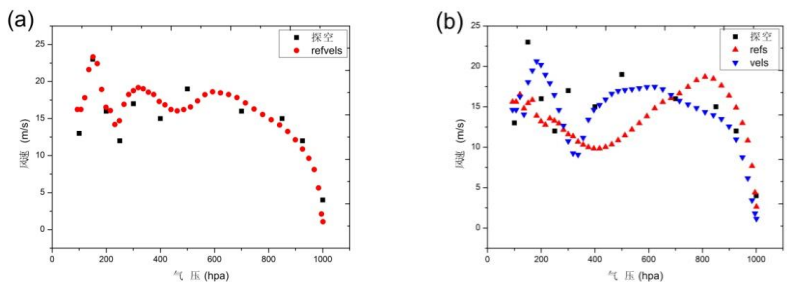

Fig.3 constracting sounding wind velocity at 00:00 with forcasting wind velocity from (a) refvels (b) refs and vels experiments

By figure 3 (a) (b), though there is a certain difference betweem refvels test forecast wind and sounding data, the basic situation and the amplitude can be better reflected. The wind speed that vels forecast not as

good as refvels test.Thus, it can be seen that the test which assimilated wind speed forecast better wind field.

4.4 Comprehensive analysis of the results

In order to compare effect of assimilation tests,we analyzed each test in forecasting divergence field and verticalrain water mixing ratio per hour.Figure4 of forecasted cross-section drawn divergence fields for 2h(22:00-00:00) from all the assimilation experiments (unit:1000g/kg),ellipsis.

Figure 4 is the forecast regional center position divergence vertical section for 2h. Judging from this situation,both the initial field assimilation and multiple time assimilation showed priority of mesoscale convection vertical structure of convergence in the lower level and divergence in the higher level. Also, the reflectivity data assimilation tests showed stronger high-level precipitation conditions than only the wind radial assimilation tests. It is proved that reflectivity assimilation played a key role in the precipitation forecast.

Figure 5 is the contrast that the tests' three hours forecast of 22:00-01:00 with TRMM satellite measured 3 hours rainfall precipitation. By contrast with other tests, we can see that there is good correspondence with the reflectivity assimilated tests (ref,refs,refvel,refvels) and precipitation TRMM satellites measured rainfall,especially multiple time reflectivity and racial wind assimilated test refvels,whose southwest false vapor weakened than refs test, wherever the control test reflect has large deviation of precipitation position. Refvel vel, ref, precipitation test for 60mm, energy 80mm 120mm, and the maximum precipitation of refvels vels refs tests, respectively achieved 160mm 60mm, TRMM 120mm, and measured rainfall 80mm only. Visibly, comprehensive examinated of rainfall precipitation and location prediction, refvels test is more reasonable.

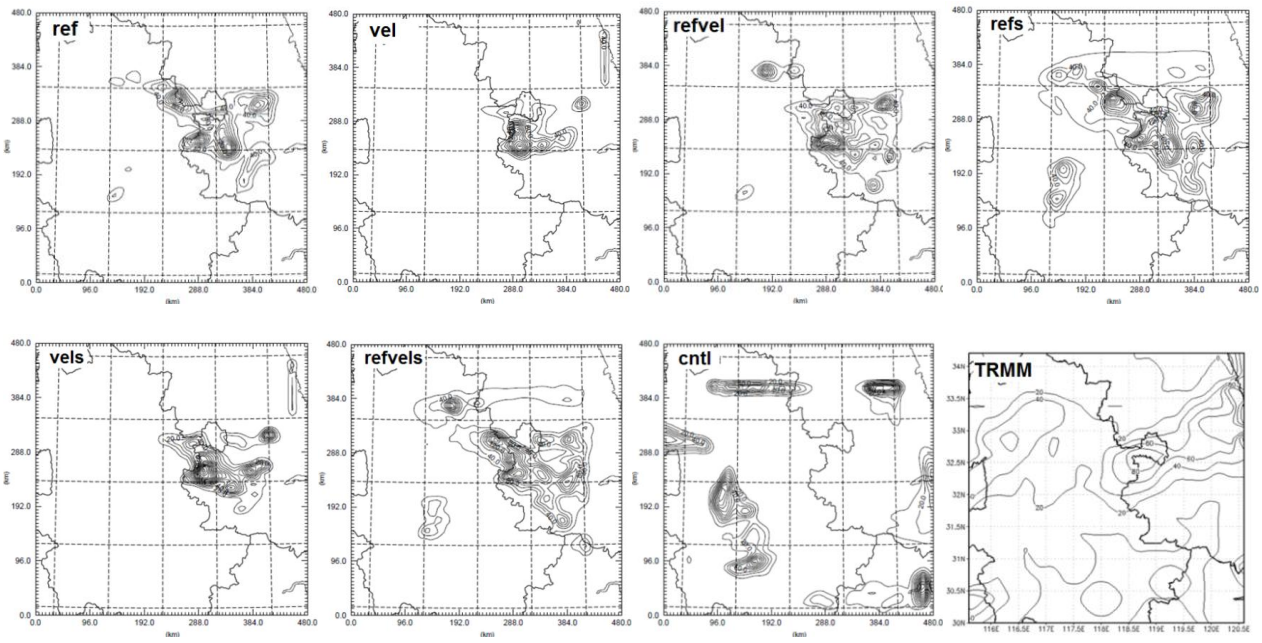

Fig.5 constrasting the amount of precipitation forecasted for 3h (22:00-01:00) from all the experiments with TRMM satellite observations of 3h precipitation

5 Conclusions

Doppler radar reflectivity and radial velocity data are added directly to the mesoscale model ARPS (The Advanced Regional Prediction System) in numerical simulation by its data processing system ADAS (ARPS Data Analysis System). The experiments include: control experiment, reflectivity assimilated

experiment, velocity assimilated experiment, both the two kinds of data assimilated, and continuous assimilion at multiple times experiment.

By simulating one rainstorm process around Jiangsu Province, we analyzed the impact of improving the initial field and getting better forecast results which brought by the two kinds of radar data added in differernt combinations, and came to the following conclusions:

(1) reflectivity data and radial velocity mainly separately adjusts the moisture field and strengthened the meso-microscale information, both the two kinds of radar data assimilated preformed better than either one kind of radar data added within 2 hours.

(2) Compared with other assimilative experiments, the predicted wind speed from the multiple times' assimilating experiment with two kinds of radar data was more close to the sounding wind speed, and the predicted position of rainfall from this experiment had better relationship with TRMM observation, with a considerable error of precipitation amount.

REFERENCE

[1] Kasahara A , Balgovind R C , Katz B. Use of satellite radio metric imagery data for improvement in the analysis of divergent wind in t he tropics. *Mon. Wea. Rev.* , 1988 , **116** : 866～883.

[2] Wei Li, Yuanfu Xie, Shiow-Ming Deng, Qi Wang. Application of the Multigrid Method to the Two-Dimensional Doppler Radar Radial Velocity Data Assimilation[J].Journal of Atmospheric and Oceanic Technology,2010,27(2):319-332.

[3] 闵锦忠;彭霞云;赖安伟;杜宁珠. 反演同化和直接同化多普勒雷达径向风的对比试验[J]. 南京气象学院学报 , Journal of Nanjing Institute of Meteorology, 2007(06).

[4] Qingyun Zhao, John Cook, Qin Xu, Paul R. Harasti Improving Short-Term Storm Predictions by Assimilating both Radar Radial-Wind and Reflectivity Observations [J].Weather and Forecasting.2008,23(3): 373-391.

[5] Gu, W., H. Gu, and Q. Xu. Impact of single-Doppler radar observations on numerical prediction of 7 May 1995 Oklahoma squall line. Preprints, Fifth Symp. on Integrated Observing Systems, Albuquerque, NM, Amer. Meteor. Soc., 2001: 139–142.

[6] Xiao Q., Zhang X., Davis C., Tuttle J., Holland G., Fitzpatrick P.J. Experiments of hurricane initialization with Airborne Doppler radar data for the Advance Research Hurricane WRF (AHW) model[J].Mon.Wea.Rev., 2009,137(9):2758-2777.

[7] Pu,Z.,Li,X.,Sun,J. Impact of airborne doppler radar data assimilation on the numerical simulation of intensity changes of hurricane dennis near a landfall [J]. J.Atmos. Sci.2009,66(11):3351-3365.

[8] Zhao, K., Xue, M. Assimilation of coastal Doppler radar data with the ARPS 3DVAR and cloud analysis for the prediction of Hurricane Ike. [J] Geophysical Research Letters,2008,
36(12),Article number L12803.

[9] Sugimoto, S., Andrew Crook, N. , Sun, J., Xiao, Q., Barker, D.M. An examination of WRF 3DVAR radar data assimilation on its capability in retrieving unobserved variables and forecasting precipitation through observing system simulation experiments [J].Mon.Wea.Rev.,2009,137,(11): 4011-4029.

[10] 杨艳蓉,王振会,杨洪平,张沛源,李柏. 多普勒雷达反射率与径向风资料在数值模式中的应用试验[J].2008,(6)

[11] 王瑾; 刘黎平;CINRAD/CD 雷达反射率因子同化对中尺度数值模式云微物理量场调整的分析.[J]高原气象 ,Plateau Meteorology

Development of Rapid Update Cycle Forecasting System Based on AREM Model and Its Real-Time Rainfall Forecasts during Flooding-Season of 2009 in China

WANG Ye-hong, ZHAO Yu-chun, PENG Ju-xiang, and LI Hong-li
Institute of Heavy Rain, China Meteorological Administration, 430074, Wuhan, China. yehongw0120@yahoo.com.cn

Abstract

AREM (Advanced Regional η-coordinated Model) model is a heavy rain numerical forecasting model and play a very important role in rainfall forecast in China, which has a special process for the large and high topography in China and takes climatic features in East Asia into consideration. Several faults are still not solved: (1) the model is initialized in a cold-start way, which usually lead to model SPIN-UP problem. (2) Radar detections are not applied in the model due to the limitation of data assimilation system. (3) A large amount of high-frequency observational data is not used due to its two-time run in a day, which results in the fact that the model forecast cannot be updated in time.

Aimed at above-mentioned faults, Wuhan Institute of Heavy Rain of CMA (China Meteorological Administration) introduced LAPS (Local Analysis and Prediction System) system and set up a 3-hourly rapid update cycle based on AREM model (AREM-RUC). It has three advantages when compared with AREM model: (1) the model is initialized in a warm-start way and the model SPIN-UP phenomena is reduced. (2) High-frequency data are used in the model, such as radar detections and intensive automatic weather station observations. The initial field contains much more mesoscale information and the model rainfall forecast is improved. (3) The AREM-RUC gives a new forecast every 3 hours according to latest observational data, which improves rainfall now-casting and short-time forecast.

AREM-RUC began to run operationally on 20 May 2009 and its forecast products were broadcast every 3 hours through the website of Institute of Heavy Rain, which played a very important role in flooding-season of 2009. The rainfall forecast statistics and the analysis of typical heavy rain process during June to December 2009 showed that AREM-RUC reduced SPIN-UP phenomena due to its warm-start run, improved a lot rainstorm forecast, especially extremely heavy rain forecast due to its 3-hourly forecast update, and gave a much more accurate forecast for mesoscale systems due to its effective assimilation of Doppler radar detections and intensive automatic weather station observations in the initial field.

1. Introduction

With the rapid development of social economy and meteorology science, people are more and more reliant on meteorology, especially for some special trades that are highly sensitive to weather such as aviation, updated weather forecast based on latest observation data is needed. Besides, state government and people pay much attention on some sudden severe weather. So, continually updating short-time nowcasting technique is an essential problem to meteorological persons.

In late 1980's, the study of weather prediction based on high-frequency observation data was started in the United States. In Sep 1994, NOAA/NCEP began to put the first Rapid Update Cycle Forecasting System into operation, which called RUC-1, with once data assimilation every 3h and the model resolution of horizontal 60km and vertical 25 levels. In later more than ten years, RUC system was developed continuously in FSL and NOAA/NCEP. At present, two 1h Rapid Update Cycle Forecasting Systems with respective resolution of 20km (RUC-20) and 13km (RUC-13) are operational run parallel in NOAA/NCEP.

In recent years, some achievements are gained in the research of Rapid Update

Cycle Forecasting System in China. Guangzhou Institute of Tropical Oceanic Meteorology built CHAF on the base of GRAPES model and its assimilation system. In this system, non-conventional detecting data of high spatial-temporal resolution such as satellite, radar, automatic station data are assimilated to generate a high -quality grid field for weather analysis. And such hourly 3D fine initial field with multi factors is also provided to forecast model, which establishes a good base to fine prediction. Beijing Institute of Urban Meteorology developed WRF-RUC, a 3h Rapid Update Cycle assimilation analysis and 3km-resolution fine numerical model forecasting system based on WRF model and its assimilation system, which uses local dense observation and remote sensing data in Beijing and is suit for Northern China. This system plays an important role in 2008 Olympic Games weather service.

AREM (Advanced Regional η-coordinated Model) model is a meso-scale heavy rain numerical forecasting model with Chinese own intellectual property rights. It shows evident advantages in East-Asia heavy rain forecast and is widely used in many operation and research organizations. In 2009 Wuhan Institute of Heavy Rain developed a Rapid Update Cycle Forecasting System Based on AREM Model （AREM-RUC）, which is significant to promote the development of AREM and improve precipitation prediction.

2. Development of AREM-RUC

AREM model is a heavy rain numerical forecasting model and play a very important role in rainfall forecast in China, which has a special process for the large and high topography in China and takes climatic features in East Asia into consideration. Several faults are still not solved: (1) the model is initialized in a cold-start way, which usually lead to model SPIN-UP problem. (2) Radar detections are not applied in the model due to the limitation of data assimilation system. (3) A large amount of high-frequency observational data is not used due to its two-time run in a day, which results in the fact that the model forecast cannot be updated in time.

LAPS（Local Analysis Prediction System， Mcginley，et al，1992，Albers，et al，1996）is developed by NOAA/FSL which can assimilate effectively multi kinds of data including satellite, radar, GPS, radio sonde, automatic station, wind profiler, microwave radiometer data etc., and provide a high special-temporal meso-scale 3D grid analysis field, which is one of the most advanced meso-scale analysis systems.

Aimed at above-mentioned faults, Wuhan Institute of Heavy Rain of CMA (China Meteorological Administration) introduced LAPS (Local Analysis and Prediction System) system and set up a 3-hourly rapid update cycle based on AREM model (AREM-RUC). It has three advantages when compared with AREM model: (1) the model is initialized in a hot-start way and the model SPIN-UP phenomena is reduced. (2) High-frequency data are used in the model, such as radar detections and intensive automatic weather station observations. The initial field contains much more mesoscale information and the model rainfall forecast is improved. (3) The AREM-RUC gives a new forecast every 3 hours according to latest observational data, which improves rainfall now-casting and short-time forecast.

3. Result of AREM-RUC real-time forecast in 2009

AREM-RUC began to run operationally on 20 May 2009 and its forecast products were broadcast every 3 hours through the website of Institute of Heavy Rain. The process is shown as Fig.1.

AREM-RUC runs for 8 times per day and provides 36h forecast. Its initial field is provided by LAPS analysis field and side-boundary condition by NCEP 3h forecast field. At 00UTC and 12UTC, LAPS assimilates the data of radio sonde, automatic station and radar, and at the else time(03、06、09、15、18、21UTC), the data of automatic station and radar are assimilated.

AREM-RUC began to run operationally on 20 May 2009 and its forecast products were broadcast every 3 hours through the website of Institute of Heavy Rain, which played a very important role in flooding-season of 2009.

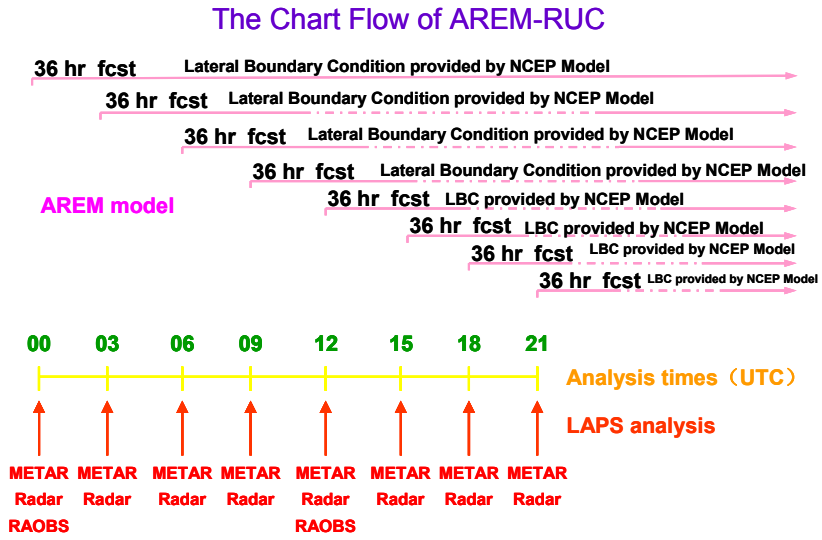

Figure 1: The chart flow of AREM-RUC

Fig.2 shows the Threat Score (TS) of the 0-24h rainfall forecast from 1 Jun to 14 Dec 2009 of AREM-RUC and other two editions of AREM model operationally run in Wuhan Institute of Heavy Rain. There are 6 TS areas: China, the Yangtse River valley, South China, North China, North-eastern China, East South-western China. Results show that for rainfall >50mm -100 and >100m in North-eastern China, the TS of AREM-RUC is lower than that of AREM-YW. For the other else rainfall amount in other else areas, the TS of AREM-RUC is always higher than that of AREM-YW and AREM-SY.

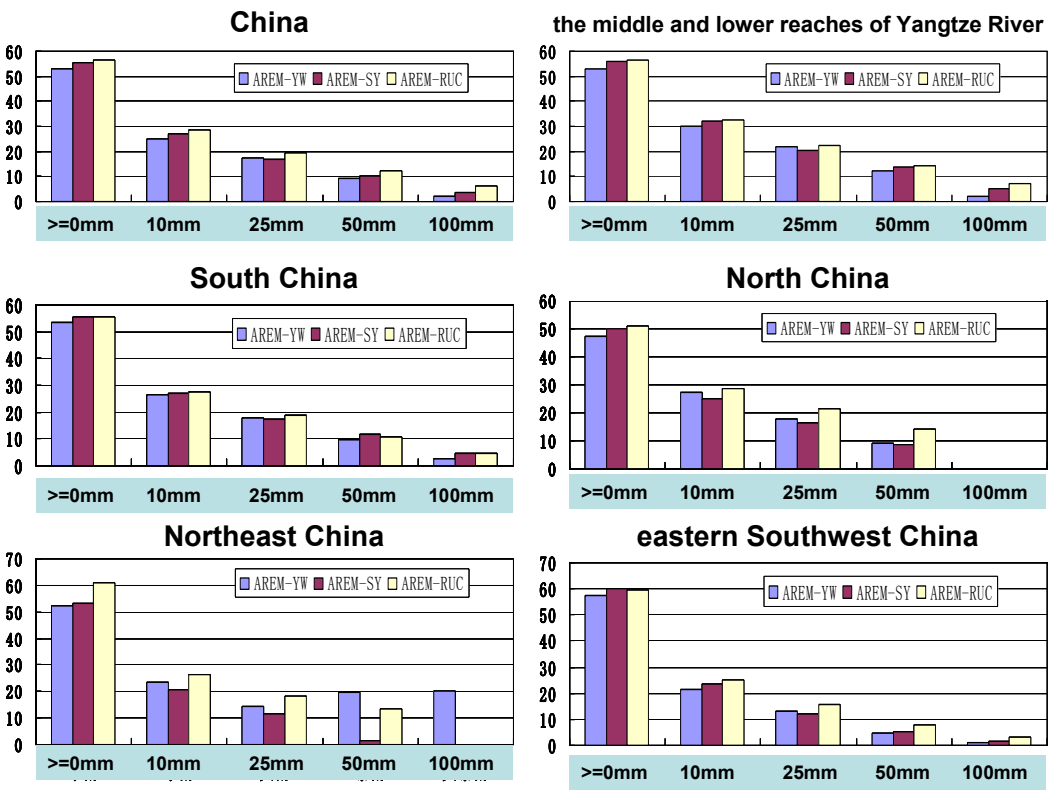

Figure 2: Threat Score (TS) of the rainfall forecast from 1Jun to 14 Dec 2009（%）

During 00UTC 29-30 June 2009, an extreme heavy rain process has occurred in the areas including southwestern Hubei, Jianghan plain, northeastern Hubei and middle-southern Anhui and the greatest precipitation is near to 300mm. This event is

successfully forecast by AREM-RUC and the rain belt range, strong rainfall center position and rainfall amount are close to observation, which is much better than the forecast result of AREM-YW and AREM-SY(Fig.3). AREM-RUC played a very important role in flooding-season of 2009.

4. Conclusion

The rainfall forecast statistics and the analysis of typical heavy rain process during June to December 2009 showed that AREM-RUC reduced SPIN-UP phenomena due to its hot-start run, improved a lot rainstorm forecast, especially extremely heavy rain forecast due to its 3-hourly forecast update, and gave a much more accurate forecast for mesoscale systems due to its effective assimilation of Doppler radar detections and intensive automatic weather station observations in the initial field.

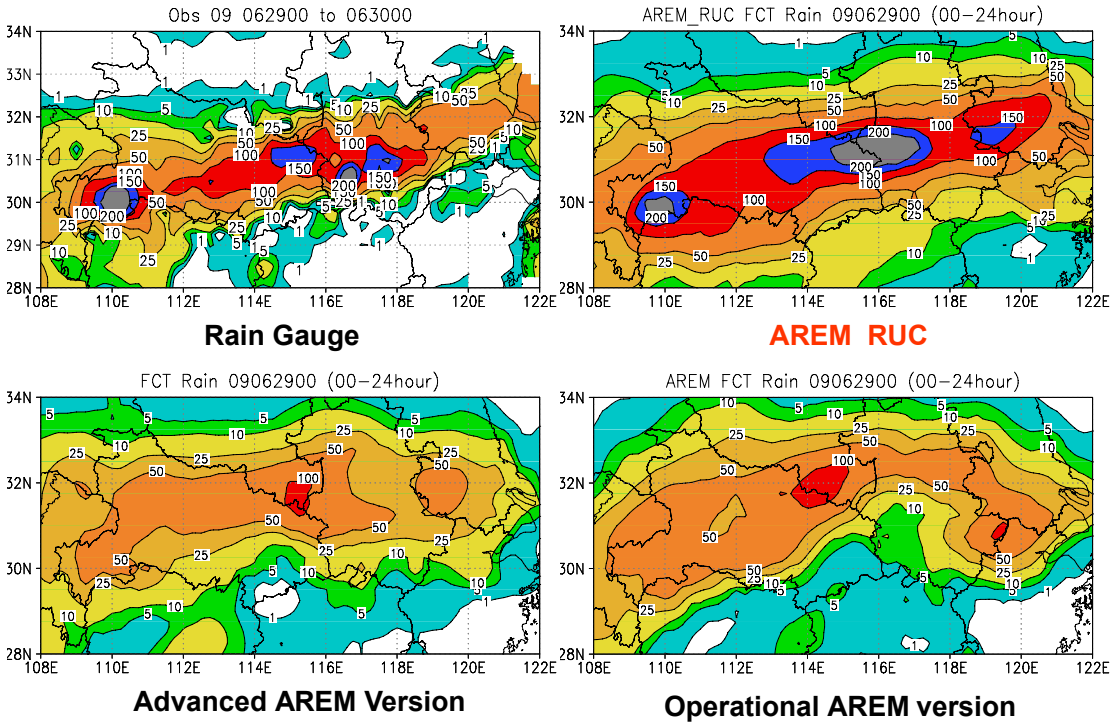

Figure 3: Precipitation during 00UTC 29-30 June 2009 (mm)

a)observation；b)AREM-RUC forecast；c)AREM-SY forecast；d)AREM-YW forecast

Acknowledgments:

This study has been supported by the following projects: Meteorological research project of public sector of Ministry of Science and Technology (NO: GYHY200706012, GYHY200906010). Scientific research project of Wuhan Institute of Heavy Rain (NO: 0903,1009)

5. References

Mcginley J, Albers S, Stamus P. 1992: Local data assimilation and analysis for nowcasting. *Adv Space Res*, 12(7): 179-188.

Albers S C, Mcfinley J A, Birkenhuer D A, et al. 1996: The local analysis and prediction system (LAPS): Analysis of clouds, precipitation and temperature. *Wea Forecasting*, 11(3): 272-287.

Chen Zitong, Huang Yanyan, Wan Qilin, et al. 2010:Rapid updating cycle assimilation and forecasting system and its experiments and analysis in flood seasons. *Journal of Tropical Meteorology*, 26(1): 49-54.

Session F

Precipitation variability and climate change

Representation of Monsoon Systems in Regional Climate Models

Bodo AHRENS, Andreas DOBLER, Steffen KOTHE
Institute for Atmospheric and Environemntal Sciences, Goethe-University Frankfurt/Main, Germany
bodo.ahrens@iau.uni-frankfurt.de

Abstract This paper shows downscaling experiments with the regional climate model COSMO-CLM in the domains of the Indian summer monsoon (ISM) and the West Africa monsoon (WAM). It discusses the representation of the monsoon systems in the regional model and the added value of regional climate simulation with respect to different driver data: re-analysis and global climate model data. The discussion is guided by the application of simple indices based on rainfall, outgoing longwave radiation, and wind shear. Major findings are that it is very difficult for the regional model to add value at the monsoon system scale and that the reasons are different for ISM and WAM.

1 Introduction

The West African monsoon (WAM) and the Indian summer monsoon (ISM) are seasonal wind reversal phenomena driven by heat lows over the Sahara/Sahel region resp. the Tibetan plateau connected with a northward displacement of the intertropical convergence zone and inland transport of moist air. Both regions receive most of its annual precipitation during the monsoon season from June to September.

It is important to understand the processes involved in the observed inter-annual variability and long-term trends of the monsoon intensities. For example, observational data indicate a decreasing trend of monsoon precipitation in West Africa over the last 30 years (Nicholson et al. 2000, Le Barbé et al. 2002), but the causes for this change are not well understood. To foster understanding of the monsoonal system often sensitivity studies with climate models are performed. These studies illustrate, for example, the importance of sea surface temperature or land-use (Vizy & Cook 2002, Charney 1975, Paeth et al. 2009). But, at the same time global and regional climate models show limited ability to simulate the monsoonal systems (Xue et al. 2010, Kothe & Ahrens 2010).

The motivation of this study is to evaluate the regional climate model COSMO-CLM for the WAM and ISM, and to learn about the reasons of model deficits. The goal is to quantify the added value by nested higher-resolution simulations in comparison to the forcing global data sets at about their scale. Here, the global data sets are the ECMWF re-analyses products and simulations with the GCM ECHAM5. Therefore, the presented evaluation focused on mean monsoonal states, spatial and inter-annual. This will lead in improvements of COSMO-CLM and its enhanced applicability in sensitivity studies, seasonal and longer climate predictions in monsoonal climate systems.

Studies of the ISM (e.g., Wang & Fan 1999, Dobler & Ahrens 2010) and the WAM (e.g., Fontaine et al. 2008) showed that certain indices are useful for the investigation of the representation of the monsoon in the model simulations. Here, we use indices based on precipitation, outgoing long-wave radiation, and zonal and meridional wind components. These are described in Sec. 3 after a short model and setup description in Sec. 2. Section 4 presents some results and this is followed by conclusions.

2 Model and model setup

The COSMO-CLM (COnsortium for Small-scale MOdeling-Climate Limited-area Model) is a state-of-the-art non-hydrostatic regional climate model (RCM). It is the climate version of the COSMO-model (see http://www.cosmo-model.org), which several European weather services use for mesoscale weather forecasting. The first climate version of COSMO-CLM has been available in summer 2002 (see http://www.clm-community.eu).

In this study we investigated two climate simulations for each monsoonal system, ISM and WAM. The setup for these two simulations was identical, but two different datasets were used as driving data at the lateral boundaries: (a) the ECMWF ERA-Interim (time period 1989 until 2008, Dx ≈0.70°) and ERA40 (1958-2000, ≈1.125°) re-analysis for WAM and ISM, respectively, and (b) ECHAM5 data (1960-2000, ≈1.88°). The computational domains with 0.44° grid-spacing of the COSMO-CLM simulations were the whole African continent and a South-Asian domain (Fig. 1). More on used parameterizations can be found in Dobler & Ahrens (2008).

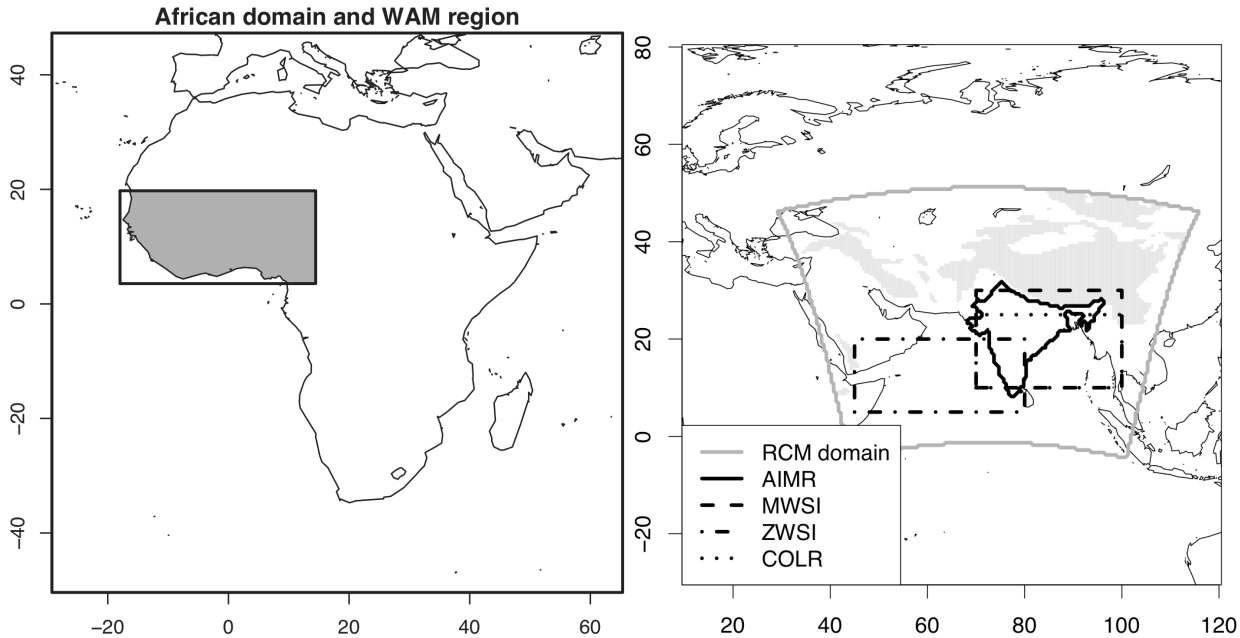

Figure 1: COSMO-CLM model domains for WAM (whole area, left) and ISM (outlined in grey, right). Also the evaluation index analysis domains are indicated. There is one common index domain for WAM (shaded grey) and several for the different indices for ISM

3 Evaluation indices and reference data

Many indices have been used to objectively describe monsoon circulation and quantify its variability. Most of these indices are based on precipitation, but other indices are based on the magnitude of mean summer vertical wind shear, or the outgoing long-wave radiation (OLR) as an indication of convection. In recent years, there has been a lot of discussion about which index is best (e.g. Wang 1999, Fontaine et al. 2008).

For this study, we chose indices based on precipitation (the well defined All India Monsoon Rainfall indes for ISM), OLR, and zonal and meridional wind components. The wind components are used to define vertical wind shear indices describing the monsoonal dynamics and monsoon cell circulation. For WAM the wind shear in 900 hPa and 200 hPA is used to define the WAMI (Fontaine et al. 2008). A larger than average WAMI represents an enhanced southwesterly monsoon flux and a stronger tropical easterly jet. For ISM the wind components in 850 hPa and 200 hPa are used in the zonal and meridional wind shear indices (ZWSI and MWSI, resp.) following Wang and Fan (1999) and Goswami et al. (1999).

Due to disagreement in the definition of the indices' domains in the literature we have chosen a common index domain for WAM and different domains for the different chosen indices for ISM as shown in Fig. 1. All data is interpolated to the grids of the respective observational reference data sets. In the following only index values for the monsoon seasons are shown.

We used the Global Precipitation Climatology Centre (GPCC) data product version 4 (see htpp://gpcc.dwd.de) as the reference dataset for precipitation. GPCC provides a dataset of globally gridded rain gauge measurements with a spatial resolution of 0.5°. For OLR we used the NASA/GEWEX SRB (Surface Radiation Budget) dataset (release 2.5, July 1983 to June 2005) on a 1° grid (Gupta et al., 2006) for WAM and data from NOAA (Liebmann and Smith 1996) for ISM. Due to the low cloud-top temperature of high convective clouds, a low OLR value indicates high convective activity. The meridional and zonal wind components for the calculation of the wind shear reference were taken from the re-analysis product of the National Centers for Environmental Prediction/National Center for Atmospheric Research (NCEP/NCAR). The NCEP re-analysis output variables were classified into four categories, depending on the relative influence of the observational data and model on the gridded variable. The wind fields were classified as "category A files", which are highly influenced by observations and can be considered to be the most reliable class of NCEP output variables.

4 Results

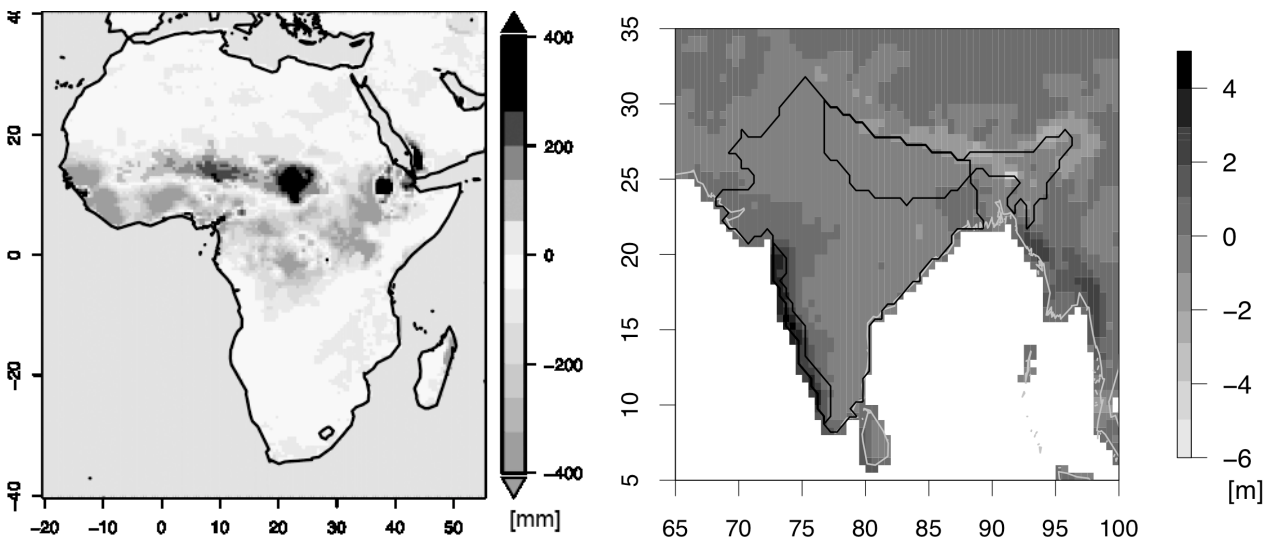

Figure 2: Monsoon mean precipitation difference of COSMO-CLM simulations driven by re-analysis data and the GPCC dataset

Figure 2 shows the mean monsoonal difference patterns of the COSMO-CLM simulations forced with ERA reanalysis with the observational data set. There are substantial differences. For example, COSMO-CLM overestimates precipitation in the Sahel and underestimates precipitation by up to 50% along the West coast and Central Africa. In both simulation, ERA and ECHAM5 driven, COSMO-CLM extends the main precipitation region too far north. In the South-Asian domain both simulations overestimate precipitation along the west coasts. COSMO-CLM with ERA forcing even overestimates precipitation by more than 100% at the western coast of India windward of the coastal mountain ridge. At the same time the model underestimates precipitation in the northern part of India, in the Himalayan foothills, with mean values of 402 mm and 340 mm for the ERA and ECHAM5 driven simulations, respectively, compared to 900 mm estimated by the observational data set.

Figure 3 compares the mean spatial precipitation fields of the different model based data sets with the GPCC data set using simple statistics. Despite the spatial patterns of differences in COSMO-CLM simulations discussed above, the regional climate model is able to add value on the simulations by the global climate model ECHAM5. COSMO-CLM is not able to improve on the re-analyses. The regional model seems to overestimate variability for ISM because of the systematic and substantial over- and underestimation in discussed regions. Thus, this is implied by large-scale differences and by errors at the sub-global data scale.

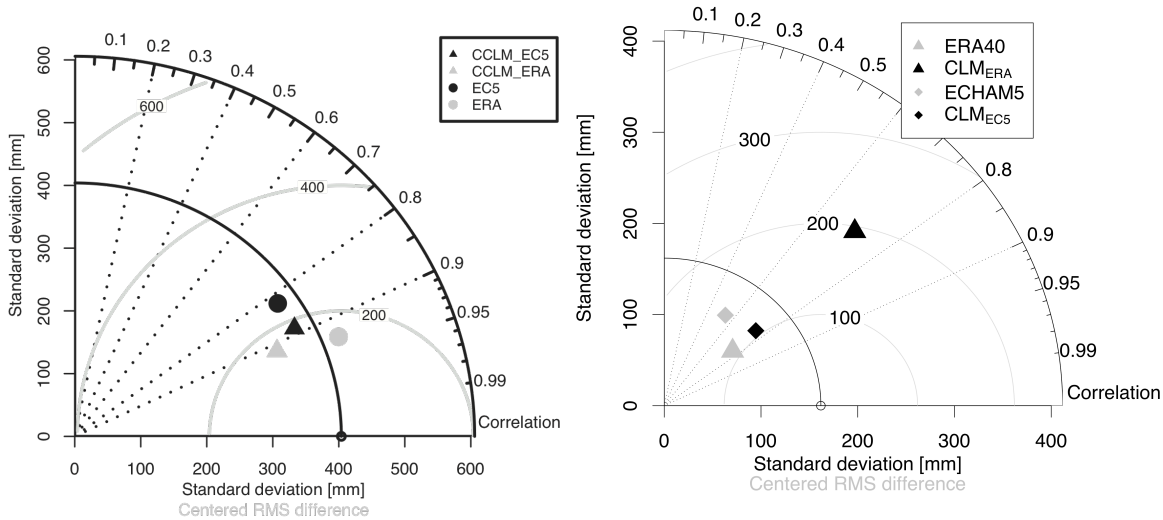

Figure 3: Taylor-diagram of the mean spatial precipitation fields for WAM (left) and ISM (right) simulated

by the global models and COSMO-CLM compared to the GPCC data set

OLR is underestimated over the ocean in all COSMO-CLM simulation.s The underestimation is even more in the ECHAM5-driven simulations than in the ERA-driven simulations, that is probably connected to higher sea surface temperatures in ECHAM5 than in ERA. These sea surface temperatures are the prescribed ones in the COSMO-CLM simulations. We used OLR as in indicator of wide-spread convective activity: grid boxes with OLR values below 180 W/m^2 are assumed to be convectively dominated. Thus, COSMO-CLM overestimates convective activity over the ocean and also over Central Africa with more than twice as many convective days in the simulations as in the observations (not shown).

Figure 4 compares the mean spatial patterns of OLR. It shows that COSMO-CLM increases spatial variability of convection, which is related to the overestimation of convection. This can be seen especially for ISM with the OLR index domain is largely over the ocean.

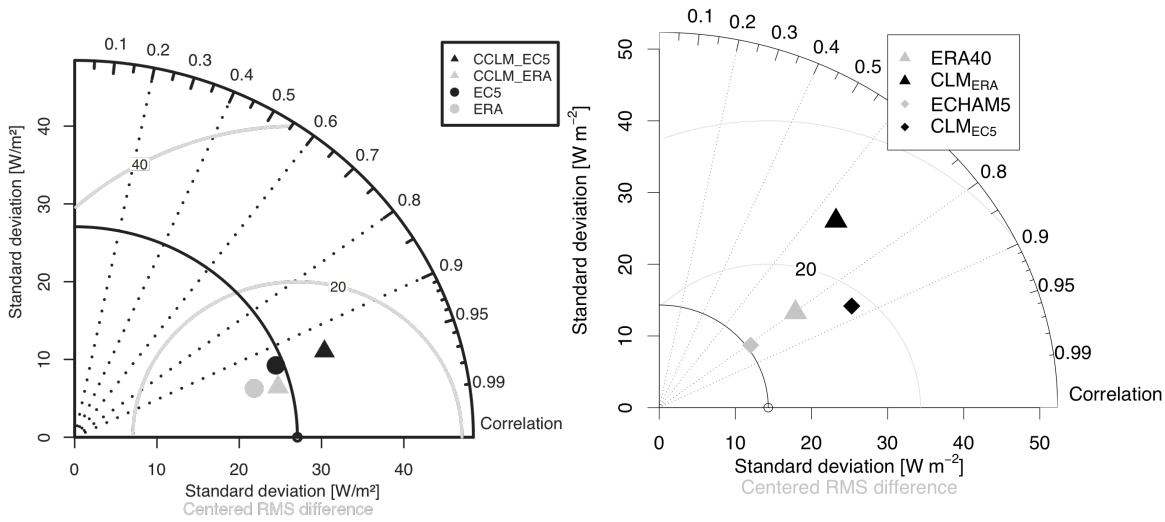

Figure 4: As Fig. 3, but for outgoing longwave radiation OLR

The dynamical indices indicate that COSMO-CLM is not able to improve the representation of the monsoonal circulation. For WAM the COSMO-CLM overestimates WAMI indicating a too intense circulation. For ISM COSMO-CLM and ECHAM5 overestimates the zonal and underestimates the meriodional wind shear suggesting that the models have difficulties in representing the monsoon Hadley circulation (Goswami et al. 1999).

Looking at temporal correlations of the analysis domain-averaged indices, we saw that the value for the precipitation and dynamical index pair is smaller than for the precipitation and OLR pair in the observational reference (0.6 and 0.9, respectively) for WAM. Both values are larger in the reference data than in all the model-based data sets. COSMO-CLM overestimates and the global models underestimate the correlation of OLR and the dynamical index for WAM. For ISM, there is anticorrelation between the time series of precipitation and OLR (note the definition of the index analysis domains). And, in all models this anticorrelation was higher than in the reference data. Thus, precipitation over India was overly influenced in the models by convection over the Arabian Sea and the Bay of Bengal.

5 Conclusions

We found that in both simulation domains COSMO-CLM was able to represent the main features of the monsoon system. As expected the regional climate model was able to improve on the forcing data given by ECHAM5 in terms of spatial distribution of precipitation. The regional model is able to better represent the complex topography; for instance, the orography of the Tibetan Plateau was better represented in the RCM because of the higher resolution. But, there was not much improvement to be seen over the ERA reanalysis data sets in the spatial distribution of precipitation, vertical wind shear, or outgoing longwave radiation, either.

COSMO-CLM showed a clear overestimation of convective activity in general, which is only partly

explained by higher sea surface tempereature in ECHAM5 than in ERA. But, nevertheless there was a underestimation of precipitation simulated in Central Africa and a-long the Himalayan foothills. The latter underestimation is related to an underestimation of precipitation and convective activity during night-time (not shown here). The overestimation of precipitation in the Sahel is related to a surface temperature warm bias over the Sahelian and Sahara region and a too intense monsoon circulation in the WAM simulation. The zonal circulation seems too intense also for ISM and this is related to the precipitation overestimation along the west coast mountain ridges. These deficiencies are at the large scale. This paper mainly discussed monsoon features, which are large enough to be also represented in the global models. The results showed that the regional climate model does not improve the global data in all aspects, and the example of precipitation underestimation along the Himalayan foothills showed that there are deficits in the regional scale too. Still, dynamical downscaling with COSMO-CLM in the monsoon regions is expected to add value if climate projection data for climate impact studies is needed.

Acknowledgments. The authors acknowledge funding from the Hessian Initiative for the Development of Scientific and Economic Excellence (LOEWE) through the Biodiversity and Climate Research Centre (BiK-F), Frankfurt am Main.

References

Charney JG (1975) Dynamics of deserts and drought in the Sahel. Q J R Meteorol Soc 101:193-202

Dobler, A., and B. Ahrens (2008), Precipitation by a regional climate model and bias correction in Europe and South Asia, Meteorol Z, 17(4), 499–509.

Dobler A, Ahrens B (2010) Analysis of the Indian summer monsoon system in the regional climate model COSMO-CLM. J Geophys Res., 115, D16101

Fontaine B, Louvet S, Roucou P (2008) Definition and predictability of an OLR-based West African monsoon onset. Int J Climatol 28(13):1787-1798

Goswami BN, Krishnamurthy V, Annamalai H (1999) A broad scale circulation index for the interannual variability of the Indian summer monsoon. Quart J Roy Meteor Soc 125:611-633

Gupta SK, Stackhouse PW, Mikovitz JC, Cox SJ, Zhang T (2006) Surface radiation budget project completes 22-year data set. GEWEX WCRP News 16(4):12-13

Kothe S, Ahrens B (2010) The Radiation Budget in Regional Climate Simulations for West Africa. J Geophys Res. In print.

Liebmann, B., and C. A. Smith (1996), Description of a complete (interpo- lated) outgoing longwave radiation dataset, Bull Am Meteorol Soc, 77(6), 1275–1277.

Paeth H, Born K, Girmes R, Podzun R, Jacob D (2009) Regional climate change in tropical and northern Africa due to greenhouse forcing and land use changes. J Climate 22(1):114–132. doi:10.1175/2008JCLI2390.1

Vizy EK, Cook KH (2002) Development and application of a mesoscale climate model for the tropics: Influence of sea surface temperature anomalies on the West African monsoon. J Geophys Res 107:4023. doi:10.1029/2001JD000686

Wang B, Fan Z (1999) Choice of south Asian summer monsoon indices. Bull Amer Meteor Soc 80(4):629-638

Xue Y, De Sales F, Lau W, Boone A, Feng J, Dirmeyer P, Guo Z, Kim KM, Kitoh A, Kumar V, Poccard-Leclercq I, Mahowald N, Moufouma-Okia W, Pegion P, Rowell D, Schemm J, Schubert S, Sealy A, Thiaw W, Vintzileos A, Williams S, Wu ML (2010) Intercomparison and analyses of the climatology of the West African Monsoon in the West African Monsoon Modeling and Evaluation project (WAMME) first model intercomparison experiment. Clim Dyn. doi:10.1007/s00382-010-0778-2

Spatial and Temporal Variability Characteristics of Precipitation in Huai River Basin during 1961-2005

LU Yan-Yu[1], WU Bi-Wen[1], Tian Hong[1] and Sun Wei[2]

（1 Anhui Climate Centre, 2 Anhui Meteorological Information Centre, Hefei 230061）

Abstract Surfaces of precipitation at resolution of 1km×1km were generated by the series data from 170 observation stations in Huai River basin from 1961 to 2005, using Kriging interpolation method. Based on the grid data series, the spatial and temporal variability characteristics of precipitation in Huai River basin were analyzed. Results showed that the higher precipitation occurred in the south of the basin, as compared with the less in the north. There is a weak negative trend with large inter-annual variabilities of annual precipitation in recent 45 years, and the rainfall of various season have different change patterns. The linear trend analyses and Mann-Kendall trend test indicated that the changing trends of precipitation did not arrive at the significant level in Huai River basin. Nevertheless, the inter-decadal variabilities of annual and flood season precipitation have obvious phase characteristics. The precipitation presents decline trend before 1990s, while an apparent increasing trend after 2000. At present, the precipitation of Huai River basin is in a phase of high climate variability. During recent 45 years, there is an evident variation in the spatial distribution of precipitation in Huai River basin, which is represented by an increase trend of precipitation in the upper and middle Huai River, and a decline trend in the northeast of basin.

Key words Kriging method, Precipitation, Huai River basin, spatial distribution, changing trend

Variability of Rainfall, Increasing trend of One Day Heavy Rainfalls in Sri Lanka in the Context of Climate Change

K.H.M.S. PREMALAL
Department of Meteorology
Colombo 07
Sri Lanka

Abstract

Global climate is changing mainly due to rapid increase of emission of greenhouse gases through the anthropogenic activities. Fourth Assessment Report (AR4) of the Intergovernmental Panel on Climate Change (IPCC) has documented that the global temperature had increased by about 0.74^0C during the period 1905 - 2006. It is also indicated that there is a strong possibility of changing climate pattern with the climate change.

Recent analysis of temperature data in Sri Lanka shows, temperature has increased by 0.2 degree Celsius per decade during the period 1951-2008. It has been observed that extreme climatic conditions related to temperature and precipitation have also been increased in Sri Lanka during the analysis period. This study was mainly focused to find out the behavior of rainfall pattern during the last 60 years with area average rainfall over the region. It shows a decreasing trend of rainfall in all 25 districts and trends are higher in wet zone (Annual rainfall > 2500mm) than dry zone (Annual rainfall < 1750). Total rainfall has decreased by an average of 9% and it varies between minimum 2 mm per year in Jaffna to the maximum 19 mm per year in Kegalle. Climatic zones also slightly shifted with the decreasing rainfall.

Though the rainfall pattern has a decreasing trend, the variability of rainfall plays an important role in different economical sectors such as agriculture, water and energy. Two periods namely, 1951-1979 and 1980-2008 were selected to compare the Coefficient of Variability (CV) and it reveals that the CV during the period 1980-2008 has increased than 1951-1979 period. Substantially high CV of rainfall could be a good measure of high rainfalls (floods) and low rainfalls (droughts) events in any region or country.

1. Introduction

Climate of Sri Lanka can be divided into four seasons namely, First inter-monsoon (March – April), Southwest monsoon (May – September), Second inter-monsoon (October – November) and Northeast monsoon (December – February) according to the rainfall pattern. Highest total area average rainfall is receiving during the Southwest monsoon and second Intermonsoon periods. About 60% of the total rainfall is receiving during these two monsoon periods. The rainfall receiving in these two periods are very much important to the economy of Sri Lanka. Because 40-45% of power demand of Sri Lanka is generated by hydro power and the reservoirs of the highlands mainly recharge during these two seasons. Lowest rainfall is receiving during the first intermonsoon. Total annual area average rainfall in Sri Lanka is 1861 mm and it is equivalent to 122 km^3 by volume.

Agriculture of Sri Lanka is one of the major income of the people in Sri Lanka and the almost total consumption of rice, vegetable and potatoes are cultivated in Sri Lanka. Rice is the staple food in Sri Lanka and it is cultivated by farmers on a small-scale in rural regions, principally in the northern and eastern plains (Lareef, 2002). Rice production is mainly dependent on rainfall.

The principal cultivation season is known as 'Maha' and is from October to March. During this season, there is usually enough water to sustain the cultivation of all rice fields. The subsidiary cultivation season, known as 'Yala' is from April to September. Usually there is only enough water for cultivation of half of the land area compared to that for Maha (Department of Census and Statistics, 1991).

From the total amount of rainfall (1861 mm) receives, 10% uses for the Irrigation, Domestic and Industrial Purposes. 31% are escape to the sea. The remaining 59% contributes for the evaporation and evapotranspiration (Ratnasara, 2006). Therefore decreasing of total rainfall, change of rainfall pattern ultimately impact for the living organism.

Therefore it is clear that, only small amount of rain water is using for the human requirement. There is a possibility to increase evaporation and evapotranspiration in Sri Lanka due to the increase of temperature. Water loss from the evaporation is 59 % from the receiving rainfall and it has calculated by considering the daily evaporation as 3 mm (Average Evaporation). But if it increases by another 1 mm per year due to increase of temperature, the contribution to the evaporation will be increased up to 79% and it will be highly impacted for the ground water recharge capacity in Sri Lanka.

Therefore the understanding, Temperature trends, present rainfall pattern and trends, possibility of heavy rainfall and the variability is very important for the sectors such as Agriculture and Water also for the economical growth of Sri Lanka.

2. Data and Methodology

Sri Lanka Meteorological Department maintains 20 meteorological stations and they measured many meteorological parameters such as Rainfall, Temperature, Relative Humidity, Wind speed and direction etc. In addition to that about 35 agriculture meteorological stations and 350 meteorological stations also maintained. The distribution is fairly good and it represents good spatial distribution. Therefore resolution of the distribution is somewhat large and taking the area average distribution will highly represent the rainfall of individual stations. Spatial changes of temperature are not higher than spatial changes of rainfall. Therefore temperature measuring network is not represents like rainfall network, but the prevailing distribution is established according to the World Meteorological Organization standards.

2.1 Analysis of Temperature

The analysis of average temperature (average of both the maximum and minimum) shows significant trend during the past few decades. The average trend is 0.2 ^{0}C (2°C per century) (Figure 2) per decade for the period 1951-2006, but it is 0.3 ^{0}C (3°C per century) for the period 1981-2006 (Figure 3). Fourth Assessment Report of IPCC (IPCC AR4, 2007) also stated that, the increasing trends have been observed across the seven sub regions of Asia. The observed increases in some parts of Asia during recent decades ranged between less than 1°C to 3°C per century.

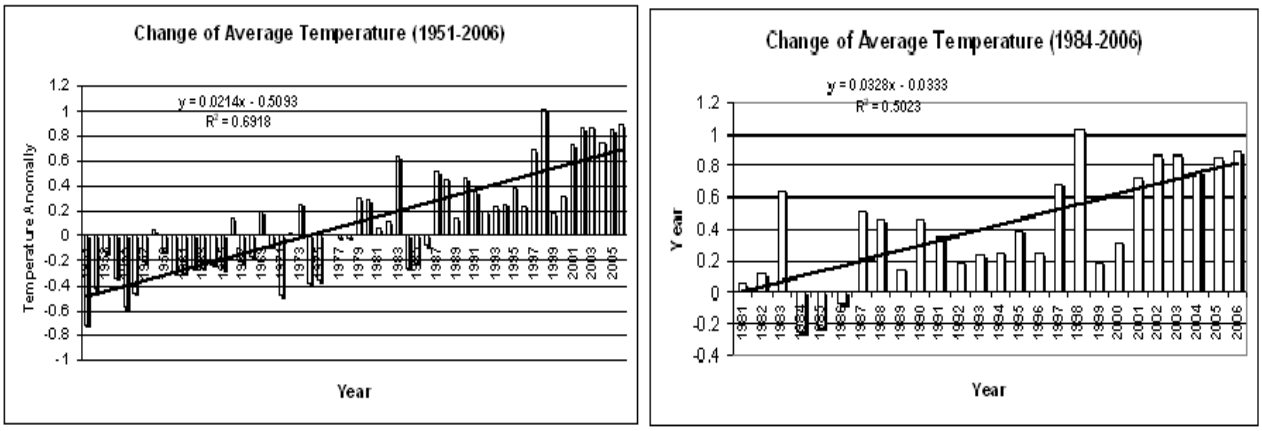

(a) (b)

Figure 1 : (a) Change of Temperature Anomally (1951 – 2006)
(b) Change of Temperature Anomally (1981 – 2006)

The trends of temperatures do not show similar behavior when considering the individual stations. The increasing trend of minimum temperature is high in the highlands and its shows 0.02^0C per decade, but the trend of maximum temperature is high in the coastal areas (Figure 2a and b).

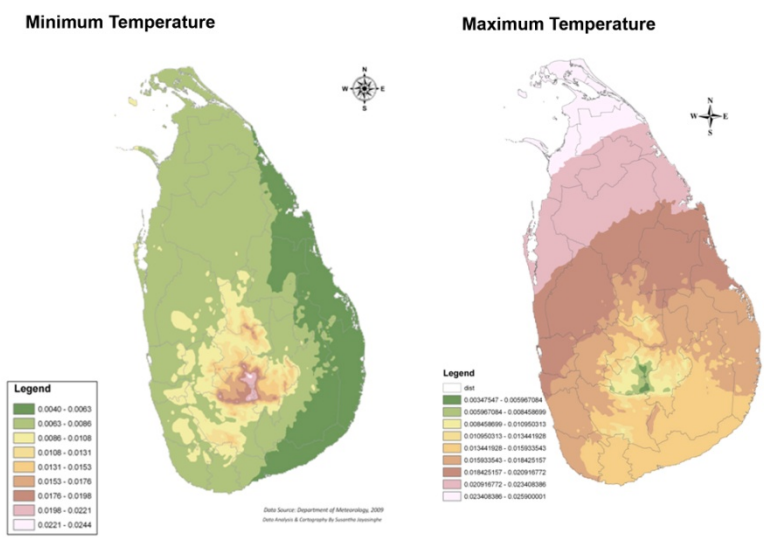

(a) (b)

Figure 2 : Trends of Maximum and Minimum Temperatures (1961-2000)

By considering the periods 1951-2006 and 1984 – 2006 (Figure 1 (a) and (b)), It is clear that the increasing trend is higher in the recent past than past few decades. IPCC AR4 pointed out that, rainfall pattern in many parts of the world has been changed and the trend of rainfall is negative in some parts and also it is positive in the other parts. Therefore the analysis of rainfall pattern is important.

2.2 Analysis of Rainfall

Due to the high density of rainfall network in Sri Lanka, it is not easy to analyze rainfall pa ttern in indi vidual stations. Therefore area av erage rainfall using T hesian Pol ygon method has tak en for this analysis. For this analy sis the rainfall da ta series for differe nt district has been s moothed by the 5 year weighted moving averages and the average value Y defined as (Samui, 1994)

$$Y = (X_{i-2} + 4X_{i-1} + 6X_i + 4X_{i+1} + X_{i+2})/6$$

Where, X_i is the rainfall at i^{th} Year.

Time series analy sis from 1951 - 2008 has been done for the diffe rent districts and it shows that significantly decrea sing trend of rainfall in ever y districts. The slopes for all 25 districts are shown in the table 1.

District	*Slope*	*R^2*	*P Value*	*District*	*Slope*	*R^2*	*P Value*
Colombo	**-9.9**	**0.3**	**0.0**	**Puttalam**	**-4.8**	**0.3**	**0.0**
Kalutara	**-13.9**	**0.5**	**0.0**	**Gampaha**	**-11.3**	**0.4**	**0.0**
Galle	**-13.3**	**0.6**	**0.0**	**Kegalle**	**-17.2**	**0.6**	**0.0**
Matara	**-9.2**	**0.4**	**0.0**	**Ratnapura**	**-7.1**	**0.4**	**0.0**
Hambantota	**-4.4**	**0.4**	**0.0**	**Monaragala**	**-11.0**	**0.6**	**0.0**
Ampara	**-12.3**	**0.5**	**0.0**	**Badulla**	**-8.2**	**0.4**	**0.0**
Baticaloa	**-8.7**	**0.3**	**0.0**	**Polonnaruwa**	**-9.3**	**0.5**	**0.0**
Trincomalee	**-6.1**	**0.2**	**0.0**	**Vavuniya**	**-5.3**	**0.3**	**0.0**
Mullativu	**-4.3**	**0.2**	**0.0**	**Anuradhapura**	**-5.1**	**0.3**	**0.0**
Jaffna	**-1.8**	**0.1**	**0.1**	**Kurunegala**	**-10.4**	**0.7**	**0.0**
Killinochchi	**-4.9**	**0.3**	**0.0**	**Matale**	**-7.6**	**0.3**	**0.0**
Mannar	**-3.0**	**0.1**	**0.0**	**Kandy**	**-16.3**	**0.7**	**0.0**
				Nuwara Eliya	**-9.9**	**0.4**	**0.0**

Table 1 : Decreasing Trend of Rainfall in Different Districts (1951-2008)

Compare the slopes of different districts and it can be concluded that the decreasing rate per year is highest in t he wet zone and in termediate zone, but it is not m uch higher in t he dry zone. T otal rainfall was decreased by an average of 8 mm per year (Figure 3) and it varies between minimum 2 mm per y ear in Jaffna (Dry Zone) to the maximum 17 mm per y ear in Kegalle (Wet Zone). Figure 3 shows that the district wise trend of rainfall during the period.

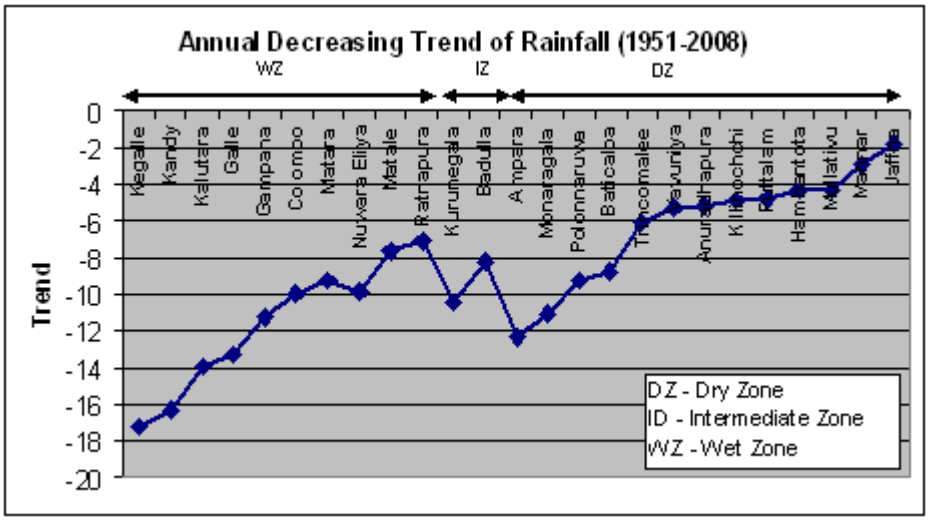

Figure 3 : Decreasing Trends of Rainfall (1951-2008)

According the analysis of rainfall trends for the period 1951-2008, it was clear that, there is a possibility to shift climate zones during recent past. As mentioned earlier there are three climate zones in Sri Lanka namely Dry zone (average rainfall below 1750 mm per annum), Intermediate Zone (average rainfall between 1750 mm and 2500 mm per annum), Wet Zone (average rainfall above 2500 mm per annum). Average rainfall for the periods 1961-1990 and 1975-2004 were calculated and it shows that the margin of the different climate zones are slightly shrinking during the recent season (1975-2004) (Figure 4).

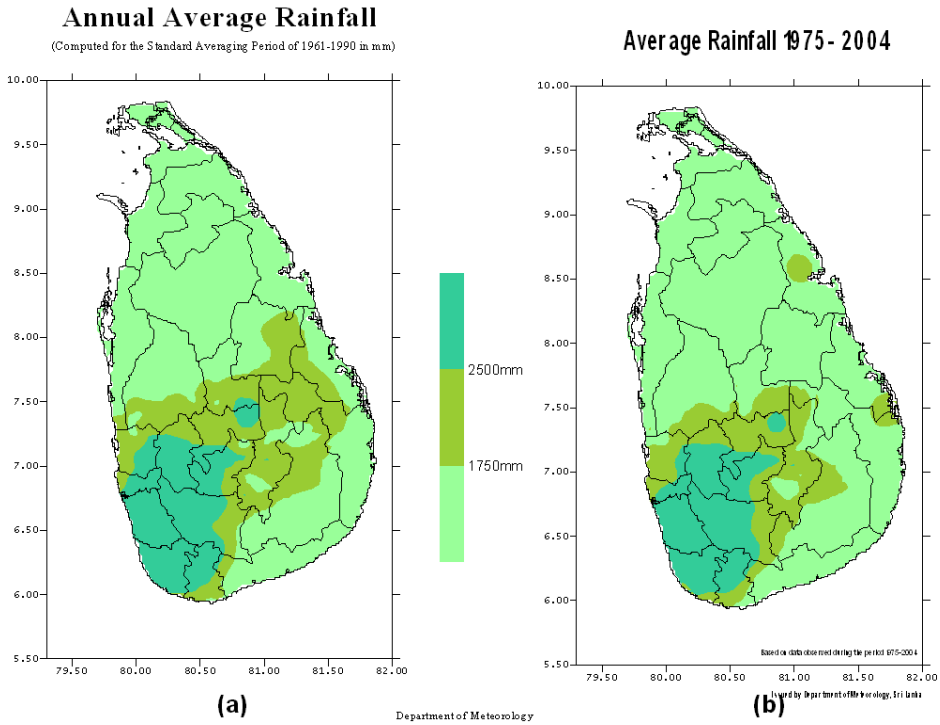

Figure 4 : Rainfall map for the Periods (a) 1961-1990 and (b) 1975-2004

Other impact for the recharge of ground water is the heavy rainfall and high intense rainfall. Recent analysis for the period 1961-2008, shows that one day heavy rainfall has been increased in the western slopes (Figure 5) (Premalal, 2008). The amount of annual rainfall is high in the western slope and hence amount of runoff will increase due to the High intensities. Therefore both the heavy rainfall and increasing evaporation due to high temperature is highly impacted for the ground water recharge. Analysis of annual rainfall shows that the total annual rainfall amount is decreasing by about 8 mm per year. Therefore it can be shown that the water sector is much vulnerable for the climate change.

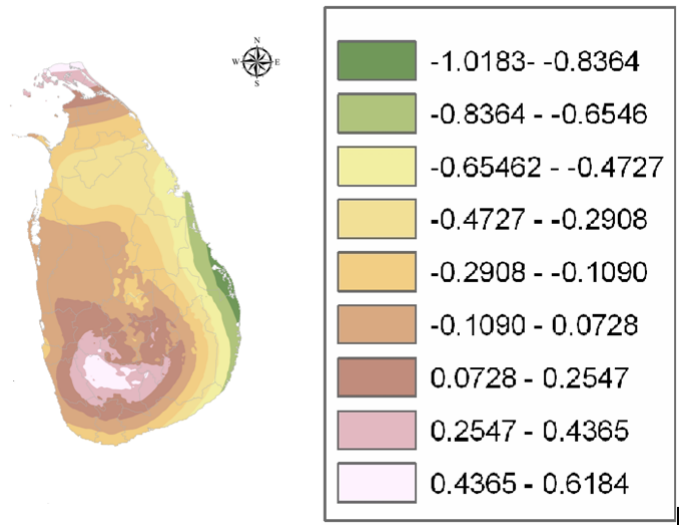

Figure 5 : Increasing Trend of One Day Heavy Rainfall Events (1961-2008)

The correct amount of rainfall and the correct onset of rain are very important for the many crops like rice in Sri Lanka. Chandrapala, 1997 shows that Maha season (Combine of South west monsoon and second inter monsoon) is most vulnerable from the variability of rainfall in the period 1961-1990 than 1931-1960. Also, Maha season is the highest cultivation season and much of the rice requirement is growing in the dry zone in Sri Lanka. The sowing of rice crop is start with the onset of Second Inter Monsoon (SIM) during the latter part of September. Recent observation shows that it did not receive SIM rainfall in correct time. Therefore Coefficient of Variation (CV) or variability has been calculated for different districts. Calculation of CV shows that, it has increased during the period 1980- 2008 than 1951-1979. The CV is high in the Dry zone and low in wet zone.

2.2.1 Analysis of Rainfall Variation

Interseasonal, interannual and spatial variability in rainfall trend has been observed during the past few decades all across Asia. Decreasing trends in annual mean rainfall are observed in Russia, North-East and North China, coastal belts and arid plains of Pakistan, parts of North-East India, Indonesia, Philippines and some areas in Japan. Annual mean rainfall exhibits increasing trends in Western China, Changjiang Valley and the South-Eastern coast of China, Arabian Peninsula, Bangladesh and along the western coasts of the Philippines (IPCC AR4, 2007).

Economy of Sri Lanka is very much depends on agriculture and the high variability of rainfall within the season will be highly impacted. According to the rainfall records of Meteorology Department, Second Intermonsoon was delayed in 2007 and 2009 comparing the last 5 years. Therefore calculating variability for different time period for different climate season will important for the policy makers to decide to adapt to the climate change.

Analysis of CV during the maha season shows that, it is high in the dry zone and gradually it is decreasing and it was not higher in wet zone. The comparison of CV for the periods 1951 – 1979 and 1980 – 2008 shows remarkable increases during the period 1980 – 2008 (Figure 6a and b). The highest changes are confined in the dry zone. Dry zone is the major area for growing rice and

the rainfall variability will highly impacted for the crop during sowing time and also harvesting time. Analysis of annual CV for different districts does not show the variability within the season or onset and withdrawal of the season. Therefore complex analysis should be done to find variability as mentioned above.

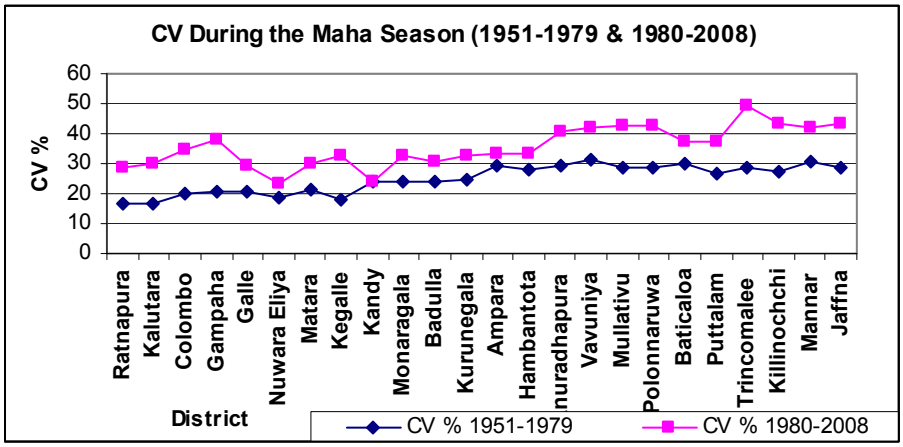

(a)

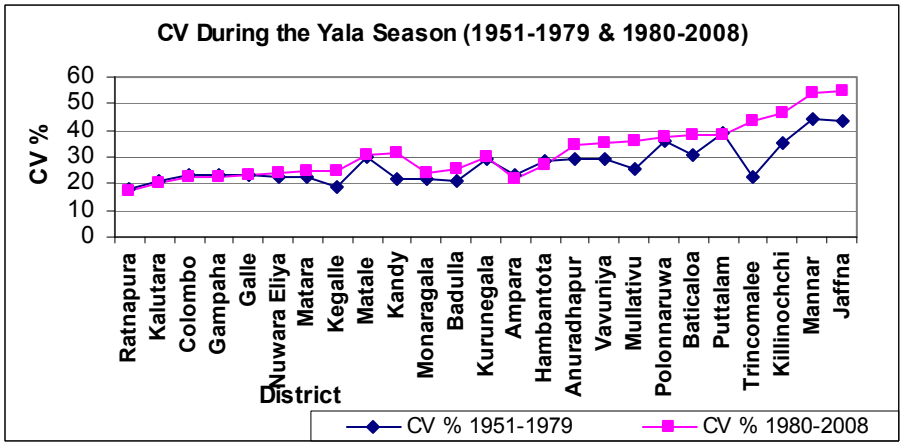

(b)

Figure 6 : (a) Rainfall Variability at different district during Maha season
(b) Rainfall Variability at different district during Yala season

3. Conclusion and Discussion

Average temperature has been increased and the increasing trend is high during the recent past. With the increasing temperature it could be seen that the climate of Sri Lanka also changed especially during the recent past. According to the analysis of rainfall it could be seen that the annual rainfall has significantly decreased. Primarily it will be impacted for the water resources and then secondly the decreasing of rainfall will impact for the sectors as agriculture and energy.

Receiving rainfall at correct time is important for the economy in Sri Lanka. But analysis showed that the variability has been increased for the last few decades. Annual rainfall variability has increased almost all over the country, but variability is high in Dry Zone than the Intermediate Zone and wet zone. The variability is higher in the recent past. Rainfall variability is much higher during the maha season than yala season.

4. Refe rences

Chandrapala, L. 1997, Comparison of Arial Precipitation of Sri Lanka on District Basis during the periods 1931-1960 and 1961-1990. Proc. National Symposium on Climate Change 7-8 March Colombo

Department of Census and Statistics. 1991. Statistical Abstract of the Democratic Socialist Republic of Sri Lanka, Colombo.

IPCC AR4 Fourth assessment Report (2007)

Ratnasara, G.V., 2006, Presented in Irrigation Department in Sri Lanka for DSWRP Project

Samui, R.P. 1994 , Rainfall Variation along the Tees ta Valley in Mountaino us Slope of Sik kim, Mausam, 45.2, 165-170.

Lareef Zubair, 2002, , El Nino Southern Oscillation influence on Rice Production in Sri Lanka, *International Journal of Climatology*, 22, 249-260

Premalal, K.H.M.S. (2008), Scientific Paper presented for the training course for Climate Change Adaptation and Mitigation, Swedish Meteorological and Hydrological Institute

Regional Impact of Climate Change in Korea Rainfall Extremes

JONGPIL KIM[1], GWANGSEOB KIM[2] and JAE HONG PARK[3]

[1]*Ph.D. Student of School of Archi. and Civil Engineering, Kyungpook National University and Researcher of Brain Korea 21, Korea (jpkim@knu.ac.kr)*
[2]*Professor of School of Archi. and Civil Engineering, Kyungpook National University and Researcher of Climate Change Research Center, Korea (kimgs@knu.ac.kr)*
[3]*Professor of Department of Civil Engineering, Semyung University, Korea (jhpark@semyung.ac.kr)*

1. Introduction

Regional impacts of climate change have demonstrated various changes in precipitation, air temperature, sea surface temperature, sea level and so on. Along with global warming, natural disasters such as flood and drought also have increased for several decades. According to the 2007 Fourth Assessment Report by the Intergovernmental Panel on Climate Change (IPCC), climate change appears clearly in hydrometeorological measurements. Also this report indicates that the occurrence of extreme events such as localized torrential downpour and heat wave was more frequent than before.

The pattern of precipitation change in South Korea can be summarized as: the total rain days per year have decreased and annual precipitation has increased therefore the number of heavy rain days (over 80 mm/day) has increased. Moreover results from the linear regression analysis of the Korea annual rainfall for 1905-2004 show that rainfall for recent 30 years has increased more dramatically than that of the whole duration (Kim et al., 2009). In the study of Schonwiese and Rapp (1997), the precipitation in Northern Europe was increased while the precipitation in Southern Europe was decreased. These studies indicate that climate change can cause different trends of precipitation through the local features. In this study, the regional impact of climate change in Korea rainfall extreme was evaluated according to the difference of elevation, degree of urbanization, longitude, latitude, inland/seaside, basins using the hourly nationwide precipitation data from 1973 to 2009.

2. Materials and Methods

2.1 Data Description

To analyze the regional impact of climate change in Korea rainfall extremes, trend analysis was performed using 59 weather station data(Fig. 1) from 1973 to 2009 which are operated by Korea Meteorological Administration (KMA). The annual maxima of consecutive rainfalls for eight rainfall durations (i.e. 1, 2, 3, 6, 12, 24, 48 and 72 hours) were analyzed using hourly precipitation measurements to evaluate the quantitative change of rainfall extremes. In addition, the number of rain days over nine thresholds (i.e. 0, 10, 20, 30, 40, 50, 60, 70 and 80 mm/day) were analyzed to evaluate the frequency change of extremes. To evaluate the regional impact in more

detail, results were analyzed for different local features such as elevations, latitudes, longitudes, inland or shore area, urbanized or unurbanized terrain and different six river basins those are Han, Nakdong, Geum, Sumjin, Youngsan and Jeju (see Fig. 2).

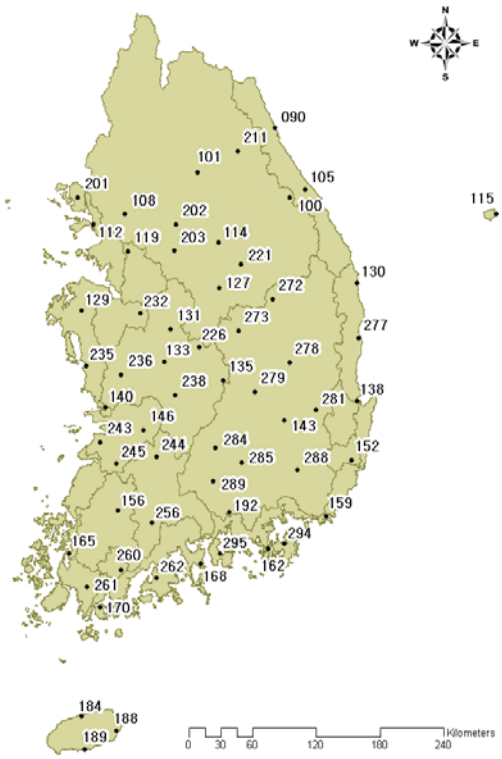

Fig. 1. Map of the 59 weather stations.

2.2 Methodology

We employed the nonparametric Mann-Kendall (MK) test to perform the trend analysis. MK test is not sensitive to statistical properties of sample measurements that are sampling size, variance, skewness and so on and also applicable to the series with missing data or outliers. This technique was first proposed by Mann (1945), and improved by Dietz and Kileen (1981). For a certain time series $\{X_k, k = 1, 2, 3, \ldots, n\}$, MK statistics can be defined as followed;

$$T = \sum_{j<i} \mathrm{sign}(X_i - X_j) \ , \quad 1 \le j \le i \le n \tag{1}$$

Where, $\mathrm{sign}(x)$ is a sign function determined by the difference between two consecutive measurements.

In the case where there is no ties and trend, under the null hypothesis the distribution of T may be approximated by a normal distribution with mean zero and variance;

$$\mathrm{Var}(T) = n(n-1)(2n+5)/18 \tag{2}$$

provided that $n \ge 10$.

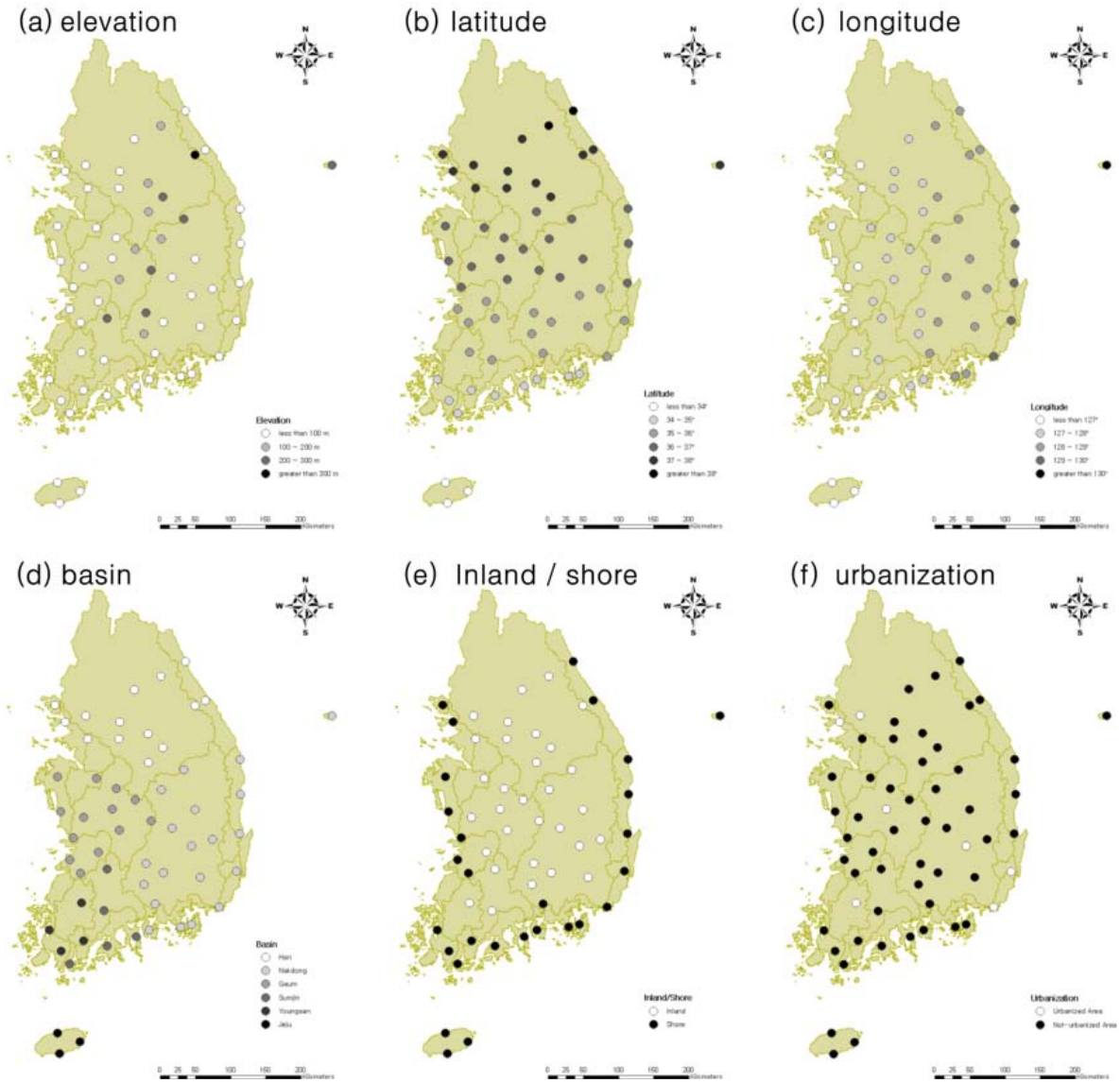

Figure 2. Map of the classified weather stations according to the different local features.

3. Results and Conclusion

In this study, overall results can be summarized that quantity and frequency of rainfall extremes increase, whereas the number of rain days over 0 mm/day decreases. The trend of the annual maxima of consecutive rainfalls has not a statistical significance but increased for all durations. And we found that the upward trend of extreme precipitation appears more clearly in higher elevations, higher latitudes, the Han-river basin and inland stations than in other local conditions (see Table 2). Also our results demonstrated that the upward trend of rain days over 80 mm/day appears clearly in higher latitudes, urbanized area and the Han-river basin (see Table 3). These variations of rainfall extremes appear more apparently in urbanized terrain than in the other. Therefore it is urgent that measures to consider these regional variations of rainfall extremes be established for water resources management, dam operation and prevention of flood disasters in South Korea.

Table 1. The linear change of annual maxima of consecutive rainfalls for each duration and annual sum of rain days over each threshold for 1973-2009.

Class	Class Mark	# of stations	annual maxima of rainfall (mm)				annual sum of rain days (days)			
			rainfall durations				thresholds (mm/day)			
			1-hr	12-hr	24-hr	48-hr	0	10	50	80
Elevation	< 100m	45	11.8	21.0	23.4	32.7	-1.7	2.1	1.7	1.1
	100~200m	7	11.4	27.1	35.6	47.3	0.1	2.3	2.0	1.3
	200~300m	6	11.8	30.3	46.8	57.8	3.4	3.7	2.5	1.4
	≥ 300m	1	19.0	67.6	106.6	119.1	4.5	7.7	3.8	1.7
Latitude	< 34°	3	26.9	40.6	38.3	37.9	-1.9	1.9	0.4	1.2
	34°~35°	9	13.3	3.0	-8.4	-7.8	-2.8	1.8	1.9	0.8
	35°~36°	15	8.9	10.7	13.5	22.2	-2.3	1.3	1.3	0.8
	36°~37°	18	7.5	18.5	28.8	42.4	-0.8	2.6	1.9	1.0
	37°~38°	12	16.1	51.9	66.5	81.9	1.2	4.1	2.7	2.0
	≥ 38°	2	19.8	59.3	66.8	73.5	6.6	2.2	3.1	2.4
Longitude	< 127°	18	10.8	17.7	16.9	29.4	-1.2	2.3	1.7	1.1
	127°~128°	19	10.2	22.3	29.4	38.2	-2.6	1.9	1.6	1.0
	128°~129°	16	14.8	31.9	38.7	45.2	-0.4	2.9	2.2	1.4
	129°~130°	5	13.5	21.3	32.3	40.9	4.0	1.3	1.9	1.3
	≥ 130°	1	9.9	24.7	49.2	86.3	6.3	9.2	5.1	2.3
Basin	Han	14	16.6	53.3	65.7	78.1	2.7	3.2	2.5	2.0
	Nakdong	20	11.2	19.1	24.7	33.9	-1.3	2.5	2.0	1.3
	Geum	13	4.4	9.2	15.5	30.9	-4.1	2.1	1.5	0.7
	Sumjin	5	11.3	7.8	6.6	9.1	2.2	0.8	1.9	0.8
	Youngsan	4	12.9	-6.5	-17.7	-15.5	-4.3	2.2	1.4	0.0
	Jeju	3	26.9	40.6	38.3	37.9	-1.9	1.9	0.4	1.2
Inland/Shore	Inland	31	10.9	26.6	35.6	48.1	-1.1	2.6	1.9	1.2
	Shore	28	13.1	20.0	21.0	27.9	-0.7	2.1	1.8	1.2
Urbanization	Urbanized	7	13.9	22.1	31.2	47.9	2.6	2.5	2.4	1.7
	Unurbanized	52	11.6	23.6	28.3	37.2	-1.4	2.4	1.8	1.1

Table 2. The number of weather stations with upward or downward trend in annual maxima of consecutive rainfall for each rain duration (significance level = 10%).

※ ▲: significantly upward trend, △: unsiginificantly upward trend,
▽: unsignificantly downward trend, ▼: significantly downward trend.

Class	Class Mark	# of stations	Rainfall Duration															
			1-hr				12-hr				24-hr				48-hr			
			▲	△	▽	▼	▲	△	▽	▼	▲	△	▽	▼	▲	△	▽	▼
Elevation	< 100m	45	8	33	4	0	9	26	10	0	6	30	9	0	8	34	3	0
	100~200m	7	3	4	0	0	2	5	0	0	2	5	0	0	2	5	0	0
	200~300m	6	2	4	0	0	2	3	1	0	3	3	0	0	2	4	0	0
	≥ 300m	1	0	1	0	0	0	1	0	0	0	1	0	0	0	1	0	0
Latitude	< 34°	3	1	2	0	0	1	2	0	0	1	2	0	0	1	1	1	0
	34°~35°	9	2	6	1	0	0	7	2	0	0	8	1	0	0	8	1	0
	35°~36°	15	0	13	2	0	0	11	4	0	1	8	6	0	1	13	1	0
	36°~37°	18	3	14	1	0	2	11	5	0	3	13	2	0	3	15	0	0
	37°~38°	12	6	6	0	0	8	4	0	0	5	7	0	0	6	6	0	0
	≥ 38°	2	1	1	0	0	2	0	0	0	1	1	0	0	1	1	0	0
Longitude	< 127°	18	3	13	2	0	3	12	3	0	3	10	5	0	4	13	1	0
	127°~128°	19	4	14	1	0	3	12	4	0	2	16	1	0	1	18	0	0
	128°~129°	16	5	10	1	0	6	7	3	0	4	10	2	0	5	9	2	0
	129°~130°	5	0	5	0	0	0	4	1	0	1	3	1	0	1	4	0	0
	≥ 130°	1	1	0	0	0	1	0	0	0	1	0	0	0	1	0	0	0
Basin	Han	14	6	8	0	0	9	5	0	0	5	9	0	0	6	8	0	0
	Nakdong	20	3	16	1	0	3	13	4	0	5	12	3	0	5	13	2	0
	Geum	13	1	10	2	0	0	8	5	0	0	9	4	0	0	13	0	0
	Sumjin	5	1	4	0	0	0	3	2	0	0	4	1	0	0	5	0	0
	Youngsan	4	1	2	1	0	0	4	0	0	0	3	1	0	0	4	0	0
	Jeju	3	1	2	0	0	1	2	0	0	1	2	0	0	1	1	1	0
Inland/Shore	Inland	31	8	21	2	0	8	18	5	0	7	20	4	0	8	22	1	0
	Shore	28	5	21	2	0	5	17	6	0	4	19	5	0	4	22	2	0
Urbanization	Urbanized	7	1	6	0	0	2	5	0	0	1	4	2	0	3	4	0	0
	Unurbanized	52	12	36	4	0	11	30	11	0	10	35	7	0	9	40	3	0

Table 3. The number of weather stations with upward or downward trend in annual sum of rain days over each threshold (significance level = 10%).

Class	Class Mark	# of stations	Threshold															
			0 mm/day				10 mm/day				50 mm/day				80 mm/day			
			▲	△	▽	▼	▲	△	▽	▼	▲	△	▽	▼	▲	△	▽	▼
Elevation	< 100m	45	1	20	20	4	0	37	8	0	9	35	1	0	12	31	2	0
	100~200m	7	1	1	5	0	0	6	1	0	2	5	0	0	2	4	1	0
	200~300m	6	1	3	2	0	1	4	1	0	3	3	0	0	2	4	0	0
	≥ 300m	1	0	1	0	0	0	1	0	0	1	0	0	0	0	1	0	0
Latitude	< 34°	3	0	2	1	0	0	3	0	0	0	2	1	0	0	3	0	0
	34°~35°	9	1	2	4	2	0	6	3	0	2	7	0	0	1	6	2	0
	35°~36°	15	0	8	6	1	0	13	2	0	0	15	0	0	2	13	0	0
	36°~37°	18	2	5	10	1	0	15	3	0	2	16	0	0	3	14	1	0
	37°~38°	12	0	7	5	0	1	10	1	0	9	3	0	0	8	4	0	0
	≥ 38°	2	0	1	1	0	0	1	1	0	2	0	0	0	2	0	0	0
Longitude	< 127°	18	1	9	6	2	0	15	3	0	6	11	1	0	6	10	2	0
	127°~128°	19	1	6	10	2	0	16	3	0	2	17	0	0	3	15	1	0
	128°~129°	16	1	5	10	0	0	13	3	0	6	10	0	0	5	11	0	0
	129°~130°	5	0	4	1	0	0	4	1	0	0	5	0	0	1	4	0	0
	≥ 130°	1	0	1	0	0	1	0	0	0	1	0	0	0	1	0	0	0
Basin	Han	14	1	7	6	0	0	12	2	0	10	4	0	0	9	5	0	0
	Nakdong	20	1	7	12	0	1	16	3	0	3	17	0	0	5	15	0	0
	Geum	13	0	5	6	2	0	11	2	0	0	13	0	0	1	11	1	0
	Sumjin	5	1	2	1	1	0	3	2	0	1	4	0	0	1	4	0	0
	Youngsan	4	0	2	1	1	0	3	1	0	1	3	0	0	0	2	2	0
	Jeju	3	0	2	1	0	0	3	0	0	0	2	1	0	0	3	0	0
Inland/Shore	Inland	31	2	11	17	1	0	28	3	0	9	22	0	0	9	21	1	0
	Shore	28	1	14	10	3	1	20	7	0	6	21	1	0	7	19	2	0
Urbanization	Urbanized	7	0	6	1	0	0	7	0	0	2	5	0	0	3	4	0	0
	Unurbanized	52	3	19	26	4	1	41	10	0	13	38	1	0	13	36	3	0

Acknowledgements

This research was supported by a grant from Construction Technology Innovation Program (CTIP) funded by Ministry of Land, Transportation and Maritime Affairs (MLTM) of Korean government.

References

Dietz, E.J. and Kileen, A. (1981). A nonparametric multivariate test for monotone trend with pharmaceutical applications. *Journal of the American Statistical Association*, Vol. 76, pp. 169-174.

Kim, G., Yim, T.K. and Park, C.H. (2009). Analysis of the secular trend of the annual and monthly precipitation amount of South Korea, *Journal of Korean Society of Hazard Mitigation*, Vol. 9, No. 6, pp. 17-30.

Mann, H.B. (1945). Nonparametric tests against trend. *Econometrica*, Vol. 13, pp. 245-259.

Schonwiese, C.D. and Rapp, J. (1997). *Climate Trend Atlas of Europe, based on observations 1981-1990*. Kluwer, Dordrecht, The Netherlands.

Implementation of the wind, NAO, AO and ENSO data in prediction of the rain rate in the North Mediterranean area by fuzzy-neural model

Oleg M. Pokrovsky
Main Geophysical Observatory, St. Petersburg, 194021, Russia, pokrov@main.mgo.rssi.ru

1. Introduction

Forecasting the weather from one month to one season ahead became economically necessary direction of predictive studies. Seasonal forecasts are possible whenever the chaotic atmospheric motion is perturbed in a predictable way by slowly varying boundary conditions, such as sea surface temperature (SST) or land conditions. The most important of these boundary conditions are the El-Nino-Southern Oscillation (ENSO) in Western Hemisphere and North-Atlantic Oscillation (NAO) in Eastern Hemisphere. A clear awareness of the origin of the long-term predictive skill began with works of Walker and Bliss (1932), Bjerknes (1969). The ENSO is the strongest climate signal in the inter-annual timescales. It has quasi-periodic behavior with dominant periods of around 2-7 years. Many others distributed around the world were discovered during last years. Although the weather is highly non-linear, perturbations to the average weather can often be taken as being proportional to the forcing, plus unpredictable weather noise. This means that simple, often linear, forecast models can be very useful in seasonal forecasting. In fact, statistical models based on linear ENSO, NAO and other teleconnections are used in many locations throughout the world (Wang, 2001). Statistical climate may be considered as the statistical set of the daily weather for a given season over a specific geographical region. Thus, the timescale of seasonal climate goes far beyond the predictability that is defined in terms of sensitive dependence on the initial atmospheric conditions. Instead, the predictability of seasonal climate is often connected with a forcing field such as SST or surface atmospheric pressure (SAP). The key to successful application of an empirical model lies in understanding the underlying physical mechanism for the relation between the predictor and the predicted fields. Unlike the dynamical models, that try to answer how a certain anomaly occurs by simulating the detailed processes, that are necessary to produce the observed seasonal anomaly, the statistical models directly try to determine the probability that a certain anomaly will occur over a specific geographical region under a known condition, in particular, the space-time structure of a given forcing, such as ENSO or NAO signal in the SST field. The effectiveness of empirical models, therefore, depends crucially on whether the relevant components (with respect to space and time scales) to be used as predictors are suitably incorporated into the prediction models, and whether the relationships between predictors and predictands are properly established (Pokrovsky, et al, 2002). The above relationships may not necessarily be linear, particularly, when mid and high latitudes are concerned. Nowadays, the use of a procedure, such as principal component analysis or a rotated version of it, to extract coherent signals has enabled the compression of climatic variables into a few guess patterns. The present paper attempts to apply the idea of a non-linear model in low-dimensional phase space (Pokrovsky, 2004, 2009b). In the terms of a low-dimensional phase space approach, fuzzy patterns are used to determine nonlinear metrics and the composition of the initial time states as well as simulating state vectors with respect to the centers of action (e.g. centers of ocean-atmosphere interactions). Fuzzy set methodology (Pokrovsky, 2000, 2009a) is used to define an empirical rule to assign a set of initial states to one of the atmospheric circulation regime sets determined by major low oscillations and represented in a few low-dimensional vector subsets. A specific meaning is assigned to the simulation trajectory in the phase space generated by an onlinear model to be close to the observing trajectory (Pokrovsky O.M., 2009b). Self-learning model is designed to approximate to the observing trajectory at the learning time interval and to evaluate deviations between model and measurement data at verification stage. The motivation for such an approach came from the following facts. First, a non-linear model might be efficient only in low-dimensional phase space because in high-dimensional space the model cannot be stable and an extremely long time is required to train

such a model. Second, we have observed that the time evolution of a specific key sea surface temperature forcing region, relevant to season scales, can often be efficiently described in a low-dimensional phase space. The possibility for constructing a low-dimensional phase space from the predictor fields allow a closer examination of their impact on the seasonal climate over a specific climate zone leading to the possibility of nonlinear and more dynamically based statistical prediction in contrast to pure statistical approaches. Our preliminary application of this method to the prediction of the winter and spring surface air temperature (SAT) over Europe showed significant improvement in the skill score (Pokrovsky, 2009b). Third, the geographical distribution of the predictive skills, as well as their time behavior, varies from one key region of sea surface temperature forcing to another. Therefore, the final optimal prediction might be achieved through a linear or nonlinear combination of the predicted results derived from different key forcing regions.

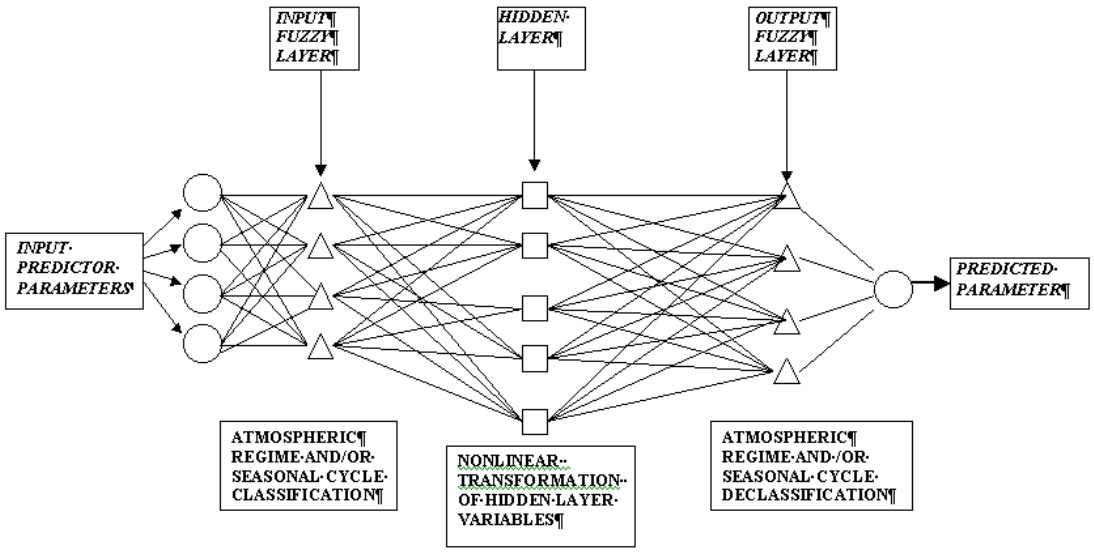

Figure 1. Fuzzy-neural model scheme

2. Forecasting methodology

The use of a neural network (NN) is a powerful nonlinear scheme based on black box statistics, where one can tune the model parameters to arrive at a good prediction, but can see neither the phase relation between the predictand and predictors, nor the origin of skills. Therefore, we assume that the predictability of seasonal climate is connected with forcing fields such as the sea surface temperature or others. The key to a truly successful application of a neural network model lies in the understanding of the underlying physical mechanism for the relation between predictor and predictand fields (Pokrovsky, 2000).We used a comprehensive neural network model, which is based on a combination of fuzzy logic modules and neural network principle structures. The general scheme of our self-learning fuzzy-neural model is presented at fig. 1. Let us consider it from the left to right direction. The left module defines the initial field assimilation as the input information. Further, this dataset should be classified in several fuzzy logic modules. It is necessary to emphasize that each input meteorological field is linked to several fuzzy sets. The classification procedure is related to diurnal or seasonal cycles or to various type of spatial distribution of meteorological parameters, e.g., type of atmospheric circulation. That means that each field should be evaluated by means of a complex procedure and then should be attributed to one of the clusters (fig.1). Nonetheless, metric distances of each field to cluster centers are taken into account in the next model layer, which is called a hidden layer. A hidden layer is designed to perform non-linear transformation of distance variables into output variables. A very

important feature of a neural network is its ability to learn. This learning is based on the simultaneous analysis of some input and output samples, which are called learning samples. As a rule, a size of learning sample is equal to one third of the general sample size. Therefore, two thirds of the general sample is implemented to evaluate the efficiency and accuracy of a neural network as a predictive tool. The structure of the hidden layers is very complicated. Each of the hidden layer modules is linked to every one of the fuzzy logic modules. The first hidden layer output is connected to the second fuzzy logic layer. Its function is designed to declassify the results of non-linear transformations, which were carried out in the hidden layer. Hence, this declassification module provides an inverse transformation from the artificial inner variables to ordinary units of meteorological parameters. The final combination of output variables leads us to the acquisition of the estimates of the predictive variables (surface air temperature, etc.). Empirical orthogonal functions (EOFs) and singular value decomposition (SVD) are the most commonly used techniques (Wang, 2001) to build a phase space. EOFs are the eigenvectors of the covariance matrix obtained from calculating covariances of time series at different spatial points. EOFs are optimal in explaining as much total variance as possible with any specific number of spatial patterns. The first EOF explains most of the temporal variance in the dataset among all possible spatial fields. The subsequent EOFs are mutually orthogonal (in space and time) and successfully explain less variance. The EOF analysis is non-local in that the loading values at two various spatial points in an EOF do not simply depend on the time series at those two points but depend on the whole dataset. This contrasts with the one-point correlation analyses used to define teleconnections, for which the patterns can be interpreted locally. A fuzzy set approach is more appropriate to approximate the temporal and spatial modes in low dimensional phase space (Pokrovsky *et al*, 2002). Certainly, there are atmosphere-ocean interactions generating a set of forward and feedback links. Some of them are nonlinear and cannot be described by simplified statistical models based on a linear regression. Therefore, a multivariate self-learning neural network model was developed to describe the predictive relationships between evolving large-scale patterns in the Northern Hemisphere sea surface temperature, surface air pressure and surface air temperature fields (predictors) and subsequent patterns in the Europe and Northern Mediterranean surface air temperature and precipitation rate (predictands). A lead interval of varying length (from 1 to 6 months) is placed between a series of consecutive predictor periods and a single predictand period. Objective evaluation of strength of such relationships is a primary aim of this study. The global monthly mean sea surface temperature, surface air temperature, rain rate and surface air pressure grid fields used in the present study were derived from the NCEP/NCAR (National Center for Environment Protection/National Center for Atmospheric Research) reanalysis data set. The dataset covers the period from January 1958 to December 1998. The annual cycle and inter-annual linear trend were removed from predictor and predictand fields. The anomalies (departure from climate means) were used in all prediction model modifications. The data used were divided into training and verification sample sets. The data contained in the verification set were used only for the evaluation of the predictive skill. It should be pointed out that the linear trend, calculated on each grid after the removal of the annual cycle is related either to artificial factors (measurement errors) or to variability having a large time scale (equivalent to longer than a century), which is not relevant to the predictive problem considered here. The amplitude of the linear trend is very small. However, it may give rise to a trajectory shifting in phase space and thus affect the selection of the nearest fuzzy set activated in the nonlinear model. Therefore, this filtering procedure might be considered as a necessary step in the present context.

3. Fuzzy classification of regime circulation and rain rate spatial distribution over Europe

Joint fuzzy analysis of SST, SAT, SAP, wind and rain fields permits us to investigate not only atmospheric circulation patterns responded to major the surface air pressure low oscillations in Atlantic-Europe area, but also to find the related spatial anomaly of the rain rate fields during all seasons, which appeared coherently with accompanied SST, SAT and SAP anomalies. The fuzzy set analysis of these fields revealed the major circulation regimes over the eastern North Atlantic and Europe. We found that there are three main regimes corresponding to seasons (Pokrovsky, 2009a): 1) winter and early spring; 2) summer, and 3) autumn. The first regime is primary zonal and closely related to type *W* in Hess-Brezowsky classification. Therefore, major anomalies of rain rate might be found in mountain areas around Europe including the Alps, Balkans and Apennines Peninsulas in Southern Europe. The summer airflow regime substantially deviates from zonal regime and to be determined by three vorticity polar systems: 1) North-Western (Scandinavia), 2) Western Mediterranean and 3) Caucasian. As an example we present here a most interesting sample which is responded to the blocking of zonal flow, when extreme weather events are most probable.

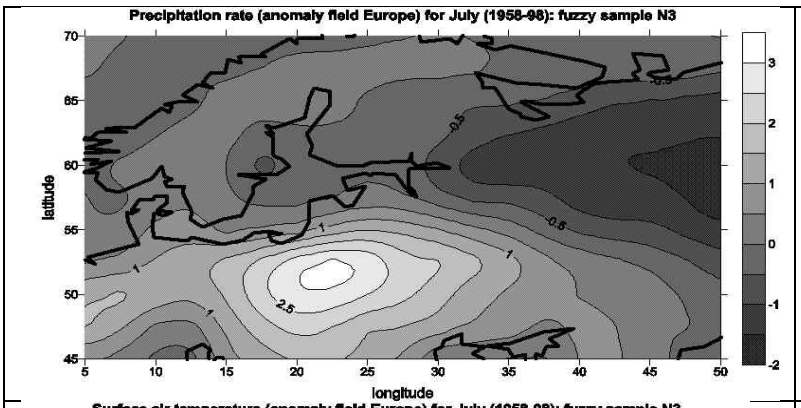

Figure 2. Fuzzy classification of July monthly rain rate in Europe (fuzzy sample N3)

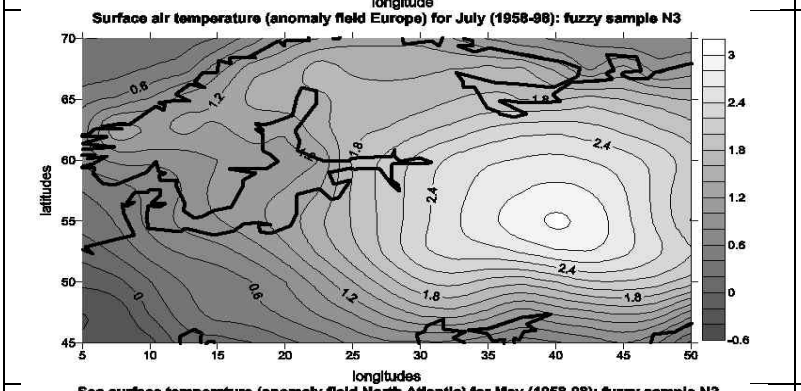

Figure 3. Fuzzy classification of July monthly surface air temperature in Europe (fuzzy sample N3)

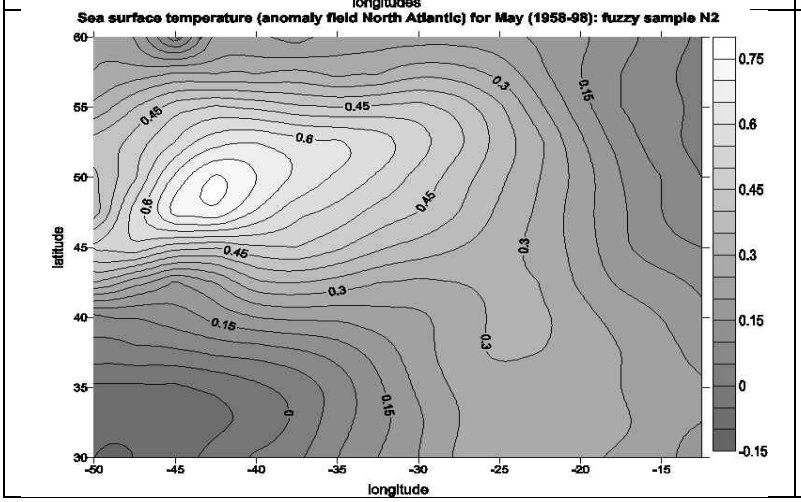

Figure 4. Fuzzy classification of May monthly SST in North Atlantic (fuzzy sample N3)

Europe is divided into the western and eastern parts with low and high atmospheric pressure large spatial scales. One example of coherent fuzzy samples in the monthly rain rate, the SAT and the North Atlantic SST anomalies are presented at fig.2-4. Very specific SST distribution in the North Atlantic (low SST in low latitude zone and high SST anomaly in middle latitude belt in April-May) inevitably led to blocking in Europe for 2-3 months. Similar information, but in reduced form contains in the NAO data. Extreme blockings occurred in 1972 and 2010 have caused floods in Central Europe and droughts in European part of Russia. Less pronounced rain rate anomalies in Russia occurred in 1992 and in 1994. Experiments with the NN predictive model permits us to obtain monthly temperature fields for various lead times. Most promising results were derived for winter-spring-summer seasons. The comparison of predictive and true fields for a two months lead time allows us to conclude that the forecast reproduces the main features of temperature and rain spatial distribution correctly. When a lead time extends to four months, the deviation of the predictive from true field rises two times. Efficiency of predictive model efficiencies was also proved by high level of skill score and correlation coefficient magnitudes: 0.5-0.7 for SAT fields. Predicted rain rate fields are characterized by lower magnitudes: 0.3-0.5.

4. Conclusion

The overall objective of this paper was to propose a self-learning model for seasonal prediction of surface air temperature and precipitation rate over Europe and Northern Mediterranean. The model was validated using a cross-validation technique and was compared to the regression technique. It is known (Cherry, 1996) that the main problem with a regression or single value decomposition approach in statistical prediction is the over-fitting problem. Pairs of most correlated predictor/predictand modes are sought for over the training period and are used in prediction. When the training sample is not long enough, the associated correlations between these pairs of modes are largely overestimated. Since these correlations are precisely the linear prediction coefficients linking predictand modes to their corresponding predictor modes (entering in the regression model), the explained variance of forecast is also overestimated. In contrast, when a sample is long, the phase space points are rather scattered and the associated correlation coefficients became underestimated, while the explained variance of forecast is also underestimated. The phase space points might be associated with the various circulation regimes. That is why these points comprise a large scattering pattern in phase space. A fuzzy set approach enables us to split this wide pattern in a number of more narrow sets of points. Each of these narrow sets is associated with a specific circulation regime.

References:

Bjerknes J., 1969, Atmospheric teleconnections from Equatorial Pacific, *Mon. Weather Rev*., v.97, p.163-172.

Cherry, S. (1996). Singular value decomposition analysis and canonical correlation analysis. *J. Climate*, **9**, 2003-2009.

Pokrovsky O.M., 2000. Land Surface Energy Exchange Simulation Based on Combined "Fuzzy Sets and Neural Networks" Approach. *Proceedings of Second Conference on Artifical Intelligence*, AMS, Boston, MA, p.21-26.

Pokrovsky O.M., R.F. Kwok and C.N. Ng, 2002. Fuzzy logic approach for description of meteorological impacts on urban air pollution species: a Hong Kong case study. *Computers and Geosciences*, V. 28, N 1, p. 119-127.

Pokrovsky O.M., 2004. Climate short-term self-learning climate model for Northern Europe. *Proceedings of the First BALWOIS conference*, paper FP-022, CD, Ohrid, Macedonia.

Pokrovsky O.M., 2009a. South European Rain Rate Modulation by NAO and Changes in Atmospheric Circulation Regimes Caused by Climate Warming. *Computers and Geosciences,* v. 35, p.897-906.

Pokrovsky O.M., 2009b. Self-learning statistical short-term climate predictive model for Europe. In a book "*Global Climatology and Ecodynamics*" (Ed. A.P.Cracknell), Springer and Praxis Publ. Chichester, UK, p. 185-210.(http://www.springerlink.com/index/t261415767644267.pdf)

Walker G.T. and W. Bliss, 1932, World weather. *Mem. Roy. Met. Soc*., v.4, p. 53-84.

Wang R., 2001, Prediction of seasonal climate in low-dimensional phase space derived from the observed SST forcing,, *J. Climate*, v.14, p.77-97.

Variability of Equatorial East African Rainfall based on Empirical Mode Decomposition derived variability components

Zablone Owiti[1] and Zhu Weijun[2]

[1,2]College of Atmospheric Science, Nanjing University of Information, Science and Technology,
[1]Kenya National Council for Science and Technology, zowiti@ncst.go.ke

Abstract

We apply the relatively new nonlinear empirical mode decomposition (EMD) method, an alternative to the traditional methods, to extract the variability components of the Equatorial East Africa (EEA) rainfall. This method is adaptive without requiring any predetermined functions and does not assume a time series to be linear or stationary prior to analysis. The gauge rainfall series for 44 stations over EEA are decomposed into modulated annual cycle (MAC), the inter-annual and decadal-to-trend variability components. MAC is an alternative reference frame that allows the annual cycle to change from year to year for defining anomalies.

The extracted rainfall components were subjected to Empirical Orthogonal Function (EOF) analysis to obtain their respective spatial and temporal structures. The dominant mode of variability of the MAC component corresponds to the rainfall regimes over the region with the southern parts of the region with unimodal rainfall regime indicating strong seasonality. It is further shown that the annual cycle is not strictly regular in frequency or amplitude for the period of study indicating changing annual cycle of rainfall.

The dominant mode of the inter-annual component corresponds to El Nino-southern oscillation (ENSO) climate variability with signals of positive rainfall anomalies in most parts of the region except the northwestern and western parts of Uganda. The decadal-to-trend variability shows a dipole pattern, with increasing rainfall trend in the northern sector and drying trend in the southern sector of the region. However, the positive trend in the northern sector of the region are reversed at coastal and lake Lake Victoria areas where weak negative trend is evident. Further, it is shown that the decadal-to-trend component captured the prominent significant fluctuations of rainfall that have been observed over the region through proxy data such as lake levels since the early 20th century.

1. Introduction

Considerable amount of research using empirical approaches has been done over the Equatorial East African (EEA) to explore the variability and prediction of rainfall on interannual to decadal time scales (Nicholson, 1986; Indeje *et al*, 2000; Rodhe and Virji,1976; among others). Most of these studies utilized techniques which assume that the studied climate variables are stationary and linear. However, for any weather or climate system, it is impossible for all the control systems including sources and sinks to be unchanged. Any disturbances in these conditions may change the basic behaviour of the system. In such a case the stationarity of the atmospheric process is modified (Yang and Zhou, 2005), hence there is a need to adopt methods that address the nonstationarity and nonlinarity in the the time series.

We address the problem of nonstationarity by using the empirical mode decomposition (EMD) (Huang et al., 1998; Huang and Wu, 2008) to understand the variability of the EEA rainfall and explore its teleconnectivity. EMD is empirical, intutive, direct, and adoptive, without requiring any predetermined functions. The decomposition is designed to seek different instrinsic modes of oscillations in any data based on the principle of local scale separation. The method does not assume a time series to be linear or stationary prior to analysis. An important component of the decomposition of a time series by EMD is the inclusion of the annual cycle, referred to as modulated annual cycle (MAC). Unlike more traditional methods, where climatology is subtracted from the data and only the anomalies are studied, this method decomposes the total signal. The annual cycle is an important

component and is retrieved as one of the components of variability in the decomposition.

2 Data and Methodology

Observed daily rainfall amounts for 44 stations across the three East Africa countries (Kenya, Uganda and Tanzania, extending from January 1962 to December 2000 was used in this study. Out of these stations, a few stations from Kenya had data dating back to early 1990s. The major method employed in this study is the Ensemble Empirical Mode Decomposition (EEMD). Other methods used included Empirical Orthogonal Function (EOF) analysis and graphical methods. The major steps in EEMD are: (a) add a white noise series to the targeted data; (b) decompose the data with added white noise into IMFs; (c) repeat step (a) and step (b) again and again, but with different white noise series each time; and obtain the (ensemble) means of corresponding IMFs of the decompositions as the final result. Detailed description of the EMD method can be found in Huang et al. (1998) and Wu and Huang, (2009). The steps to decompose a time series and to extract modes of variability by the EEMD method are as follows:

1. The EEMD technique is used to extract IMFs from the raw data series as described in the previous section (detailed procedure is in Huang and Wu, 2008);
2. The components (containing some annual cycle signal as well as some longer timescale variations) obtained from step 1 is combined and then one more single EMD decomposition is done on the combined series;
3. The resulting first IMF from step 2 is the final Modulated Annual Cycle (MAC) component;
4. The sum of the first components before the components combined in step 2 is the final high frequency component;
5. The combination of the residual from step 3 and the components after the components combined in step 2 showing interannual variability is the final interannual component; and
6. The the last remaining components from step 5 are combined as the final decadal-to-trend component.

The above decomposition and reconstruction process separates a raw series from each station an interannual component, and a decadal-to-trend component.

3 Results and Discussion

3.1 Spatial and Temporal Structure of Variability Components

Figure1 provides example of the major timescale components derived for Dagoretti station rainfall series using the EEMD technique. In this study only MAC and lower frequency components were considered for further analysis. The temporal and spatial variability of rainfall over EEA of thess time-scales are presented in the following sub-sections.

3.1.1 Modulated Annual Cycle (MAC)

Figure 2 (a) shows the spatial pattern for the leading eigenmode,EOF1, with variance of 35%, for the MAC component of the EEA rainfall which exhibits a north-south orientation. Positive loadings dominate the southern part of the region with negative loadings over the northen parts. The inter-tropical convergence zone (ITCZ) which sweeps across the region twice a year and determines the seasonal cycle and climatological rainfall pattern is largely responsible for the bimodal rainfall pattern experienced over many parts during March to May (long rains) and October to December (short rains). However, over southern part, unimodal climate regime dominates, with a single well defined wet season occurring during boreal winter. This implies that the seasonality of the annual cycle of rainfall is strong over this part of the region as depicted in Figure 2(a) compared to northern parts of the region which experience more than one rainfall season in a year. The parts dominated by negative and weak loadings in Figure 2 characterized by trimodal regimes since they often receive significant amounts of rainfall during July through September.

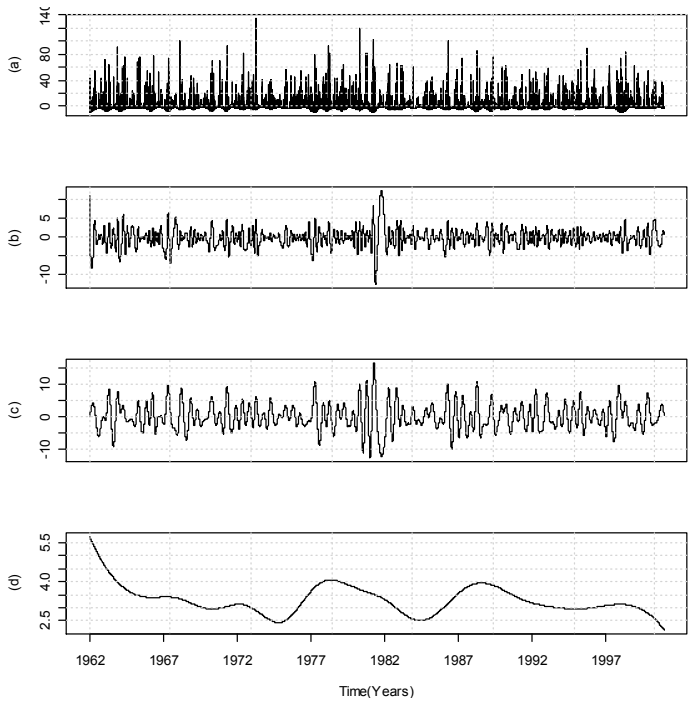

Figure 1: Components of daily rainfall at Dagoretti station for 1962-2000. (a) high frequency component; (b) MAC component; (c) interannual component; and (d) decadal-to-trend component.

The coastal region of EEA also receive rainfall in most parts of the year due to the effect of the Indian Ocean. Figure 2(b) of the corresponding EOF1 PC series shows that the annual cycle is not strictly regular in frequency or amplitude indicating a changing annual cycle of rainfall. The spatial pattern for the EOF2 (with variance of 24%) and its corresponding time-series (not shown) depicts significant positive loadings over parts affected by the local circulation systems. The remaining parts of the region exhibit weak loadings implying weaker effect of local systems in the annual cycle. Again as in EOF1, the EOF2 series indicates the modulation of the annual cycle with some years having stronger amplitude of annual cycle.

3.1.2 Interannual Variability

Figure 3 shows the pattern of the first eigenvectors (EOF1) of the monthly interannual rainfall componets and its corresponding PC series. The first and second patterns account for 30% and 8% of the total variance. The first EOF pattern (Figure 3a) is positive in most parts of the region except the northwestern, and western parts of Uganda that has weak negative signal. The highest values are concentrated in the eastern parts of the region. The loading patterns for MAM and OND (figures not shown) were generally simmilar with those of monthly series, with only slight differences. The corresponding first PC time series for the interannual component (Fig. 3(b)) shows variations throughout the data span. The periods with maxima values all coincided with warm ENSO events except Jul 1961 – May 1962 and Sep 1967 – Aug 1968. These two periods however coincided with the build up of positive anomalies over the Indian Ocean (positive Indian Ocean Dipole). For the years with minima values, two periods i.e. Sep 1964 – Jul 1965 and Oct 1998 – May 2000 coincided with the cold ENSO events while the others coincided with neutral ENSO phase. These results indicate that the first EOF of the interannual component for EEA is consistent with ENSO and Indian Ocean SST variability. The major warm ENSO events correspond to the high peaks of the time series especially for the OND season. The ENSO event of 1997 is however distinctly conspicuouse in all the first EOF PCS series for three cases considered.

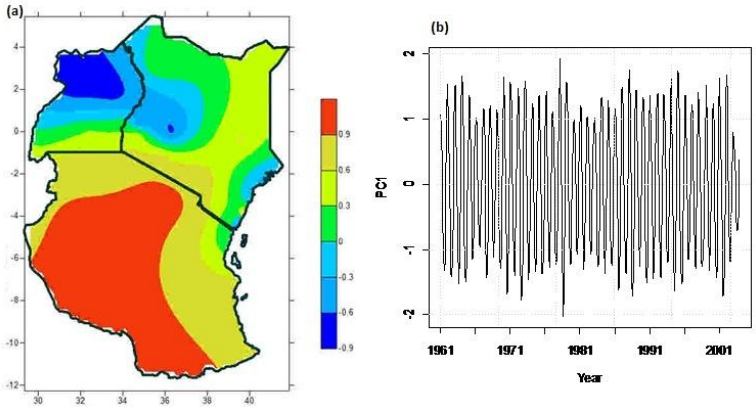

Figure 2: (a) The leading spatial mode – EOF1 (explains 35% of the total variance) of EOF analysis of MAC component; (b) its coresponding PC.

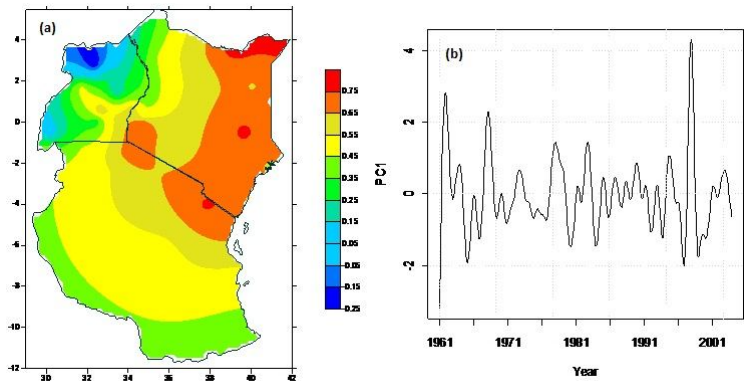

Figure 3: (a) The first spatial mode – EOF1 (explains 30% of the total variance) of EOF analysis of interannual component; (b) its coresponding PC

3.1.3 Decadal-toTrend Variability

The first EOF of the decadal-to-trend (Figure 4) variability explains 28% of the total variance of that time scale. Its loadings (Fig. 4 (a)) shows a dipole pattern, with positive loadings (increasing rainfall trend) in the northern sector and negative loadings (drying trend) in the southern sector of the region. However, the positive (increasing trend) loadings in the northern sector of the region are reversed at coastal and lake areas where weak negative loadings (drying trend) are evident. The corresponding PC series (Fig. 4 (b)) exhibits a decline from its highest levels in early 1960s to the lowest level in early 1970s, with an increase in amplitude that reaches a maximum in mid 1990s and then a decline in late 1990s. The highest amplitude in the early 1960s correspond to the period when the region recieved the heaviest rainfall in that century leading to the rise of Lake Victoria by several metres (Nichlson, 1986). Figure 5 (a) compares well with results of Nicholson and Yin, (2001), in which lakes of East Africa were used as indicators of environmental and climatic change on long time scales. The major fluctuations in the rainfall series are captured in the lake levels of their results.

Further we note that from the adoptive decadal-to-trend components for particular stations (for example Figure 5 for Garissa and Kisumu and other stations not shown), there is no distinctive trend in rainfall. However some stations from northern part of Kenya (Moyale, Lodwar and Garissa) showed a general positive trend. This observation somehow point in the same direction as the results of the climate model experiments using AR4 climate scenarios (IPCC, 2007) based on the gridded model data. They showed that East African climate is likely to become wetter, particularly in the Short Rains (October to December) and particularly in northern Kenya, in the forthcoming decades.

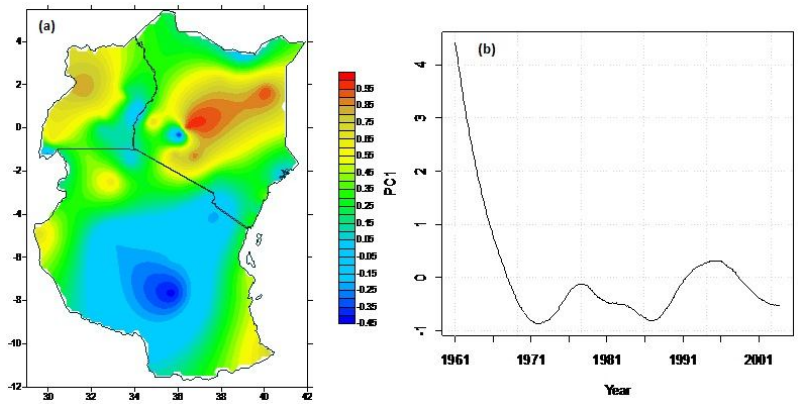

Figure 4: (a) The first spatial mode – EOF1 (explains 28% of the total variance) of EOF analysis of decadal-to-trend component; (b) its coresponding PC.

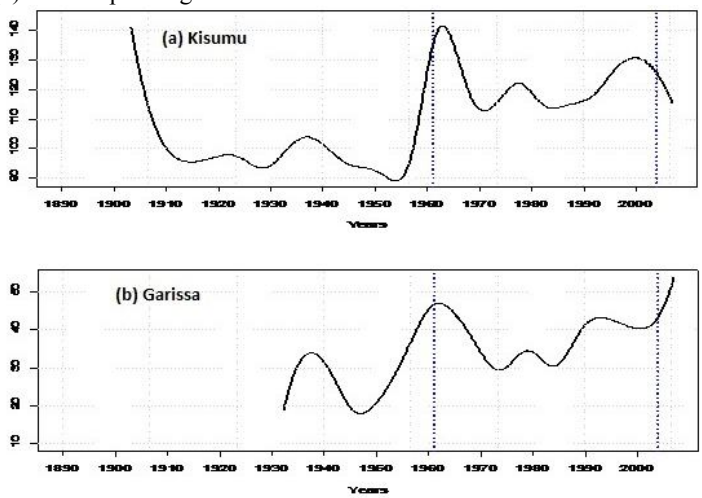

Figure 5: Adoptive decadal-to-trend componet extracted by EEMD method at (a) Kisumu and (b) Garissa from 1903-2006 and 1931-2006 respetively. The vertical dotted lines indicade the data period that was used in EOF analysis (i.e the period corresponding to the PCs time series in Figure 4).

4. References

Huang, N. E. , Z. Shen, and S. R. Long, M. C. Wu, E. H. Shih, Q. Zheng, C. C. Tung, and H. H. Liu, 1998: The empirical mode decomposition method and the Hilbert spectrum for non-stationary time series analysis, *Proc. Roy. Soc. London*, **454A**, 903-995.

Indeje, M., F. H. M. Semazzi, and L. J. Ogallo, 2000: ENSO signals in East African rainfall and their prediction potentials. *Int. J. Climatol*. **20**, 19-46.

IPPC, 2007: Report of Intergovernmental Panel on Climate Change, M.L. Parry, O.F. Canziani, J.P. Palutikof, P.J. van der Linden and C.E. Hanson, Eds., *Cambridge University Press*, Cambridge, UK.

Nicholson, S. E. 1986a: The spatial coherence of African rainfall anomalies—interhemispheric teleconnections. *J. Clim. Appl. Meteorol*., **25**, 1365–1381.

Nicholson, S. E., and X. Yin, 2001: Rainfall conditions in equatorial East Africa during the nineteenth century as inferred from the record of Lake Victoria. *Climatic Change*, **48**, 387–398.

Rodhe, H. and Virji H, 1976: Trends and periodicities in East African rainfall. *Mon. Wea. Rev*. **104**, 307-315.

Wu, Z., and N. E Huang, 2009: Ensemble Empirical Mode Decomposition: a noise-assisted data analysis method. *Advances in Adaptive Data Analysis*. **1**, 1-41.

Yang, P., and X. Zhou, 2005: On nonstationary behaviors and prediction theory of climate systems. *Acta Meteorologica Sinica*, **63**, 556-570.

Session G

Quantitative Precipitation Forecasts

Ongoing developments on Limited Area Ensemble Forecasting and the coordination role of TIGGE LAM

Tiziana Paccagnella
ARPA-SIMC, Hydro-Meteorological and Climate Service of the Emilia-Romagna
Regional Agency for Environmental Protection, Bologna, Italy, tpaccagnella@arpa.emr.it

Acknowledgments

Part of this presentation is based on the TIGGE LAM plan still under writing and I wish to aknowledge the co-authors and particularly Josh Hacker, David Parsons and Richard Swinbank.

I really wish to thank all the colleagues who sent me update information about their present activities: Jan Barkmeijer, Neil Bowler, Jing Chen, Jun Du, Claude Fisher, Inger Lise Frogner, Jiandong Gong, Nils Gustavson, Joshua Hacker, Trond Iversen, Ake Johansson, Mate Mile, Josè Antonio Garcia Moya, Ken Mylne, Yong Wang, Xue Ming, Chiara Marsigli, Andrea Montani, Olivier Nuissier, Nigel Roberts, Kazuo Saito, Susanne Theis, Zoltan Toth.

I apologize but, due to obvious editing restrictions, I could not give appropriate visibility to their contributions in this abstract.

Introduction

Ensemble forecasting was initially introduced to improve the predictability of atmospheric motions and processes at medium range and at the synoptic scale. These successful applications, together with the necessity to improve the predictability of severe /high impact weather events, led the scientific meteorological community to develop Ensemble Prediction Systems (EPS) based on Limited Area Models (LAM) to benefit of the higher attainable horizontal resolution.

Considering that Global EPS are moving to higher and higher resolution, the main added value from LAM EPS will be in the representation of phenomena at the convective-permitting/resolving scale. This is an important contribution if considering that high impact/severe events usually are strongly determined or enhanced by a mesoscale or convective scale component. Many open scientific and technical challenges are to be tackled and scientific issues cover a wide spectrum of problems, most of them common to Global EPS: mesoscale predictability, proper representation of the different sources of uncertainty, efficient methods to generate perturbations, interaction of local perturbations with those transmitted by the driving global systems, calibration of non Gaussian fields, verification of intense and rare events etc.etc.

LAM EPS: Scientific issues

The primary goal of EPS is to represent and quantify the uncertainty associated with numerical weather prediction. This uncertainty is due to the many approximations and errors affecting the modelling chain both during the assimilation of the meteorological observations and during the model integration. A "good" EPS should provide forecast scenarios statistically indistinguishable from the real atmospheric evolution, quantify the system uncertainty by means of the ensemble spread with the same amplitude of the forecast error, and should also provide a better deterministic forecast based on the ensemble mean (at least for upper air fields). Going from global to LAM EPS, the process to represent forecast uncertainty is even more intricate since larger scale perturbations (hereafter referred as larger perturbations) interact with perturbations generated to represent smaller scale errors (hereafter referred as local perturbations) typical of LAM forecasting.

A lot of research work has been done and is being doing with specific focus on the local perturbations on the initial conditions and on the model trajectories (e.g. Hacker et al 2010, Wang 2010 (talk at this conference) , Marsigli 2009, Montani et al. 2010, Li et al, 2008, Jing 2010 (talk at this conference), Wang 2010 (talk at this conference)). It is reasonable to expect that local perturbations will be relatively more important in the shortest time range and at very high resolution (1-3 km up to 24 hours). It is again reasonable to assume that consistency with boundary perturbations will sustain better the development of local perturbations, but methodologies to assure this consistency is still matter to be investigated. One of the most recent and advanced work in this direction has been done recently by the Met. Office (Bowler and

Mylne, 2009) where it is confirmed the limited period of survival of local perturbations in the initial conditions and the difficulties in drawing final conclusions in this sense.

Representation of details in lower boundary conditions is increasing steadily with more complex land-surface models and space-borne sensors. Those details can then exert more impact on a short-range mesoscale forecast and we expect this "branch" of perturbations will play a greater role in the future. Not much work on this subject has been done up to recently but, also considering the forthcoming increasing in horizontal resolution, methodologies to obtain proper perturbations in soil and surface parameters need to be developed and tested. (Mile 2010). Recent work (by Hacker,Snyder et al, 2010) showed that this task may prove formidable because atmospheric preconditioning can result in forecasts sensitive to small-amplitude uncertainty. Soil moisture is one of the most difficult soil parameter to be estimated. Due the poorness of available observations, and to the strong dependency on local soil properties, in numerical forecasting practice the soil moisture field is often computed as the field which produce the better near surface parameters forecast. It is well known that, especially if large scale forcing is weak, the impact of the soil moisture on local meteorological parameters can be extremely relevant and it is evident the importance of deriving proper methodologies to describe and account for the uncertainty in this field (Sutton et al 2006).

Topography has always been a big issue in numerical modelling since its effect on the atmospheric flow involves many phenomena. Going down with the mesh size, its representation can be more realistic but, especially in region with complex and steep orography, it is still necessary to apply some smoothing to avoid numerical instabilities or other problems like unrealistic precipitation at the grid scale. Many of the model parameters related to orography and to its subgrid variance are tunable and their setting is almost always based on sensitivity performed on a limited set of cases. Uncertainty related to these effects should be also investigated and represented in high resolution LAM EPS.

Multi Model – Multi Boundaries approach is also being exploited in several implementations (e.g. Garcia-Moya et al 2009; Marsigli 2009, Lin 2010 (talk at this conference)) during these years with promising results. The comparison of the benefits of well-calibrated single-model vs multi-model LAM EPS systems should also be explored also taking into account the extra-work required to have available suitable reforecast datasets. Where domains overlap a natural avenue for exploring and exploiting "ensembles of ensembles" may be possible for longer periods. An interesting application of the added value from the combination of a LAM EPS and a Global EPS is give by the NORLAMEPS system (Frogner et al. 2006). NCEP SREF and Canadian REPS will also be combined within NAEF (http://www.emc.ncep.noaa.gov/gmb/ens/NAEFS-5th/Session_5/Methot%20naefs-workshop-summary.pdf)

The development and testing of convective permitting EPS is now an "hot topic" in several centres (e.g at the University of Oklahoma (Clark et al 2010), at Meteo-France based on the Arome model, at DWD based on the COSMO model, at the Met Office based on the Unified Model, at NCEP based on the two NMM and ARW models) and this issue is particularly relevant in a mid-term planning since Global EPS systems are still far from these finer scale configurations. To keep going with the increase in horizontal resolution, it is very important to carry on studies about the predictability at the convection-resolving scale to support the design of the future LAM EPS systems.

Calibration is required to have highly reliable and sharp probabilistic forecasts. Because the expense of producing large data sets appropriate for calibration is substantial, most calibration research has been completed with global models from operational centres with longer archives, and in many cases simplified versions of global models. Mesoscale variability introduces further challenges to statistical methods. For example, mesoscale error modes may be less Gaussian and further may not be well defined by any known parametric distribution. Activities in this direction are ongoing (Diomede et al 2010 (talk at this conference) but more research is needed.

The definition of comprehensive verification techniques is always an issue especially when high resolution precipitation forecasts is considered (Barbara Brown 2010, talk at this conference; Anna Ghelli 2010, talk at this conference). LAM EPS probabilistic verification should also allow a fair intercomparison between Global EPS and Km scale ensembles. One of the greatest challenge for regional EPS systems is to accurately assess the probability of (relatively rare) extreme events, which often are far more important in terms of societal impact than "normal" weather. It is well known that the evaluation of forecast skill concerning extreme weather events is really critical due to poor statistics associated to these events. How best to do this? Is an alternative approach to e.g. ensemble bias correction required in order to best support the accurate forecasting of extreme events, as opposed to the forecasting of normal weather?. Much has

been done but much is still needed to progress in this direction. Weather type oriented verification is extremely important and international cooperation is necessary to constitute the necessary observational databases. Evaluate the general performance of regional EPS systems of LAMs coupled to application models (hydrology, air quality, …), and assess the benefit of the non-atmospheric uncertainty information to end users is also part of a comprehensive estimation of the added value coming from LAM EPS.

Data assimilation at the convective-permitting (and down to resolving) scale is a big issue also due to the lack of defined balances driving physical processing at the finer mesoscale. The importance of assimilating high resolution non conventional data make this branch of present NWP even more challenging. During the last decade, Ensemble Based data assimilation is doing big progresses but, especially at the fine scales in the scope of LAM EPS, research is still young and the impact of ensemble based technique still to be fully exploited. Both Hybrid techniques and fully Ensemble Based systems are under development and testing in many centres and european consortia.

LAM EPS and TIGGE LAM

The TIGGE-LAM panel was set up by the GIFS-TIGGE working group to coordinate the contribution from LAM EPS to the THORPEX Interactive Grand Global Ensemble (TIGGE; http://tigge.ecmwf.int/) and to the proposed Global Interactive Forecast System (GIFS). According to the THORPEX core objectives, GIFS-TIGGE is focussed on the optimization of the use of Ensemble Forecasting to maximize the forecast skill. TIGGE LAM is intended to coordinate actions to evaluate which are the events whose predictability can be improved by the use of LAM EPS. TIGGE LAM (http://www.smr.arpa.emr.it/tiggelam/) should define how best to implement ensemble prediction systems to address regional and local situations and specific high-impact weather types. TIGGE LAM activity should be developed by providing guidelines, coordinating activities and fostering research with the following main objectives:

- to contribute to the definition of scientific issues to advance LAM EPS
- to reinforce the link and cooperation with the other WWRP working groups with crossing competences.
- to support and foster research on LAM EPS by promoting actions to make the access to LAM EPS products easier and by coordinating / stimulating / participating to specific initiatives to address the relevant scientific issues
- to coordinate the archiving of limited-area ensemble forecasts by providing standards and guidelines and as a complement to the TIGGE archive
- to facilitate the interoperability of the different LAM-EPS
- to facilitate the implementation of new LAM EPS

To foster the Regional Focus, the Panel is being restructured in Regional Sub-Groups to make more efficient the interactions with the THORPEX Regional Committees, regional forecast centres and the national hydro meteorological services.

The different LAM EPS groups have been included in the TIGGE LAM mailing list and the metadata on the different LAM EPS systems (at least some of them) have been collected and are available on the TIGGE LAM web site (at: http://www.smr.arpa.emr.it/tiggelam/?search&Metadata). In Table 1, present LAM EPS systems are listed.

TIGGE LAM activities connected to TIGGE were mainly related to products archiving and format standardization. Following what already done by TIGGE a list of TIGGE LAM output parameters was defined together with the specific for the GRIB2 coding (http://www.smr.arpa.emr.it/tiggelam/?search&parameters). A sub-set of these output parameters have been classified as High Priority, and the Panel proposed to archive them at the three TIGGE Archiving Centres, NCAR, ECMWF and CMA. Europe is working to implement this archive; CMA is also planning to follow the Panel proposal. A good link with other Working Groups, Programmes and initiatives have also been established. It is envisaged that regional ensembles from TIGGE LAM will contribute to the development of the GIFS, by optimizing the use of the products of the existing systems and via the participation to relevant RDPs and FDPs. Products based on LAM EPS systems, where available, will supplement products available from the global TIGGE data, and demonstrate the additional benefit obtainable from higher resolution ensembles.

WWRP, THORPEX and GIFS-TIGGE represent a perfect opportunity to coordinate LAM EPS activity both at scientific and implementation level. WWRP offers the opportunity to have cross-coordination with the closely related working groups. THORPEX provides the organizational basis to LAM EPS to contribute to the improvement of We ather For ecasting with spe cific reference to Regional HIW. GIFS TIG GE represents the main reference since TIGGE LAM must complement global EPS by adding value where and when higher resolution and local optimization can play a substantial role.

The TIGGE LAM Plan is still under writing. The main scientific issues will be detailed within the Plan together with all the i nitiatives whic h are necessary to exploit at best the u nique po tential com ing from being part of these Programmes.

Table 1: List of LAM EPS

LAM EPS System	Status	Institute -Consortium	Contact person
Europe			
OMSZ LAMEPS	Operational	Hungary	Máté Mile
ALADIN LAEF	Operational	ZAMG / Austria	Yong Wang, Florian Weidle
AEMET-SREPS Op	erational	AEMET/Spain - HIRLAM	Jose Antonio Garcia Moya
NORLAMEPS Op	erational	Met.NO	Inger-Lise Frogner, Trygve Aspelien
MOGREPS	Operational	Met Office/UK	Ken Mylne
SRNWP PEPS	Operational	DWD /Germany - SRNWP	Sebastian Trepte
COSMO-LEPS	Operational	ARPA-SIMC/Italy - COSMO	Andrea Montani
COSMO-SREPS	Preoperational	ARPA-SIMC/Italy - COSMO	Chiara Marsigli
GLAMEPS	Dev/ Preoperational	DNMI-Univ Oslo/Norway - HIRLAM ALADIN	Trond Iversen
PEARCE	Operational	Meteo-France / France	Laurent.Descamps
AROME EPS	Research	Meteo-France / France	Olivier Nuissier
DMI - HIRLAM	Development	DMI	Xiao Hua Yang
USAM LETKF	Development	USAM/Italy Lu	cio Torrisi
Africa			
South Africa	Development	South Africa Weather Service	Eugene Poolman, Stephanie Landman
Botswana	Under Planning	Botswana Weather Service	Galebonwe Ramaphane
Asia			
CMA-WRF LEPS	Preoperational	CMA/China	Jiandong Gong
JMA MRI EPS	Research	MRI/Japan	Kazuo Saito
Korea	Research	Korean Met Administration	Hee Sang Lee
Vietnam	Development	Vietnam Weather Service	Mrs. Do Le Thuy, Mr. Le Duc
United States			
NCEP-SREF Op	erational	NCEP	Jun Du
U.S. Air force Mesoscale Ensemble	Operational	U.S. Air force	J. Hacker, C. Snyder
Convective Scale EPS	Research	Univ Oklahoma	Ming Xue
UWME	Research	Univ Washington /USA	Clifford Mass
EnKF	Research	Univ Washington /USA	Greg Hakim
Univ. Oklahoma	Research	Univ Oklahoma	David Stensrud
NOAA/OAR/ESRL/GSD Res	earch	NOAA/OAR/ESRL/GSD Isido	ra Jankov
Canada			
CMC LAM EPS	Preoperational	MS / Canada	Martin Charron

References

Bowler NE and K.R. M ylne. 2009. Ensemble tran sform Kalman filter perturbations for a reg ional ensemble prediction system Q. J. R. Meteorol. Soc. 135: 757–766 (2009)

Clark, A. J., W . A. Gallus, Jr. , M. Xue, and F. Ko ng, 20 10: Convecti on-allowing an d co nvection-parameterizing en semble forecasts of a mesos cale convective vort ex and ass ociated severe weather. Wea. Forecasting, Accepted.

Frogner I. L. . H. Ha akenstad , T. I versen 2006. L imited-area ense mble predictions a t the N orwegian Meteorological Institute Q. J. R. Meteorol. Soc. (2006), 132, pp. 2785–2808

García-Moya, J . A., Call ado, A., S antos, C, S antos-Muños, D. and Si marro, J., 20 09: Predictability o f Short-Range Forecasting: A Multi- model Appro ach. No ta Téchnica 1 del Serv icio de Predeci bilidad y Predicciones Extendidas. Agencia Estatal de Meteorología. Spain.

Hacker, J., C. Sny der, S.-Y. Ha, and M. Pocerni ch, 20 10: Linear an d n onlinear resp onse t o parameter variations in a mesoscale model. Tellus A. Under revision.

Hacker, J., S.-Y. Ha, C. Snyder, J. Berner, F. Eckel, E. Kuchera, M. Pocernich, S. Rugg, J. Schramm, and X. Wang, 2010: The U.S. Air Force Weather Agency's mesoscale ensemble: Scientific description and performance results. Tellus A. Under revision.

Hamill TM, 2006: Ensemble-based atmospheric data assimilation. Predictability of Weather and Climate (p. 124-156). Cambridge University Press.

Li X., M. Charron, L. Spacek, G. Candille 2008. A Regional Ensemble Prediction System Based on Moist Targeted Singular and Stochastic Parameter Perturbations. MWR, 136, 443-461.

Marsigli C. 2009. Final report on priority project SREPS (Short Range Ensemble Prediction System). Technical report of the COSMO consortium available at: http://www.cosmo-model.org/

Mile Mate 2010. Status and Developments of ALADIN LAMEPS at HMS. Available at: http://hirlam.org/

Montani A., D. Cesari, C. Marsigli and T. Paccagnella 2010. Seven years of activity in the field of mesoscale ensemble forecasting by the COSMO– LEPS system: main achievements and open challenges. Submitted to TELLUS A- Under revision

Saito K., M. Hara, H. Seko, M. Kunii and M. Yamaguchi, 2010b: Mesoscale ensemble prediction system of MRI/JMA at B08RDP Part1: Comparison of initial perturbation methods. Tellus.(submitted)

Saito K., H. Seko, M. Kunii and T. Miyoshi, 2010c: Mesoscale ensemble prediction system of MRI/JMA at B08RDP Part2 : Effect of the lateral boundary perturbation in breeding and local ensemble transform Kalman filter. Tellus.(submitted)

Sutton C, Hamill TM, Warner TT. 2006: Will perturbing soil moisture improve warmseason ensemble forecast? A proof of concept. Monthly Weather Review 134: 3174-3189.

The Regional Ensemble Prediction System(REPS) at CMA and its application to heavy rainfall forecast in monsoon season in China

Jing Chen,Guo Deng, Yinglin Li, Xiaoli Li, Jiandong Gong,
Xiaocong Wang. Jiangkai Hu

The Center of Numerical Weather Prediction,CMA
chenj@cma.gov.cn

1. Introduction

To improve the probabilistic forecast of the heavy rain events in summer season in China, the Center of Numerical Weather Prediction(CNWP),CMA developed regional ensemble prediction system (REPS).The REPS took advantage of achievements at high resolution deterministic mesoscale prediction model, data assimilation system and experiences from development of global ensemble prediction system at CNWP. The real time operational running of REPS is started from Jun 2010. Results showed that the REPS could give much more information comparing with control run. However, it was found that spread of REPS was small compared with observations and forecast errors, the forecasting error for control run was obvious, and mesoscale ensemble products were still not good enough for site- and time-specific forecasts, but it demonstrated good ability to capture the high impact weather event.

2.Developments of REPS/CNWP

The control model of REPS was the Weather Research and Forecasting model (WRF V2.2) over a limited area domain, which is covering China. Its horizontal resolution is 0.15 x 0.15 degree. The initial perturbation technique is based on the breeding of growing modes (BGM), which is a simple and inexpensive method to generate growing modes of the atmosphere. This method simulates data assimilation process and considers the errors in real data at the same time. The BGM-based initial perturbation in mesoscale ensemble prediction model was rescaled in a forecasting cycle, then produced 60-hour prediction twice a day at 00UTC and 12 UTC respectively. Lateral boundary conditions are obtained from global ensemble prediction system at CMA, in which 15 members participated in total, and each output of GEPS corresponds to one member of REPS. Efforts were made to include as much meso-scale data in

the initial field as possible based on the WRF ensemble forecasting flow and its designed model prediction flow by using 3-DVAR assimilation in 6-hour cycles.

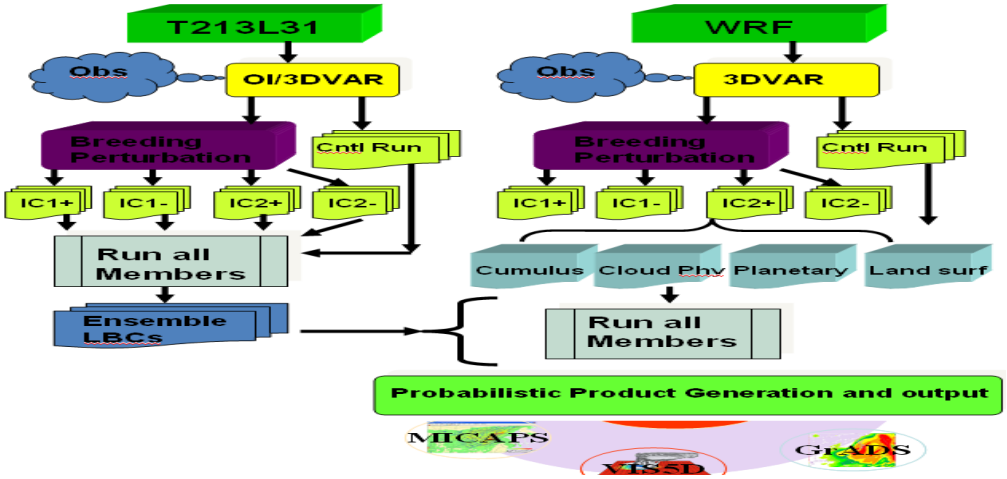

Fig.1 Flow chart of regional ensemble prediction system.

The experimental cases showed that the physical process perturbation, compared with initial condition perturbation, had greater impacts on the spread of ensemble prediction, To represent model error uncertainties, multi physics process was employed in the REPS(table 1).

Table 1 Multi-physics configuration of REPS/CNWP

members	microphysics	Convective parameterization	Planet boundary layer
Ctrl.	Lin scheme	Betts	MYJ
Pair 1	Lin scheme	KF	YSU
Pair 2	Lin scheme	Betts-Miller	YSU
Pair 3	Lin scheme	Betts-Miller-Janjic	YSU
Pair 4	Lin scheme	KF	MJY
Pair 5	WSM6	Betts-Miller	MJY
Pair 6	WSM3	Betts	MJY
Pair 7	WSM3	Betts	YSU

3. The performance of REPS/CNWP

The performance of REPS, are accessed for a 1-month period (July 07 2010 to Aug. 11 2010). The verification is performed by using analyzing field. Figure 2, 3 and 4 show the RMSE&SPREAD, CRPS for the T2m, MSLP and temperature at 850hPa, respectively. Obviously for all the verification variables, the RMSE of ensemble mean is smaller than the control one and the spread is

much smaller and grow slow. But the value of CRPS are all smaller than 1.5K, which is reasonable. The results provide the confidence to put the REPS into operational running.

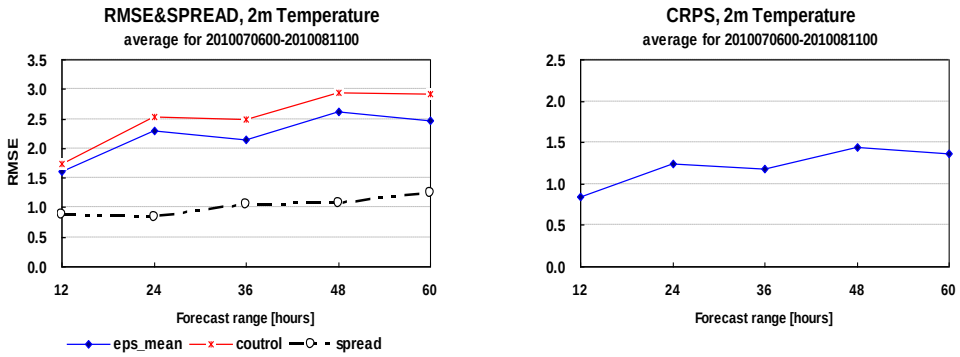

Fig. 2 The RMSE &SPREAD of ensemble mean (a) and CRPS(b) for 2m Temperature prediction

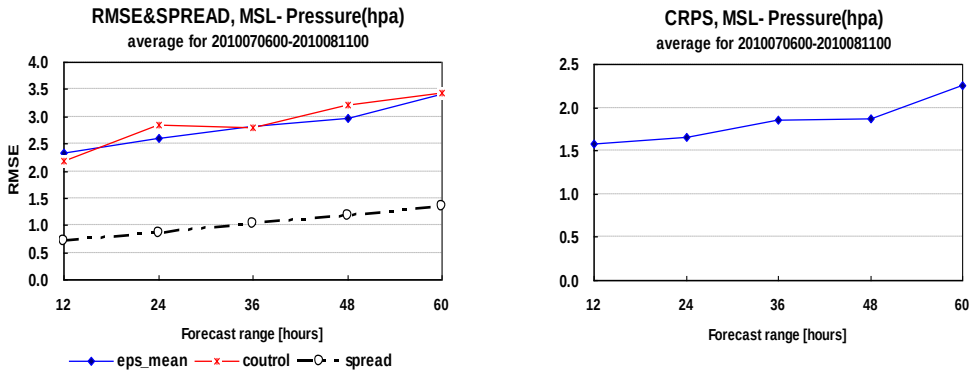

Fig. 3 The RMSE &SPREAD of ensemble mean (a) and CRPS(b) for MSLP(1000 hPa)

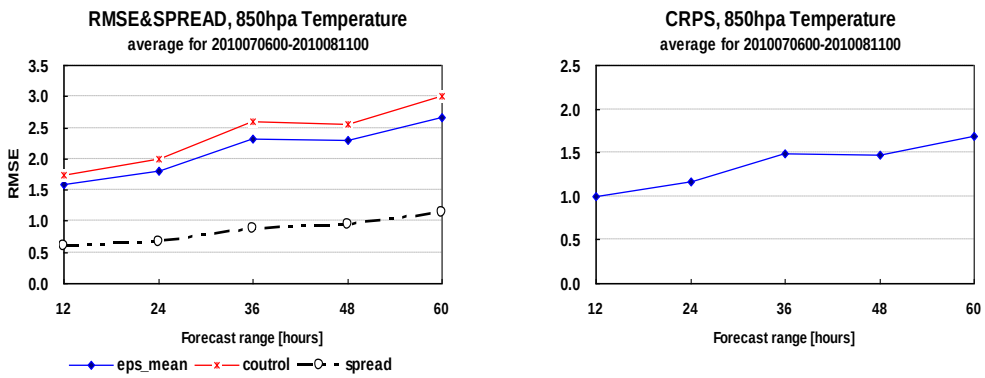

Fig. 4 The RMSE &SPREAD of ensemble mean (a) and CRPS(b) for 850hPa Temperature

4. Examples of application in monsoon season

One advantage of ensemble forecasting is to represent various uncertainties of weather forecasts. Conventional ensemble products based on model outputs were provided to forecasters. These products included the ensemble mean, ensemble spread, probability of occurrence of some phenomena, stamp charts

Two selected examples of REPS forecast products for HIW events in monsson season are presented in some detail. The first example is an squall line happened in Henan Province (June 3 2009). This squall line process was not predicted by forecasters, but it was found in retrospect that some REPSs had predicted gale. The second case was a successful forecast for the heavy rainfall in Yangtze river on July 9, 2010. From these case, comparing to deterministic forecasts, the advantage of REPS products for predicting the complex small-scale summer system over China was very obvious.

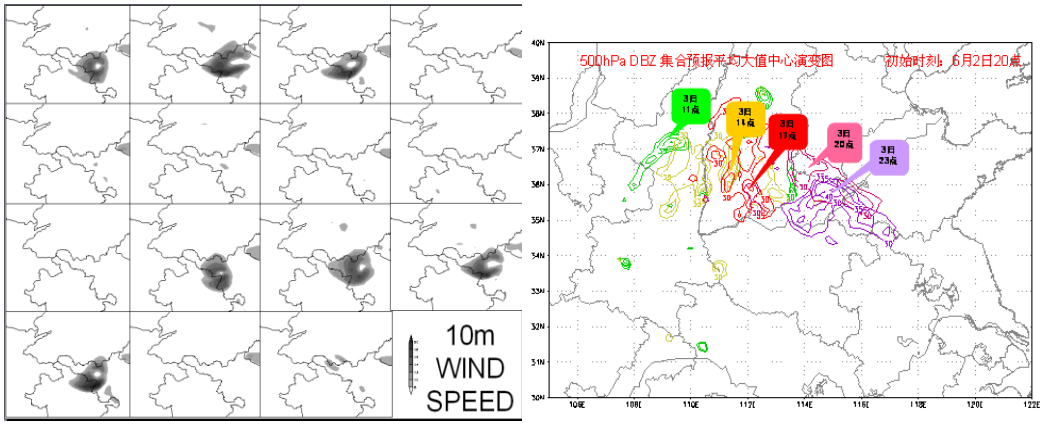

Fig.5 Stamp chart of 10m wind speed and ensemble mean of modeling radar reflection at 500hPa layer for 12h forecasts , which were initialized on 00Z June 3, 2009

5. Future plans

The Global/Regional Assimilation and Prediction System (GRAPES) has been recently developed for the next generation medium-range operational model at China Meteorological Administration (CMA).CNWP will developed GRAPES-based REPS. The initial perturbation is still a key point of REPS, so CNWP plan to develop initial perturbation such as Singular Vectors, Ensemble Transform Kalman Filter.

Ensemble forecast of tropical cyclone motion using RAMS model and Breeding of Growing Modes method

Tran Tan Tien[1], Cong Thanh[1]

[1] *Meteorology hydrology and oceanography of Faculty, ,Ha Noi University of Science. 334 Nguyen Trai, Thanh Xuan, Ha Noi, Viet Nam*

1. Introduction

In recent years the world as well as in Vietnam, the global model and regional models have been studied to improve both dynamic and physical processes to solve problems and weather and climate forecast The problem is interested in forecasting problem is: Data observer, data assimilation, integral models and evaluate the results predicted. To improve the quality of forecasting, early in 1990, ensemble forecast method was introduced. The contents of this method is the combination of the results forecast of the following: using a model with multiple inputs, using multiple models with inputs, each model using an input .

First of all, do not understand about the state of the atmosphere plays an important role. Small differences in initial atmospheric states could amplify the predicted big future in unstable conditions (Lorenz, 1963, 1965, 1993; Thompson, 1957) and NCEP centers have shown this intelligence. Initial conditions uncertainty plays an important role in creating the initial field. Currently the world's fifth most common way to create initial conditions uncertainty the following: Monte Carlo approach, Time-Lagged approach, Breeding approach, Singular Vector approach and methods Coupling with data assimilation [1].

For forecasting storms, Abersons and colleagues (2001) have used the noise from the NCEP global model, but research only very little improvement in storm track. Zhang and Krishnamuti (1997, 1999), Krishnamuti and MacKey (2001) has pointed out the difference in forecasts between control and perturbed models run allow direct communication with (EOF). Cheung and Chan (1999 a, b) applied three methods: Monte Calo, lagged-averaged, BGM to forecast TC motion with the barotropic model, the results show that, using improved methods of BGM has been over 40% of the predicted results. Cheung (2001) used MM5 model predictions and evaluation, the results indicate that Monte Calo method is lower than predicted in the test method BGM for better results in the first 36 hours. 2001, Puri and colleagues studied the forecasting system storm track in Europe with noise created by the original singular vetor method. They pointed out that approval of the orbit is highly sensitive to the platform using singular vector.

In this study, the number weather prediction (NWP) model assuming perfect, prediction error is only due to initial conditions trigger. Therefore, the key point of this method of creating a set of initial conditions slightly different for some models predict. In other words, the key to success is the combination of the effectiveness of the method of jamming the original field. The methods of creating original (initial seed) and raising the noise on the model used for global and regional models to predict the meteorological fields for the future.

In this study the authors have used the BGM method to generate an ensemble of initial meteorological fields for forecasting members.

2. Create initial seed and breeding in order to forecast typhoon track

2.1 Domain and grid configuration

To experiment forecast typhoon track by RAMS the domain and grid configuration were chosen : domain prediction of 161 x 161 grid points, 28 km horizontal resolution, center in 15^0N and 110^0E . The domain computer size is 4508 x 4508 km2. Calculation domain covers the whole territory of Vietnam and part of China, ensuring limited error diffusion calculation domain in mind, just consider the influence of the northeast monsoon store, derived from high Syberi pressure and other tropical center pole. Border south of the calculation domain at about -5^0S, with the goal of a better description advantages southwest monsoon in summer, blowing from the

southern hemisphere through the equatorial region of Southeast Asia . Number of vertical is 26, in which pressure on the colleges is 10 mb. Step time integrals are set to 60 seconds.

2.2 Create initial seed and breeding approach

In this process of initially cr eating Ti me-Lagged ap proach, t he conten ts o f this method are as follows: Using data analyzed by the OBS 48,42,36,30 hours before the time of making predictions and integrate the RAMS model to 24 hours before predicted. Select each corresponding pair of a field and subtract to create a perturbation field (D1, D2, ..., D6). We finally normalize the resulted perturbation field associated with each pair to the original noise (Figure 1a).

Results of how to create noise is the noise created originally for each of six fields (te mperature and wind components). The noise will be adopted to find the fastest growing mode.

The breeding method based on the idea of two authors Toth and Kalnay (BGM) [2]. The contents of this method as follows:

a / Create any noise and standardized as described above
b / Add and subtract noise has standardized with analysis field and integral model 6 hours with initial boundary condition is used to update the NCEP.
c / The two fields took effect predicted for the new noise D at the time t +6
d / Standardization of this interference by the formula

$$\mathbf{D^*} = S.D$$

Where

$$S = C / \Delta P$$

$$\Delta P = \sqrt{\frac{\sum_{1}^{N}\left[T^{p}_{850} - T^{n}_{850}\right]^2}{N}}$$

N is the number of grid points

T^{p}_{850}, T^{n}_{850} : is the value of a p air of positive and n egative predictions of the temperature field in the 850mb, C is a coefficient (chosen by experience).In the worke it was chosen C = 1.2

e/ Repeat from step b/ service at T00 (Figure 1b) we find the noise development

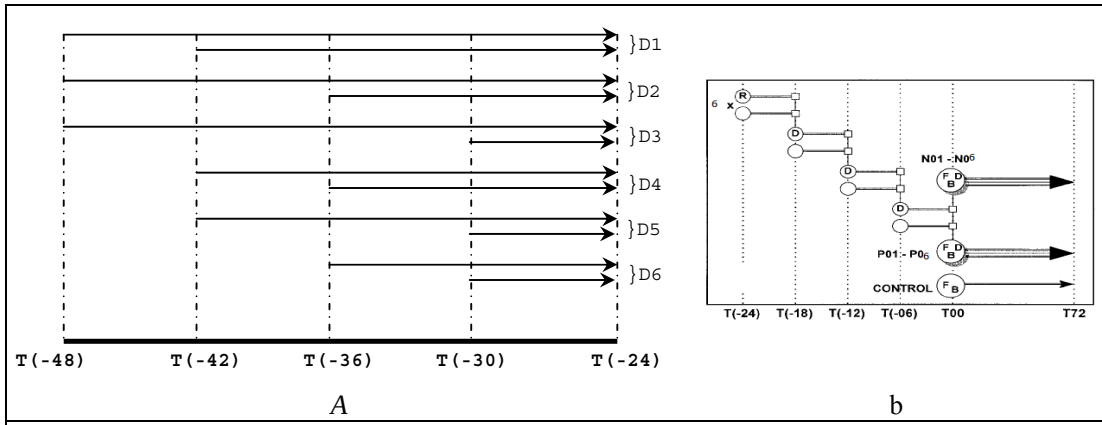

A b

Figure 1: *Create initial seed and BGM approach*

2.3 Initial data

Using global GFS data with a resolution of 1x1 degrees Theodolite interpolation of grid computer updates the weather station data and sea surface temperatures average week NCEP

3. Some results

Authors experimental method of creating initial seed and breeding to create the initial fields for

wind field (u and v) and temperature field [3], [4] to predict the storm track for ChanChu on May 13th, 2006

3.1 Evolutions of ChanChu storm (12-17/5/2006)

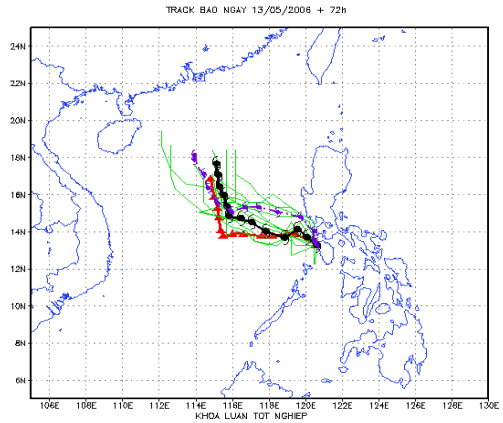

***Figure 2**. Forecast 72 hours in storm track by RAMS model on May 13, 2006*
Storm track control forecast: broken lines with circular dots;
Storm track from member prediction: instant thin lines (12 lines)
trajectory forecast combination: lines associated with circular dots;
Best track (Japanese copies): lines associated with the triangle

This is a very powerful storm, formed from the eastern Philippines on 12/5. Storm moved rapidly west northwest. Morning on 16/5, as to about 115 degrees longitude east, storm changed direction to move quickly to the north (Figure 2). , Night on 17/5 storm landed on the mainland province of Guangdong (China) [5].

Using the method of BGM to test predictions for this storm. For six of the original data, we used by the Obs 00, 06, 12, 18h on May 11, 2006 as the original data and the integral model RAMS to the time of 00h on May 12, 2006. Have taken effect had a pair of field prediction by Time-Lagged approach has created six of modes of the RAMS model.

Breeding of model RAMS with temperature, wind of the initial seed D1 in Chan Chu strorm as follows: add, subtract for temperature, wind in the all level's initial seed D1 with temperature, wind of all level's GFS 00h field on May 12, 2006 (T-24), the results created a new pair of field prediction.

Integral for this pair of field time to 06h on May 12, 2006 (T-18), looking at the forecasting performance of pairs (T-18) and standardized according to the formula presented in the BGM method. Field temperature, wind has been standardized and them have been add and subtract with the temperature, wind field in the GFS 12 h on May 12, 2006 (T-12), integrals of this pair to 18h on May 12, 2006 (T-06), predicted to result in (T-12) limit for 6 hours of temperature, wind field has found effective and standardized had add and subtract with plus temperature, wind field in the GFS field (T-6).

Continued interference in the integral pair (T-6), search performance and standardized temperature, wind field in the all level, we have been temperature, wind field of D1 (add and subtract with temperature, wind fields of GFS at 00 h on May 13, 2006 (T00), two new fields were created as two component predictions.

Thirteen fields were used as above to create 3-day forecast from the 7h on May 13, 2006 the meteorological field. Using DownHill method to determine the center of the storm predicted sea level pressure level. Storm track prediction is presented on Figure 5. Best track data used to evaluate the distance error, Along Track Error and across Track Error for Chan Chu storm. Evaluation results are presented in Table 1. From Table 1 shows predicted inspection RAMS

model results predict rate moves in the first 42 hours of delay (ALTE <0) and the difference of movement compared to the storm track (ACTC> 0), 30 hours after moving faster speed (ALTE> 0), movement offset to the left compared with the best track (ACTC <0).

Table 1: Table distance error (DE), Along Track Error (ALTE) and across Track Error (ACTE) of control forecast of RAMS model (CF) and mean of members (MM).
(The time of 7h forecast on May 13, 2006)

Term	DE(km)		ALTE (km)		ACTE(km)	
	CF	MM	CF	MM	CF	MM
6 11	4	63	-113	-62	15	13
12 16	0	67	-160	-60	15	29
18 19	8	70	-176	-67	90	-20
24 16	**8**	**36**	**-92**	**-25**	**140**	**27**
30 18	3	86	-75	-43	167	74
36 17	6	107	-74	-52	159	94
42 15	0	123	-74	-56	130	110
48	**168 14**	**7 165**		**125**	**27**	**76**
54	186 13	3 181		127	-43	40
60	219 12	8 215		124	-44	35
66	250 13	3 246		118	-42	61
72 16	**7**	**93**	**154**	**78**	**-66**	**50**

BGM method results predicted storm track better than control forecast, moving direction and distance error. Specific cases applies BGM approach in 24, 48 and 72 hours of the Along Track Error is -25, 125, 78 km, Across Track Error is 27, 76, 50 km, the distance error is 36, 147, 93 km. Meanwhile, the case of forecasting storm track with control forecast have Along Track Error is -92, 165 and 154 km, Across Track Error of 140, 27, -66 km, the distance error is 168, 168, 167 km. Especially in this case, the model predicts the direction of the storm track was 48 hours before (Figure 2) the distance error at the 168 km redirects in case of BGM and 147 km to the cases control forecast (Table 1)

3.2. Assessment of storm forecasting methodology adopted by Breeding of Growing Modes method across the entire sample.

Based on the sample of storm research, the authors make the orbit predicted storm track by RAMS model (Figure 3) and to evaluate the distance error based on seven hurricanes.

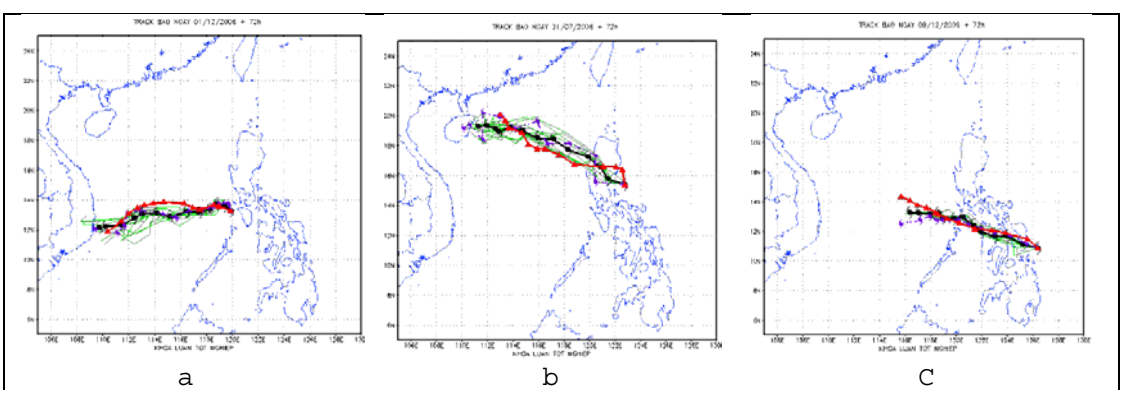

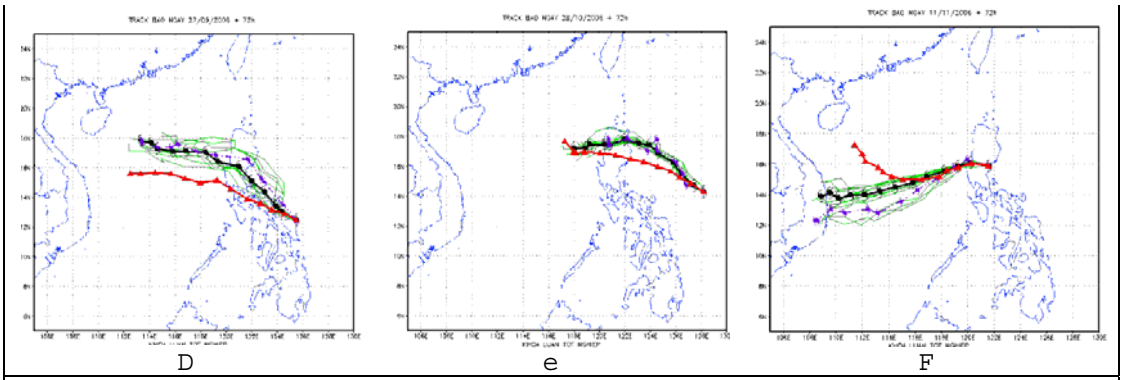

***Figure 3**. Forecast 72 hours in 6 storms track by RAMS model on May 2006*
Storm track control forecast: broken lines with circular dots;
Storm track from member prediction: instant thin lines (12 lines)
trajectory forecast combination: lines associated with circular dots;
Best track (Japanese copies): lines associated with the triangle

Reviews: From Figure 3 shows the results of ensemble forecasting method is a good with Durian (Figure 3.a), Prapiroon (Figure 3.b), Utor (Figure 3.c), Chan chu (Figure 2), Cimaron (Figure 3.e) and Chebi hurricanes (Figure 3.f). While the results predicted com ponents o f the Xangsane hurricane (Figure 3.d) have not been real trajectory of the storm.

Table 2: Mean distance error of 7 storms

MPE		
Term (h)	**BGM method (km)**	**Control forecast (km)**
6 72		70
12 75		75
18 103		105
24 101		134
30 120		164
36 139		165
42 151		178
48 137		203
54 148		233
60 145		266
66 174		302
72 153		324

Table 2 presents the results of average distance error of the en tire sample size for 7 storms in 2006. From the results in Table 2 on the average error distance of the entire sample with the test plan shows:

At the time of initial forecasts, the storm position in these plans nearly equal and relatively close to the l ocation of the ob servation position of the storm. The average error distance in each time forecasting 12, 24 and 36 hours of ensemble forecast respectively 75, 101 and 139 km. While in the control forecast error is worth 75, 134 and 165 km, another error negligible difference.

Term growth forecasts, the error location of the control forecast to increase much faster than forecast schemes BGM method. Specific term in the forecast 48, 60 and 72h, error of BGM method are 137, 145 and 153 km while the error for the control forecast are 203, 266 and 324 km.

Thus we have seen in the cases considered, BGM method for error location nearly 100 km of the storm track than control forecast in the forecast period 48, 60 and 72h. Thus, the BGM method increases the accuracy with the term forecasts predict 2 to 3 days.

4. Conclusion

Applying the BGM method and forecasting 7 storms track by 2006 with RAMS model forecast shows 72 hours when a result better than the case using control forecast, namely 171 km to improve with 72 hours term. In case of storms predicted this, the spread of the track component contains the best track of the storm forecast and control forecast. Results entirely consistent with the theory of ensemble of Kalnay is be good when the noise is positive and negative interference of the spread of the two predicted control forecast and the best track [6]. This result shows the effectiveness of the BGM method in the predicted storm and opened the possibility to apply the forecasting storm in Vietnam.

5. Reference

[1] Jun Du, Uncertainty and Ensemble forecast, *Lecture*

[2] Toth, Z., and E. Kalnay, 1997: Ensemble forecasting at NCEP and the Breeding method. *Monthly Weather Review*, **125**, 3297-3319.

[3] Xiaqion g ZHOU and Johnny C.L.CHEN, Ensemble forecasting of tropical cyclone motion using a baroclinic model, advances atmospheric sciences, vol. 23, No.3, 2006, 342-354

[4] Yong WANG and Alexander KANN,ALADIN Limited Area Ensemble Forecasting, *AMS online journal*

[5] Annual meteorological 2006, Hydro-Meteorological *Agency of Mid-Central Viet Nam Regional*

[6] Eugennia Kalnay, Ensemble forecasting and data assimilation

Blending a probabilistic nowcasting method with a high resolution ensemble for convective precipitation forecasts

Kirstin Kober[1], George C. Craig[12], **Christian Keil[1]**

[1]Meteorologisches Institut der Ludwig-Maximilians Universität München, Germany
[2]Deutsches Zentrum für Luft- und Raumfahrt, Institut für Physik der Atmosphäre, Oberpfaffenhofen, Germany
email: *kirstin.kober@lmu.de*

1. Introduction

Nowcasting and NWP are two different methods to address the challenge of accurately forecasting convective precipitation for short lead times. It is known that nowcasting methods that are based on extrapolation of observations perform quite well for very short term prediction (0-1 hour) as in this time frame the motion of convection can adequately be described by advection. For longer lead times, the skill of nowcasts decreases quite rapidly as the temporal evolution of the precipitation field can not be represented. High-resolution NWP is able to resolve convection. NWP models can simulate the temporal evolution of the precipitation field, but have difficulties with the representation of the initial state of the atmosphere. Due to the strengths and weaknesses of both methods, a skillfull forecast over lead times from 0 to 8 hours has to be a combination of both methods. The inherent uncertainty of the methods and of meteorological situations requires a probabilistic approach.

2. Data and Methods

The forecasts based on radar observations (2 km resolution) are calculated with the radar tracking algorithm Rad-TRAM (Kober and Tafferner 2009). This algorithm is extended with a module based on the Local Lagrangian method (Germann and Zawadzki 2005) to calculate the probability of exceeding the threshold of 19 dBZ for different lead times up to 8 hours (Kober et al. 2010). Therefore, the fraction of pixels above the threshold is calculated in a search area with lead time dependent size. This value is shifted to consider the motion of the field with the displacement vector calculated in the original algorithm, again depending on the lead time.

For the forecasts based on NWP, an experimental ensemble based on COSMO-DE model is used (2.8 km resolution). The model is started daily at 0 UTC with 24 hour forecasts. The COSMO-DE-EPS (Gebhardt et al. 2010) considers uncertainties of the lateral boundary conditions and the model physics and consists of 20 members. Based on the fields of synthetic radar reflectivities in 850 hPa, probabilistic forecasts are derived with three approaches. First, as traditionally applied on ensembles, the fraction of members above the threshold at each grid point is calculated. Second, each member is treated as a deterministic solution and the neighbourhood method (Theis et al. 2005) is applied. Here, the variability of the solution in time and space is considered and the fraction of pixels above the threshold in a predefined search area is calculated around each grid point. Third, the mean of the 20 neighbourhood members is calculated. This means, this method considers three sources of uncertainty: the imperfectness of the model, the lateral boundary conditions and possible timing and location errors. Finally, 22 different probabilistic forecasts are available at each forecast time.

The probabilistic model forecasts are calibrated with the reliability diagram statistics method (Zhu et al. 1996) for each of the three methods separately. This results in lower probability maxima for all three methods and more similar forecasts. The reliability com-

ponent of the Brier score is reduced for all methods.

3. Quality of Probabilistic Forecasts

The quality of the forecasts based on Rad-TRAM and COSMO-DE-EPS is evaluated with different measures to consider different aspects of quality: the Brier score and its decomposition, reliability diagrams, ROC curves and the area underneath them, and a version of the CSRR. Furthermore, the quality is evaluated in two set-ups. First, the development of quality with lead time is investigated to consider the dependence on different meteorological regimes. Second, and that is presented here, the development of quality is investigated with lead time.

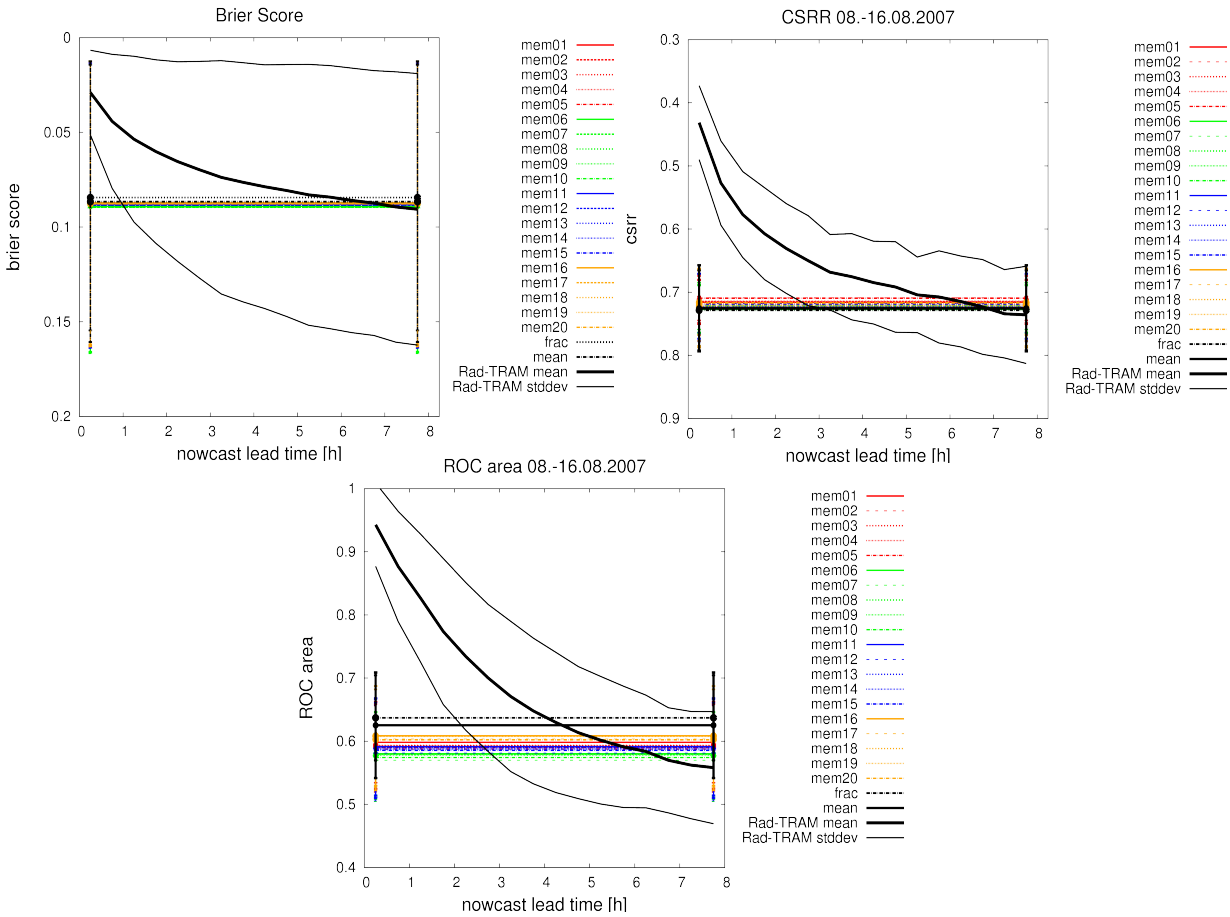

Fig.1: Development of Brier score, CSRR, and area under ROC curve with lead time for Rad-TRAM and calibrated COSMO-DE-EPS forecasts from 8 to 16 August 2007.

Figure 1 shows the development of skill with lead time over the investigated period from 8 to 16 August 2007 with the Brier Score, the CSRR, and the ROC area as well for Rad-TRAM and COSMO-DE-EPS. It can be seen in all scores that Rad-TRAM has very high skill in the first forecast hours that decreases to the low skill of the model for long lead times. The skill of the COSMO-DE-EPS forecasts is constant due to the set-up of the ensemble. The mean values cross around 5 to 7 hours, so that then the NWP forecasts have more skill than Rad-TRAM. Considering the variability of the mean over the investigated period further increases the cross-over time frame.

4. Blending of Rad-TRAM and COSMO-DE-EPS probabilities

In this study, the two forecast methods are combined additively. Therefore, weighting func-tions have to be defined. This is conducted following Kilambi and Zawadzki (2005). As the standard deviations are smallest in CSRR, the temporal development of Rad-TRAM's quality using this score defines its weighting function:

$$w_r(\tau) = 2.11 - \frac{1}{1 - CSRR(\tau)^{2.8}}$$

As the weights should sum to 1, the weighting function for all 22 COSMO-DE-EPS fore-casts is calculated with

$$w_c(\tau) = 1 - w_r(\tau)$$

Figure 2 displays the resulting weighting functions. While for lead times up to 5.75 h more weight is given to Rad-TRAM, the ensemble forecasts dominate the weighting afterwards. However, at the maximum lead time of 8 hours, Rad-TRAM still contributes to the blended forecast due to the small differences in quality of both forecast sources for long lead times (cf. Fig.1). This is in contrsat to very short lead times when only one component (Rad-TRAM) is used.

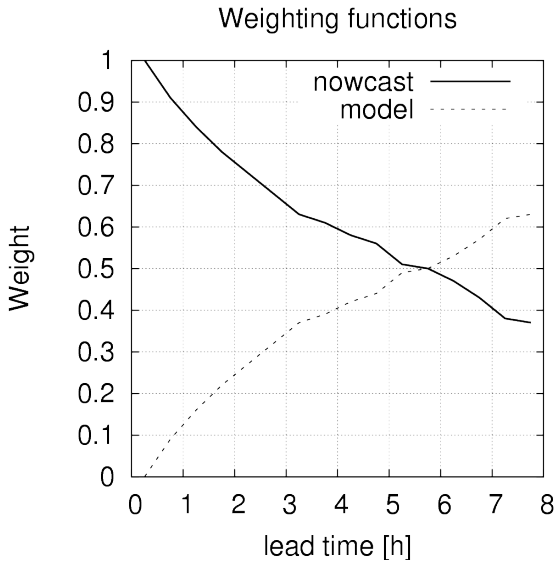

Fig.2: Weighting functions for Rad-TRAM and COSMO-DE-EPS for the blending procedure.

The blending procedure multiplies, depending on lead time, the respective weight on the probabilistic forecasts and sums the products**:**

$$P_{blend,i} = w_r(\tau) * P_{LL}(\tau) + w_c(\tau) * P_{EPS,i}$$

For all 22 COSMO-DE-EPS forecasts, the same weight is applied as the differences between the approaches are small (cf. Fig.1).

Figure 3 illustrates an example of the blending procedure with the components and the resulting combined fields for two different lead times. In the upper row, the maximum weight is at Rad-TRAM and in the lower at the COSMO-DE-EPS forecasts. Only the fraction method is shown due to clarity. It can be seen that for short lead times (upper row, τ=1.25h), the sharp structures of the Rad-TRAM forecasts (Fig.3a) can be clearly identified

in the combined field (Fig.3c). For long lead times (lower row, τ=7.25h), the combined field is dominated by the forecast with the fraction method. Figure 3 shows that the additive combination provides a smooth transition from one forecast source to the other. The blended probability fields are senseful and seamless combinations of the components.

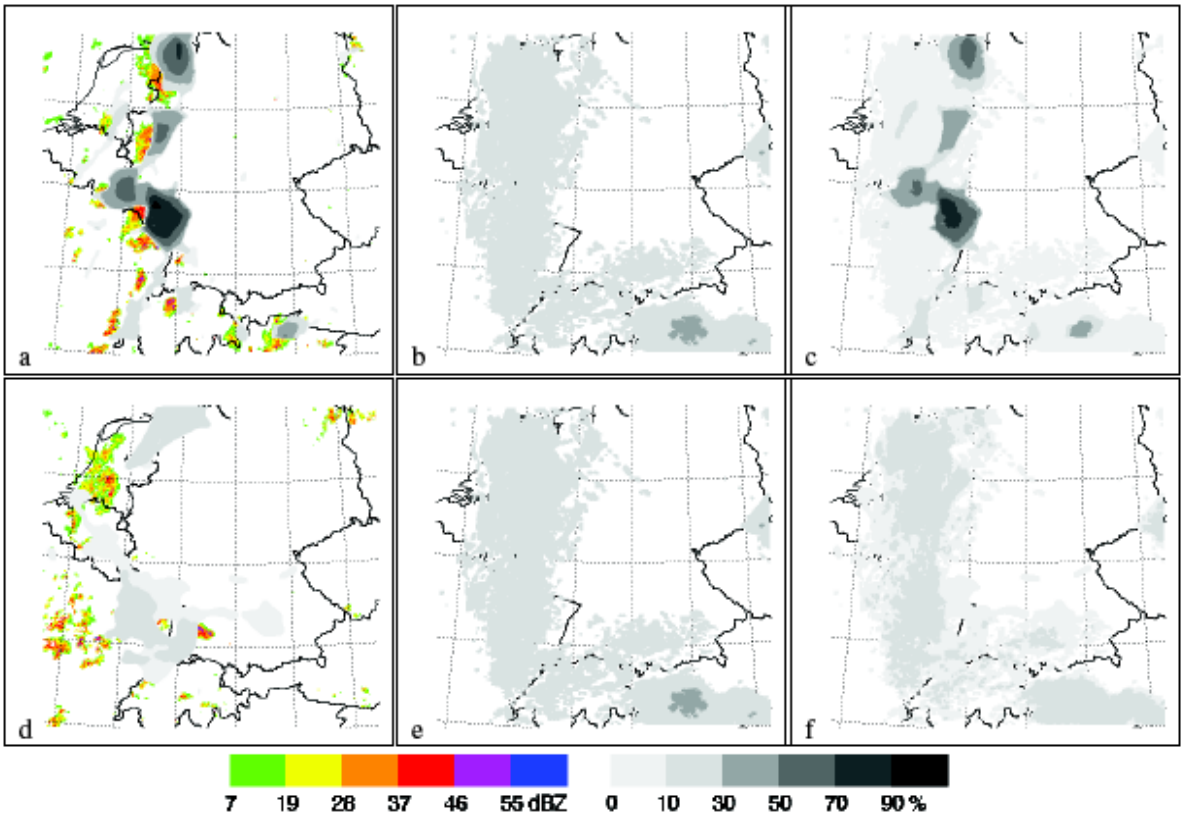

Fig.3: Combined probabilities for 12 August, 23:15UTC (c and f) with components from Rad-TRAM (a and d) and COSMO-DE-EPS fraction method (b and e) for τ=1.25h (a-c) and τ=7.25h (d-e). Observations used to initialise the Rad-TRAM forecasts are shown in colour in the background of panels (a) and (d).

Nevertheless, the value of the blending procedure must be proven in comparison to the forecast quality of the components (Fig.1) with the quality of the blended probability field. The combined fields should at least reproduce the skill of each component for various lead times. Fig.4 displays the quality of the blended forecasts with the Brier score, the CSRR, and the area under the ROC curve as evaluated for the single compontent. In comparison to Fig. 1 it is evident, that the combined fields show in all score the expected behavior. For short lead times, the skill is in the range of Rad-TRAM and the differences between the solutions are small. With increasing lead time, the differences increase as well. For long lead times, the skill is in the range of the respective COSMO-DE-EPS forecasts. For lead times around the cross-over times where the skill of both components is equal, the blending procedure even improves the skill of the forecasts. For example, in the ROC area, after 4 hours Rad-TRAM has lost 32% of its initial skill, whereas the combination with the fraction method still attains 73%.

5. Conclusions

In this work, a framework has been established to calculate and combine probabilistic forecasts from an observation based nowcasting method with forecasts from a high resolution ensemble. This enables to represent the phenomena of interest on the same scale. The combination provides seamless probabilistic forecasts that maintain the

skill of the best respective component and even improves them in the time around the cross-over point. One promising possiblity to reduce variabiltity in the results and likewise improve their reliability would be the consideration of synoptic regimes in the derivation of the calibration and weighting functions (Done et al. 2006). The performance of the model could be improved through the usage of a time-lagged ensemble including data assimilation.

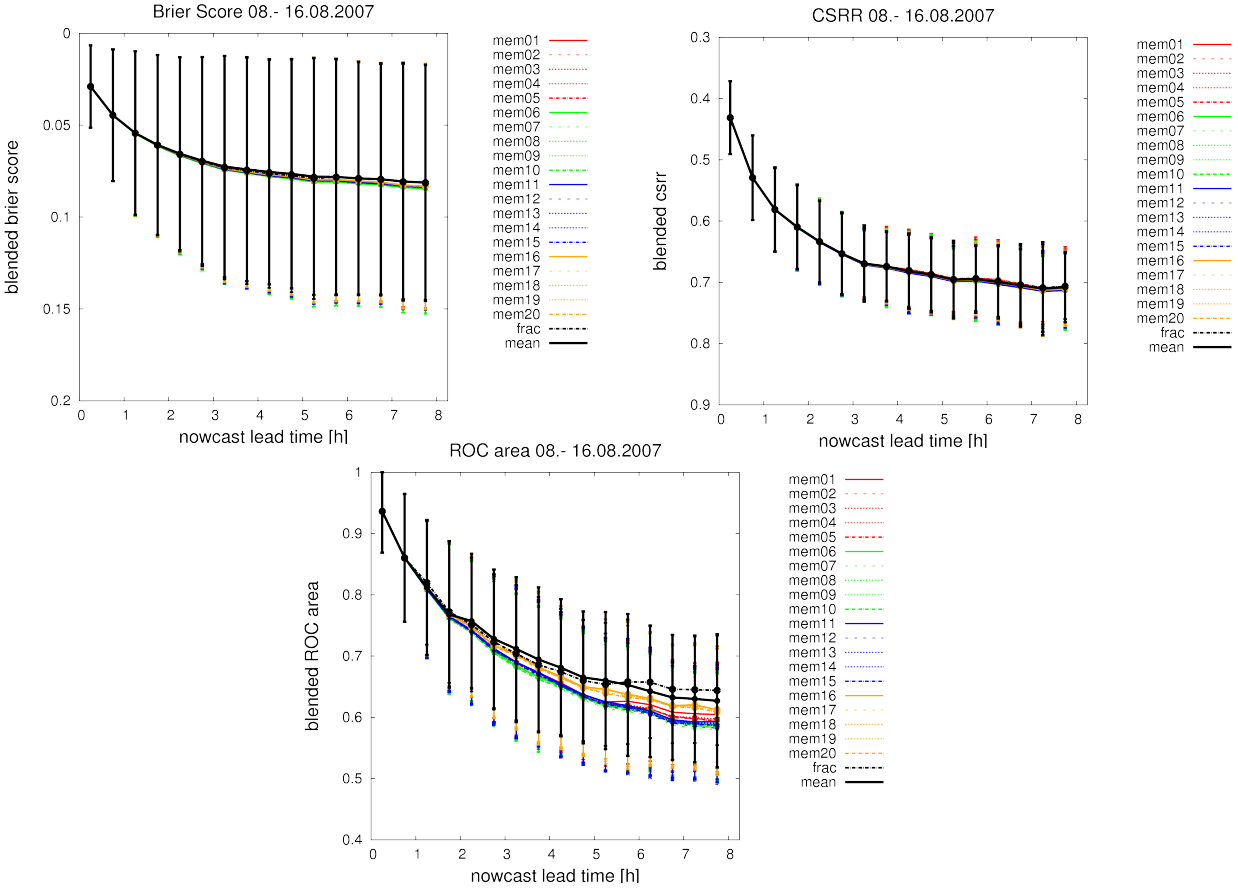

Fig.4: Development of Brier Score, CSRR, and area under ROC curve with lead time for blended probabilities from 8 to 16 August 2007.

References

Done, J., Craig, G.C., Gray, S., Clark, P. and Gray, M.: 2006, Mesoscale simulations of organized convection: Importance of convective equilibrium, *Quart. J. Roy. Meteor. Soc.* **132**, 737-756.

Gebhardt, C., Theis, S., Paulat, M. and Bouallegue, Z. B.: 2010, Uncertainties in COSMO-DE precipitation forecasts introduced by model perturbations and variation of lateral boundaries, *submitted to Atmos. Res.* .

Germann, U. and Zawadzki, I.: 2004, Scale Dependence of the Predictability of Precipitation from Continental Radar Images. Part II: Probability Forecasts, *J. Appl. Met.* **43**, 74-89.

Kober, K. and Tafferner, A.: 2009, Tracking and nowcasting of convective cells using remote sensing data from radar and satellite, *Meteor. Z.* **1**, 75-84.

Kober, K., Craig, G.C., Keil, C. and Dörnbrack, A.: Blending a probabilistic nowcasting method with a high resolution ensemble for convective precipitation forecasts, *submitted to Quart. J. Roy. Meteor. Soc.*.

Theis, S., Hense, A. and Damrath, U.: 2005, Probabilistic precipitation forecasts from a deterministic model: a pragmatic approach, *Meteorol. Appl*. **12**, 257-268.

Probabilistic QPF from a realtime multi-model storm-scale ensemble forecast system

Fanyou Kong[1], Ming Xue[1,2], and Xuguang Wang[1,2]
Center for Analysis and Prediction of Storms[1] and School of Meteorology[2],
University of Oklahoma, USA, fkong@ou.edu

1. Introduction

Producing skillful and reliable probabilistic QPF is a challenging task, especially when high-resolution NWP is involved. In support of NOAA Hazardous Weather Testbed (HWT) Spring Experiment, in the past four years since 2007 the Center for Analysis and Prediction of Storms (CAPS), in collaboration with the Storm Prediction Center (SPC) and the National Severe Storm Laboratory (NSSL) and funded by the NOAA CSTAR program, had conducted unprecedented and highly successful real-time storm-scale ensemble forecast (SSEF) experiment (Xue et al. 2007, 2008, 2009; Kong et al. 2007, 2008, 2009). In 2010 spring, under the new three-year CSTAR grant and with newly added collaborations with DTC, AWS, and HPC, the CAPS storm-scale ensemble forecasting system (SSEF) has been brought to a new level. Major changes in SSEF for the 2010 HWT Spring Experiment include: The forecast domain has been expanded to cover the entire continental United States (Figure 1), increasing total computing grid points by ~40% compared to the 2009 domain; The total number of ensemble members is increased to 26, consisting of two WRF dynamical cores (ARW and NMM) and the Advanced Regional Prediction System (ARPS); New double-moment microphysics schemes coming with WRF V3.1 are included in some ARW members; A large set of ensemble post-processed products from a 15-member sub-ensemble that consists of multi-model, IC and LBC perturbation, and radar analysis members are generated and made available near real-time to the HWT participants.

This extended abstract presents an overview of the storm-scale ensemble system and examples of the real-time ensemble QPF products. Some ensemble evaluation statistics are also presented.

2. Experiment overview

The CAPS 2010 Spring Program ran from 26 April 2010 to 18 June, encompassing the NOAA HWT 2010 Spring Experiment that is officially between 17 May and 18 June. This experiment period is shifted into mid-June to accommodate Aviation Weather Testbed activity. Three numerical weather models are used to produce a 26 member 30 h ensemble forecast during weekdays, covering a full-CONUS domain (Figure 1) at 4 km horizontal grid spacing. Nineteen members are produced using the Advanced Research WRF core (ARW), five members are produced using the WRF Nonhydrostatic Mesoscale Model core (NMM), and two members are produced using the Advanced Regional Prediction System (ARPS). Both WRF cores are the V3.1.1 release.

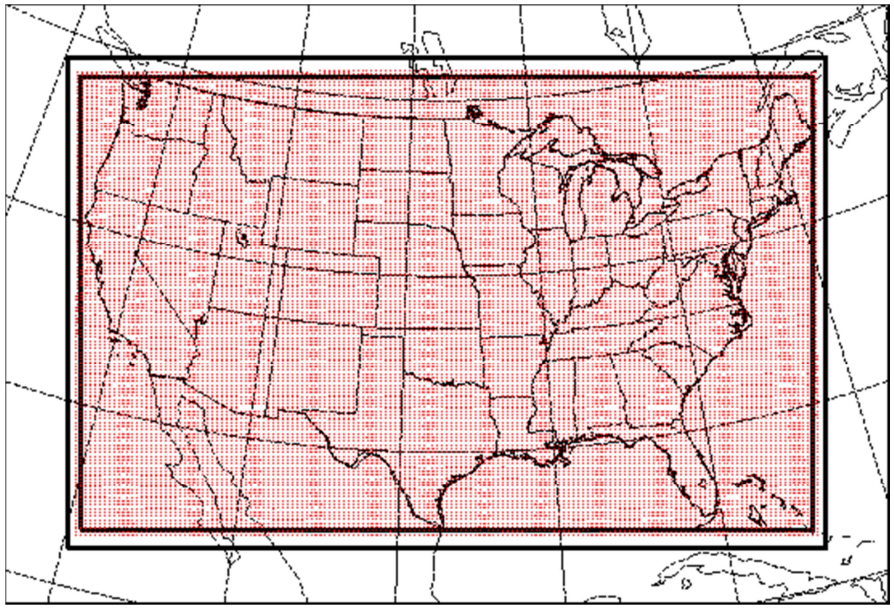

Figure 1. Computational domains for the 2010 Spring Experiment. The outer thick rectangular box represents the domain for performing 3DVAR/Cloud Analysis (1200×780). The red dot area represents the WRF-NMM forecast domain (790×999). The inner thick box is the domain for WRF-ARW and ARPS forecast and also for common verification (1160×720).

All forecasts are initiated at 0000 UTC, using NAM 12 km (218 grid) 00Z analyses as background for initialization with the initial condition perturbations for the ensemble members extracted from the NCEP Short-Range Ensemble Forecast (SREF). Doppler radar radial wind and reflectivity data from over 140 available WSR-88D stations within the domain are assimilated through ARPS 3DVAR and Cloud Analysis package into all but three members (one from each model group). All 4 km ensemble forecasts are performed on Athena, a Cray XT4 supercomputer system with 18000+ computing cores, at the NSF sponsored National Institute of Computational Sciences (NICS) in the University of Tennessee.

Table 1-3 outline the configurations for each individual members of each model group (arw, nmm, and arps). cn refers to the control member, with radar data analysis, c0 is the same as cn except for no radar data is analyzed in. m3 – m19 are members with either initial perturbation or physics perturbation or both added on top of cn initial condition. NAMa and NAMf refer to 12 km NAM analysis and forecast, respectively. ARPSa refers to ARPS 3DVAR and Cloud Analysis using NAMa as the background. For the perturbed members arw_m5~m14 and nmm_m3~m5, the ensemble initial conditions consist of a mixture of bred and ET perturbations coming from the 21Z SREF perturbed members (4 WRF-em (ARW), 4 WRF-nmm (NMM), 2 ETA-KF, 2 ETA-BMJ, and 1 RSM-SAS) and physics variations (grid-scale microphysics, land-surface model (LSM), and PBL physics). New in 2010 Spring Experiment is the addition of three random perturbation members (arw_m3~m5) and five extra physics-perturbation-only members (arw_m15~m19). Two types of random perturbations are added, one is Gaussian type perturbation and another is Gaussian perturbation plus a recursive filter with convective storm scale length. The physics-perturbation-only members are added

to help assessing impacts from different microphysics and PBL schemes. The lateral boundary conditions come from the corresponding 21Z SREF forecasts directly for those perturbed members and from the 00Z 12 km NAM forecast for the non-SREF-perturbed members.

Table 1. Configurations for each individual member with WRF-ARW core. NAMa and NAMf refer to the 12 km NAM analysis and forecast, respectively. ARPSa refers to ARPS 3DVAR and cloud analysis

member	IC	BC	Radar	microphysics	LSM	PBL
arw_cn	00Z ARPSa	00Z NAMf	yes	Thompson	Noah	MYJ
arw_c0	00Z NAMa	00Z NAMf	no	Thompson	Noah	MYJ
arw_m3	arw_cn + random pert	00Z NAMf	yes	Thompson	Noah	MYJ
arw_m4	arw_cn+RF-smoothed pert	00Z NAMf	yes	Thompson	Noah	MYJ
arw_m5	arw_cn + em-p1+recur pert	21Z SREF em-p1	yes	Morrison	RUC	YSU
arw_m6	arw_cn + em-p1_pert	21Z SREF em-p1	yes	Morrison	RUC	YSU
arw_m7	arw_cn + em-p2_pert	21Z SREF em-p2	yes	Thompson	Noah	QNSE
arw_m8	arw_cn – nmm-p1_pert	21Z SREF nmm-p1	yes	WSM6	RUC	QNSE
arw_m9	arw_cn + nmm-p2_pert	21Z SREF nmm-p2	yes	WDM6	Noah	MYNN
arw_m10	arw_cn + rsmSAS-n1_pert	21Z SREF rsmSAS-n1	yes	Ferrier	RUC	YSU
arw_m11	arw_cn – etaKF-n1_pert	21Z SREF etaKF-n1	yes	Ferrier	Noah	YSU
arw_m12	arw_cn + etaKF-p1_pert	21Z SREF etaKF-p1	yes	WDM6	RUC	QNSE
arw_m13	arw_cn – etaBMJ-n1_pert	21Z SREF etaBMJ-n1	yes	WSM6	Noah	MYNN
arw_m14	arw_cn + etaBMJ-p1_pert	21Z SREF etaBMJ-p1	yes	Thompson	RUC	MYNN
arw_m15	00Z ARPSa	00Z NAMf	yes	WDM6	Noah	MYJ
arw_m16	00Z ARPSa	00Z NAMf	yes	WSM6	Noah	MYJ
arw_m17	00Z ARPSa	00Z NAMf	yes	Morrison	Noah	MYJ
arw_m18	00Z ARPSa	00Z NAMf	yes	Thompson	Noah	QNSE
arw_m19	00Z ARPSa	00Z NAMf	yes	Thompson	Noah	MYNN

Table 2. Configurations for each individual member with WRF-NMM core

member	IC	BC	Radar	mp_phy	lw_phy	sw-phy	sf_phy
nmm_cn	00Z ARPSa	00Z NAMf	yes	Ferrier	GFDL	GFDL	Noah
nmm_c0	00Z NAMa	00Z NAMf	no	Ferrier	GFDL	GFDL	Noah
nmm_m3	nmm_cn+nmm-n1_pert	21Z SREF nmm-n1	yes	Thompson	RRTM	Dudhia	Noah
nmm_m4	nmm_cn+nmm-n2_pert	21Z SREF nmm-n2	yes	WSM 6	RRTM	Dudhia	RUC
nmm_m5	nmm_cn + em-n1_pert	21Z SREF em-n1	yes	Ferrier	GFDL	GFDL	RUC

Table 3. Configurations for each individual member with ARPS

member	IC	BC	Radar	Microphysics	radiation	PBL	Turb	sf_phy
arps_cn	00Z ARPSa	00Z NAMf	yes	Lin	Chou/Suarez	TKE	3D TKE	Force-restore
arps_c0	00Z NAMa	00Z NAMf	no	Lin	Chou/Suarez	TKE	3D TKE	Force-restore

3. QPF products

A total 36 days of complete set of ensemble forecasts were produced throughout the experiment period. Post-processed QPF products from the SSEF were generated in realtime, including probability matching mean, frequency-based ensemble probability,

and neighborhood probability of accumulated precipitation. Model forecast QPF and probabilistic QPF (PQPF) has been evaluated using various verification metrics and compared to the operational 12-km NAM forecasts. The PQPF from SSEF outperforms that of NAM and SREF in many case dates. Figure 2 shows examples of ensemble-based deterministic QPF product, the probability matching mean, and two PQPF products, the frequency-based probability and neighborhood probability. All match the observation (NSSL QPE product) well, even with a 30 h lead time.

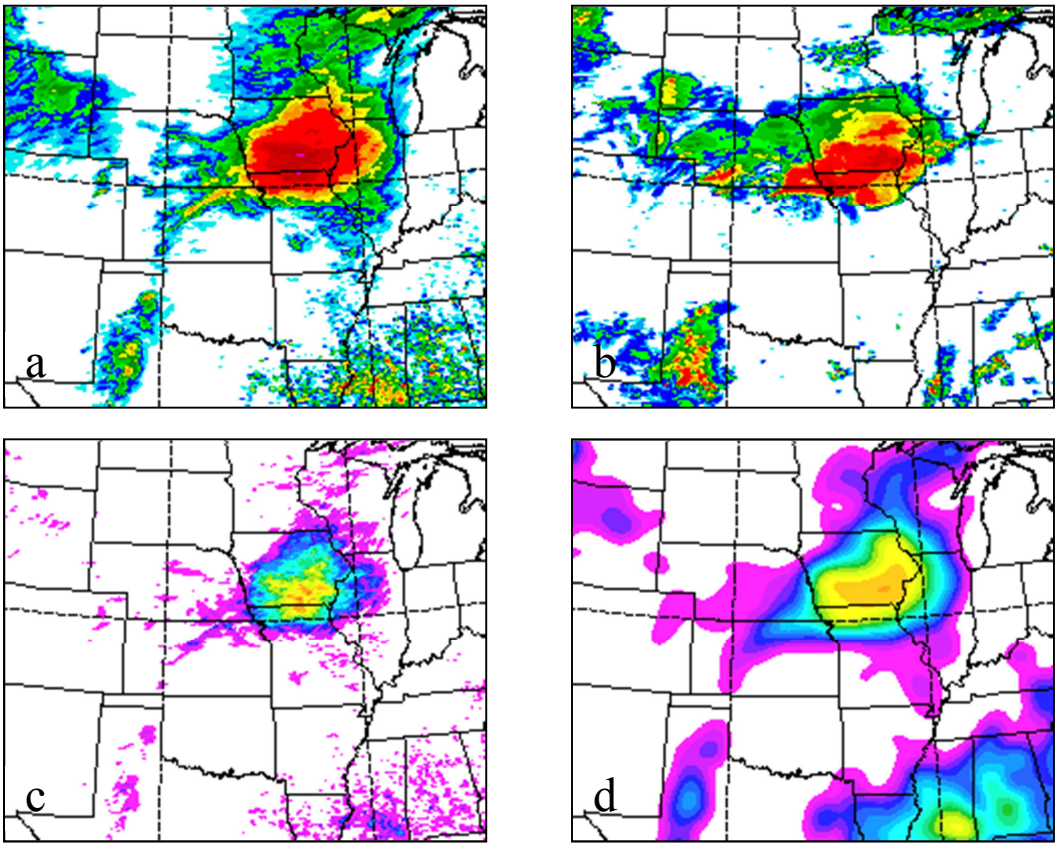

Figure 2. 30 h forecast QPF products of the 6-h accumulated precipitation, valid 0600 UTC 2 June 2010. (a) Probability matching mean, (b) NSSL QPE (observation), (c) ensemble probability for the threshold of 1", and (d) neighborhood probability for the threshold of 1".

The equitable threat scores (ETS) of 3-h accumulated precipitation forecast from individual SSEF ensemble members, ensemble mean and probability matching mean, as well as the operational NAM (12 km grid spacing) , calculated over the 36 days of data, are shown in Figure 3. The thick lines, one from each model group, represent the control member of the corresponding group. It is clear that all high-resolution, convection-resolving members outscore the operational NAM QPF, especially with higher thresholds. The probability matching mean outperforms individual members as well as the classic ensemble mean.

Skill scores and reliabilities of PQPF, both frequency-based and neighborhood-based, and among different subsets of ensembles have been evaluated. New approach to produce probability matching mean QPF has been explored.

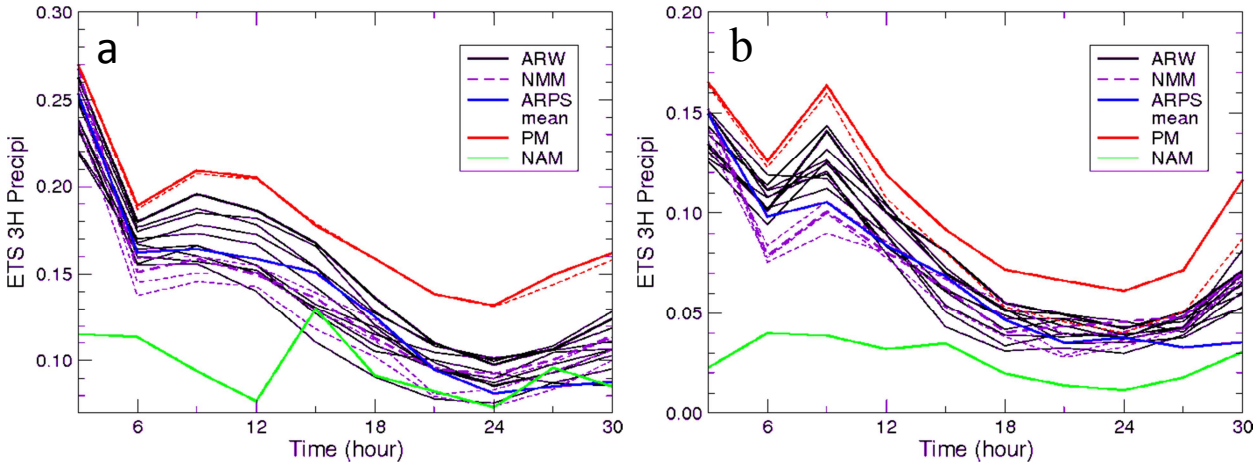

Figure 3.ETS scores of the 3-h accumulated precipitation forecasts from the 15-member sub-ensemble and the operational NAM over 36 days, for the threshold of 0.01" (a) and 0.5" (b).

Acknowledgements

This research was mainly supported by a grant to CAPS from the NOAA CSTAR program. Supplementary support was also provided by NSF ATM-0802888, and other NSF grants to CAPS. The realtime forecasts presented here were produced at the National Institute of Computational Science (NICS) at the University of Tennessee. A supercomputer of the Oklahoma Supercomputing Center for Research and Education (OSCER) was used for some of the ensemble post-processing.

References

Kong, F., and co-authors, 2007: Preliminary analysis on the real-time storm-scale ensemble forecasts produced as a part of the NOAA Hazardous Weather Testbed 2007 Spring Experiment. *Preprints, 22th Conf. on Weather Analysis and Forecasting and 18th Conf. on Numerical Weather Prediction* Amer. Meteor. Soc., Park City, UT, 3B.2.

Kong, F., and co-authors, 2008: Real-time storm-scale ensemble forecast experiment - Analysis of 2008 spring experiment data. *24th Conf. Several Local Storms*, Savannah, GA, Ameri. Meteor. Soc., Paper 12.3.

Kong, F., M. Xue, K.W. Thomas, J. Gao, Y. Wang, K. Brewster, K.K. Droegemeier, J. Kain, S. Weiss, D. Bright, M. Coniglio, and J. Du, 2009: A real-time storm-scale ensemble forecast system: 2009 spring experiment.. 23rd Conf. Wea. Anal. Forecasting/ 19th Conf. Num. Wea. Pred., Omaha, NB, Amer. Meteor. Soc., Paper 16A.3

Xue, M., and co-authors , 2007: CAPS realtime storm-scale ensemble and high-resolution forecasts as part of the NOAA hazardous weather testbed 2007 spring experiment. *22nd Conf. Wea. Anal. Forecasting/18th Conf. Num. Wea. Prediction*., Amer. Meteor. Soc., Park City, UT, Paper 3B.1.

Xue, M., and co-authors, 2008: CAPS Realtime Storm-scale Ensemble and High-resolution Forecasts as Part of the NOAA Hazardous Weather Testbed 2008 Spring Experiment. *Preprints*, *24th Conf. on Severe Local Storm*, Amer. Meteor. Soc., Savannah, GA, Paper 12.2.

Xue, M., and co-authors, 2009: CAPS realtime multi-model convection-allowing ensemble and 1-km convection-resolving forecasts for the NOAA Hazardous Weather Testbed 2009 Spring Experiement. 23rd Conf. Wea. Anal. Forecasting/19th Conf. Num. Wea. Pred., Omaha, NB, Amer. Meteor. Soc., Paper 16A.

Development of QPF approaches in NMC/CMA

Jian LIN[1], Xing JIANG[1], and Kan DAI[1]
Fanghua ZHANG [1], Xuekuan MA [1] and Lin DONG[1]
National Meteorological Center[1], CMA
linjian@cma.gov.cn

1. Introduction

To meet the needs of economy growth and public community, especially needs of the weather services on some important societal activities, such as Olympic Games and National Day's Celebration, fine quantitative precipitation forecast (QPF) is of great importance. In May 2008, QPF section is set up in NMC to be mainly responsible for providing QPF products with an interval of 6 hours in the coming 24 hours. The operational QPF system involves in some new data, including real-time data (radar, AWS et al.) and new NWP data.

At present, the QPF forecast just provide the distribution of the different rainfall grade shown by different isolines, such as light, moderate, heavy rain, rain storm and so on. There is no quantitative precipitation forecast in deed. In order to obtain the real QPF products, some QPF approaches should be developed , for instance, multi-model rainfall ensemble forecast based on different rainfall models, which can be regarded as an essential rainfall forecast. Meanwhile, meso-scale ensemble probability forecast and ingredient-based methodology are also used as supplements and corrections for QPF. In this paper, our attempts to develop the above mentioned approaches.

2. Multi-model rainfall ensemble forecast

For the use of numerous NWP data in QPF, the major challenge is how to use them in the limited time and how to improve the forecast efficiency and accuracy. Short range ensemble forecasting (SREF) of quantitative precipitation (Du J, 1997, Stensrud D J, 2000, Du J, 2002) can increase the forecast accuracy. Due to the inability of ensemble mean results to the extreme rainfall event, multi-model rainfall ensemble forecast, with the consideration of the shape of rainfall belt and intensity of rainfall, is applied in the operation of QPF, of which the weight of different model is decided by the similarity degree (Li Kaile, 1986) of different rainfall forecast of models in terms of stepwise regression (Chen Liqiang, 2005). This method takes into account the diversity and probability distribution of the rainfall forecast of different models.

Fig 1 presents the flow chart of multi-model rainfall ensemble forecast. According to the verification of routine operation, the rainfall forecasts of T639, EC, Japan and NCEP models are of better performance and chosen to the members of multi-model rainfall ensemble forecast.

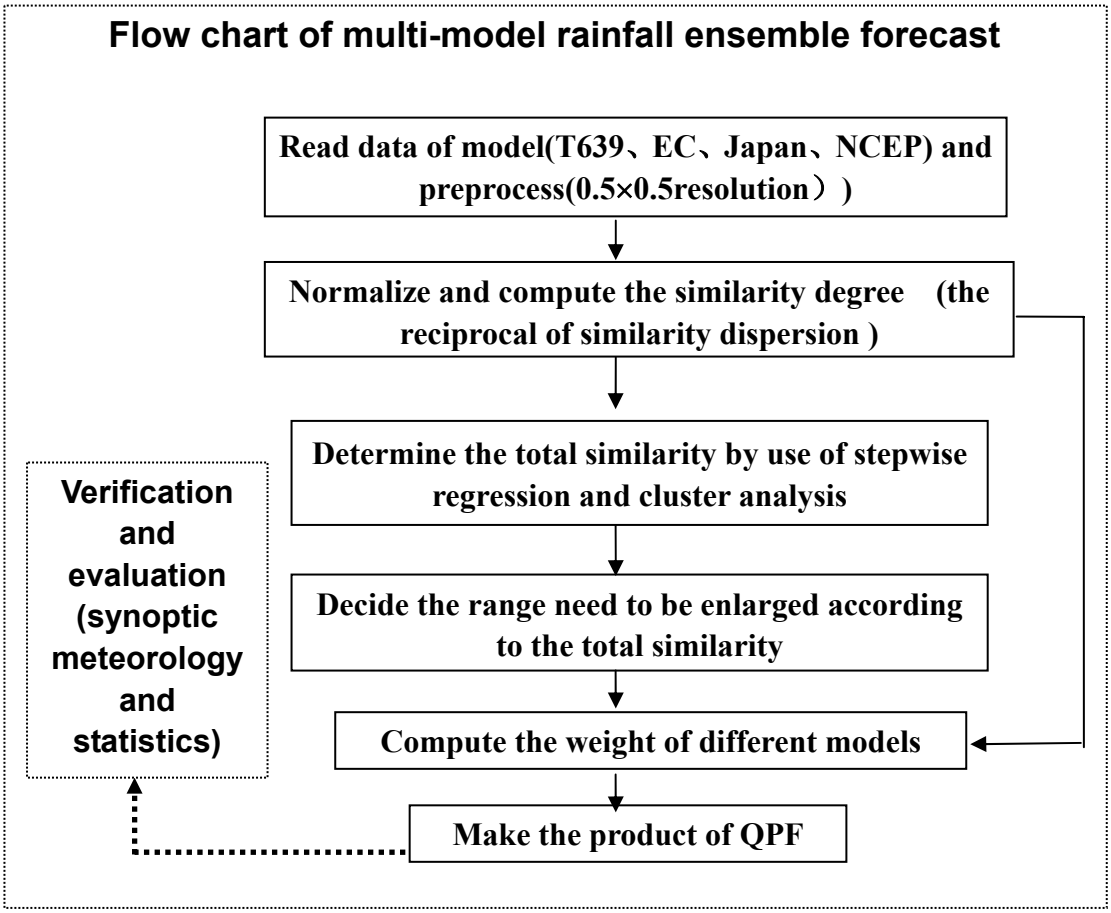

Fig 1. Flow chart of multi-model rainfall ensemble forecast

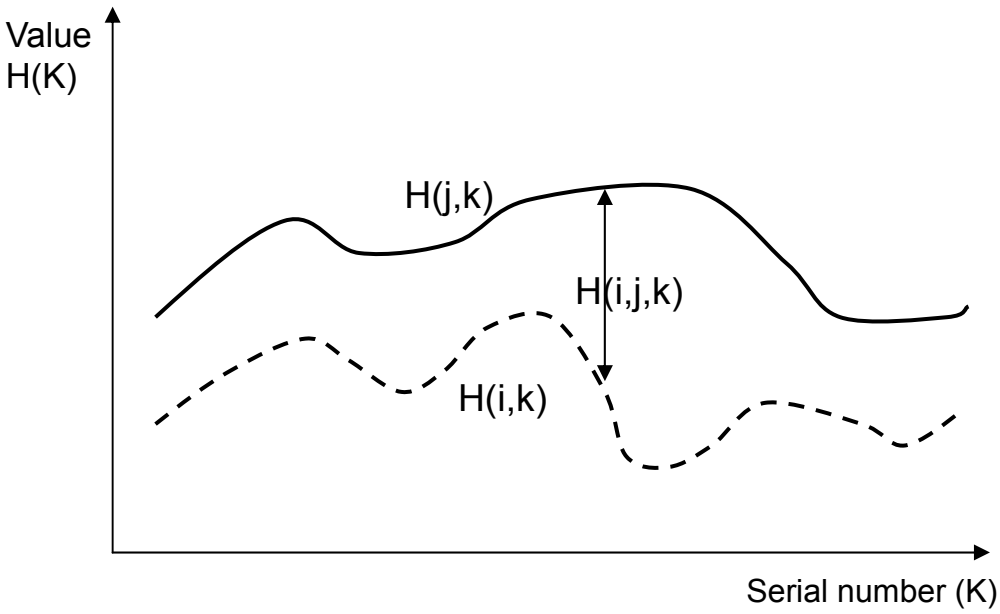

Fig 2. Schematic diagram of similarity discrete degree

As shown in fig 2, $H_{ij}(k)$ indicates the difference value of factor (k) between sample i and j, $H_{ij}(k) = H_i(k) - H_j(k)$. E_{ij} is the total mean difference of all factors(k=1,……,m),

$$E_{ij} = \frac{1}{m}\sum_{k=1}^{m} H_{ij}(k).$$

D_{ij} is the so-called value coefficient which represents the difference degree of the total mean value between two samples, $D_{ij} = \frac{1}{m}\sum_{k=1}^{m}\left|H_{ij}(k)\right|$.

R_{ij} means the shape coefficient reflecting the discrete degree of the difference of each factors between two samples to total mean difference, $R_{ij} = \frac{1}{m}\sum_{k=1}^{m}\left|H_{ij}(k) - E_{ij}\right|$.

C_{ij} indicates the similarity discrete degree, $C_{ij} = \frac{1}{2}(D_{ij} + R_{ij})$. Where, $0 < C(i,j) \le 1$. Smaller $C(i,j)$, more similar the two sample. When the two samples coincide, $D_{ij} = 0$, $R_{ij} = 0$, $0C_{ij} =$ 。

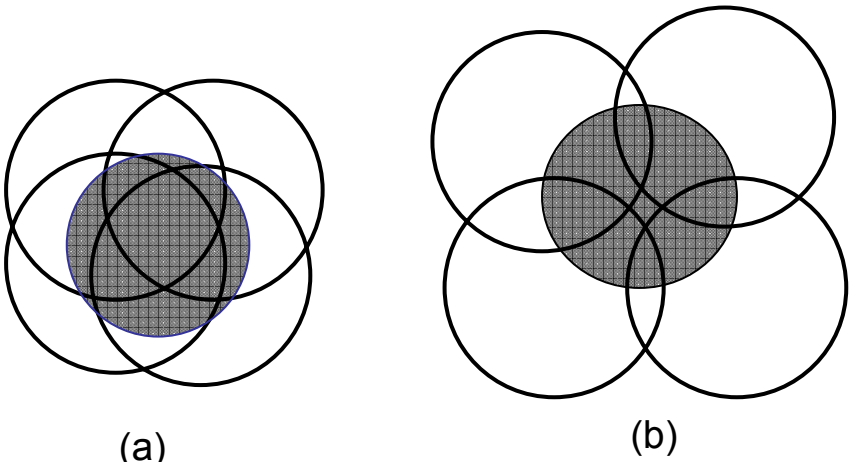

Fig 3. Schematic diagram of the heavy rain forecasting area of ensemble members (○) and the most possible heavy rain area (●) in the case of (a) forecasts of members are close (convergent) and (b) forecasts of members are different (divergent)

Total similarity degree is decided by the stepwise regression and cluster analysis, and then determines the extended radius. As shown in Fig 3, the similarity degree is larger in the case of Fig 3(a) verse 3(b), thus a higher certainty and less for the range to be enlarged are expected. The overlapping area through enlarging the range has the highest possibility for heavy rain. The probability distribution of rainfall is taken into account. The method can advance the forecast accuracy and enhance the forecast capacity of extreme weather events.

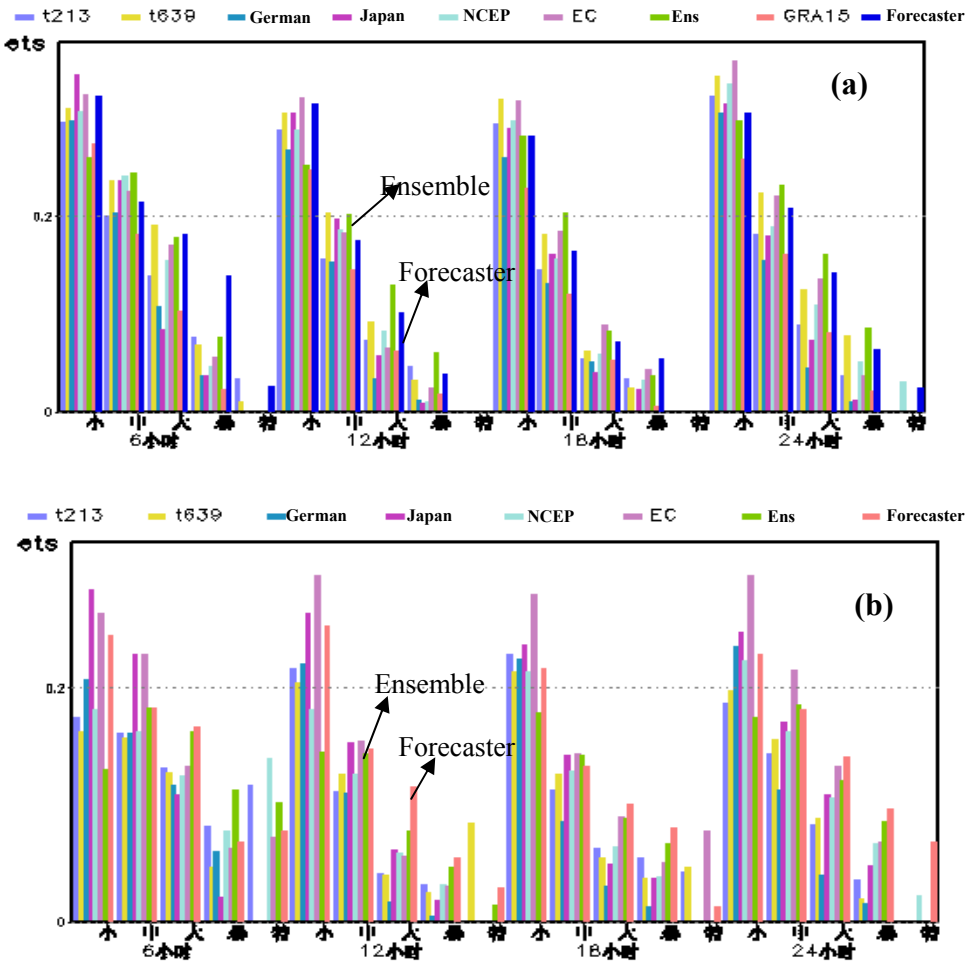

Fig 4. Ts skill scores for the different grades of 6hr accumulated precipitation in the different models in June (a) and July (b), 2010

Operational verification shows that the perf ormance of multi-model ensemble is m uch better than the single model. Figure4 displays the Ts skill score for the different grade of 6hr accumulated precipitation for different models and forecaster in June (a) and Ju ly (b.), 2010. In June, the multi-model ensem ble has genera lly m uch better perf ormance than th e single model, especially for th e grades ab ove the m oderate rain. Meanwhile, forecaster didn't refer to the results of multi-model ensemble and g et a lower T s skill scor e than the multi-model ensemble forecas t. In J uly, with referring to the ensem ble forecast, the forecaster got the highest Ts skill score. It should be pointed out that Ts skill score of the ensem ble method for the light rain is no t as good as th e ind ividual m odel because the area is en larged when forecasts of members are divergent. In addition, the model forecast usually underestimated the extreme rainfall, thus the correction should be applied to the ensemb le forecast for the extreme rainfall. It is also true for the case of 24hr ensem ble forecast. 24hr forecast accumulated from 6hr ensem ble is better th an 24hr ensem ble forecast, which is p robably related to the detail consideration of 6hr rain belt shape and strength.

3. Meso-scale ensemble probability forecast

Meso-scale ensemble probability forecast (Elizabeth E. Ebert et al, 2009, Hamill, T.M., 2001) has been found to be a useful supplement of QPF. At present, we develop some 6hr rain products based on WRF meso-scale ensemble probability forecast, such as stamp charts, ensemble mean and discrete degree charts, probability-matched ensemble mean (PM) charts, maximum precipitation distribution charts, percentage probability forecast products, serial charts(plumes, ensemble box and whisker, probability forecast). Ensemble mean(Fig.5a) smoothes the information of low forecast predictability indicated by discrete degree, which can capture the precipitation center of high probability but underestimate the maximum rainfall and artificially enhance the area of light rain. Probability-matched ensemble mean (PM) charts (Fig.5b) are consistent with ensemble mean but the maximum rainfall is forecasted better and area of light rain is more effectively controlled. At the same time, Talagrand diagram are used to verify the discrete degree of ensemble forecast and reliability diagrams are applied to examine the relationship between forecast probability and observation frequency. Both of them are very useful in QPF.

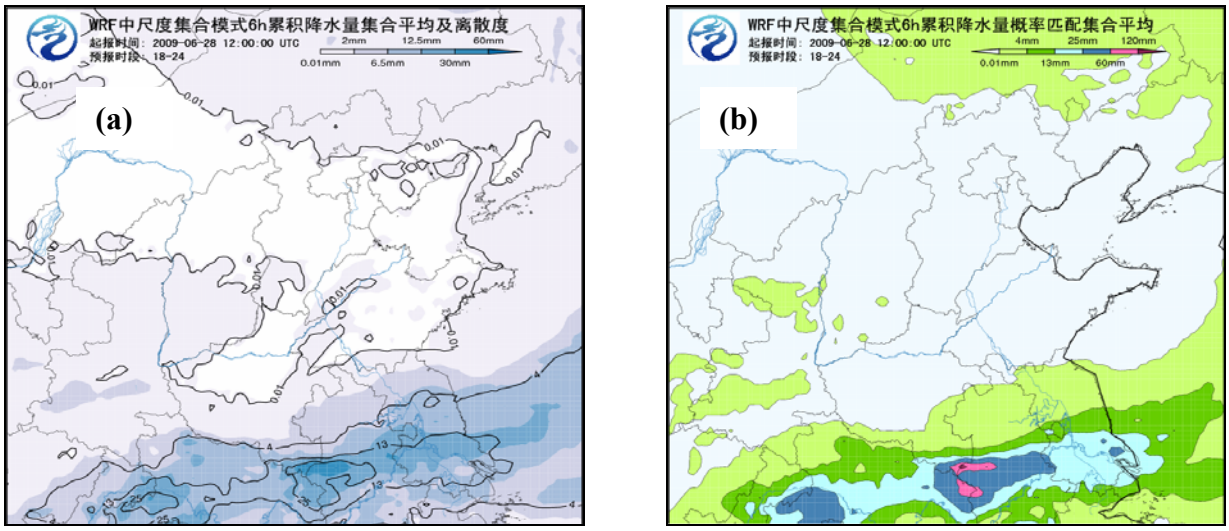

Figure5. Ensemble mean and discrete degree charts (a) and probability-matched ensemble mean (PM) charts (b)

4. Ingredients-based methodology

One of the significant problems for the multi-model ensemble forecast and meso-scale ensemble probability forecast lies in the ignorance of synoptic circulation information.

Doswell et al. (1996) first put forward Ingredients-Based Methodology (IBM), a new forecast method for flash flood. In China, this method is applied to the heavy rainfall forecast by Zhang et al (2010) and Li et al (2006). Although the rainstorms share common dynamic and thermodynamic environmental conditions, their physical ingredients significantly differ in the different heavy rainfall types in China.

The application of the numerical weather prediction (NWP) outputs to synthetically analyze the dynamic and thermodynamic environmental condition and basic physical ingredients in forecasting heavy rainfall is crucial to the success of ingredients-based

methodology. However, the operation appliance of this method is quite difficult, especially for 6hr QPF, because the relationship between the basic ingredients and heavy rain is not the same for the different heavy rainfall event. For example, statistic based on hundreds stations with over 60mm in 6 hours show that the divergence of about 20% stations are positive at 850hPa and negative at 200hPa(Fig.6),which didn't agree with the traditional mode for the occurrence of heavy rainfall.

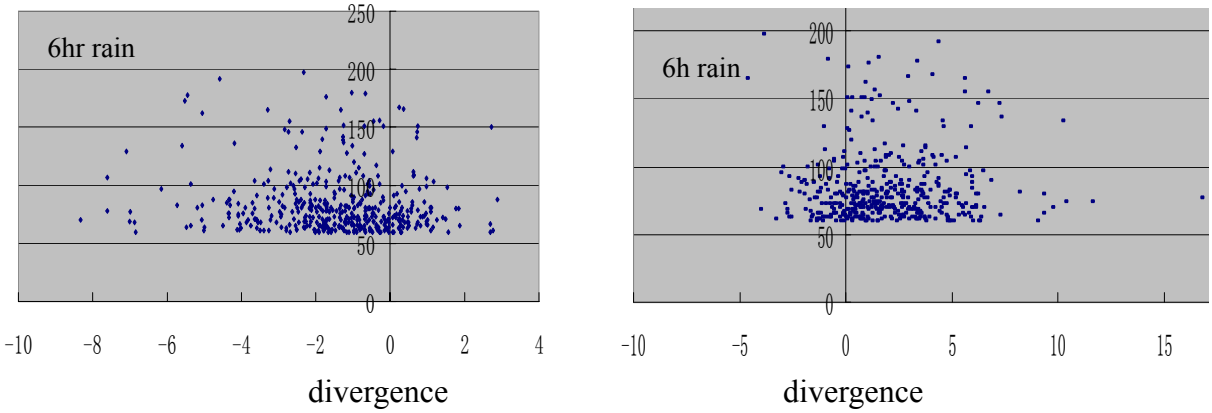

Fig 6. Divergence at 850hPa (a) and 200hPa(b) for the stations with over 60mm in 6 hours and the station percentage of different level heavy rain at the beginning (left) and end (right) (c)

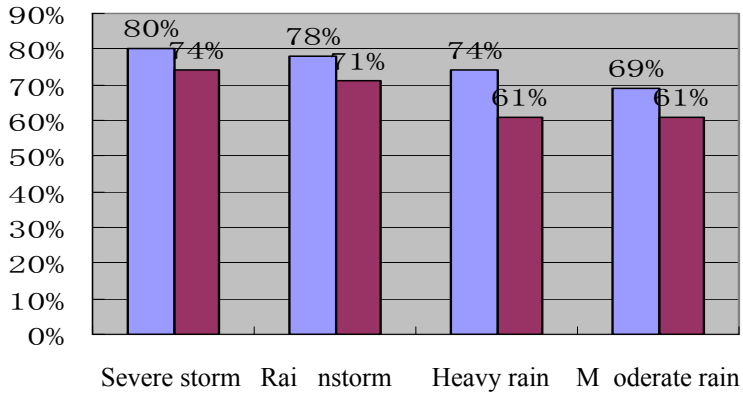

Fig 7. Percentage of stations for different rainfall grades with the low-level(850hPa) convergence

As demonstrated in figure7, stronger the rain, higher percentage of station with the lower-level convergence no matter for the beginning or the end stage of the rainfall. Generally the percentage at the beginning of heavy rain is higher than that at the end. It is no doubt that divergence at low level is an important indicator for the heavy rain, but the threshold value is difficult to determine. This is the big challenge for the ingredients-based methodology.

Reference

Li Kaile, 1986: A new similarity parameter and its application. ACTA Meteorological Sinica (in Chinese), 44(2), 174-183

Chen Liqiang, Zhou Xiaoshan,Yang Sen, 2005: quantitative precipitation forecasts method for short-range ensemble Forecasting. Journal of Nanjing Institute of Meteorology (in Chinese), 28(4), 543-548

Du J, Mullen S L,1997: Sanders F . Short range ensemble forecasting(SREF) of quantitative precipitation[J]. Mon. Wea. Rev, 125 (10), 2427-2459

Du Jun, 2002: Present situation and prospects of ensemble numerical prediction. Journal of Applied meteorological Science (in Chinese), 13(1), 16-28

Stensrud D J, Bao J W, Warner T T ., 2000: Using initial condition and model physics perturbations in short range ensemble simulations of meso-scale convective system . Mon. Wea. Rev, 128 (7), 2077-2107.

Doswell C A III, Brooks H E, Maddox RA . 1996: Flash flood forecasting: An ingredients-based methodology. Wea. Forecasting, 11:560-581

Zhang Xiaoling, Tao Shiyan, Sun Jianhua, 2010: Ingredients-based heavy rainfall forecasting. Chinese Journal of Atmospheric Sciences (in Chinese), 34(4):754-766

Li Jun, Li Wujie, Liao Yishan, 2006: An Ingredients-Based Methodology of Forecasting Heavy Rain of Meiyu Front. Metorological Monthly (in Chinese), 32(9), 3-8

Elizabeth E. Ebert, Anthony Salemi, Michael A. Turk, Michelle A. Spampata, and Sheldon J. Kusselson, 2009: Validation of the Ensemble Tropical Rainfall Potential (eTRaP) for Landfalling Tropical Cyclones, 89th Annual Meeting of the American Meteorological Society, Phoenix, Arizona

Hamill, T.M., 2001: Interpretation of rank histograms for verifying ensemble forecasts. Mon. Wea. Rev., 129, 550-560.

Research and Operation on Quantitative Precipitation Forecast (QPF) in DPR of Korea

KIM thaejin
Central meteorological research institute , DPR of Korea
shma@co.chesin.com.

The dynamic method, the empiric and statistic method, the short-time extrapolation method by using of synoptic observations were used for QPF in the past few years.

In the dynamic method the amount of precipitation is determined as the accumulation by horizontal transport of vapor and the condensation by vertical motion of air. In case of heavy rain, the large scale factors, medium and meso-scale factors by to pography and convection instability were added to them .
In the empiric and statistic method, the distribution of the precipitation amount, analyzed with seasons and pressure systems, was used for the corresponding region forecast and the discriminant regression equation was made out for the classified forecast of precipitation amount.
The principle component analysis and the cluster method were developed and used for the medium rage 5 days forecast.

In the recent days with the rapid development of numerical weather forecast, the study for transfer-methods by using NWP output is being carried out.
The BP multi-layer structure of Neural Network is designed and is implemented operationally now. In this method, the amount of precipitation is divided by several grades and forecasted successively by occurrence probability of each grade, but the results obtained are not yet reached to the satisfied level.
On the other hand, on the basis of analysis on atmosphere background and cloud data from satellite, which cause heavy rain in some region, the conception model for rainstorm occurrence is developed and used for very short range forecast.
The research for higher resolution of time-space scales at QPF is being studied now but it has some difficulty at the consideration of medium and meso scale disturbance and detailed topographic factors.

It would be expected that the reasonable choice of the factors that fully present regional precipitation amount is necessary for QPF, which requires more study such as sophisticated analysis on observation and NWP output, some numerical simulation for singular process and the introduction of advanced model.

Quantitative Precipitation Forecasts during the HMT-West campaign

Huiling Yuan[1, 2], Isidora Jankov[1, 3], Steve Albers[1, 3], and Zoltan Toth[1]
Collaborators: Tim Schneider[1], Allen White[1], Martin Ralph[1], Ed Tollerud[1], Tara Jensen[4], John Halley Gotway[4], Linda Wharton[1], Dan Birkenheuer[1], Paul Schultz[1], Curtis Alexander[1, 2]

1. NOAA/ESRL/Global Systems Division
2. Cooperative Institute for Research in Environmental Sciences (CIRES), University of Colorado, Boulder, CO
3. Cooperative Institute for Research in the Atmosphere (CIRA), Colorado State University, Fort Collins, CO
4. NCAR/Developmental Testbed Center (DTC)

Ensemble forecasts have been implemented since 2005 in NOAA/ESRL/GSD for the Hydrometeorological Testbed (HMT)-West program in California. New ensemble forecasts have been configured during the winter season 2009-2010. The ensemble suite includes 9 members with mixed dynamic cores and microphyscics in the WRF model, driven by a subset of Global Ensemble Forecast System (GEFS) members. The 9 km forecasts run to 114 hr, with the 3-km nested domain covering central California running to 12 hr. This study focuses on analyzing the performance of quantitative precipitation forecasting (QPF) and probabilistic QPF (PQPF) and comparing ensemble forecasts at different resolutions (9 and 3 km) as well as deterministic runs from High-Resolution Rapid Refresh (HRRR, 3 km). The algorithm to calibrate PQPF will be investigated for the new ensembles. The precipitation verification dataset is based on the NCEP Stage IV data and gauge observations. The precipitation data was applied to run a distributed hydrological model for generating ensemble streamflow.

A numerical study of aerosol effects on regional precipitation

Yan Yin and Hui Xiao
Key Laboratory of Meteorological Disaster of Ministry of Education
Nanjing University of Information Science & Technology, NO. 219 Ningliu Road, Nanjing, 210044, China，yinyan@nuist.edu.cn

1. Numerical Model and Experiment Setup

1.1. Description of the experiments

A rainstorm occurred in Shanxi province, China, on June 13, 2007 is simulated using the Weather Research and Forecasting (WRF) mesoscale model coupled with the Morrision's double-moment bulk microphysical scheme (Morrison et al., 2005). The microphysics scheme predicts the number concentrations and mixing ratios of five hydrometeor species (cloud droplets, small ice, rain, snow, graupel) and includes a detailed treatment of droplet activation based on the scheme of Abdul-Razzak and Ghan (2000). The initial spectra of aerosol particles are given by three lognormal distribution functions and the size distributions of the hydrometeor species are represented by gamma functions.

Two cases with different aerosol conditions are considered. A 'continental case' (C-case) and a 'polluted-continental case' (P-case). These cases are constructed by considering different fraction of aerosol particles are water soluble. Sensitivity tests are conducted and are compared to understand the response of cloud microphysical processes and precipitation to the changes in concentrations of aerosol particles.

1.2. Case description

The WRF model is integrated for a 30-h period from 1400 LST, 12 June 2007, to 2000 LST, 13 June 2007. The model is configured with two nested grids with spacing of 30 km (141×120 grid points) for domain 1, and 10 km (151×121 grid points) for domain 2. The domain 1 is centered at 40°N and 106°E. A rainstorm that developed over the Shanxi province of China from 02 LST to 13 LST, 13 June 2007, is simulated in this study. At 500hPa, 0200 LST, 13 June 2007, there were two troughs located at the eastern of Europe and the eastern of Russia respectively, while the ridge closed to Baikal (not shown). The base of trough of East Asia was divided into two parts, one of that run through Hetao area, and the 500 hPa height field showed a low system over the Shandong Peninsula associated a warm moist easterly flow back of the system, resulting in a convergence zone over North China.

2. Results

2.1. Precipitation

The process lasted for 18 hours. The precipitation data shown here is extracted from MICAPS (Meteorological Information Comprehensive Analysis And Process System). The simulation shows that the simulated rainfall regions and intensity are generally consistent with observations, but the simulated rainfall belt is a little to the

westward of the observation. The maximum value of 18-h observed precipitation is between the C-case and the P-case, while the maximum value in the P-case can reach 50 mm, about 10 mm larger that in the C-case, whereas the observed maximum value of precipitation is 44 mm.

Figure 1 shows the difference of 18-h integrated rainfall amount (mm) between the C-case and P-case. The area with the largest difference of 21 mm appears in the east part of Shanxi province, while the area with rainfall decreased more than 12 mm concentrated in the west of Shanxi province. Although the maximum value of accumulated rainfalls in the P-case is greater than the C-case, the grid-averaged of rainfall amount is reduced by about 0.8% in the polluted case (15.4 mm) as compared with the clean case (15.27 mm), indicating that the polluted aerosols have a positive contribution to precipitation, at least for the case simulated here.

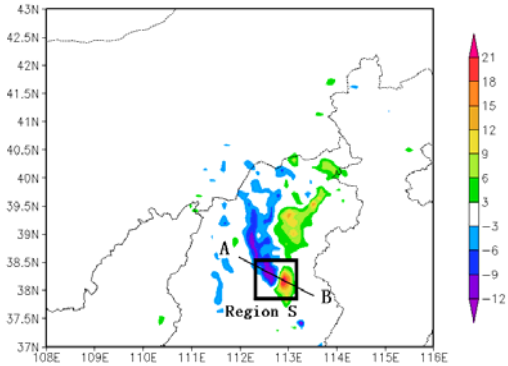

Fig. 1 The difference of 18-h integrated rainfall amount (mm) between C-case and P-case

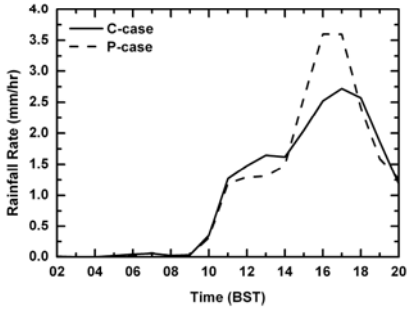

Fig. 2 Grid-averaged rainfall rate over the region of S

From the above results one can conclude that increase in the aerosol concentrations has little influence on the total precipitation, however, the effect of the concentration of aerosol on the location of precipitation is significant. There are the maximum of 18-h cumulative rainfall and two cores with the increased precipitation and the decreased precipitation in the region S (Figure 1). Therefore, we mainly lay stress on the analysis in the region S. Figure 2 displays the grid-averaged rainfall rate over the region of S. Two main periods of rainfall over the whole process are 11-14 LST and 14-18 LST, and the dramatic comparison of grid-averaged rainfall rate between the P-case and the C-case occur in 13 LST and 16 LST respectively. The averaged rainfall rate in the C-case which is more than 1.64 mm/hr greater than that in the P-case at the early stage (13 LST) and about 1.07 mm/hr less than that in the P-case at the later stage (16 LST).

2.2. Mixing ratio and number concentration of hydrometeors

Region S contains two cores with both increased and decreased precipitation, we make vertical cross sections along line AB (Fig. 1) to show the mixing ratio and number concentration of various hydrometeors. At 1300 LST, 13 June 2007, the

maximum cloud water mixing ratio in the P-case is increased by about 0.05 g/kg compared with that in the C-case, and the corresponding number concentration are 130 $mg^{-1}$and 80 mg^{-1}, respectively. In the P-case, the cloud base is at 775 hPa and the 0℃ isotherm is at 625 hPa. The maximum velocity of updraft in the C-case is greater than that in the P-case emerging below the 0℃ isotherm. Figure 3 displays the average vertical profiles of hydrometeors mixing ratio along line AB at 1200 BST June 13. In addition to cloud water, the mixing ratios of hydrometeors in the C-case are larger than that in the P-case. The rain water mixing ratio in the C-case and the P-case are 0.13 g/kg and 0.1 g/kg at 675hPa and 0.034 g/kg and 0.024 g/kg at surface, respectively.

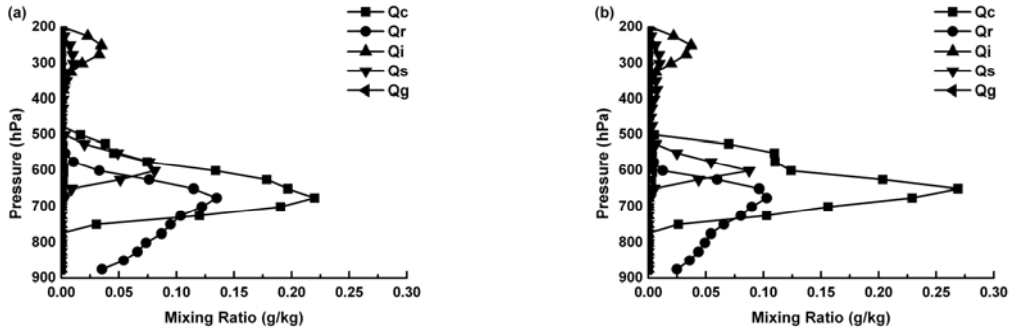

Fig. 3 The average vertical profiles of hydrometeors mixing ratio along line AB at 1300 BST June 13 : (a) C-case; (b) P-case

Although the ice mixing ratio in the P-case is less than that in C-case, the number concentration of ice is apparently higher than that in the C-case. The maximum value of snow mixing ratio in the C-case and the P-case are 0.081 g/kg and 0.087 g/kg, while the maximum value of graupel mixing ratio are 0.0027 g/kg and 0.0043 g/kg respectively. In contrast, the number concentration of graupel in the P-case is 6 times more than that in the C-case. In other word, the diameter of graupel particle in the P-case is much less than that in the C-case, corresponding to the terminal fall speed, and the graupel particle in the C-case easier fall from cloud. At the early stage (13 LST), the mixing ratio of ice phase particles is much less than liquid phase particles, and maximum updraft and the main cloud are below the 0℃ isotherm.

The result that the precipitation at 13 LST, to a larger extent, dependent on the warm microphysical processes, and that an increase in the aerosol concentration can lead to an increase in cloud water and a decrease in rain water is similar to previous studies (e.g., Givati and Rosenfeld, 2004; Lynn et al., 2007). At 1600 LST. (not shown), the increases of maxing ratio of snow, rain water, and graupel are remarkable in the P-case at 16 LST compared to that at 13 LST, while the decreases in the C-case. The maximum velocity of updraft in the P-case is much greater than that in the C-case emerging above the 0℃isotherm. In the C-case, the maximum

mixing ratio of cloud water is decreased by about 0.21 g/kg compared to that at 13 LST, indicating that the precipitation dependent on the warm microphysical processes and trend to dissipate. In contrast, the mixing ratio of snow and graupel in the P-case are increased by about 0.4 g/kg and 1.2 g/kg while that are few at the early stage, implicating that the precipitation in the P-case dependent on the cold microphysical processes at the later stage. Khain et al. (2005) stated that an increase in the concentration of aerosol leads to a low collision rate and a delay of raindrop formation, resulting in a larger vertical velocities and a more water that rides to the freezing level. The results obtained here are consistent with theirs, although the cloud systems are different.

Table 1 Source-sink terms of raindrop and its maximum conversion rate due to various microphysical processes

Source-sink terms of raindrop	Description	Maximum values at 1300 LST ($10^{-3}\cdot g\cdot kg^{-1}\cdot s^{-1}$)		Maximum values at 1600 LST ($10^{-3}\cdot g\cdot kg^{-1}\cdot s^{-1}$)	
		C-case	P-case	C-case	P-case
PRA	Accretion of cloud droplets by rain	0.6	0.55	0.3	1.8
PRACS	Accretion of snow by rain	0.45	0.4	0.035	1.6
PRC	Autoconversion of droplets to form rain	0.027	0.006	0.0039	0.0014
PGMLT	Melting of graupel to form rain	0.0008	0.014	0	0.9
PSMLT	Melting of snow to form rain	0.0001	0.011	0	0.013
PRE	Evaporation of rain	-0.33	-0.22	-0.16	-0.35

2.3. Conversion rate of the source-sink terms

Table 1 shows the source-sink terms of raindrop and the maximum conversion rate due to various microphysical processes along line AB. It is obvious from this table that accretions of cloud droplets and snow are the main source terms of raindrop. Although the value of the term of autoconversion of droplets is small, it plays an important role in the formation of initial raindrop. An increase in aerosol concentration likely results in a decrease of the cloud droplet size and lead to a reduction in autoconversion of droplets. At 13 LST, the value of autoconversion of droplets in the C-case is about 5 times greater than that in the P-case, and also larger at 16 LST. The low rate of autoconversion of droplets leads to the formation of a large number of small droplets with a low sedimentation, resulting in an increase of accretion of cloud droplets by rain. At 16 LST, the terms of accretion of cloud droplets and snows in the C-case are far below that at 13 LST, resulting in a decrease in rain at the later stage. In contrast, the maximum conversion rate of the melt of graupel and accretion of snow by rain in the P-case are increased at 16 LST. The microphysical characteristics of precipitation that snow and graupel particles become the main sources for rain, is a little different from the mechanism of cold frontal precipitation in South China (Shi et al.,2008). In addition, cloud droplet is the main sources for the increase of snow and graupel, which is adequate in the P-case. Thus,

an increase in concentration of cloud droplet, resulting from the increase of aerosol number concentration enhances the rainfall at the later stage.

3. Summary and Conclusions

A rainstorm occurred in Shanxi province on June 13, 2007 is simulated using the Weather Research and Forecasting (WRF) mesoscale model coupled with the Morrision's double-moment bulk microphysical scheme. Sensitivity tests are conducted and are compared for different background conditions to understand the response of cloud microphysical processes and precipitation to changes in concentrations of aerosol particles. The results show that the total rainfall amount is reduced by about 0.8% in the polluted case as compared with the clean case, but a more intensive rainfall rate at the central region of the rained area and no significant change in rainfall area are observed in the former case than in the latter. Snow and graupel are the main sources for rain at the surface. In the polluted case considered here, higher concentration of aerosol particles leads to the decrease of warm rain at the early stage, and consequently more numerous snow particles can grow by coagulations with cloud droplets and rain droplet in the air for longer, intensifying precipitation at the later stage.

Acknowledgements:

This study was partially funded by the Public Meteorology Special Foundation of MOST (Grant No. GYHY200706036), the National Natural Sciences Foundation of China (Grant No. 41030962), and the "Excellent Creative Research Team in Jiangsu Universities" program.

Reference

Abdul-Razzak, H. and Ghan, S. J. 2000. A parameterization of aerosol activation 2. Multiple aerosol types. J. Geophys. Res., 105, 6837–6844.

Givati, A. and Rosenfeld, D. 2004. Quantifying precipitation suppression due to air pollution. J. Appl. Meteor., 43(7): 1038-1056.

Khain, A., Rosenfeld D, and Pokrovsky, A. 2005. Aerosol impact on the dynamics and microphysics of deep convective clouds. Quart. J. Roy. Meteor. Soc., 131(611): 2639-2663.

Lynn, B. H., Khain A., Rosenfeld, D., et al. 2007. Effects of aerosols on precipitation from orographic clouds. J. Geophys. Res., 112, D10225, doi:10.1029/2006JD007537.

Morrison, H., Curry J. A., Khvorostyanov, V. I. 2005. A new double-moment microphysics parameterization for application in cloud and climate models. Part I: Description. J. Atmos. Sci., 62: 1665-1677.

Shi, Y., Lou, X., Deng, X., et al. 2008. Simulations of mesoscale and microphysical characteristics of cold front clouds in South China. Chinese Journal of Atmospheric Sciences (in Chinese). 32(5): 1019-1036.

The Challenge of LAMEPS on Quantitative Precipitation Forecast

Yong WANG[1] and Simona TASCU[2]

[1]Central Institute for Meteorology and Geodynamics, Austria, wang@zamg.ac.at
[2]National Meteorological Administration, Romania

1. Introduction

Over recent years Limited Area Model Ensemble Prediction System (LAMEPS) has become more important as a scientific tool for improving prediction of heavy rainfall, and several LAMEPSs have been developed and run operationally. Compared to global EPS, additional challenges posed for a LAMEPS with high quality, with more details, in particular, quantitative precipitation forecast (QPF) to be covered with confidence.

At ZAMG (ZentralAnstalt für Meteorologie und Geodynamik), the Central European regional ensemble system ALADIN-LAEF (Aire Limitée Adaptation Dynamique Développement InterNational – Limited Area Ensemble Forecasting, Wang and Bellus et al., 2010) has been developed in frame of the international cooperation of ALADIN/LACE (Limited Area modelling in Central Europe), and run quasi-operationally since 2007. The core of ALADIN-LAEF is ALADIN-AUSTRIA, it is the operational configuration of ALADIN at ZAMG (Wang et al. 2006). ALADIN-LAEF has a horizontal resolution of 18 km and 37 vertical levels. There are 17 members in ALADIN-LAEF, of which the first 16 members are perturbed. Their LBC perturbations are provided by the first 16 ECWMF-EPS (Leutbecher and Palmer, 2008) members. The 17th ALADIN-LAEF member obtains IC and LBC from the ECMWF EPS control forecast. We employ the Blending method for dealing with the atmospheric IC perturbation, which combines the large scale uncertainty generated by global EPS with the small scale perturbations resolved by LAM (Bellus et al. 2010); and the Non-Cycling Surface Breeding (NCSB) technique for generation of surface initial conditions perturbation (Wang and Kann et al. 2010).

In this paper we briefly describe the recent research results carried out at ZAMG for addressing the following challenges of LAMEPS on QPF.

2. What is the strategy to cope with the interaction between larger scale perturbations given by the driving global EPS and "local" perturbations generated specifically for the LAMEPS?

One of the key requirements for a LAMEPS is that the scale of the perturbation should be in accordance with the scales of variability resolved by the model. On the other side, the LAM perturbations should be consistent with the perturbation coming through the lateral boundary, e.g. the large scale forcing from the global EPS model.
The dynamical downscaling of ensembles of global model for generating IC perturbation in LAM, which is used in most operational LAMEPSs, is from the nature incapable to meet this requirement.

To handle with the interaction between larger scale perturbations given by the driving global EPS and "local" perturbations generated specifically for the LAMEPS, we implemented the Blending method in ALADIN-LAEF for generation of IC

perturbations. Blending combines the large-scale uncertainty generated by ECMWF Singular Vector (SV) with the small-scale uncertainty generated by breeding with ALADIN model. The combined perturbation has the feature that its large-scale part of the perturbation is from ECMWF SV, and the small scale part is from ALADIN breeding. Through breeding the blended perturbation attempts to give the best estimate of the actual errors in the initial analysis based on the past information of the flow, whereas the SV contain future information of possible forecast error. The initial perturbation is now consistent with the LBC perturbation in large scale part, both of them from ECMWF SV perturbation. The small-scale uncertainty in the analysis is more detailed and accurate due to the higher resolution and more balanced orographic/surface forcing of the LAM breeding.

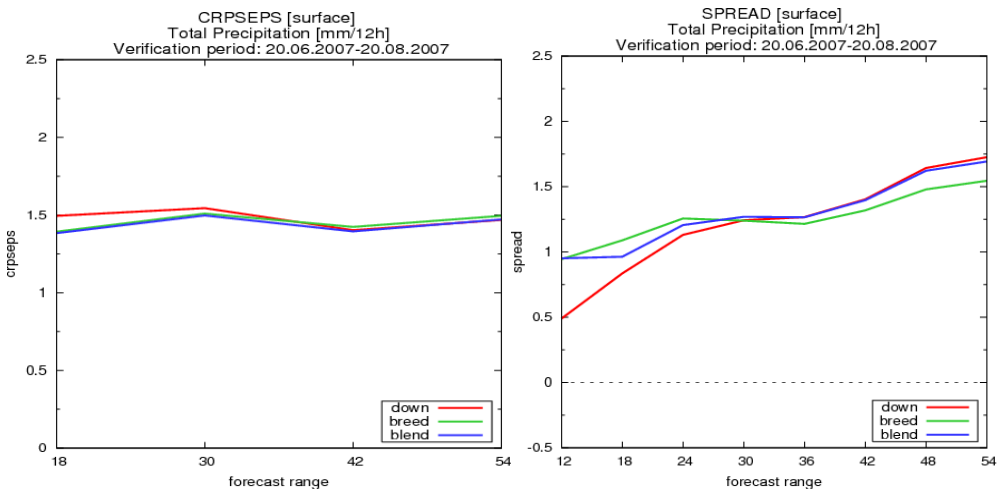

Figure 1. Verification of ALADIN-LAEF 12h accumulated precipitation forecast of experiments DOWN (in red, dynamical downscaling), BRED (in green, ALADIN Breeding) and BLEND (in blue, ALADIN Blending). Left: Continuous Rank Probability Score; Right: ensemble spread, averaged statistics over central Europe and a two-month summer period.

The Blending technique is a spectral technique using standard non-recursive low-pass Dolph-Chebyshev digital filter. The detailed description and discussion of Blending, in particular the technical implementation in ALADIN-LAEF, are given in Bellus et al. (2010).

Figure 1 shows the comparison of Blending and breeding on ALADIN-LAEF precipitation forecasts for a two months period. Regarding the probabilistic score measured by Continuous Rank Probability Score, the outperformance of Blending to Breeding is found, in particular, in the late forecast hours after 30h. It is obviously due to the impact of the LBC perturbation. Blending has the large scale perturbations which are consistent with the LBC perturbations. Breeding initializes a similar spread in the early hours, but the growth of perturbation is slower than Blending. The generation of perturbation by breeding conflicts somehow with the LBC perturbation from ECMWF SV, the benefit of using Blending comes clear in the later lead time after 30 hours.

3. How can we generate the surface perturbation in LAMEPS?

The representation of uncertainties in the surface initial conditions is important for the quality of ensemble QPF. To improve the forecast reliability and ensemble dispersion, a strategy for perturbing surface initial conditions, Non-Cycling Surface Breeding (NCSB) has been proposed. The strategy combines short range surface forecasts driven by perturbed atmospheric forcing and the breeding method for generating the perturbation to surface initial conditions. As Breeding, the simulation of growing error is started by introducing perturbations in the atmosphere. The perturbed atmosphere is not randomly, but downscaled from a global EPS. The regional model is then integrated up to 6 or 12 hours with the perturbed atmospheric ICs and LBCs, but the same surface initial state. The difference between the 6 or 12 hour surface forecasts and the corresponding new surface analyses is rescaled, and then added to the corresponding new surface analysis. This pseudo-breeding run is restarted every time with a new perturbation of the atmosphere obtained from the global EPS. This non-cycling feature ensures that the initial surface perturbation in LAMEPS is only driven by the atmospheric perturbations from the global EPS. It will be very probably introducing model drifting problem if the impact of the short range LAM forecast is put into the surface initial conditions continuously (Cycling) after several months. More information and the performance of NCSB on precipitation forecast are given in Wang and Kann et al. (2010)

4. Does LAM perturbation outperform the dynamical downscaling of global EPS?

In current operational LAMEPSs, the dynamical downscaling of global EPS perturbation remains the most attractive way for simulating the initial uncertainties. This is because of simplicity and good performance. Some studies indicate that the dynamical downscaling is slightly skilful than the regional perturbations ensemble with ETKF or targeted SV. However, one has to keep in mind that the regional small scale uncertainty cannot be explicitly simulated in a LAMEPS with dynamical downscaling, which is usually just following the governance of the global ensemble that is driving it. As known there are significant forecast uncertainties on meso-scale, short range and in local details. The representation of those meso-scale uncertainties in a LAMEPS is particularly useful for QPE.

Investigation has been done to compare QPF of ALADIN-LAEF with Blending and downscaling. As shown in Figure 1, clear positive impact of Blending can be seen in the first 24 hours. It demonstrates that downscaling of ECMWF SV perturbation is not optimally designed for the early forecast range. In the late forecast hours downscaling performs same as Blending, it is obviously due to the impact of the LBC perturbation.

5. What is the more added values of LAMEPS to its driving global EPS?

To answer this essential question related to LAMEPS, we have compared the performance of ALADIN-LAEF (16 members) with ECMWF EPS (50 members), one of the most advanced operational global EPS. A set of standard ensemble and probabilistic forecast verification methods has be applied to evaluate the performance of ALADIN-LAEF and ECMWF EPS. In Figure 2 Continuous Ranked Probability Skill Scores (CRPSS) of 12h accumulated QPF of ALADIN-LAEF and ECMWF EPS are shown. It is evident that ALADIN-LAEF is more skillful for the short range forecast than ECMWF EPS.

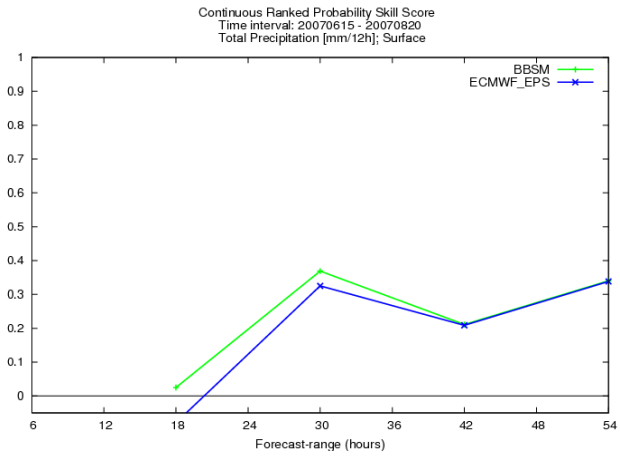

Figure 2. Comparison of CRPSS of 12h accumulated QPF between ALADIN-LAEF (in green, BBSM) and ECMWF EPS (in blue, ECMWF_EPS); averaged CRPSS statistics over central Europe and a two-month summer period.

6. Is LAMEPS adding value to its existing high resolution deterministic Limited Area Model (LAM) forecast?

Model and analysis related errors contribute to the eventual loss of predictive skill. Ensemble forecasting method has proved to be a successful way for handling those errors in the model. A high resolution deterministic LAM, on the other side, is still a necessary for the weather forecast. The question is then very naturally raised. We tackled this challenge in the way: **a)** comparison of LAMEPS with time lagged ensemble of high resolution deterministic LAM runs; **b)** comparison of LAMEPS ensemble mean/median with high resolution deterministic LAM forecast.

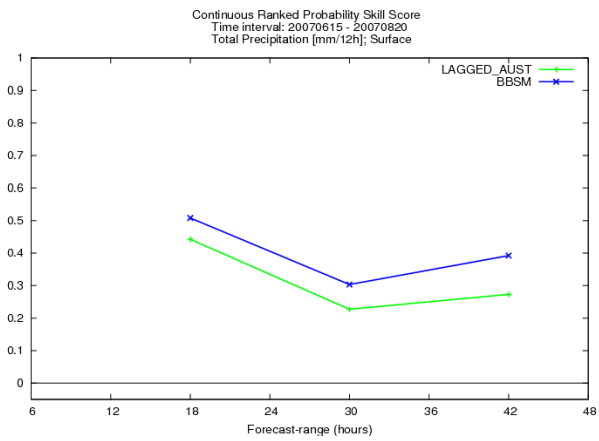

Figure 3. Comparison of CRPSS of 12 h accumulated QPF between ALADIN-LAEF (in blue, BBSM), the time lagged ensemble of ALADIN-AUSTRIA (in blue); averaged CRPSS statistics over central Europe and a two-month summer period.

The comparison of ALADIN-LAEF (17 members; 18km resolution) with the time lagged ensemble of ALADIN-AUSTRIA (5 members; 9.6km resolution) is shown in Figure 3. The CRPSS of ALADIN-LAEF is clearly superior of the time lagged ALADIN-AUSTRIA ensemble. Figure 4 presents the Equitable threat score (ETS) of 12h accumulated precipitation forecast of ALADIN-LAEF ensemble mean/median and of ALADIN-AUSTRIA. More skill with ALADIN-LAEF can be observed than the forecast of ALADIN-AUSTRIA, the ensemble median performs the best.

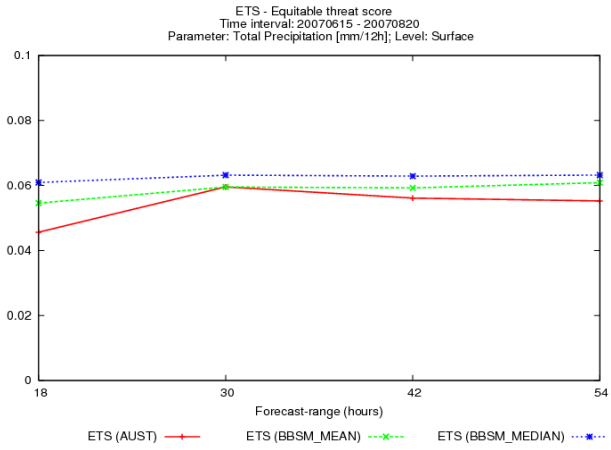

Figure 4. Comparison of ETS of 12h accumulated QPF between ALADIN-LAEF ensemble mean (in green), ensemble median (in blue) and ALADIN-AUSTRIA (in red); averaged ETS statistics over central Europe and a two-month summer period.

7. Conclusions

Experiments have been carried out with ALADIN-LAEF for answering essential questions related the LAMEPS on QPF. Answers can be given from the research:

- ✓ The combination of the large scale perturbation from global EPS with LAM perturbation, which are consistent with the large scale forcing from LBC, is quite beneficial for the LAMEPS QPF.
- ✓ Introduction of the surface perturbation improves the LAMEPS forecast.
- ✓ LAM perturbation can outperform to the dynamical downscaling of global EPS.
- ✓ LAMEPS adds more values to its driving global EPS.
- ✓ LAMEPS has more skills than its high resolution deterministic LAM forecast.

Acknowledgements

We gratefully acknowledge all the colleagues who have contributed to ALADIN-LAEF, in particular, Bellus, Schmeisser, Weidle and Wittmann. The work has been partly funded by LACE and ÖAD.

References

Bellus M, Wang Y, Geleyn JF, Tian W. 2010: A new method for initial perturbation generation in LAMEPS: Blending. In preparation for *Monthly Weather Review.* Available from the authors on request.

Leutbecher M., Palmer TN. 2008. Ensemble forecasting. *J. Comput. Phys.*, **227**, 3515–3539.

Wang Y, Haiden T, Kann A. 2006: The operational Limited Area Modelling system at ZAMG: ALADIN-AUSTRIA. *Österreichische Beiträge zu Meteorologie und Geophysik*, **37**, ISSN 1016-6254.

Wang Y, Kann A, Bellus M, Pailleux J, Wittmann C. 2010: A strategy for perturbing surface initial conditions in LAMEPS. *Atmospheric Science Letters* **11:** 108-113, DOI: 10.1002/asl.260.

Wang Y, Bellus M, Wittmann C, Steinheimer M, Weidle F, Ivatek-Sahdan S, Kann A, Tian W, Ma X, Bazile E. 2010: The Central European limited area ensemble forecasting system: ALADIN-LAEF. In revision, *Quarterly Journal of the Royal Meteorological Society.*

Global QPF and QPE: Where do we have trouble to achieve them?

C. Lu, H. Yuan, E. I. Tollerud, and N. Wang
NOAA Earth System Research Laboratory, Boulder, CO 80305, USA

1. Introduction

Today, many weather forecast centers are capable of providing quantitative precipitation forecasts (QPF) based on numerical weather prediction (NWP) models. Complementarily, global satellite precipitation retrievals provide quantitative precipitation estimations (QPE) that can be used for real-time monitoring or validation of QPF. However, how much confidence do we have in these two informational sources? How accurate are they? and how consistent is between the two? In this study, assessments of both a global QPE from a satellite precipitation product and corresponding global QPF from a global NWP model are conducted using available global land-based gauge data. We devise a scale decomposition technique, coupled with seasonal and spatial classifications, to evaluate these inaccuracies. The results are then analyzed in context with various physical precipitation systems, including heavy monsoonal rains, light Mediterranean winter rains, and North American convective- and midlatitude cyclone-related precipitation.

2. Global QPF and QPE datasets

The National Center for Environmental Prediction's (NCEP) Global Forecast System (GFS) is the U. S. operational global weather forecast model (Kanamitsu 1989; NOAA/NCEP Office Note 2003). Figs. 1a and 1d display these 1-day GFS forecasts of 24-h accumulated precipitation for Northern Hemispheric winter and summer seasons (defined as October to March and April to September, respectively).

Figures 1b and 1e show U.S. National Oceanic and Atmospheric Administration's (NOAA) satellite data products, called CMORPH [Climate Prediction Center MORPHing technology (Joyce et al. 2004)], which provides 6-hourly precipitation amounts on a $0.25^{o} \times 0.25^{o}$ grid for a near-global domain. Fig. 1b and 1e show the resulting averaged 24-h precipitation amounts estimated by CMORPH for winter and summer seasons (defined above), respectively. The CMORPH dataset comes from the IR-PMW merged satellite estimates.

A set of global precipitation analyses based on ~7000 quality-controlled gauge stations around the world provided by the Global Precipitation Climatology Centre (GPCC) are used in this study. The global distribution of these gauge stations can be found in Schneider et al. (2008). Figs. 1c and 1f show the gauge rainfall analyses for daily precipitation over the world's continents averaged for winter and summer seasons, respectively, in parallel with the forecasts and satellite estimates in other panels. Several potential problems associated with global rain gauge analyses are discussed by Ebert et al. (2007). First, the gridded gauge data tend to have a relatively smooth field compared to actual point measurements. Second, in mountainous areas, gauge observations tend to underestimate topographically forced precipitation amounts. Third, analyses are not accurate over some parts of the world where gauge stations are sparse, such as in Africa and South America. When verifying global NWP model and satellite-retrieved precipitation fields using the GPCC gauge analysis, we will take into consideration of the possible adverse effects presented by inaccuracies in our verification "truth".

3. How consistent between global QPF and QPE?

The averaged root-mean-square (RMS) errors computed for winter and summer seasons, respectively, are displayed on figs. 2a and 2b. As expected, errors are typically large in heavy precipitation systems in the tropics and decrease towards higher latitudes. For example, the discrepancy between forecasts and satellite estimates of precipitation in the Asian-Australian monsoon constitutes the largest precipitation errors in both seasons and can be as large as 15 mm/day. Persistent errors (in the sense of occurring in both seasons) are also found for intense rain systems associated with large-scale flow convergence over the oceans, such as the inter-tropical convergence zone (ITCZ) and the South Pacific convergence zone (SPCZ). Scattered errors over both oceans and continents are conjectured to relate to convective storms, because they display seasonal variations. For example, in the Northern-Hemispheric summer, the U.S. and China have relatively large errors, while in winter, these errors mostly occur in the Southern-Hemispheric continents, particularly in southern Africa, Australia, and South America. The RMS error between the GFS and CMORPH over the winter in Europe, particularly around the Mediterranean, although not large, poses another weather regime. The model and satellite uncertainties involved in these light winter rains may be of different origins than those intense rain-producing weather systems mentioned above.

It should be noted again that the errors displayed in Fig. 2 may arise from either GFS precipitation forecasts or CMORPH precipitation retrievals. However, the fact that these discrepancies exhibit apparent distinctive seasonal, geographical, and storm scale-related signatures suggests that the errors that produce them may be separable and that their physical causes might therefore be analyzable. To do so, we select several focused windows (various rectangular domains) in Fig. 2 to examine in greater detail what causes these verification differences. Within each window we use land-based gauge measurements as observational truth.

4. Towards understanding of uncertainties in global QPF and QPE

With the scale-decomposition technique discussed above, we can examine various types of rain-producing storms around the world. In particular, we focus on seasonal precipitation forecasts and estimates rendered by the GFS and CMORPH over the various regions selected in Fig. 2a and 2b.

4.1. Asian-Australian monsoon

In the summer phase of the Asian-Australian monsoon, the Asian continent serves as a relatively warm source in comparison with surrounding oceans, so that monsoonal flows converge over land, especially over the Indian subcontinent, South China, and Southeast Asia. Precipitation associated with this feature can be considered to be at large scales. Therefore, we use the 1000 km-scale wavelet filter to decompose the precipitation fields from GFS, CMORPH, and GPCC. From examination of the monsoon region (figures are not shown), we can see that the GFS tends to over-forecast, and CMORPH tends to underestimate monsoonal rains when compared with gauge observations. For example, the GFS over-forecasts rainfall on the west coasts of India and Burma, Southeast Asia, the South China coast, Indonesia, and New Guinea, while CMORPH slightly underestimates in these areas. This is verified in the scatter plots of Fig. 8. Comparing figs. 8 (c) and (d), one can see that for intense rainfall categories, such as those greater than 100 mm/month, there are more GFS events (points) than CMORPH events (points), and that these events tend to fall above the diagonal line for GFS and below the diagonal line for CMORPH. CMORPH correlates with GPCC slightly better than GFS. The correlation coefficients are not good overall for both model forecasts and satellite estimates. One of the reasons for this may be density and representativeness problems with the verification gauge data. Because many rain gauge measurements in the monsoon region are located on small-island

countries, the $1^o \times 1^o$ GPCC rainfall analyses may not provide a sufficient database for verification.

In the winter phase, monsoonal flows converge over the tropical oceans and the northern portion of Australia. For this case, in order to examine the details of the convective storms, we select a 200 km-scale wavelet to decompose the precipitation fields from GFS, CMORPH, and GPCC. The corresponding scatter plots in Figs. 9(g) and 9(h) show the correlations between GFS and GPCC, and between CMORPH and GPCC. A pattern similar to that of the summer large-scale monsoon precipitation is seen here also; the GFS largely over-forecasts and CMORPH slightly underestimates the monsoon convective storms. However, the overall correlation of both GFS and CMORPH with gauge observations has dropped significantly. We speculate that significant spatial and temporal displacement errors of both model and estimates have become dominant at these small scales.

4.2. North America extratropical and convective storms

Over the North American continent, one can see from Fig. 2a and 2b that the GFS and CMORPH precipitation fields mainly diverge on the west and east coast in winter, and over the Central Plains in summer. These differences are likely related to storm track forecast errors in winter and to severe thunderstorms in spring and summer. Therefore, we first applied a 1000 km-scale wavelet to the winter precipitation fields from GFS, CMORPH, and GPCC. Figs. 9(d) and 9(e) show the corresponding scatter plots. The GFS tends to slightly over-forecast winter extratropical storms as they move inland onto the west coast and as they exit off the east coast. The CMORPH fields, on the other hand, largely underestimate the precipitation for both land-falling and exiting winter storms. For this reason, the GFS surprisingly shows much stronger correlation than the CMORPH estimates.

For summer convective storms, the wavelet decomposed precipitation fields at 200 km. The corresponding scatter plots are shown in 8(g) and 8(h). As with the Asian monsoon, correlation coefficients drop significantly for both GFS and CMORPH when smaller precipitation scales are applied. Here, however, it appears that both GFS and CMORPH have exaggerated precipitation related to convective activity in the U.S. The GFS and CMORPH in the present study also both show strong signals for North American monsoon rainfall.

4.3. Europe and Mediterranean rains

During the verification period, Europe did not experience significant precipitation (northern Europe is excluded in the current CMORPH domain), except in the Mediterranean region. Mediterranean precipitation during winter typically consists of light and relatively uniform rainfall. We consider these to be a result of large-scale precipitation systems. The GFS performs reasonably well, with slight overforecasts in the Balkan Peninsula and in Ireland/England. Fig. 9(a) shows a fairly good correlation between GFS forecast and gauge analysis. By contrast, CMORPH underestimates winter precipitation over all of Europe. In particular, it fails to capture precipitation over Ireland, the west coast of the U.K., and the Atlantic coast of Spain and Portugal. In the Mediterranean region, CMORPH also underestimates winter rains. These failures result in a large number of underestimates in comparison with gauge data, as shown in Fig. 9(b).

4.4. South American large-scale tropical and terrain-induced rainfall and convective storms

South America is another region where GFS and CMORPH showed significant differences in both seasons (Fig. 2). To understand the cause of these differences, we examine large-scale

precipitation in the Northern summer (Southern winter) and convective storms in the Northern winter (Southern summer) over the South American domain.

In Northern summer, most of South America is in their dry season. Rainfall is mostly concentrated in the northernmost part of the continent, along the Equator, and along the southern tip of the continent near the Andes. The scatter plots confirm this impression (Figs. 8e-8f). From the results, it is clear that the GFS tends to over-forecast rainfall both in the north and in the south along the Andes, while CMORPH estimates capture the tropical rainfall very well but underestimates the topographic rainfall along the Andes.

During the Northern winter when much of South America is in their wet season, many convective storms are generated over the continent. In the distributions of convective-scale precipitation, both GFS and CMORPH suggest tremendous convective activity and large amounts of rain produced by storms in the Amazon basin. However, rain gauge analysis indicates modest rainfalls. In addition, the rain gauge analyses exhibit a smoother pattern than either the GFS or the CMORPH fields. This may indicate that there are not sufficient rain gauge measurements in the Amazon basin. As a result, the scatter plots show a large number of over-forecasts and overestimates for convective events by the GFS and by CMORPH satellite retrievals [Figs. 9(i)-(j)]. In particular, there is almost no correlation between the GFS forecasts and GPCC gauge analyses. There is a slightly larger correlation between CMORPH and GPCC, possibly because CMORPH estimates are more sensitive to the larger stratiform rainfall areas. In addition, the NWP model also tends to generate too much mountain-induced precipitation along the Cordillera (in the north) and Andes (in the south). These topographic features are missing in the gauge analysis, possibly due to insufficient observations as mentioned in section 2.

4.5. African tropical and savanna rains

Over much of Africa, rainfall is a part of the ITCZ, which migrates north and south relative to the Equator with the change in seasons. The decomposed large-scale precipitation features for Africa during the Northern summer showed that on both sides of the tropical rains, there are two dry areas with virtually no precipitation. The northern portion of Africa (the Sahara Desert) is located in the subtropical-high belt, where rain is scarce year-round. The southern portion of Africa is largely savanna plain where Northern Hemispheric summer is the dry season.

Compared to gauge analyses, the GFS forecasts large-scale rains reasonably well, with some intense rains (over 300mm/month) being underforecast and others overforecast [Fig. 8(a)]. The CMORPH, on the other hand, shows problems for the African large-scale tropical rains. First, it overestimates rain area, so that there are many light-rain events above the diagonal line in Fig. 8(b). Second, the CMORPH does not capture intense rain areas, so that there are many heavy-rain events situated below the diagonal line in the figure.

African savanna rains appear in the Northern-Hemispheric winter, but disappear in the summer, in the southern portion of Africa (figure not shown). In the wet season, thunderstorms produce heavy rainfall over the savanna. The gauge rainfall analyses are quite smooth. In fact, there are more similarities between the GFS and CMORPH than between either one and the GPCC. This may again reflect the problem of insufficient rain gauge observations over this region. As a result, the scatter plots show that both GFS and CMORPH inflate the rain areas and intensity relative to gauge observations, and the correlation scores are extremely low [Figs. 9(e)-(f)].

5. Conclusions

We first computed RMS error between global QPF against a set of satellite-based global QPE on a daily basis. The results identified the areas where large differences exist. In order to

determine the origin of these differences, we compared both to a set of global gauge analyses. Table 1 summarizes our findings.

In general, both GFS forecasts and CMORPH satellite estimates capture the large-scale precipitation systems better than they do convective-scale storms (see Table 1). However, the satellite estimates are slightly better at handling (with marginally better correlation scores) the convective-scale precipitations than the NWP model. This may reflect the fact that the model's convective parameterization generates storms with significant spatial displacement and temporal phase errors. The model has a tendency to over-forecast precipitation for both large-scale and convective-scale storms, while satellite retrievals tend to underestimate intense rainfall amount but to overestimate stratiform-rain areas. CMORPH precipitation analysis also appears to present problems along coasts, where it tends to underestimate precipitation amount and fails to distribute the rain area deep enough over land. This may indicate an effect of surface emissivity differences over the ocean and land, to which satellite retrievals are typically subject.

The above results are based on the verification of the NWP model and satellite precipitation fields against the GPCC gauge analyses, which are treated as observational "truth". From Table 1, we see that in regions of dense gauge data available, global model QPF tends to outperform satellite-retrieved QPE. This is especially true for large-scale precipitation systems in North America and European-Mediterranean regions. However, in several cases studied, such as in the South America and Africa domains, the correlation scores for GFS or CMORPH precipitation fields with GPCC analyses were extremely low. We conjecture that these problems are related to the uncertainties in the verification data itself. It is well known that gauge measurements are very sparse in the Amazon River basin in South America and in the savanna plain in Africa (Schneider et al. 2008). Therefore, it is not surprising that in these situations the model and satellite are more similar than either to gauge analyses. The possible problems involved in the gridded gauge analyses are summarized in Table 1. Further investigations for these cases or areas with better verification datasets are recommended.

References

Bech, C., J. Grieser, and B. Rundolf, 2004: A new monthly precipitation climatology for the global land areas for the period 1951 to 2000. Available at: http://www.dwd.de/en/FundE/Klima/KLIS/int/GPCC/GPCC.htm

Ebert, E. E., J. E. Janowiak, and C. Kidd, 2007: Comparison of near-real-time precipitation estimates from satellite observations and numerical models. *Bull. Amer. Meteor. Soc.,* **88**, 47-64.

Joyce, R. J., J. E. Janowiak, P. A. Arkin, and P. Xie, 2004: CMORPH: A method that produces global precipitation estimates from passive microwave and infrared data at high spatial and temporal resolution. *J. Hydrometeor.*, **5**, 487-503.

Lu, C., H. Yuan, E. Tollerud, and N. Wang, 2010: Scale-dependent uncertainties in global QPFs and QPEs from NWP model and satellite fields. *J. Hydrometeor.*, **11**, 139-155.

Kanamitsu, M., 1989: Description of the NMC Global Data Assimilation and Forecast System. *Wea. Forecasting*, **4,** 335-342.

NOAA NCEP, 2003: Global Climate and Weather Modeling Branch, *NOAA/NWS/NCEP Office Note*, **442**, [http://www.emc.ncep.noaa.gov/officenotes/newernotes/on442.pdf.], 1-15.

Schneider, U., T. Fuchs, A. Meyer-Christoffer and B. Rudolf, 2008: Global Precipitation Analysis Products of the GPCC. Available at: http://gpcc.dwd.de

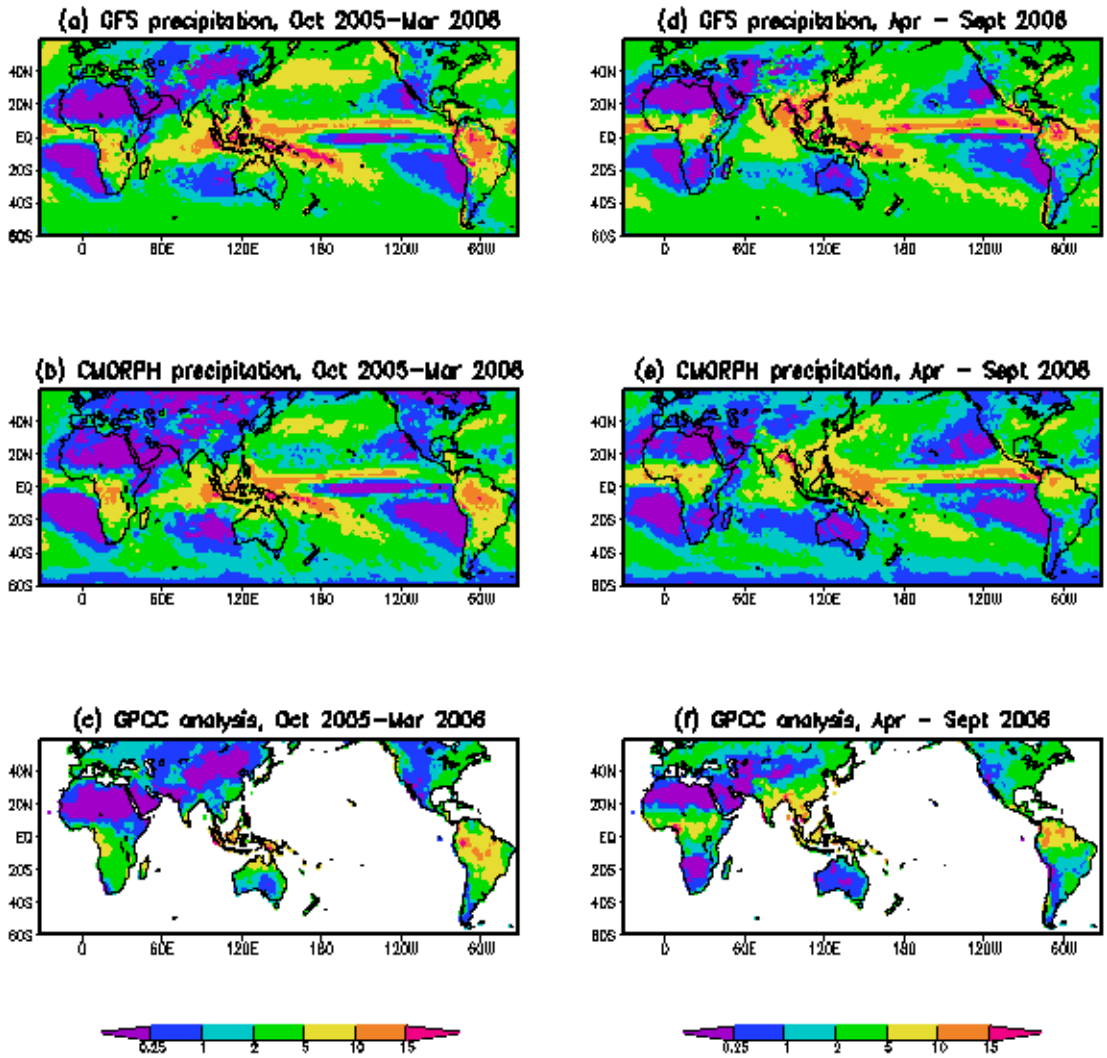

Fig. 1: The global distributions of averaged daily precipitation (unit: mm/day) for winter (left column) and summer (right column) seasons. (a) and (d) are the 1-day forecast fields from the GFS, (b) and (e) are 24-h estimates from CMORPH, and (c) and (f) 24-h analyses from GPCC.

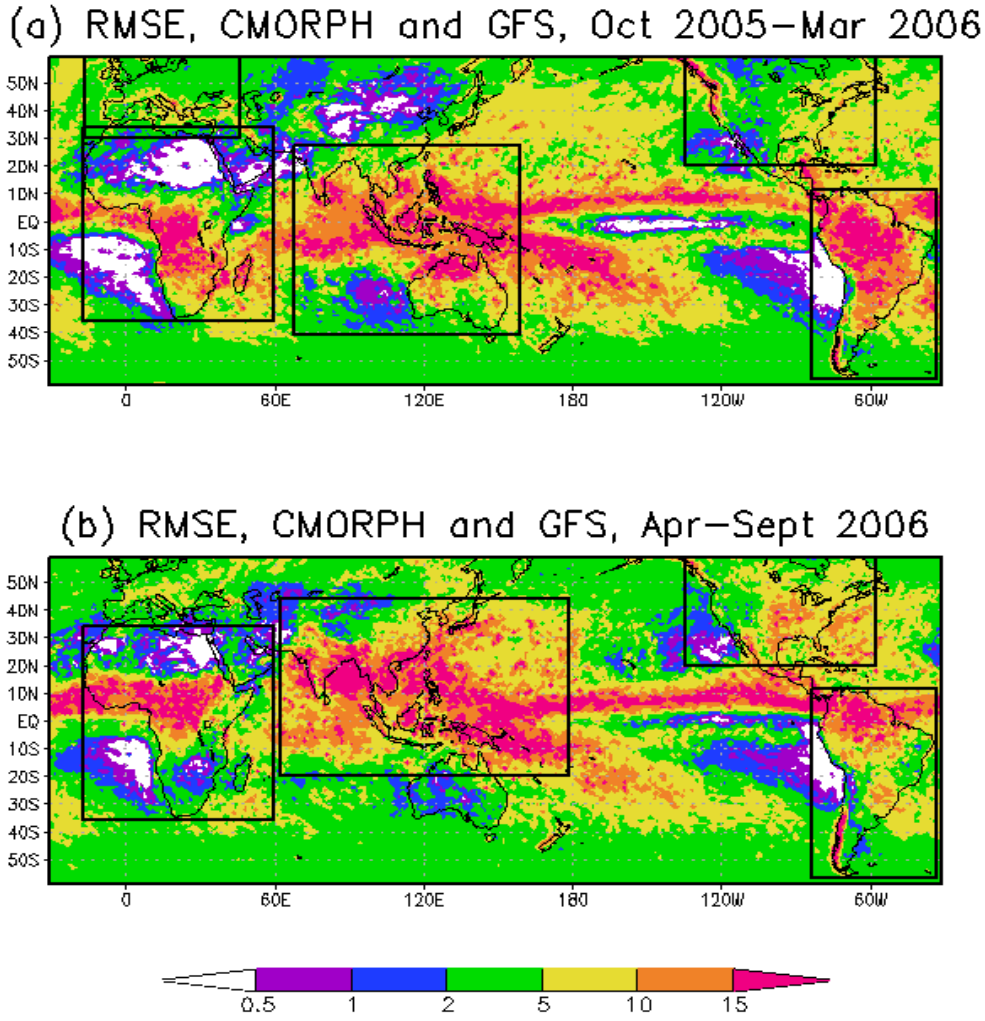

Fig. 2: The global distribution of averaged root-mean-square error (unit: mm/day) between GFS and CMORPH for (a) winter and (b) summer, respectively. The rectangular boxes are the selected focused regions for the further analyses.

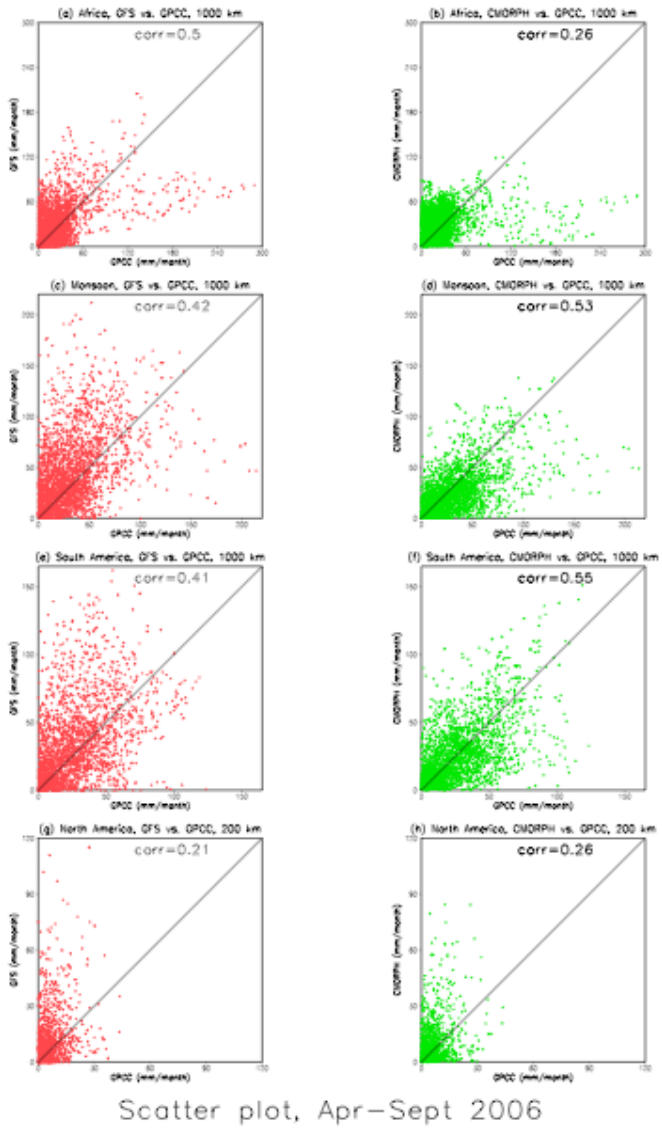

Fig. 3: Scatter plots showing the correlations between (a) GFS and GPCC (Africa, 1000-km scale), (b) CMORPH and GPCC (Africa, 1000-km scale), (c) GFS and GPCC (monsoon, 1000-km scale), (d) CMORPH and GPCC (monsoon, 1000-km scale), (e) GFS and GPCC (South America, 200-km scale), (f) CMORPH and GPCC (South America, 200-km scale), (g) GFS and GPCC (North America), and (h) CMORPH and GPCC (North America, 200-km) for monthly averaged precipitation.

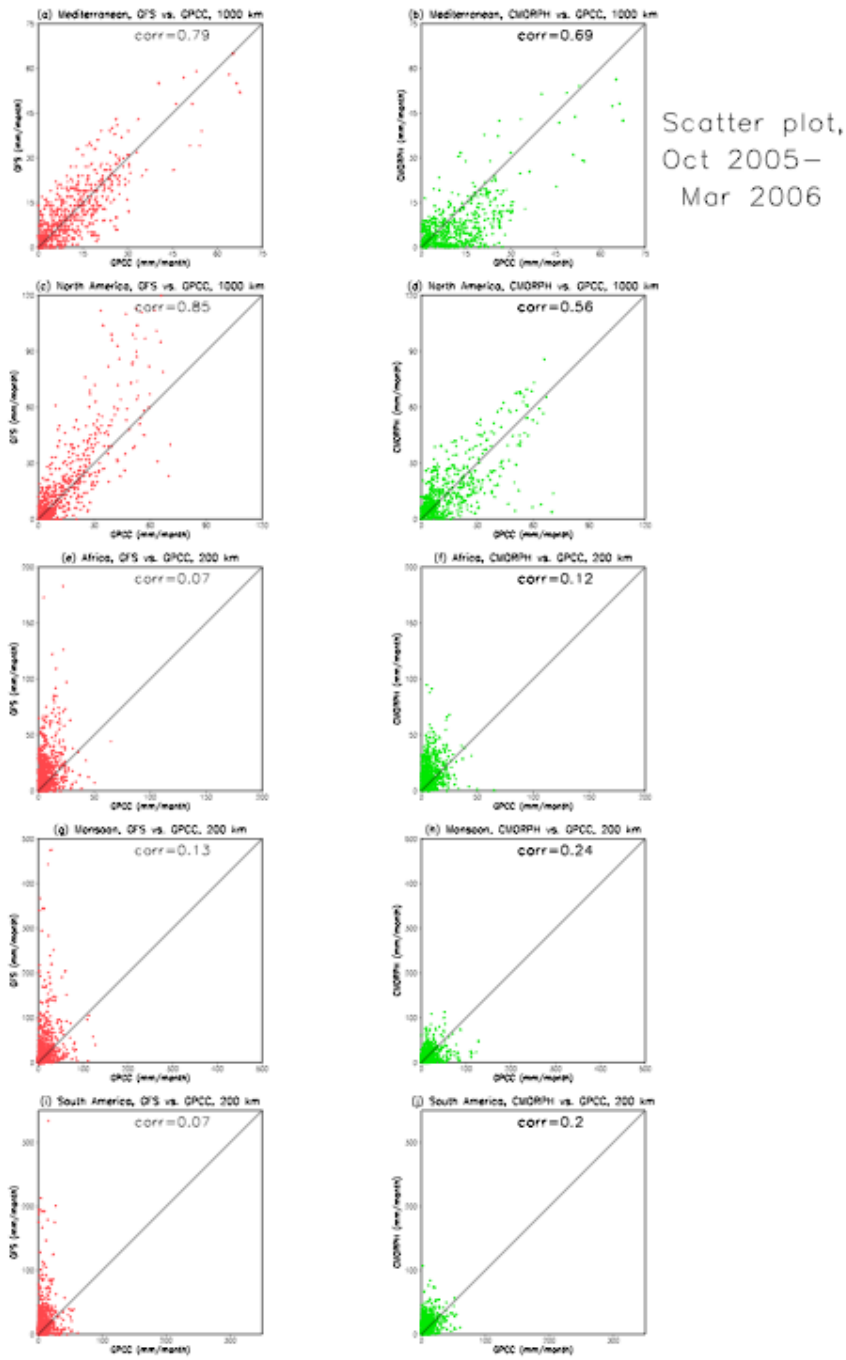

Fig. 4: Scatter plots showing the correlations between (a) GFS and GPCC (Mediterranean, 1000-km scale), (b) CMORPH and GPCC (Mediterranean, 1000-km scale), (c) GFS and GPCC (North America, 1000-km scale), (d) CMORPH and GPCC (North America, 1000-km scale), (e) GFS and GPCC (Africa, 200-km scale), (f) CMORPH and GPCC (Africa, 200-km scale), (g) GFS and GPCC (Monsoon, 200-km scale), (h) CMORPH and GPCC (Monsoon, 200-km), GFS and GPCC (South America, 200-km scale), (h) CMORPH and GPCC (South America, 200-km) for monthly averaged precipitation.

Storm types region and season	QPF (GFS)	QPE (CMORPH)	Verification data (GPCC)
Summer monsoon (large scale)	Corr=0.42 overforecast intense rain	Corr=0.53 underestimate west coast problem	possible analysis problems for gridded data
Winter monsoon (convective scale)	Corr=0.13 overforecast strong convective rains	Corr=0.24 underestimate strong convective rains	possible analysis problems for gridded data
North America winter storms (large scale)	Corr=0.85 slightly overforecast storm tracks	Corr=0.56 underestimate west coast problem	
North America summer storms (convective scale)	Corr=0.21 overforecast strong convective rains	Corr=0.26 overestimate stratiform rain areas	possible mountainous rain gauge problems specially for North American monsoon
European−Mediterranean winter precipitation (large scale)	Corr=0.79 slightly overforecast	Corr=0.69 largely underestimate	
South America tropical rains (large scale)	Corr=0.41 overforecast	Corr=0.55 coastal problem	possible station coverage problems
South America summer storms (convective scale)	Corr=0.07 possible overforecast	Corr=0.20 possible overestimate stratiform rain areas	also topographic−forced precipitation problems
Africa tropical rains (large scale)	Corr=0.50 slightly overforecast	Corr=0.26 underestimate intense rains overestimate rain areas	possible station coverage problems
Africa Savanna rains (convective scale)	Corr=0.07 possible overforecast	Corr=0.12 possible overestimate stratiform rain areas	possible station coverage problems

Table 1: Summary of verification results for global QPF and QPE for selected storm types, domains, and seasons.

Multiscale Spectral Structures of Tropical Rainfall over Maritime Continent Simulated by NRCM and Observed by Satellites

Hsiao-ming Hsu, Joseph J. Tribbia, and Mitchell W. Moncrieff
National Center for Atmospheric Research

Tropical circulations are strongly affected by tropical convection, and heat released by producing rainfall is the primary energy source. In this investigation, the tropical rainfall obtained from numerical experiments of different resolutions and retrieved from satellite observations are analyzed spectrally in both space and time. In addition to diurnal and intraseasonal peaks, temporal and spatial power-law scaling of different exponents are revealed and discussed. The temporally averaged spatial spectra show smooth spectral transitions from steep exponents at high wavenumbers to gentle exponents at low wavenumbers, representing a fundamental change in statistical structures from non-stationary processes at small scales to stationary processes at large scales. For analyzing the time evolution of spatial variances wavenumber by wavenumber, the spatial exponent spectra are generated, and the high- and low-frequency exponents of the temporal spectra behave differently between the low- and high-wavenumber ranges. For the low-wavenumber range, the low-frequency exponents are gentler than the high-frequency ones, and they tend to reach exponents between -1 and -2. However, for the high-wavenumber range, they tend to be a constant around -1.5 for the scale less than 100 km. Although there are a few quantitative differences between the modeled and the retrieved, essential spectral structures are quite similar. Thus, the tightly coupling of tropical rainfall in both time and space is demonstrated, and implies that rainfall/convection and circulation in the Tropics is a non-separable system in scales.

Regime-dependent forecast uncertainty of convective precipitation

Christian Keil and George C. Craig
Meteorologisches Institut der Ludwig-Maximilians-Universität, München, Germany
Email: Christian.Keil@lmu.de

1. Introduction

Predictability, or forecast uncertainty, can be addressed with ensemble techniques (Kalnay 2003). While ensemble prediction systems (EPS) are well established at synoptic-scale medium range weather forecasts (see. e.g. Molteni et al. 1996), the design of short-range convection-permitting EPS is difficult due to the poor knowledge of the mechanisms promoting rapid error growth, the various sources of uncertainty and limited computing resources (Kong et al 2006). Recently, a first step towards a convection-permitting EPS (employing a horizontal grid spacing of 2.8 km) was done at Deutscher Wetterdienst (DWD) by following a multi-boundary and multi-parameter approach taking into account uncertainties in the lateral boundary conditions and model physics (Gebhardt at al. 2010).

Forecast uncertainty of convective precipitation is influenced by all scales, but in different ways in different meteorological situations. Done et al. (2006) investigated the dynamical role of the synoptic and mesoscale environment in controlling the local characteristics of convective precipitation and proposed two different regimes. During forced (or equilibrium) convection the amount of precipitation is controlled by the large-scale production of Convective Available Potential Energy (CAPE). In the second, local-forced (or non-equilibrium) regime, CAPE is available, but the extent to which it produces convection and precipitation is restricted by the availability of triggers sufficient to overcome a convective inhibition energy (CIN). Triggers include boundary layer convergence regions or local maxima in temperature or moisture. Since these are typically driven by local orographic or surface flux variability, they may be hard to predict, even if the large-scale meteorological situation is known.

These distinct meteorological regimes can be identified by considering a time scale of convective adjustment τ_c (Done et al. 2006). This scale is an estimate of the rate at which CAPE is being consumed by convective heating. If the convective time scale is only a few hours, and thus short compared to the time scale over which the large-scale environment evolves (say 1 day) the convection will remove CAPE as fast as it is created, and the rate of creation of CAPE controls the amount of convection. On the other hand, if the convective time scale is similar to, or longer than, 1 day, convection is acting too slowly to remove the CAPE, and there must be local factors controlling its rate.

The goal of this study is to identify a regime-dependent forecast uncertainty of convective precipitation using the convection-permitting COSMO-DE-EPS covering a 9 day period during the COPS field campaign (Convective and Orographically induced Precipitation Study, Wulfmeyer et al. 2008). Our hypothesis is that forced-frontal convective precipitation associated with synoptic weather patterns may be predictable for several days and is primarily governed by lateral boundary conditions in limited area models. In contrast, single convective cells developing during air-mass convection situations, which of themselves are predictable only for a matter of hours, are frequently triggered by local, small-scale processes enforced e.g. by

mountain ridges and are anticipated to react sensitively to changes in the model physics.

2. Tools and ingredients

2.1 The convection-permitting ensemble

The high resolution ensemble prediction system COSMO-DE-EPS is based on the operational, deterministic COSMO-DE model (Baldauf et al. 2006) with a horizontal resolution of 2.8km and 50 vertical levels up to 30 hPa. It is put in ensemble mode by combining lateral boundary conditions of four different global models with five variations of physical parameterizations for a total of 20 ensemble member forecasts. The different lateral boundary conditions stem form the COSMO-SREPS ensemble (Marsigli et al. 2008) and comprise the global models of the European Centre for Medium Range Weather Forecast (ECMWF, member 1-5), the GME model of DWD (member 6-10), the GFS system of the National Center of Environmental Prediction (NCEP, member 11-15) and the Unified Model of the UK MetOffice (member 16-20). The five physics perturbations are accomplished in a non-stochastic and uniform approach by varying exactly one parameter for each perturbation (Table 1). These parameters are chosen to maximize the variability of convective precipitation. The COSMO-DE-EPS is started daily at 00 UTC with a forecast range of 24 hours. Note that COSMO-DE-EPS is still experimental and the setup used for this study does not represent the current status.

Here COSMO-DE-EPS fields of synthetic radar reflectivity at 850 hPa pressure surface are used as a proxy for precipitation intensities and to assess forecast quality employing radar observations. In COSMO-DE synthetic reflectivities are calculated with a forward operator using information from the hydrometeor distribution of rain, snow and graupel at every grid point. The forecast quality is computed hourly 15 minutes after the full hour due to data availability.

2.2 Observation data

Forecast quality is validated using hourly instantaneous radar data of the European Composite. It is provided by DWD and covers an area of 1800km x 1800km over Europe. Here, a subdomain of southwestern Germany and northeastern France centered over the COPS observation region is evaluated. The European radar composite delivers instantaneous radar intensities given in six reflectivity classes (7, 19, 28, 37, 46, 55 dBZ) on a horizontal grid with a resolution of 2km x 2km.

2.3 The convective time scale

The convective adjustment time scale τ_c used in this study is defined by Done et al. (2006). The rate of change of CAPE due to release of latent heat is estimated from the rainfall rate i_R and we may derive the following expression for τ_c:

$$\tau_c = \frac{\mathrm{CAPE}}{\frac{\mathrm{dCAPE}}{\mathrm{dt}}} = \frac{\mathrm{CAPE}}{0.045 \cdot i_R}$$

A threshold value of convective time scale τ_c must be identified to distinguish between equilibrium and non-equilibrium convection. Done et al. (2006) suggest a typical synoptic time scale would be a day or more. Over land, changes in forcing

associated with the diurnal cycle are likely to be important, so a shorter threshold time scale τ_c of around 6 hours is used in this study (as in Molini et al. 2010).

3. Results

Forecasts of COSMO-DE-EPS are continuously available from 8 to 16 August 2007 covering various meteorological situations during the COPS field experiment. Here an examination of the entire period applying the convective adjustment time scale to identify regime-dependent forecast uncertainty is shown. A detailed case-study on the meteorological conditions during IOP15 on 12 August and an inspection of the forecast performance of the ensemble members as seen by stamp maps and two scores highlighting the different flow regimes that day is presented by Keil and Craig (2010).

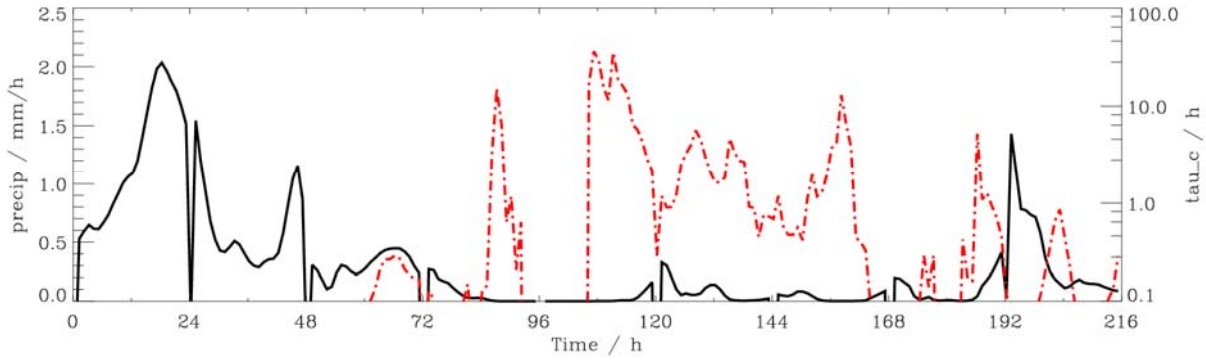

Figure 1. Time series of the ensemble mean total precipitation (solid line) and the mean convective time scale τ_c averaged over the COPS domain shown in Fig.1 for the entire period from 8 to 16 August 2007.

In Figure 1 the time series of the mean total precipitation in conjunction with the mean convective time scale averaged over the 360 x 360 km ^{2} COPS region is displayed. The period can be split in different episodes: from 8 to 10 August the situation is dominated by strong precipitation intensities and small convective time scales due to a prevailing upper-level trough across central Europe leading to an easterly flow in the COPS region. On 11 August the flow pattern changed and the next 3 days (12-14 August) are characterized by small mean precipitation amounts and a predominantly large mean convective time scale indicating weakly forced conditions at the synoptic scale. On the last two days (15 and 16 August) the meteorological conditions were predominantly governed by synoptic-scale disturbances crossing the COPS region.

The behaviour of the mean frequency bias score (FBI) and its spread is condensed in Figure 2 showing the scatter diagram for the entire period. Here, the convective time scale is used to stratify the data points into locally forced situations (τ_c > 6h, open circles in Fig.2) and forced-frontal situations (τ_c < 6h, dots in Fig.2). Overall, both flow regimes can be separated fairly well. During the locally forced regime the mean FBI is characterized by low mean FBI (FBI < 0.3) and high spread FBI. On the other hand, the synoptically forced regime is characterized by higher mean FBI and lower spread FBI. Seen by the convective time scale perspective, we may revisit the meteorological interesting conditions including the regime change on 12 August. These data points are highlighted in Figure 2. During the late afternoon

triggered convection conditions prevailed, characterized by a strong sensitivity on the physical perturbation, and hence showing a large forecast uncertainty (low mean FBI and large spread FBI). This is confirmed by the convective time scale attaining values larger than 6 hours, as is typical for locally forced, triggered convection meteorological regimes. In the late evening and at night the approaching surface cold front accompanied by precipitation causes a regime change. Now, the rainfall is less sensitive to the physical perturbations, that is, the precipitation forecast exhibits a smaller uncertainty, and the convective time scale attains values less than 6 hours, typical for synoptically-forced situations.

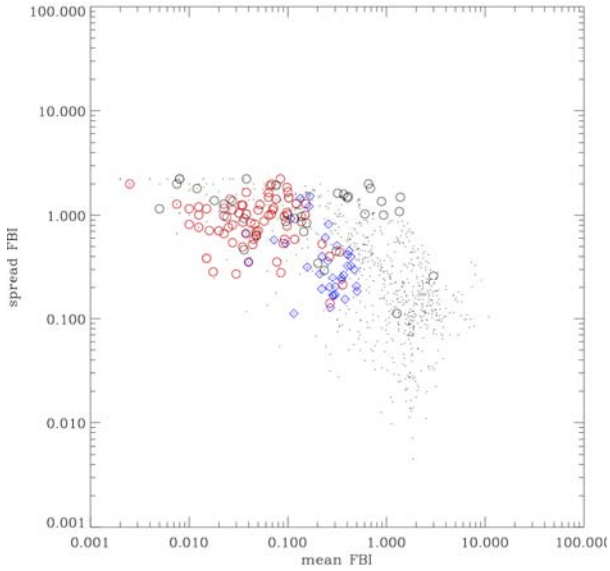

Figure 2. Scatter plot of the mean FBI (any symbol is the average over the same driving model or the same physical perturbation) versus its spread FBI for the entire period. The open circles denote the values when the convective timescale is larger than 6h indicating the triggered convection regime, the dots the values when the timescale is less than 6 hours indicating equilibrium conditions governed by synoptic-scale forcing. The red circles indicate values for 12 August and a timescale larger 6h, while the blue diamonds the values on that day when the timescale is less than 6h.

4. Conclusions

First results of the convection-permitting COSMO-DE-EPS system allow for an examination of the forecast uncertainty of convective precipitation during a nine day period during the COPS field campaign in August 2007. Two distinct meteorological regimes can be distinguished depending on the control of convection as measured by the mean and spread FBI and the convective adjustment time scale. Firstly, during triggered convection situations the precipitation forecast of COSMO-DE-EPS reacts sensitively to changes in the model physics, and the convective time scale attains values of more than a few hours (here a threshold of 6 hours was selected). Convective precipitation is primarily governed by local processes like orography or boundary layer phenomena leading to a large forecast uncertainty. Secondly, during forced-frontal convection situations, the precipitation is controlled by synoptic forcing that is determining the creation of instability. This regime is characterized by short convective time scales.

Currently a re-forecasting project using the COSMO-DE-EPS for the entire summer 2009 is underway at DWD. It is planned to apply the presented methodology on this large data set. In future it is planned to examine the potential of the convective adjustment time scale as a quantity to construct a flow-dependent convection-permitting EPS directed towards adaptive ensemble modeling.

Acknowledgments. We thank Deutscher Wetterdienst (DWD) and Deutsches Zentrum für Luft- und Raumfahrt (DLR) in Oberpfaffenhofen for providing the COSMO-DE-EPS forecast data and the radar observations, respectively. CK acknowledges funding from the German Research Foundation (DFG) priority program on Quantitative Precipitation Forecasts (SPP1167). This work has been performed during the COST731 Action of the European Science Foundation.

References

Baldauf, M., K. Stephan, S. Klink, C. Schraff, A. Seifert, J. Foerstner, T. Reinhardt, and C.J. Lenz, 2006: The new very short range forecast model LM-K for the convection-resolving scale. *Second THORPEX International Science Symposium*. Extended Abstracts, Part B, 148-149, Available online at http://www.pa.op.dlr.de/stiss/proceedings.html.

Done, J.M., G. C. Craig, S.L. Gray, P.A. Clark, and M.E.B. Gray, 2006: Mesoscale simulations of organized convection: Importance of convective equilibrium. *Quart. J. Roy. Meteor. Soc.*, 132, 737 – 756.

Gebhardt, C., S.E. Theis, M. Paulat, and Z. Ben Bouallegue, 2010: Uncertainties in COSMO-DE precipitation forecasts introduced by model perturbations and variation of lateral boundaries. *Atmospheric Research*, In revision.

Kalnay, E., 2003: Atmospheric Modeling, Data Assimilation, and Predictability. Cambridge University Press, 341 pp.

Keil, C. and G. C.Craig, 2010: Regime-dependent forecast uncertainty of convective precipitation. *Met. Z.*, submitted.

Kong, F., K. K. Droegemeier, an N. L. Hickmon, 2006: Multi-resolution ensemble forecasts of an observed tornadic thunderstorm system. Part I: Comparison of coarse- and fine-grid experiments. *Mon. Wea. Rev.*, 134, 807 - 833.

Marsigli, C., A. Montani, and T. Paccagnella, 2008: The COSMO-SREPS ensemble for short-range system: analysis and verification on the MAP D-PHASE DOP. *Joint MAP D- PHASE Scientific Meeting - COST 731 mid term seminar*, 19-22 May 2008, Bologna, Italy 9-14.

Molini, L., A. Parodi, N. Rebora, and G. C. Craig, 2010: Classifying severe rainfall events over Italy by hydrometeorological and dynamical criteria. *Quart. J. Roy. Meteor. Soc.*, submitted.

Molteni, F., R. Buizza, T. N. Palmer, and T. Petroliagis, 1996: The ECMWF ensemble prediction system: Methodology and validation. *Quart. J. Roy. Meteor. Soc.*, 122, 73-119.

Wulfmeyer, V., et al., 2008: The Convective and Orographically induced Precipitation Study: A Research and Development Project of the World Weather Research Program for improving quantitative precipitation forecasting in low-mountain regions. *Bull. Amer. Meteor. Soc.* 89(10), 1477-1486.

Rainfall forecasts from the Met Office variable resolution convective scale NWP model over the UK

Yong Ming Tang, Humphrey W Lean, and Jorge Bornemann
Met Office, Joint Centre for Mesoscale Meteorology (JCMM), United Kingdom
yongming.tang@metoffice.gov.uk

1. Introduction

Forecasting severe convection and quantitative precipitation in NWP is a major challenge. The current conventional approach of parameterizing convection has had only limited success. The alternative approach using higher resolution models which allow convection to be explicitly resolved is costly. Further, such high resolution models are usually used only over small areas, nested inside coarser resolution models which do not explicitly resolve convection. The mismatch of the grids and the model physics at the boundary of the limited-area fine resolution model can be a major source of model error. To overcome this difficulty, we have developed a variable grid, fine resolution, limited area numerical model. The variable resolution model has been tested for a number of events with the grid size varies smoothly from coarse resolution at the outer boundaries to a uniform 1.5 km in the interior of the domain. This will replace our exiting 4 km resolution NWP model and become the Met Office new NWP operation forecasting model. Here we will describe our new variable resolution NWP model configuration, and present some test results using this variable grid model compared with conventional nesting model.

2. Model description

The Met Office horizontal variable resolution UM shares the dynamical core with the regular resolution UM. However the horizontal grid spacing is no longer uniform. Instead we have designed a variable resolution grid which varies smoothly from a high resolution area in the interior domain to a coarse resolution outer domain. The whole model domain is divided into three regions. The inner high resolution uniform resolution region, the outer coarse resolution region, and in between is the transition zone (see Figure 1. In this variable resolution transition zone, the grid varies smoothly from fine resolution in the middle to coarse resolution toward the the outer boundaries in each direction. As described by Davies (1983), amongst several other works, a smoothly-varying grid can help to avoid the numerical errors introduced by the variable grid structure, such as local flow distortion and degradation caused by the resolution increase, or wave reflection caused by the spurious group velocity change due to the resolution change.

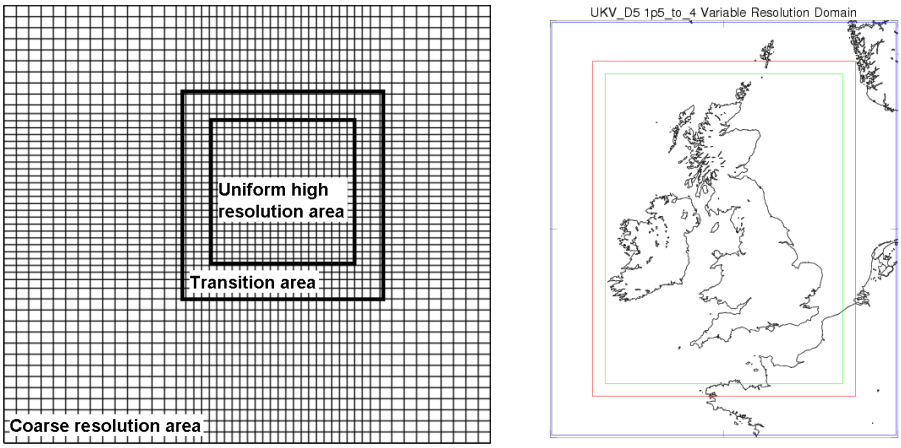

Figure 1: A schematic picture of a variable resolution grid (L) and model domain (R).

In each of the horizontal dimensions (see Figure 1), we define a uniform fine resolution area in the middle, with a grid length Δs. The grid length is then stretched at a constant stretching (or inflation) factor r, that is $\Delta s_{i+1} = r\Delta s_i$. until the grid size Δs reaches its desirable coarse resolution length. We then extend the domain to a further uniform coarse resolution region in the outer domain, as described in Cote et al. (1998). This is a very effective way to stretch the grid, for each successive doubling of resolution, only $\ln 2/\ln r$ number of points is needed. Typically, if $r = 1.1$, a 1 km fine resolution domain in the middle, and a 14-point variable resolution zone, so that the resolution is stretched to 4 km. Four model domains were used in this study; UKV (Met Office UK variable resolution model), UV1p5 (1.5 km high resolution model domain in the 1.5 to 4 nested model, which is also the inner domain of UKV), UV4 (4 km UM model, which is the same size as UKV and provide boundary values for UK1p5) and UVR (The nested model system comtains UK1p5 and UK4)

3. Cases studies

A variety of cases were run, including some very strong sharp frontal systems (08 Jan 2008 and 17 June 2009), and some weak scattered shower events (14 Apr 2008). Each run was for 18 forecasting hourr. As expected, in all the cases we studied the UKV and UK1p5 produced very similar results over the UK1p5 domain. Both models shared the same dynamic core and both have a better representation of the orography and land-sea contrasts than UK4. In Figure 2(a) we plot the area-average rainfall rate over the UK1p5 domain as a function of the forecasting time averaged over all 16 runs. The UK1p5 and UKV model data are first aggregated onto the 4 km model grid. The general agreement between the three models is very good. As explained by Lean et al. (2008), we should expect all models to start with a very small rainfall rates at $T + 1$ then increases to $T + 6$ as the explicit convection spins up. However, the rainfall rate values at this stage are normally too high, which is a well known over-shoot problem. It is clear that the UK4 model over-shoots more; as its rainfall rate is more than 10% at the peak hours than UKV and UK1p5. Figure 2(b) shows the number of cells as a function of rainfall rate threshold (mm/hr) over the UK1p5 domain averaged over all cases. There are

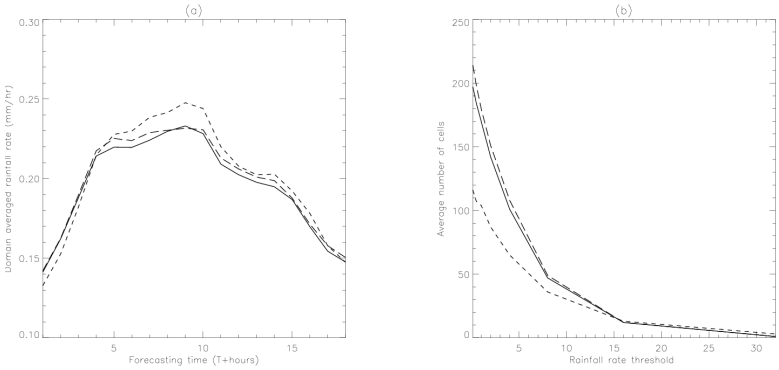

Figure 2: (a) Domain-averaged rainfall rate over the UK1p5 domain from all 16 runs. (b) Cell numbers as a function of rainfall rate threshold (mm/hr) over the UK1p5 domain averaged over all cases. The UK1p5 and UKV model data are aggregated onto the 4 km grid. The solid lines are from the UK1p5 model, the long-dashed lines are from the UKV model and the short-dashed lines are from the UK4 model.

significant difference, as much as 50%, between the models, especially at the lower end of the rainfall rate threshold. This discrepancy is again mainly caused by the spin-up issue combined with boundary updating in UK4 model. When we compare UK1p5 and UKV, both figures show very good agreement, but there is a slight systematic bias. That is UKV produces more rain at the beginning of the forecasting hours, and more cells at the lower end of the rain-rate threshold. In Figure 3 we show the accumulated

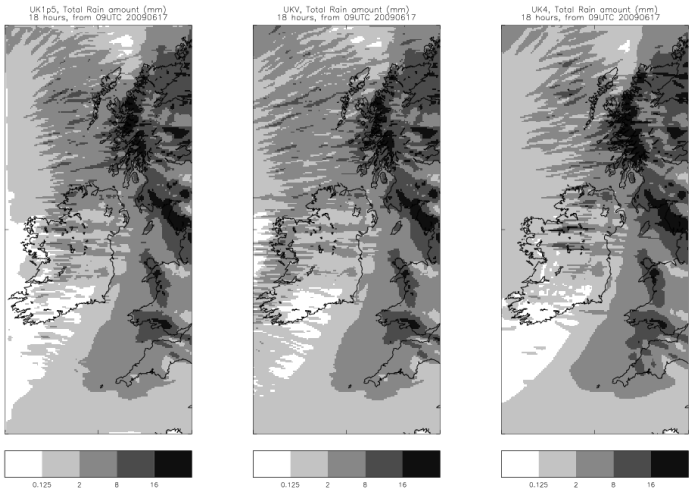

Figure 3: Total rain amount over the 18 hours forecasting period for a 17 Jun 2009 case in the west of UK1p5 doamin. from UK1p5 (left) UKV (middle) and UK4 (right).

rainfall amount over the forecasting period from the south west of the UK1p5 model domain for a secific case (17 June 2009). Although for a large part of the model domain all models produce similar results, we can see that there are discrepancies mostly along the western inflow boundary area of the UK1p5 domain. UK1p5 has less rain cells and the rain cells are more streaky in shape while the representation of rainfall is better in UKV. To examine this further, Figure 4 shows the meridional averaged rainfall amount

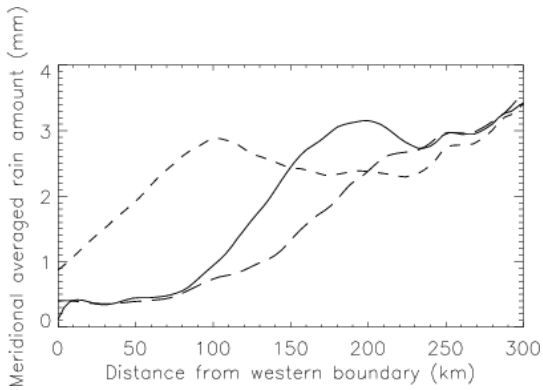

Figure 4: Meridional average total rain amount over the 18 hours forecasting period for 17 Jun 2009 case. The solid line is from 1.5 km UK1p5 model, the dotted line is from the UKV model and the dashed line is from UK4.

across the model domain.

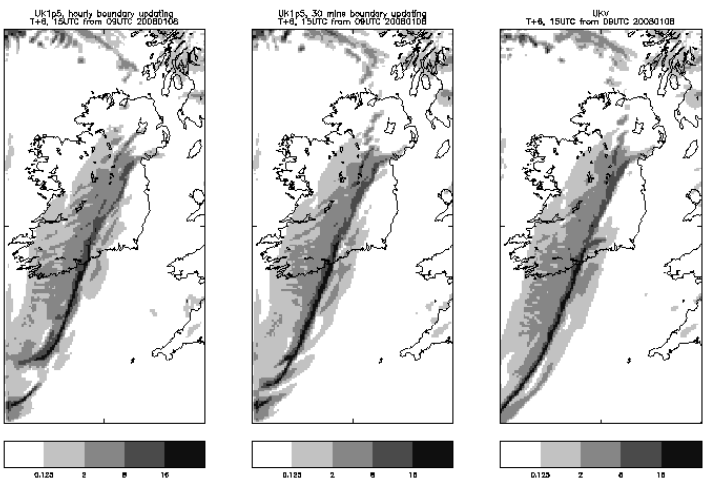

Figure 5: Surface rain rate at T+6 forecasting time for 08 Jan 2008 case in the south west of UK1p5 doamin. The left and middle panels are from the nested 1.5 km UK1p5 model, the left one with hourly boundary updating and the middle panel with 30 minutes boundary updating. The right hand side panel is from the UKV model .

Next we consider a case (Jan 08 2008) when a strong cold front crossed from West to East in the evening with strong and sharp line convection. All models show similar representations of the front, and when compared with radar observations, the representation of the line convection is remarkably good. In Figure 5 we show the forecasting rainfall rate at T+6 hours. While all models are similar overall, there are some visible differences. For instance, the (cold) frontal lines in the fine resolution models UKV and UK1p5 are thinner and sharper, and the streaky structures typically associated with the cold front are more pronounced. Also, the boundary updating in the nested model has a profound effect on the spin-up of the frontal line structure.

4. Summary and discussion

We have described a variable-grid, fine-resolution, limited-area numerical model, with an initial aim to obtain an improvement in the operational forecasting of convective initiation and precipitation. All models capture the main features well, such as the initiation of the convective storm initiation and the frontal line convection. But when significant differences do occur, it is mainly in the area of the inflow boundaries, and in the showers initiated behind the frontal system. Here the UKV model is particularly superior because, as noted above, it can be regarded as a closely coupled two-way nested model with boundary updating at every time step, while the smooth transition between the inner high resolution area and the outer region in effect enlarges the region of validity. In addition UKV does not need the large data transfer associated with the boundary forcing in conventional nested models. Consequently, we expect the adoption of UKV to lead to a positive impact on convective initiation, especially for convergence lines and advecting showers.

References

Cote, J., Gravel, S., Methot, A., Patoine, A., Staniforth, A. and Roch, M. 1998, The operational CMC-MRB global environmental Multiscale (GEM) model. Part I: Design consideration and formulation, *Mon. Wea. Rev.*, **126**, 1373-1395.

Davies, H.C., 1983, Limitations of some common lateral boundary schemes used in regional NWP models, *Mon. Wea. Rev.*, **111**, 1002-1012.

Lean, H.W., Clark, P.A., Dixon, M., Roberts, N.M., Fitch, A., Forbes, R. and Halliwell, C., 2008, Characteristics of high-resolution versions of Met Office Unified Model for forecasting convection over the United Kingdom, *Mon. Wea. Rev.*, **136**, 3408-3424.

Value of high resolution forecasts: convective climatology point of view

Martina Suaya
National Weather Service, Argentina
msuaya@smn.gov.ar

1. Introduction

The current state of the art in numerical models for weather prediction and the accessibility of computing power makes it possible to a larger meteorological community to obtain, run and produce high resolution forecasts. These forecasts are only limited by computed power and initial conditions, whereas papers about their quality can be found in the literature. From parameterization to explicit schemes in convection, still more computing is needed as well as nested domains into mesoscale models. The National Weather Service of Argentina has been running operationally a 30km resolution ETA model since 2003 and a nested non hydrostatic 10km one since 2006. The later is only available in 10°x10° box centered on high density and rich region of Argentina where high precipitation events are frequent. Non explicit convection model schemes are run at this center in operational basis although some attempts are performed in experimental mode.

Following the increase in resolution of global models is the intention over the next year to migrate from the hydrostatic 30km resolution ETA model, to a 10km version of the same model but run in non-hydrostatic mode over the whole domain of responsibility of the Argentine National Weather Service (RCMS Buenos Aires), that is from 90W to 30W, and from 65S to 20S. The performance of the operational ETA/SMN model has been evaluated over the last years and it resulted satisfactory in reproducing synoptic scale features, some local characteristics (sea breeze), as well as thermodynamic state of the atmosphere in general. Parameters such as precipitation, maximum and minimum forecasts among others have shown good results (Ciappesoni 2005, Suaya 2009). Feedback from forecasters has been encouraging although in general regarding precipitation a dry bias is observed, in particular for high precipitation seasons.

More detailed on the forecast provided and guidance is on demand. In particular, focus is on mesoscale systems where high precipitation is frequently observed and is usually underforecast by the 30km ETA model resolution. For example the number of days with 50mm totals or more for Buenos Aires city is on average for the summer (December to March) of 1-2 days per month. In Spring there's also a secondary maximum explained by the circulation present in this time of the year which favors the formation of storms (i.e. cold atmosphere and insolation). High precipitation rates over the city can easily result in flooding, with all the inconveniences it can bring in a large city.

What we can expect from a 30km resolution forecast model is to reproduce accurately the large-scale environment that feeds the convective storms but by

itself it is incapable of providing specific, detailed guidance on the timing and location of precipitation or the type and characteristics of the systems that produced the precipitation (Xue et al. 2001, 2003). In that sense it's the purpose of this study to assess qualitatively the benefits of a 10km and non-hydrostatic model in comparison with the coarser resolution one. Following Weisman (2008), one approach to asses the benefits of higher resolution models is to address the climatological behavior of the convection. In that sense on the following sections some results of frequencies, monthly totals and systems evolution in terms of precipitation will be discussed. No attempts are made to match forecasts with observation on the strictly sense to avoid the discussion of resolution issues. It's left for later papers to discuss verification statistics more rigorously and objectively.

2. Data and results

Only daily precipitation totals from the observational network available at the Argentine National Weather Service (NWS) database is used. This data undergo consistency checks on operational basis and on differed mode. The models to be analyzed are those operative at the NWS, which are the Regional ETA/SMN, 30km horizontal resolution, 38 levels in the vertical. It is run in a hydrostatic mode with parameterized convection (Betts-Miller-Janjic scheme). This model is nested to the Global Forecast System model (NCEP) of the same cycle. The High Resolution model is run in a non-hydrostatic mode and with a 10km horizontal spacing and is nested to the Regional ETA/SMN model. The domain of 10km model is a 10°x10° box centered on high density and rich region of Argentina (called Pampa), Uruguay and part of Brasil where high precipitation events are frequent. No other differences in configuration between models are present. Only the 12–36h forecast period based on the 0utc cycle was used for the model precipitation data to avoid spinup and overlapping model forecasts.

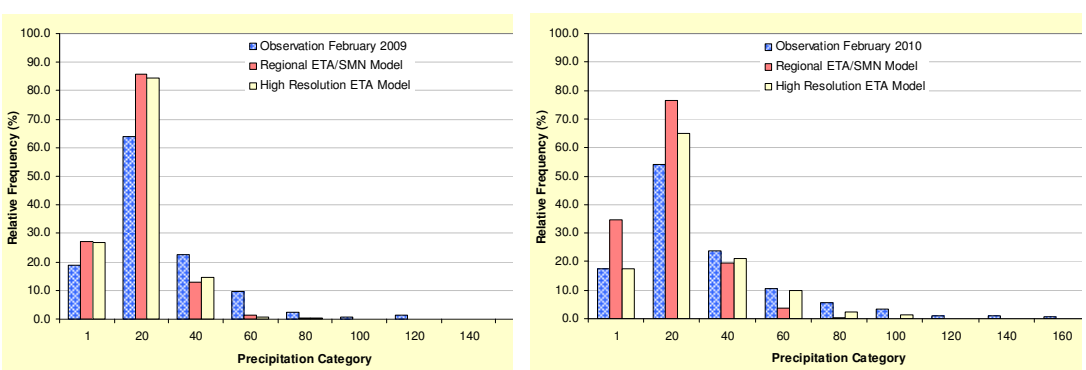

Figure 1: Relative frequency of days with precipitation observed, forecasted by the Regional Model (30km) and the High Resolution model (non hydrostatic, 10km) for the categories 1,20,...60mm. February 2009 on the left and 2010 on the right

The climatological character of the convection during the experimental period can be summarized in the graphics of Figure 1, which show for each month the number of observations with precipitation between the selected categories,

normalized by the total number of days with precipitation (no precipitations points are not considered). The model forecasts were taken from the nearest point. We can see for all cases that both models represent the monthly frequency of observed precipitation, with maximum frequency in the 20 to 40mm and a sudden drop to the 60mm and higher categories. For almost all the month and categories analyzed, the high resolution adjusts better to the observations. In Table 1 the extreme categories are presented showing that the total number of cases with high precipitation is better represented by the High Resolution model while the Regional model clearly shows a dry bias above 100mm.

Table 1: As Figure 1 but for the total number of cases observed during the two summer seasons considered for the highest precipitating categories.

Category	OBS	High Resolution	Regional ETA/SMN
100	37	**28**	0
120	14	**6**	2
140	9	0	0
160	6	0	0

In terms of monthly totals, both models represent the same precipitation patterns, but the high resolution model can attain higher values when a convective month is present. One of such example is shown in Figure 2, where we can appreciate differences of more than 200mm between models, and comparing to the observations the high resolution has the best fit, while the Regional ETA/SMN model under forecasted significantly the monthly totals.

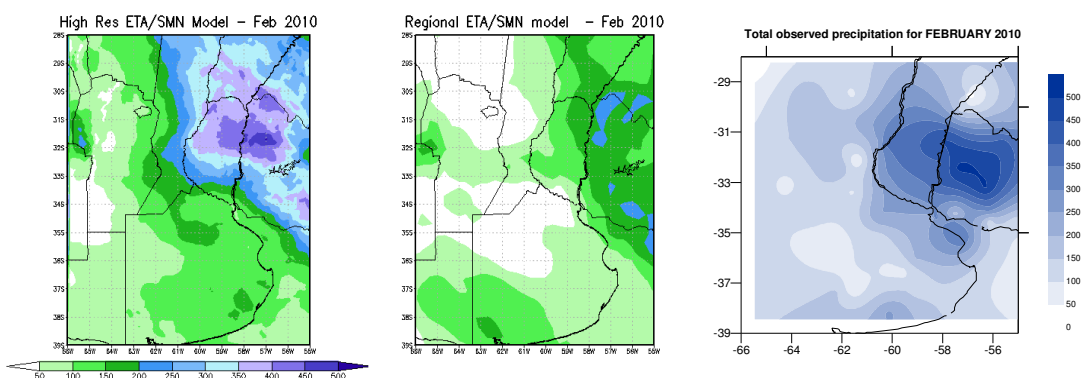

Figure 2: Monthly precipitation totals of 12-36hs forecast from the Non Hydrostatic High Resolution forecast ETA model (left) and Regional ETA model (center), and observed (right) for February 2010

Looking into daily totals we can see that the differences observed in Figure 2 come from particular days where high precipitation was forecasted and observed (Figure 3).

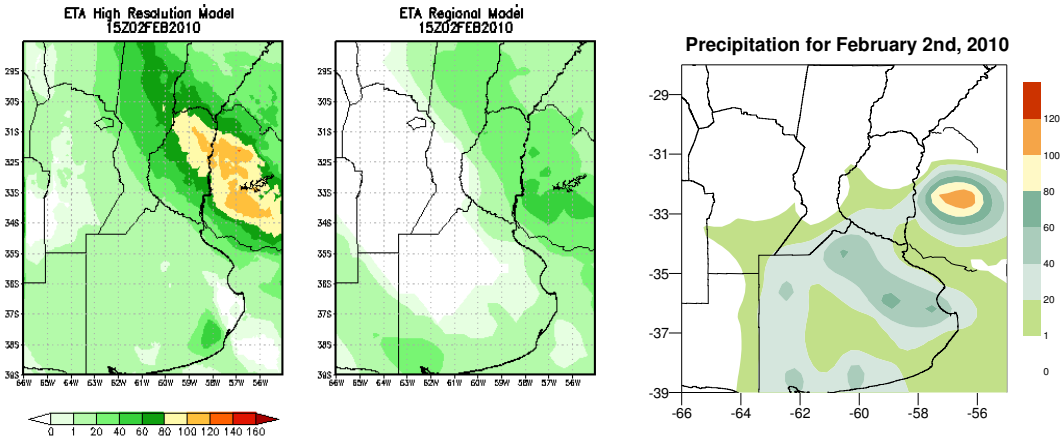

Figure 3: Non hydrostatic High Resolution forecast (left) and Regional ETA model (center) for February 2nd, 2010. Observed precipitation on the right.

From the 8 months analyzed (summer 2009 and 2010), only those months with high precipitation events show discrepancies between models. Studying the monthly totals and comparing to the observations, no significant wet bias (indicating false alarms) stands out for neither model.

From the 265 days analyzed only 37 (14% of cases) presented significant differences between daily forecasted precipitations. In general these differences where in terms of intensification and in most cases between the categories 40-80mm. Comparing these cases with observations we se that High Resolution model performed significantly better than the Regional Model (25 cases against 12 cases), and in terms of location both models have similar skill. The difference in intensity for all cases is also shown in Figure 4 (right) where we can see the highest difference in the 20mm bin, indicating that the High resolution model might result in wetter forecasts than the Regional model, at least in the higher precipitation amounts.

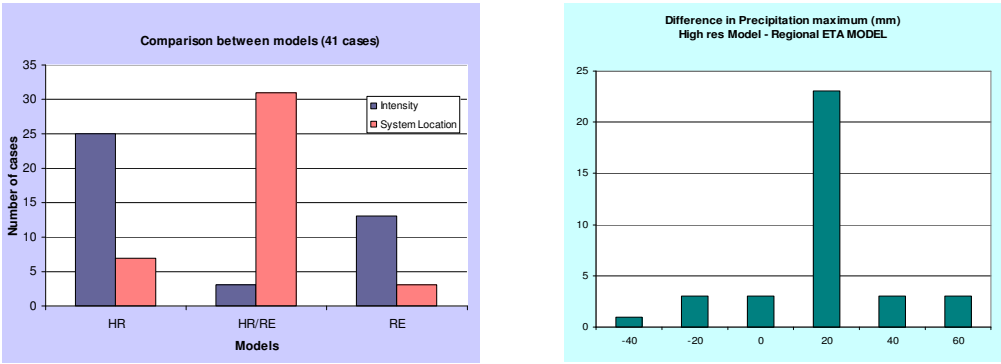

Figure 4: Graphics showing statistics of the comparison between the two configurations of the ETA model considering only those cases where significant difference on daily accumulated precipitation or location of systems was observed (subjective and visual selection). On the right, number of cases where Intensity or System Location performed better for each model, and on the left difference in maximum precipitation (High Resolution Model minus Regional ETA/SMN Model) for every meteorological system present on the selected days.

3. Conclusions

The 30km resolution ETA/SMN model was compared with 10km and non hydrostatic one in terms of their climatology in the high precipitation categories to asses the value added with later. Results show significant differences between models. In particular the High resolution model shows ability in activation the convection that results in higher precipitation amounts when convective systems where present. Both resolution and hydrostaticity might play a significant role in activating convection, which cannot be assessed in this study but it can be inferred that hydrotaticity plays a major role in intensifying the system (as shown figure 3).

The value added with the high resolution model was subjectively evaluated, showing that much improvement could be obtained in the forecasts. Better performance in all precipitation categories was shown but in particular in higher bins. When dry conditions are present both models have similar skills.

4. References

Ciappesoni, H.H., y R. Valdivieso: Verificación de los Pronósticos Públicos y del Modelo ETA/SMN del Servicio Meteorológico Nacional Argentino durante el año 2003 Y 2004. Congremet IX, 2005.

Suaya, M., y R. Valdivieso, 2009: Modelo ETA SMN 2003-2008 - usos, experiencias y resultados. Congremet X/Climet XII, 2009.

Weisman Morris L., and coauthors: Experiences with 0–36-h Explicit Convective Forecasts with the WRF-ARW Model. Weather and Forecasting, June 2008, vol. 23, 407-437.

Xue, M, and Coauthors, 2001: The Advanced Regional Prediction System (ARPS)—A multi-scale nonhydrostatic atmospheric simulation and prediction tool. Part II: Model physics and applications. Meteor. Atmos. Phys., 76, 143

Can Multi-model ensemble forecasts improve probability of precipitation forecasts compared to single model ensemble forecasts?

Laurence J. Wilson[1] and **Anna Ghelli[2]**
[1]*Environment Canada*
[2]*European Center for Medium Range Weather Forecasts*
lawrence.wilson@ec.gc.ca

1. Introduction

The TIGGE (Thorpex Interactive Grand Global Ensemble) project was designed to encourage research to determine the advantages of merging ensemble forecasts from different centers. Most verification studies using the TIGGE database have so far focused on the evaluation of upper air variables with respect to gridded analyses. For example Park et al (2007) looked at the performance of the models in terms of geopotential height at 500hPa and temperature at 850hPa. Johnson and Swinbank (2009) discussed the advantages of model combinations using geopotential height at 500hPa and mean sea level pressure. They also considered 2m Temperature in their evaluation, but still with respect to analysis data. Yi He et al (2008) studied the benefits of multimodel ensembles in a hydrological context and more recently Froude (2010) compared the performance of the ensemble systems when used for tropical cyclone forecasts. In general, these studies show that improvements in probabilistic forecasts can be obtained from combined ensembles compared to single model ensembles, especially if the models used in the combination are of relatively high quality, but the magnitude of the improvement has not been found to be large.

We have been using the TIGGE database to try to answer the question of the benefits of combined ensembles for a long-period sample of precipitation forecasts. The main goal of this work is to try to answer the TIGGE question posed above in a more user-friendly way, which is by comparing directly with surface observations rather than analysed data. This approach has the advantage that no model dependence is introduced into the verification dataset. This is particularly important when comparing the quality of several different systems since none of the systems is given an unfair advantage or disadvantage compared to the others by use of truth data which has been processed using one of the candidate models. Furthermore, exactly the same data is used for the verification of all the ensembles. We also wish to obtain as representative a result as possible, by using a long time period for the model evaluations.

We emphasize at the outset that this is a work in process. The results presented below are samples recently obtained, and we continue to analyse the results and to carry out further experiments using different verification measures, and for different regions. Most of the work has so far been done for Europe where a dense network of rain gauge observations is available, but efforts are underway for Canadian stations, and other regions will need to be evaluated before the TIGGE question is fully answered. The methodology and data are described in the next section, followed by sample results,

and some preliminary interpretation of the results. More results will be presented at the meeting.

2. Verification methods and data

One year of ensemble forecasts from 7 of the 10 ensembles in the TIGGE database was used in this study. A simple criterion based on model availability was adopted to select the seven ensembles. They are ECMWF (ECMF), JMA (RTJD), UKMO (EGRR), NCEP (KWBC), CMA (BABJ), CMC (CWAO) and BoM (AMMC). A comprehensive model description can be found on the TIGGE portals (http://tigge.ecmwf.int) and in Park et al. (2008). The ensemble forecasts were interpolated to a common 1x1 degree grid in order to have a uniform dataset with the same number of grid points.

For the European region verification, observation data was obtained from European meteorological offices and consists of high spatial density networks of both synoptic and climatological stations. The data are quality controlled and were upscaled to the 1 by 1 degree grid by computing averages over gridboxes. Since the observation network is sufficiently dense, gridbox average precipitation values were computed and used in the verification only if there were at least 9 observation sites in the gridbox. Further details of the upscaling method are described in Ghelli and Lalaurette (2000) and Cherubini et al. (2002). The advantages of this method for verification are that there is no model information used in the observation data processing and that the observation data retains its local characteristics, while the upscaling removes sub-grid scale information that cannot be represented in the models. The verification focused on 24h precipitation accumulations, for the year Oct 1, 2007 to Sept 30, 2008.

For the Canadian verification, rain gauge observations were obtained from 20 first order widely- spaced stations. With this data, we are lucky to have one station in a 1x1 degree grid box, and so the verification necessarily becomes a single-station verification with the observations matched to the forecasts at the nearest gridpoint. This is equivalent to estimating the grid box average precipitation using one observation, and so is consistent with the method used for the European data. However, there is no upscaling, so the verification is a more absolute and severe assessment of the quality of the models in terms of their ability to forecast precipitation at a point. If increases in model resolution are accompanied by increases in the accuracy of model forecasts at smaller scales, then the gap in quality revealed by these two verification approaches should narrow.

In order to carry out complete diagnostic forecast verification, one normally needs to use a variety of different verification measures, each of which describes different attributes of the forecast quality. For this study, we began with reliability diagrams, their associated scores, and the relative operating characteristic curve. The first assess the degree of agreement between the forecast probability and the conditional frequency of occurrence of the predicted event ("reliability"), while the last assesses the ability of the forecast to discriminate situations preceding the event from those preceding the non-event ("Discrimination"). "Events" were defined as the occurrence of 24h precipitation

amounts over thresholds, 1, 3, 5, 10, 15, 20, 25, and 30mm. For each of these events, reliability tables, brier scores, reliability and resolution, and the area under the ROC curve are being computed for three 3 month seasons (DJF, MAM, and JJA), for each ensemble separately, for all ensembles combined, and for combinations of the "best" four ensembles, and "worst" 4 ensembles. In combining ensembles, no debiasing was done, since it is not clear from previous studies that debiasing improves the performance of the combined ensemble compared to combinations of the raw ensembles. (See, for example, Candille et al 2010)

3. Sample Results

Figure 1 shows two reliability tables for the European area, one for the lowest threshold and one for a more "significant" threshold of 25 mm. For the low threshold, all the ensembles show at least a reasonable degree of reliability, while the Canadian ensemble is the most reliable. For the more significant threshold of 25mm, all of the ensembles significantly overforecast the probabilities. However, the ECMWF ensemble shows the best result since it has attempted forecasts of probabilities as high as 60 or 70% without significant loss of reliability for this relatively rare event.

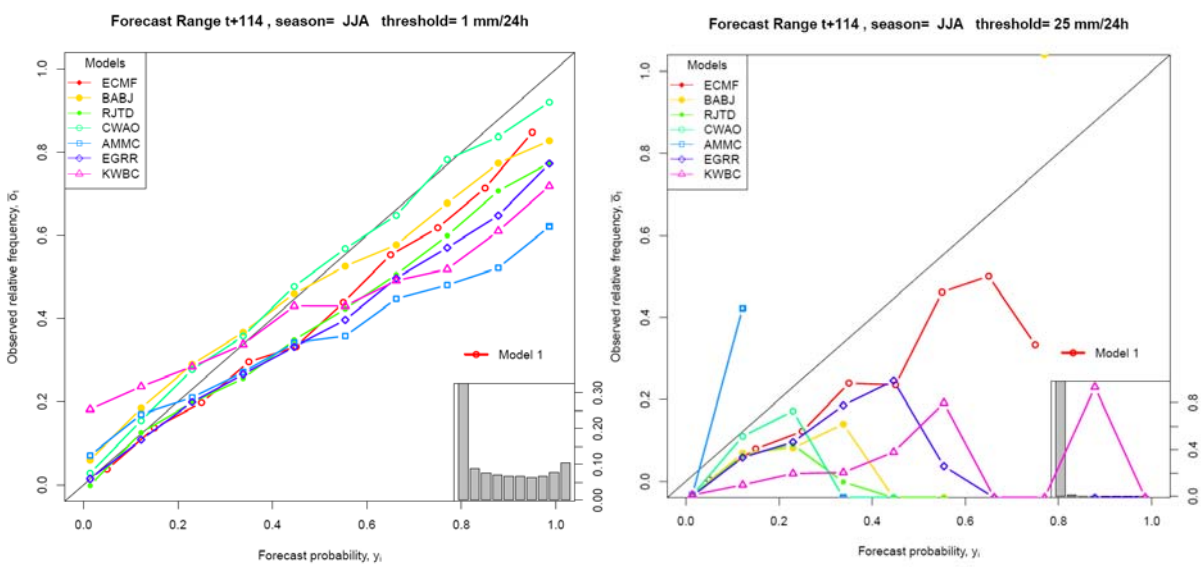

Figure 1. Reliability of single model ensemble forecasts, summer 2008, 114 h forecast, for thresholds of 1mm /24h (left) and 25 mm / 24 h (right).

Figure 2 shows four plots of the area under the ROC curve for each of the seven ensembles and for an ensemble created by combining all seven together, for the winter season. It can be seen from the figure that the performance of the ECMWF ensemble is always the best of the single model ensembles but that usually the combined ensemble outperforms all of the single model ensembles. The advantage of the multimodel ensemble is much more pronounced for the higher threshold than for the lower threshold (note also the difference in ordinate scales in this figure). A quick check of some of the other threshold results revealed that, at least for the winter season, the

difference between the COMB ROCA and the best of the single model ROCAs increased with increasing threshold.

The ROCA values are generally rather high, especially for the shorter range forecasts. Given that the ROCA was computed over the whole verification sample, all of Europe, for the 90 day season, it is likely that much if not most of the discrimination comes from the relative ability of the models to distinguish “wet” stations from “dry” stations and “wet” days from “dry” days. That is, these results might be showing differences in the models’ abilities to represent the precipitation climatology of Europe rather than showing discrimination of individual events at different locations. Tests are being carried out to check this hypothesis.

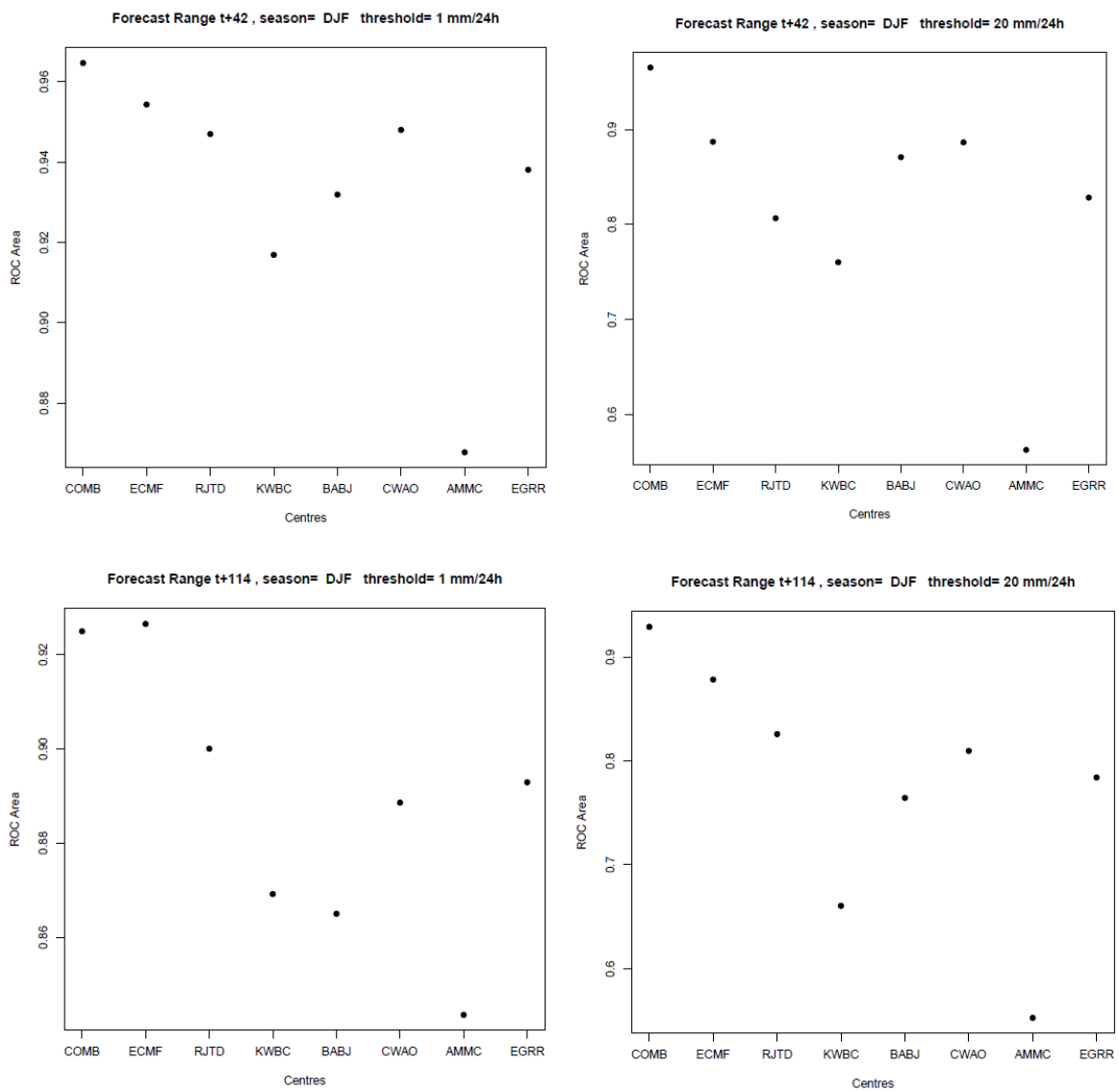

Figure 2. ROC areas for each of the seven single model ensembles and the combined ensemble (COMB) for the winter season for 42h forecasts (top) and 114h forecasts (bottom). Precipitation threshold is 1mm/24h (left) and 20 mm/24h (right).

In addition to combination of all the ensembles (ALL or COMB), combinations of the four best (4BEST: ECMWF, JMA, CMC and UKMO), two best and two worst (2BEST2WORST: ECMWF, JMA, BoM and CMA), and four worst (4WORST: BoM, CMA, NCEP and UKMO) were evaluated.

Figure 3 summarises the performance of the four different combinations. The ROC Area for the 4B is slightly better than ALL, while the 4W has the lowest value of the score. The score for the 2B2W combination is in between the 4B and 4W performance, which might be expected. This is a positive result, since it shows that it is possible to improve on the grand ensemble (which already improves on the single model ensembles), by selecting a few high quality models. Once again, one must note the ordinate scale of the figure; the differences are small for this low threshold and short range forecast.

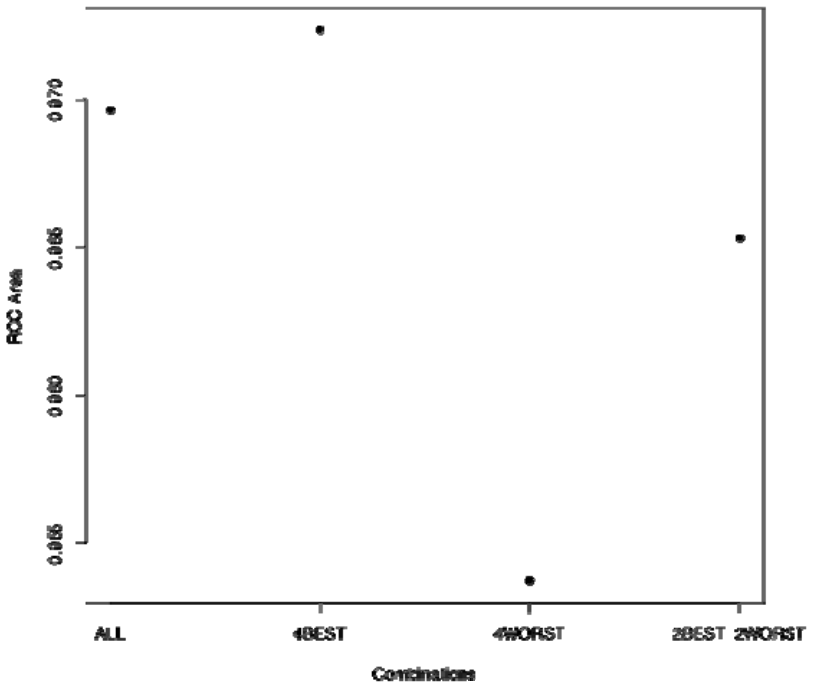

Figure 3: Relative performance of the combined ensembles for threshold 5mm / 24h, 42h forecast: 4BEST, 2BEST2WORST, 4WORST and ALL (all ensembles).

The work with the Canadian data is not as far advanced as for the European data. Figure 4 gives an example of ROCs and corresponding area obtained for the 20 Canadian stations, over the full year of data, for the CMC model and the ECMWF model. The ECMWF model shows a slightly larger ROCA area for these 6 day forecasts, but neither ensemble has significant discriminating ability at this range. The much lower ROCA values reflect the fact that this verification is with respect to single station data.

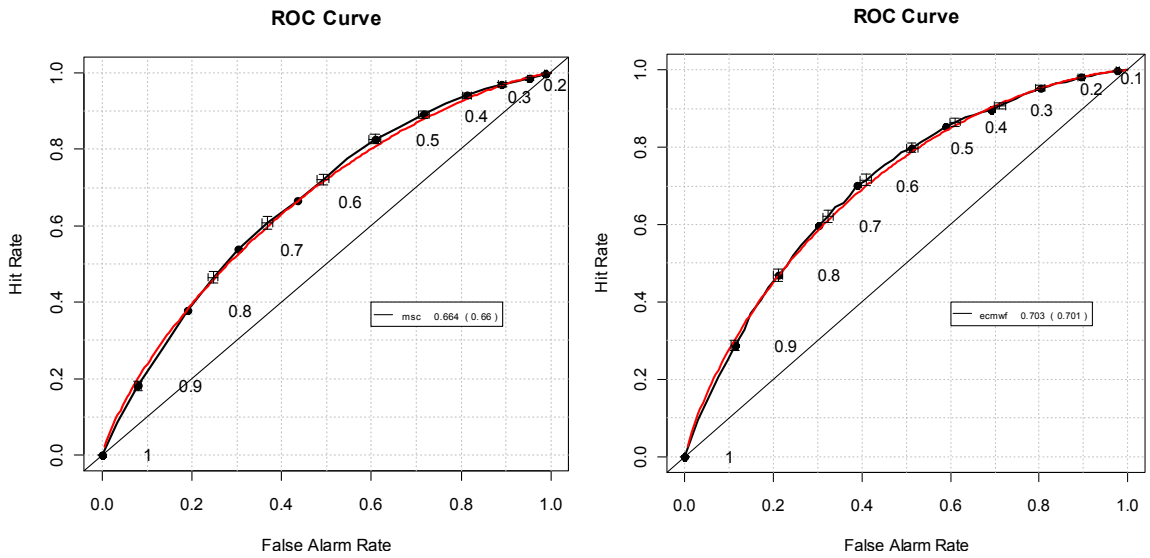

Figure 4. ROC curves and areas for one year of CMC ensemble forecasts (left) and ECMWF ensemble forecasts, 144h projection. The threshold is 1mm/ 24h. The red curves are the bi-normal model fit to the points and the black lines with the plotted points represent the empirical ROC. Boxes around the plotted points are the 5 to 95% bootstrap confidence intervals.

4. Discussion and Future work:

These results are very preliminary, but so far suggest that there is value in combining ensembles to predict precipitation amounts. This is consistent with experience with the North American Ensemble Forecast System (NAEFS), where the combination of the Canadian and NCEP ensembles has led to significantly improved ensemble forecast probabilities for both centers. If further tests support the preliminary result shown here that the advantage of multi-model ensembles increases for higher precipitation thresholds, then this would be significant, for it would indicate that multi-model combinations are important for the improvement of forecasts of high impact weather events. Whether the advantages are large enough to justify the extra effort of blending ensembles on an operational basis remains to be determined.

Much work remains to be done. The following is a non-exhaustive list of investigations that need to be undertaken to settle the TIGGE question for surface data:
-For the ROC results, determine the source of variations in discriminant ability to answer the question: “Does the combined ensemble improve the ability to distinguish significant precipitation events at specific times and places?”
-Verify the forecasts using other complementary verification measures for probability forecasts: reliability diagrams, brier scores and components, and the CRPS.
-Assess the ability of the single model ensembles and combined ensembles to predict high impact precipitation events, using distribution-fitting methods and evaluating the extremes of the predictive distribution

-Carry out the verification for other regions of the world. In addition to Canada, it is important to evaluate surface ensemble forecasts for areas where models (and ensembles) tend to perform relatively poorly, such as in the tropics.
-Verify other surface weather elements: temperature, wind, clouds.

5. References

Candille, G., S. Beauregard, and N. Gagnon, 2010 : Bias correction and multiensemble in the NAEFS context or how to get a 'free calibration' through a multiensemble approach, *Mon. Wea. Rev*., In press.

Cherubini, T., Ghelli, A., and Lalaurette, F., 2002: Verification of precipitation forecasts over the Alpine region using a high-density observing network. *Weather and Forecasting,* **17**, 238–248.

Froude, L, 2010: TIGGE: comparison of the predicted Northern Hemisphere Extratropical cyclones by different Ensemble Prediction Systems, *Weather and Forecasting*, **25**, 819-936.

Ghelli, A. and Lalaurette, F., 2000: Verifying precipitation forecasts using up-scaled observations. *ECMWF Newsletter* **87**, ECMWF, Reading, United Kingdom, 9–17.

Johnson, C. and Swinbank, 2009: Medium-range multimodel ensemble combination and calibration *Q. J. R. Meteorol. Soc.* **135**: 777–794 (2009)

Park, YY, Buizza R, Leutbecher M. 2008. TIGGE: preliminary results on comparing and combining ensembles. *Q. J. R. Meteorol. Soc.* **134**, 2029–2050.

Yi, He, Fredrik Wetterhall, Hongjun Bao, Hannah Cloke, Zhijia Li, Florian Pappenberger, Yuzhong Hu, Desmond Manful and Yingchun Huang, 2010: Ensemble forecasting using TIGGE for the July – September 2008 floods in the Upper Huai catchment: a case study, *Atmos. Sci. Let.* **11**: 132 – 138

Improvement of Poor Man's Ensemble Precipitation Forecast in Mountainous Regions of Australia

Jingru DAI[1], Michael MANTON[1], Steven SIEMS[1]
[1]*Monash University, Melbourne, Australia*
jingru.dai@monash.edu

Accurate prediction of precipitation is very important for water management and planning especially over a water catchment area. The Australia Bureau of Meteorology's Poor Man's Ensemble (PME) forecast for daily rainfall combines quantitative precipitation forecasts to give deterministic and probabilistic rainfall forecasts (Ebert, 2001,2002). However, the 100km by 100km forecast map of PME is too coarse to delineate detailed features of orographic precipitation in mountainous areas. In winter observation errors can arise when precipitation may fall as snow in strong winds rather than rain and there are limited points for verification.

A statistical approach has been developed to improve the PME forecast for the Snowy Mountains region of south eastern Australia. Clustering analysis is employed to identify different meteorology regimes using nearby Wagga-Wagga atmospheric sounding variables. PME precipitation forecasts have been verified for each of the regimes using Snowy Hydro Ltd (SHL) high-quality precipitation gauges across the region. A linear regression is adopted for each regime using sounding variables and PME forecast value to calibrate the daily precipitation forecast. Three-year winter evaluation (2005 to 2007) shows around 20 percent improvement in terms of mean square error for nowcasting and 1-day ahead forecasts.

How sensitive are probabilistic precipitation forecasts to the choice of ensemble generation method?

Juan J. Ruiz[1,2] and Celeste Saulo[1,2]
[1]Dept. of Atmosphere and Ocean Sciences, Faculty of Exact and Natural Sciences, University of Buenos Aires, Buenos Aires, Argentina
[2]Centro de Investigaciones del Mar y la Atmósfera (CONICET-UBA), Buenos Aires, Argentina

1. Intruduction

As described by Wilks and Hamill 2007, errors in PQPF forecast have several sources, including initial conditions and model errors. These two particular error sources motivate two different approaches for ensemble generation: the initial and boundary condition perturbation ensemble (Toth and Kalnay 1997, Molteni et al 1996 among many others) and ensembles with different formulation of model physics or multimodel ensembles (Ebert et al. 2001, Krishnamurti et al. 1999, Park et al. 2008). The main objective of this paper is to evaluate which approach leads to a better PQPF skill over our region of interest and also to perform a comparison between perturbed initial conditions and/or perturbed physics generated ensembles with simpler and computationally cheap ensembles like the one proposed by Theis et al. 2005, which only takes into account displacement errors in the forecasted field.

2. Methodology

2.1 Ensemble generation

Three different ensemble generation strategies are tested in this work, all of them are implemented using the Weather Research and Forecasting (WRF) model Advanced Research WRF (ARW) dynamical core version 2.0 (Skamarock et al. 2005). In all experiments horizontal resolution is 40 km, and 31 vertical sigma levels have been used with the model top located at 50 hPa. Model domain is shown in Figure 1.

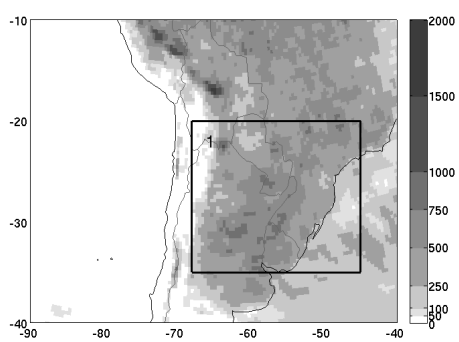

Figure 1: Regional ensemble domain and CMORPH total precipitation (in mm) between December 15th 2002 and February 15th 2003 (shaded). The black box indicates the area used for verification and calibration.

Breeding ensemble:

This is a single model, single configuration ensemble with perturbations introduced in the initial and boundary conditions using breeding of the growing modes technique (hereafter breeding) (Toth and Kalnay 1993) with a rescaling period of 6 hours. The ensemble consists of 11 members (5 pairs of perturbed members and a control run) integrated up to 48-hour lead time.

Boundary conditions are provided by a global ensemble based in the Medium Range Forecasts model with T62L28 resolution (aproximately 2.5 horizontal resolution). The unperturbed initial condition (control run) is obtained from the Global Data Assimilation System (GDAS) analysis with 1° x 1° resolution. The experiment starts on 15th December 2002 and ends by 15th February 2003, and the regional ensemble forecasts are initialized at 1200 UTC.

Multimodel ensemble:

WRF framework allows the use of different parameterizations for convection, boundary layer mixing, surface processes, cloud microphysics and radiation. In this work, this capability is used to construct a multi model ensemble based on the same dynamical core (ARW) but using different choices for model physics. Initial and boundary conditions, as well as model domain are the same for all members and correspond to the control run of the breeding system described above. Table I sumarizes the different parameterizations used for each ensemble member.

Member	Convection	PBL	LSM
1	KF	YSU	NOAH
2	BM	MYJ	NOAH
3	BM	MYJ	5 layer
4	GRELL	YSU	RUC
5	GRELL	MYJ	NOAH
6	BM	YSU	RUC
7	KF	MYJ	NOAH
8	KF	YSU	5 layer
9	KF	YSU	RUC
10	BM	YSU	NOAH
11	BM	MYJ	RUC

Table I: Schemes used for each ensemble member for the representation of convection, PBL and the surface processes.

Spatially shifted ensemble:

This ensemble is a synthetically generated ensemble which does not require of multiple model runs. It simply consists of spatially shifted forecasts generated from a single control run. This approach has been introduced by Theis et al. (2005). The main idea of this strategy is to account for uncertainty in the location of forecasted features. In this case the control run of the breeding ensemble is used to construct the spatially shifted ensemble; the maximun allowed shift is 3 grid points in any direction which gives an ensemble size of 49 ensemble members.

2.2 Calibration methodology

Calibrated probabilities were computed using the ensemble mean (i.e. the different skill of each ensemble member was not taken into account) because previous experiments (Ruiz and Saulo, 2010, submitted) have shown that the inclusion of this information does not lead to a significant improvement in PQPF skill. A Gamma distribution was fitted to the mean forecasted precipitation errors as in Slougther et al (2007) where the gamma parameters are functions of forecasted precipitation.

CMORPH (Climate Prediction Center Morphing Technique, Joyce et al. 2004) precipitation estimates were used for calibration and verification of the PQPFs.

3. Evaluation of PQPF skill

This section presents the results associated with the sensitivity of the PQPF skill to the method used for the ensemble generation. Figure 2, shows the BSS and its resolution component diference with respect to the breeding ensemble, for all the ensemble systems tested. The reliability component is very similar in all cases so it is not discussed here. For this particular lead time (24 hours) the shifted ensemble shows the best results, while both ensembles perform better than the breeding one.

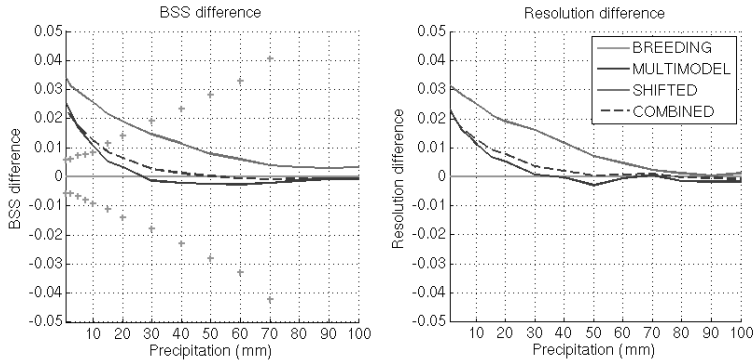

Figure 2: BSS difference with respect to the breeding ensemble, for the multi model, spatially shifted and combined ensembles. Breeding ensemble (ligth grey solid line), multimodel ensemble (black solid line) shifted ensemble (grey solid line). The grey crosses in the left panel, indicate the 90% confidence limit.

The multimodel and breeding ensembles can be also combined into a larger one consisting of 21 members as suggested in Hou et al. 2001. This combination –denoted as COMBINED- outperforms the multimodel ensemble, particularly for thresholds above 5 mm (Figure 2). Figure 2 also suggests that most of the differences between the various ensemble systems are related with the resolution component of the BSS.

The improvement achieved by the shifted ensemble is surprising because this is bassically a cost free ensemble where differences among members are not flow dependent and also are not related with errors in model formulation as in the rest of the ensembles. This behavior suggests that a simple spatial smoothing can effectively remove unpredictable components of precipitation field at short lead times. However for 48 hours lead time this particular approach has a slightly better skill than breeding but significantly worse than the multi model or the combined ensemble (not shown). The simpler smoothing approach can only take into account position errors but cannot represent uncertainty associated with the existence of a precipitating system or its intensity. This type of uncertainty can only be addressed with a dynamic ensemble.

As the shifted ensemble shows good results but suffers from fast forecast skill loss with lead time, it seems natural to combine the shifted approach with multimodel, breeding and combined ensembles. To do this, shifted ensembles have been derived from each ensemble member of the multimodel, breeding and combined ensembles using a maximun shift of 1 grid point, due to memory limitations. The resulting ensembles are going to be referred to as shifted multimodel, shifted breeding (both with a size of 99 members) and shifted combined (with at total size of 189 members). Results for 24-hour lead time compared with multimodel ensemble performance are shown in Figure 3, as BSS diferences with respect to the multimodel ensemble.

Shifted multimodel and shifted combined ensembles show the largest improvement at low thresholds. The shifted breeding is slightly worse than the multimodel for lower thresholds but is the best approach for thresholds above 20 mm. However, it should be noted that for higher thresholds, differences are below the significance level. As discussed before, changes in BSS are due to differences in the resolution component of the score. Similar results were obtained for 48-hours lead time, indicating that when the shifted approach is combined with a dynamical ensemble the loss in forecast skill with forecast length is corrected.

4. Conclusions

Different ensemble generation strategies have been compared for PQPF generation over South eastern South America during the 2002-2003 warm season. CMORPH precipitation estimates have been used in order to work with a more complete precipitation dataset for calibration and verification.

The PQPF derived from two dynamically generated ensemble systems was compared with a very simple ensemble system (the shifted ensemble) which only takes into account the uncertainty associated with the possition of rain areas. This simple ensemble proves to be quite competitive at short forecast ranges (less than 24 hours); yet, its skill drops rapidly with increasing lead time. The success of this simple approach for short lead times suggests that dynamic ensemble approaches are not good enough to represent forecast uncertainty during the first 24 hours. It seems that more specific methods are needed to better represent uncertainty at short forecast ranges.

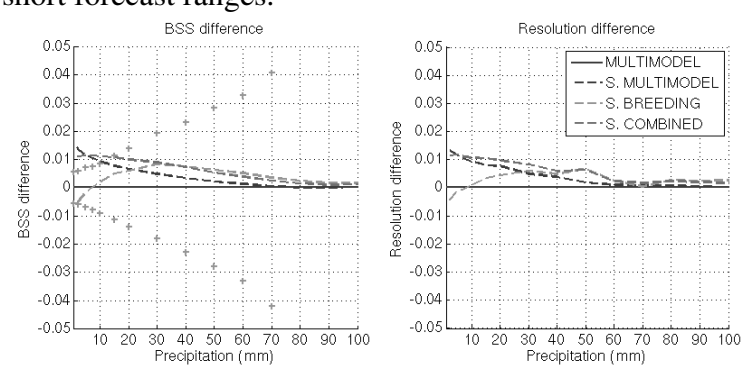

Figure 3: BSS and resolution difference between the multimodel ensemble (black solid line) and the shifted multimodel ensemble (black dasehd line), shifted breeding ensemble (light grey dashed line) and shifted combined ensemble (dark grey dashed line). Grey crosses in the left panel, indicate the 90% confidence limit.

Among dynamically generated ensembles tested, the multimodel ensemble based on different configurations available in the WRF model, outperformed the breeding ensemble. Still, the improvement obtained from the combination of breeding and multi model ensembles is not very large. This suggests that most of PQPF error during this particular time of the year (i.e. Southern Hemisphere summer) arises from errors in model physics rather than problems in the initial and/or boundary conditions. During this particular season, most of the precipitation predicted by different configurations results from the convective parameterization, further emphasizing the importance of appropriate model physics in determining precipitation fields. Along the same line, it could be considered that relatively low performance of the breeding ensemble, could be due to the length of the rescaling period, which could be adjusted to capture smaller scale and faster growing perturbations associated with mesoscale and convective scale processes and thus more appropiate to be used during the warm season (Kalnay and Silva Dias, 2009, personal communication).

Among the alternatives that have been evaluated, the most important improvement has been obtained with the combination of the multi model ensemble approach and the spatial shift technique even at 48-hours lead time. This approach is particularly interesting and promising for implementing high resolution ensembles in small operational or research centers for which computational costs largely restrict ensemble size.

Although all the results showed in this paper were obtained using CMORPH, results based on the use of a dense rain gauge network available over the region during the selected period were similar. Most of the experiments were also carried out over a tropical region located over Northern Brazil which also exhibits a similar behaviour although the skill of the PQPF was lower than that for the region discussed in the paper.

Acknowledgments

This study has been supported by the following projects: UBACyT X204, CONICET PIP 112-200801-00399. The research leading to these results has received partial funding from the European Community's Seventh Framework Programme (FP7/2007-2013) under Grant Agreement N° 212492 (CLARIS LPB. A Europe-South America Network for Climate Change Assessment and Impact Studies in La Plata Basin).

References

Ebert, E. E., 2001: Ability of a Poor Man's Ensemble to Predict the Probability and Distribution of Precipitation. *Mon. Wea. Rev*., **129**, 2461-2480.

Ebizuzaki, W., and E. Kalnay, 1991: Ensemble experiments with a new lagged average forecasting scheme. *WMO Report* #15.

Hou, D., E. Kalnay, and K. K. Droegemeier, 2001: Objetive Verification of the SAMEX`98 Ensemble Forecast. *Mon. Wea. Rev.*, **129**, 73-91.

Joyce, R. J., J. E. Janowiak, P. A. Arkin, and P. Xie, 2004: CMORPH: A method that produces global precipitation estimates from passive microwave and infrared data at high spatial and temporal resolution. *J. Hydromet*., **5**, 487-503.

Krishnamurti, T. N., C. M. Kishtawal, T. E. LaRow, D. R. Bachiochi, Z. Zhang, C. E. Willford, S. Gadgil, and S. Surendran, 1999: Improved weather and seasonal climate forecast from multi model superensemble. Science, 285, 1548-1550.

Molteni, F., R. Buizza, T. N. Palmer, and T. Petroliagis, 1996: The ECMWF Ensemble Prediction System: Methodology and validation. *Quart, J. Roy. Meteor. Soc*., **122**, 73-119.

McLean Sloughter J., J., A. Raftery, T. Gneiting, and C. Fraley, 2007: Probabilistic Quantitative Precipitation Forecasting Using Bayesian Model Averaging. *Mon. Wea. Rev*., **135**, 3209-3220.

Park, Y., R. Buizza, and M. Leutbecher, 2008: TIGGE Preliminary results on comparing and combinning ensembles. Quarterly Journal of the Royal Meteorological Society, 134, 2029-2050.

Skamarock, W. C., J. B. Klemp, J. Dudhia, D. O. Gill, D. M. Barker, W. Wang, and J. G. Powers, 2005: A description of the Advanced Research WRF Version 2. NCAR Tech Notes-468+STR

Theis, S. E., A. Hense and U. Damrath, 2005: Probabilistic precipitation forecast from a deterministic model: a pragmatic approach. Meteorological Applications, 12, 3,257-268. doi10.1017/S1350482705001763

Toth, Z., and E. Kalnay, 1997: Ensemble Forecasting at NCEP and the Breeding Method. *Mon. Wea. Rev*., **125**, 3297-3319.

Wilks, D. S., 1995: Statistical Methods in the Atmospheric Sciences: An Introduction. International Geophysics Series, Vol. 59, Academic Press, 467 pp.

Multimodel consensus forecasting of the precipitation using TIGGE data

ZHI Xiefei, ZHANG Ling

Key Laboratory of Meteorological Disaster of Ministry of Education, Nanjing University of Information Science and Technology, Nanjing 210044

1. Introduction

The extreme events from 11 January until 2 February 2008 brought severe low temperature and icy weather to broad regions in central and southern China, which caused billions of dollars worth of direct economic loss and hundreds casualty. These extreme icy weather events were closely linked to the change in the Middle East jet stream (MEJS), which intensified and shifted southeastward (Wen et al. 2009). Wang et al. (2008) indicated that the very active AO is a very important factor which leads to the anomalous atmospheric circulation and thus these severe weather events. During the events more frequent blockings over Eurasia were observed (Zhang et al. 2009; Zhou et al. 2009). Meanwhile, the subtropical western Pacific high (SWPH) was stronger and its ridgeline was farther north than normal. The anomalous high slowed down the eastward movement of weather systems to the Pacific and was favorable for the convergence of water vapor over central–southern China (Wen et al. 2009; Zhang et al. 2009). Further study indicated that extraordinarily strong convections over the maritime continent and South China Sea may play an important role in the formation of the anomalies of the SWPH during early 2008 (Zhang et al. 2009).

Nowadays, the numerical weather prediction (NWP) has become the major guidance in our daily weather forecast. However, the skill of extended range forecast for surface temperature and rainfall using available NWP models is still not satisfactory to address the detailed aspects of extreme weather events. Multimodel superensemble forecast method is a practical post-processing technique capable of reducing model output errors (Krishnamurti et al. 1999; 2000a; 2000b; Yun et al. 2003; Mutemi et al. 2007; Zhi et al. 2009a; Lin et al. 2009). Zhi et al. (2009b) and Lin et al. (2009) applied the multimodel superensemble technique in the forecasting of the surface temperature in Northern Hemisphere. The forecast skill of the multimodel superensemble with fixed training period is higher than that of the ensemble mean and the best individual model for the 24h-144h surface temperature forecast. The superensemble with running training period has superior forecast skill to that with fixed training period for the 24h-168h forecast. Further study indicates that bias-removed ensemble mean can considerably reduce the RMSEs of the 24h-144h surface temperature forecast as well. In this study, the bias-removed ensemble mean forecasting experiment was performed for the precipitation in central and southern China during the extreme weather events in early 2008 to improve the extended range forecast skill of the high-impact weather events.

2. Data and methods

Based on the daily mean temperature and 24h total accumulated precipitation in southern part of China (102.5°E-122.5°E, 22.5°N-35°N) from 1952 to 2008, the features of the extreme events with low temperature and abundant precipitation during the period from 10 January until 2 February 2008 have been investigated which are fitted by the Generalized Pareto Distribution (GPD) proposed by Hosking (1990). The 24-216h ensemble forecast data of the 24h accumulated total precipitation during the period from 1 January until 31 January 2008 are taken from European Centre for Medium-Range Weather Forecasts (ECMWF), Japan Meteorological Agency (JMA), National Centers for Environmental Prediction (NCEP), and China Meteorological Administration (CMA) in the TIGGE Data Archive Portal. In addition, the NCEP/NCAR reanalysis data and the TRMM 24h accumulated total precipitation from 1 January to 10 February 2008 are used as the "observed data" for verification of the forecasts.
The consensus forecast experiments of the 24h accumulated total precipitation are conducted by using the multimodel ensemble mean (EMN), the bias-removed multimodel ensemble mean with fixed training period (BREM) and the bias-removed multimodel ensemble mean with running training period (R-BREM), respectively. The root-mean-square errors (RMSEs) and the precipitation rank threat score (TS) are utilized to evaluate the forecast skills of the surface temperature and 24h accumulated total precipitation, respectively.
The multimodel ensemble mean (EMN) is calculated as follows,

$$EMN = \frac{1}{n}\sum_{i=1}^{n} F_i \qquad (1.1)$$

where F_i is the *i*th model forecast, and *n* is the number of forecast models involved.
The bias-removed ensemble mean (BREM) is calculated as follows,

$$BREM = \overline{O} + \frac{1}{N}\sum_{i=1}^{N}(F_i - \overline{F}_i) \qquad (1.2)$$

where F_i is the *i*th model forecast value, $\overline{F}_i$ is the time mean of the *i*th model forecast over the training period, $\overline{O}$ is the time mean of observed state, *N* is the number of models. The root-mean-square error is written as

$$RMSE = [\frac{1}{N}\sum_{i=1}^{N}(F_i - O_i)^2]^{\frac{1}{2}} \quad (i = 1 \cdots N) \qquad (1.3)$$

where F_i is the *i*th sample forecast value, and O_i is the *i*th sample observed value.

3. The multimodel ensemble forecasts of the precipitation

Due to cold surges, four successive major precipitation processes affected central and southern China during the period from 10 January until 2 February 2008, which caused low temperature, snowstorms and freezing rain over the southern part of China. As shown in Figure 1, more than a third of stations in the southern part of China were covered by the extremely abundant precipitation with 50 years return period, and the extremely low temperature with 50 years return period occurred in the Guizhou and western Hunan province as well. The concurrence of low temperature and large precipitation caused the extreme icy weather over the southern part of China.
Based on the precipitation 24-216h ensemble forecasts of ECMWF, JMA, NCEP and CMA in

the southern part of China during the period from 1 January until 31 January 2008, the multimodel consensus forecasts of the 24h accumulated total precipitation have been conducted for the forecast period from 16 to 31 January 2008. Similar to the procedure mentioned in section 4, 6 days training period was chosen as the optimal training period and the TRMM (Tropical Rainfall Measuring Mission) precipitation data were chosen as the "observed data". Threat score (TS), also known as the critical success index (Schaefer, 1990),

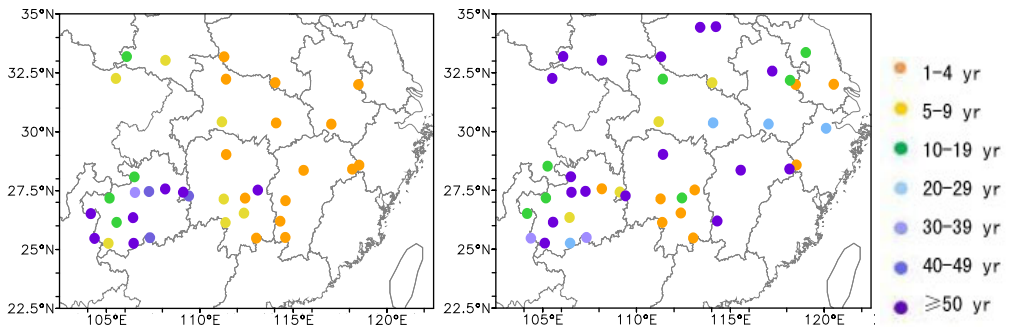

(a) **(b)**

Fig.1. The extreme daily mean temperature (a) and 24h accumulated total precipitation (b) distribution for different return periods during the period from10 January to 2 February 2008.

or equitable threat score (ETS) which is a modification of the threat score to explain the correct forecasts as a result of chance (Gilbert, 1884), is used at the National Centers for Environmental Prediction (NCEP) almost exclusively as the most important variable for verification of the skill in precipitation forecasting (Mesinger, 2008). In this study, TS with different ranks was utilized to evaluate the precipitation forecast skills of different individual models and multimodel consensus forecasts. It is defined as follows,

$$TS = \frac{NA}{NA + NB + NC}$$

with NA denoting the total number of correct forecasting points, NB the total number of false alarm points, and NC the total number of forecast miss points.

Figure 2 shows the TS score of 24h accumulated total precipitation forecast for sprinkle and moderate rain over central and southern China during the period from 25 January until 1 February 2008 with the forecast time from 24-216h, including the CMA, JMA, NCEP, ECMWF, multimodel ensemble mean and bias-removed ensemble mean with running training period. Comparing forecasts of the sprinkle (0.1-10mm/24h) rain of the individual models, the forecast skills of the JMA model are the best among four models except for the 24h forecasts. With increasing precipitation ranks, the TS scores of the individual models decrease considerably. For the moderate rain (10-25mm/24h) forecasts over central and southern China, the TS scores of the JMA model contain large fluctuations and the ECMWF forecasts are more stable, while the forecast skills of the CMA model are not satisfactory. In order to obtain better forecast skills, the ensemble forecasts of the JMA, ECMWF and NCEP models were selected to carry on the multimodel consensus forecasts. The TS scores have been improved by using the R-BREM technique for most forecast time except for 72h and 216h forecasts compared with the ECMWF forecasts which have the best performance among four models. For the moderate rain forecasting, the 24h-192h TS scores of the R-BREM technique are higher than those of

the individual models and the EMN technique.

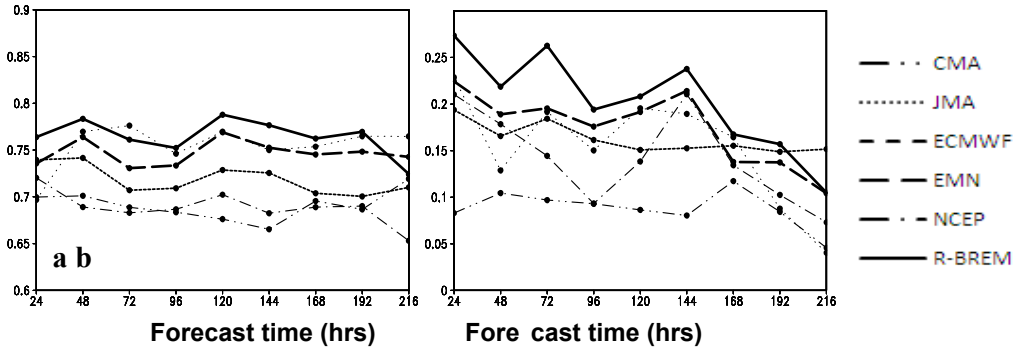

Fig.2 TS scores of the 24h accumulated total precipitation forecast using different individual models, EMN and R-BREM techniques for sprinkle (a) and moderate rain (b) over central and southern China during the period from 25 January to 1 February 2008.

It should be noted that due to the discontinuity of the precipitation distribution, the selection of the training period length plays an important role in the precipitation forecasts by using the R-BREM technique. In this study, the optimal training period length is chosen based on the precipitation characteristics over central and southern China in January 2008. The optimal length of the training period may vary with variables, regions and seasons.

4. Conclusions

The multimodel consensus forecasting experiments have been conducted by using the ensemble forecasts of ECMWF, JMA, NCEP and CMA taken from the TIGGE archives. For the sprinkle forecasts over central and southern China, the R-BREM technique has the best performance in terms of TS scores for the 24-192h forecasts except for the 72 forecasts among all individual models and multimodel consensus techniques. For the moderate rain, the forecast skill of the R-BREM technique is superior to those of individual models and multimodel ensemble mean.

It should be noted that the selection of the training period length is very important for the forecasting of both the surface temperature and the precipitation by using the R-BREM technique. The optimal length of the training period may vary with variable, region and season.

Acknowledgements

This work is supported by the Special Scientific Research Fund of Meteorological Public Welfare Profession of China under Grant No. GYHY200906007.

References

Gilbert, G. F., 1884: Finley's tornado predictions, Amer. Meteorol. J., 1, 166–172.

Hosking, J. R., 1990: L-moments: Analysis and estimation of distributions using linear combinations of order statistics. J. R. Statist. Soc., B52: 105-124.

Krishnamurti, T. N., Kishtawal C. M. et al., 1999: Improved weather and seasonal climate

forecasts from multimodel superensemble. Science, **285**, 1548-1550.
Krishnamurti, T. N., Kishtawal C. M. et al., 2000a: Improving tropical precipitation forecasts from a multi analysis superensemble. J. Climate, **13**, 4217-4227.
Krishnamurti, T. N., Kishtawal C. M. et al., 2000b: Multimodel superensemble forecasts for weather and seasonal climate. J. Climate, **13**, 4196-4216.
Krishnamurti, T. N., Surendran S. et al. 2001: Real time multianalysis/multimodel superensemble forecasts of precipitation using TRMM and SSM/I products. Mon. Wea. Rev., **129**, 2861-1883.
Lin C. Z., Zhi X. F. et al. 2009: Multi- model superensemble forecasts of the surface temperature using the TIGGE data. Journal of Applied Meteorological Science, 20 (6): 706-712.
Messinger F., 2008: Bias Adjusted Precipitation Threat Scores, Adv. Geosci., 16, 137–142,
Schaefer, J. T., 1990: The critical success index as an indicator of warning skill, Wea. Forecasting, 5, 570–575.
Wen M., Yang S., et al., 2009 : An analysis of the large-scale climate anomalies associated with the snowstorms affecting China in January 2008. Mon. Wea. Rev., 137: 1111-1131.
Yun, W.-T., Krishnamurti T.N., 2003: Improvement of the superensemble technique for seasonal forecasts, *J. Climate*, **16**, 3834-3840.
Zhang L, Zhi X. F., 2009: The features and possible causes of the extreme event with freezing rainand snow over the southern China in early 2008. Abstracts, Climate change and tropical climatic hazards in Asia Oceania : 6th Annual Meeting of Asia Oceania Geosciences Society. Singapore: AOGS, 2009.
Zhang Z. Y., Gong D.Y. et al., 2009: Anomalous winter temperature and precipitation events in southern part of China. Journal of Geographical Sciences, 19:471-488.
Zhi X. F., Lin C. Z. et al. 2009a: Superensemble forecasts of the surface temperature in Northern Hemisphere middle latitudes. Scientia Meteorologica Sinica., 29 (5): 569-574. (in Chinese)
Zhi X. F., Lin C. Z. et al. 2009b: Multimodel superensemble forecasts of surface temperature using TIGGE datasets. Abstracts, Predictability of weather and climate: 6th Annual Meeting of Asia Oceania Geosciences Society. Singapore: AOGS, 2009.
Zhang L, Zhi X. F., and Pan J. L., 2010: An analysis of the winter extreme precipitation events on the background of climate warming in southern China. J. Trop. Meteor.(in Press).
Zhou W, Chan J. Extreme low temperature and icy weather in south China in January 2008. Abstracts, Climate change and tropical climatic hazards in Asia Oceania :6th Annual Meeting of Asia Oceania Geosciences Society. Singapore: AOGS, 2009.

The Development of Ensemble Prediction System in WHIHR

LI Jun , WANG Minghuan ,Lin Chunze
Wuhan Institute of Heavy Rain/CMA, Wuhan 430074
lijun@whihr.com.cn

A Short-Range Ensemble Forecast system is under development by perturbing initial conditions and lateral boundary conditions based on a regional model, AREM (Advanced Regional Eta Model), which has 11 members in 37km horizontal resolution over China. Two strategies in perturbing IC were compared to examine an optimal approach in building a regional ensemble prediction system (EPS): one is directly applying perturbations from a global EPS to the regional EPS(a downscaling of a global EPS,Sch-1), and another is generating own perturbations by the regional model itself(BGM,Sch-2). The following four results can be seen.(1) By evaluating ensemble spread and probabilistic forecasts, it shows that the "Sch-2" seems to be superior to the "Sch-1" in this preliminary study (Fig.1).(2) No matter what IC perturbation strategies were applied,ensemble-based forecasts, ensemble mean and probabilistic forecasts, are in general outperform single control and operational forecast. (3) The ensemble spread and forecast skill are positively correlated quite well on domain average,the spatial correlation between spread and forecast error is about 40-45% on average.

The system was running daily and evaluated during flood season in 2009, The results show that ensemble forecasts are in general outperform single deterministic forecasts with additional forecast information, the ensemble means of precipitations of low thresholds are more skillful than the ensemble means of precipitations of high thresholds(Fig.2) . It show that probabilistic forecast seems to be more usefull for the higher forecast skill than ensemble mean and control forecast(Fig.3).Furthermore, the decision-making forecast will be more,scientific by a comprehensive analysis of various ensemble products comprehensively.

In overall, ensemble spread is underdispersive comparing to the forecast error. At least the partial reason for the underdispersion is due to the lack of consideration in model physics uncertainty, which is a subject to be explored during the next phase of this EPS development.

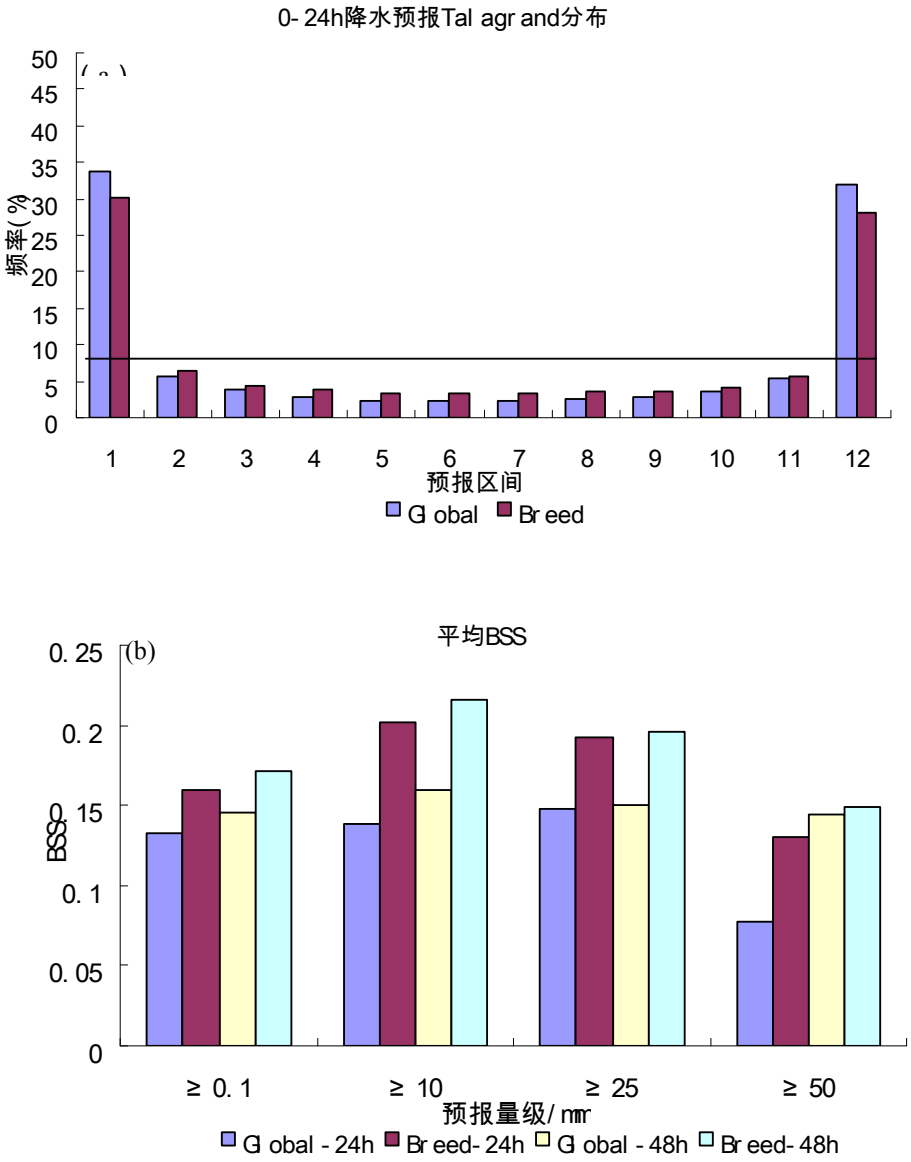

Fig.1 The Talagrand distribution histogram of precipitation forecasting for 0-24h and the average value of BSS

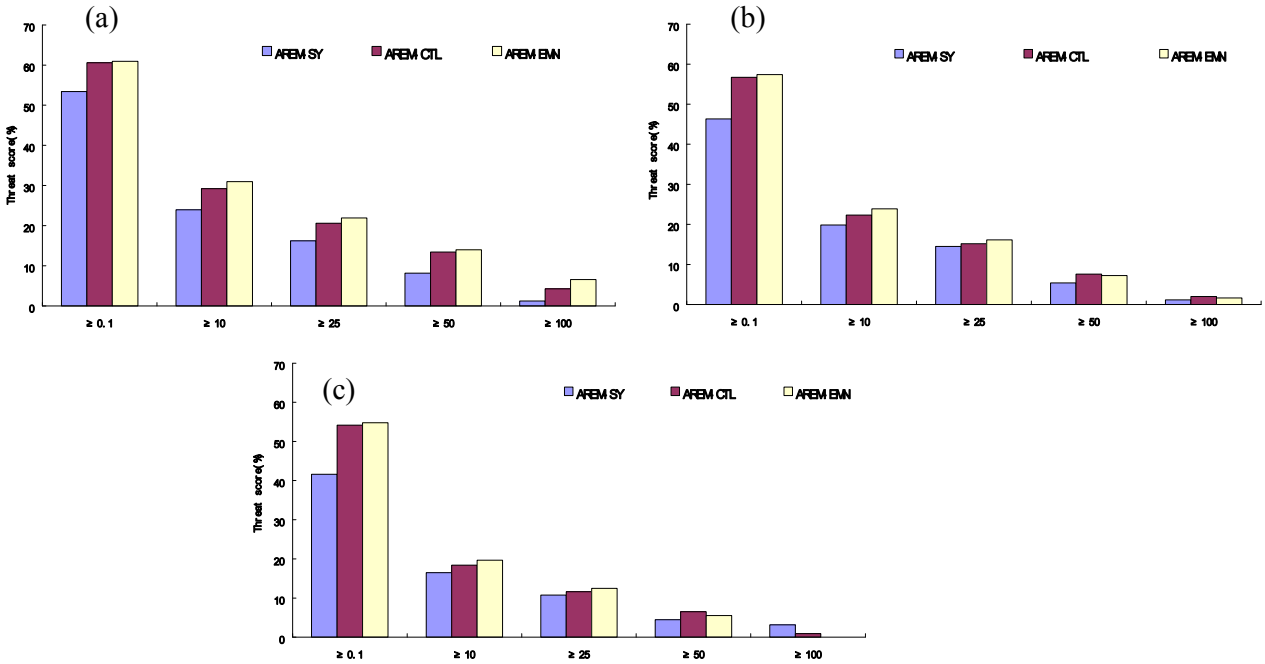

Fig.2 The threat score of different precipitation forecasting (a)for 0-24h,(b)for 24-48h and (c)for 48-72h

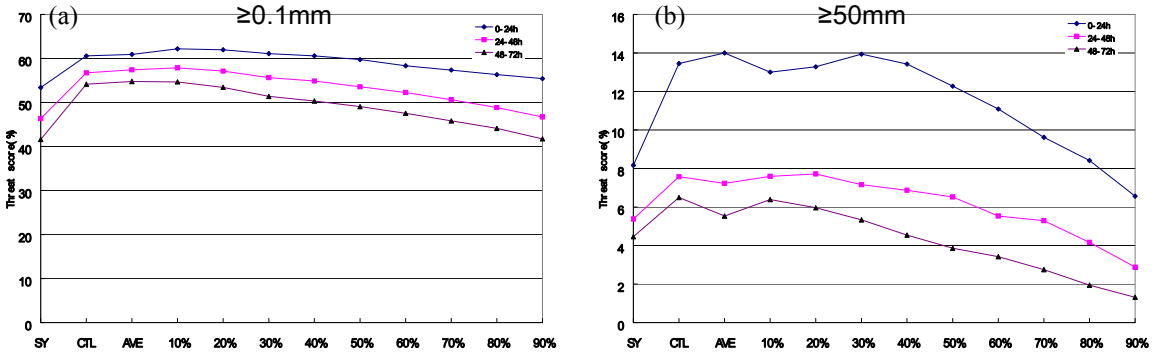

Fig.3 The threat score of SY,CTL and different probabilistic forecasts thresholds (a)for ≥0.1mm,(b)for ≥50mm(the score of defferent forecast lead time was represented by different line type)

Poster Presentations

Coupling Ensemble weather predictions with Xinanjiang model for flood forecast

Hongjun BAO[1] Linna ZHAO[1] Yi HE[2] Pappenberger Florian[3]

1. *National Meteorological Center, China Meteorological Administration, P. R. China*
2. *Department of Geography, King's College London, Strand, London, WC2R 2LS, UK*
3. *European Centre for Medium-Range Weather Forecasts (ECMWF), Shinfield Park, Reading, RG2 9AX, UK*

baohongjun@cma.gov.cn

1. Introduction

The incorporation of numerical weather prediction (NWP) into a flood forecasting model can increase forecast lead times from a few hours to a few days. Single deterministic weather forecast from NWP can't take uncertainties and systematic biases into consideration and hence often fail to replicate weather variables correctly. Ensemble Prediction Systems (EPS) have evolved over the last decade to simulate the effect on weather forecasts of observation uncertainties, model uncertainties (e.g. due to a lack of resolution, simplified parameterization of physical processes and effect of unresolved processes), imperfect boundary conditions and data assimilation assumptions (Park et al., 2007). An EPS is interpreted by Buizza as a system based on a finite number of deterministic integrations and regarded as, so far, the only feasible method in meteorology to predict probability density function beyond the range of linear error growth. EPS forecasts from a single weather centre only account for part of the uncertainties originating from initial conditions and stochastic physics (Roulin, 2006). Other sources of uncertainties, including numerical implementations and/or data assimilation, can only be assessed if a grand ensemble (GE) of EPS from different weather centres are combined (Goswami et al., 2007). When various models that produce EPS from different weather centres are aggregated, the probabilistic nature of the ensemble precipitation forecasts is better retained and accounted for (He et al., 2009, 2010; Bao,2009). An ensemble of weather forecasts can be used on catchment hydrology and provide improved early flood warning as some of the uncertainties can be quantified (Cloke and Pappenberger, 2008).

To this end, a case study was carried out using five TIGGE forecast centres: The Xinanjiang model (Zhao, 1992) was used to simulate the discharge. The study area is the Xixian catchment, located upstream of the Huaihe River. The aims of this paper are to (1) develop atmospheric-hydrologic flood forecasting model cascade driven by TIGGE ensemble forecasts, and (2) apply the model cascade to the Xixian catchment and compare the simulation results driven by TIGGE forecasts and raingauge observation.

2. The data and the test catchment

The Huaihe River is located between latitudes 31°N and 35°N and longitudes 112ºE and 121ºE. It originates in the Tongbai Mountains of Henan Province, and flows over four provinces in east-central China. The length of the main channel of the Huaihe River is 1000 km and the

total catchment area is 1.912×10^5 km^2. Its mean annual precipitation and runoff depth is approximately 888 and 240 mm respectively. The runoff coefficient ranges from 0.1 (northeast) to 0.6 (southwest). The Xixian catchment, located between latitudes 31.5°N and 33.0°N and longitudes 113.0ºE and 115.0ºE in the upstream of the Huaihe River, has a drainage area of 8826 km^2 and is situated in the south of Henan province, China. The catchment average annual precipitation is 1145 mm, 50% of which is within the period of the flood season (June-September). Ten rainfall stations and one hydrological station are available in the Xixian catchment.

Observed hydro-meteorological data were obtained from China Meteorological Administration (CMA). When the study was conducted, EPS data was available from five centres in the TIGGE database with the majority delivering EPS from January 2007 onwards. The flood event took place in July 2007 was selected as the flood event in the test case. Table.1 lists the five weather centres and their numbers of ensemble forecasts.

Table 1. List of the meteorological forecast centres used in the case study

Country/Region	Weather centre	Centre Abbriviation	Centre Code	Ensemble menbers
Canada	Canadian Meteorological Centre	CMC	BABJ	14+1
China	China Meteorological administrator	CMA	CWAO	14+1
Europe	European Centre for Medium-Range Weather Forecasts	ECWMF	ECMF	50+1
UK	UK Met Office	UKMO	EGRR	23+1
USA	National Centres for Environmental Prediction	NCEP	KWBC	14+1

3．Application and result analysis

The majority of the weather centres delivered global EPS data from January 2007 onwards. This study focused on one flood event that took place in July 2007. The flood warning level at the Xixian station is 41.50 m and corresponds to a discharge of 4034 m^3/s. The warning level was reached at 0000 (UTC) on 15 July 2007 for the studied flood event and exceeded in the subsequent one day.

3.1 Precipitation input evalution

The precipitation forecasts Pf were retrieved from five weather centres in the TIGGE archive, namely Canadian Meteorological Centre (CMC), China Meteorological Administration (CMA), European Centre for Medium-Range Weather Forecasts (ECMWF), UK Met Office (UKMO), and National Centres of Environmental Prediction (NCEP). The forecasts of 11 July 2007 from NCEP were excluded from this study due to an error that occurred during data extraction. For the selected five centres, each provides one ‘central’ unperturbed analysis and a number of forecasts with perturbed initial conditions. All forecast members were assigned equal weights (Park et al., 2007). The consequent inference is based on the principle of equal probability of selection. The original medium-range forecasts are corrected in ca. 25×25 km resolution (He et al, 2009; 2010). They were interpolated to areal averages of ten

sub-catchments to be used as inputs for the Xinanjiang model. Buizza pointed out that consistency between forecasts issued on consecutive days is a desirable property of a forecasting system, therefore we examined the feature by visually comparing $\boldsymbol{P_f}$ of small, moderate and heavy precipitation with thresholds of 0.0~9.9mm, 10~24.9mm, over 25mm respectively. These thresholds are defined by the National Meteorological Centre of CMA. In this paper, the threat scores (TS) method (Guan et al, 2006; Zhao et al, 2010) was employed to evaluate the performance of the five weather centres and their grand ensemble. TS ranges from 0 to 1, with 0 indicating no skill and 1 perfect.

TS shows that the five EPSs and grand ensemble have diferent peformance for -small precipitation. Scores of CMA, ECMWF and NCEP, ranged from 0.46 to 0.67 with TS and from 0.92 to 1.49 with bias score (B) with lead time ranging from 24hours to 240 hours, is slightly better than that of CMC and EGRR. In the range of moderate precipitation, EGRR performs better than other 4 centres. Five EPSs all have the TS value below 0.30, which indicated that these events were rarely captured. Grand ensemble has a slightly better TS value than CMA and CMC.

3.2 Discharge simulation

All ECMWF forecast members issued on 12 July 2007 displayed the best agreement for the rainfall event occurred on 13 July 2007. Similarly, the amount and timing of the rainfall between 13 July 2007 and 15 July 2007 were best forecasted with 2-day lead time, i.e. from 14 July 2007 to 16 July 2007. For lead times longer than two day, the 51 ECMWF forecast members demonstrated a fairly consistent signal representing an intensive rainfall event but one could not tell the exact date and time it was to occur as the spread of forecast members was rather large. For example, forecasts issued on 10 July 2007 indicated a large precipitation event would possibly occur on 15 July 2007. Less than 10% of the forecast members predicted it was to occur on 15 July 2007. The situation improved on 13 July 2007 when most forecast members clustered closer to each other than on the previous day of issue (over 70% members agreeing on 15 July 2007). Disagreements between probabilistic and single forecasts can be used as an indication of potentially low predictability and vice versa. The progress of agreement amongst forecast members evolved from longer to shorter lead times demonstrates the EPS forecasts become more predictable as it is getting closer to the actual event. In comparison to the observed discharge, the ensemble of $\boldsymbol{Q_f}$ was underestimated by approximately 10-30% for all forecast members varying from day to day. In this study, $\boldsymbol{Q_{50}}$ is very comparable with the $\boldsymbol{Q_{sim\text{-}raingauge}}$.

The ensemble of $\boldsymbol{Q_f}$ was evaluated using a warning table, where observations were compared with simulations. The warning table shows the forecasts ability to predict the individual events. The studied flood event is well predicted by all centres with a lead time of 10 days (see Fig.1 for warning level). However, making use of multiple centres from the TIGGE archive did not always show a better performance than using a single EPS centre. This indicates grand ensemble does not necessarily lead to a better performance than a single EPS. Techniques for combining multiple centres should be investigated in the future.

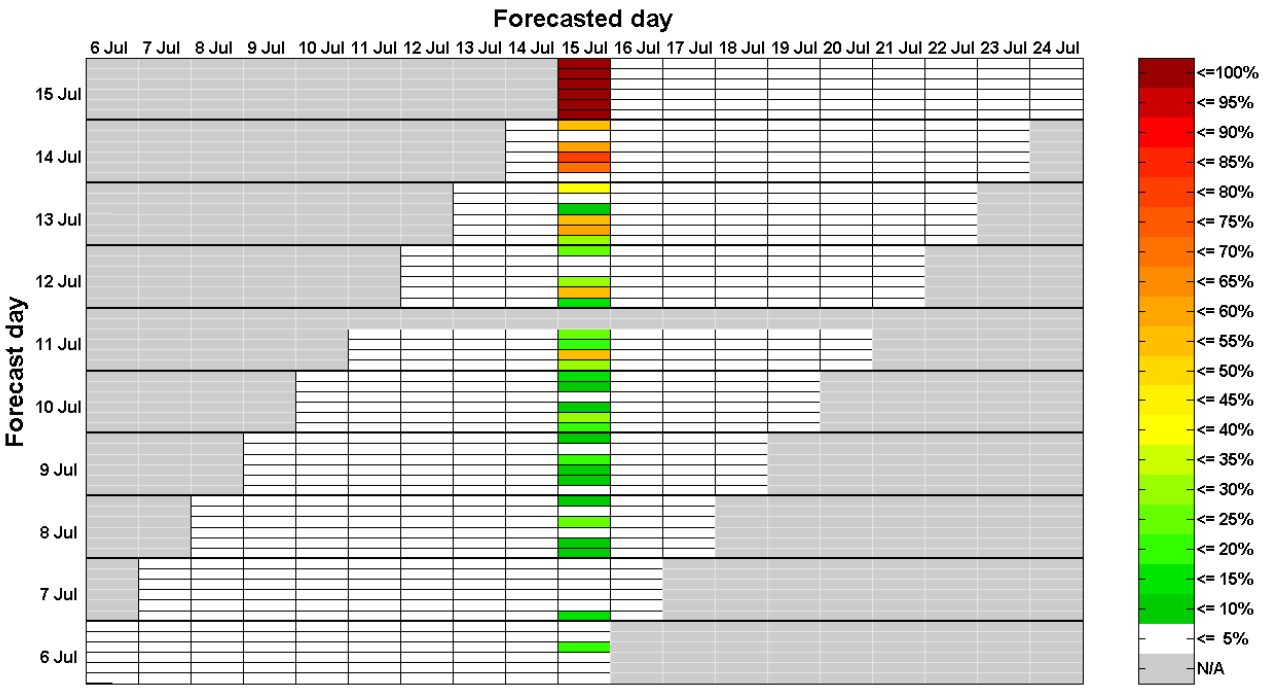

Figure 1 The warning table for the studied flood event. The six horizontal bars from bottom to top represent the five centres (CMC, CMA, ECWMF, UKMO, NCEP), and the ensemble of the five forecast centres.

4． Conclusion and outlook

A coupled atmospheric-hydrologic flood forecast model driven by the TIGGE ensemble forecasts is set up to study the potential benefits of using the TIGGE database in flood forecasting in the upper reaches of Xixian catchment during the 2007 flood seasons. Xinanjiang model is applied for forecasting rainfall-runoff process. The results demonstrate that the TIGGE archive is a promising tool for issuing a fairly reliable warning as early as 10 days in advance with producing forecasts of discharge comparable with the observed discharge. Lead times can be potentially improved, which holds great benefit for flood management and preparedness.

The techniques for how to deal with multi-model weather predictions is necessarily to focused on. In this study, the principle of equal probability of selection was applied. Multiple EPS inputs should be used with great caution as they have different error structures and cannot be easily combined (Cloke and Pappenberger, 2009; He et al,2010). Different weather forecasts may be assigned a different weight coefficient, which might improve the performance of the grand ensemble.

A spatial and temporal correction to the ensemble weather predictions to resolve discrepancies in the spatial distribution and timing should be developed for flood forecast. The precision of rainfall forecast affects an offset of the peak in term of timing and magnitude that led to the partial failure in early flood warning in hydrological forecasting.

Acknowledgements

This work was supported by the Research Fund for Commonweal Trades (Meteorology) (Grant numbers: GYHY200906007 and GYHY201006037), and the Innovation China UK (ICUK) programme (Grant number KCL24).

References:

Bao, H. J. *Coupling EPS-Hydrologic-Hydraulic Model for Flood Forecasting*. Ph. D. Dissertation. Nanjing: Hohai University. (In Chinese), 2009.

Cloke H. L., Pappenberger F. Evaluating forecasts for extreme events for hydrological applications: an approach for screening unfamiliar performance measures. *Meteorological Applications*, **15**(1): 181-197. 2008.

Cloke H. L., Pappenberger F. Ensemble flood forecasting: A review. Journal of hydrology,375:613-626. 2009.

Guan C G, Wang K M, Chen X H. Analyses and Verfications of T213 Rainfall Forecast from 2002 to 2005. *Meteor*.Mon.32(8):70-76,2006. (in Chinese)

He Y, F Wetterhall, H.L. Cloke, F Pappenberger, M Wilson, J Freer, and G McGregor. Tracking the uncertainty in flood alerts driven by grand ensemble weather predictions, Meteorological Applications, Special Issue: Flood Forecasting and Warning, 16(1): 91 - 101. 2009.

He Y, F Wetterhall, Bao H J,H L Cloke, Li Z J,F Pappenberger, Hu Y Z, D Manful and Huang Y C. Ensemble forecasting using TIGGE for the July-September 2008 floods in the Upper Huai catchment: a case study, Atmosphereric Science Letters.DOI:10.1002/asl.270. 2010.

Park YY, Buizza R, Leutbecher M. TIGGE: preliminary results on comparing and combining ensembles. ECMWF TM 548, European Centre for Medium-Range Weather Forecasts (ECWMF), Reading, UK. 2007.

Roulin E. Skill and relative economic value of medium-range hydro-logical ensemble predictions. *Hydrology and Earth System Sciences Discussions* **3**: 1369–1406. 2006.

ZHAO L.N., et al.2010: Assessment of Probabilistic Precipitaiton Forecasts for HUAIhe Catchment Using TIGGE Data ,*Meteor*.Mon.,36(7):133-142. (in chinese)

Zhao, R. J. The Xin'anjiang model applied in China. *Journal of Hydrology*, 135(1-4), 371-381. [doi: 10.1016/0022-1694(92)90096-E] . 1992.

Convection over the Taunus Mountains: Distribution, Tracks and Life Cycle

Christoph Brendel and Bodo Ahrens
Institute for Atmospheric and Environmental Sciences, University of Frankfurt
christoph.brendel@iau.uni-frankfurt.de

1. Introduction

Deep convection belongs to one of the most intensive atmospheric processes on earth. Deep convection is often associated with heavy rainfalls, wind gusts, hail and lightning. In some cases, strongly depending on favourable meteorological key parameters, the development of tornados is possible (DOSWELL 2001). These natural hazards can result in high damages, insurance costs and sometimes loss of human lives. Convective processes occur on the local- and mesoscale, and are highly variable in space and time in their occurrence and intensity. For this reason forecasting of convection in detail is difficult. Especially the areas of formation, the tracks of single convective cells and their behaviour are not predictable. Rain gauge networks are also not able to detect convective precipitation in its totality and therefore a high-resolution long-term climatology of deep convection does not exist. Regarding these problems there was a motivation to find out how convective cells occur and trace over complex terrain, e.g. low mountain ranges. There are some examinations about the influence of mountainous areas on convection done in the USA. On the one hand the aim was to identify regions, which initiate convection depending on different stream directions (BANTA and SCHAAF 1987) and on the other hand the suggestion was to investigate the influence of the Colorado Rocky Mountain Range on the diurnal cycle of convective precipitation for two summer seasons (KARR and WOOTEN 1976).

2. Area of Investigation

The area of investigation is located in the German low mountain ranges with focus on the Taunus Mountains (Fig. 1). The Taunus Mountains consist of three parts: a main ridge (a) that is orientated from southwest to northeast; a northern part with some side ridges orientated from southeast to northwest, separated by a large valley/basin (b) into a western (c) and an eastern part (d); and a southern narrow zone (e) dropping off steeply to the Rhein-Main-Basin.

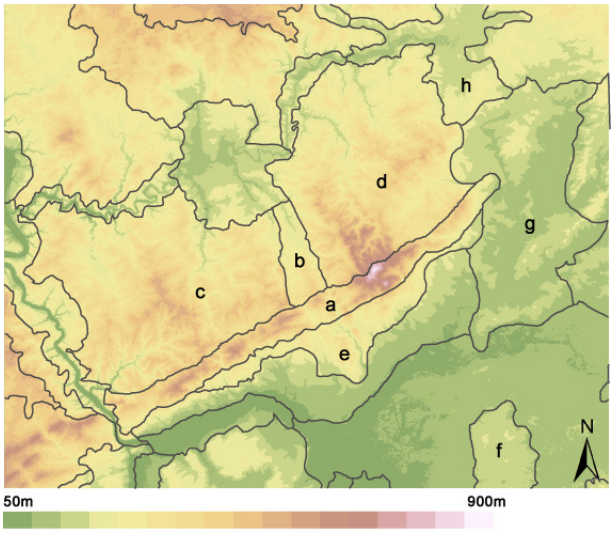

Figure 1: Area of investigation, digital elevation model (shaded), area borders of unspoiled nature (grey lines), dimension of the whole area (80km north-south and 100km west-east)

3. Data

For the investigation the weather radar data for the time period March 2000 – December 2007, provided by the German Weather Service (DWD), were taken into account. The advantage of this radar product is the high temporal (5 min) and spatial (1 km) resolution. Disadvantages are some shadowing effects caused by the highest mountain peaks due to the precipitation scan of the radar, which allows only the scan of the lowest layer. For further investigations, the output of convective cells and tracks has been subdivided into different stream directions, based on the objective weather classification of the DWD.

4. Method

Based on an existing tracking algorithm (STEINACKER et al. 2001) a simple algorithm was created to filter radar images, to identify convective cell cores, and to determine the tracks for every single cell core.

A 2-dimensional Gauss filter was used to smooth the radar images with a standard deviation σ of 0.85. The filter matrix consists of 7 x 7 grid points. The necessity of the filter is explained by remaining clutter and the precipitation structure in general, which can have weak secondary cell cores. After filtering they merge with primary cell cores and this make the identification of convective cell cores more clearly for the automatic algorithm.

To identify convective cell cores, two basic conditions have been defined to distinguish between convective and stratiform precipitation. On the one hand an intensity threshold for convective cell cores has to be considered, which was set to 8.12 mm/h. On the other hand the spatial variability of convective precipitation has to be considered. To check these conditions a 7 x 7 grid point matrix was again taken into account. The algorithm checks the differences in precipitation from the central grid point to the surroundings. Potential cell cores must have a larger precipitation intensity than its direct surrounding grid cells, and grid cells in larger distance to the central grid point of the matrix must have a certain precipitation difference to them.

For tracing convective cell cores from one time step to the next time step, additional data were needed. Thus, six hourly means of NCEP/NCAR reanalysis data for u- and v- wind vectors have been used (HARRIS 2008). To recover a cell core in the next time step from a radar image, a displacement vector, based on the reanalysis wind data, will indicate the expected position of the cell core. From the end of this displacement vector a searching area is defined to look for cell cores. In the case the algorithm finds a cell core within this area an identical ID number is assigned, otherwise the cell core is dissolved or a cell core beyond the area is assigned with a new ID number. A shortcoming of the algorithm is that merging and splitting of convective cells cannot be considered and the assumption that convective cell cores always shift with the mean stream direction of the troposphere.

5. Results

The whole dataset consists of 89671 cell cores, which mostly occur under southwesterly flow direction (59.6%). The second most frequently-occuring weather type for convective cells is the northwesterly flow (18.1%), followed by the undefined flow direction (17.3%) and the southeast (3.9%) and northeast (1.1%) flows. To get an overview of the large dataset of convective cells and their tracks, a line density per km^2 was calculated within a radius of 1.5km. Figure 2 shows the most interesting stream directions for the whole period of investigation. First of all the results show different regions for the highest densities of convection, highly depending on the stream direction. Southwesterly flows show a very high density of convective tracks caused by the eastern side ridge of the Taunus Mountains (c), which moves to the Wetterau Basin (g) and Lahn Valley (h) east of the Taunus Mountains (Fig. 2). The western part of the Taunus Mountains (d) shows significantly lower densities. Northwesterly flows show a significant high density of convective tracks at the Odenwald Foothills (f)

in the southeast of the investigated area (Fig. 2). Much less densities are located across the whole Taunus Mountains, but with a slightly higher density north of the Main Taunus Ridge (b,c,d). The comparison between summer and winter shows a more homogenous distribution of convection during the summer period than for winter times (not shown).

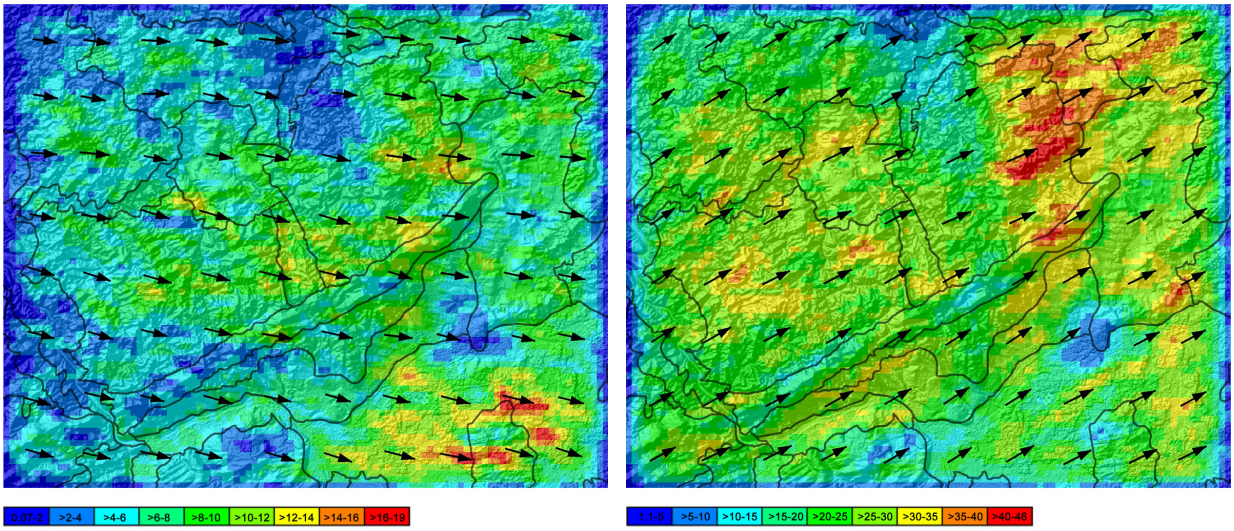

Figure 2: Density of convective tracks (shaded) for northwesterly flow (left) and southwesterly flow (right), mean track direction of convective cell cores (arrows), area borders of unspoiled nature (grey lines)

6. Conclusion

The distribution of convection is highly heterogeneous over the area of investigation. The number of convective cell cores does not much correlate with elevation but some specific elevated areas have a large influence on convection. Considering the shadowing effect at the highest mountains, it is still a little bit surprising that there seems to be only a small influence by the Main Taunus Ridge to the occurrence and initiation of convection. Especially southwesterly flows show an enhanced initiation of convection due to mountain ridge perpendicular to the flow, and additionally, a further development of the cells downwind the mountains.

Acknowledgments

The PF-Radar data were obtained from Elmar Weigl, DWD

References

BANTA, R. M. and SCHAAF, C. B. (1987): Thunderstorm Genesis Zones in the Colorado Rocky Mountains as Determined by Traceback of Geosynchronous Satellite Images. Monthly Weather Review 115 (2). 463-467.

DOSWELL, C. A. III (ed.) (2001): Severe Convective Storms. Meteorological Monographs 50. American Meteorological Society. Boston. 570.

HARRIS, I. (2008): NCEP/NCAR Reanalysis: http://www.cru.uea.ac.uk/cru/data/ncep/ (03/01/2009)

KARR, T. W. and WOOTEN, R. L. (1976): Summer Radar Echos Distribution Around Limon, Colorado. Monthly Weather Review 104 (6). 728-734.

STEINACKER R., DORNINGER, M., WÖLFELMAIER, F. and KRENNERT, T. (2000): Automatic Tracking of Convective Cells and Cell Complexes from Lightning and Radar Data. Meteorology and Atmospheric Physics 72 (2-4). 101-110.

Flash flood forecasting by coupling radar-based precipitation and distributed hydrological model

YANGBO CHEN[1], Haolan Zhou[1], Qiwei Ren[1]
[1]The Sun Yat-sen University, Center on Natural Harzards Research,

eescyb@mail.sysu.edu.cn

1. Introduction

Flooding is one of the most serious natural disasters in China, and has caused huge losses year by year. The devastating floods was not only observed in large river basins, but also in the newly developed urban area, particularly in the south and southeast coastal area where the fastest economic development has been observed in the past decades, and also frequently heavy rain caused by tropical storms. Flood forecasting has played key role in flood management, particularly for saving lives, so to advance the flood forecasting techniques and improve the flood forecasting accuracy has long been the goal of hydrological communities. This paper presented some research results in coupling physically based distributed hydrological model with radar estimated precipitation, for flash floods both in river basins and coastal urban areas. The method is called by the author as new generation flood forecasting method.

2. CINRAD radar in Guangzhou and precipitation estimation

CINRAD(Chen, et. al., 2009) is China's latest generation weather radar that can detect heavy rain at an interval of 5-6 minutes at 9 elevation angles in the precipitation detection mode with a maximum radius of 460km. It is expected that CINRAD will contribute to the observation of extreme storms and estimate precipitation quantitatively over much of populated China at high temporal and spatial resolution. A preliminary study to Guangzhou CINRAD data quality control and precipitation estimation carried out by Chen, et. al.(2009) showed that it is possible to couple the CINRAD estimated precipitation with the distributed hydrological model for flood forecasting. In this study, the Guangzhou CINRAD is used to estimated the precipitation for both in the Liuxihe River basin and Dongguan City area.

3. Liuxihe Model

Liuxihe Model is a physically based distributed hydrological model(Chen, 2009, Chen, et. al., 2010). The model has several sub-models, including Basin Digitization Model (BDM), Data Preparation Model(DPM), Evaportranspiration Model (EM), Runoff

Production Model (RPM), Runoff Routing Model (RRM) and Parameter Deriving Model(PDM). The BDM divides the studied basin into a number of cells horizontally, which are further divided into 3 layers vertically. All cells are classified as hillslope cells, river cells and reservoir cells according to their flow accumulation; each cell having its own properties and model parameters. The DPM prepares data for every cell including DEM, soil type, land cover type, channel cross-section size, which is used to derive model parameters, and rainfall, which is either estimated from weather radar or interpolated from rain gauges. EM calculates the evaportranspiration occurring in the cells, and RPM determines the runoff produced in every cell. The runoff modelled includes surface runoff, interflow and underground flow. The saturation excess mechanism is employed to determine the surface runoff while the interflow is calculated using Campbell's equation. Cell by cell RRM routes the runoff produced to the basin outlet. The runoff routing is divided into hillslope routing and river routing. The PDM derives model parameters physically based on the cell's properties, categorized as unadjustable and adjustable parameters. Unadjustable parameters, that include flow direction and slope of the hillslope cell, are derived directly from the cell's properties. For the adjustable parameters, the initial values are proposed first based on the cell's properties, and then sensitivity analysis is performed cell by cell to test the model's performance sensitivity. Based on the sensitivity analysis, the parameters are adjusted to improve the model performance with an iterative procedure.

4. River basin flash flood simulation

The proposed new generation flood forecasting method has been studied extensively in Southern and Southeast China for river basin and urban area flood forecasting. The scale of the studied river basins includes small, medium and large-sized catchments, with the drainage area low to 92km ^{2}, and high to 10,000km ^{2}. For most of the cases only gridded precipitation interpolated from rain gauges were used, but in Liuxihe Reservoir Basin, the CINRAD radar estimated precipitation was tested. The Liuxihe Reservoir Basin(Chen, et. al, 2010) is located in a tributary of the upstream of Liuxihe River Basin in southern China. The basin is mountainous with a drainage area of 539 km^2. A dam is built in the outlet of the basin named as Liuxihe Dam. The area is humid, and was affected by floods frequently.

Data of 13 flood events in the past decades were collected. Precipitation from 6 rain gauges was collected for all the 13 events, but radar reflectivity for precipitation estimation from the Guangzhou CINRAD was retrieved only for 3 events. The reservoir inflows for all 13 events are derived from the water balance equation based on the observed reservoir operation records during the events. The precipitation from 6 rain gauges was interpolated to grid cells with the spatial resolution at 100m based on the Thysson Polygon method. Based on the algorithm for precipitation estimation with Guangzhou CINRAD(Chen, et. al., 2009), the radar data was first quality controlled, and then was used to estimate the precipitation, and corrected with rain

gauges. Fig. 1 shows the event accumulated precipitation for flood event no. 2 and no. 5. From Fig. 1, it can be s een that the spati al precipitation distribution over the whole basin is rather uneven.

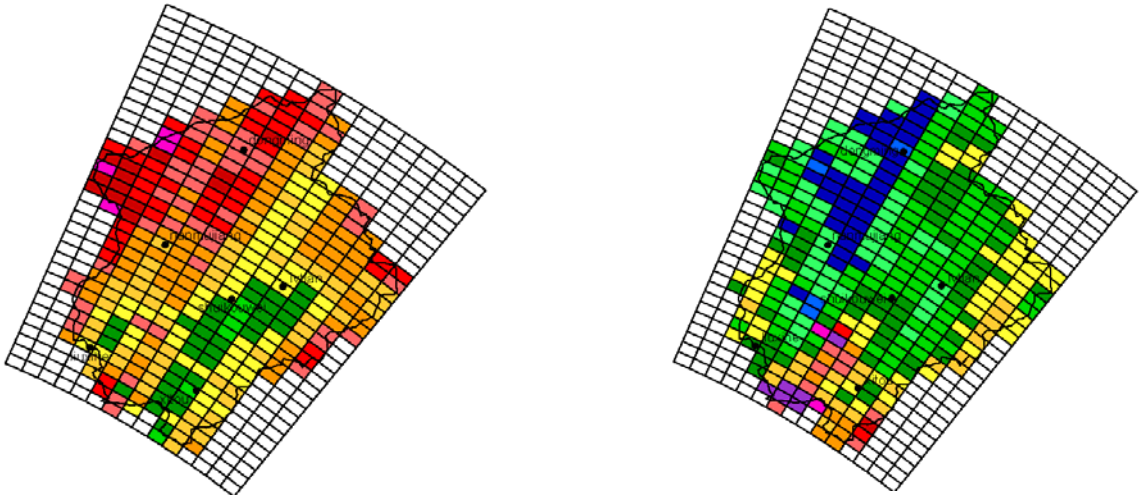

(a) Flood Event No. 2 (b) Flood Event No. 5

Fig. 1 Event-accumulated precipitation estimated from Guangzhou CINRAD

The Liuxihe Model was set up in the studied basin at a spatial resolution of 100m grid cell, the DEM was surveyed locally at the spatial resolution of 100m, while the soil type and land cover type data are downloaded from the public domains. The model parameters are determined based on the observed flood events with rain gauges precipitation. Then floods were simulat ed with both radar and rain gauges estimated precipitation, Fig. 2 is the simulated results.

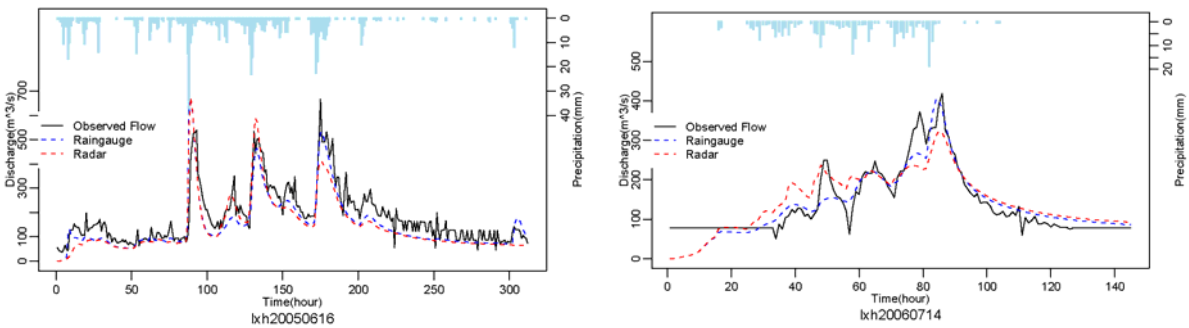

(a)Simulation result of flood event No. 2 (b) Simulation result of flood event No. 5

Fig. 2 Liuxihe Reservoir Basin flood simulation results

From the results of Fi g. 2, it can be seen that the resu lts simulated with rain gauges precipitation and radar estima ted precipitation are com parable, and fit the observed flood processes reasonably good.

5. Urban area flash flood simulation

Dongguan City is the one of the fastest developing city in southern China, which is

located along the south coastal. Dongguan city observed more frequent, much heavier storms in the past decade, and is the becoming the fourth most severe storm rain region in Guangdong Province. Due to the dual implication of high economic development and severer storm, the city experienced serious flooding and losses in the past decade. The new generation flood forecasting method was studied and validated in the downtown area of Dongguan City.

The studied area, with a drainage area of around 200km ^{2}, is a downtown area with high density population and commercial buildings, while the most parts of the rivers are covered with concrete roads. The whole area was first divided into several drainage area based on the DEM and river networks as showed in Fig. 3(a), and then it was further divided into polygon cells as showed in Fig. 3(b), and the pipeline network is delineated with a survey data in recent years.

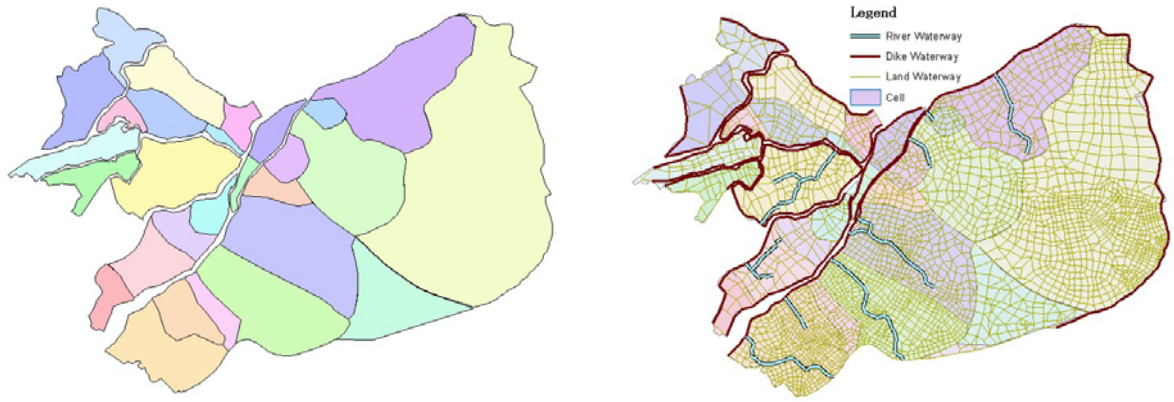

(a)sub drainage area division (b) cell division

Fig. 3 Flood simulation model set up for Dongguan City downtown area

Data for two floods occurred in recent year was collected, one in July of 2006 that was induced by Typhoon Bilisi, another one is induced by Typhoon Fengshen in June of 2008. Precipitation from rain gauges for both storm was collected, and radar data for 2006 storm was also collected. Fig. 4 shows the radar and rain gauges estimated precipitation respectively of 2006 storm.

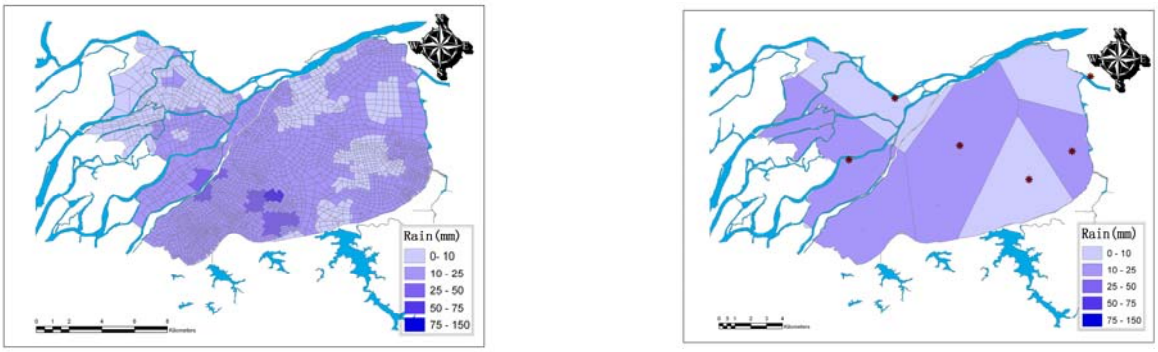

(a)radar estimated precipitation (b) rain gauge estimated precipitation

Fig. 4 Precipitation estimated in Dongguan City downtown area

The floods were simulated with both precipitation estimated from rain gauges and radar, Fig. 5 shows the simulated water depth for 2006 storm. There are some differences between the results with radar and rain gauges estimated precipitation, but in overall, both the simulated results fit the observation reasonably.

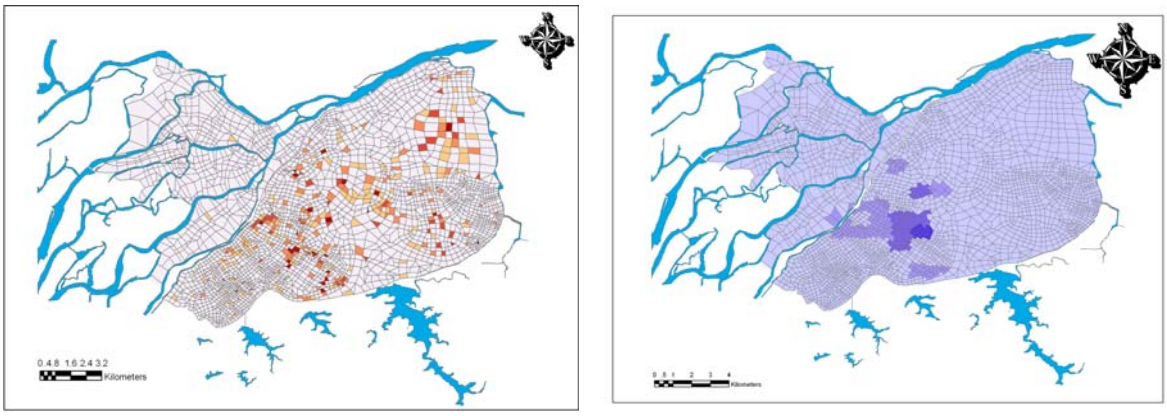

(a)result with radar precipitation (b) result with rain gauges precipitation

Fig. 5 Dongguan City downtown area flood simulation results

Conclusion

The method proposed in this paper is new one, the preliminary research results show that it is promising for flash flood forecasting, but it is still in its early stage towards the real-time operational use. Further efforts are still needed in China to apply this method in China such as high resolution data acquisition, uncertainty studies for flood forecasting, including uncertainties in radar based precipitation estimation, model uncertainties and real-time operational uncertainties, and real-time implementation environment and educational enforcement.

Acknowledgements

This study was supported by the research grant from the department of Sciences and Technology of Guangdong Province(grant no. 2009A030302003), National Sciences Foundation of China(grant no. 50479033) and the Ministry of Water Resources of China(grant no. 2007SHZ1-38).

References

Chen, Y., 2009: Liuxihe Model. *Sciences Press*, Beijing, China.

Chen, Y., Ren, Q., Huang, F., Xu, H. & Cluckie, I. D., 2010: Liuxihe Model and its modelling to river basin flood. *Journal of Hydrologic Engineering*. DOI:10.1061/(ASCE)HE.1943-5584.0000286.

Chen, Y., Zhu X., Han, J. & Cluckie, I. D., 2009: CINRAD data quality control and precipitation estimation. *Water Management*, 162(WM2), 95-105, doi: 10.1680/wama.2009.162.2.95.

Statistical Prediction of China Summer rainfall Using Regression

Xingang Dai[1] Zhi Cheng[2] Ping Wang[3]
RCE-TEA[1], Institute of Atmospheric Physics, Beijing 100029, Lanzhou University[2], Lanzhou 730000, Chinese Academy of Meteorological Sciences[3], Beijing 100081
daixg@tea.ac.cn, chengzhi@tea.ac.cn

This study focuses on inter-seasonal weather prediction for China using statistical methods. The interaction between East Asian monsoon and westerly is one of the key mechanisms that determining major character of summer climate pattern in China. Many studies have found several important physical factors that exert considerable impacts on the summer climate, which are ENSO cycle, the North Atlantic oscillation (NAO) and spring snow cover over Tibetan Plateau. A linear regression equation consisting of the factors is suggested to make summer rainfall prediction. The ENSO cycle is described by two spring SSTA trends referring developing and decaying phases of an El Nino event, respectively, corresponding to quite different climate pattern in East China. Severe floods often appear in southern China in second phase, and a dry climate usually appears in the north of China in the first phase. An inverse pattern of the summer rainfall against El Nino is the characteristics of La Nina event. On the other hand, anomalous westerly in mid-latitudes is in connection with NAO phase which influences the quasi-stationary waves on the zonal flow and blocking location and frequency being correlated to the summer rainfall pattern Besides, previous spring snow cover over the plateau could influence the coming summer rainfall. Statistics revealed that the more the snow cover, the more the rainfall along Changjiang River valley, and vice versa. There are two approaches in predicting the rainfall pattern. The first is to predict the East Asian Monsoon index, by which the predicted rainfall field is made basing on regression method. The second is directly to predict regional rainfall by the regression equation. And the regional predictions are then distributed to every weather station according to recent statistics between the station and regional rainfalls. The station or regional prediction is then employed to estimate extreme weather event according to 'Extreme Value Theory" (GEV) in our case study. Finally, statistical conditions are discussed for the predictors and expected prediction.

Comparison of calibration techniques for a limited-area ensemble precipitation forecast using reforecasts

Tommaso Diomede, Chiara Marsigli, Andrea Montani, and Tiziana Paccagnella
ARPA-SIMC, HydroMeteorological and Climate Service of the Emilia-Romagna Regional Agency for Environmental Protection, Bologna, Italy, tdiomede@arpa.emr.it

1. Introduction

The calibration of the precipitation forecasted at high resolution is currently a challenge for the ensemble community working with Limited Area Models, especially with respect to the improvement of the forecast skill for rare events. The potential of using reforecasts to achieve this goal has been shown in recent studies (Hamill et al., 2008; Fundel et al., 2010). In the present work, thirty years of reforecast of one member of COSMO-LEPS (the Limited-area Ensemble Prediction System based on the non-hydrostatic limited-area model COSMO) were used for testing the calibration strategy. Three calibration techniques were considered: Cumulative Distribution Function, Linear Regression and Analogs. The analog-based method was implemented in terms of the similarity of precipitation field, as well as in terms of the similarity of upper air fields representing the synoptic pattern.
The impact of the application of these techniques to the ensemble precipitation forecasts operationally provided by COSMO-LEPS (10 km of horizontal resolution) in the years 2003-2007 was verified over the Emilia-Romagna Region (Northern Italy), Switzerland and Germany. The calibration of COSMO-LEPS is a part of the project CONSENS (CONSolidation of COSMO ENSemble), developed within the framework of COSMO (COnsortium for Small-scale MOdeling), which aims at consolidating the COSMO ensemble forecasting systems for the mesoscale.

2. Data and methodology

The calibration strategy was based on historical forecast and observed rainfall data available over the areas under investigation. Thirty years of reforecast of one member of COSMO-LEPS were run by MeteoSwiss. One reforecast run with a 90-h lead time was available every three days from 1971 to 2000. This model climatology is used to calibrate forecasts of all lead times, without considering the time dependency of model bias. (Fundel et al., 2010). According to the model climatology, the observed precipitation data were collected over the period 1971-2000 for Emilia-Romagna and Switzerland; rather, the observed data over Germany were available only for the period 1989-2000. The rainfall data were interpolated on the model grid points which cover the areas under investigation using the nearest neighbour method for Emilia-Romagna, the SYMAP method (Frei et al. 2006) for Switzerland and the inverse-squared-distance weighting method based on the nearest three gauges for Germany. The 24-h rainfall amounts span the daily time window 08:00-08:00 UTC for Emilia-Romagna and the daily time window 06:00-06:00 UTC for Switzerland and Germany. The calibration techniques tested in this work provide corrections based on the Cumulative Distribution Function (hereafter, CDF), the Linear Regression (hereafter, LR) and the Analog method. The choice of these methodologies is due to the need of improving the quantitative precipitation forecasts (QPFs) provided by COSMO-LEPS, especially as an input to hydrological models. Thus, techniques which enable a calibration of QPFs and not only of the probabilities of exceeding a

threshold were selected. The described methodologies were used to calibrate each member of COSMO-LEPS. The basic implementations of the CDF and LR methods were developed by generating a seasonal correction function for each model grid point. Each function was defined by using the historical data forecasted and observed over each grid point for that specific season.. This approach generates correction functions that are location (i.e. grid point) specific. For the CDF method, the calibrated 24-h QPF was determined by comparing the reforecast and observed CDF curves. The value of the observed data which had the same probability of occurrence of the current 24-h QPF was used as the corrected QPF value. For the LR method, the parameters of the regression line estimated on the basis of reforecast and raingauge historical data were used to correct the current 24-h QPF value. The analog-based methodology was applied using two implementations, which differ about the meteorological field used for the analog search. In the first implementation, the analog search was performed in terms of the similarity of the forecasted precipitation fields over the area under investigation. In the second implementation, the analog search was performed in terms of the similarity of the forecasted circulation patterns, evaluated in terms of the geopotential at 700 hPa, 12 UTC (hereafter, Z700), over a spatial domain which is significant for the area under investigation to relate the synoptic circulation to the precipitation at ground. In the following of this paper, the first implementation of the analog-based method is referred to as “ANL” and the second implementation as “anlZ”. In both the implementation, for each 24-h lead time, the root-mean-square (rms) differences between each member of the current forecast and each reforecast day were computed, and averaged over the grid points. Then, the historical date with the smallest rms difference was chosen as the date of the analog day, then the gridded raingauge recordings of that past day were used as the calibrated QPF value.
The effect of the calibration process was verified for 24-h QPFs operationally provided by COSMO-LEPS in the years 2003-2007. The probabilistic verification was carried out in terms of the attributes diagram and the Brier Skill Score (BSS). The verification was performed for each grid point with respect to percentiles of the climatological distribution of observed 24-h precipitation as threshold for the verified events.

3. Results

3.1 Comparison of the methodologies over Emilia-Romagna, Switzerland and Germany

The statistical analyses, evaluated for different seasons, thresholds and forecast ranges, reveal an increase of forecast reliability and skill for the calibrated ensembles over Switzerland and Germany, except when the anlZ method is applied. However, the skill improvement resulting from the forecast calibration is small for Germany. No significant improvements of forecast reliability and skill are obtained for the calibrated ensembles over Emilia-Romagna; even, a worsening of the ensemble performance is obtained for the autumn season. Generally, the raw and calibrated ensembles provide overconfident forecasts and the calibrated forecasts show more reliability at lower probabilities. The greatest amount of skill improvement resulting from forecast calibration is obtained over Switzerland. The choice of the best methodology depends on the area under investigation. On the one hand, the ANL method provides the best performance over Switzerland; on the other hand, the CDF and LR methods are to be preferred for Germany. For Emilia-Romagna, the decision about the best

calibration method is not definite, depending on the threshold of the verified event. Generally, forecasts of lower precipitation events are more skilful than forecasts of higher precipitation events. A performance decay with the increase of lead time is evident. Comparing the performance over Emilia-Romagna, Switzerland and Germany, the raw forecasts show more skill in autumn, spring and winter over Emilia-Romagna and Germany than over Switzerland. Rather, the performance for summer is better over Switzerland than over Emilia-Romagna and Germany. The calibrated forecasts has more skill over Switzerland and, with a lesser extent, Germany than over Emilia-Romagna. The Figures 1 and 2 display results only for the autumn and spring seasons, considering the 80-th percentile of the 24-h climatological rainfall amount as verification threshold.

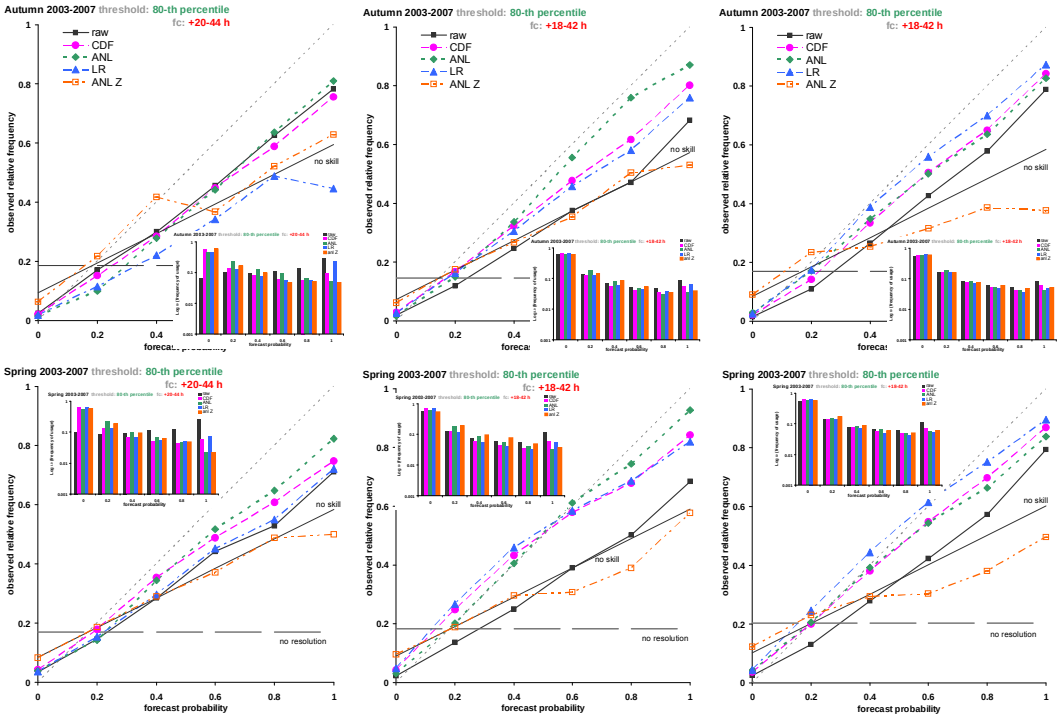

Fig 1. Attributes diagrams for the raw and calibrated ensembles over Emilia-Romagna (left panels), Switzerland (middle panels) and Germany (right panels) in autumn (first row panels) and spring (second row panels) at day 1 lead time, for the 80-th percentile threshold. The solid black line with squares is for the raw ensemble, the dashed fuchsia line with circles is for the ensemble calibrated by CDF, the dotted dark green line with diamonds is for the ensemble calibrated by ANL, the dot-dashed blue line with triangles is for the ensemble calibrated by LR and the double dot-dashed orange line with empty squares is for the ensemble calibrated by anlZ. The inset histograms denote the frequencies of the use of the forecasts for each probability bin.

3.2 Testing weather-specific correction functions over Emilia-Romagna

The lack of a remarkable improvement (especially over Emilia-Romagna) resulting from the application of the proposed calibration methods suggested the need of defining specific correction functions which should be able to link the model error to the meteorological situation. Actually, the poor performance of calibration can be ascribed to the lack of a strong relationship between forecast and observed data, which hampers to highlight a model error which has a systematic dependence on geography, orography and flow direction. To overcome this problem, the use of calibration functions which are weather-regime dependent is proposed. In particular, an easy way of doing this has been tested, building calibration functions which were specific for underestimation and overestimation model conditions.

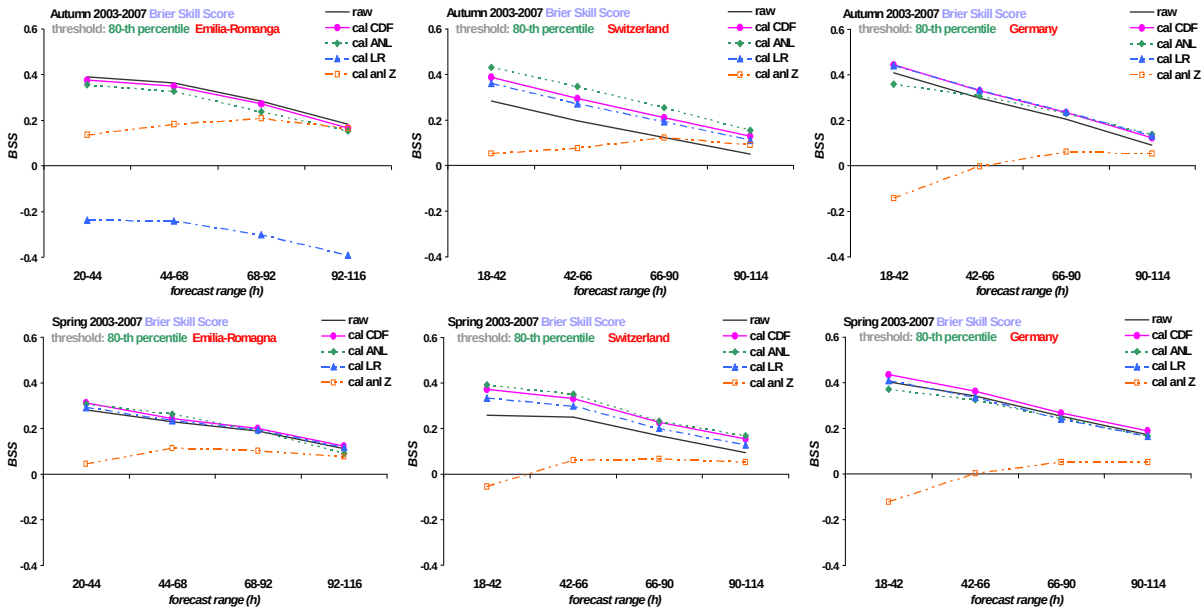

Fig 2. BSS for the raw and calibrated ensembles over Emilia-Romagna (panels on the left), Switzerland (panels in the middle) and Germany (panels on the right) in autumn (first row panels) and spring (second row panels), as a function of the lead time of the forecast. Skill at the 80-th percentile threshold. The solid black line is for the raw ensemble; the solid fuchsia line with circles is for the ensemble calibrated by CDF; the dotted green line with diamonds is for the ensemble calibrated by ANL; the dot-dashed blue line with triangles is for the ensemble calibrated by LR and the double dot-dashed orange line with empty squares is for the ensemble calibrated by anlZ.

The basic idea of this approach was that, for each model grid point and season, the training sample of 24-h rainfall forecast and observation was divided in order to pool data which correspond to, respectively, underestimated and overestimated forecast. Then, a criterion needed for evaluating if the actual forecast corresponds to an underestimation or overestimation model condition. Finally, the corresponding calibration function was applied.

A preliminary test on such a approach was carried out for the Emilia-Romagna case study. The calibration functions used for this test were based on the LR method. Different predictors were tested for the evaluation of the underestimated or overestimated model condition. The selected predictors were: the best analog in terms of rainfall field, Z700, Q700, the combination Z700-Q700, and the mean fields of Z700 and Q700 (specific for each flow regime). For the approach based on analogy, given a certain lead time, the best analog of the actual forecast is searched in terms of the selected predictor. For each model grid point, the forecasted and observed precipitation data of each past analog day were compared to determine if the forecast was overestimated or underestimated. Then, the current forecast is evaluated as an overestimation or underestimation model condition on the basis of what occurred in the selected past analog days. Finally, the specific calibrating function corresponding to the forecasted model condition was used. For the approach based on the mean field of Z700 (or Q700), the current forecast of Z700 (or Q700) was compared, separately, against the mean fields of Z700 (or Q700) corresponding to, respectively, the historical overestimated and underestimated forecasts occurred for a fixed flow regime. Unfortunately, the results are not satisfactory (Fig 3), as the performances of the calibrated ensembles are generally quite worse or similar to the performances of the raw ensemble. Therefore, the selected predictors seem to be not useful within such an approach for evaluating if the meteorological model is currently providing an underestimated or overestimated

24-h rainfall forecast. Nevertheless, the results obtained on the basis of a perfect forecast about the under- or over-estimation model condition are quite encouraging, showing that there is room for the improvement of the forecast by means of such a calibration approach (Fig. 3, lines labelled with “2LR PP” in the graph’s legend).

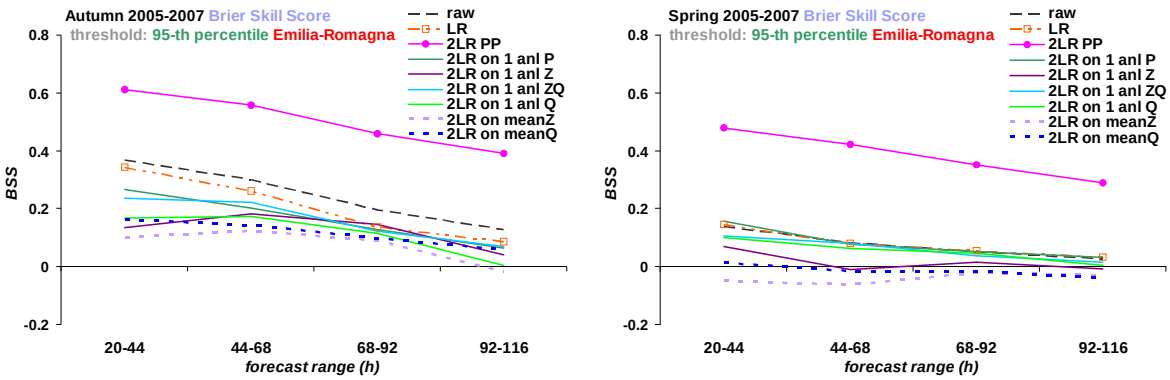

Fig 3. BSS of the raw ensemble and the ensembles calibrated by different weather-regime dependent implementations of the LR method over Emilia-Romagna, as a function of the forecast lead time. Skill at the 95-th percentile threshold. Results refer to the autumn (left panel) and spring (right panel) in the years 2005-2007, as Q700 was available only for such a period in the archive of COSMO-LEPS. The different implementations of the LR method are based on different predictors used for evaluating if the current forecast is providing an underestimated or overestimated 24-h rainfall amount: observations (2LR PP); best analog of rainfall field (2LR on 1 anlP), Z700 (2LR on 1 anlZ), combination Z700-Q700 (2LR on 1 anlZQ), Q700 (2LR on 1 anlQ); similarity of the current Z700 (2LR on meanZ) and Q700 (2LR on meanQ) fields to the corresponding mean field for a specific flow regime.

Conclusions

The statistical analyses revealed a positive impact of the calibration process over Switzerland and Germany; rather, no significant improvements resulted over Emilia-Romagna. The choice of the best calibration method depends on the area under investigation. Results suggested the need of generating correction functions which are weather-regime dependent, as the model error is likely to have a systematic dependence on geography, orography and flow direction. As a future development, a multi-variable approach will be tested for improving this evaluation. This proposed approach should be based on the evaluation of upper air fields at different levels and times by means of a Principal Component Analysis, in order to find a better matching of the space-time evolution of the synoptic pattern.

References

Frei, C., Schöll, R., Fukutome, S., Schmidli, J., Vidale, P. L., 2006: Future change of precipitation extremes in Europe: Intercomparison of scenarios from regional climate models. *J. Geophys. Res.*, **111**, D06105.

Fundel, F., Walser, A., Liniger, M.A., Frei, C., Appenzeller, C., 2010: Calibrated Precipitation Forecasts for a Limited Area Ensemble Forecast System Using Reforecasts. *Mon. Weather Rev.*, **138**, 176-189.

Hamill, T.M., Hagedorn, R., Whitaker, J.S., 2008: Probabilistic forecast calibration using ECMWF and GFS ensemble reforecasts. Part II: Precipitation. *Mon. Wea. Rev.*, **136**, 2620–2632.

Quantitative Precipitation Estimation Using Neural Networks and Multi-sensor Data

SOHYUN CHO[1] and GWANGSEOB KIM[2]

[1]Graduate *student of Department of Civil Engineering, Kyungpook National University and Researcher of Brain Korea 21, Korea (shcho35@knu.ac.kr)*
[2]*Professor of Department of Civil Engineering, Kyungpook National University and Researcher of the Research Center of Flood Defense Technology for Next Generation, Korea (kimgs@knu.ac.kr)*

In recent decades, many studies are getting focused on the climate change throughout the world and the damage from natural disasters has been getting worse. Flood disaster had especially caused the biggest damage on the record in Korea peninsula. Almost of the annual rainfall sum falls intensively in summer season like a typhoon and heavy rain season in Korea. And the quantity of precipitation has increased over recent years while the number of rain days has decreased. Since these variation properties of rainfall in Korea, it is hard to forecast the future weather conditions. But accurate results from precipitation forecasting are essential for protecting many lives from the flood disasters and managing water resources. Therefore we tried to improve quantitative precipitation estimation using neural networks (NN) and multi-sensor data such as satellite images, Automatic Weathering Systems (AWSs) measurements, Numerical Weather Model (NWM) outputs and Sea Surface Temperature (SST). In addition, we chose pixels in the East Asia which have high correlation coefficient between multi-sensor data and Korea precipitation measurements. In the results, we found that precipitation estimation with 3 to 6-hour lead time was highly correlated with observed precipitation data.

ANALYSIS FOR TURBULENCE AND WIND GUST FACTOR IN SURFACE LAYER AFFECTED BY TYPHOON

Huang Shicheng[1] Zhou Jialing[2] Wang Wenlan[2] Zhang Bing[2] Zhang Bei[2]

1 *Jiangsu Institute of Meteorological Sciences, Nanjing* 210008

2 *Jiangsu Provincial Observatory, Nanjing* 210008

Email: zh_jialing@hotmail.com

Based on the turbulence data obtained with wind gradient data from the ultrasonic anemometer on the meteorological tower near Qingdao Coast, during the period of Typhoon Matsa and Khanun landfalling over the eastern China in 2005, six strongwind periods in which average wind speed per 10 min exceeding 8 m/s were selected. With the aid of the vector analysismethod, the turbulence characteristics, such as average wind velocity and direction change, turbulence and wind gust factors in surface layer in East China during the the period of typhoon landfalling are analyzed.

Gale appeared in large area of Qingdao City during the periods of the typhoons landing the East China. In the case of Matsa, the maximum wind speed from Qingdao observation reached 20.8m/s (8 on the Beaufort scale), while the one from Tuandao reached 24.0m/s (9 on the Beaufort scale). Although the routine of Typhoon Kahnun was further away from the turbulence observatory than the one of Matsa, the maximum wind speed still reached 18.0m/s(8 on the Beaufort scale). The sequential wind data were obtained by ultrasonic anemometer during the periods of the Typhoon Matsa and Typhoon Kahunm affected Qingdao City.

In the paper, a subsample with the time interval being 10 minutes was consisted of 6000 observation records which were three dimensional wind (referred as Ux, Uy, Uz) and temperature every 0.1 seconds. According to the wind speed changing of the two case, 720 subsamples were selected and the number of those of wind speed exceeding 8.0m/s were 395.

In the study, polynomial fitting method was used to eliminate non-stationary fluctuating wind speed tendencies so that gust velocity was the stationary random process. Time-height distribution of horizontal averaged wind speed U during the periods affected by the two cases was shown in Fig.1.

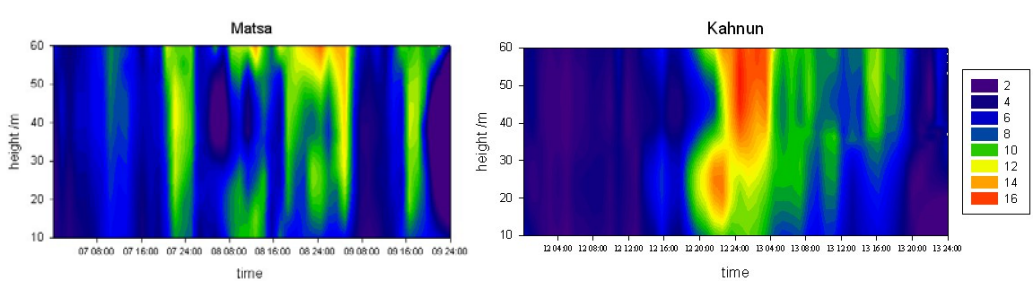

Fig1. Time-height distribution of horizontal averaged wind speed during the periods affected by Typhonn Matsha and Kahnun (unit:m/s)

The results show that during the periods affected by typhoon, the turbulent fluctuation is instable, the horizontal and vertical wind velocity and direction change rapidly. Even though the tracks of the typhoons moved into the sea are different, and the turbulence intensities are obviously different in surface layer during different strongwind periods, according to Iu > Iv > Iw. The evolution of gust factor and turbulence is the same in the two typhoon processes. The turbulence and the gust factor increase significantly, when wind velocity is increasing and direction is changing.

References

[1] Chen Lianshou , Ding Yihui. A Panorama of Northwestern Pacific Typhoon. Beijing : Science Press ,1979. 22~25

[2] Yang Huijuan, Li Ning and Lei Yang. FEATURES OF TYPHOON IN SOUTHEAST COASTAL REGIONS OF CHINA IN THE RECENT 54 YEARS. Scientia Meteorologica Sinica,2007,2794):413~418

[3] Chen Yuling , Zhou Jun and Ma Fenhua. RECENT PROGRESS OF STUDY ON CHINA LANDFALLING TYPHOONS. Scientia Meteorologica Sinica,2005,25(3):319~329

[4] LIU Xue-gang, LUO Zhe-xian, TENG Dai-gao and DAI Kan1. Warm Sector Structure Change of Typhoons in Atmospheric Boundary Layer during Its Whole Life Period. Journal of Nanjing Institute of Meteorology,2007,30(3):320~327

[5] HUANG Xin-qing, LUO Zhe-xian and TENG Dai-gao.Preliminary Analysis on Three-Dimensional Structure of Typhoon during Formation. Journal of Nanjing Institute of Meteorology,2007,30(5):648~656

[6] Song Lili, Mao Huiqin, Zhi Shiqun and et al.ANALYSIS ON BOUNDARY LAYER TURBULENT FEATURES OF LANDFALLING TYPHOON. Acta Meteorologica Sinica,2005,63(6):915~920

[7] XIAO Yi-qing, SUN Jian-chao and LI Qiu-sheng.Turbulence integral scale and fluctuation wind speed spectrum of typhoon:an analysis based on field measurements. Journal of Natural Disasters,2006,15(5):45~53

[8] PENG Jiang-liang, WU Xi, JIANG Zhi-hong and LIU Hong-nian.Comparison of Turbulent Characters over Urban and Suburban Surface Layer in Nanjing Winter. Journal of Nanjing Institute of Meteorology,2008,28(1):21~29

Research and Application of Typhoon Gale Disaster Evaluation Methods --Taking Sutong Bridge as Example

Huang Shicheng[1] Zhou Jialing[2] Wang Wenlan[2] Zhang Bing[2] Zhang Bei[2]

1 *Jiangsu Institute of Meteorological Sciences, Nanjing* 210008

2 *Jiangsu Provincial Observatory, Nanjing* 210008

Email:zh_jialing@hotmail.com

As the impact of global climate change, extreme weather phenomena such as storms, increased temperature is an indisputable fact. As the major investment project, a massive social and economic benefits significantly, and therefore the impact of severe weather has also increase sensitivity. Jiangsu in east China sea by the territory of Riverside, by a variety of weather system, weather and climate complexity, frequent severe weather, small-scale weather systems are relatively active, heavy rain, with rain, thunderstorms, typhoons, tornadoes, hail, squall lines, cold, frost, wind, snow, fog in the region major severe weather [1]. Summer and autumn of tropical cyclones (typhoons), is affected the most serious kind in East China severe weather system, its main hazard is the wind greatly affect a wide range of hazards long duration and often accompanied by heavy rain and heavy rain, in the coastal and river areas of the storm surge can cause a rare [2]. Typhoon winds, especially 8 typhoon winds, construction and operation of the project has a great influence on the typhoon's strong winds and other weather disasters, impact assessment is to design safety, construction safety requirement.

Wind in the typhoon disaster in China has been a lot of analysis of the results of these researches, as the unit of administrative division to study the specific project for typhoon wind disaster area Local research is rarely mentioned. Research shows that climate statistical methods, can reveal the bridge site of temporal and spatial distribution of typhoon disasters. The Monte Carlo (Monte-Carlo) method is to solve the problem of small samples of uncertain design, is a random number to simulate the test method. The method of using random sampling observation by observation of the sample value statistics, the realization of the research system simulation.

In this paper, Su Tong Bridge, for example, from 1949 to 2007, the bridge site typhoon wind data in their respective districts, by climate analysis, statistical analysis and Monte Carlo simulation of disaster damage, typhoon winds of the project area to assess disaster. So as to construction of large bridges and other large complex transportation projects, reasonable and effective, standardized job in disaster preparedness events, the maximum to avoid risks. The results showed that:

(1) bridge site from 1949 to 2007 typhoon in their respective districts 7, 22 typhoons crossing the edge or external airstream typhoon 146 typhoon affected bridge site area average of 2.5. Typhoon bridge DC from May end to 11 later this month are at risk of typhoons, but in July beginning of the September mid-typhoon occurrence frequency is relatively concentrated, the typhoon-prone period, which in August is the typhoon up to the month. 7 September the

typhoon affected the number of bridge site area ratio of the total area in the north of bridge site to reach 84.9% of Nantong, Changshu City, south of the bridge site area 87.7%. Seriously affect the appearance of the bridge district board level 8 typhoon gusts above average 0.78. The impact of typhoon winds, gale winds occurred mainly in the southeast and the north side direction, while the southwest wind appears less likely. Seriously affect the bridge site area for more than eight hours for the impact of typhoon winds in summer and autumn 6 to 10 months, concentrated in July-September, in the bridge area north of Nantong, Changshu, respectively, south of the typhoon winds of the total 93.3%, 88.4%, Among them, most likely in August, in the bridge north and south, respectively, 34.9%, 44.4%.

(2) This article Sutong a case, the bridge district board 8 typhoon winds of expected loss index of 0.2821, the potential economic losses of 206.75 million yuan, accounting for the province typhoon expected loss index of 48%, which bridge site area along the coast of the special geographical location and Nantong in Jiangsu Province, Changshu is the place across the province is closely related to a major hurricane.

(3) by Su Tong Bridge disaster of typhoon winds also show that large-scale construction project planning and future operations should pay particular attention to the landing here, crossing the typhoon disasters and external influence airflow caused by the typhoon wind weather, construction tower cranes, etc. facilities should avoid setting up in the wind direction to avoid the risk of disasters caused by typhoon winds. The study also found that, even if the typhoon winds in June and in October the chances appears smaller, but still great harm. Therefore, the typhoon wind project area should be proactive disaster prevention, prevention, and should establish project areas for environmental monitoring weather warning system, to receive and distribute timely typhoon forecasting and warning, and a corresponding typhoon emergency response procedures.

In general, the more developed areas of regional economic population density, industrial density, the higher the level of industrialization, in which case a small probability of extreme weather disasters are causing huge economic losses, the paper winds of Typhoon Bridge Disaster preliminary risk assessment studies to try similar projects can provide a reference meteorological disaster assessment. It is noteworthy that the typhoon winds and torrential rain disaster includes two aspects of disasters, this disaster loss estimates consider only the typhoon winds, expected yield loss index and the calculation of the potential economic loss is limited, we will be strong winds and typhoons typhoons and storms in the risk assessment and risk management typhoon further study.

References

[1] JIANG D L, YAN J Y. Climate of Middle and Lower Reaches of Changjiang River. [M].Beijing: China Meteorological Press, 1991, 151-272.

[2] CHEN L S, DING Y H. Northwest Pacific Typhoon Introduction [M]. Beijing: Science Press, 1979, 440-488.

[3] TIAN H, MA K Y,LIN Z S. Analysis Of The Heavy Rain And Strong Wind Of Landing Typhoon on The Coasts of South And East China[J], Quarterly Journal Of Applied Meteorlolgy,1999,10(S1):148-152.

[4] YANG Y H, LEI X T. Statistics Of Strong Wind Distribution Caused By Landfall Typhoon In China[J]. Journal of Tropical Meteorology, 2004, 20(6):633-642.

[5] Forecasting Group of Jiangsu Provincial Weather Bureau. Important weather analysis and prediction in Jiangsu [M].Beijing: China Meteorological Press, 1988, 79-80.

[6] LIU C, HUANG S C, ZHANG Z Y, et al. Sutong Bridge Meteorological Observation and Wind Factors Computing Report [R].Nanjing: Jiangsu institute of meteorological science, 2002, 56-57.

[7] OU J P,DUAN Z D,CHANG L. Typhoon Risk Analysis For Key Coastal Cities in Southeast China[J]. Journal of Natural Disasters, 2002, 11(4):10-17.

[8] HUANG C F. Risk Assessment of Natural Disaster Theory & Practice [M] Beijing: Science Press, 2005, 24-25.

[9] ZHANG J Q, LI N. Quantitative methods and applications of risk assessment and management on main meteorological disasters [M].Beijing: Beijing Normal University Press, 2007, 284-272.

[10] XU S L. Fortran Common Algorithm Procedures Set[M].Beijing: Tsinghua University Press,1995,502-503.

Study on Spatial-Temporal Distribution and Variation of Jiangsu Summer Precipitation

Jiang Wei Lü Jun

Jiangsu Meteorological Bureau, Nanjing **210008**

Extended abstract

1 The temporal and spatial distribution of rain during summer in Jiangsu province

1.1 The analysis of Empirical Orthogonal Function (EOF)

According to the summer precipitation data obtained in 63 stations of Jiangsu from 1961 to 2008 , the spatial-temporal distribution were analyzed with EOF, the first 3 eigenvectors' total variances have exceeded 70%, which basically represent the rain's spatial distribution feature during summer in the recent 50 years in Jiangsu, while the other eigenvectors' total variances are relatively less influential.

The first eigenvectors' variances contribution is 45%, which is a positive value according to the data of 59 stations in Jiangsu, it represents the first type of characteristics of the rain's space distribution during summer in Jiangsu province, that means the whole province teems with rain or lacks rain.

The second eigenvectors' variances contribution is 23%, it represents the second type of characteristics of the rain's space distribution during summer in Jiangsu province, in that eigenvectors got from stations in Southern areas of Yangtze River are positive while eigenvectors from the others are negative, that means to take the Yangtze river as the boundary, the spatial distribution of rain in the south is in contrary to that in the north, e.g. when the amount is much in the south, it is less in the north, or vice versa.

The third eigenvectors' variances contribution is 7%, the eigenvectors that most stations reckoned among areas between Huaihe Valley and Yangtze River are positive, and that of the other stations are negative. It represents the third type of characteristics of the rain's space distribution during summer in Jiangsu province: the rain is relatively more (less) in areas between Huaihe Valley and Yangtze River while in the other areas is less (more).

According to the analyses of the time coefficient corresponded with the first 2 eigenvectors (chart omitted), the first principal component is concluded that the 1965, 1974, 1980, 1987, 1991, 2003 are the typical years when the rain throughout Jiangsu is much more than mean value; 1966, 1967, 1978, 1994 are representative years with much less rain than average value in Jiangsu. From the second principal component we can find that 1965, 1972, 1990, 2000, 2003, 2005 are the quite typical years with more rain in the north and less in the south; 1987, 1991, 1999 are the typical years with less rain in the north and more in the south. To sum up, typical years with relatively more rain or less are well-distributed, it appears all the time. However, the typical years when the rain in the north is opposite to that in the south appear in the recent 20years, especially since the 1990s, it happens more frequently. in addition. 1965、1987、1991.2003 can be concluded into both of the distribution type, it can be found that the effect of EOF is not good enough, so based on EOF method and taking REOF, this article will make further analysis of the feature of the temporal and spatial distribution of precipitation in summer in Jiangsu Province.

What's more, the two curves also show less significant upward or downward trend, indicating that nearly 48 years in Jiangsu Province, there is no significant increasing or decreasing trends of rainfall in summer.

1.2 The analysis of Rotated Empirical Orthogonal Functions (REOF)

In the preceding analysis, on the basis of EOF, We take the first 3 principal components to rotate, and then we get different types of distribution in precipitation patterns in Jiangsu province. The first rotated eigenvector's variance contributes to 23 %. The distribution characteristic of the eigenvector is shown in figure 1a: The high load primarily concentrated in the Yangtze River and the most areas south of it, named Southern areas of Yangtze River-centered precipitation patterns. The second rotated eigenvector's variance contributes to 22%, the distribution characteristics of the eigenvector is shown in figure 1b: The high load primarily concentrated in Huaihe Valley and northern areas of it called Huaihe-Valley-centered- Precipitation distribution patterns. The third rotated eigenvector's Variance contributes to 28%, the distribution characteristics of the eigenvector is shown in figure 1c: The high load primarily concentrated in most areas between the Yangtze River and Huaihe Valley, and also includes the southwest region of Jiangsu province, called areas between the Yangtze River and Huaihe Valley centered Precipitation distribution patterns.

After analyzing three eigenvector of each corresponding period of comparison map (figure 2), the three curves' maximum or minimum well reflect the relevant area of very wet or dry year. In the middle of the 1960s and 1970s, years with abnormal rainfall too much or too little came frequently in northern areas of Huaihe Valley; years with less rain were quite frequent in southern areas of Yangtze River. In the early 1970s, droughts and floods often happened abnormally among areas between Huaihe Valley and Yangtze River. From the late 1970's to the late 1980's, the whole province enjoys a relative stability in precipitation changes, hardly with any exceptions. From 1990s to now, northern areas of Huaihe Valley and southern areas of Yangtze River entered a period of abnormal and frequent droughts and floods, and strength kept intensing.

The three parts that is divided by summer precipitation are in coincide with land distribution of Jiangsu, so it can be put into forecast business practice.

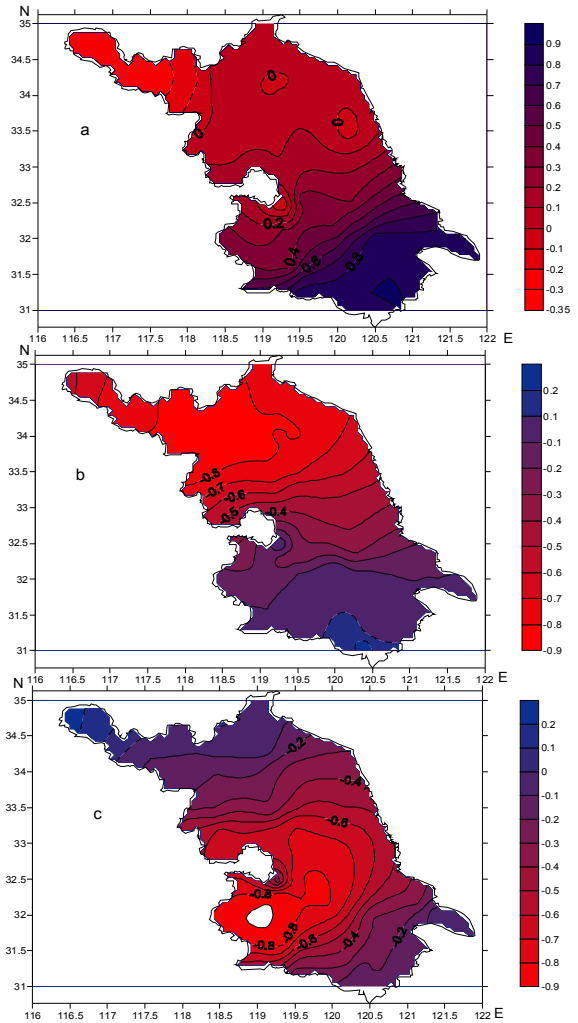

Fig.1 The first, second and third eigenvector fields of REOF

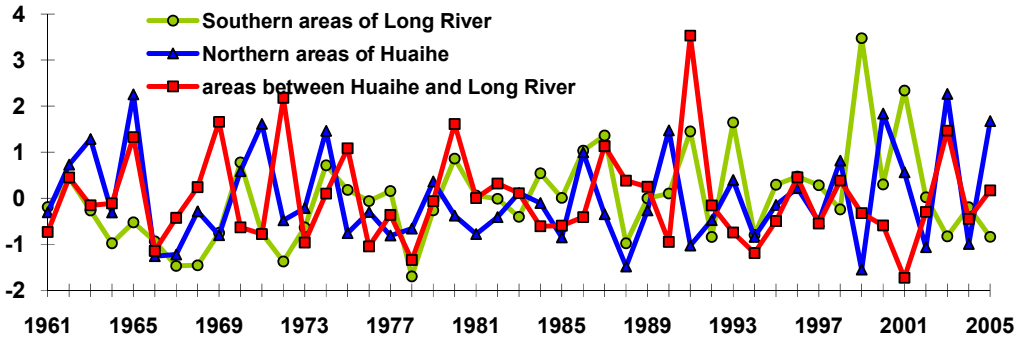

Fig.2 The time series of PCA

2 Inter-decadal Characteristics

The fig3 suggest that from the 1960s to the middle of the 1970s, the abnormal drought or flood years occurred easily in Northern areas of Huaihe Valley, and most years of less precipitation occurred in Southern areas of Yangtze river, and during the 1970s, the

precipitation in southern areas of Huaihe Valley was negative anomaly. From the late 1970s to 1980s, the variety of provincial precipitation relatively stays stable , and the precipitation in areas of Huaihe Valley was positive anomaly while negative anomaly in most other areas. From 1990s to now, in Northern areas of Huaihe and Southern areas of Yangtze River, the frequency and intensity of abnormal drought or flood years increased, and the regional drought or flood years increased clearly. In 1990s the rain was relatively heavy in southern areas of Huaihe Valley during summer. Since the 21st century, the years with relatively heavy rain in summer are quite common and the type of northern areas of Huaihe Valley appears more frequently.

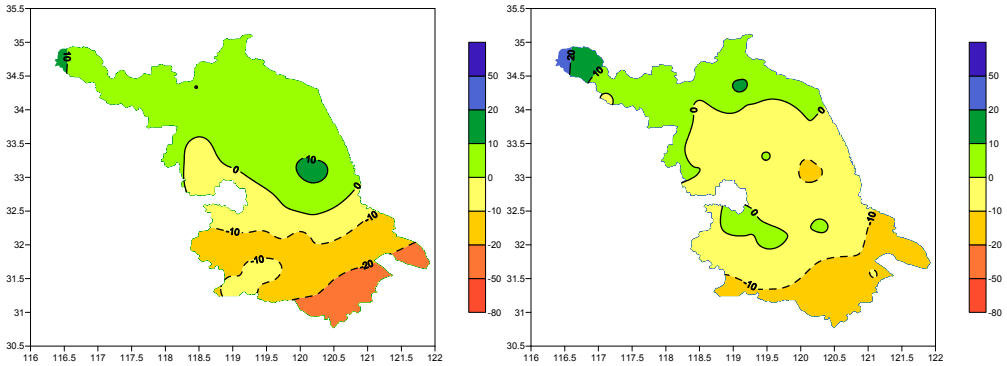

(a) (b)

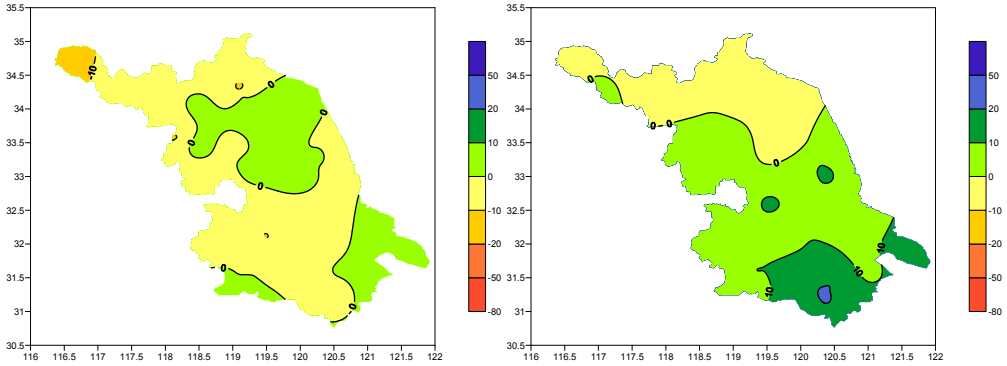

(c) (d)

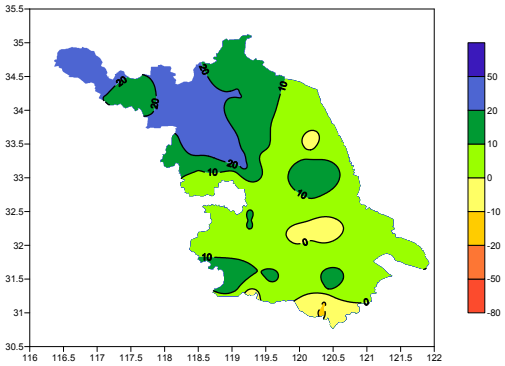

(e)

Fig. 3 Interdecadal Change of space distribution of the rainfall in summer of Jiangsu during 1961-2009, (a) in 1961-1970, (b) in 1971-1980, (c) in 1981-1990, (d) in 1991-2000, (e) in 2001-2008

3 The temporal and spatial distribution of summer rain day number

From 1961 to nowadays, the number of summer rainstorm days (≥50mm/day) in Jiangsu is keeping gro wing (0. 18d/10y), especially since 21st century, it has p osed a dramatically increase (0.82d/10y). There are some regional differences among the summer rainstorm day numbers of three different areas of Jiangsu. Fro m 1961 to now, the tre nd of the increasing numbers in Southern areas of Yangtze River is more apparent than that in Northern areas of Huaihe Valley and areas between Huaihe River and Yangtze River. But since this century the days of Northern areas of H uaihe Valley increased more clearly. Meanwhile the events of heavy rain greater than 100 mm or more has increased remarkable in recent years.

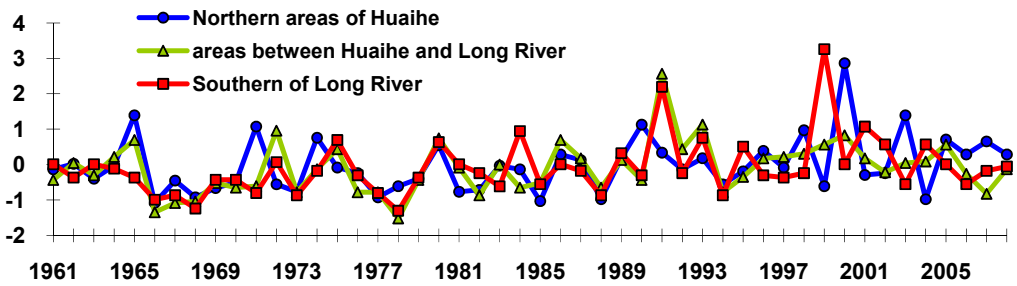

Fig 4 the time series of summer rainstorm day number

4 the exceptions of summer rainstorm

As a whole, preci pitation extremes increased in Jiangsu from 1961 to 2 008, especially from this century. For example, the 24-hour rainfall in Xiangshui station of northern Huaihe Valley e hit an historic milestone of Jiangsu Province since the founding of China, reaching 737.3 millimeters i n August 30, 200 0. As another example t he 24-hour rainfall of five stati ons reached the extreme value since the stations had meteorological record, the five stations were Yangzhou (249.0 millimeters), Y izheng (27 4.6 millimeters), Jiang pu (3 01.4 millimeters), Nanjing (207.2 millimeters), and Danyang (279.4 millimeters).

Key Words: Spatial-temporal distribution, summer precipitation, rainstorm day number, the events of heavy rain

References

Li Zhenghua, Zhu Jinhong, Cai Jingning, Wang Shaowu 2005: Flood in Huaihe Valley since 1470. Meteorological Monthly, 31(6), 24-28.

Cai M in, Di ng Yuguo, J iang Zhi hong, 2007: E xtreme Preci pitation E xperimentation o ver Eastern China Based on L-moment Estimation. Plateau Meteorology 26(2), 309-318.

Chen Huai, Wang Yongbo, Shi Neng, 2001: Climate secular change and base state over the mid-lower reaches of Yangtze River. Scientia Meteorologica Sinica, 21(1), 44-53.

Li Xiaodong, Zhu Yafen, Qian Weihong, 2002: Spatiotemporal Variations of Summer Rainfall over Eastern China during 1880–1999. Advances in Atmospheric Sciences, 19 (6), 1055-1067.

W. Qian, X. Lin, 2005: Regional trends in recent precipitation indices in China. Meteorology and Atmospheric Physics, 90, 193-207.

U. Fuentes, D. Heimann, 2000: An Improved Statistical-Dynamical Downscaling Scheme and its Application to the Alpine Precipitation Climateology. Theoretical and Applied Climatology 65, 119-135.

The characteristic change and analysis of its cause of recent precipitation in DPR of Korea

KIM thaejin, SONG Chol Man
Central meteorological research institute , DPR of Korea
shma@co.chesin.com.

In this paper, the statistical research and analysis on the characteristic changes of precipitation appeared since the early part of the 21st century in DPRK, and on clarifying its cause was described at various aspects.

Available data and methodology are as follows;
Observation data of precipitation amount (since 1918yr) at main meteorological stations and climatological stations,
The northern hemisphere 500hPa height (NCEP reanalysis data)
The Global and the East Asian regional climate research results presented recently,
Correlation analysis method
Linear and multi-regression analysis
Composite method of charts

The inter-decadal and inter-annual change of precipitation amount and specially the regional precipitation distribution in July, August was analyzed by mean and variation coefficient and the recent change of summer seasonal Changma was also analyzed.
In order to clarify the cause of changes in precipitation, the atmosphere circulation background fields and the natural factors (solar activity, ice and snow cover, volcanic activity) and the human factors (change of greenhouse gas Co2 concentration, deforest, desertification) and the factor analysis to climate change were used.

The conclusion obtained in this paper is that the annual mean precipitation amount, especially summer season precipitation had the decreasing trend since 1960 's and the increasing trend in Autumn season precipitation after 2000yr and the intensity of rainstorm was strengthen remarkably compared with previous time.

The study showed that the strengthening of zonal circulation in East Asia compared with the mid-20st century and the relative weakening of East Asia monsoon from it and the rapid increase of the co2 concentration in the air was closely related to the recent change at precipitation.

An hourly updated convection-allowing forecast System in Shenzhen region

Fanyou Kong[1], Hongping Lan[3], Weimin Wang[4], Fei Cai[3], Xiangming Sun[3], Xunlai Chen[3], Yunheng Wang[1], Ming Xue[1,2], and Jidong Gao[1]
Center for Analysis and Prediction of Storms[1]
and School of Meteorology[2], University of Oklahoma, USA
Shenzhen Meteorological Bureau[3]
Shenzhen Institute of Advanced Technology, Chinese Academy of Sciences[4]
fkong@ou.edu

1. Introduction

Recent achievement in radar data assimilation and the increasing computing power allow operational experiments to be performed to assess benefits and limitations of convection-allowing NWP on high-resolution QPF (Kong et al. 2007, 2008, 2009, 2010; Xue et al. 2007, 2008, 2009). An hourly updated WRF-ARW based forecasting system has been developed and run in realtime mode since March 2010 in Shenzhen Meteorological Bureau in Southeast China. It is a collaborative effort among the Center for Analysis and Prediction of Storms (CAPS), Shenzhen Meteorological Bureau (SZMB), and Shenzhen Institute of Advanced Technology (SIAT). The storm-scale forecasting system, called HAPS (referring to Hourly Assimilation and Prediction System), has a domain that covers the entire Guangdong province at 4km grid spacing and produces 6-h forecasts every hour, utilizing all seven S-band Doppler radars in the province by analyzing both reflectivity and radial wind into ICs using ARPS 3DVAR and cloud analysis package. This is the first step of a three-phase plan aiming to develop an advanced data assimilation and forecasting system in Shenzhen and surrounding region. The second phase will extend the forecasts to 12 h with expanded domain and analysis of other available observations in next 12 months. The third phase, taking another 12-18 months, will develop into a storm-scale ensemble forecasting system capable to produce high-resolution probabilistic forecasts of storms and precipitation.

This extended abstract provides an overview to the HAPS forecast system, with some example cases from the realtime products. Three companion papers to this conference will present case verifications of some high profile heavy rain events, and sensitivity experiments aiming to identify key factors affecting QPF skill.

2. HAPS overview

The Hourly Assimilation and Prediction System (HAPS) has a domain of 840km by 600km at 4 km grid spacing, covering entire the Guangdong province (Figure 1). The forecast model is the Weather Research and Forecast model system (WRF-ARW) V3.0.1.1, aided with the Advanced Regional Prediction System (ARPS) package to provide radar analysis and post-production of forecast fields. The ARPS 3DVAR and cloud analysis modules are used for realtime analysis of radar data (both radial wind

and reflectivity) from seven WSR-98D Doppler radars in the region. Every hour, HAPS produces a 6 h forecast over the 4-km domain within 30 min past the hour, with a wide range of QPF and other weather forecast products including 6-min interval reflectivity animation movies available in realtime to SZMB forecasters.

In order to assure realtime storm-scale forecasts, two background forecasts are initiated at 00 and 12 UTC, respectively, at 12 km grid spacing covering a larger region (Figure 1) using 0.5deg GFS analysis and forecast as IC and LBC to provide quasi-realtime IC background and LBCs for the 4 km storm-scale (or convection-allowing) forecasts. The LBCs for these background forecasts are updated every 3-h (from GFS). Each 12 km background forecast produces 48 h output, written every hour. GFS dataset are directly downloaded to SIAT computing system from NCEP data site. The GFS data lag time in average ranges from 5 - 5.5 h. As a result, a 12 UTC background forecast is used to drive storm-scale forecasts starting next 00 UTC and later, and a 00 UTC background forecast is used to drive storm-scale forecasts starting next 12 UTC and later.

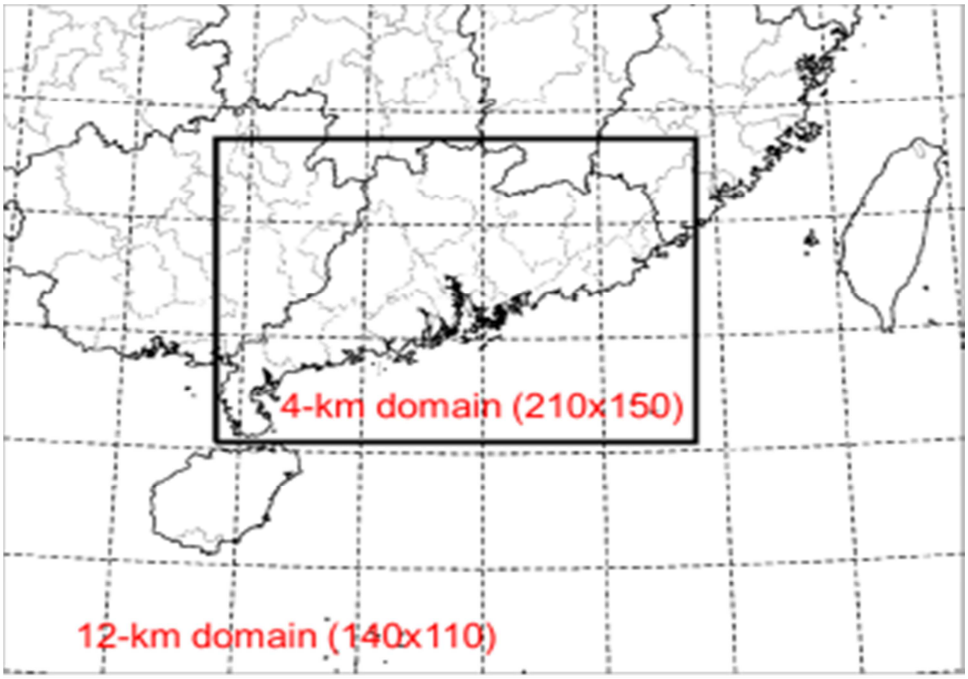

Figure 1. HAPS domain (4-km) and the background forecast domain (12-km).

Storm-scale forecasts over the 4 km grid are produced hourly. Taking 00 UTC forecast as an example, it uses the 12-h forecast that is initiated 12-h ago at 12 UTC on the previous day as background, add reflectivity and radial wind data valid at 00 UTC, observed from seven WSR-98D Doppler radars in the region, through the ARPS 3DVAR and complex cloud analysis module, and integrate 6 hours forward until 06 UTC. The LBCs used for producing this forecast are hourly output from the same background forecast (13-, 14-, 15-, 16-, 17-, and 18-h in this example). Similarly, the storm-scale forecast initiated at 12 UTC uses the 12-h forecast that is initiated 12-h ago at 00 UTC on the same day as background, and adds radar data valid at 12 UTC. In a situation when the current background forecast is not available due to lack of proper

GFS dataset or any other reason, the previous background forecast will be used. For example, if the 00 UTC background forecast is not available, the 12 UTC storm-scale forecast will then use the 24-h forecast from the previous day (12 UTC initialization) as background, and use as LBCs the 25-, 26-, … 30-h forecasts.

All forecasts, including pre- and post-processing, are performed on SIAT's Linux cluster - Dawning 5000 super computer system. The Dawning 5000 system has 72 computing nodes, each equipped with four AMD Shanghai 8374HE 2.2GHz quad-core processors (total 16 processors, or cores) with 32GB memory (2GB per core). Four computing nodes, with a total 64 computing processors, are dedicated to HAPS by SIAT.

3. Forecast products

QPF products from the storm-scale (4km) forecasts, including 1-h, 3-h, and 6-h accumulated precipitation and derived reflectivity, along with other forecasted weather variables such as 2-m temperature and 10-m wind, are available to forecasters in Shenzhen Meteorological Bureau within 30 min after each forecast initialization at the top of the hour. Figure 2 shows example QPF images with the observed 6-h rainfall map alongside.

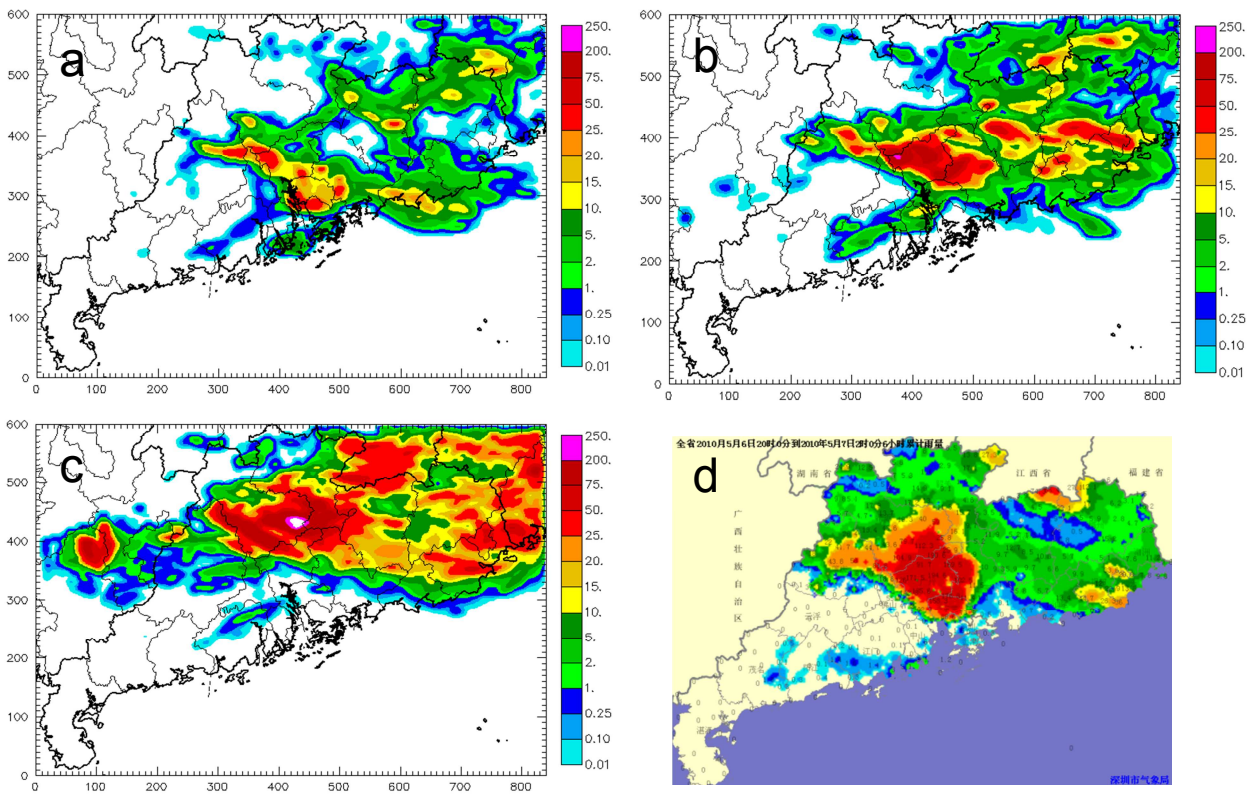

Figure 2. HAPS predicted 1-h (a), 3-h (b), and 6-h (c) accumulated precipitation valid 0200 UTC 7 May 2010, along with the observed 6-h rainfall (d).

Preliminary evaluations help identified approaches to improve HAPS for producing accuracy of storm-scale QPF, including the analysis of available non-radar observations

such as surface observations from AWS stations, the expansion of forecast domain to alleviate LBC impact, the use of advanced data assimilation including cycling of radar and other observation data. These are the main focus in the second phase.

Acknowledgements

This project is supported by a grant to CAPS from the Shenzhen Institute of Advanced Technology, Chinese Academy of Sciences. The realtime forecasts are produced on the SIAT supercomputing facility.

References

Kong, F., and co-authors, 2007: Preliminary analysis on the real-time storm-scale ensemble forecasts produced as a part of the NOAA Hazardous Weather Testbed 2007 Spring Experiment. *Preprints, 22th Conf. on Weather Analysis and Forecasting and 18th Conf. on Numerical Weather Prediction* Amer. Meteor. Soc., Park City, UT, 3B.2.

Kong, F., and co-authors, 2008: Real-time storm-scale ensemble forecast experiment - Analysis of 2008 spring experiment data. *24th Conf. Several Local Storms*, Savannah, GA, Ameri. Meteor. Soc., Paper 12.3.

Kong, F., M. Xue, K.W. Thomas, J. Gao, Y. Wang, K. Brewster, K.K. Droegemeier, J. Kain, S. Weiss, D. Bright, M. Coniglio, and J. Du, 2009: A real-time storm-scale ensemble forecast system: 2009 spring experiment.. 23rd Conf. Wea. Anal. Forecasting/ 19th Conf. Num. Wea. Pred., Omaha, NB, Amer. Meteor. Soc., Paper 16A.3

Kong, F., M. Xue, and X. Wang, 2010: Probabilistic QPF from a realtime multi-model storm-scale ensemble forecast system. Third WMO QPF/QPE Conference, Nanjing, China.

Xue, M., and co-authors, 2007: CAPS realtime storm-scale ensemble and high-resolution forecasts as part of the NOAA hazardous weather testbed 2007 spring experiment. *22nd Conf. Wea. Anal. Forecasting/18th Conf. Num. Wea. Prediction*., Amer. Meteor. Soc., Park City, UT, Paper 3B.1.

Xue, M., and co-authors, 2008: CAPS Realtime Storm-scale Ensemble and High-resolution Forecasts as Part of the NOAA Hazardous Weather Testbed 2008 Spring Experiment. *Preprints*, *24th Conf. on Severe Local Storm*, Amer. Meteor. Soc., Savannah, GA, Paper 12.2.

Xue, M., and co-authors, 2009: CAPS realtime multi-model convection-allowing ensemble and 1-km convection-resolving forecasts for the NOAA Hazardous Weather Testbed 2009 Spring Experiement. 23rd Conf. Wea. Anal. Forecasting/19th Conf. Num. Wea. Pred., Omaha, NB, Amer. Meteor. Soc., Paper 16A.

Downscaling precipitation for weather forecast using high resolution terrain data and multi-model predictions

Anwei Lai[1] **,** Chunze Lin[1]**,**Chunguan Cui[1] , Jun Li[1] ,
Institute of Heavy Rain, CMA, Wuhan
laianwei@hotmail.com

Abstract

In this work nonlinear downscaling is used to establish empirical relationship between different numerical weather model predictions and observed rainfall over the middle and south China. The numerical weather predictions mainly include rainfall forecasts of global models, mesoscale model and diagnosis rainfall from mesoscale model. The global numerical weather models are T639 model from China and Japan global model. The mesoscale model, AREM, is the operational model of Insitute of Heavy Rain, CMA, Wuhan. We use the high resolution terrain data and AREM synoptic-scale circulation calculated the rainfall of terrain forcing and rainfall of moisture flux divergence. The final objective is application the artificial neural network(ANN) to the four kinds rainfall for downscaling the precipitation about 2-3km resolution for diurnal rainfall forecast. The results indicated that the downscaling precipitation of ANN method not only is reasonable for moderate intensity rain but also maybe better to describe the fine structure of the high intensity rain events.

1. Introduction

Rainfall prediction on scales of the order of a few kilometers in space is a necessary ingredient to the fine weather forecast. But the high resolution numerical model should be more computer costs. So the downscaling precipitation is very useful for the operational weather forecast. Many approaches have been researched and operated in the world (Rebora, 2006). As is well-known to all, the different scale numerical models have themselves advantages of rainfall prediction. In this study nonlinear downscaling, BP (Back Propagation), is used to establish empirical relationship between different scale numerical weather model predictions and history observed rainfall over the middle and south China. The numerical weather predictions mainly include rainfall forecasts of global models, mesoscale model and diagnosis rainfall from mesoscale model. The rest of this paper is organized as follows. The data and methodology is introduced in section 2. To illustrate the working of the method and to test its performance ,in section 3 we apply the approach to one intense rainfall event and one month continuous experiments. Section 4 is devoted to discussion and conclusions.

2. Data and methodology

We used four kinds of simulated precipitation, such as global numerical model precipitation, mesoscale numerical model precipitation, terrain impact diagnosed precipitation and moisture flux diagnosed precipitation. The global numerical models include Chinese operational model T639 and Japanese operational model. The mosescale model is an operational meso-scale numerical model AREMv2.3 in Wuhan

Institute of Heavy Rain of CMA. The ingredients of two diagnosed rainfall are the AREM outputs and high resolution DEM (Digital Elevation Model) data. The fig.1 is illustrated the schematic of the downscaling precipitation. Before the BP method is carried out, the five rainfalls are preprocessed by interpolation and pyramid matching (Zinner et al., 2002;Keil and Craig, 2007) to remove the displacement error. The resolution of final prediction is about 3km one tenth of the resolution of mesoscale weather numerical model.

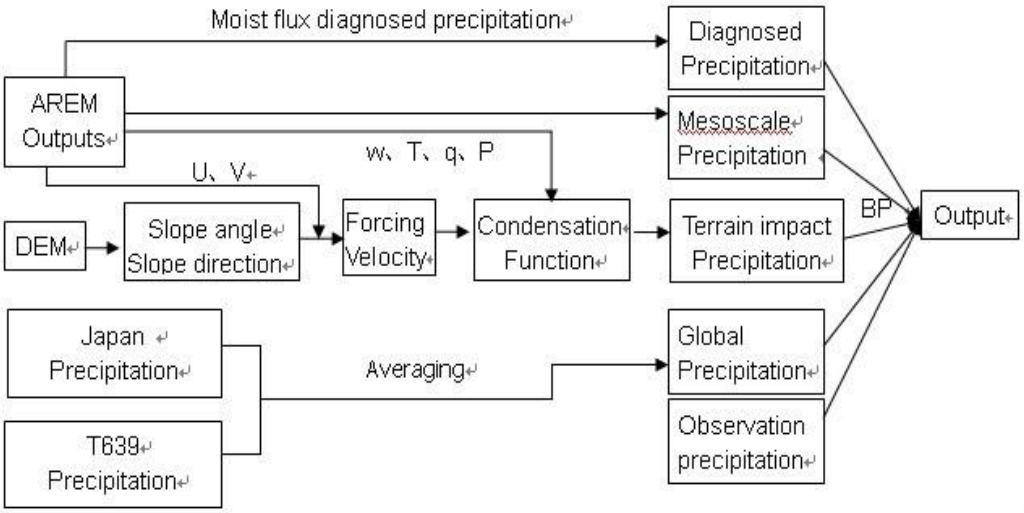

Fig.1. The schematic illustrating the downscaling precipitation

3. Results

During the 0100 UTC June,2010 to 0200 June,2010 a intense rainfall event occurred in south of China. The maximum rainfall was 211.7mm at Yulin station in Guangxi province. The results shown in Fig.2 is more suitable for the heavy rain. It can get fine structure of the heavy rain, but the lower resolution inputs precipitation can not describe the phenomena. But the region of rainfall ⩾10mm and ⩽25mm is wider than the observation. The threat score of downscaling and global precipitation for one month test in Fig.3 indicated that the method had the positive impact on heavy rain. But the threat score of ⩾1mm, ⩾10mm and⩾25mm rain are lower than the global model. It maybe results from more false positive of downscaling approach.

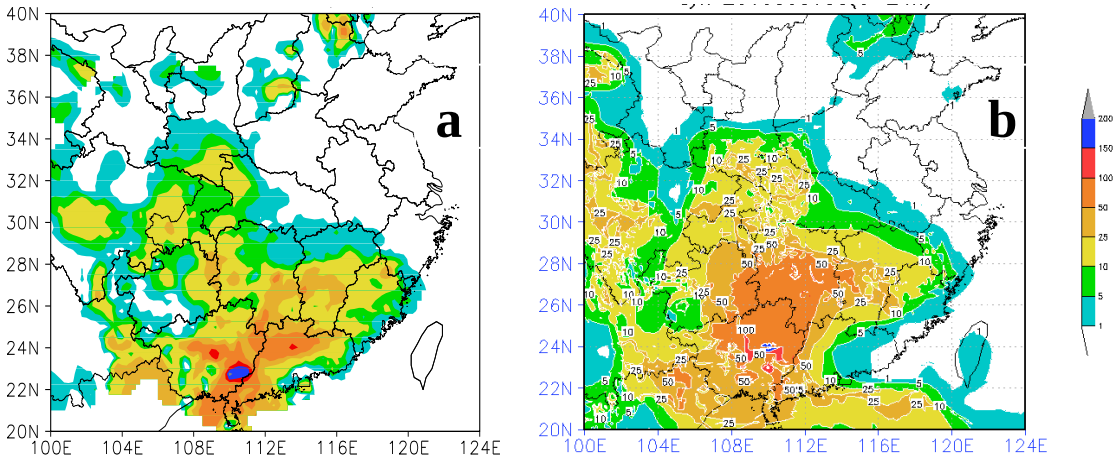

Fig.2. The 24h accumulated precipitation for (a) observation, (b) downscaling.

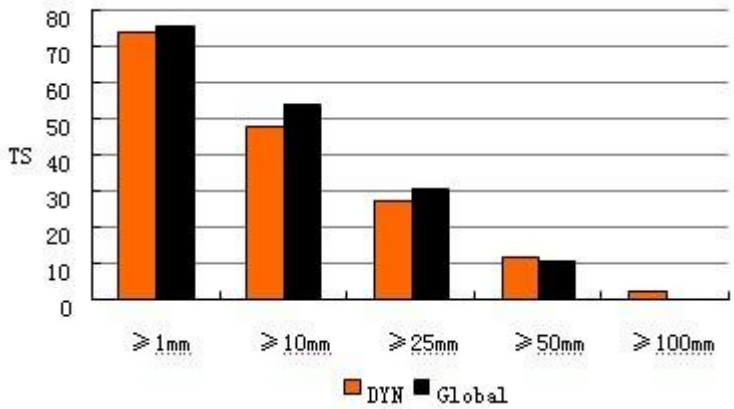

Fig.3. The threat score(TS) of 24h accumulated precipitation
(red histogram is downscaling, black histogram is global model)

4.Discussion and conclusions

The approach discussed in this paper maybe more suitable for more than 50mm precipitation and more false positive for others. The method maybe takes advantage of the different scale numerical model, but the result seriously depended on the numerical model predictions. So the system error of numerical model is vital to the performance of the method. The further work will be focus on the remove the system error.

Acknowledgment

This study has been supported by the following projects: Meteorological research project of public sector of Ministry of Science and Technology (NO.GYHY200906010, Scientific research project of Wuhan Institute of Heavy Rain (NO.0903).we also thanks to researcher Zhibin Wang and Xuzan Gu in Institute of Heavy Rain, CMA, Wuhan for giving suggestion.

References

Rebora N. et al. 2006:RainFARM: Rainfall downscaling by a filtered autoregressive model. J. of Hydrometeor., 3,724-738.

Zinner T. et al, 2008: Tracking and monitoring severe convection from onset over rapid development to mature phase using multi-channel Meteosat-8 SEVIRI data. Mon. Wea. Rev.,135,3248-3259.
Keil C. and Craig G.,2007: A displacement-based error measure applied in a regional ensemble forecasting system. Meteor. Atmos. Phys.,101,191-210.

A Kalman Filter based QPF calibration system

Hongping LAN[1], Fanyou KONG[2], Jiajia He[1] and Xunlai CHEN[1]
Shenzhen Meteorological Bureau[1],
Center for Analysis and Prediction of Storms, University of Oklahoma, USA[2]
hp2068@sina.com

China Shenzhen Meteorological Bureau, the Center for Analysis and Prediction of Storms, and the Shenzhen Institute of Advanced Technology, in a collaborative effort, developed a realtime radar data assimilation and forecasting system, called HAPS – referring to Hourly Assimilation and Prediction System. Using WRF-ARW modeling system with a grid spacing of 4km, HAPS analyzes radar data from seven S-band Doppler radars in the region every hour and produces 0-6 h QPF. HAPS QPF has longer lead time compared to typical nowcasting systems, but location and intensity errors exist. A method is proposed to calibrate HAPS 0-6h QPF using Kalman Filter technique and blend with 0-3h nowcasting QPF.

Past QPF and corresponding QPE are first matched in locations. Intensities of QPF and QPE of the same locations are analyzed to obtain intensity calibration field, which will be applied to future forecasts to form calibrated QPF. Two location matching methods,, object matching and correlation coefficient matching, are tested and the later is selected. The working flow is : The correlation coefficient of the past 2h HAPS QPF and corresponding QPE is calculated over a 500km by 500km region. If the correlation coefficient is greater than 0.25, the QPF and QPE are classified to have same location and their intensity difference field, assuming Gaussian noise distribution, is filtered using Kalman Filter method to have a smoothed calibration field. Weighting factors are applied to the nowcasting QPF and HAPS QPF to produce intensity calibrated and nowcasting calibrated QPF. Verification against automatic rain gauge data shows higher ETS scores for the calibrated QPF compared to those without calibration.

Probability Distribution of Summer Daily Precipitation in the Huaihe Basin of China

Li LIANG[1,2], **Linna ZHAO**[2], Yuanfa GONG[1], Fuyou TIAN[2], and Zhi WANG[2]
1. Chengdu University of Information Technology, Chengdu, China
2. National Meteorological Center, China meteorological Center, P. R. China
zhaoln@cma.gov.cn

1. Introduction

Huaihe basin is located in eastern part of China which is between the Yellow River and Yangtze River, composing the Huaihe river, Yihe river, Shuhe river and Sihe river, and its watershed area is about 270,000 square kilometers. As the weather and the changes of climate are complex in the basin, both the drought and flood disasters happened frequently here. As a result, it caused serious damages not only to people's lives, property but also to the sustainable development. The precipitation from June to August is about 53% of the annual precipitation (Cheng, 2004). Therefore, the precipitation from June to August is the main factor to determine whether drought or flood will occur and also the level of flood.

Many researches have been carried out related to the spatial distribution of precipitation. Gregory et al. (2007) used gamma distribution to represent monthly rainfall in Africa. It shows that the gamma distribution is well suited to fit precipitation data and better to distinguish rainfall regimes. Nevertheless, the research on statistical characteristics of the spatial and temporal distribution of the precipitation probability in the Huaihe basin is a littler bit to hear more. The paper investigated the summer daily precipitation in the Huaihe basin based on statistical analysis. It reveals the features of the probability distribution of precipitation in the Huaihe basin over the lately 28 years, so as to provide scientific guidance to the best understanding of the precipitation pattern of the Huaihe basin and necessary climatic background for the daily precipitation forecasts.

2. Data and Methodology

The method introduced in this research is developed by using the daily precipitation records of meteorological rain gauges of 158 intensified observation sites in the Huaihe basin, during the summer from 1980 to 2007, which is defined from May 31 to August 31 every year, totally 28 years. The daily precipitation data of 158 sites are reserved to study after excluding the sites which were removed or new established during the 28 years. The research area and sites' location are illustrated as Figure 1.

The density function of gamma distribution is used to estimate the probability distribution of daily precipitation. Specifically, a model proposed by Katz (1977) is used, which assumes that the probability distribution of daily precipitation is related to whether the day before the rainy day is dry or wet. Since the probability distribution of daily precipitation is related to whether the preceding day is dry or wet, and therefore the

Fig.1. The Illustration of the test catchment and the locations of 5 stations in the test area. (①, ②, ③, ④and⑤represent for Xixian, Fuyang, Shangqiu, Huaian and Lianyungang rain gauge site, and the black triangle represents the hydrographic station, representatively.).

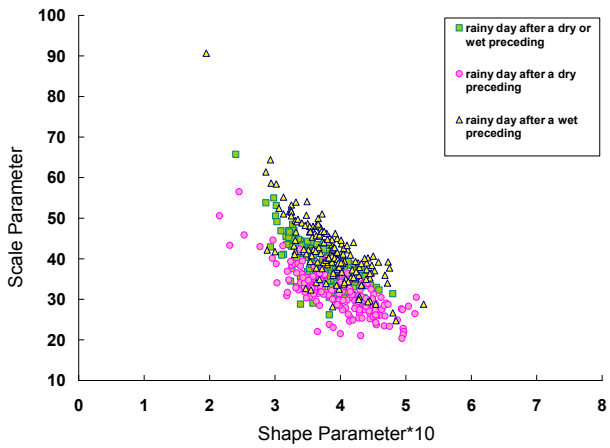

Fig 2. The scatter of shape parameter and scale parameter of gamma distribution of daily precipitation over Huaihe basin.

stochastic process of precipitation could be described by a dual variable, that is, ((J_{n-1}, X_n), n = 1, 2, 3 ... ...), where J represent the *nth* day is a rainy day (daily precipitation > 0 mm) as J equal 1, and it represent the *nth* day is not a rainy day as J equal 0. X_n is the precipitation of the *nth* day. The dual variable (J_{n-1}, X_n) express that the probability distribution of the *nth* day's precipitation is related to whether the *(n - 1)th* day is rainy.

The gamma distribution density function is shown in Equation (1). The complete gamma function is shown in Equation (2) (Gregory et al., 2007)

$$f_i(x) = \frac{1}{\beta_i^{\alpha}\Gamma(\alpha_i)}\left(\frac{x}{\beta_i}\right)^{\alpha_i - 1}\exp\left(-\frac{x}{\beta_i}\right) \quad \ldots\ldots \quad (1) \quad , \quad \Gamma(\alpha_i) = \int_0^{\infty} e^{-t} t^{\alpha_i - 1} dt \quad \ldots\ldots \quad (2)$$

Where x > 0, α_i , β_i > 0, i = 0, 1, 2. That is correspond to the unconditional rainy days, rainy day which has a dry preceding day (J_{n-1} = 0, J_n = 1) and rainy day which has a wet preceding day (J_{n-1} = 1, J_n = 1) separately. The samples of rainy days of 158 sites in the Huaihe basin are investigated according to these three types, and both the rainy day which has a dry preceding day and the one has a wet preceding day are conditional rainy days. The shape parameter α_i and the scale parameter β_i, as well as the $\bar{x}_i$ and s_i^2, are estimated by the maximum likelihood estimation(Gregory et al., 2007), that is, $\beta = \frac{\bar{x}}{\alpha}, \alpha\beta^2 \approx s^2$. Finally, the probability density function $f_i(x)$ is calculated in a certain interval according to the formula (1) and (2).

3 . Result

3.1 The parameter analysis of the unconditional and conditional rainy days

Sixteen stations were investigated as representative stations from five catchments respectively, the upper stream, the part stream between Wangjiaba dam and Bengbu station, the part stream between Bengbu station and Hongze Lake, the Yishu river watershed and the downer stream of Huai river below Hongze lake (Fig. 1).

The shape parameter is less one order of magnitude than the scale parameter(Fig.2), indicating that the basin is a scale dominated region(Gregory et al. , 2007), we knew that this kind of region is likely to have variable rain and more extreme events. During the 1980 to 2007, flood or drought occurs about every two years in the Huaihe basin. The relatively dry period is from 1985 to 1988 and from 1992 to 1999. Severe drought occurred in 1999, flood occurred in 1991, 2003, 2007 (Bi. et al, 2004).

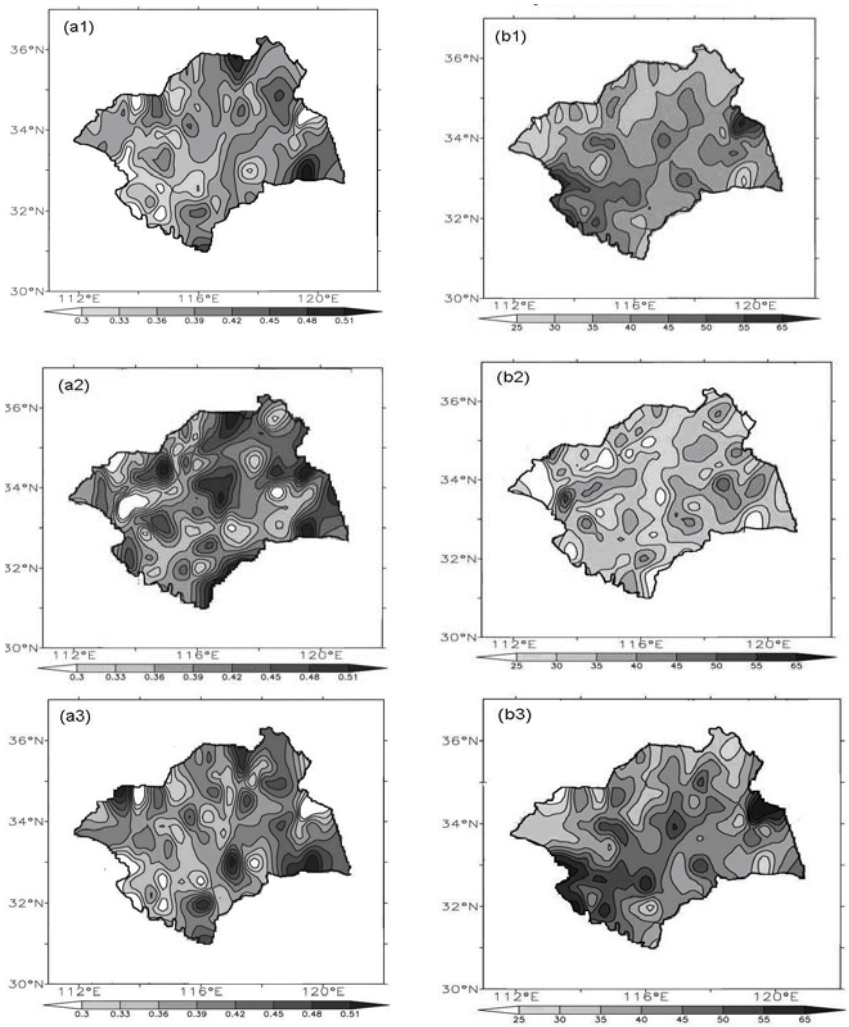

Fig .3 Spatial distribution of shape and scale parameter on rainy days after a dry or wet preceding (a1 and b1), rainy days after a dry preceding (a2 and b2) and rainy days after a wet preceding (a3 and b3), respectively.

The values of shape parameters of three rainy day types were all below 0.5(Fig 3.a1~a3), this is indicating that the Huaihe basin does not belong to shape dominated region. It can be seen clearly (Fig 3.a2~a3) that the distribution of conditional rainy days' shape parameter indicate more details of precipitation distribution which is more approximating the real situation.

It is clear that the values of scale parameters of the Huaihe basin were above 30 (Fig3.b1~b3). As the scale parameter is large, the distribution of precipitation probability shows large variability. Further analysis shows that these scale parameters of such three types have large differences, mostly, i.e. $\beta_1 < \beta_0 < \beta_2$. The amounts of precipitation of the rainy days which has a dry preceding day are smaller than that of a wet preceding day. Under the condition that the rainy day has a dry preceding day, the confluence area of Sha river and Ying river, the eastern part of the Huaihe river and the part stream between Wangjiaba dam and Bengbu station of Huai river of the Huaihe River, the eastern part stream between Bengbu station and Hongze Lake of Huai river, and the downer stream of Huai river below Hongze lake are all the areas of a higher probability of large precipitation amount. Under the condition that the rainy day has a wet preceding day, the eastern part of the Yishu river watershed, the region near the Wangjiaba dam are the center of a higher probability of large precipitation amount.

3.2 Probability distribution of da ily precipitation of unconditional and conditional rainy days

The probability distribution of daily precipitation of certain type of rainy days can be created by using the estimated shape parameter and scale parameter of gamma distribution. Five rain gauge sites, such as Xixian, Fuyang, Shangqiu, Huaian and Lianyungang were investigated as representative stations from the five catchments respectively. To evaluate how accurately the probability density function of gamma distribution reflect the historical situation, here give the gamma distribution density function and sample frequencies of the daily precipitation at representative stations under the condition that the rainy day has a dry preceding day(Fig. 4).

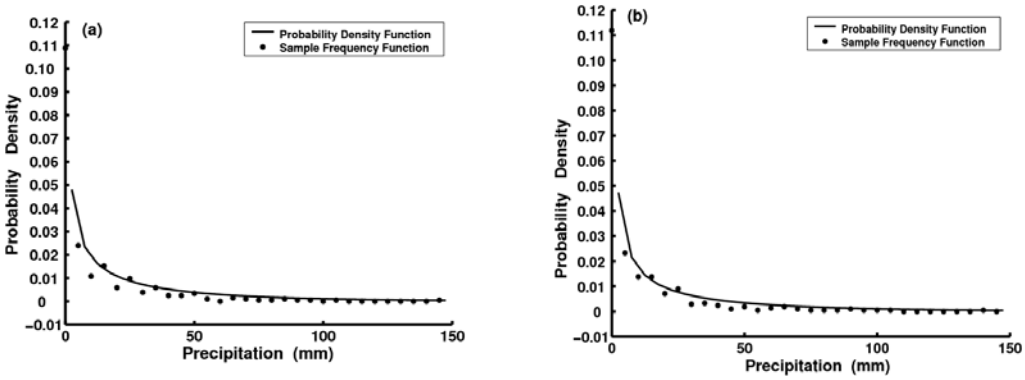

Fig.4 Gamma distribution density function(solid line) and sample frequencies function(dot line) of the daily precipitation under the conditions of a dry preceding day at representative stations of Xixian (a), Fuyang (b), respectively.

Furthermore, both the probability density curve of the gamma distribution and the sample frequency curve present the shape of reverse “J” (Fig. 4). The fitness of the two curves increased with the daily precipitation. As a result, it illustrates that the gamma distribution function can well describe the probability distribution of the daily precipitation under the two conditions. Although the estimation of the gamma distribution parameters is influenced by the content of samples and random vibration

(Wu et al., 2004), the probability density function of gamma distribution can better fit the frequency of the samples by using the daily precipitation records of 28 years in the Huaihe basin .To some extent, it reduced the influence that the random oscillation of the samples caused to the estimate of the probability distribution of daily precipitation.

4 . Conclusion and discussion

From the view of estimated parameters of gamma distribution, Huaihe basin is the "scale-dominated" region where is likely to have variable rain and more extreme events. It illustrates that the extreme more or less rainfall events (i.e. drought or flood) often occurs in the Huaihe basin.

Combining the probability density function of gamma with spatial distribution of scale parameter, it has been found that the precipitation amount of the rainy days which has a dry preceding day is smaller than the ones that have a wet preceding day. Under the condition that the rainy day has a dry preceding day, the confluence area of Sha river and Ying river, the eastern part of the Huaihe river and the part stream between Wangjiaba dam and Bengbu station of Huai river, the eastern part stream between Bengbu station and hongze Lake of Huai river, and the downer stream of Huai river below Hongze lake are all the areas of a higher probability of large precipitation amount. Under the condition that the rainy day has a wet preceding day, the eastern part of the Yishu river watershed, the region near the Wangjiaba dam are the center of a higher probability of large precipitation amount.

Through the Kolmogorov-Smirnov (K-S) test and the comparison between the gamma distribution probability density function of the five representative stations， such as Xixian, Fuyang, Shangqiu, Huaian and Lianyungang station， and the sample frequency of the daily precipitation records, it is proved that the gamma distribution function can be a adequate fitting to the probability distribution of the precipitation in summer of the conditional rainy days, which were given a wet or dry preceding day, of the Huaihe basin. The probability density distribution function *Γ,* to a certain extent, overcomes the influence that the random oscillation of the samples caused to the estimate of the probability distribution of daily precipitation. Applying the gamma distribution to get the probability distribution of maximum amount of daily precipitation in certain days is certainly a future avenue of research.

Acknowledgements

This work was supported by the Research Fund for Commonweal Trades (Meteorology) (Grant number: GYHY200906007 and GYHY201006037).

References (omitted)

THE IMPACT OF NORTH PACIFIC SUBTROPICAL HIGHS UPON ENSO ON THE INTERANNUAL TIMESCALE

LI Yi[1], YANG Xiu-qun[2], HUANG Shi-cheng[1]

(1. Jiangsu Institute of Meteorological Sciences, Nanjing 210008, China;

2. Institute of Severe Weather and Climate, Nanjing University, Nanjing 210093, China)

E-mail: judyliyi@sohu.com

Abstract

Along the subtropics of the Northern and Southern Hemispheres, there exist belts of the subtropical highs. Due to the sea-land terrains, the belts of subtropical high usually split into several cells, and the cells are named subtropical highs. They dominate the activities of the subtropical synoptic systems and locate between the tropical easterlies and mid-latitude westerly. They are the ligament of the interaction between the tropical and extra-tropical circulation system. Some researchers[1-3] suggest that the anomalous subtropical high can lead to abnormal weather and climate, and it's closely related with the monsoon, precipitation, ENSO events, and so on[4,5]. ENSO is the strongest signal[6] of interannual climate variability in the tropical Pacific and has an important impact upon the global interannual climate variability[7,8]. ENSO events are often associated with the anomalous wind in the subtropical trade-wind zone[9], so they are also have very close relationship with the subtropical high system north of the trade-wind zone. In our preliminary study, we also find that the North Pacific subtropical high can impact on ENSO and trigger the occurrence of ENSO events.

In this paper, by using NCEP atmospheric reanalysis data, Hadley center sea surface temperature, and SODA6 oceanic reanalysis data from UMD (University of Maryland), contraposing the whole North Pacific subtropical high system, we first define several indices which quantitatively describe the 500 hPa subtropical high and the SLP subtropical high to analyze the interannual variations of the 500 hPa subtropical high and the SLP subtropical high. Then, we reveal the characteristics of the anomalous SLP subtropical high leading ENSO events and its triggering role for the establishment of an ENSO event on the interannual timescale. Results show that on the interannual timescale, the preceding anomalous SLP subtropical high can trigger the occurrence of ENSO events, and the anomalous surface wind field over the western tropical Pacific associated with the SLP subtropical high plays an important role during the above process by using the methods of correlation and composition.

In Fig 1a, we can know that when SLP subtropical high becomes weak, the corresponding summertime SLP weakens and a cyclonic circulation appears. The subtropical trade wind south of the subtropical high also becomes weak. The strong northwest wind appearing in the western Pacific subtropical high region will influence this area along with the abnormal westerly in the western tropical Pacific. The abnormal westerly may cause the western equatorial Pacific thermocline to deepen, and spread eastward in the form of Klevin wave, causing the SST in eastern equatorial Pacific to arise and the warm SST to develop. Finally, a matured El Nino (DJF(0)) event forms in winter. Comparing the Fig. 1b with Fig.

1c, we can see in Fig. 1b that when the SLP subtropical high weakens, the sea level pressure is anomalously west and weak in the summer(JJA(0)) of the El Nino developing period. At this time, the westerly over the south of subtropical high becomes anomalously strong and extends southward, and converges with the western tropical Pacific westerly anomalies. And then, a significant El Niño event will occur in the following autumn and winter through the above process. In Fig. 1c, when the SLP subtropical high weakens, although the sea level pressure field is also reduced, the location of the cyclonic circulation center moves eastward and northward, and no significant equatorial westerly wind anomalies appears at this time. So, there is no El Niño event in winter. All these have shown that when the SLP subtropical high is anomalously west and its intensity becomes weaker, which will benefit the subsequent occurrence of an El Niño event.

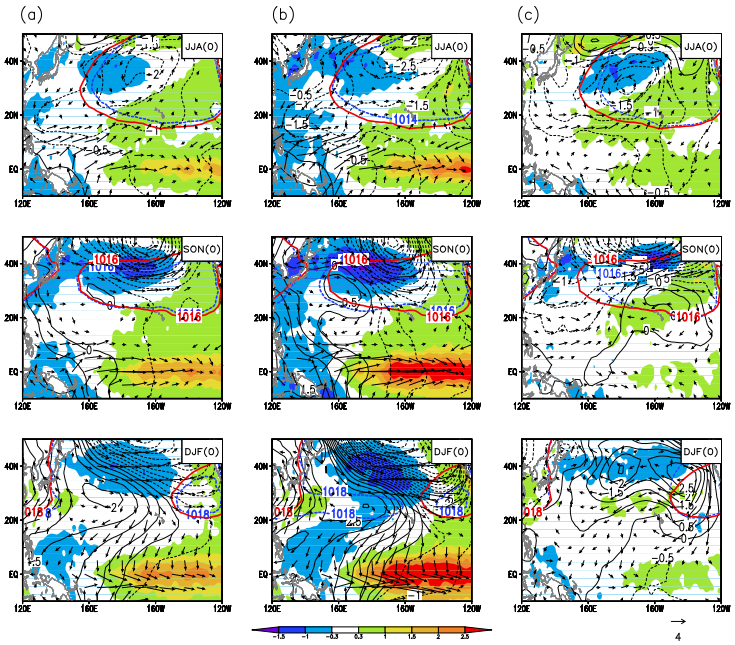

Fig. 1 Composite summertime and following autumntime、wintertime sea level pressure anomaly in hPa（contour）, sea surface temperature anomaly in □（shaded） and surface wind anomaly in m/s（vector）in terms of years with weaker summertime surface subtropical high minus those in terms of years with stronger summertime surface subtropical high. Left panel (a) is based on all of the weaker and stronger summertime surface subtropical high years (17 years), middle panel (b) the years with ENSO events followed (10 years) and right panel (c) the years without ENSO events followed (7 years)

The marine component of the ENSO event is characterized by anomalous warming or cooling of sea surface temperature in the tropical eastern Pacific Ocean. The sea surface temperature changes are mainly caused by the following factors: air-sea heat flux, horizontal advection, vertical advection, diffusion effect and so on. In the previous analysis, we found the subtropical wind anomaly in the early summer which is associated with the subtropical high anomalies played an important role in the formation of ENSO event. When the subtropical high weakens, unusual cyclonic circulation appears over the subtropical region, and the associated wind anomalies affect the subtropical and tropical coastline areas. This subtropical abnormal wind induces the westerly anomalies in tropical regions, which reduce the intensity of cold water upwelling over the tropical area. And the westerly anomalies appear on both sides of equator. According to the Sverdrup relationship, wind stress curl is

negative in the northern hemisphere, it leads the convergence of warm water over equatorial region and influences the distribution of the heat flux. As a result, the equatorial eastern Pacific sea temperature will rise and trigger the El Niño onset. Fig. 2 shows the differences of the physical fields between the strong subtropical high years and weak subtropical high years. Fig. 2a is the composite diagram of the fields' differences under the (JJA0) anomaly in Figure 1b. Fig. 2b and 2c are the surface wind stress and the ocean surface current field anomalies respectively in the summer before the onset of El Niño when the SLP subtropical high appears changes.

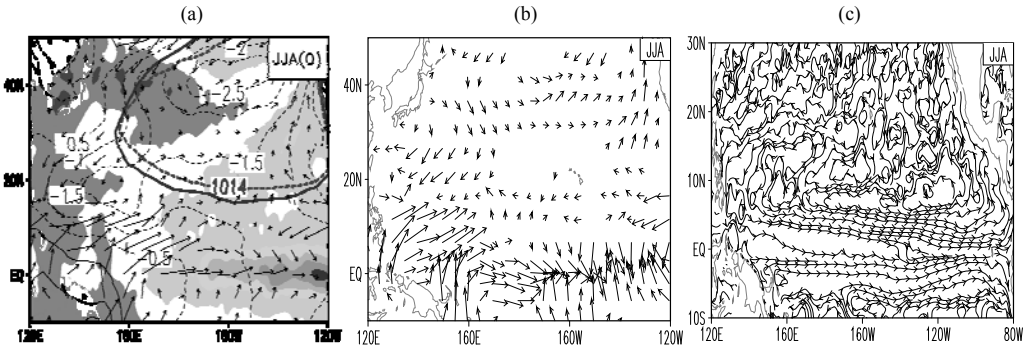

Fig. 2. The composite of summertime (a) surface wind anomaly、(b) surface wind stress anomaly and (c) the ocean surface current anomaly in the El Nino developing year.

References:

[1] ZHU Cong-wen, He Jin-hai, Tan Yan-ke. Characteristics of the northern hemisphere sub-tropical high seasonal splitting over the Asian monsoon sectors and its possible mechanism [J]. J. Trop. Meteor., 2004, 10(02): 160-170.

[2] CHEN Lie-ting, WU Ren-guang. The joint effects of SST anomalies over different Pacific regions on summer rainbelt patterns in eastern China [J]. Chinese Journal of Atmospheric Sciences, 1998，22(05):43-51

[3] WANG Xiao-chun, WU Guo-xiong. The analysis of the relationship between the spatial modes of summer precipitation anomalies over China and the general circulation [J]. Chinese Journal of Atmospheric Sciences, 1997，21(2):161-169

[4] YU Dan-dan, Zhang Ren, Hong Mei et al. A characteristic correlation analysis between the Asia summer monsoon memberships and west Pacific subtropical high [J]. J. Trop. Meteor., 2007, 23(1):78-84

[5] CAI Xue-zhan, Wen Zhen-zhi, Wu Bin. Relationship between west Pacific subtropical high and ENSO and its influence on rainfall distribution of rainy season in FUJIAN [J]. J. Trop. Meteor., 2003，19(1):36-42

[6] YANG Xiu-qun, Guo Yan-juan, Xu Gui-yu et al. Comparison of global spation-temporal structures between interannual and interdecadal climate variations [J]. Journal of NANJING university (natural sciences), 2002, 38(3):308-317

[7] TORRENCE C，WEBSTER P J. Interdecadal changes in the ENSO-Monsoon system [J]. J Climate, 1999, 12(8): 2679-2690.

[8] WANG Cheng-lin, Zou Li. West Pacific subtropical high's interannual variability and relativity to ENSO [J]. J. Trop. Meteor., 2004, 20(2):137-144.

[9] ANDERSON B T. Tropical Pacific sea-surface temperatures and preceding sea level pressure anomalies in the subtropical North Pacific [J]. J Geophys Res, 2003, 108(D23): 4732.

Establishment and Verification of Multi-model Ensemble Forecast System *

Lin Jian[1] Jiang Xing[1] Jiang Yuan[2]

[1]National Meteorological Center, Beijing, 100081

[2]State Key Laboratory of Severe Weather(LaSW) Chinese Academy of Meteorological Sciences, Beijing,100081

Jiangx@cma.gov.cn

Abstract

Using 6h and 24h accumulation precipitation product from T639, Japan, European centre and NCEP of National Meteorological Centre operational as ensemble prediction members, adopting “two steps set” as ensemble prediction method, setting up 6h precipitation multi-model ensemble forecast system initially. The system preprocess the model precipitation products that entering into the integration first, then uses analogy deviation method to determine the similarity of each member, takes gradually merge method to clustering the members , according to the similarity between each member with the other members, determines the weight index of each member, eventually brings out a new multi-model precipitation product. The currently system includes 6 hours step accumulation precipitation product in 48 hours and 24 hours step accumulation precipitation product in 72 hours,

.The research is jointly funded by China Meteorological Administration infrastructural project

two times each day at 0000UTC and 1200UTC. The system does not depend on the historical data ,calculates speedy, which can satisfy the needs for operation. In the mean time, the weather inspection and statistics testing shows that, the product improves the forecast ability for extreme precipitation, and has been applied well in daily operation and weather security services of the Shanghai Expo.

key words: quantitative precipitation forecast(QPF) ; multi-model ensemble forecast; assemble method

Multi-model Ensemble QPF for Southeastern China Using Bayesian Model Averaging

Mu Xiao[1], Yumeng Tao[1], Qingyun Duan[1], Zhang Guoping[2] and Zhao Linna[2]
1- Beijing Normal University, Beijing, China
2- China Meteorological Administration, Beijing, China

Abstract: TIGGE database contains 10-16 day ensemble quantitative precipitation forecasts (QPFs) produced by numerical weather prediction (NWP) models from about 10 NWP centers around the world. How to make use of the different ensemble QPFs has been a subject of intense research interest. This paper discusses how to use Bayesian Model Averaging (BMA) to combine ensemble QPFs from different NWP models. Ensemble QPFs from three NWP models are used in this study: China Meteorological Administration (CMA), Japanese Meteorological Administration (JMA) and US National Center for Environmental Predictions (NCEP). The study area is the Southeastern China. Preliminary results are presented in this paper.

1. Introduction

Numerical weather prediction (NWP) models are an indispensible tool in today's society, providing vital weather information for people so they can plan for their daily activities and prepare for severe weather hazards such as snowstorms, typhoons and flash floods. Traditionally NWPs produce singled valued deterministic forecast products such as quantitative precipitation forecasts (QPFs). More recently, forecast products such as ensemble QPFs from NWPs become popular because these products provide not only the most likely weather forecasts, but also associated uncertainty information. World Meteorological Organization (WMO) sponsored an international research programme known as THORPEX (The Observing system Research and Predictability Experiment), with an overall aim to accelerate improvements in the accuracy of one-day to two-week high impact weather forecasts. One key THORPEX activity is THORPEX Interactive Grand Global Ensembles (TIGGE) project, undertaken by scientists from different NWP centers around the world. TIGGE has assembled 10-16 day ensemble QPFs since 2006 from about 10 NWPs.

The accuracy and reliability of the ensemble QPFs from a given NWP in the TIGGE database vary greatly, depending on the product types, locality and seasonality. It has been shown that even simple arithmetic average of forecasts from multiple models generally outperforms any individual forecast [Weigle et al. 2008]. The advantages of multi-model averaging in enhancing the skill of weather predictions have led to the development of more sophisticated averaging approaches such as the super-ensemble approach [*Krishnamurti et al*., 2000]. Recently, Raftery et al. [2005] developed a Bayesian Model Averaging (BMA) scheme and applied it to generate multimodel ensemble weather forecasts. BMA forecasts weigh individual forecasts from competing models based on how well each model forecasts agree with the corresponding observations. It provides not only the most likely forecasts, but also a realistic description of the forecast uncertainty [Raftery et al.. 2005; Sloughter et al., 2007; Duan et al., 2007].

Here, we are going to employ the BMA scheme developed by Raftery et al. [2007] and apply it to generate multimodel ensemble QPFs by making use of ensemble QPFs from different models in the TIGGE database. The purpose of this paper is to demonstrate if BMA multimodel ensemble QPF is better individual ensemble QPFs. The organization of this report is organized as follows. Section 2 reviews the BMA methodology. Section 3 describes data and experimental design. Section 4 presents the results. Section 5 provides summary and conclusions.

2. The Bayesian Model Averaging (BMA) method:

The BMA scheme generates multimodel probabilistic forecast, $p(y|f_1,\ldots,f_k)$, conditioned on individual ensemble forecasts, $\{f_1,\ldots,f_k\}$, from all models:

$$p(y|f_1,\ldots,f_K) = \sum_{k=1}^{K} \omega_k h_k(y|f_k) \tag{1}$$

where $h_k(y|f_k)$ is the PDF conditioned on f_k ; ω_k is the posterior probability of forecast f_k being the best one.

We can use Logistic regression method to represent the probability of rain on a given day:

$$\text{logit } P(y=0|f_k) \equiv \log \frac{P(y=0|f_k)}{P(y>0|f_k)} = a_{0k} + a_{1k} f_k^{\frac{1}{2}} + a_{2k}\delta_k \tag{2}$$

where the $P(y>0|f_k)$ means to rain, and δ_k is a predictor, equal to 1 if f_k= 0 and equal to 0 otherwise.

Given a raining day, we use Gamma distribution to fit the precipitation amounts:

$$g_k(y|f_k) = \frac{1}{\beta_k^{\alpha_k}\Gamma(\alpha_k)} y^{\alpha_k - 1} \exp\left(-\frac{y}{\beta_k}\right) \tag{3}$$

The means and variances of the fitted Gamma distributions can be estimated by $\alpha_k = \mu_k^2/\sigma_k^2$ and $\beta_k = \sigma_k^2/\mu_k$, where $\mu_k = b_{0k} + b_{1k} f_k + b_{2k}\delta_k$ and $\sigma_k^2 = c_0 + c_1 f_k$. Incorporating Eqs. (2) and (3) into Eq. (1), the BMA probabilistic QPF can be expressed as:

$$p(y|f_1,\ldots,f_K) = \sum_{k=1}^{K} \omega_k [P(y=0|f_k) I(y=0) + P(y>0|f_k) g_k(y|f_k) I(y>0)]$$

$$\text{s.t.}\begin{cases}\text{logit}\,P(y=0|f_k) \equiv \log\frac{P(y=0|f_k)}{P(y>0|f_k)} = a_0 + a_1 f_k^{\frac{1}{3}} + a_2\delta_k \\ g_k(y|f_k) = \frac{1}{\beta_k^{\alpha_k}\Gamma(\alpha_k)} y^{\alpha_k - 1}\exp\left(-\frac{y}{\beta_k}\right)\end{cases} \tag{4}$$

a_{0k}, a_{1k}, a_{2k} and b_{0k}, b_{1k}, b_{2k} can be estimated for all models using forecasts and observations from the training period. As for c_0, c_1 and ω_k, we can use expectation-maximization (EM algorithm) to get the estimated values.

3. Experimental design and data

We obtained ensemble QPFs from three NWPs in the TIGGE database (see Table 1). We restricted our study area to Fujian Province in the Southeastern China. For demonstration purpose, we used two months of data to train the BMA (from 15th June to 14th August, 2009).

Table 1 Models used

Models	Source	Ensemble size
BABJ	China Meteorological Administration	15
KWBC	National Center for Environmental Prediction	21
RJTD	Japan Meteorological Agency	51

4. Results and discussions

Fig. 1 displays the raw ensemble QPFs of the three models along with observational data during the training period. The solid line represents the observation. The box and whisker plots indicate the means, plus/minus one standard deviations, and maximum and minimum of the raw ensemble QPFs. A good ensemble forecast should have as many observations inside the ensemble ranges as possible.

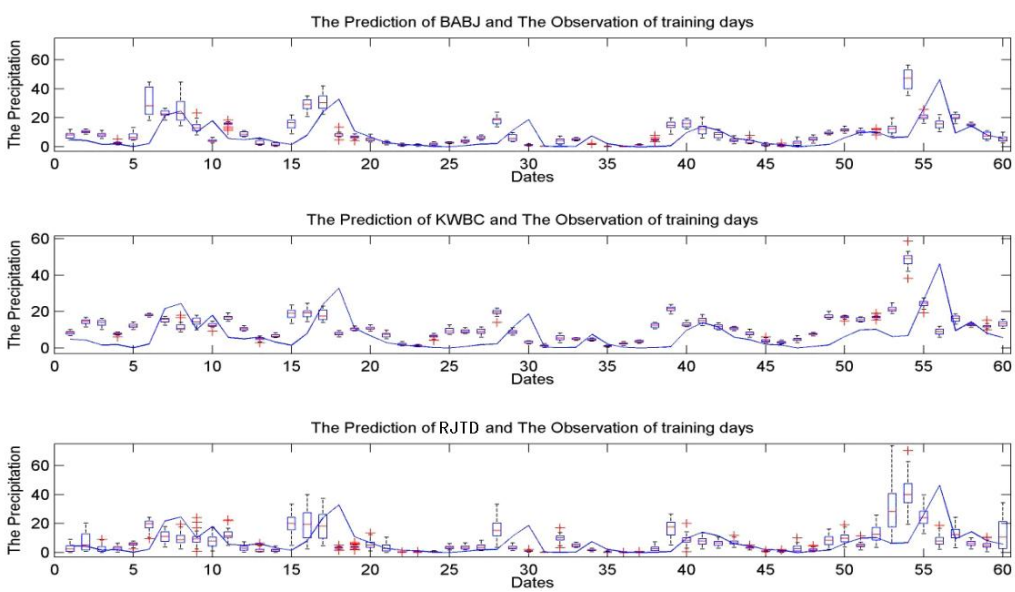

Fig.1. Forecasts compared with observations of 60-training days.

Employing the BMA model presented in Section 2, we conducted a simple numerical study to generate BMA multimodel ensemble QPFs. By using 60-days of training data to fit the Logistic and Gamma models, we estimated BMA weights and all of parameters for the BMA model (Table 2).

Table 2 The weights and parameters of the BMA model

	weights	a_0	a_1	a_2	A	B	c_0	c_1
BABJ	0.756	0.104	-0.723	0.456	1.235	0.26	0.495	0.242
RJTD	0.146	-0.31	-0.499	0.656	1.355	0.228	0.495	0.242
KWBC	0.098	0.31	-0.725	0.11	1.363	0.171	0.495	0.242

Table 2 shows that BABJ model receives the highest weights of the three, while KWBC model receives virtually none, suggesting that BABJ has the highest skill among the models and KWBC model has no skill at all. A visual inspection of Fig. 1 indicates that the spread of KWBC is very small and observations are mostly outside the KWBC ensemble ranes. This implies that KWBC is overconfident.

To compare the performance of the BMA produced ensemble QPFs and the raw ensemble QPFs from the three models, we computed several performance metrics including RMS (Root of Mean Square), MAE (Mean Absolute Error) and CRPS (Continuous Ranked Probability Score) (For all of these performance metrics, smaller values imply better performance). The comparison results are shown in Table 3.

Table 3 The RMS, MAE, CRPS values of raw and BMA ensemble QPFs

RM		S	MAE	CRPS
Raw Models	BABJ 8407.1		11.96	5.18
	KWBC 7189.0		11.75	6.49
	RJTD 2389.3		6.95	10.70
BMA 204.2			1.37	3.18

Table 3 shows the advantages of BMA ensemble QPF over the individual raw QPFs as all of the performance metrics of the BMA ensemble QPFs are clearly superior to those the raw ensemble QPFs. RMS, MAE and CRPS are indicators of accuracy. In order to illustrate how well the ensemble QPFs are calibrated against the observations, we calculated the 90% confidence intervals of the different ensemble QPFs. For a well-calibrated ensemble, 90% confidence intervals should contain approximately 90% of the observations. Table 4 exhibits the calibration results for the BMA and raw ensemble QPFs. The results indicate that BMA ensemble QPF has the best calibration as it is closest to 90%, while KWBC ensemble QPF is the least calibrated.

Table 4 The number of observations inside the 90% confidence intervals

BMA		BABJ	KWBC	RJTD
Percentage (%)	0.81	0.16	0.08	0.49

5. Summary and Conclusions

We presented a BMA scheme developed by Raftery et al. [2005] and Sloughter et al. [2007] and applied it to generate multimodel ensemble QPFs for Fujian Province of the Southeastern China. With 2 month of training data, we estimated the BMA weights and BMA model parameters. Among the three NWPs, the BABJ model seems to perform better than the other two models based on the training data. The spread of RJTD model is very small, but poorly calibrated. The BMA ensemble QPFs are more accurate and better calibrated than the raw ensemble QPFs generated by the NWPs. This study suggests that BMA is a very promising statistical tool to post-processing the raw ensemble forecasts.

Acknowledgement: The authors acknowledge financial support provided by Chinese Ministry of Science and Technology 973 Research Program [Grant #: S2009041002].

References:

Duan, Q., N. K. Ajami, X. Gao, and S. Sorooshian (2007), Multi-model ensemble hydrologic prediction using Bayesian model averaging, Adv. Water Resour., 30, 1371–1386, doi:10.1016/j.advwatres.2006.11.014.

Raftery, A. E., T. Gneiting, F. Balabdaoui, and M. Polakowski (2005), Using Bayesian model averaging to calibrate forecast ensembles, Mon. Weather Rev., 133, 1155–1174, doi:10.1175/MWR2906.1.

Sloughter, J.M., A.E. Raftery, T. Gneiting, and C. Fraley (2007), Probabilistic Quantitative Precipitation Forecasting Using Bayesian Model Averaging, Mon. Wea. Rev., 135, 3209-3220.

Weigel, A.P., M.A. Linniger, and C. Appenzeller,(2008), Can multi-model combination really enhance the prediction skill of probabilistic ensemble forecasts? *Quart. .J. Roy.Meteor. Soc*., 134, 241-260.

Verification of QPFs in hydrological catchments applying the novelty SAL technique utilizing QPEs based on a local analysis system and radar data

Pertti NURMI, Sigbritt NÄSMAN and Erik GREGOW

Finnish Meteorological Institute
P.O. Box 503, 00101 Helsinki, Finland
pertti.nurmi@fmi.fi

1. Introduction

Object-oriented or feature-based verification techniques are well suited for the verification of spatial Quantitative Precipitation Forecasts (QPF) in hydrological basins that have clearly defined lateral boundaries. SAL (acronym for Structure – Amplitude - Location), developed by Wernli et al. (2008), is a relatively new object-based verification measure which has gained rather wide popularity in Europe since its introduction. This technique has been applied for hydrological catchment verification at the Finnish Meteorological Institute (FMI) quite actively (Nurmi and Näsman, 2008, 2009a,b, 2010).

SAL has three distinct components which consider the aspects of structure (S), amplitude (A), and location (L) of a precipitation field in a pre-defined domain, in our case a relatively large (30 000 square km) river catchment in the southwestern part of Finland (Figure 1). The amplitude component (A) measures the relative deviation of the domain-averaged QPF from the observations within the domain. Positive A values indicate an over-estimation of total precipitation and, consequently, negative values indicate under-estimation. Regarding the components S and L, coherent precipitation objects are identified separately in the forecast and in the observations, but with no matching to each other being performed of these objects. The location component (L) combines information about the displacement of the forecast precipitation field's center of mass and about the error in the weighted-average distance of the precipitation objects from the total field's center of mass. The structure component (S) produces positive values if the precipitation objects are too large and/or too flat, whereas negative values are the outcome when the objects are too small and/or too peaked. In an idealistic situation, a perfect forecast would produce zero values for each of the components, S=A=L=0. A comprehensive account on the SAL technique is given in Wernli et al. (2008).

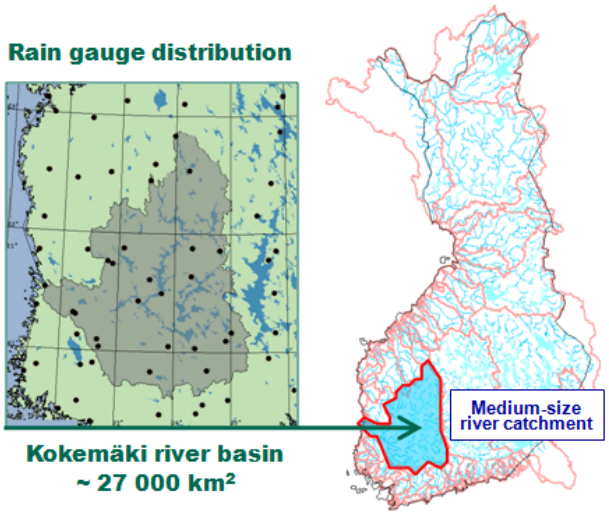

Figure 1. Kokemäki river catchment in Finland, with the rain gauge distribution enlarged on left

Typically (e.g. in the case of Wernli et al., 2008), rain gauge observations are being used as "the observed truth" in SAL verification. One may want to argue that the spatial coverage of a given rain gauge network is not sufficient for realistic precipitation verification. The situation naturally varies from country to country and from area to area. The Finnish rain

gauge coverage is definitely not satisfactory to enable reliable verification. This can be confirmed by looking at Figure 1, where also the rain gauge distribution is shown within the domain under study.

The “observed truth”, or the best “truth estimate”, is a fundamental issue in all forecast verification activities and every verification application. Originally, simply rain gauge data were exploited in analyzing and quantifying the observed state of precipitation. However, there remains a big representativeness issue due to the potential scarcity of observing rain gauge stations within the given domain(s) or catchment(s). To broaden our perspective on precipitation verification and to overcome the representativeness problem, radar-derived Quantitative Precipitation Estimates (QPE) based on FMI’s operational weather radar network were first applied. Unfortunately, also radar data exhibit well-known (and also not-so-well-known) pitfalls. The latest addition to the verification artillery is to use QPEs based on FMI’s pre-operational in-house modification of the Local Analysis and Prediction System (LAPS) (Albers et al., 1996).

The LAPS version of FMI produces three-dimensional analysis fields of a number of weather parameters, precipitation being one of them. The LAPS products are used mainly in now-casting but utilization of LAPS analyses for verification purposes was considered of additional value of the application. LAPS adopts data fusion to perform a high-resolution analysis using statistical methods on top of a coarser resolution background state. The first-guess background field is the latest ECMWF forecast with its current horizontal resolution of c. 16 km. The fine-scale structures of the resulting 3D-analyses are extracted from the observations. Therefore, LAPS relies strongly on the existence of high-resolution observations and especially on the availability of remote sensing data. The present FMI implementation of LAPS is capable of processing and ingesting several types of in-situ and remotely sensed observations like Synop/Metar and road weather observations, sounding data, radial radar winds/reflectivity (C-band) and various satellite data. There are currently two LAPS domains being operated and producing hourly analyses, one covering the Helsinki Testbed domain with a 1 km resolution, and the other covering the whole of Finland with a 3 km resolution.

The SAL verification methodology was applied in the given hydrological river catchment (Figure 1) to deterministic QPFs originating from ECMWF and from two configurations of FMI’s operational regional limited area HIRLAM model. The RCR (Reference) version of HIRLAM runs at a similar 16 km resolution as the ECMWF deterministic forecasting system, whereas the meso-beta scale, MB71, version of HIRLAM boasts a 7.5 km horizontal resolution. It is the operational practice of FMI’s shift forecasters to produce grid-edited QPFs based on the NWP guidance (ECMWF, HIRLAM) at their disposal. These QPFs, referred to as MET_Edit in this paper, representing forecasters’ interpretation (or end product) of expected precipitation patterns were used as additional verifiable forecast products, applying SAL.

Following the introduction, we present SAL verification results for QPFs based on four origins: (i) ECMWF, (ii) HIRLAM_RCR, (iii) HIRLAM_MB71, (iv) MET_Edit, using QPEs from three sources: (a) rain gauges, (b) radar, (c) LAPS. Statistical results are presented as seasonal averages and the data coverage is two years, from autumn 2008 to summer 2010.

2. Results

Figure 2a shows a case example from summer 2010, highlighting how different a QPE field can look like based on available, or used, observational data. The left-hand-side precipitation distribution is based on rain gauge data, only, utilizing the Kriging analysis

method. One can see two bulls eye rainfall maxima at two individual gauge stations, with more than 50 mm of precipitation during the given 24-hour period. Nothing of them is seen on the radar-derived precipitation field in the center panel of the figure. The right-hand-side LAPS generated QPE has much of the same elongated rain band structure as the radar based distribution. However, the LAPS analysis seems to have captured some of the features of the northern rainfall maxima recorded by the rain gauge at that site. The QPFs produced for this summer case by the three models, ECMWF, HIRLAM_RCR and MB71, presented in Figure 2b, show marked differences. As expected, the coarser models (ECMWF, RCR) have less fine-scale details than the MB71 version of HIRLAM.

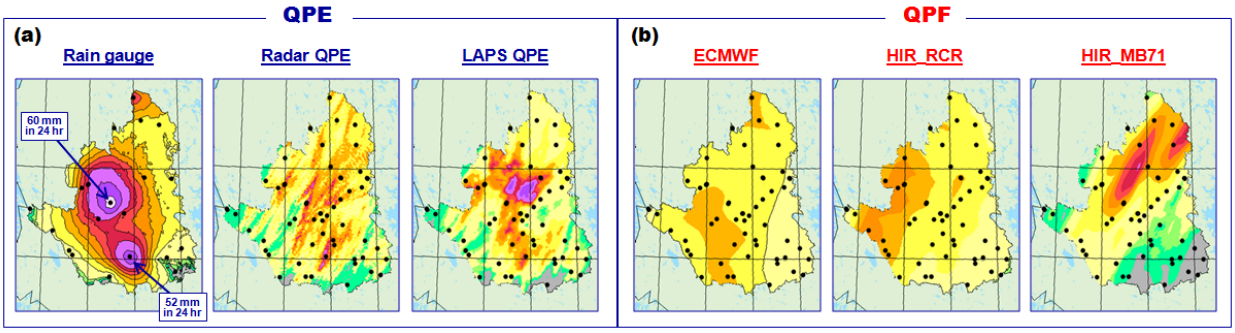

Figure 2. 24-hour accumulated rain gauge (Kriging), radar-derived and LAPS based QPE (a), and corresponding ECMWF, HIRLAM_RCR and MB71 QPFs (b), 14 July 2010.

From the SAL statistics in this case (not shown) it is difficult to make too strong conclusions. Each of the models was verified against gauge, radar and LAPS analyses, individually, i.e. we had nine pairs of comparisons. The best S (structure) scores (i.e. smallest values) were assigned to MB71, with S values of -0.27, 0.43 and 0.40 for the gauge/ radar/ LAPS reference, respectively. The highest S values were reported for ECMWF.

The amplitude (A) and location (L) components are more of a mixed bag and there is no clear signal of which model would perform best in this summer case. For the amplitude, RCR would score best and MB71 worst when using gauge comparison. When comparing against radar or LAPS the differences in A are very small and the absolute values also small, indicating good performance. The L values are generally very small for all models and when using whatever comparison. This is a feature we have noticed also in our earlier studies and this SAL behavior requires more thorough investigation.

The most typical way to present SAL statistics is to construct a two-dimensional, x-y plot of S (x-axis) vs. A (y-axis), where each individual plot marker indicates one S-L value pair for each 24-hour precipitation event during a given time period. Figures 3a and 3b show such a scatter plot for the summer period of 2010 by using radar and LAPS as the verifying “truth”, respectively. It should be noted that we had for the very first time the possibility to utilize LAPS based QPE in verification during the summer of 2010.

One can immediately see the generally very high S values. Using LAPS as the verifying QPE produces somewhat smaller values than the radar-derived QPE. It is satisfactory to note that the, relatively speaking, best scores (i.e. lowest S values) are gained by the finest scale MB71 model, with average values of 0.99 and 1.29 for LAPS and radar comparison, respectively. The large S values are probably the result of not up-scaling our QPEs to the model resolutions, i.e. the results at least partly reflect implications from comparing QPFs and QPEs of differing resolutions.

The best amplitude (A) scores during summer 2010 (Figures 3a and 3b) were achieved, on average, by the meteorologists’ grid-edited forecasts, with no bias (i.e. A ~ 0) visible.

It would be an attractive result if the meteorologists were able to add value on the NWP guidance they're utilizing in their forecasting process. However, the deviation around the mean A is large. There appears to be some over-estimation of the precipitation amplitude for all of the models in this comparison.

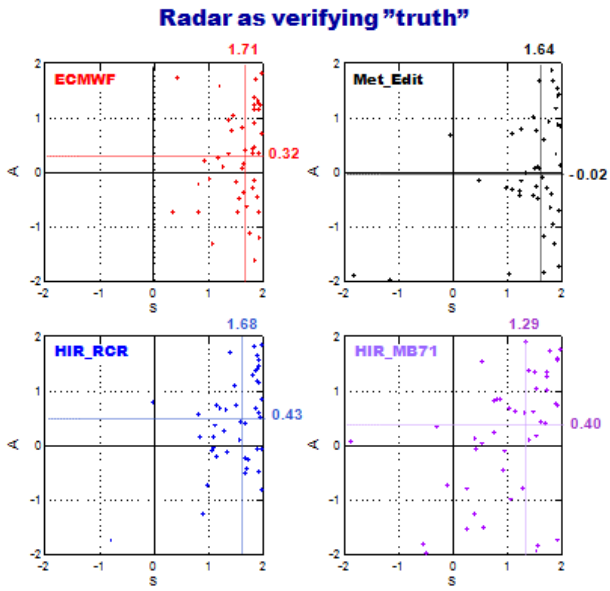

Figure 3 (a) S vs. A plots in the Kokemäki river catchment for individual 24-hour precipitation accumulations during summer 2010 for ECMWF, HIRLAM RCR and MB71, and for human edited forecasts, MET_Edit using Radar QPE as verifying "truth".

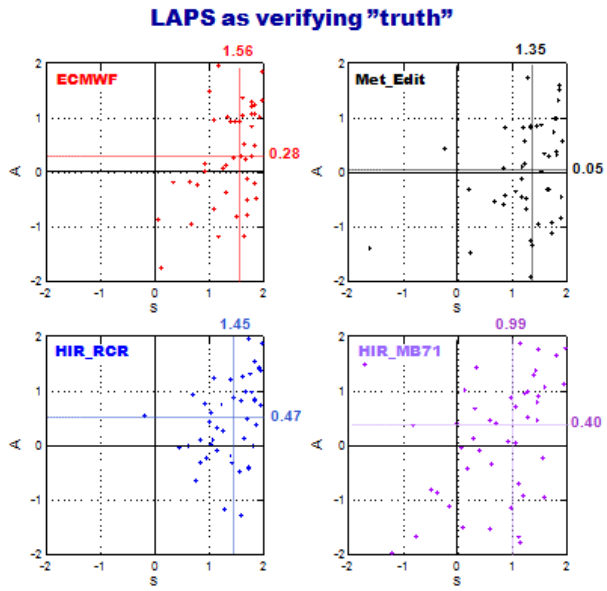

Figure 3 (b) As Figure 3 (b) but using LAPS QPE as verifying "truth".

Aggregated seasonal SAL statistics from autumn 2008 until summer 2010 are shown as Table 1. Each of the four rows represent seasonal SAL component averages for the four QPF products when using radar-derived QPE as verifying analyses. The last box on the right shows, for comparison, SAL statistics based on LAPS QPE. As mentioned earlier, this was the first time when such analyses were available for verification purposes. The best/worst component values are indicated by green/red numbers. One can see most red numbers of the structure (S) component systematically associated with ECMWF and most of the green ones with the high resolution MB71 model. This is in line with what was seen already in the scatter plots of Figure 3 for summer 2010. Interpretation of the results for the amplitude (A) is not at all as clear as the situation seems to be somewhat different from season to season. The location (L) values are generally very small and the best/worst scores are, therefore, not highlighted at all.

Table 1. Aggregated seasonal SAL statistics for ECMWF, HIRLAM RCR and MB71 and for human edited forecasts, MET_Edit, using radar QPE as verifying "truth". For summer 2010, corresponding statistics are shown for LAPS QPE (rightmost column).

	Autumn 2008			Winter 2009			Spring 2009			Summer 2009			Autumn 2009			Winter 2010			Spring 2010			Summer 2010			Summer 2010			
	Radar			Radar			Radar			Radar			Radar			Radar			Radar			Radar			LAPS			
	S	A	L	S	A	L	S	A	L	S	A	L	S	A	L	S	A	L	S	A	L	S	A	L	S	A	L	
ECMWF	1.00	.69	.16	1.28	.11	.14	1.54	.52	.38	1.73	.69	.37	1.53	.30	.32	1.38	-.45	.13	1.04	.32	.22	1.71	.32	.44	1.56	.28	.37	ECMWF
HIR_RCR	.97	.79	.17	1.09	-.05	.14	1.47	.57	.32	1.66	.70	.37	1.40	.46	.30	1.16	-.45	.14	1.11	.44	.15	1.68	.43	.39	1.45	.47	.29	HIR_RCR
HIR_MB71	.70	.48	.17	.84	-.31	.16	1.29	.31	.29	1.49	.41	.35	1.22	.31	.22	.98	-.72	.14	.86	.29	.18	1.29	.40	.42	0.99	.40	.33	HIR_MB71
MET_Edit	.93	.40	.18	.97	-.61	.18	1.43	.09	.29	1.65	.28	.37	1.33	-.03	.26	1.15	-.57	.14	1.13	.18	.20	1.64	-.02	.42	1.35	.05	.36	MET_Edit

3. Conclusions

SAL behavior is still somewhat unclear to the authors. Some further investigations, especially into the location component (L), are called for. Comparison of SAL with some of the traditional verification scores as well with some other features-based verification measures (e.g. CRA, MODE) might be an interesting topic for further study.

The SAL verification methodology has not yet been adopted by the hydrological community in Finland and presumably not elsewhere, either. Therefore, its potential operational implementation remains an open issue. Also, meaningful QPF thresholds (e.g. for 24-hour precipitation accumulations) for given hydrological basins would need to be defined. The threshold of only 0.1 mm per 24 hours applied in this study is definitely not one that would per se be relevant for any hydrological action taking.

QPE based on LAPS analyses is under active research at Finnish Meteorological Institute, and LAPS awaits operational implementation in the foreseeable future. Understanding of observation uncertainty is one of the key issues in forecast verification. Much more research is required in this context.

The overall statistics show that increase in model resolution seems to produce (relatively speaking) better SAL scores, at least for the structure component S. Comparisons between the LAPS vs. radar-based "truth QPE", which was performed for the very first time in summer 2010 in Finland, do show considerable differences in the verification results, and this would signal that the QPE issue is not yet being solved.

References

Albers, S., J. McGinley, D. Birkenheuer, and J. Smart, 1996: The Local Analysis and Prediction System (LAPS): Analyses of clouds, precipitation, and temperature. *Wea. and Forecasting*, **11**, 273-287.

Nurmi, P. and S. Näsman, 2008. QPF Verification in Hydrological Catchments with the Object-oriented SAL Measure. *American Geophysical Union (AGU) Fall Meeting (San Francisco, 15-19 December 2008)*. http://www.agu.org/meetings/fm08/index.php/Program/HomePage

Nurmi, P. and S. Näsman, 2009a. SAL in hydrological catchments. *4th International Verification Methods Workshop (Helsinki, Finland, 8-10 June 2009)*. http://space.fmi.fi/Verification2009/Booklet_FINAL_2009-05-29.pdf

Nurmi, P. and S. Näsman, 2009b. Object-oriented SAL Verification in Hydrological Catchments of Finland. *Post-processing and Downscaling Atmospheric Ensemble Forecasts for Hydrologic Applications, HEPEX Workshop (Toulouse, France, June 15-18, 2009)*. http://hydis8.eng.uci.edu/hepex/Workshops/postprocesswksp/postprocwksp.html

Nurmi, P. and S. Näsman, 2010. Verification Activities within COST Action 731: QPF verification in hydrological catchments utilizing the SAL technique and radar-derived QPE information. *6th European Conference on Radar Meteorology (ERAD) (Sibiu, Romania, 6-10 September 2010).*

Wernli, H., M. Paulat, M. Hagen and C. Frei, 2008: SAL _ A Novel Quality Measure for the Verification of Quantitative Precipitation Forecasts. *Mon. Wea. Rev.,* **136,** 4470-4487.

Analysis on a permanent elongate convective System of rainfall

PuMeijuan[1] QinDanyu[2] XiaYing[1] Zhangxuerong[3] XieLingyun[1] Zhang bei[1]

(1 Jiangsu Provincial Meteorological Bureau, Nanjing, 210008，)
(2 National satellite Meteorology Center, Beijing, 100081)
(3 Nanjing University of Information Science & Technology, Nanjing, 210044)
Email:pumeijuan@126.com

1. Introduction

Mesoscale Convective System (MCS) is one of the important weather system that may cause thunderstorm, gale, tornado, rainstorm and many other disastrous weather. Maddox defined MCC from the MCS for the first time by using satellite images in late 1980s. Anderson and Arritt defined another kind of MCS: a Permanent Elongate Convective System (PECS)—a flat meso-α system which has a longer life cycle and an eccentricity of 0.2-0.7. Data of automatic weather stations(AWS), NCEP/NCAR global $1^o \times 1^o$ reanalysis and satellite data are used to investigate the dynamical and thermo-dynamical mechanism of a PECS which cause the heavy rainfall in center of Jiangsu Province on July 4-5th, 2003. The results indicate some new important references for rainstorm forecasting.

2. General synoptic situation

From 4th 20:00 to 5th 20:00 July, there was a regional heavy rainfall process occurred in the middle of Jiangsu Province. 31 counties' daily precipitation reached 50mm, in which 23 counties' daily precipitation greater than 100mm. Nanjing reached 207.2mm and break the record since 1905. And Yangzhou' daily rainfall reached Unprecedented 261.1mm.

For the hourly GOES-9 satellite cloud top temperature(TBB), we defined $T_{BB} \leq -32$℃ as convective cloud , $T_{BB} \leq -52$℃ as stronger convective cloud and $T_{BB} \leq -70$℃ as the most strongest convective cloud region of this process. It shows the convective cloud($T_{BB} \leq -32$℃) is the main meso-scale influence system and exhibit typical permanent elongate convective System characteristics, the eccentricity is 0.5-0.6. The position and allocation of up and low level jet stream, shear line on 700hPa and 500hPa, the edge of subtropical high on 500hPa and the convergence line of MeiYu front provided advantageous environmental conditions for PECS development.

3. Analysis on the activities and the caused rainfall of the PECS

According to the hourly T_{BB} contour charts from 20:00 4th to 20:00 5th , we can find six PECS clouds which affected on this strong rainfall process.

As the 2nd PECS cloud for an example, there were 4 scattered comma convective clouds born in the weak convective area in middle-eastern of AnHui Province at 23:00 4th July, which developed to be PECS at 00:00 5th in the course of moving eastward. Meanwhile, T_{BB} dropped from -62℃ to -70℃. Then the clouds developed quickly and at 3:00 5th and became a permanent elongated shape, of which the area of $T_{BB} \leq -32$℃ reached 171561 square kilometers. Then the cloud kept on extending southeastward. At 03:00 5th, the 3rd clouds moved eastward and combined with the 2nd cloud, which resulted in an intensive PECS developed rapidly, T_{BB} got below -75℃. The area of $T_{BB} \leq -32$℃ is 229770 square kilometers At 06:00 5th. Meanwhile, the meso-β clouds corresponding to the $T_{BB} \leq -70$℃ area of the 3rd cloud developed quickly. The MβEC clouds corresponding to the $T_{BB} \leq -70$℃ area of 2nd cloud moved southeastward. At the 9:00 5th, the whole clouds kept on moving eastward and became

weaker, and at the 13:00 5th the cloud moved out of JiangSu Province. The MβEC clouds of T_{BB}≤-70℃ lasted for 14 hours and weakened to the clouds of T_{BB}≤-52℃. And at 17:00 5th ,the clouds of T_{BB}≤-52℃ lasted for 17hours and disappeared over the sea.

The moving eastward and combination of the 2nd and 3rd cloud is the main system which causing the rainfall along the YangZi River and in the south area in JiangSu Province. The rainfall happened in Nanjing during the two clouds combined. The development can be seen as 4 phases: born phase(23:00 4th ～00：00 5th), developing phase(01:00～05:00 5th) , developed phase(06:00～08:00 5th) and perishing phase(09:00～13:00 5th). The phase during 01:00～05:00 5th was the concentrated rainfall phase in Nanjing, and at the 02:00 5th the minimum T_{BB} was below -75□. At 03:00 5th, the hourly rainfall was 57.3mm and 49.6mm in Jiangpu ang Nanjing respectively. The peak value of the rainfall is corresponded with the valley value of the minimum TBB. The rainfall and the TBB had negative correlation, i.e. lower the TBB is, stronger the precipitation is. The PECS going through developing and weakening with moving eastward, it caused heavy rainfall in YangZhou,ZhenJiang ,ChangZhou and NanTong.

From the evolution of the clouds above, the PECS has a distinct character that is the MβEC clouds lining along the direction from southwest to northeast and new clouds being born and back-building. The clouds distribution and direction have correspondence with the shear line in low level and have important relation with the sustainment of the shear line and beneficial dynamic and thermal conditions.

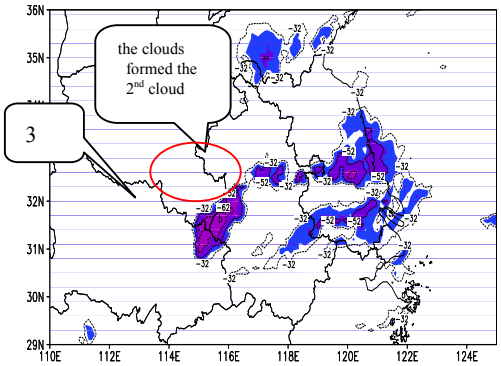

Fig1. T_{BB} at 23:00 4th July

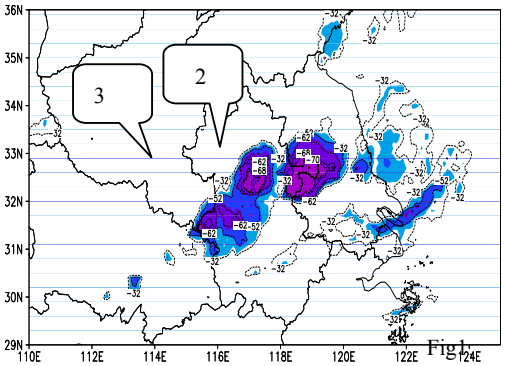

Fig2. T_{BB} at 00:00 5th July

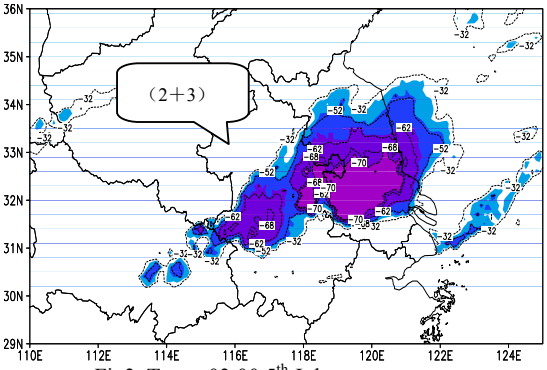

Fig3. T_{BB} at 03:00 5th July

4. the dynamic and thermal conditions of PECS development.

The PECS was excited and developed in the north edge of 500hPa subtropical high and at right entrance of the 200hPa up-level jet stream, where the distance from the ridge of subtropical high about of 7-8 latitudes. Meanwhile, the PECS located at the left of the southwest low-level jet stream on 700hPa and 850hPa or the south of the shear line. The up-level divergence, low-level convergence and strong ascending motion formed very important conditions that can prompt the meso-scale system

PECS grow. The evolution of meso-scale PECS relates well to the evolution of positive vortex belt. The meso-scale PECS cloud cluster develops strongly because of the strong vertical motion caused by the vertical development of the nearby vortex belt. And it will be weaken or disappear when the vortex belt inclines, which results in the vertical motion weakening, and the related rain terminates at the same time.

The low-level moisture and warm instability energy accumulation provided the energy for develop of the PECS. PECS and the heavy rainfall area is in the high value area of K>34℃, the heavy rain center moving towards as similar as the big value of K>36℃. the helicity coupled the vertical velocity with vertical vorticity, which shows effectively the potential instability happen. Over the rainfall area ,the middle-low level is the positive helicity area, that the positive value center reach $8\times10^{-6}m/s^2$ near the 600 hPa. The up level is the negative helicity area ,which the value center reach $-5\times10^{-6}m/s^2$. The occurrence and development of the heavy rainfall and PECS is in correspondence similarly with helicity space distribution.

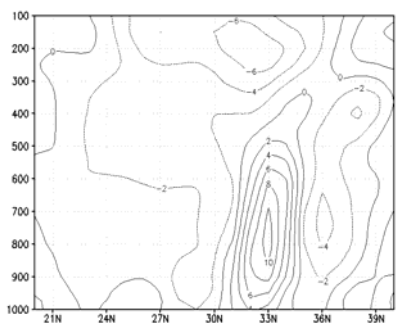

Fig 4. vertical section along 119ºE of vorticity at 08:00 5th July

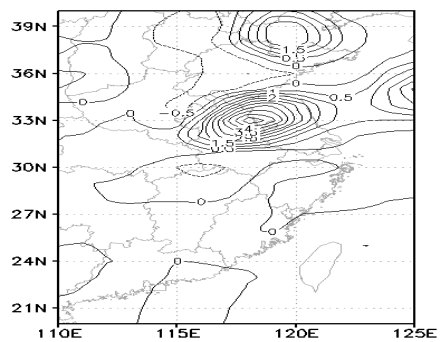

fig5 helicity on 700hPa at 02:00 5th July in 2003

5. Conclusions

(1)The PECS causing the JiangSu heavy rainfall is made up of many MβEC clouds which corresponding to the low-level shear line, and lining along the direction from southwest to northeast. And new clouds are born and back-building which have merged into PECS. The distribution and direction had correspondence with shear line in low level.

(2) The heavy rainfall areas matched with TBB<-70□, lower the TBB is, stronger the precipitation is. During the mature period, the minimum temperature is below -75□, the convection break through the troposphere.

(3)The strong up-level divergence,low-level convergence and ascending motion stimulated the meso-scale convection system in MeiYu front. The cyclonic vorticity which built up the cumulus convection activity was due to the PECS being with the positive vorticity region of the band area corresponding with the shear line. The evolution of meso-scale PECS relates well to the evolution of positive vortex tube. The Meso-scale PECS cloud cluster develops strongly because of the strong vertical motion caused by the vertical development of the vortex tube nearby. And it will be weaken or disappear when the vortex tube inclines, which results in the vertical motion weakening, and the related rain terminates at the same time.

(4)PECS and the heavy rainfall area is in the high value area of K>34□, the heavy rain center moving towards as similar as the big value of K>36□ . The helicity coupled the vertical velocity with vertical vorticity ,which shows effectively the potential instability happen. The occurrence and development of the heavy rainfall and PECS is in correspondence similarly with helicity space distribution.

3rd Conference on QPE /QPF and Hydrology. World Meteorological Organization, Nanjing, China, Oct.18-22,2010.

Radar-based Quantitative Precipitation Estimation for the Cool Season in Mountainous Regions

Youcun Qi*[1,2], Jinzhong Min[2], Jian Zhang[1], David Kingsmill[3], Kenneth Howard[1]

[1]NOAA/National Severe Storms Lab

[2]Nanjing University of Information Science and Technology

[3]NOAA/Earth System Research Lab

1 Introduction

This paper presents a case study of radar-derived quantitative precipitation estimation (QPE) for the cool season in the complex terrain of California as shown in Fig.1, with a focus on developing a VPR correction algorithm for orographically enhanced precipitation processes. It was commonly observed that precipitation amounts increase with distance up a mountain slope when a deep, moist layer of air rises over the mountain barrier. The increase is more significant with higher freezing levels since condensed moisture requires time to accumulate on particles before they reach the ground. The case to be discussed occurred on 13-14 October 2009 in the central and northern California. At the beginning of 13th of October 2009, a very wet and windy storm struck central and northern California. This storm was fueled by unusually strong upper jet energy across the Pacific and a surge of tropical moisture from former super typhoon Melor, which struck Japan earlier on the 8th of October 2009. It brought intense precipitation to the central and northern California. Rainfall estimations are computed from WSR-88D observations with the developed VPR correction algorithm. For this winter storm, the rainfall estimation skill was increased using the new VPR correction algorithm, and the root mean square errors of 48hr rainfall accumulation compared to gauge was reduced from 2.09 inch (before VPR correction) to 1.55 inch (after VPR correction). The new VPR correction algorithm is described in the next section, and detailed case study results are presented in section 3. The last section, section 4, provides a summary.

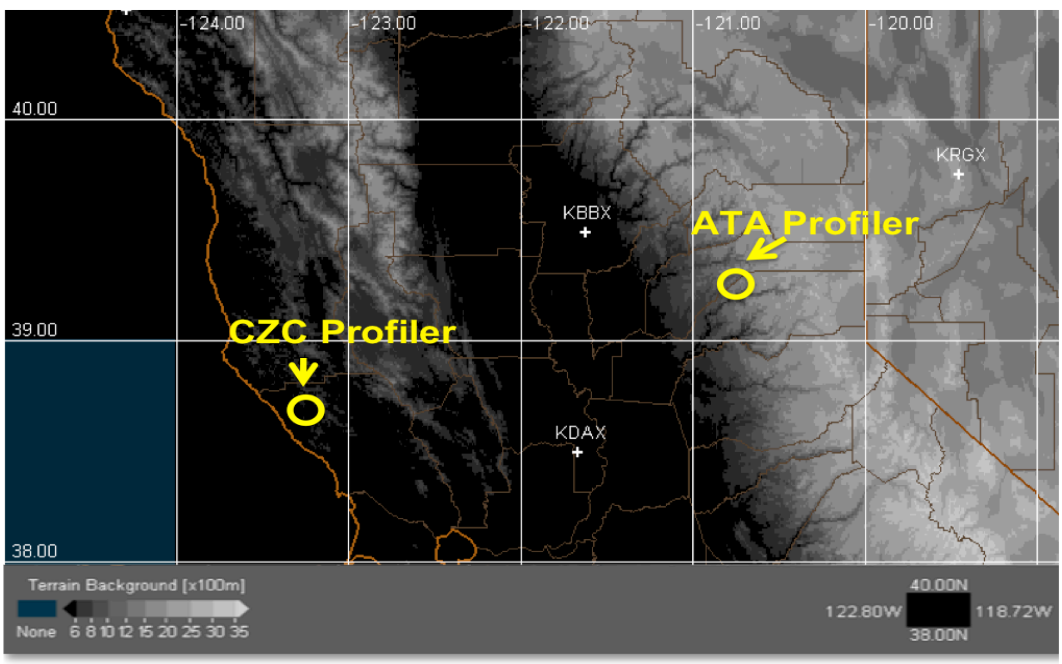

Fig.1 Map of the study domain.

* Corresponding author : Youcun Qi, 120 David L. Boren Blvd., Suite 2100 Norman, OK 73072-7304;
E-mail: youcun.qi@noaa.gov

2. Methodology

In order to obtain an accurate radar QPE in the current study was generated with the following 5 steps:

1), Minimizing ground clutter contaminations in the QPE through a reflectivity quality control (QC);

2), Reducing QPE errors due to orographic process, bright band, and radar beam sampling in the ice regions through a VPR correction;

3), Mitigating discontinuities in the QPE due to beam blockages through a new way of deriving the hybrid scan reflectivity;

4), Mosaicing HSR fields from multiple radars on to a common QPE analysis grid;

5), Reducing QPE errors by applying spatially varying Z-R relationships representing different microphysical processes across the analysis domain.

The current study, we mainly focused on step2 developing a robust and effective VPR correction algorithm. This module is an extension of the technique developed by Zhang and Qi 2010 (hereafter, ZQ10), in which radar QPE errors associated with a bright band were corrected using single tilt apparent VPRs. The detailed VPR correction scheme is discussed in the rest of this section.

2.1 Generate apparent vertical reflectivity profile (AVPR)

The first step of the new VPR correction involes computing apparent VPRs by taking azimuthal mean of reflectivities from predefined precipitation areas with potential bright band contamination (ZQ10) and with radar sampling in the ice region. Each AVPR is computed for an individual tilt, and the areas are delineated according to the following criteria: 1) VIL (vertically integrated liquid, Greene and Clark 1972) <6.5 kg/m^2; 2) Beam blockage < 50%; 3) Reflectivity>=15dBZ and composite reflectivity > 30dBZ (to capture bright band peak) for bright band areas; 4) Reflectivity > 0 dBZ or composite reflectivity >30 dBZ for ice regions.

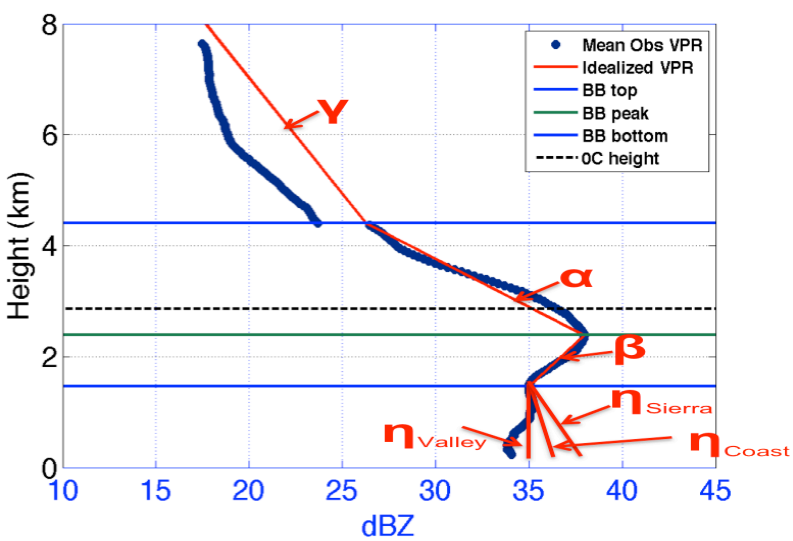

Fig.2 The conceptual VPR model used in the current study. The blue dots represent the observed VPR, and the red line is the idealized VPR. The blue lines are bright band top (upper) and bottom (below). The solid green and dashed black lines are bright band peak and the 0°C height, respectively.

The orographic enhancement effect (e.g., Kitchen et al. 1994) is shown as an increase of areal mean reflectivity with decreasing height in the mean radar AVPR below the bright band bottom (Fig.2). Vertical pointing precipitation profiler radar data are used to derive the VPR slope for the orographic effect in the current study. The profiler data were obtained from two S-band precipitation profiler radars deployed during the National Oceanic and Atmospheric Administration (NOAA) Hydro-meteorological Test-bed (HMT, http://hmt.noaa.gov) in Nov. 2005 to Apr. 2006. The radars were located in Cazadero (CZC) near the west coast of California and in Alta (ATA) on the California Sierras as shown in Fig.1. These profiler radars measure time evolutions of the reflectivity structure along a vertical column with high

temporal (1min) and spatial (60m) resolution. Two orographic VPR slopes are derived, One is the west coast orographic VPR slope generated from CZC, and the other is the Sierra slope derived from ATA. For the central valley, the VPR slope is set to zero below bright band, meaning no orographic enhancement to the precipitation in the region.

2.2 Parameterize apparent VPR

Each single tilt AVPR is parameterized with a linear model (Fig.2), and the linear model is described by apparent bright band top, peak, and bottom heights and piece-wise linear segments with different slopes (α, β, γ and η). Three η slopes for three different areas (west coast η_{coast}, central valley η_{valley} and east mountain η_{sierra}) as shown in Fig.2. η_{coast} (1.87dBZ/km) and η_{sierra} (3.5dBZ/km) are average value obtained from CZC and ATA respectively. For η_{valley}, we still set it zero because no profiler data can be obtained from the central valley.

2.3 Apply apparent VPR

The VPR correction is applied to the observed reflectivity field to obtain an estimated reflectivity near the ground, assuming a horizontally invariant vertical reflectivity structure. The correction is applied to each individual tilt and is only applied to areas with potential bright band contamination and with radar sampling in the ice region. Specifically, the areas for correction must meet the following criteria: 1) Height of the reflectivity bin is above the apparent BB bottom. 2) VIL<6.5kg/m^2; 3) Reflectivity >20dBZ or composite reflectivity >30dBZ in the bright band region; 4) Reflectivity >5dBZ or composite reflectivity >30dBZ in the ice region.

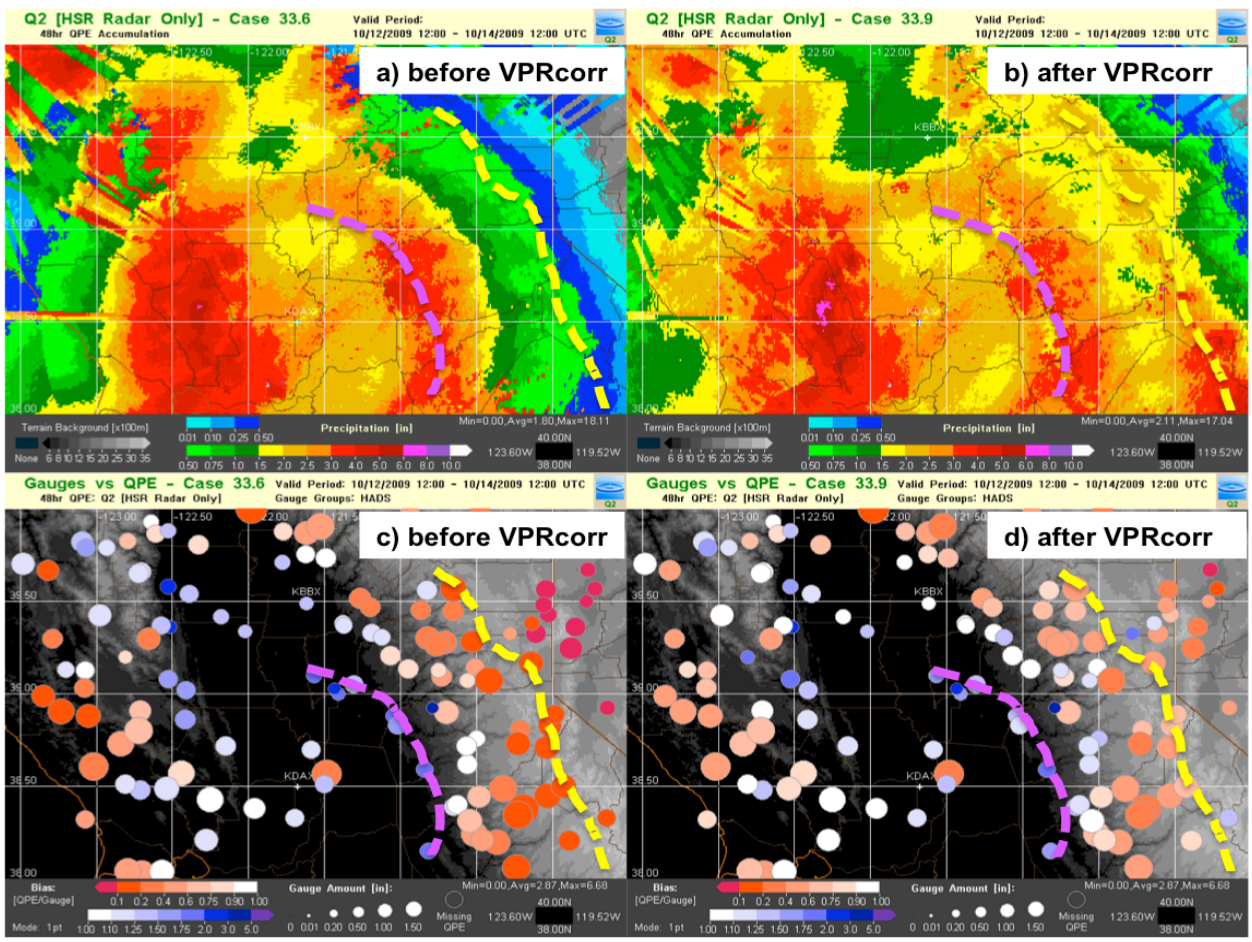

Fig.3 Hybrid scan reflectivity field at 12Z Oct. 14, 2009 before (a) and after (b) the VPR correction. The bias ratio field between radar estimated and gauge observed 48-hr rainfalls before (c) and after (d) the correction are also shown. The dash purple lines indicate the bright band area, and the dash yellow lines indicate the area where radar was sampling in the ice region.

3. Case study results

The case to be discussed occurred on 13-14 October 2009 in the central and northern California. At the beginning of 13th of October 2009, a very wet and windy storm struck central and northern California. This storm was fueled by unusually strong upper jet energy across the Pacific and a surge of tropical moisture from former super typhoon Melor, which struck Japan earlier on the 8th of October 2009. It brought intense precipitation to the central and northern California. In the current study, multiple VPRs are derived, one for each tilt. Each VPR (e.g., BB area and ice region) is obtained by taking azimuthal average of reflectivities along constant range circles at 1 km interval. This VPR represents the mean vertical reflectivity structure as sampled by the radar at different ranges on a given tilt, including the beam broadening effect. Reflectivities in a given tilt above the bright band bottom are adjusted down to the BB bottom level (Fig.2) using the idealized VPR for the same tilt. After they reach the BB bottom, they will be adjusted down to the ground using orographic slopes according to different area and terrain heights. A hybrid scan reflectivity field is then constructed using the VPR corrected reflectivities. Since the VPR correction was applied down to the ground level, the beam broadening effect was totally corrected.

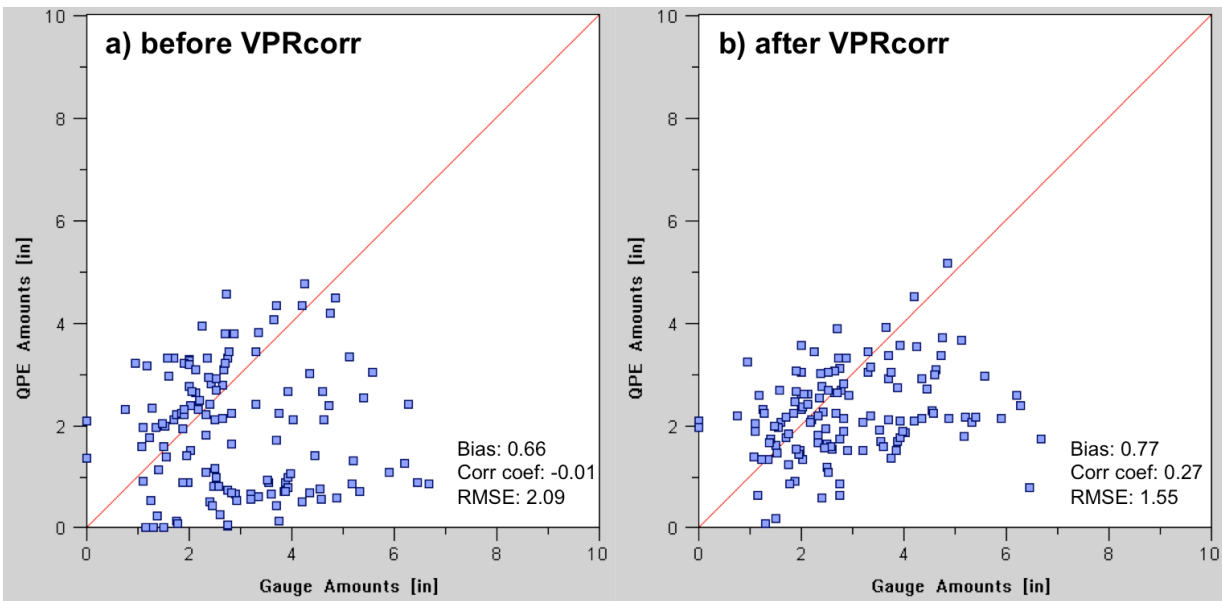

Fig. 4 Scatter plots of event total rainfalls from the radar QPE versus gauge observations before (a) and after (b) the VPR correction.

Figure 3 shows example hybrid scan reflectivity fields before (Fig.3a) and after (Fig.3b) the VPR correction. As a result of the VPR correction, reflectivities are reasonably reduced in the bright band area (indicated by the dashed purple line) and significantly increased in the ice region (indicated by dashed yellow line). The corrected rainfall field shows a more physically realistic and continuous distribution of reflectivity that is free of circular discontinuities. The bias ratio between radar QPE and gauge observations showed that the overestimation in the bright band area (dash purple lines in Figs. 3c and 3d) was slightly reduced by the VPR correction, while the underestimation was significantly mitigated where the radar was sampling in the ice region (dash yellow lines in Figs. 3c and 3d), and the improvement was relatively large.

Scatter plots of the radar 48hr rainfall accumulations before and after the VPR correction versus gauge observations are shown in Fig.4. It is apparent that the VPR correction mitigated overestimations and underestimations, and resulted in the radar QPE that agrees better with the gauge observations (Figs. 4bvs. 4a). The root mean square errors (rmse) decreased from 2.09 inch to 1.55 inch, and the bias is increased from 0.66 to 0.77. The correlation coefficient was increased from -0.01 to 0.27.

4.Summary

A new VPR correction was developed to reduce radar QPE errors due to bright band and radar sampling in ice regions. Further, an adjustment procedure was developed to account for the orographic precipitation process in the mountainous regions. The new VPR correction sheme successfully reduced overestimations in bright band area and improved underestimation in regions with radar sampling in the ice region. The new radar QPE technique will be implemented within the NSSL's National Mosaic and Q2 system (Vasiloff et al 2007; Zhang et al. 2009; http://nmq.ou.edu) for evaluation in real time across the Contiguous United States.

Acknowledgments

Major funding for this research was provided under NOAA's Hydro-Meteorological Testbed (HMT) program and partial funding was provided under NOAA-University of Oklahoma Cooperative Agreement #NA17RJ1227.

.

References

Zhang J. and Qi Y., 2010: A real-time algorithm for the correction of bright band effects in radar-derived QPE. *J. Hydrometeorology.* Accepted.

Greene, D. R. and R. A. Clark, 1972: Vertically Integrated Liquid Water—A New Analysis Tool. *Mon. Wea. Rev.* **100**, pp. 548–552

Vasiloff, S. V., D.J., Seo, K. Howard, and coauthors, 2007: Improving QPE and very short term QPF: An initiative for a community-wide integrated approach. *Bull. Amer. Meteor. Soc.*, ***60***, 1048-1058.

Zhang, J., K. Howard, S. Vasiloff, and coauthors, 2009: National Mosaic and multi-sensor QPE (NMQ) system: description, results and future plans. *Preprints, The 34th Conf. on Radar Meteorology*. Amer. Meteor. Soc. 5–9 Oct. 2009, Williamsburg, VA. Paper 7A.1

3rd Conference on QPE /QPF and Hydrology. World Meteorological Organization, Nanjing, China, Oct.18-22,2010.

Correction of Radar QPE Errors Associated with Partial Bright Band Observations Near the Ground

Youcun Qi*[1,2], Jian Zhang[1], Kenneth Howard[1], David Kingsmill[3]

[1]NOAA/National Severe Storms Lab

[2]Nanjing University of Information Science and Technology

[3]NOAA/Earth System Research Lab

1. Introduction

The melting of aggregated snow/crystals often results in an enhancement of the reflectivity observed by weather radars, and this is the so-called bright band (BB). The primary cause of the enhancement is a rapid increase in the dielectric constant of hydrometeors at the top of the melting layer followed by an increase of fall velocities of melting snowflakes toward the end of the melting process. The locally high reflectivity causes significant overestimation in radar quantitative precipitation estimates if no appropriate correction is applied. When the melting layer is very close to the ground, it often occurs that only a partial bright band can be observed by the radar. Since no information is available below the BB can be obtained from radar observations, the partial BB often leads to large overestimations in radar QPEs. To correct for these large errors, an empirical relationship of BB peak and BB bottom is developed from high-resolution precipitation profiler data. The empirical relationship is combined with the BB top and peak information from the apparent vertical profile of reflectivity (VPR) and an estimated BB bottom is derived. Radar QPEs are then corrected based on the estimated BB bottom. The methodology has been tested for two events over the plain area in the United States. The method is shown to be very effective in reducing the overestimation errors, and the corrected radar rainfall estimates compared much better with gauge observations than those without the correction.

*Corresponding author : Youcun Qi, 120 David L. Boren Blvd., Suite 2100 Norman, OK 73072-7304;
E-mail: youcun.qi@noaa.gov

2. Methodology

a. S-Band Precipitation Profiler Data Analysis

The profiler data used in this study were obtained from two S-band precipitation profiler radars deployed during the National Oceanic and Atmospheric Administration (NOAA) Hydro-meteorological Test-bed (HMT, http://hmt.noaa.gov) in Nov. 2005 to Apr. 2006. The radars were located in Cazadero (CZC) near the west coast of California and in Alta (ATA) on the California Sierras. These profiler radars measure time evolutions of the reflectivity structure along a vertical column with high temporal (1min) and spatial (60 m) resolution (e.g., White et al, 2000, Matrosov et al, 2006). The data used in the current study was 5-min averages of the 1-min observations.

Total of 6336 vertical reflectivity profiles were analyzed in the current study. Among them, 2037 (605 from CZC and 1432 from ATA) were identified as to have a low but complete bright band. The criteria for having a low and complete bright band are: 1) there was only one peak below the 0°C height, where the 0°C height was obtained from a nearby sounding; 2) the peak must be well-defined in that an inflexion can be found both above and below the peak; 3) the inflexion points must be at least 100 m away from the peak (i.e., the bright band peak is at least 200 m wide); 4) the peak reflectivity must be at least 6 dBZ higher than the reflectivities of the top and bottom; 5) the bottom of the peak must be less than 500m above the radar height. From these profiles, the reflectivites of bright band peak (Z_{peak}) and bottom (Z_{bttm}) were recorded. The BB bottom reflectivity is subjectively

selected and it is usually the reflectivity several points (typically 100 ~300 m) below the bottom inflexion point.

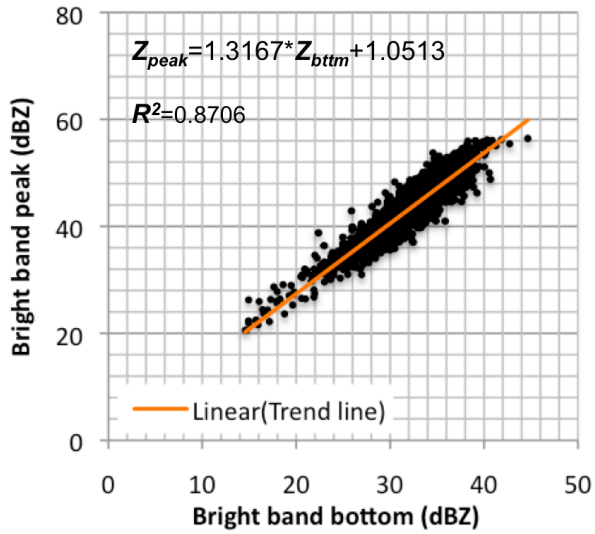

Fig. 1. Linear relationship between the bright band peak and bottom reflectivities measured by the S-Band precipitation profilers. The data are from 2037 observed profiles recorded in widespread stratiform precipitation.

The manually identified BB bottom (Z_{bttm}) and peak reflectivities (Z_{peak}) are plotted in Fig. 1, and a linear relationship is fitted to the data:

$$Z_{peak}=1.3167*Z_{bttm}+1.0513 \qquad (1)$$

This relationship has a slope larger than unity indicating that the BB peak intensity increases faster than the BB bottom intensity (Kitchen et al. 1994). The correlation coefficient is 0.94, which suggests that more than 87% of the variability in the reflectivity of bright band bottom can be explained by variations in the reflectivity of bright band peak. This indicates that, for well-defined bright band events, the peak and bottom relationship has relatively small spatial and temporal variations since the profiler data were obtained over a time period of seven months and in two locations 290 km apart. It provides a high degree in confidence towards using the empirical relationship for the VPR correction of bright band effects.

b. VPR correction for a low bright band in radar reflectivity observations

The empirical relationship between BB peak and bottom intensities derived from the profiler data were used to refine the VPR correction method in Zhang and Qi 2010 (Hereafter, ZQ10). The VPR correction in ZQ10 was applied based on a 2-piece linear model fitted to the bright band layer in an apparent VPR (Fig. 3 in ZQ10). Assuming that the reflectivity below the apparent BB bottom is constant, the reflectivities in bright band area can be corrected for surface precipitation estimation according to (Eqn. [9] in ZQ10).

When the apparent BB peak is too close to the ground (i.e., when the melting layer height is less than 1500 m and the apparent BB peak height is less than 1000 m relative to radar site level), an apparent BB bottom cannot be directly obtained from AVPR. In the current study, BB bottom reflectivity is derived from the empirical Z_{peak} – Z_{bttm} relationship (Eqn.[1]) assuming that Z_{peak} in the profiler empirical relationship is approximately equal to the apparent BB peak reflectivity. The beam broadening effect was neglected because the effect is relatively small when the BB peak is below 1 km above radar level.

After the BB bottom reflectivity is obtained, a BB bottom height h_b is computed from Eqn.(2a) with the newly derived BB bottom reflectivity – if the apparent BB peak is less than 250 m above radar level or the difference between BB peak Z_{peak} and the reflectivity at the bottom of the VPR is less than 2 dBZ. Otherwise, the new BB bottom height is computed by Eqn.(2b).

$$h_b = \begin{cases} h_p - (Z_{bttm} - Z_{peak})/\alpha \text{----------}(a) \\ h_p + (Z_{bttm} - Z_{peak})/\beta \text{----------}(b) \end{cases} \qquad (2)$$

where Z_{bttm} is the new BB bottom reflectivity derived from the empirical relationship. α and β are the apparent VPR slopes above and below the bright band peak; and h_p and h_b are the heights of the apparent bright band peak and bottom respectively (ZQ10).

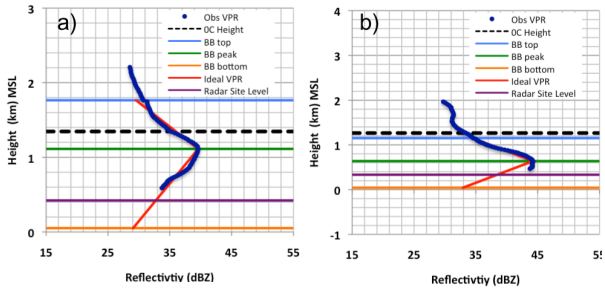

Fig. 2. Apparent VPRs (blue dots) and associated linear VPR model (red lines) for (a) KABR at 1000UTC 06 Oct. 2009, (b) KEAX at 1700UTC 19 Feb. 2010.

Once the idealized BB VPR is obtained, a reflectivity correction factor, ΔZ(r), is computed from the VPR according to the following:

$$\Delta Z(r) = \begin{cases} \alpha \bullet [h(r) - h_p] + \beta \bullet [h_p - h_b]; - - - h(r) > h_p \\ \beta \bullet [h(r) - h_b]; - - - - - - - - - - h(r) \le h_p \end{cases} \quad (3)$$

$$Z_c(r)\big|_{r \in BBA} = Z_o(r)\big|_{r \in BBA} - \Delta Z(r)$$

Here, r is the range from the radar to any given gate and h(r) is the height of the beam axis at the gate; $Z_o(r)$ and $Z_c(r)$ represents the observed and VPR corrected reflectivities at any given gate within a BBA, respectively. For a bright band situation, $\Delta Z(r)$ is usually positive, thus the correction would only reduce the observed reflectivities after the correction. $\Delta Z(r)$ can become negative when h(r) – h_p is so high that $\alpha \bullet \left[h(r) - h_p\right] > \beta \bullet \left[h_p - h_b\right]$, and equation (3) may be potentially used to correct for underestimations in radar-derived QPE when the radar beam is sampling upper part of precipitation clouds (i.e, the snow/ice region). However, this correction may not be very accurate if only one slope is considered above the BB peak.

3. Case study results

In the current study, multiple VPRs are derived and then applied for correction, one for each tilt. These mean observed VPRs account for the beam spreading effects because the reflectivity were averaged at the same range on a single tilt, instead of over multiple tilts at a certain height. When applying the correction back to observed reflectivity, the beam spreading effects are implicitly accounted for. This approach was found to be superior to the single-VPR approach, where one mean VPR is computed from observations of multiple elevations angles at closer ranges and then applied to the far ranges. Experiments with the single-VPR approach resulted in some circular discontinuities (not shown) because the VPRs could not accurately account for the beam spreading at different ranges. Using the VPRs for each tilt, the correction is adaptive to the range variation of the beam width and the BB distribution, and discontinuities in the corrected fields are minimized. Figure 3 shows example reflectivity fields before and after the VPR correction. The inflated reflectivity in bright band area was corrected. The corrected fields showed physically consistent distributions and were free of circular discontinuities that were usually caused by non-representative BB top/bottom heights in single-VPR approaches.

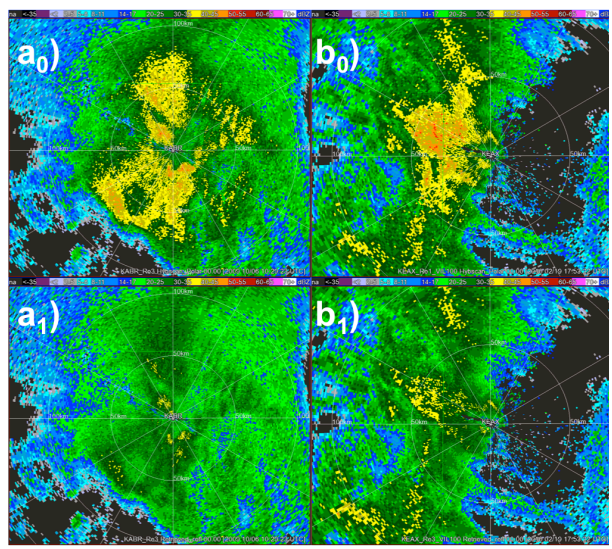

Fig. 3. Base level reflectivities (upper row: a_0, and b_0) before AVPR correction, (low row: a_1, and b_1) after AVPR correction. The two columns are images from (*column 1*) KABR at 10Z Oct 06, 2009, and (*column 2*) KEAX at 17Z Feb 19, 2010.

The hybrid scan reflectivity field is converted into rain rate using one Z-R relationship ($Z=200R^{1.6}$). The rain rates are aggregated into hourly rainfalls and

compared to the surface gauge observations. Figure 4 shows a comparison of hourly radar rainfall estimates before and after the BB VPR correction against gauge observations for the two events shown in Fig.3. The significant overestimations in radar-derived QPE of the KABR (Fig.4a), and KEAX (Fig.4b), were successfully reduced by the VPR correction. Radar estimates after the correction agreed much better with the gauge observations than those before VPR correction.

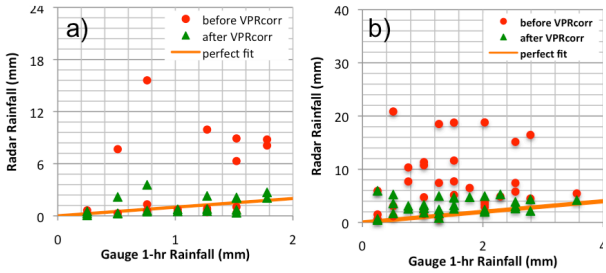

Fig. 4 Scatter plots of hourly radar precipitation estimates versus gauge observations before (red dots) and after (green triangles) a VPR correction. The data are from (a) KABR at 1100UTC 06 Oct. 2009, (b) KEAX at 1700UTC 19 Feb. 2010.

4. Summary

High temporal and spatial (vertical) resolution profiler data from two sites were analyzed and an empirical BB peak and BB bottom relationship was obtained. The empirical relationship was combined with the apparent vertical profile of reflectivity (VPR) from volume scan radars to find the BB bottom height and intensity where a BB bottom cannot be identified from the apparent VPR. The new BB bottom identification method consistently reduced the overestimation errors in radar-derived QPE after the VPR correction, and the VPR corrected radar-derived QPE agreed well with rain gauge observations. The VPR correction is most effective and robust for radars in flat lands because of relative uniform spatial distributions of BB.

Acknowledgments

The authors are thankful to Dr. Pengfei Zhang for many discussions that greatly helped this study. Major funding for this research was provided under NOAA's Hydro-Meteorological Testbed (HMT) program and partial funding was provided under NOAA-University of Oklahoma Cooperative Agreement #NA17RJ1227.

References

Allen B. White, James R. Jordan, Brooks E. Martner, and Bruce W. Bartram, 2000: Extending the dynamic range of an S-band radar for cloud and precipitation studies. *J. Atmos. Oceanic Technol.,* 17, 1226- 1234.

Zhang J. and Qi Y., 2010: A real-time algorithm for the correction of bright band effects in radar-derived QPE. *J. Hydrometeorology.* In press.

Kitchen, M., R. Brown, and A. G. Davies, 1994: Real-time correction of weather radar data for the effects of bright band, range and orographic growth in widespread precipitation. *Quart. J. Roy. Meteor. Soc.,* 120, 1231–1254.

Matrosov, S.Y., Cifelli R., Kennedy P.C., Nesbit S.W., and Rutledge S.T. 2006: A comparative study of rainfall retrievals based on specific differential phase shifts at X- and S-band radar frequencies. *J. Atmos. Oceanic Technol.*, 23, 952-963.

QPF verification using object-oriented methods to investigate the benefits of higher resolution models

Carlos Santos [1], Anna Ghelli[2], Imanol Guerrero [1] and Laura Ferranti [2]
[1]Agencia Estatal de METeorologia
[2] European Centre for Medium Range Weather Forecast

csantosb@aemet.es

Abstract
Quantitative precipitation forecasts (QPF) from NWP models used at the European Centre for Medium-Range Weather Forecasts (ECMWF) are assessed using an object-oriented verification method, the SAL measure (Wernli et al 2008). This method provides quantitative and detailed information about different aspects of QPF, a complementary method to assess performance of high resolution models, which are usually penalized by classical scores.

1. Introduction

Numerical Weather Prediction (NWP) models are improving quickly due to the fast progress in computational and satellite resources, development in data assimilation, dynamics and parametrization of physical processes. One of the current challenges is the mesoscale horizontal resolution, and new difficulties arise, not only for model development, but also in validation techniques.

NWP classical verification issues have been often related to spatial scale of models and observations: representativeness of observations, impact of interpolation methods, relative loss of statistical significance or independence due to spatial and temporal correlation, and interpretation of different scores according to spatial scale. New verification methods deal with patterns and structures, a complementary approach to assess model performance, for instance fuzzy verification and feature/object oriented methods.

In the context of QPF verification, the Structure-Amplitude-Location (SAL) measure (Wernli et al., 2008) is a feature-oriented measure that describes precipitation forecast skill, when verified against gridded observations, that gives quantitative and detailed information in terms of its different components. This information can be used to assess model performance from a different perspective, as well as to use it as further help in forecasting guidance.

The SAL measure has been used to assess the ECMWF high resolution deterministic model and control member from the Ensemble Prediction System for 2008 over Central Europe. The verification assessment is further enhanced by taking into account pre-defined climatological regimes, which are used to stratify the dataset. The climatological regimes are computed using 28 years of re-analysis data (Era-Interim and ERA 40). The results of this verification exercise will be presented and they give a fair assessment to high resolution models when compared with coarser models. Further research is needed on the fine tuning of the SAL algorithm. Section 2 describes the methodology, section 3 describes the forecasts and observations databases, while results are discussed in section 4. Conclusions are drawn in section 5.

2. Methodology

a. upscaling observations

High resolution observations (HR) are upscaled (Cherubini et al, 2002) to obtain a precipitation analysis on a selected regular grid. For each gridpoint an estimate of observed precipitation is selected using one of the different existing methods, depending on the purpose of the study. A simple method is to take the average of the observations inside the gridbox; inverse distance weighting (IDW, Sodoudi, 2009) gives good results for 24h accumulated precipitation. Even though there are other possible estimation methods, IDW has been selected for this study. Any observations within a distance d from the gridbox center, where d can be the grid resolution or some proportion related (in fig. 1 d/sqrt(2) is shown), is considered. Then, the observed precipitation estimate is computed as:

$$R = \sum r^{-\alpha} R_i / \sum r^{-\alpha} \quad \text{with } \alpha=2$$

For HR networks dense enough to cover the grid, this method can overcome the problem of missing data at most resolutions. The distance d can be selected, to some extent, according with the network density. Each model is compared with observations gridded at its resolution; in this way fair comparisons can be done.

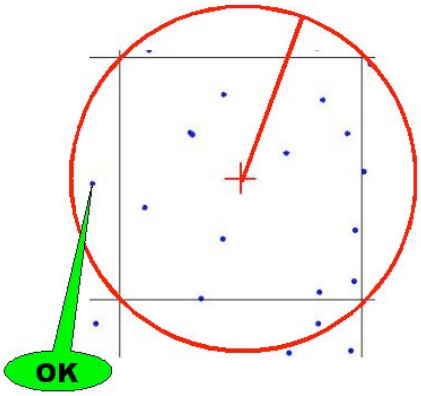

Fig. 1. Selection of observations in the upscaling method used here

b. The SAL method

The Structure-Amplitude-Location (SAL) method is an object-oriented verification method used to overcome limitations of classical methods. A detailed description can be found in Wernli et al (2004). The three components of SAL give an indication on the Structure, Amplitude and location of the error.

Negative values of the structure component S mean that forecast objects are too small or too peaked, while positive ones mean too large or too flat. Amplitude values correspond to the usual precipitation bias. Location component L ranges from 0 to +2, the larger the worse location of the center of mass or the relative position of the objects. For the three components, the closer to zero the better the forecast field.

3. Data sets

QPFs over Central Europe (45-55N, 5-15E) on 2008 (366 days) have been compared with the HR observations available (provided by the different member states and collected at ECMWF). Daily precipitation (06-06 UTC) from the High-resolution deterministic forecast (T799) and the Ensemble Prediction System (EPS) control forecast (T399) models have been assessed, using the 00UTC run and forecast steps t+54 and t+126 to represent the short and the medium range respectively. About 3000 stations provided data that have been gridded to 0.25 deg for T799 and to 0.50 deg for T399.

4. Results

The results relative to the time step t+54 for T799 are presented in subsection (a). In (b) and (c) the impact of different stratifications is examined, while (d) and (e) show comparisons of T799 with T399 (impact of resolution) are shown.

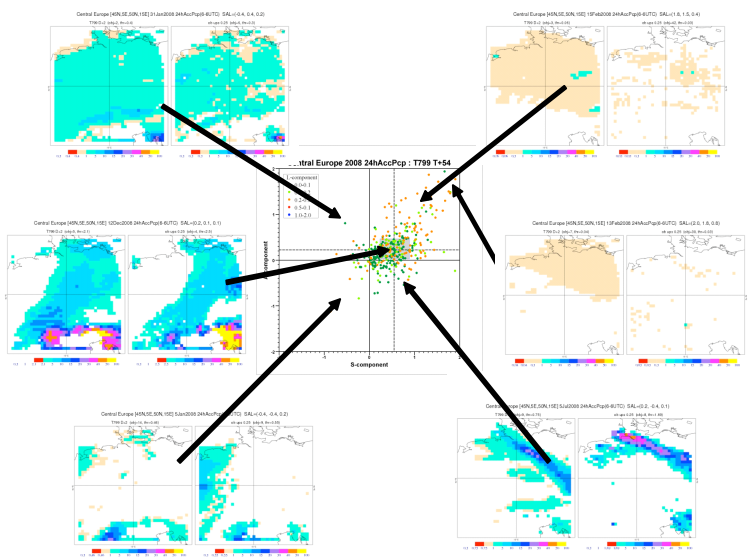

Fig 2: T799 SAL plot and six selected forecast-observation plots.

a. T799

The SAL plot can help in understanding and comparing precipitation pattern. In a SAL plot, the X and Y-axes

measure the S and A components respectively, while L is plotted in different colours. A point in the plot describes SAL results for one comparison (one day of the period). The dashed lines show the median of the S and A distributions, while the shadowed rectangle shows the inter-quartile ranges (IQR). Each quadrant in the plot can be interpreted as follows: quadrant I for larger structures, larger precipitation (pcp); II for smaller structures (or less variance), larger pcp; III for smaller structures, lower pcp; IV for larger structures, lower pcp; IQR for better QPF; large Ls for clear bad location. The SAL plot for T799 over the domain and period described in section 3 is shown in figure 2, together with six selected plots (one for each group) of forecast-observation pairs. This SAL plot indicates over-population over I and IV, indicating larger structures, as well as the already-known positive bias, and also some cases of bad location.

b. Impact of light precipitation bias

A filter has been applied to remove all days with precipitation less than 2mm/24h in order to overcome a well known bias of the numerical model..

The impact of this bias can be further examined by stratifying summer-winter results, plots shown in fig. 3. The impact of light precipitation days is much more important in winter, as expected, when many cases of large precipitation are predominant; the overpopulation of quadrant I is small, while SAL components improve. These are clear indications that above this 2mm maximum precipitation threshold the model overcomes this known bias problem. Similar results (not shown here) have been found for other resolutions (T399), and other forecast steps (t+126). Therefore results shown in following subsections use this filter (2mm) in order to avoid this known bias.

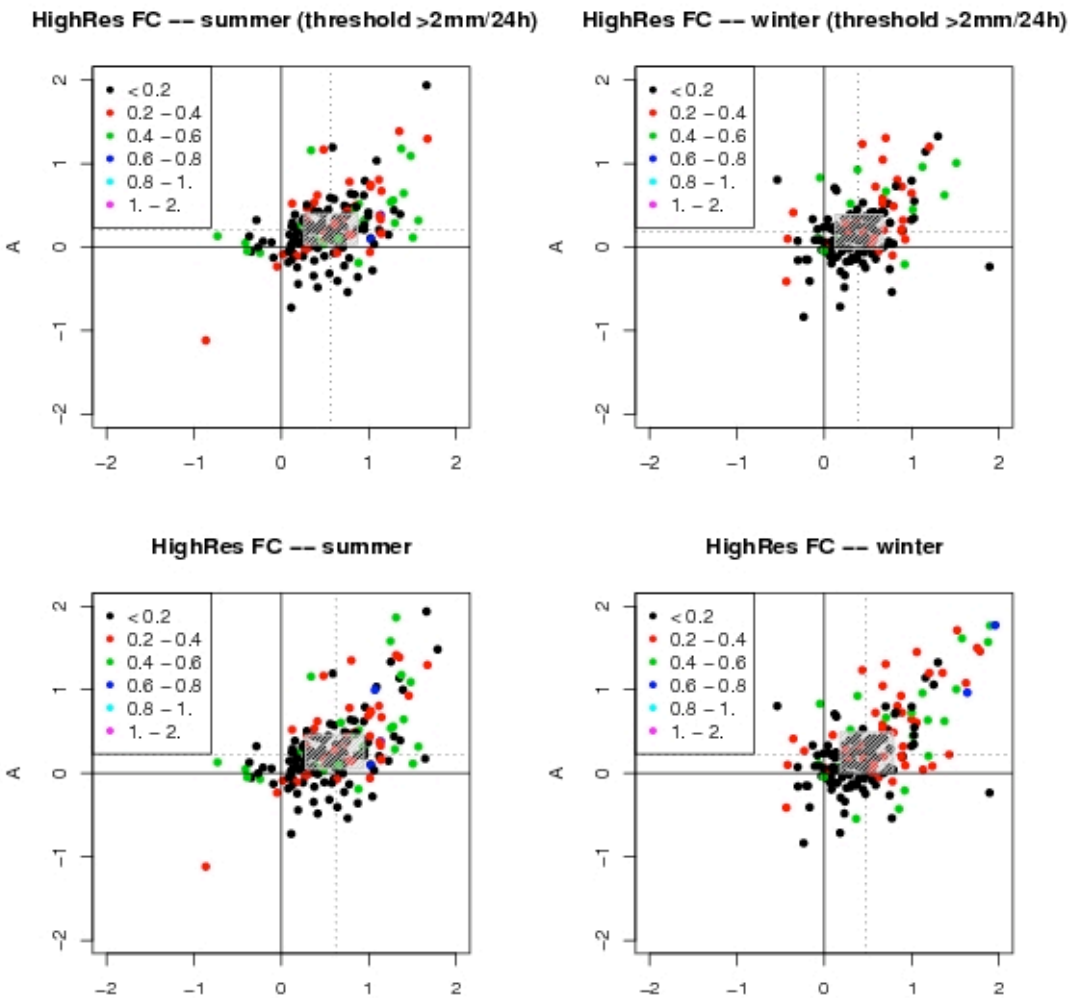

Fig. 3: Sal for the T799 model filtering out the small amounts of precipitations . Summer (left column), and winter (right column)

c. Stratification on weather regimes

Further information can be obtained taking into account pre-defined climatological regimes, which are used to stratify the dataset. The climatological regimes are computed using 28 years of re-analysis data (Era-Interim and ERA 40), gathering days in four different clusters: Blocking, NAO+, NAO-, and Atlantic ridge. Figure 4 shows the weather regimes and plots for these four clusters.

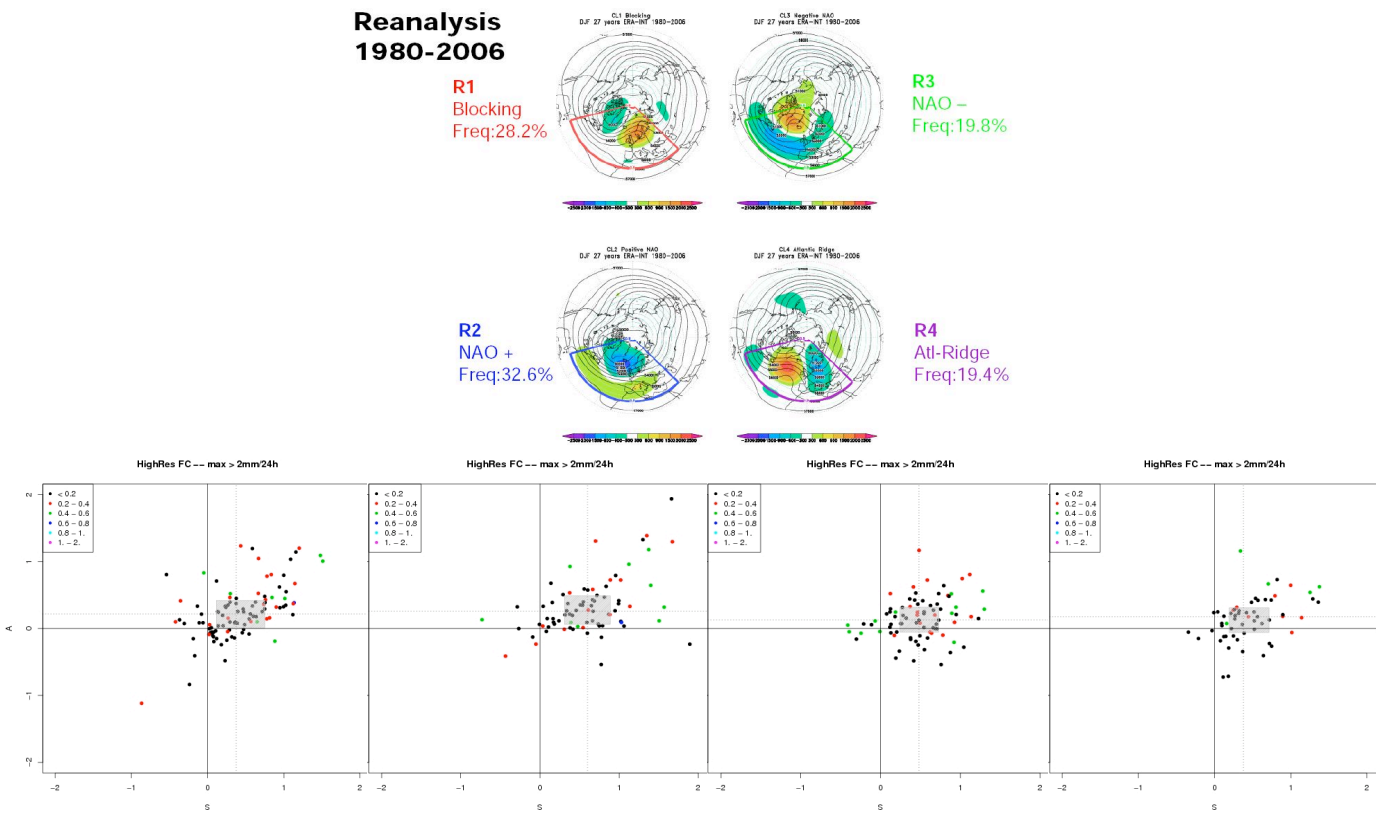

Figure 4: Patterns and SAL plots for the four weather regimes described in the text.

The kind of precipitation patterns expected for the different weather regimes is consistent with the SAL plots: in the Blocking case (cold and dry winters) the cloud of points shows positive slow and overpopulation of quadrant I, positive A and S. NAO+ (warm and wet winters, many cases of LSP) shows worse S (larger structures) and more overpopulation on I. In NAO- (cold and snowy winters, larger amounts of daily precipitation) the cloud of points is centralized, with a close to zero A component. Atlantic ridge (warm and dry winters) case shows a slightly positive slope but cloud of points much more centralized and very good locations.

d. T799 and T399: impact of resolution

Figure 5 compares SAL plots for T799 (~25km) and T399 (~50km), showing similar SAL patterns (consistently, each one resolves patterns at its own resolution with similar performance): over-population over I and IV, indicating larger structures, as well as the already-known positive bias, and also some cases of bad location. T799 gives therefore more valuable QPF as it provides patterns of similar quality with higher resolution. This kind of assessment using classical scores (e.g. root mean square error) can give better scores to the coarser grid model.

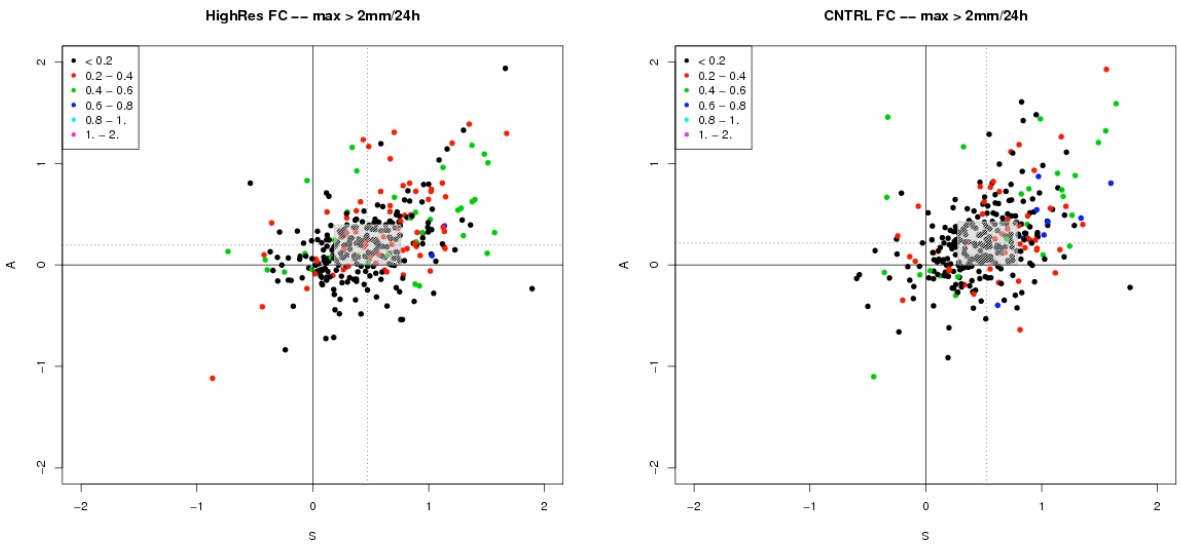

Figure 5: SAL plots for T799 and T399

5. Conclusions

Several problems arise using NWP classical verification methods when it comes to deal with HR forecasts; for instance, the double penalty problem can give better scores to coarser grid models, so new methods must be explored to assess NWP in fast development on their way to spatial mesoscale. The Structure-Amplitude-Location measure (a case of object-oriented method) gives quantitative and detailed information about different aspects of model QPF performance, assessing the skill of a model in representing precipitation patterns at its own resolution, and can help understand (both modellers and users) features improvement in QPF.

Performance of daily QPF from ECMWF models (both high resolution deterministic and EPS control forecast) has been assessed using SAL method, over Central Europe for 2008.

ECMWF T799 D+2 QPFs over Central Europe 2008 show overestimation of structure size (S), positive bias (A), location to improve (L), and number of objects distribution to improve as well. T799 and T399 perform similarly, each one at its own resolution, this means that T799 provides QPFs with the same performance but higher resolution, thus more valuable forecasts.

By selecting only those cases with maximum precipitation over a 2mm the assessment shows better performance, overcoming a known problem of positive bias in light precipitation cases. This behaviour is shown to be consistent by stratifying cases in winter and summer. Furthermore, using a clustering method to stratify the sample in four different weather regimes (NAO+, NAO-, Blocking and Atlantic Ridge), results show an overall consistency with this behaviour.

Results look promising and some further research is needed. Clustering algorithms with a higher level of complexity must be explored. The selection of the factor f used for the precipitation threshold in the object construction ($R^* = f\ Rmax$) could be related with regional sensitivity, weather variability, etc. Though the stratifications described (seasonal and flow-dependent) provide a large amount of information, some others can be explored as well.

6. Acknowledgements

Marcus Paulat (DWD), Matthias Zimmer (Univ. Mainz) and Heini Wernli (Univ. Zurich) kindly provided the original SAL source code. Interesting discussions with the former, as well as with Pertti Nurmi (FMI) and Martin Göeber (DWD) helped in a deeper understanding of the SAL method. Special thanks must be given to ECMWF Member States for providing data from their HR observation networks.

7. References

Ahrens, B., And A. Beck, 2008: On upscaling of rain-gauge data for evaluating numerical weather forecasts. *Meteor. Atmos. Phys.*, **99**, 155-167, doi:10.1007/s00703-007-0261-8.

Cherubini T, Ghelli A, Lalaurette F (2002). Verification of precipitation forecast over the alpine region using a high density observing network. *Weather Forecast*, **17(2)**:238-249.

Sodoudi, S., Noorian, A., Ged M. and Reimer E., 2009: Daily precipitation forecast of ECMWF verified over Iran. *Theor. Appl. Climatol.*, **99**,39-51, dpi:10.1007/s00704-009-0118-9.

Wernli, H., M. Paulat, M. Hagen, and C. Frei, 2008: SAL Novel Quality Measure for the verification of Quantitative Precipitation Forecasts. *Mon. Wea. Rev.*, **136**, 4470-4487.

Quantitative Precipitation Forecasting using CSEOF-CCA in Korea

Mingdong Sun[1], Gwangseob Kim[2], and Jae Hong Park[3]
[1]Department of Civil Engineering, Kyungpook National University and Researcher of Brain Korea 21, Korea, mingdongsun@hotmail.com)
[2]Department of Civil Engineering, Kyungpook National University and Researcher of Climate Change Research Center, Korea,kimgs@knu.ac.kr)
[3]Department of Civil Engineering, Semyung University, Korea, (jhpark@semyung.ac.kr)

1. Introduction

Among the all different variables of meteorology, precipitation is the major source of water for agriculture, industry and municipal water use, which is also the most important for the hydrological cycle. Presently precipitation becomes the major subject in the field of meteorology and hydrology research and gets attention in the climate change research due to the significant variation in the amount and intensity. There have been many studies about forecasting of precipitation for different regions (Robinson, 2006, Peel, 2008, Becker et al 2006, Jin et al 2005). Barnston et al. (1996) used the canonical correlation analysis (CCA) which describes the correlation relationship between prediction and the global sea surface temperature and precipitation. In this study, the CCA method was applied to forecast the temporal patterns evolution of precipitation which was obtained from decomposition of observational data via EOF and Cyclostationary EOF analysis. Thus, this study primarily focuses on the most conspicuous component of seasonal cycle and evolution of the Korea precipitation variable. Through comparison between the prediction outcome and observation from temporal view, in search of the better statistical methodology of effectively forecast the precipitation. The schematic procedure of this study is illustrated in figure 1.

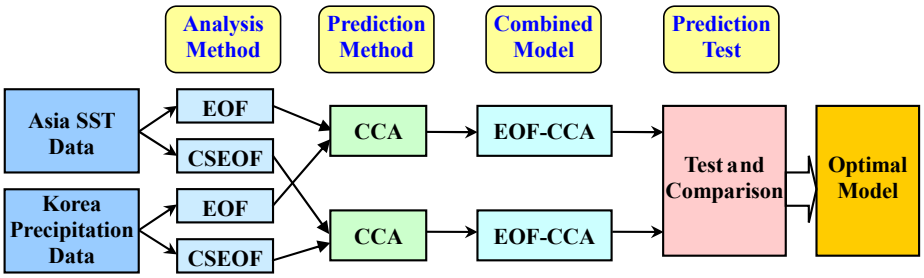

Fig 1. Flow chart of analysis and prediction model

2. Methodologies and Data Description

2.1 Methodology

In the EOF analysis, space-time data $D(r,t)$ are represented in terms of the loading vectors (L) and their principal component (PC) time series: $D(r,t)=\sum PC_n(t)L_n(r)$, where $L_n(r)$ and $PC_n(t)$ are specific spatial patterns and their temporal evolutions respectively.

The CSEOF analysis is described in detail by Kim and North (1997). In the CSEOF analysis, a space-time datum are $D(r,t)$ represented as $D(r,t)=\sum PC_n(t)CL_n(r,t)$, $CL_n(r,t)=LV_n(r,t+d)$, where $CL_n(r,t)$ are cyclostationary loading vectors (CSLVs) and $PC_n(t)$ are their corresponding principal component (PC) time series, The spatial patterns is further constrained to be periodic with d.

Canonical correlation analysis seeks vectors a and b such that the random variables $a'X$ and $b'Y$ maximize the correlation $\rho=cor(a'X,b'Y)$. The random variables $U=a'X$ and $V=b'Y$ are the first pair of canonical variables.

2.2. Data description

There are two parts data in this study, Korea precipitation and sea surface temperature, which respectively obtained from Korea Water Management Information System Data Set and International Comprehensive Ocean-Atmosphere Data Set (ICOADS).

These SST data come from ICOADS, and the spatial coverage is global grid 2.0 degree latitude×2.0 degree longitude, the grid 0°N-45°N, 75°E-150°E over Ease Asia which have 456 months (1972-2009) records of data are used in this research. And 61 stations in Korea which have 444 months (1973-2009) records of data are used for the current study. The available data maintained with extensive quality control and calculation of average of 3 months data, which are the most important processes for studying the frequency and intensity.

3. Analysis and Results

The EOF technique and CSEOF technique have been applied to the average of 3 months precipitation data of 61 stations during 36 years in Korea. The twelve leading EOF and CSEOF modes of SST data respectively account for 96.84% and 99.96% of the total variance; and the twelve leading EOF and CSEOF modes of precipitation data respectively account for 97.12% and 97.62% of the total variance. The main motivation for employing this technique in the present study is to investigate the physical processes associated with the evolution of the precipitation from the observation data. The first leading principal component time series of EOF and CSEOF analysis are shown in figure 2.

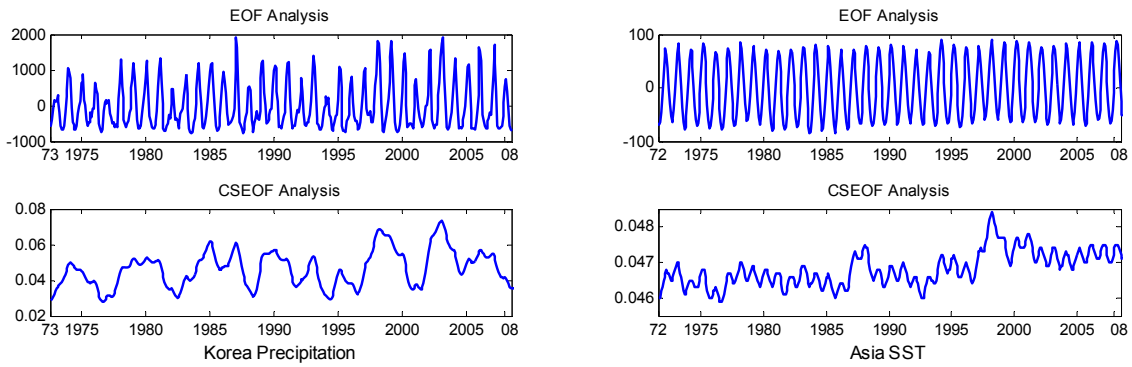

Fig 2. Principal component time series of EOF and CSEOF model

Based on the twelve leading temporal patterns of EOF and CSEOF, CCA method was applied to these obtained princ ipal component time series respec tively with different lag month, the average correlation coefficient with different lag m onths are shown in table 1.

Table 1. Average correlation coefficients with different lag month

Lag Month	0	3	6	9	12
EOF-CCA	0.3109	0.3360	0.3197	0.3106	0.2926
CSEOF-CCA	0.4342	0.4313	0.4313	0.4259	0.4215

From the table, we can fi nd that the average correlati on coefficients of CSEOF-CCA model are better than EOF-CCA model's.

Then accor ding to the function of EOFs and CSEOFs technology and extrapolation with spatial patterns, we sele cted the lag 0 month, 3 months, 6 months, 9 months, 12 months temporal patterns prediction and re versed to the precipitation pr ediction located at 61 stations. According to t he above analy sis and prediction, these two combined forecasting models prediction re sults wer e comp ared with precipit ation observation of 2009. In the test of these two combined models' prediction, the scatter plots on the prediction and observation are shown in figure 3.

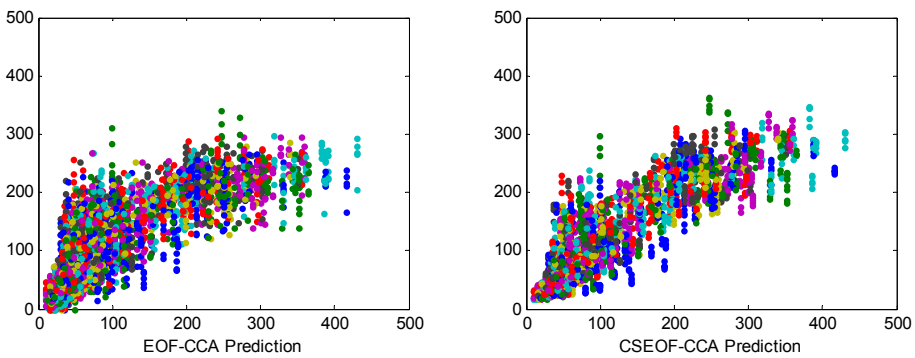

Fig 3. Scatter plots on the prediction and observation

From the temporal view, the monthly av erage of prediction and observation were

calculated respectively, the comparisons between prediction from different methods and observation are presented in figure 4.

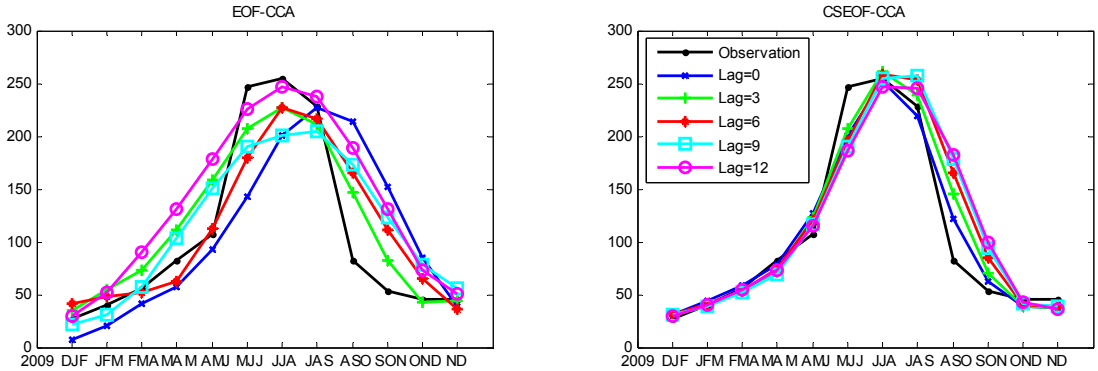

Fig 4. Comparison between observation and prediction using EOF-CCA and CSEOF-CCA

There are some statistical quantitative verification measures of prediction's method were calculated to evaluate the model performance. The statistical verification's contrastive consequence is provided in table 1 for these two models.

Table 2. The statistical quantitative verification measures of predictions

Index		SSE	R^2	RMSE	Average Absolute Error	Average Relative Error
EOF-CCA	Lag=0	44084	0.46	63.31	44.01	0.59
	Lag=3	11703	0.86	32.62	25.19	0.30
	Lag=6	16783	0.79	39.06	27.38	0.36
	Lag=9	23404	0.71	46.13	34.98	0.42
	Lag=12	27390	0.66	49.90	35.30	0.49
CSEOF-CCA	Lag=0	4335	0.95	19.85	12.96	0.15
	Lag=3	6389	0.92	24.10	15.33	0.18
	Lag=6	11459	0.86	32.28	19.64	0.22
	Lag=9	15223	0.81	37.20	22.25	0.26
	Lag=12	16382	0.80	38.59	22.15	0.25

From the above contrast figures and the standard of verification, we can found that the CSEOF-CAA combined prediction model has taken a more approximate performance, and has displayed the variation trends and evolution characteristics precipitation and variability along with recurrent seasons in Korea. So the CSEOF-CCA combined model is deemed the better prediction model.

4. Conclusions

Cyclostationary EOF analysis and CCA (CSEOF-CCA) prediction method is applied

to quantitative precipitation forecasting in Korea. Sea surface temperatures (SSTs) in the East Asia are used as predictors. The averages of 3 month data of SST in the East Asia and of precipitation in Korea are comprehensively analyzed and forecasting using the EOF-CCA technique and CSEOF-CCA technique respectively, and then compared the outcome evolved from prediction with observation. The results of this study indicate that the CSEOF-CCA prediction method has taken a more approximate performance; the average correlation coefficients with different lag month in CSEOF-CCA are all higher than in EOF-CCA model, the contrast figures and the verification standard clearly show that the CSEOF-CCA model is the more effective on forecasting seasonal precipitation in Korea, and it has presented the variation trends and evolution characteristics of the precipitation along with recurrent seasons. So it is conclusion that the CSEOF-CCA model is potentially effective and useful in forecasting seasonal rainfall variations in Korea.

Acknowledgements

This research was supported by a grant (code# 1-9-3) from Sustainable Water Resources Research Centre of the 21st Century Frontier Research Program in Korea. The thoughtful and useful comments of two anonymous reviewers are gratefully acknowledged.

References

Robinson, P.J., 2006: Implications of long-term precipitation amount changes for water sustainability in North Carolina. *Physical Geography*, **27**(4), 286-296.

Peel, S., Wilson, L.J., 2008: A Diagnostic Verification of the Precipitation Forecasts Produced by the Canadian Ensemble Prediction System. *Weather and Forecasting*, **23**(4), 596-616.

Becker, S, Gemmer, M, and Jiang, T., 2006: Spatiotemporal analysis of precipitation trends in the Yangtze River catchment. *Stochastic Environmental Research and Risk Assessment*, **20**(6), 435-444.

Jin, Y.H., Kawamura, A., Jinno, K., and Berndtsson, R., 2005: Detection of ENSO-influence on the monthly precipitation in South Korea. *Hydrological Process*. **19**(20), 4081-4092.

Barnston, A.G. and Smith, T.M., 1996: Specification and prediction of global surface temperature and prediction from global SST using CCA. *Journal of Climate*, **9**(11), 2660-2697.

Kim, K.Y. and North, G.R., 1997: EOFs of harmonizable cyclostationary processes. *Journal of Atmospheric Sciences*. **54,** 2416-2427.

Probabilistic prediction of July-August-September rainfall in Cameroon

TCHINDA TAZO Simplice
Department of National Meteorology - Cameroon
E-mail: simplicetazo@gmail.com

Introduction

Rainfall plays a key role in the socio-economic activities in Cameroon whose economy depends heavily on rain-fed agriculture. July-August-September (JAS) is the peak month's period of highest rainfall and more than 90% of extreme precipitation events occur during this period. Therefore, application of science for prediction and early warning with good lead time are vital in enhancing agricultural production and water management.

Generally it is not possible to predict day to day changes beyond a week but possible to say something about the likely conditions averaged over three months. The probabilistic prediction of July-August-September rainfall is an indication of average precipitation conditions in the three months, across a region. It aims to determine if the next rainy season will probably be above normal, near normal or below normal. This forecast does not represent only the choice of the most likely scenario (preferred), but the distribution of possible outcomes of the three predefined scenarios: "wet", "normal" or "dry."

The objective of this presentation is to highlight the path taken by the Meteorological Service of Cameroon for over ten years in the provision of seasonal forecasts.

Genesis of the Process

Cameroon entered in seasonal forecasting through the first Regional Climate Outlook Forum organized by the African Centre of Meteorological Applications for Development (ACMAD) and called PRESAO (Prévisions Saisonnières en Afrique de l'Ouest, le Tchad et le Cameroun). This forum brings together each year since 1998, climate forecasters from West Africa, Chad and Cameroon in order to develop a consensus forecast of precipitation for the region. The forum is held during the month of May and the target period of the forecast is July-August-September (JAS). The choice of this period takes account of two facts: firstly, the three months are the wettest for the region and secondly previous research has established teleconnections between rainfall during this period and surface temperatures of some ocean areas. The first fact stated above shows that the period JAS is a high risk period for the management of water resources. The second fact indicates that there are real opportunities to make a forecast of precipitation for the concerned period.

Thus, thanks to the technical and scientific support of ACMAD and its partners, Cameroon for more than a decade takes place in the development of national seasonal forecasts for the JAS period.

Fundamentals basis of our seasonal forecasting

The seasonal forecasts are developed based on interactions between the ocean and atmosphere. These interactions are responsible for an indirect influence of the Sea Surface Temperatures (SSTs) on rainfall. Thus the SSTs are explanatory variables use to predict the rainfall which is the response variable. The relationship between the two parameters can be put into mathematical equation through the construction of models.

Construction of models

The concept of predictor and predictand

The **predictor**: it is the parameter that influences and which is used to predict. In our case the predictor used are Sea Surface Temperatures extracted from the specific boxes. These boxes are mainly ATL NW (20N-40N/30W-10W), ATL EQ (0-10S/30W-10E), NINO3 (10S-10S/150W-90W), and also EOF.
The **predictand**: this is the parameter which reacts. In our case it is the cumulative rainfall, meaning the sum of the monthly totals for the period.
The Principal Component Analysis (PCA) method was used to divide the country into five rain fall zones that are: Zone Sahel; Zone Plateau; Zone Montagne; Zone Côtière; Zone Forêt. The zonal index is then calculated for each zone from the cumulative rainfall.

The statistical approach

It is to conduct statistical investigations to establish the mathematical equation expressing the physical relationship between existing predictand and predictor. The methods used include simple correlation to measure the degree of relationship between seasonal rainfall and SSTs, Multiple Linear Regression (MLR) analyses to establish the statistical model and contingency tables for verification.

At the beginning of the process the first statistical models were built using the rainfall normal for the period 1961-1990. The equations below represent these models for each zone:

1. **Zone_SAHEL = 0.06 – 0.05 NINO789T**
2. **Zone_PLATEAU = -0.16 + 0.06 EA45T + 0.03 NWA56T**
3. **Zone_MONTAGNE = -0.04 + 0.11 EA34T – 0.14 EOF56**
4. **Zone_COTIERE = 0.053 – 0.006 X NINO5T**
5. **Zone_FORET=- 0.25+0.05EA34T+0.02NIN45T+0.06 EOF56**

In the next steps of the process models were renewed in 2009 with the use of rainfall normal for 1971-2000. A new approach that combines the dynamic method to the statistical method was then introduced.

The statistical-dynamical approaches

This innovative approach was conceived and is implemented by International Research Institute (IRI) who has developed software for seasonal forecasting named Climate Predictability Tool (CPT). This software allows almost all the necessary operations for seasonal forecasting modeling. The new approach abounds several innovations including:

- The increase in the number of predictors with the inclusion of 850 hpa wind (zonal and meridional components);
- An introduction to downscaling, say the production of the forecast for a local area (station);
- Use of several statistical techniques for model development (CCA, PCR, MLR); …etc

Figure 1 below is a CPT window display during the research of the best predictor for Cameroon.

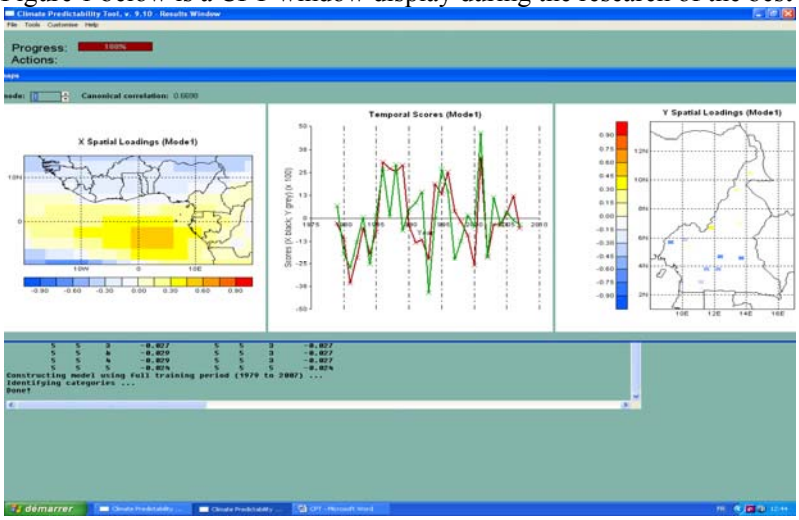

Once the models are obtained, they are used to produce the forecast.

Forecast

It is issued once the SSTs data used in different models are available. Usually in early May, the forecast should be prepared. The results from different techniques are brought together to build a unique forecast. For guidance, forecasts from some Global Producing Centers (GPC) are consulted and compared. The final forecast is obtained by consensus.

Forecasts are made for Three equi-probable categories of below-normal (dry conditions), near-normal (around the average), and above-normal (wet conditions). A probability is assigned to each category, indicating the chance of the particular category to occur during the target season. For example, a forecast presented as 20 30 50 should be understood as 20% chance of total precipitation being in the above-normal category, 30% normal and 50% below-normal. The use of probability is partly due to the inherent variability of the atmosphere.
Figure 2 below presents an example of the seasonal rainfall forecast for JAS 2008 rainfall in Cameroon.

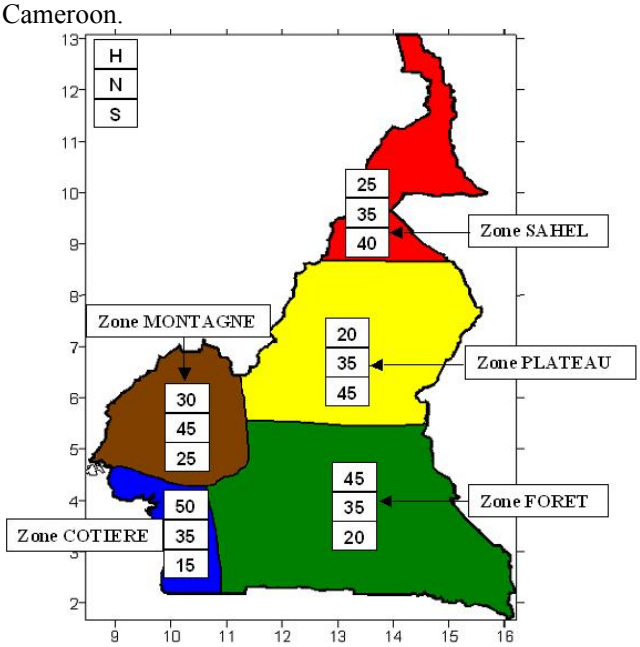

The use of the CPT provides the ability to produce an estimate of precipitations quantities for each station. The CPT also produce one map for each category of the forecast thus three map in total. An exemple is figure 3 below.

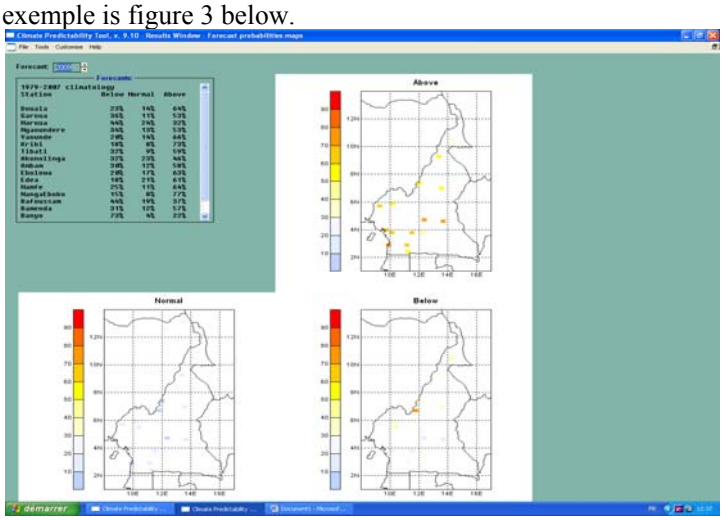

The forecast is then distributed to different users through various channels including RaNet (Radio and Internet) network. It should be recall that on request some specific users can obtain tailored climatic products at the Department of National Meteorology. These products include: onset/cessation of the rain; dry spell; risk of early sowing…etc

Verification and evaluation

The success of forecast is based on its quality and its use. At the end of each season a quality check of the forecast is made. The ‹‹Rank Probability Skill Score (RPSS) ›› method is used for verification of seasonal forecasts in Cameroon.
The map below shows the results of an audit conducted in 2008

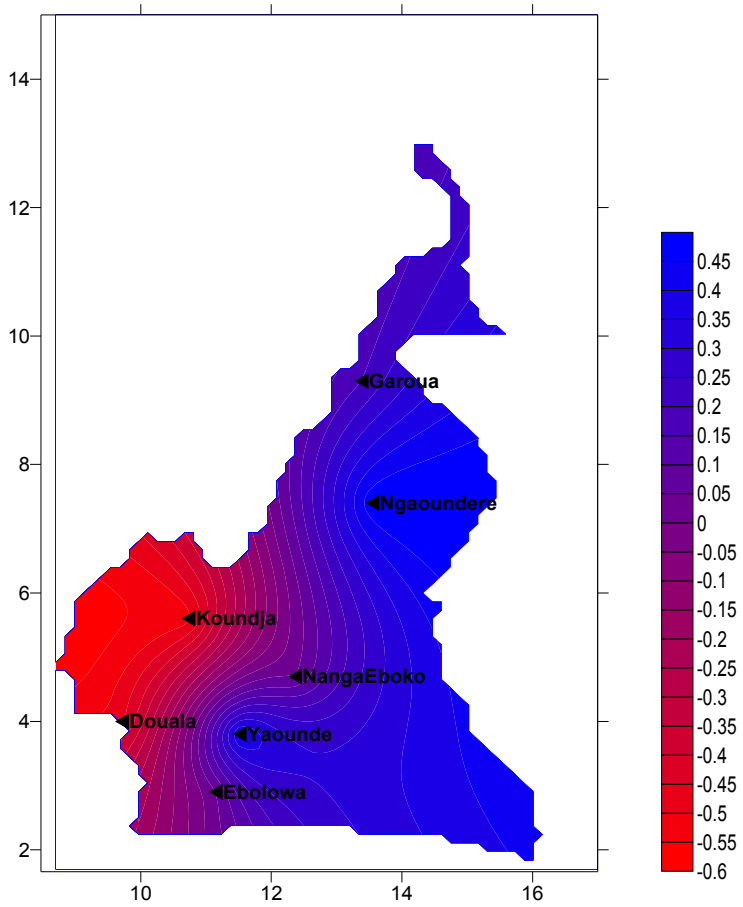

Conclusion

In order to satisfy their users with more precise climatic information the Department of National Meteorology of Cameroon has being able over time to adapt itself to new techniques to improve its products. The use of research results in the field of quantities precipitations forecast will continue to enrich the range of available products and possibly increase the reliability of forecasts.

REFERENCES

- Charles Mutai: 2000, Diagnosis and predictability of East African rainfall on intraseasonal to interannual timescale.
- Christopher Oludhe: 2002, Deterministic and probabilistic prediction approaches in seasonal to inter-annual climate forecast. Proceedings of an expert group meeting for regional association I (Africa) Banjul, Gambia.
- Guillermo J Berri: Practical application of seasonal to interannual climate prediction and decision making in agriculture and water resources management in Africa.
- NOAA-OGP: Jan 1999, An experiment in the application of climate forecast
- Washington, R. and Downing, T. E: 1999, seasonal forecasting of African rainfall: prediction responses and household food security, the geographical journal 165, 255-274.
- Climate Prediction Center (CPC) Website: http://www.cpc.noaa.gov/
- National Oceanic and Atmospheric Administration (NOAA) website: http://www.noaa.gov/
- International Research Institute (IRI) website: http://www.iri.columbia.edu/
- E F. Chavaux : 1991, Evaluation et vérification de la qualité des prévisions météorologiques.

Application of TCFM cloud motion wind in the analysis of Typhoon case study

WANG Zhen-hui[1, 2], ZHANG Lei[1, 2], YANG Yan-rong[1, 2, 3] ,ZHAN Yi-zhe[1, 2], ZHANG Zhi-guo[1, 2]

1. Key Laboratory of Meteorological Disaster of Ministry of EducationKLME, Nanjing University of Information Science & Technology,Jiangsu Nanjing 210044, China;
2. School of Atmospheric Remote SensingPhysics, Nanjing University of Information Science & Technology, Jiangsu Nanjing 210044,China;
3. College of Forest Resources and Environment, Nanjing Forestry University, Jiangsu Nanjing 210037, China

EXTENDED ABSTRACT:

1.INTRODUCTION

TCFM cloud motion wind technique is a new technique for tracking cloud with combination of Fourier phase analysis and maximum correlation (TCFM) to improve the precision of cloud tracking.In this article, TCFM technique is employed to retrieve cloud motion vectors for severe tropical storm “Morakot” from geostationary meteorological satellite FY-2C image series with a 30min interval on August, 2009. The retrieved data are assimilated at 1h interval into the numerical model ARPS (the Advanced Regional Prediction System) by means of its data analysis system ADAS for forecasting. And two other tests are designed for comparison: the control experiment with no data assimilated and the experiment with sounding data assimilated into the initial field.

2.TCFM TECHNIQUE

TCFM technique is based on the combination of Fourier phase analysis and maximum correlation.Firstly, the relevant rate in the second cloud goal of the search area to find the matching module A module,to get the module B,based on the difference between the position calculated the integer pixel displacement x_0. If module A and B match completely,then we consider that there's no sub-pixel exists,the mean velocity of the clouds in the direction X is $V = x_0/\Delta t$,otherwise,we consider that the difference between the two modules is produced by clouds of sub-pixel displacement,then we use the Fourier phase analysis technique to calculate sub-pixel displacement x’,combine x_0 and x’to get the final mean velocity: $U = (x_0 + x^{'})/\Delta t$. Use the same method,we can get the mean velocity of the direction Y.

3.ASSIMILITION OF THE CMW VECTORS

This paper selects the process of weather before landing of the "Moracot"to simulate,research mainly by precipitation. Use the satellite data of FY2-C,through the TCFM technology to get the CMW data which contains wind velocity,latitude and longitude,pressure of the simulation moments. Range is (90°E, 135.7°E)、(5.5°N,51.2°N).The test period for model integral was set from 0000 to 0600UTC,on August 7th,2009,totally 6 hours.And the corresponding background field was provided by reanalysis data from NCEP with the resolution of 1°×1 °. Simulation used one nested model which had 101×101 grid points with a horizontal resolution of 27km and 35 layers with a vertical resolution of 500m. The center was at (123.4°E, 23.7°N).The warm rain microphysics and Kain-Fritsch convective cumulus parameterization were used in coarse and fine grids. There were three test scheme designed,test one is control test noted cntl which simulate none data,test two joined the sounding data into initial fields and noted snd. Test three joined CMW data from the start of every 1 hour,and noted as cmw.

4.RESULTS ANALYSIS

4.1 Wind Field

Compared with the three experiments (cmw,snd and cntl) at 00:00,there's no big difference in the structure of the u-v horizontal wind fields,only the cmw has more vectors than the others and it been more clearly in the vortex structure of the Morakot,as it seen in Fig.3.The 6-hour integral experiment reveal that this vortex structure maintained and strengthened.

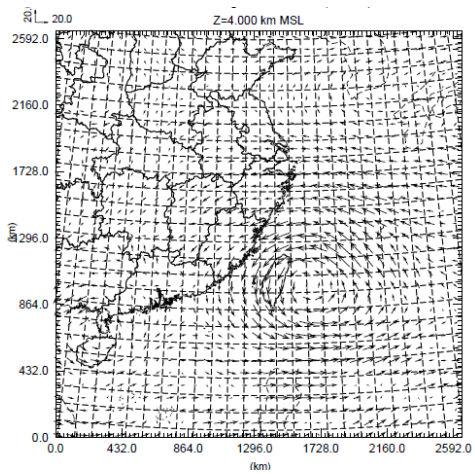

Fig.3 the initial wind field after the cloud motion wind data added

Compared u,v,w winds fields in individual shows that snd and cntl were roughly same in all altitude while cmw was stronger. Details can be seen in Fig.4.

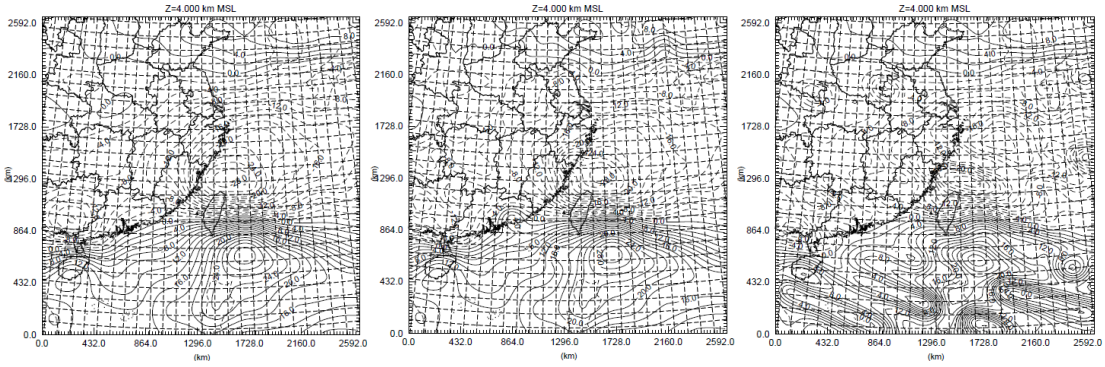

(a1)cntl (a2)snd (a3)cmw

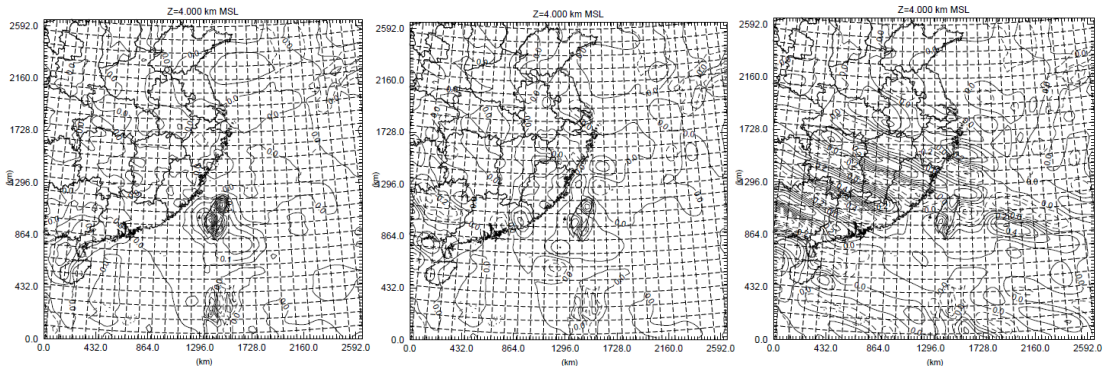

(b1)cntl (b2)snd (b3)cmw

Fig.4 the wind field for cntl,snd and cmw experiments at the initial time (a)U wind (b) W wind(4km height ,unit:m/s)

4.2 Cloud Water

As joined the cloud wind data at 00:00,the simulation result of typhoon eye in height along the typhoon path near the wall region appeared a strong upward motion,as height as roughly 16 km,which indicated that Typhoon wall area has very strong meso-scale activities.4km height of vertical wind field is given by the Fig.3(b3),while cntl and snd without such a structure.Three test corresponding position landscare mixing ratio (qc) greater value area as shown in Fig.4a. Combining analyzed levels of wind field in Fig.2,the initial moment of the sounding data assimilation and cloud track wind data test,their qc were located on the basic outline of typhoon periphery. And three tests of forecast six hours clouds water content (Fig.4b),long time continuous assimilated clouds motion winds data test showed the qc is mainly distributed in the typhoon profile,and somehow enhanced.

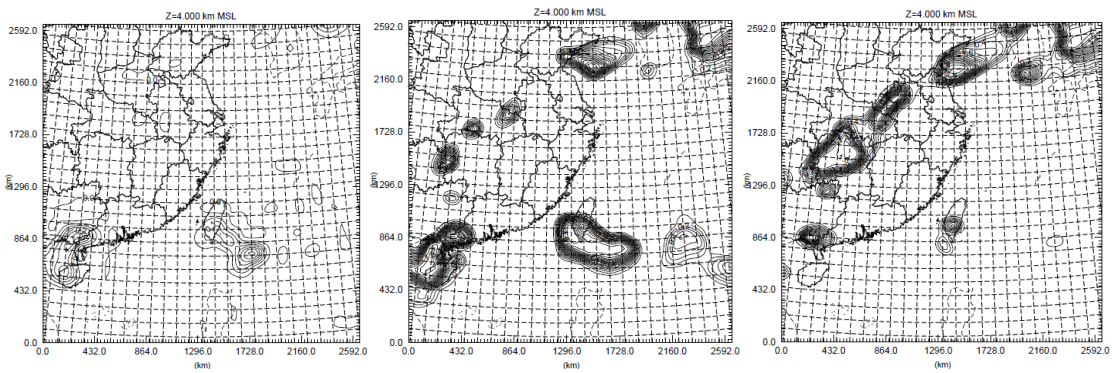

(a1)cntl (a2)snd (a3)cmw

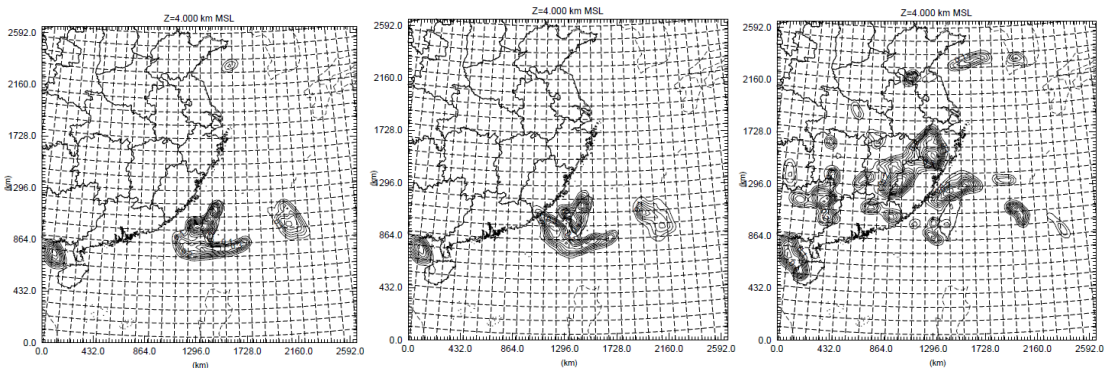

(b1)cntl (b2)snd (b3)cmw

Fig.5 the cloud water mixing ratio of the cntl,snd and cmw experiments at (a) initial time and (b) forecasting for 6h (unit: g/kg)

4.3 Divergence Field

This study also contained the vortex fields of the three experiments of the initial time and forecasting for 6-hour,as in the Fig.6.

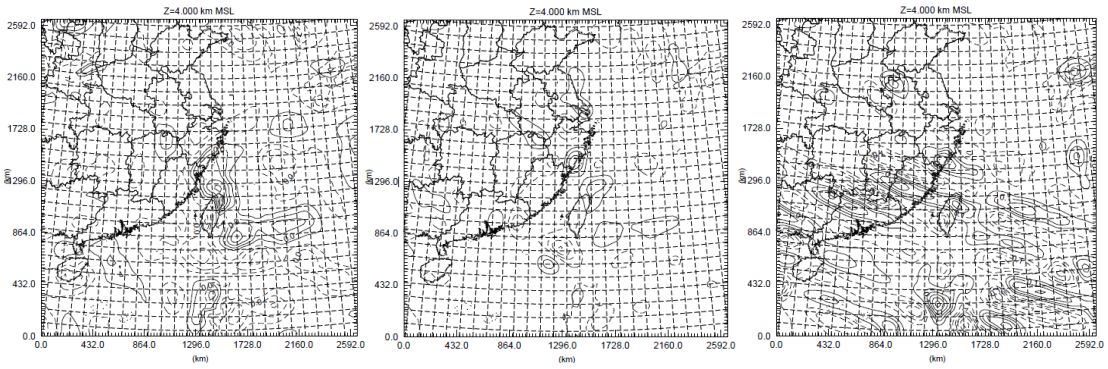

(a1)cntl (a2)snd (a3)cmw

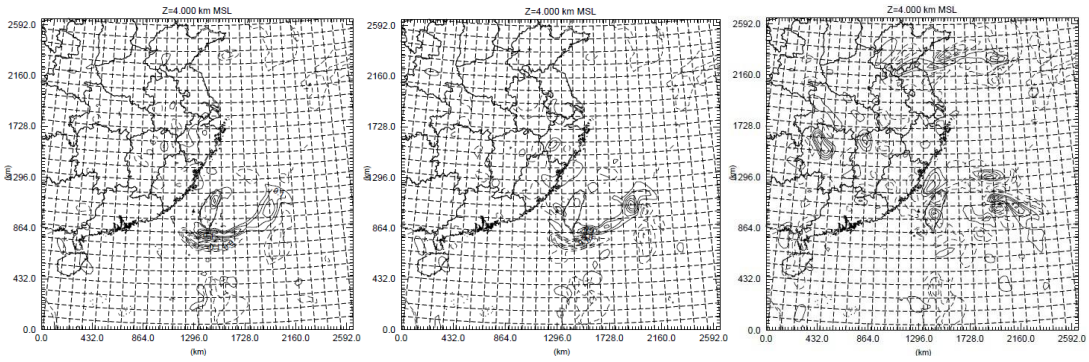

(b1)cntl (b2)snd (b3)cmw

Fig 6 the divergence of the cntl,snd and cmw experiments at (a) initial time and (b) forecasting for 6h (divergence *1000，unit: g/kg)

4.4 Rainfall

The total precipitation forcasted from the cntl,snd and cmw experiments for 3-hour (00:00-03:00) and 6hour (00:00-06:00) show in the Fig.7 as well as the average rainfall field observed by TRMM.

By comparing,it is clearly that only the cmw mathches the TRMM well in location and quantity whether in 3-hour or 6-hour.

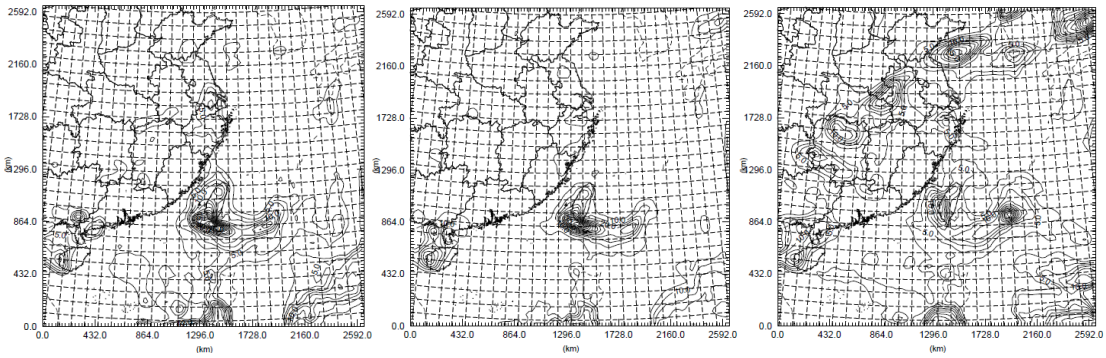

(a1)cntl (a2)snd (a3)cmw

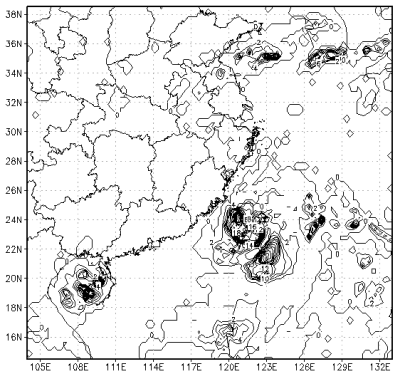

(a4)3h average rainfall observed by TRMM

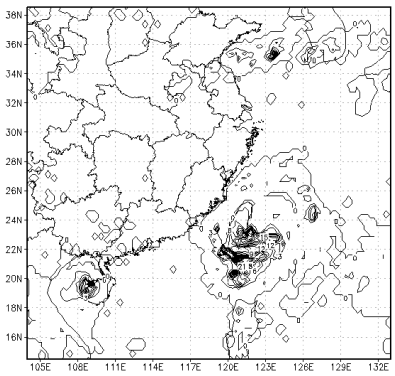

(b4)6h average rainfall observed by TRMM

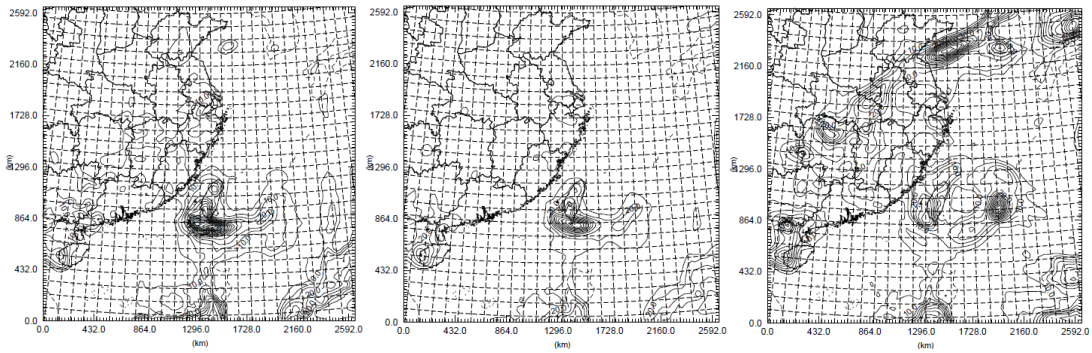

(b1)cntl (b2)snd (b3)cmw

Fig 7 the total precipitation forcasted from the cntl,snd and cmw experiments for (a) 3h 00:00-03:00 (b) 6h 00:00-06:00

5.CONCLUTIONS

The assimilation experiments of "Morakot" conducted in this article are meaningful to the application of the assimilation of the remote sensing data with meteorological satellite.By comparing the forecasting results of the three experiments, conclusions are drawn as follows:

(1) Initial vertical wind field is effectively adjusted after the CMW data assimilated into ARPS, which generates a severe conveciton lasting until the end of simulation.The water vapor centers locate at the same area as the severe convection, which provides advantageous conditions in eye wall area.

(2) There is no much difference in horizontal wind field, water vapor mixing ratio,snow and hail mixing ratio among the three tests.But the influence of cloud mixing ratio appeared from the beginning of the initial time, and the impact of cloud ice mixing ratio, cloud water mixing ratio strengthened and manifested gradually with the integral carried on.

(3) By comparing with TRMM observation of precipitation for 3h and 6h,it showed that, the experiment which CMW data assimilated continuously prevails over either the sounding data assimilated or the control experiment on precipitation simulations, bringing about a better result for forcasting position and the amount of precipitation.

REFERENCES

[1] 王振会，杨艳蓉，肖稳安等. TCFM 技术的卫星导风数据在台风模拟中的应用初探. 遥感学报,2009,13(3):515～521.

[2] 张守峰，王诗文. 应用卫星云导风进行台风路径预报试验. 热带气象学报，1999,15(4):347～355.

[3] 冯业荣. 云迹风资料在热带气旋移向预报中的应用. 气象,1999,25(12):11～16.

[4] 河惠卿，王振会，金正润，李峰，徐爱淑. 三种云导风资料及其对台风数值预报影响试验的比较分析. 热带气象学报,2009,25(1):82～88.

[5] Purdom J F W. Detailed cloud motions from satellite imagery taken at thirty second, one and three minute intervals. Proc. to the 3rd International Wind Workshop. Ascona,Switzerland,10～12 June,1996. EUM P-1: 137～145.

[6] Wang Z H, Browning K A and Kelly G A. Verification of the Tracking Technique Used in an Experimental Cloud Motion Wind Inferring System. JCMM Report. University of Reading, 1997.

[7] 李峰，王振会，官莉，何惠清. 两种导风方法在台风路径分析中的应用比较研究. 气象科学，2009,29(3):330～334.

[8] 许建明，王振会. 傅立叶相位分析导风技术的适用范围和相位重叠分析[J]. 气象科学，2004，24(3):312～313.

[9] 朱平. TCFM技术及其在云导风中的应用研究. 硕士学位论文. 2007.

Title: Methodological and experimental studies of data assimilation techniques on the convection-permitting scale

Volker Wulfmeyer

Summary:

Data assimilation (DA) on the convection-permitting scale is a key research topic in atmospheric sciences. On the one hand, this is due to the expected high positive impact on the prediction of high-impact weather events, particularly in terrain with complex land-surface and orographic properties. On the other hand, severe challenges occur due to non-linearity of model physics and non-Gaussian error stastistics of model background and observations. We present an overview of DA techniques which have the potential to improve the forecast skill using convection-permitting models and ingesting many observations which have not been routinely used yet. We are focusing on variants of the stochastic EnKF and compare this with the expected performance of 3DVAR. Hybrid combinations of variational and ensemble-based techniques and the consideration of non-Gaussian statistics are also discussed.

Analysis of Convective Precipitation and Lightning Based on Multi-scale Wavelet Edge Detection

XU MINGYI[1, 2], WANG ZHENHUI[1, 2], PAN JIAWEN[1, 2]

[1] *Key Laboratory of Meteorological Disaster of Ministry of Education , Nanjing University of Information Science &Technology, Nanjing 210044, P. R. China*

[2] *School of Atmospheric Physics, Nanjing University of Information Science & Technology 210044, P. R. China*

sweetydaisy@163.com

Quantitative precipitation estimation has always been a target for us meteorologists. In 1960s, man has discovered that precipitation surge after lightning flashes [1]. Zhang Yijun et al. discussed the correlation between precipitation and lightning and found that lightning activities were well related to strong precipitation but poor related to weaker precipitation [2]. Zhou Yunjun et al. pointed out that there was significant correlation between convective precipitation and lightning, the function of average precipitation and flashes can be established using non-linear fitting method: R= 1.692lnF-0.273, related coefficient is 0.8641[3].

Since lightning is well related to convective precipitation and unlike rain gauge, radar and satellite, lightning locating system has a wider detection range, no limit to radar shadow but a higher resolution and lower cost, using lightning to estimate convective precipitation is quite a good approach, providing a new method and complement[4-6].

This article borrows ideas from multi-scale wavelet edge detection algorithm and applies it to radar reflectivity data processing in order to effectively identify convective cloud echo region, then convective precipitation obtained from echo inversion is analyzed with lightning [7].

1 multi-scale wavelet edge detection algorithm

(1) Preprocessing of radar reflectivity data: radar data are interpolated to gridding in rectangular coordinate system using hybrid approach, which, the size of grids is 1km* 1km.

(2) This process is dealing with the radar data with wavelet transform, obtaining maximum modulus of each scale. Assume there are J scales [8].

(3) Borrow ideas from Wavelet Edge Detection, images of each scale are dealt with self-adapting threshold and modulus maximum method, now we can get image "Edge" of each scale.

(4) Reconstruction of the J scale (the last scale): the three high frequency components are replaced with "Edge", then new image "IM_J" of J scale was obtained with replaced high frequency components and low frequency component by taking inverse wavelet transform.

(5) Replace the three high frequency components of J-1 scale with "IM_J", then reconstruct

The work is supported by China Commonweal Industry Research Project GYHY200806014.

new image "IM_{J-1}" of this scale. And so on, we can get the reconstructed image "IM_1" of the first scale, that is, the Multi-scale Wavelet Edge Detection image.

(6) Finally, the denoised image is obtained by median filtering.

2 Case study

Take a weather process of severe thunderstorm and heavy precipitations happened in Nanjing on July 6, 2009 to July 7, 2009 as case study, and choose 180 minutes of this process when there are relatively densely lightning flashes and precipitation. Convective cloud echo regions are then recognized with multi-scale wavelet edge detection algorithm using radar reflectivity data from Longwang station every 6 minutes.

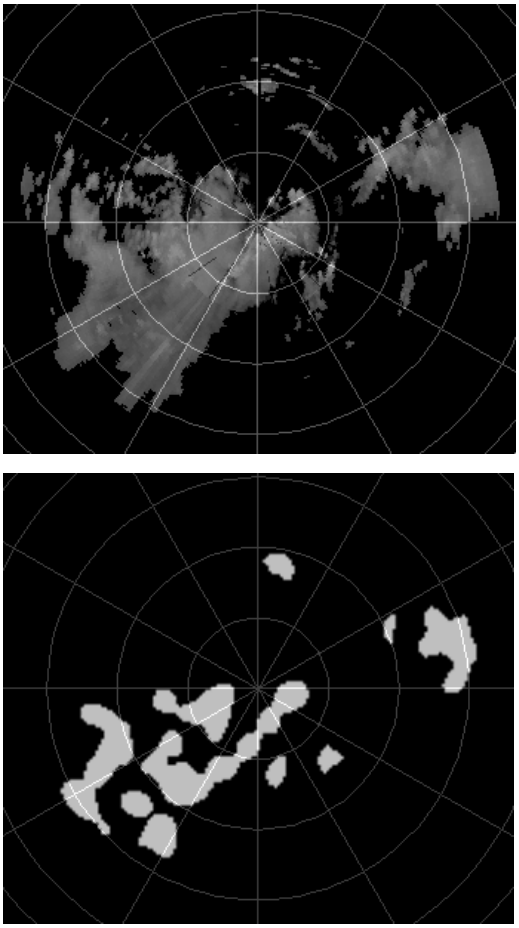

Fig1 23:18, July 6 2009, original radar reflectivity and convective echo recognition

After that, corresponding convective precipitation is inversed with Z-I relation [9]. At the same 6 minutes, lightning flashes are calculated, so the relation between convective precipitation and lightning can be analyzed.

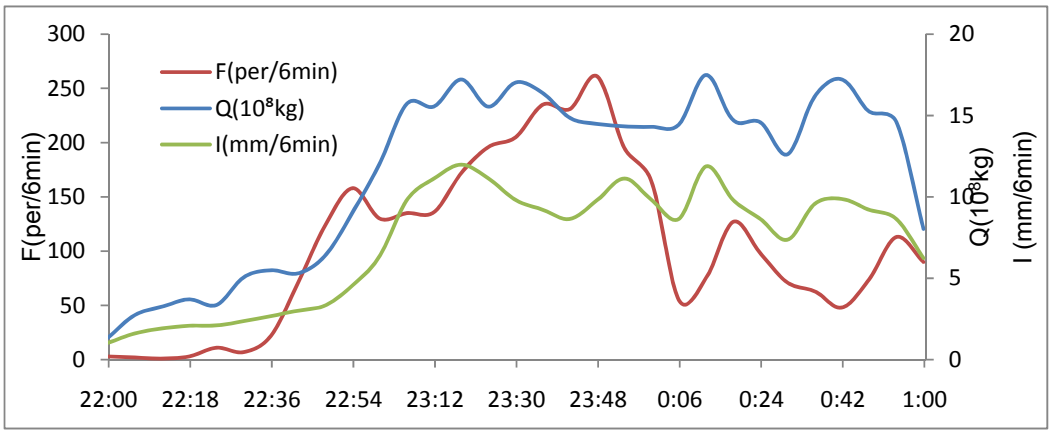

Fig2 timing diagram of Q, I and F

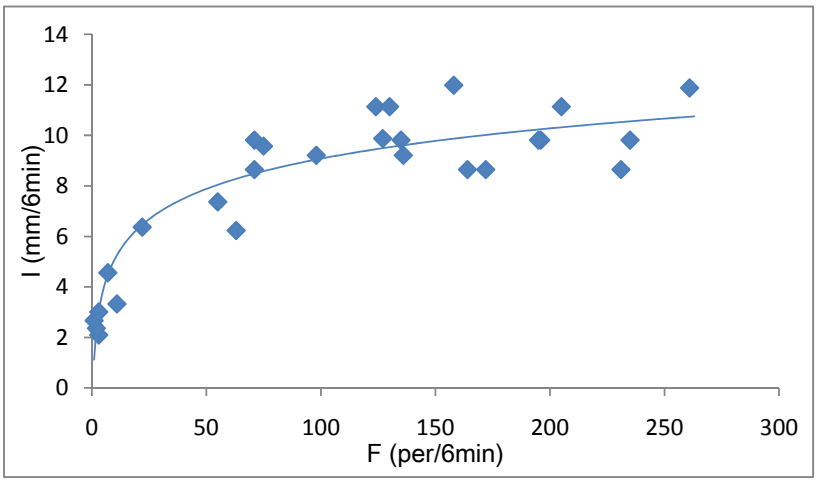

Fig3 fitting curve of I and F

Results show that rainyields per flash (RPF) ranks from 7.47×10^{7} to 4.46×10^{8} kg, average value is 1.72×10^{8}kg; non-linear curve fitting equation of precipitation intensity(I, mm/6min) and lightning frequency(F, flashes/6min) is I=1.728ln F+1.122, related coefficient is 0.8044.

References

[1] Moore C B, Vonnegut B, Vrablik E A, et al. Gushes of rain and hail after lightning [J]. J Atmos Sci, 1964, 21 (6) : 646-665.

[2] Zhang, Y.J, Hua, G.Y, Yan, M.H. The correlation analysis of electric activity, convection and precipitation in convective cloud and stratus[J]. Plateau Meteorology. 1995, 14 (4): 396-405.

[3] Zhou, Y. J, Qie, X. S. A study of the relationship between cloud-to-ground lightning and precipitation in the connective weather system in China[J]. Acta Meteorologica Sinica. 1999, 2(57).

[4] Stener M, Houze R A , Yuter S E, Jr Climatological characterization of three-dimensional storm structure from operational radar and rain gauge data[J]. Journal Applied Meteorology, 1995, 34(9):1978-2007.

[5] Churchill D D, Houze R A, Jr. Development and structure of winter monsoon cloud

clusters on 10 December 1978[J]. Journal Atmospheric Sciences, 1984, 41(6):933-960.
[6] Bigge rstaff M I, Listem ass S A. An improved scheme for convective/stratiform echo classification us ing rad ar reflectiv ity[J]. Jou mal Applie d Meteorology, 20 00, 39(1 2): 2129-2150.
[7] Yan, J, He, X.H, Wang, H.M, Convective cloud identification algorithm based on weather radar image [J]. Journal of Computer Applications. 2009, 29(12).
[8]Chen, F . I mage e dge detection based on multi-resolution wav elet transform ation [J]. Computer Engineering and Applications. 2009, 45(27),160-162.
[9] Zh ong, L .Z, Gu, S.S, Liu , L .P. A Alg orithm Id entifying Con vective and Strariform i n Mixed Precipitation and Its Application to Estimating Precipitation [J]. Plateau Meteorology. 2007, 26(3).

Research on the Relationship between Attenuation Coefficient andRadar Reflectivity Factor for Spherical Particles in Clouds at mm Wavelengths

TENG Xu [1,2] , WANG Zhenhui [1,2] , JI Lei [2] , ZHAO Fenghuan [2]
[1]Key Laboratory of Meteorological Disaster of Ministry of Education，Nanjing University of Information Science & Technology, Nanjing 210044, P. R. China
[2]School of Atmospheric Physics, Nanjing University of Information Science & Technology 210044, P. R. China
tuantuan2000@hotmail.com

1 Introduction

Because of millimeter wavelengths close to the scale of cloud particles, more and more millimeter radar systems are being used to detect cloud and small precipitation particles. When using millimeter wavelength radars, the attenuation caused by cloud and precipitation particles' scattering and absorption together with the water vapor and oxygen absorption at millimeter wavelength must be take into account. In order for the actual need of mm wavelengths cloud radar data processing, presuming that the cloud particles are sphere particles, by sampling cloud drop size spectra which follow the K- M distribution and the rain drop size spectra which follow the Gamma distribution for 1330 times, respectively, and by adopting the Mie scatter theory formula for computing scattering, absorbing and back-scattering cross-sections, the attenuation coefficient k and radar reflectivity factor Z are calculated for 3.2 and 8.6 mm wavelengths and the k-Z relationship has been obtained.

2 Methods

The attenuation of millimeter cloud radar echoes

$$k = k_{air} + k_{cloud}$$

k_{air} can be calculated by the atmospheric absorbing Liebe mode(Liebe, 1985), k_{cloud} can be obtained by the k-Z relationship.

By formulas $k = \int_0^{D_{\max}} N(D)Qt(D)dD$ and $Z = \int_0^{D_{\max}} N(D)D^6 dD$, the k-Z relationship can be presented as $k = aZ^b$ (Wang, 2000).

Presumed the droplet size distribution of precipitation follow the Gamma distribution (Clark, 1974):

$$N(D) = C_1 D^m \exp[-(3.67+m)D/D_0]$$

while the droplet size distribution of cloud(include water cloud and ice cloud) follow the K-M distribution(Marshall, etal,1948):

$$N(D)=C_1 D^2 \exp(-l\,D)$$

The ranges of the DSD(droplet size distribution) parameters for cloud and precipitation were set separately according to domestic observations.
By numerical simulation and sampling to droplet size distribution for 1330 times, the k and Z at 3.2 millimeter wavelength and 8.6 millimeter wavelengths were got, then the coefficient α&β were counted statistically, and the k-Z relationship $k = aZ^b$ at the two wavelengths were finally obtained .

3 Results

3.1 The k-Z relationship in water cloud

The parameters of the K-M distribution(C_1 、 l) were dicided by cloud droplet number concentration(N) and liquid water content(M)，the ranges of N and M were set as

$$10 < N < 1000 \quad (cm^{-3}), \qquad 10^{-4} < M < 1\ (g/m^3)$$

The k-Z relationship for small sphere particles in water cloud were obtained.(Fig.1)

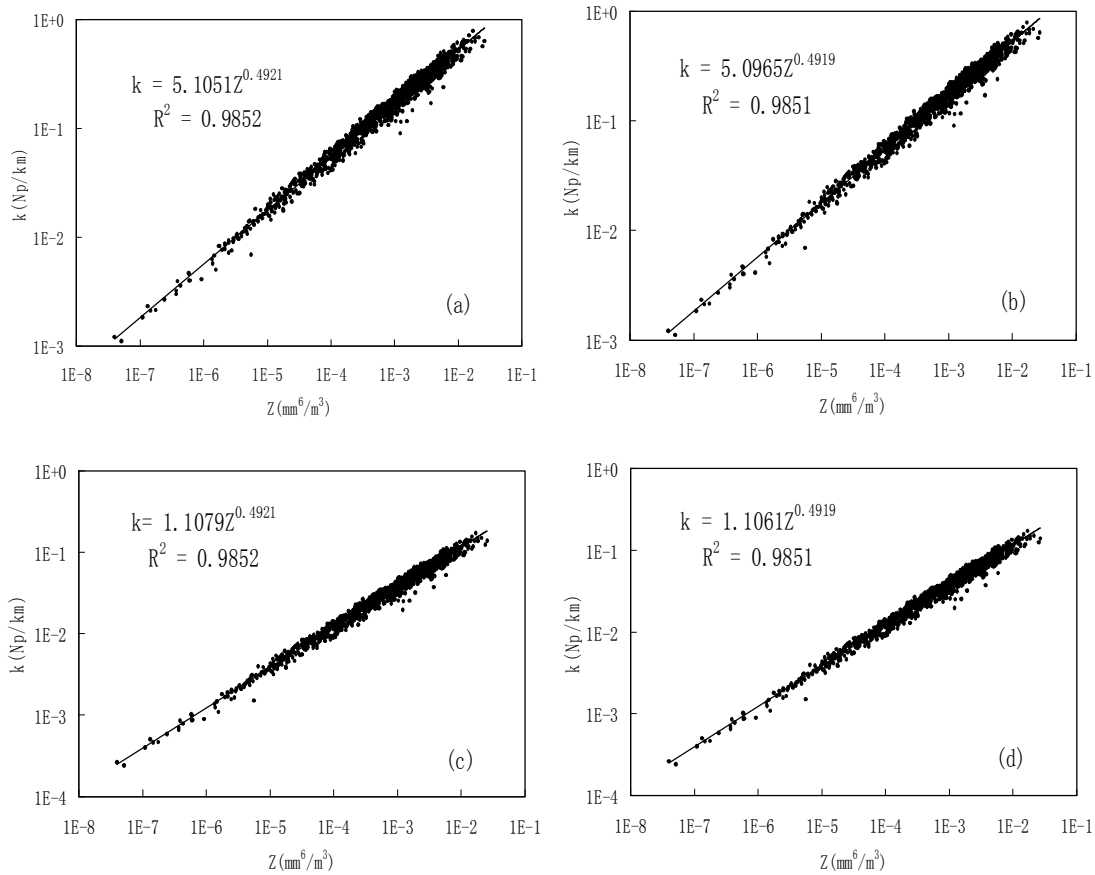

Fig. 1 The k-Z relationship for small sphere particles in cloud.
（a）λ=3.2mm,Dmax=0.006 cm,（b）λ=3.2mm,Dmax=0.01 cm
（c）λ=8.6mm,Dmax=0.006 cm,（d）λ=8.6mm,Dmax=0.01 cm

3.2 The k-Z relationship in ice cloud

The parameters of the K-M distribution(C_1、 l) were dicided by ice concentration(N) and ice water content(IWC)，the ranges of N and IWC were set as

$$10^{-4} < N < 10\ (cm^{-3}),\qquad 10^{-4} < IWC < 10^{-1}\ (g/m^3)$$

The k-Z relationship for small sphere ice particles in cloud were as followed:

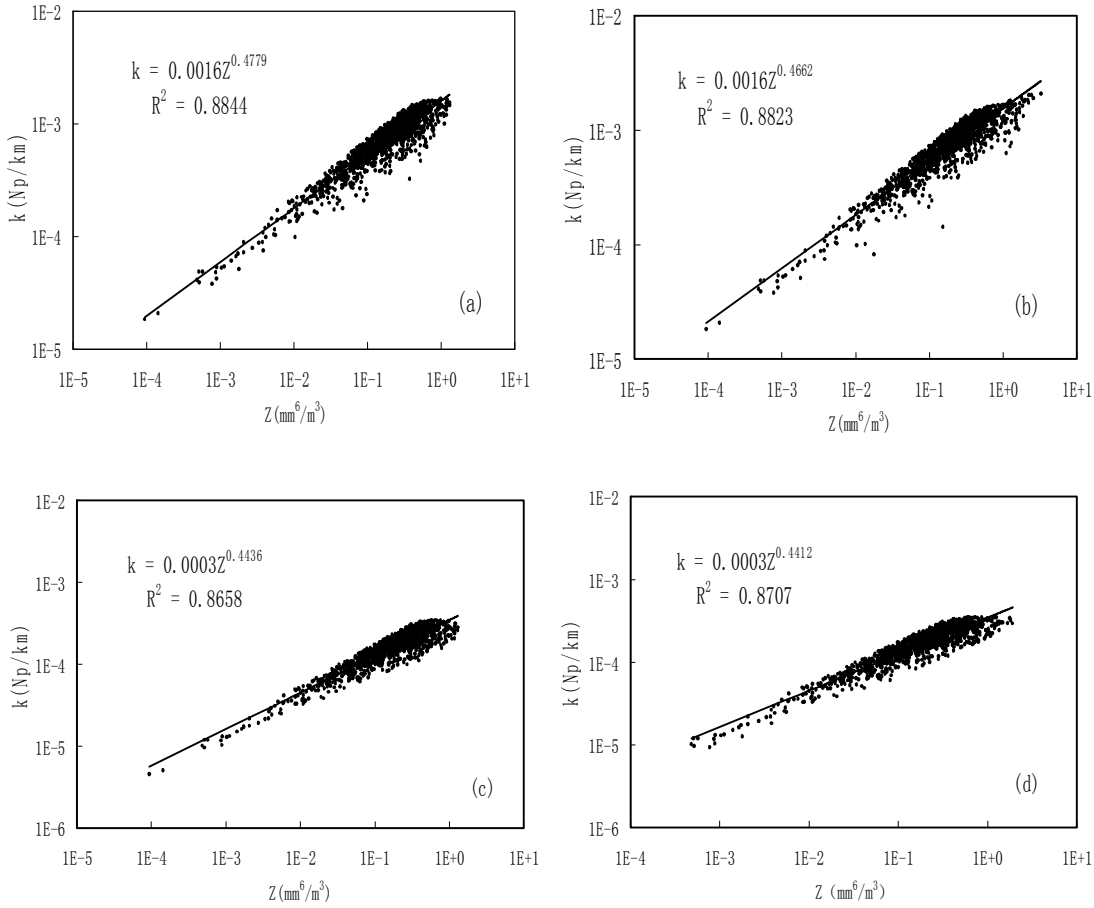

Fig.2 The k-Z relationship for small sphere ice particles in cloud.
（a）λ=3.2mm,Dmax=0.02 cm,（b）λ=3.2mm,Dmax=0.04 cm
（c）λ=8.6mm,Dmax=0.02 cm,（d）λ=8.6mm,Dmax=0.04 cm

3.3 The k-Z relationship in precipitation

The ranges of the parameters of the Gamma distribution(C_1、 m 、 D_0) were set as

$$0.00015 < C_1 < 0.15\text{，}\quad -1 < m < 4\text{，}\quad 0.015 < D_0 < 0.1$$

The k-Z relationship for small sphere particles in precipitation were as followed:

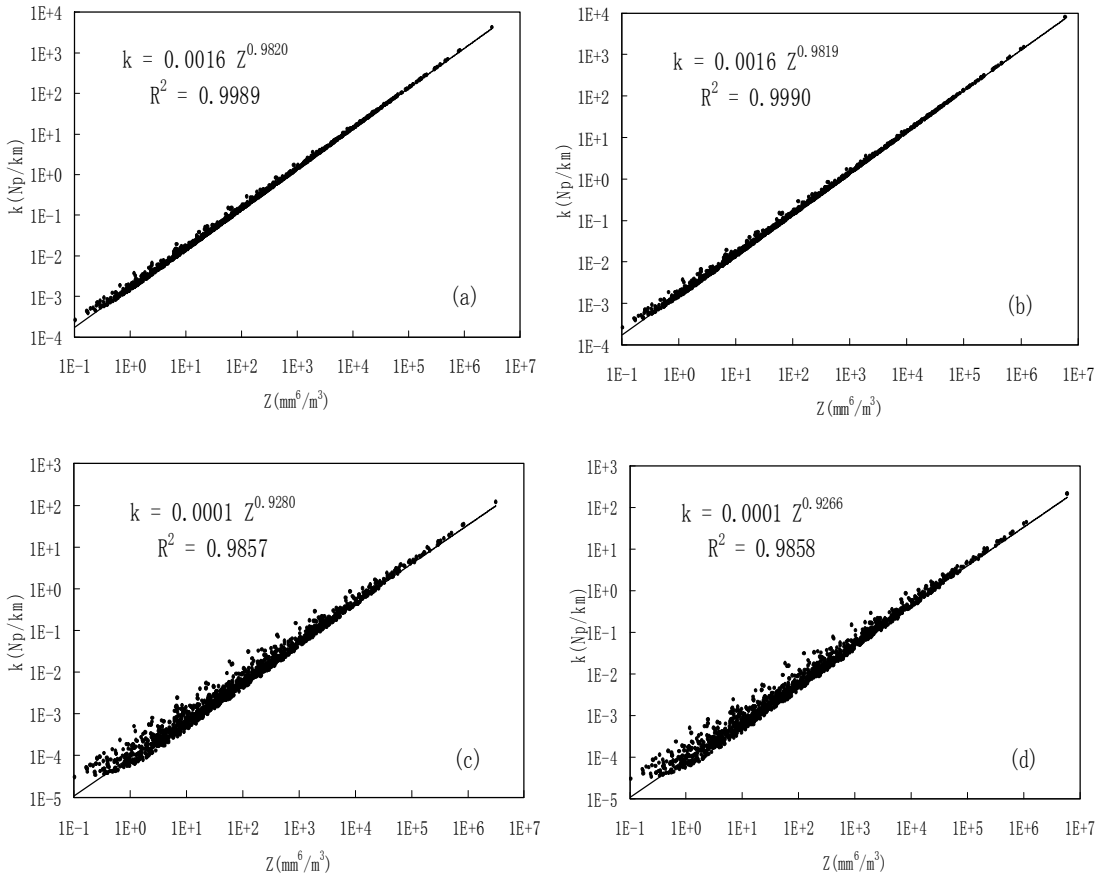

Fig.3 The k-Z relationship for small sphere particles in precipitation.
（a）λ=3.2mm,Dmax=0.5 cm,（b）λ=3.2mm,Dmax=1.0 cm
（c）λ=8.6mm,Dmax=0.5 cm,（d）λ=8.6mm,Dmax=1.0 cm

4 Conclusion

By numerical simulation and sampling to drop size spectra of cloud and precipitation which followed the Gamma distribution for 1330 times, the k-Z relationship of the cloud and precipitation particles at 3.2 millimeter wavelength and 8.6 millimeter wavelength were obtained separately. Viewing on Graph1 – Graph3，the coefficient α&β of the k-Z relationship had a good stability at 3.2 millimeter wavelength and 8.6 millimeter wavelength . As far as α&β were concerned, the maximum particles diameter (Dmax) had little impact on the k-Z relationship, and the correlative coefficient (R^2) were above on 0.85, which indicated the k-Z relationship had a statistical significance. Moreover, on the condition of the same droplet size distribution and the same value of Dmax, the attenuation of the radar echoes at 3.2 millimeter wavelength were much serious than that at 8.6 millimeter wavelength. It shows the attenuation at the 3.2mm is 5-10times larger than that at 8.6mm under the same conditions of the drop size spectra. which were going to be applied into the further

research on the correction for attenuation to millimeter wavelengths radar echoes. The k-Z relationship coefficients were available for attenuation correction of mm radar, and the formulas were going to be applied into correction for 3.2 and 8.6 mm radar attenuation.

References

Liebe H J.(1985):An updated model for millimeter wave propagation in moist air [J].Radio Sci , 20 (5) : 1069~1089.

Wang Zhenhui, Zhang Peichang.(2000):Relationship between attenuation of microwaves by polydisperse small spheroid particles and their radar reflectivity factor. Acta Meteorologica Sinica,58(1):123~128.

Clark TL.(1974): A study in cloud phase parameterization using the gamma distribution[J]. J Atmos Sci, 31(1):142~155.

arshall J S, Palmer W M.(1948):The distribution of raindrops with size[J]. Meteor,5(1):165~166.

Relationship between the interannual variation of the intensity of low-frequency oscillation for rainfall and the number of the heavy precipitation process over the lower reaches of the Yangtze River valley

Yang Qiuming, Huang Shicheng, Li Yi
Jiangsu Meteorological Institute, Nanjing 210008, China
E-mail: yqm0305@263.net

Abstract

Intraseasonal oscillation (ISO) [1-5] is a strong signal source in the extended-range weather changes. The formation and changes of ISO patterns associated with the extended-range rainfall over the lower reaches of Yangtze river valley (LYRV) in summer are very complicated, and many problems remain to know further. It is importance for further understanding these connections in theoretical meaning and practical value.

To better understand the low-frequency oscillatory variation of rainfall over LYRV (average of the 25 stations for the region (118.0°—122.5°E, 30.5°—32.0°N)), a non-integer spectral analysis[6] of the daily rainfall for May 1—August 31 in 1961—2005 is performed. It is found that the primary periods that have statistical significance at a 95% confidence level are of 10—20 days, 20—30 days, and 60—70 days (Figure 1). The variation of the low frequency oscillation of the rainfall has an important influence on the heavy precipitation process. Figure 2(a) shows the interannual variations of the number of the heavy precipitation process over LYRV (average of daily precipitation in this region is greater than or equal to 25 mm) in May—August from 1961 to 2005. Similarly, the non-integer spectral analysis is also conducted for this time series. The results show that the variation of the number of the heavy precipitation process over LYRV is mainly of oscillations of 2.0 and 11.2 years, but the long-range trend is less significant.

To study the relationships between the interannual intensity variation of the low-frequency oscillation of rainfall over the different ranges of frequency and the number of the heavy precipitation process over LYRV, the correlation coefficients are computed between the statistical parameter *F* series (Figure 1) corresponding to the individual periods (non-integer) and the number of the heavy precipitation process over LYRV in May—August. Figure 2(b) displays the correlations between the number of the heavy precipitation process and intensity of the periods (statistical parameter *F* series) on the time scale of 10—70 days. It follows that the number of heavy precipitation process over LYRV has a strongly positive correlation with the intensity of its 28-day oscillation (with the correlation coefficient of 0.452 and statistically significant at a 99% confidence level). And it has a significantly positive correlation with that of the 18-day oscillation (with the correlation coefficient of 0.319 and statistically significant at a 95% confidence level), but has an insignificant relationship with that of the 30—70-day oscillation. It is then concluded that the variations of the intensity of the 20—30-day and 10—20-day oscillations have a significantly positive correlations with the heavy precipitation process over LYRV. The strong and weak years of these two oscillations are associated with normal to anomalously more and normal to anomalously less number of the heavy precipitation process over LYRV. These relationships are of indicative guidance for the climatic pre-

diction of the heavy precipitation process over LYRV. Therefore, it is realistically important to work hard on improving the study on the 20—30-day and 10—20-day oscillations of rainfall over LYRV and their connections to the principal circulation patterns on the subseasonal time scales[7].

Since the relationship between the intensity of the 20—30-day oscillation of daily rainfall and the number of heavy precipitation process over LYRV is the most significant, the evolution of the 20—30-day oscillation would provide a better indicative significance for the extended-range forecasting during the 10—30 days.

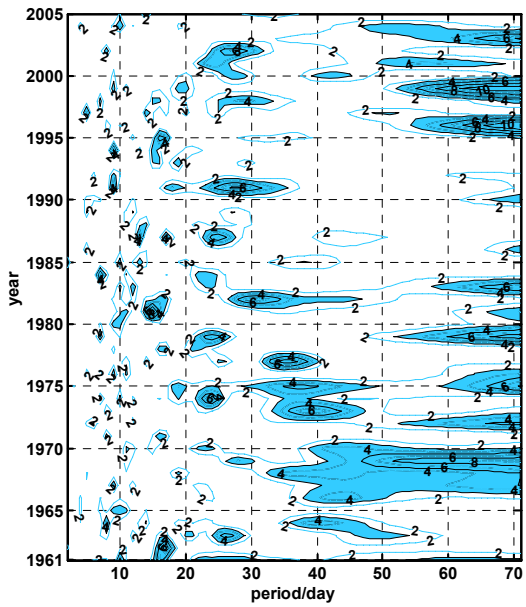

Figure 1 Interannual variations of the periods for the daily rainfall over the lower reaches of Yangtze River valley (LYRV) in May—August during the period of 1961—2005. Shaded areas with the 95% significance level. The shaded regions give a 95% significance level test of two-dimensional non-integer power spectra (statistical parameter F >3.50) for the regression equation corresponding to the non-integer period, with the individual periods (non-integer) as the abscissa and the time (year) as the ordinate

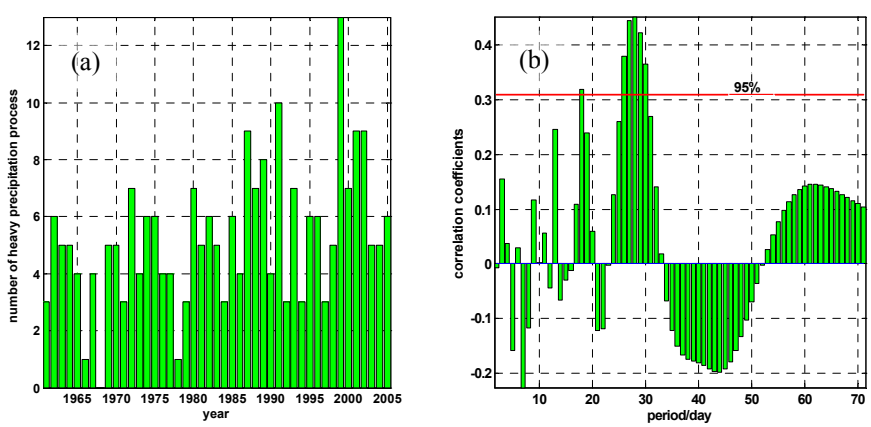

Figure 2 (a) Time series of the number of the heavy precipitation process over LYRV in May—August from 1961 to 2005 and (b) correlations between the number of the heavy precipitation process and the intensity of the periods on the timescale of 10–70 day, which the significant level of 95 % is represented by horizontal dashed line.

Reference

1 Madden R A, Julian P R. Detection of a 40—50 day oscillation in the zonal wind in the tropical Pacific. J Atmos Sci, 1971, 28: 702—708.

2 Madden R A, Julian P R. Observation of the 40—50-day tropical oscillation—A review. Mon Weather Rev, 1994, 122: 814—837.

3 Waliser D E, Lau K M, Stern W, et al. Potential predictability of the Madden-Julian oscillation. Bull Amer Meteorol Soc, 2003, 84(1): 33—50.

4 Wang H J, Han J P, Zhang Q Y, et al. Brief review of some CLIVAR-related studies in China. Adv Atmos Sci, 2007, 24(6): 1037—1048.

5 Wang B. Thrusts and prospects on understanding and predicting Asian monsoon climate. Acta Meteorologica Sinica, 2008,22(4):383-403.

6 Schickedanz P T, Bowen E G.The computation of climatological power spectra. J Appl Meteorol, 1977, 16: 359—367.

7 Ding Y H and Liang P. Extended range forecast Basing on MJO (in Chinese). Meteorological Monthly, 2010,36(7): 111-122.

Study on Mechanism of an Extra Rainfall Process Caused by the Remainder of Typhoon FUNGWONG

YIN Dong-ping W U Hai-ying ZENG Ming-jian ZANG Bei
Jiangsu Provincial observatory, Nanjing 210008, China

1 INTRODUCTION

Torrential rainfall caused by typhoon landfall required not only sufficient water vapor, but also convective instability energy transported to the storm region. As the storm intensified, positive vorticity extended to mid-level and divergence on the high-level increased, so that strong vertical motion occurred in the storm region [1-5].The studies on structure evolution characters of landfall neutercanes showed that basically symmetry vertical structure transformed to baroclinic asymmetry in the period of metamorphosis phase, and also found the neutercane intensified was related closely to the westerly upper-level trough's intensity [6-7]. For example, in the extraordinary storm case occurred over Chuhe area on July 31~August 1, 2008, caused by the depression weakened from Fung-wong typhoon two days later. The Chu River rose rapidly , with Xiaoqiao hydrologic station water level in Pukou rose to 12.62m from 7.5m in 30 hours which was only 1cm lower than the highest water level record(12.63m).

2 REAL-TIME PRECIPITATION

According to the raininess and the time for the extraordinary storm case, we divided it into two phases (see Fig.1). In the first phase, the severe precipitation region was centered around Hanshan in Anhui Province from 2300 BT(Beijing Time),31st Jul to 0800 BT, 1st Aug with maximum precipitation in 6 hours reaching 202mm (in the period of 2100 BT,31 Jul ~ 0600 BT,1st Aug). Moreover the maximum precipitation of 269mm occurred at Chuzhou in Anhui Province, from 2000 BT, 1st to 0200 BT, 2nd Aug.

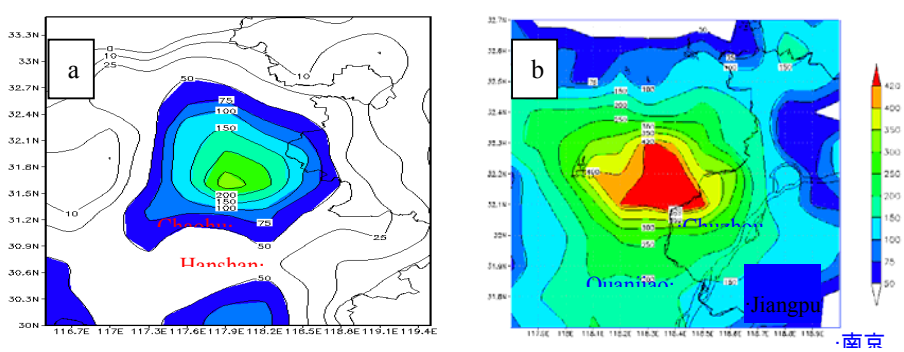

Fig.1 Precipitation distribution in the adjacency area of Jiangsu and Anhui Province
a from 2000 BT,31 Jul ~0800 BT, 1 Aug; b from 1500 BT,1st Aug ~ 0800 BT,2nd Aug
(Unit: mm)

3 WEATHER SYSTEM

Typhoon Fung-wong genesis to the eas tern ocean of Philipp ines on July 25, 2008. At 2200 BT, July 28, it decreased as tropical storm at Fuqing City in Fujian Province and moved northwest by north after being in northeastern of Jiangxi fro m northwestern of Fu jian. The typhoon decreased gradually after landing and moving on. When it reached Jiangxi Province, Fung-wong rounded Huan g Mountain an d turned northeast al one Changjiang Riv er o n t he south slope of Dabie Mount an d maintained stably ov er the border of Jiangsu and Anhui. After 2000 BT, 31 Jul, there existed a low pressur e system below 500 hPa with its center over Chuhe region, while souther appered over Nanjing. At that moment, a deep trough existed below 500hPa replacing the intact de pression circulation be fore. Th e s outherly je t axis veer ed from south-north to northeast-southwest for the reason that the Fung-wong moving northward and the subtropical high str engthened a nd e xtended west ward. Meanwhile the re ex isted a southwest j et convergenced below 850hPa. At 0800h, 1st Aug, trough in westerlies on 500hPa moved eastward to the north between the high and low circulation with east erly over Nanjing, which form ed head wind with westerlies.

4、JET STREAM EFFECT ON TORRENTIAL RAIN

4.1 Water vapor transportation function

It is evident from the ti me-height cr oss section of moisture flu x di vergence alo ng the heavy rainfall center at(32°N ,118°E)that water vapor from west side of southly jet and those from S outh Sea c onvergenced o ver t he torr ential rain region. In th e peri od of rai ning, t he water vapor transportation and convergence increased obviously and developed upward. In a word, the d eepen of moisture th ickness ov er the sever rai nfall was relevant with the wat er transportation by low-level southwester jet and tip ascending motion.

4.2 Mesoscale convective system triggered by low-level jet

In the fir st ph ase of se ver precipitation, th e depression circulation d ecreased b y Fung-wong r e-developed b y virtue o f stable barometric l ow structure transfor med wit h southwest warm and moisture air flow surging into the heavy rain region, which leading to the souther fluctuation. Under the condition, ascending motion reinforced over the eastern of the barometric low and the convective cluster moving into the Chuhe region grew rapidly.

In the seco nd phase, southwest jet and col d air from western Hetao Ar ea met an d their strength equal, so that a cold air dam came into being while warm and moisture air damming on the south side of the cold da m. In consequence, southwest f low at t he b ack of the je t reinforced and the baroclinicity intensified. Mesoscale convective system was triggered by the invasion of cold air which made the disturbance enhanced.

4.3 Mesoscale convective system driven by boundary layer jet fluctuation

In order to study the ro le of s outhwest jet on differen t lev el aff ect on sever rainfall, numerical si mulation about b oundary lev el jet w as carried o ut. The preci pitation over t he Chuhe region concentrated on the period of time from 2000 BT, 1st to 0200 BT, 2nd Aug, which corresponding to the phase for the boundary jet enhanced again at the back. The souther developed at the back of the b oundary je t en hanced the low level convergence in the torrential rain region,

which promoted the shear line development on the north side of the back of jet and a confined ascending air was compelled.

5、MERIDIONAL WIND FLUCTUATION

To explore the low level cold air movement characteristics in the period of precipitation, meridional wind temporal evolution was carried out with the grid data at the point (32°N,118°E) averaged for ten days after the typhoon Fung-wong landfall. The time-height cross section show that northern disturbance increased and it was centered from 800 to 400hPa. The disturbance reached the maximum value at 2000 BT, 1st Aug. So the increasing and developed downward do favor to the sufficient release of the unstable energy in warm and moisture flow.

6、DEVELOPMENT OF MESOSCALE VORTICITY AND ASCENDING VELOCITY

The positive vorticity center value increased and overlapped with the vertical velocity centre. As the ascend motion decreased, the intensity of the precipitation weakened in the period of 08h~14h, 1st Aug.

The torrential rain restarted after 1500 BT 1st Aug in the course of cold air strengthening and mid-level vorticity and vertical velocity increasing.

7、CONCEPTUAL MODEL OF THE EXTRAORDINARY STORM PROCESS

With the aid of TECPLOT, a 3D visualization software, the streamline field and correlative were analyzed by using NCEP/NCAR global reanalysis data with horizontal resolution 1° by 1° (see Fig.2). The plot showed the typhoon exhibited a typical spiral ascend structure with transition zone between anticyclonic rotation and heterogeneous cyclonic below 450hPa. The cyclonic rotation vorticity structure existed a spindly shape and its horizontal scale reached maximum in the vicinity of Z=8. Until 2000 BT, 30 July, the typhoon Fung-wong still maintained the intact spiral vortex structure with intensive ascending motion to the right side.

In the next period of the severe rainfall case, the spiral vortex transformed into a tilting ascending flow(see Fig.2b). It is evident from Fig.2b that the joint effects by cold air invading from diverse direction at mid-level and warm and moisture air surging into at the low-level led to the another severe precipitation.

Fig.2 Conceptual models of the extraordinary storm caused by the typhoon Fung-wong
a for the first rainfall case; and b for the second case

(the origin of coordinates is (20°N，110°E)，y-/x-axis of coordinates denote the grid number，the distance between the grids represent the latitude/lontitude. The number of 1 to 21 beside the z-axis denote the isobaric surface as 1000、975、950、925、900、850、800、750、700、650、600、550、500、450、400、350、300、250、200、150 and 100hPa)

8、CONCLUSION

1）In the case, a southwest jet maintained below 850hPa, which brought out the sufficient release of the unstable energy over the Chu River area.

2）The extraordinary storm occurred in Hanshan region was triggered by weak north wind fluctuation on the troposphere mid-level which enhanced the unstable energy. When the left back side of the low-level jet just was over the Chuhe region, abundant warm and moisture air surged into the area resulting in the tilting ascendant which increased the low-level barometric gradient. Therefore the decreased typhoon cyclone can maintain and develop.

3）The extraordinary storm trigger mechanism in Chuhe region first caused by mid-level cold air stirring from the northern, and unstable energy released successively from high level to low level was in favor of the precipitation carrying on.

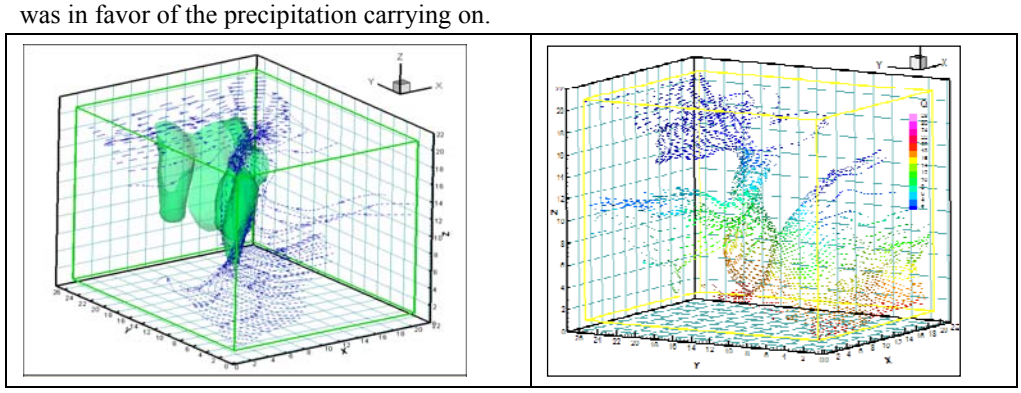

4）Exploration on the boundary jet stream show that the southerly reinforcement at the back of the jet could drive the development of the shear line on the north, promoting the convergence around heavy rain area and cyclonic vorticity enhancement, so that a confined and deep upward flow was compelled. The jet reinforced the mesoscale convective system motivation further so that convection cells generating and merging. Under the organization of steering current, the convection cells continuous recruit into precipitation area and accelerate the rainfall intensity.

References

[1] SUN Shu-Qing and ZHOU Yu-Shu. Advances in Meso-Scale Dynamical Analysis of Torrential Rain Systems in Recent Years in China. Chinese Journal of Atmospheric Sciences, 2007, Vol 31(6):2710～2811

[2] DUAN Li and CHEN Lian-Shou. Diagnostic Analysis and Numerical Study of Torrential Rain Associated with the Tropical Storm Fitow (0114). Chinese Journal of Atmospheric Sciences, 2005, Vol 29(3):343~353

[3] GUO Hu, DUAN Li, YANG Bo and et al. Mesoscale and Microscale Analysis on a Local Torrential Rain Event in Fragrant Hills Area of Beijing on July 9,2006. Jurnal of Applied Meteorological Science,2008,Vol 1993 ）: 265~274

[4] ZHU Pei-jun, ZHENG Yong-guang and TAO Zu-yu. Kinetic Energy Buget of Typhoon During Extratropical Transition. Acta Scicentiarum Naturalum Universitis Pekinesis, 2005, Vol 41(1):93~103

[5] XU Ai-hua, YE Cheng-zhi, OUYANG Li-cheng and et al.The Diagnostic Analysis of the Track and Precipitation of Typhoon “Rannaim” After Landfall. Journal of Tropical Meteorology,2006,Vol 22(3):229~236

[6] ZHU Pei-jun, CHEN Min, TAO Zu-yu and WANG Hongqing. Numerical Simulation of Typhoon Winnie(1997) After Landfall Part II: Structure EVolution Analysis. Acta Meteorologica Sinica,2002,Vol 60(5):560~567

[7] LI Ying, CHEN Lian-shou and LEI Xiao-tu. Numerical Study On Impacts of Upper-level Westerly Trough On The Extratropical Transition Process of Typhoon Winnie(1997). Acta Meteorologica Sinica,2006,Vol 64(5):552~561

[8] LIN Yong-hui, LIAO Qing-hai and WANG Peng-yun. A Possible Developing Mechanism of Low Level Jet ——The Inertial Instability of Gravity Wave. Acta Meteorologica Sinica, 2003, Vol 61(30):374~378

Development of a Localized Radar-Rain Gauge Co-Kriging QPE Scheme for Potential Use in Quality Control of Real-time Rainfall Data

Hon-yin YEUNG[1], Chun MAN[2], Alan SEED[3] and **Sai-tick CHAN**[1]
Hong Kong Observatory[1], *Chinese University of Hong Kong*[2],
Centre for Australian Weather and Climate Research[3]
Lead author's email address: hyyeung@hko.gov.hk
Presenting author's email address: stchan@hko.gov.hk

1. Introduction

Quality control (QC) is required before automatic rain gauge (RG) data, e.g. typical tipping-bucket RG, can be used quantitatively due to various types of systematic and random errors, caused by various factors including wind, wetting, evaporation, splashing, calibration, finite sampling, mechanical failure, funnel blockage, signal transmission interference, power failure, etc (Habib, 2001). Among the random errors, those arising from contamination during data transmission through radio telemetry systems and blockage of the rain gauge itself by external obstructions, like insects or fouling by birds, are crucial in heavy rain monitoring and assessment. While telemetry errors usually contaminates a single observation with an extreme value, a blocked gauge will return zero or unreasonably small values that fall well within the climatological range and are therefore difficult to detect. A QC procedure based on spatial consistency checking is proposed in this paper. Major techniques employed include a localized quantitative precipitation estimation (QPE) scheme based on the co-Kriging of radar and rain gauge data, as well as statistical analysis of the RG-QPE residuals in search for suitable QC criteria.

2. Data Sets

The two major data sets used in this study are (a) radar reflectivity at constant altitude and (b) 6-minute rainfall accumulation data from the networks of Hong Kong and Guangdong province of China. A total of 14 convective rainfall events occurred during 7 February – 1 June 2010 were selected for algorithm development and one event for performance assessment. The reflectivity data came from a mosaic of two S-band Doppler weather radars in Hong Kong updated every 6 minutes. The reflectivity signals were subjected to spurious filter and clutter filter control. To minimize the effect of anomalous propagation, the reflectivity data used for co-Kriging were sampled at 3 km above mean sea level. They are gridded onto a 480x480 rectangular array (about 1-km grid spacing), covering an area of 512x512 km^2 centred at Hong Kong. To make the co-Kriging calculation tractable, a 1-out-of-5 data thinning strategy was applied to the gridded reflectivity data, reducing the effective resolution to about 5.3 km. The rain gauge data is provided by two independent networks from Hong Kong and Guangdong, which together contain more than 1,200 real-time gauges. In this study, only the subset within the radar reflectivity domain was considered. At each update time, about 50 rain gauges would be available from Hong Kong but the actual availability from Guangdong could vary from 500 to 900 with a nominal number around 750. Roughly speaking, the average gauge separation over the two networks is about 10 km but the distribution is uneven with much higher density over the Pearl River Delta region, reducing the separation to about 5 km. Both the update schedule and rainfall accumulation periods are different in the two networks. In this study, the 6-minute accumulations with a 6-minute update cycle were chosen for combined analysis. To match these requirements, only about one third of the Hong Kong rain gauges could be used. Besides, the sensitivities of the rain gauges are also different. While the minimum rainfall amount to tip is 0.1 mm in Guangdong, that required by Hong Kong gauges is 0.5 mm.

3. Radar-Rain Gauge Co-Kriging

Borrowing ideas from geostatistics, the ordinary co-Kriging technique was explored for optimal combined analysis of rain-gauge measurements (as primary data) and reflectivity deduced rainfall (as subsidiary data). For rainfall events, especially those associated with intense convection, short-duration accumulations could vary significantly across space and haphazardly over time. We might therefore treat such quantities as random variables and apply ordinary co-Kriging analysis to combine them. Here, we did not assume any second order stationarity for the local mean and variance of these random variables. Instead, we assumed intrinsic stationarity and work directly with variograms. For background information on intrinsic stationarity, variograms, ordinary co-Kriging and the general solutions to the system of equations, interested readers are referred to the reference books by Wackernagel (1998) or Webster & Oliver (2001), as well as journal papers by Goovaerts (1998) and Phillips *et al.* (1997). For previous applications of the geostatistical technique to radar and rain-gauge data, reference could be made to Creutin *et al.* (1988), Schuumans *et al.* (2007) and Velasco-Forero *et al.* (2009). In the next two paragraphs, we summarized

the main points in our estimation for the rainfall variograms, which are vital to the calculation of individual data weights, and configuration of the localized co-Kriging analysis.

The variograms and cross-variogram are assumed to be dependent only on the distance separation h between a pair of rain gauges or radar grid points and not on the location of the pair of points or the orientation of the two points relative to each other, i.e. isotropy. The validity of isotropy will be discussed in Section 7. During each rain gauge update, the number of possible gauge pairs varies significantly making individual variogram estimation difficult and unreliable in real-time. If we further assume that the spatial structure of a particular type of rainfall system changes slowly, which is often the case for widespread and persistent rainstorm situations, we could pool data pairs at different update times together to make variograms more representative. Even with such considerations, the resulting experimental variograms would still be far from smooth and not suitable for solving the systems of co-Kriging equations. In real-time situations, dynamic modelling of the variograms will offer the most accurate spatial description of individual rainfall events but its automation may not be robust in practice. Instead, a more practical strategy of pooling all 14 rainfall cases together to prepare a single set of average variograms was proposed here. Fig. 1 (a)-(c) show the resulting three average variograms with their corresponding theoretical variograms (exponential model with nugget effect) annotated.

It is known that in Kriging or co-Kriging, data closer to an estimation point will have screening effect on more distant observations, thereby reducing the latter's weights (Wackernagel, 1998). Moreover, the actual set of variables/equations has to be kept to a manageable number if the computation is to be completed within a data update cycle, which is 6 minutes for the networks of Guangdong and Hong Kong. From Fig. 1, the ranges of both gauge-gauge and radar-radar variograms are within 40 km. Although the average gauge-radar cross-variogram hinted for an unbounded variance, individual cross-variograms (not shown) were bounded with a range generally less than 60 km. We therefore considered a radius of 50 km for setting the size of a circular neighbourhood for performing co-Kriging analysis. With such localization, we found that the average number of enclosed rain gauges is 10 or more. At most locations, the maximum number of enclosed rain gauges are well above 20. We further checked in two cases that the co-Kriging QPE will become stabilized as the neighbourhood size was increased to about 30 km and beyond. The number of radar grid points within the neighbourhood is fixed to be about 270.

4. Characteristics of RG-QPE Residuals

To quantify the amount of spatial consistency or inconsistency of a rain gauge data with respect to the co-Kriging estimate, we calculated RG-QPE residual defined as:

$$\xi = 10\log\left(G/K\right) = 10\log G - 10\log K$$

in units of decibels (dB) and studied their frequency distributions. In the above formula, G denotes the short-duration accumulation reported by a rain gauge and K the corresponding radar-rain gauge co-Kriging estimate. We also studied the RG-QPE residual in linear scale, i.e. $D \equiv G - K$, and call D as "RG-QPE departure" for the sake of easy reference. To make ξ well defined for all possible G and K values, an offset (0.08 mm) slightly less than the sensitivity of the Guangdong rain gauges (0.1 mm) was added when either of them was zero. We calculated both the residuals and departures for all the 14 rainfall events and compiled the resulting distributions as shown in Fig. 2 (a) and (b). It is noted that peaks show up in the positive tail of the departure distribution at 25.5 mm and beyond, signifying unreasonably large rain gauge values as compared to their reference QPE. Such peaks constitute one QC criterion (see Section 5 below). For false zeroes or unreasonably small rain gauge data, such kinds of abnormalities are rather subtle to be detected as they are typically buried well within the broad central peak of the distributions. To unearth the hidden mines, we need to throw away the uninterested samples, i.e. those with K equal or close to zero, as well as those bearing a relatively small estimation error. The absolute RG-QPE departure standardized by the QPE estimation error σ, i.e. $\delta = |G-K|/\sigma$, was used to select the data samples of interest. When K deviates significantly from a vanishing G, δ tends to be large especially when σ is small. We plotted in Fig. 2(c) and (d) the reduced distributions obtained by throwing away samples with $\delta \le 2$ and $\delta \le 3$ respectively. As shown in Fig. 2(c), a peak started to emerge in the negative tail of the reduced distribution around -12 dB, signifying some unreasonably large negative residuals attributable to false zeroes or unreasonably small gauge values. The peak remained visible as the distribution was further reduced by retaining only those samples with $\delta > 3$ (Fig. 2(d) refers). This discovery constitutes another QC criterion as summarized in Section 5 below.

5. Rain Gauge Data QC

Based on the previous discussions and results mentioned in Section 3 and 4, we proposed a simple QC procedure for short-duration rainfall accumulation reported by automatic rain gauges as follows:

(i) pre-QC screening to retain only those data lower than a preset threshold value G_c;

(ii) perform spatial consistency check on data retained in step (i) —

- calculate a reference QPE using localized radar-rain gauge co-Kriging;
- calculate the RG-QPE residual, departure and standardized departure; and
- compare against preset threshold values (denoting ξ_c, D_c and δ_c respectively);

(iii) assign QC flags "P" (for pass) or "R" (for reject) as follows:

- if $D \geq D_c$, flag "R";
- else, if $\delta \geq \delta_c$ and $\xi < \xi_c$, flag "R";
- otherwise, flag "P".

For the 6-minute rain gauge data from Guangdong and Hong Kong, the following set of threshold values was selected for testing: $D_c = 25$ mm, $\delta_c = 2$ and $\xi_c = -12$ dB. Note that the results were relatively insensitive to the choice of δ_c and higher values may also be used. The pre-QC screening is necessary, otherwise unphysically large rainfall data may contaminate the co-Kriging QPE and ruin the subsequent QC decision. From the maximum instantaneous Jardi rainfall rate of 513 mm/h registered in Hong Kong in 1971, G_c was set to be 51.3 mm in 6 minutes. We assumed the same threshold value is applicable to other rain gauge locations in Guangdong.

6. Performance Assessment

As our localized co-Kriging scheme excludes observation data at the estimation point, the RG-QPE departures mentioned in Section 4 could also be used for cross validation purpose. To avoid faulty rain gauge data, we only counted cases with $|D| \leq 10$ mm (implying δ generally above 20). From these, the root-mean-square error of the 6-minute co-Kriging QPE was estimated to be about 0.36 mm with a vanishing mean error. We noted from the scatter plot of K versus G (not shown) that the co-Kriging QPE tended to underestimate the 6-minute accumulations, which is not surprising as the most important piece of observation is purposely omitted. Despite this sub-optimal aspect, the co-Kriging QPE is still considered useful because the QC criteria as described in Section 5 above are not very sensitive to the absolute values of the QPE itself. As illustrated in Fig. 3, the co-Kriging rainfall map (a) captures the spatial details as shown in the radar picture (b) and reflects the rainfall intensity indicated by the rain gauge readings. For comparison, the rainfall distributions analyzed from pure radar reflectivity (stratiform-rain Marshall-Palmer relation) and rain gauge data (Barnes method) alone were also shown in Fig. 3(c) and 3(d) respectively.

The effectiveness of the QC procedure was assessed via an in-depth study with the case of 22 May 2010. The major rainfall episodes occurred from 8:00 a.m. to 12:24 p.m. and the QC procedure was applied to all the 27,635 6-minute rain gauge reports available during the period. Among these reports, 22,197 registered 0.0 mm and the remaining 5,438 at 0.1 mm or above. Out of the 22,197 reported zeroes, the QC algorithm rejected 183 reports (about 0.8%). Eyeball counter-checking revealed that 55 of which could be retained as true zeroes as they were recorded by rain gauges located on the edge or just ahead of some approaching rain bands. Out of the 5,438 non-zero reports, the QC algorithm rejected 30 (about 0.6%), which were mainly 0.1 mm. Eyeball counter-checking retained 6 of them. Overall, the rejection ratio is about 0.8% (totaling 213 out of the total 27,635 data processed). Among these rejected data, 29% (61/213) were suspected to be wrongly rejected according to eyeball counter-checking. With respect to the entire set of data samples, the portion of wrong QC as suspected by human eyes amounted to about 0.2% (61/27,635). To further assess the false-zero detection rate of the QC algorithm in heavy rain situations, we conducted an objective test targeting to simulate situations where gauges covered by an intense rain band were clogged. Firstly, a total of 562 reports with $K \geq 1$ mm and $G \geq 2$ mm were selected. Besides ensuring a significant rainfall rate, this selection can also minimize the number of ambiguous situations such as having a rain gauge located on the edge of a rain band. Secondly, each such rain gauge report was replaced by a bogus zero and then the QC procedure was re-applied. A total of 514 successful rejections were resulted, implying a false-zero detection rate of about 91%. Examination on the unsuccessful detections showed that they were all marginal cases with both δ and ξ close to their respective thresholds (i.e. $\delta_c = 2$ and $\xi_c = -12$ dB). That means higher detection rate could have been achieved if the thresholds were lowered (at the expense of a higher false alarm rate, of course).

It was noted that there was no extremely large faulty readings in this particular case. As such, we cannot assess the automatic detection rate for this kind of rain gauge error directly. Instead, we conducted a second objective test similar to the one for false zeroes. All the 22,069 true zero reports were used this time. To make allowance for estimation error, the bogus rain gauge data was set to be 25.5 mm in each turn. A total of 21,690 bogus data were successfully rejected, resulting in a detection rate of 98.3%. In the remaining cases, the corresponding QPE estimates from the co-Kriging analysis were all greater than 0.5 mm, resulting in the failure of the

QC test to reject the bogus faulty readings. For rainy situations, an objective test to assess the corresponding QC performance for erroneously large readings has yet to be devised and conducted.

7. Discussions

The problems identified during QC performance assessment were mainly of two types, namely underestimated reference QPE by co-Kriging and the detailed design of the QC algorithm. To address the QPE issue, radar-deduced rainfall accumulation may be improved by using a reflectivity-to-rain rate conversion formula more representative of the convective climatology of the region. Secondly, the reflectivity thinning strategy could be adjusted to allow higher density of radar grid points in order to capture highly localized intense convective cells. To this end, major optimization of the co-Kriging solver will be required as the total number of variables/equations will be increased non-linearly. Apart from the underestimated QPE trend, ambiguous situations as discussed in Section 6 also existed where a rain gauge is located on the edge of a rainy area. At first sight, this might seem to prompt for consideration of anisotropy. To address this issue, we studied the gauge-gauge variogram using the data at 11:30 am on 22 April 2010. It was a classic case of SW-NE oriented squall line moving mainly from west to east with a small southward component. The blue and red variograms in Fig. 1(d) corresponded to gauge pairs oriented NE-SW and NW-SE respectively. It is evident that the two variograms differ appreciably only in the farther range, say beyond 40 km with essentially the same correlation range. This justified our earlier assumption of isotropy for the co-Kriging neighbourhood. And this short-range isotropy is expected to hold in general due to the use of 6-minute accumulation, which only reflects the rainfall distribution over a very short time scale (a typical rain band, including squall line, may travel only a few kilometers and any anisotropy caused by advection along the direction of motion will not be apparent). The fast motion speed (of order 40 km/h) of the squall line in this case could also help smear out any anisotropy. Yet the "edge" ambiguity is believed to be a genuine issue requiring further treatment in the future.

As for the design of the QC algorithm, one possible improvement may be achieved by considering also longer period accumulations, e.g. 30-minute or 60-minute, valid at the same time of the 6-minute rainfall. These information could be even more useful for identifying false-zero type of errors as they are likely to persist in time in general. Except at the 30- and 00-minute of the hour, currently there was no direct report of such longer-period accumulations from the Guangdong network during each update. If required, such accumulations have to be composed from the "raw" 6-minute data, a process in which data availability will introduce another QC problem. Another issue revealed in assessing the QC performance for large errors is that the simple check of $D \geq D_c$ is insufficient for discriminating rain gauge reports that are not particularly large but are nevertheless inconsistent with the amount of rainfall seen from nearby gauges or radar reflectivity values. Skill similar to those explained for detecting false zeroes may be explored in the future.

8. Concluding Remarks

A localized version of co-Kriging analysis was developed specifically for QPE using rain gauge and radar reflectivity data taken in a subtropical environment of southern China, where highly uneven convective rainfall distributions are common in spring and summer. Such co-Kriging QPE provides a kind of "proxy" for measuring spatial consistency and a method for rain gauge data QC. Potential application of such technique in quality control over real-time rain gauge rainfall with short accumulation periods was explored. Preliminary validation findings based on selected cases in Guangdong and Hong Kong showed that the proposed QC scheme performed satisfactorily with high error detection rate. Under the existing radar data thinning strategy, the current co-Kriging solver requires a few minutes to complete a QC cycle for all gauges on a commodity Intel PC installed with Core i7 CPU at 2.67 GHz and Intel Math Kernel Library. But as discussed in Section 7, denser radar grid points is deemed necessary and a major optimization exercise will be required for enhanced operational performance. The limited coverage of Hong Kong radars confined the present study to a range of about 256 km, leaving the quality of about one quarter of the 1,200 gauges unchecked. Combined use with Guangdong radar data will be pursued to overcome the coverage limitation, as well as mitigating the range issue with reflectivity. In the future, the QC algorithm will be enhanced to cater also for the 5-minute accumulations provided by the other two thirds of rain gauges in Hong Kong. Moreover, 60-minute accumulations will also be explored for possible further enhancement to the current algorithm.

Acknowledgements

The authors wish to acknowledge and thank the Guangdong Meteorological Bureau for providing the rain gauge data in Guangdong used in this study. Thanks also go to Dr. Carlos A. Velasco-Forero for his critical review on the preliminary research results from this study.

References

Creutin, J.D., *et al*, 1988: Rain Measurement by Raingage-Radar Combination: A Geostatistical Approach. *J. Atmos. Oceanic Technol.*, **5**, 102-115.

Goovaerts, P., 1998: Ordinary Cokriging Revisited. *Mathematical Geology*, **30**, 21-41.

Habib, E. et al, 2001: Sampling Errors of Tipping-Bucket Rain Gauge Measurements. *J. Hydrol. Eng.*, **6**, 159-166.

Phillips, D.L., *et al*, 1997: Use of auxiliary data for spatal interpolation of ozone exposure in southeastern forests. *Environmetrics*, **8**, 43-61.

Schuurmans, J. M., *et al*, 2007: Automatic Prediction of High-Resolution Daily Rainfall Fields for Multiple Extents : The Potential of Operational Radar. *J. Hydromet.*, **8**, 1204-1224.

Velasco-Forero, C.A., *et al*, 2009: A non-parametric automatic blending methodology to estimate rainfall fields. *Advance in Water Resources*, **32**, 986-1002.

Wackernagel, H., 1998: *Multivariate geostatistics An introduction with applications*, 2nd Edition, Springer, Berlin.

Webster, R. & M. Oliver, 2001: *Geostatistics for Environmental Scientists*, Wiley, England.

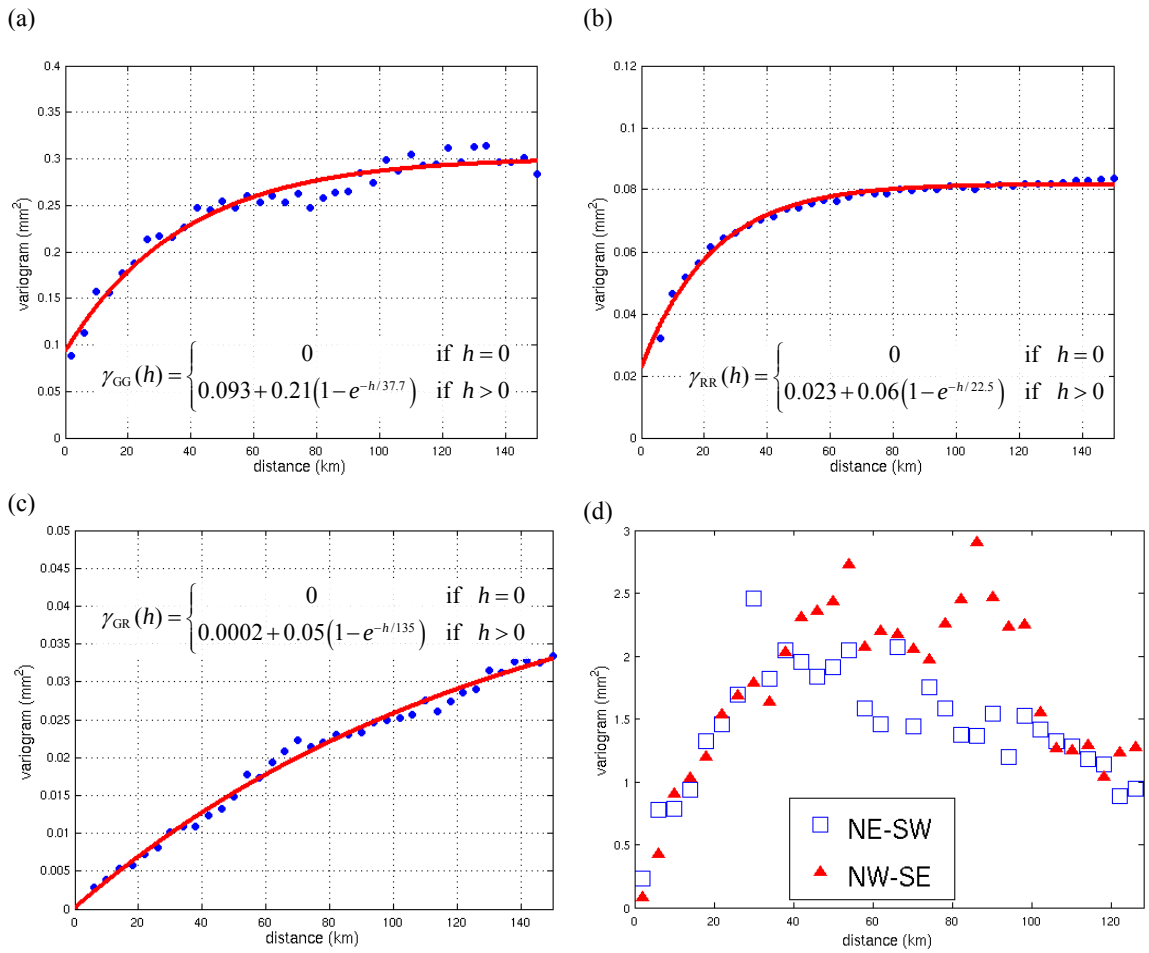

Fig. 1 Average variograms and cross-variogram generated from 14 cases selected during 7 Feb – 1 Jun 2010. (a) gauge-gauge variogram; (b) radar-radar variogram; and (c) gauge-radar cross-variogram. The respective theoretical variograms are annotated and shown as a red curve in each plots. Plot (d) is the gauge-gauge variogram generated using the case data of 11:30 am on 22 April 2010 for studying anisotropy. The blue and red variograms in (d) corresponded to gauge pairs oriented NE-SW and NW-SE respectively.

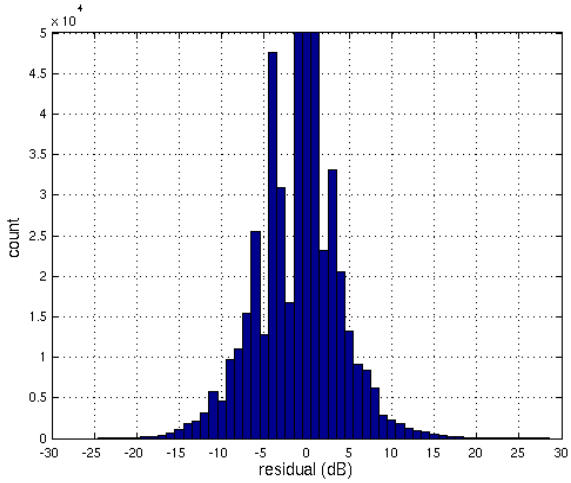
x 10^4
count
residual (dB)

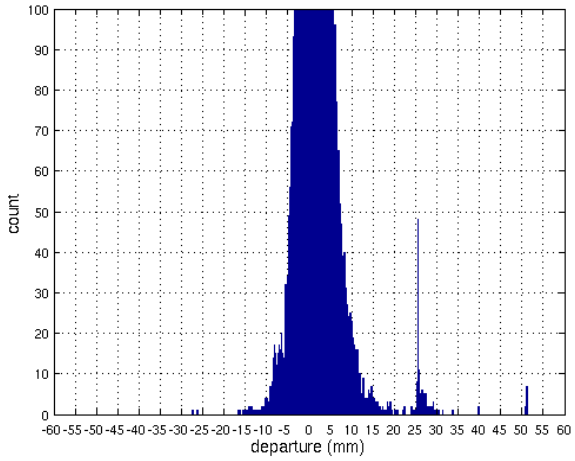
count
departure (mm)

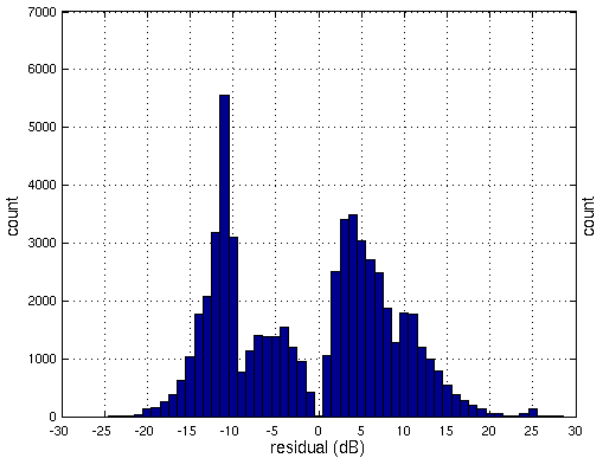
count
residual (dB)

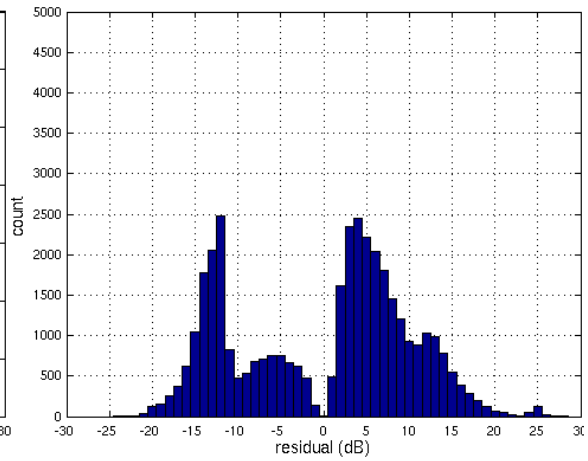
count
residual (dB)

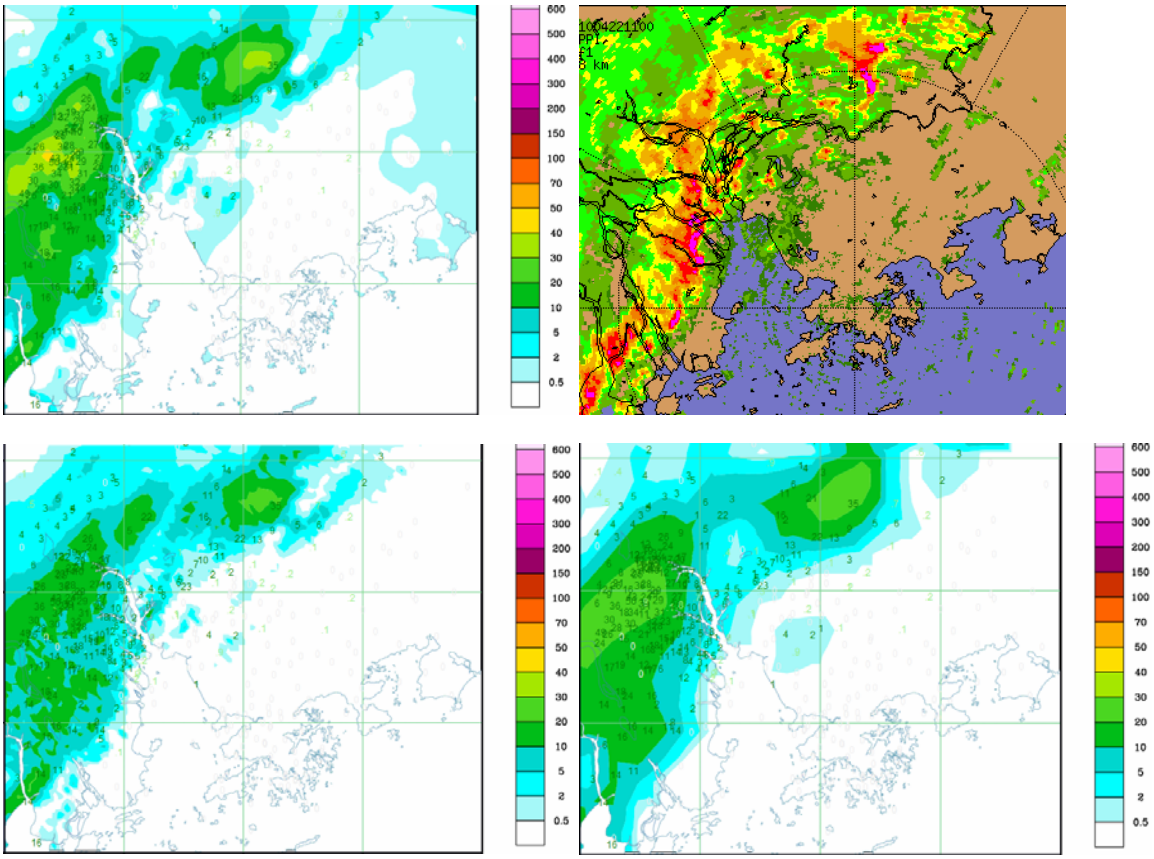
1004221100
PPI
f1
8 km
600
500
400
300
200
150
100
70
50
40
30
20
10
5
2
0.5

The Impact of Parameterization of Cloud Microphysical Processes on Convective Precipitation Forecasting

Yan Yin, Qian Chen and Hui Xiao
CMA Key Laboratory for Atmospheric Physics and Environment,
Nanjing University of Information Science & Technology, NO. 219 Ningliu Road,
Nanjing, 210044, China，yinyan@nuist.edu.cn

1. Introduction

Cloud microphysical processes play critical roles in vertical distribution of atmospheric moisture and heat, and bring great uncertainty to precipitation prediction, especially for severe rainfall events. Due to the limitation of computer power, parameterized microphysical schemes are usually utilized in weather forecasting models and climate models. Different parameterizations of cloud microphysics can lead to large discrepancies in precipitation simulations. Li et al. (2009) suggested that single-moment schemes could significantly overestimate precipitation, especially with the Lin scheme, whereas precipitation amounts simulated with two-moment schemes were comparable with the measurements. Khain and Lynn (2009) compared their simulation results obtained using the weather research and forecast (WRF) model with spectral (bin) microphysics and compared with that obtained from the Thompson bulk-parameterization scheme. They found that the difference in vertical velocity, cloud structure and precipitation obtained by different schemes is much larger than the changes caused by variation of aerosol concentration within each scheme.

In the present study, we perform simulations using WRF model with different parameterization schemes for cloud microphysical processes to investigate the efects of parameterization of cloud microphysics on precipitation for a deep convective system.

2. Description of Microphysical Schemes and Numerical Experiments

Four bulk parameterizations for cloud microphysical processes have been used in the numerical experiments, including the Lin, Thompson, Milbrandt-Yau and Morrison schemes. The Lin scheme is mainly based on the work of Lin et al. (1983) and Rutledge and Hobbs (1984). The saturation adjustments are based on the work of Lord et al. (1984) and Tao et al. (1989). Thompson scheme is a two-moment scheme for rain, and it employs many techniques found in sophisticated spectral (bin) schemes using lookup tables (Thompson et al., 2008). Milbrandt-Yau scheme is the two-moment version of Milbrandt-Yau (2005) microphysics scheme, and it predicts the zeroth and the third moments of the size spectrum of each hydrometeor category and uses the diagnostic equations for the shape parameter, based on the mean-mass diameter. As the Milbrandt-Yau scheme, Morrison scheme is also a double-moment scheme that predicts mixing ratio and number concentration of five types of hydrometeor species, including cloud droplets, cloud ice, snow, rain and graupel (Morrison et al., 2009).

A deep convective system developed over Beijing area from 0500 UTC to 1200 UTC, 31 May 2005, is considered in this study. The thermodynamic profiles observed over Beijing meteorological observatory at 00:00 UTC on 31 May 2005 are shown in Fig. 1. Version 3.2 of the WRF model is run for a 24-h period from 0000 UTC, 31 May 2005, to 0000 UTC, 1 June 2005, over the domain shown in Fig. 2. The model is configured with three nested grids with spacing of 27 km (150×150 grid points) for domain 1, 9 km (136×136 grid points) for domain 2, and 3 km (64×70 grid points) for domain 3. Domain 1 is centered at 40.0ºN and 116.5ºE. The modeling system employs the Mellor-Yamada-Janjic TKE PBL scheme, the thermal diffusion land-surface scheme. Kain-Fritsch cumulus parameterization scheme is used in the 27- and 9-km domain, and no cumulus parameterization is used in the 3-km domain.

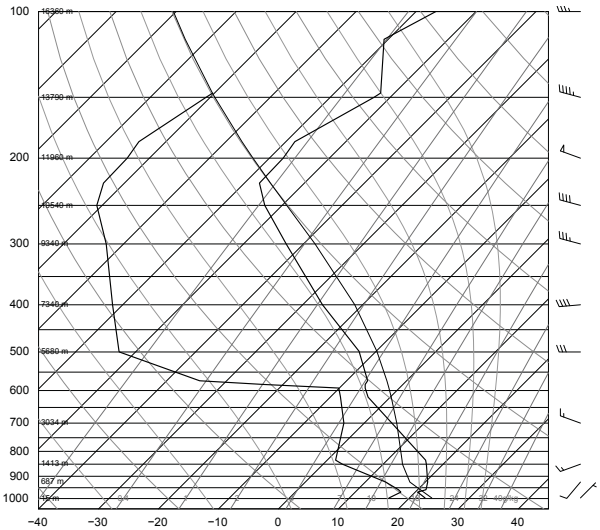

Fig. 1 Vertical profiles of temperature (right thick line) and dew point temperature (left thick line) of Beijing station at 00:00 UTC on 31 May, 2005.

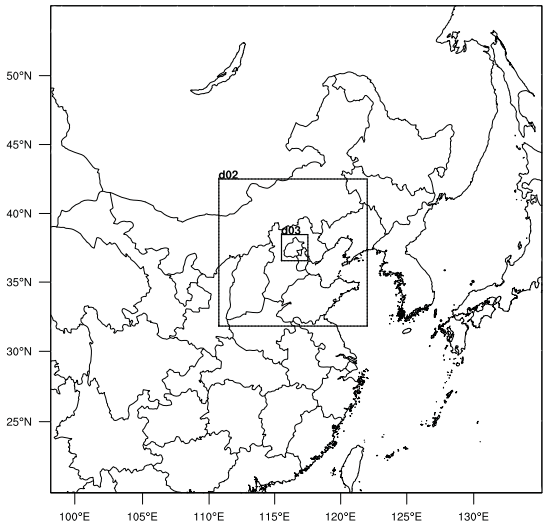

Fig. 2 Nested grid domains.

3. Results

3.1 Comparison of radar reflectivity

Figure 3 presents the simulated radar reflectivity from two single-moment microphysical schemes (Lin and Thompson scheme) and two double-moment schemes (Milbrandt-Yau and Morrison scheme) at 10:00 UTC on 31 May 2005. It is revealed that radar reflectivity simulated by single-moment scheme yields more pronounced convective core, especially with Lin scheme. Li (2009) suggested that overestimated of radar reflectivity by the Lin scheme is due to more warm rain but less ice particles produced in the microphysical processes. But in this study, it is difficult to determine which scheme is more realistic, due to lacking of real-time measurements.

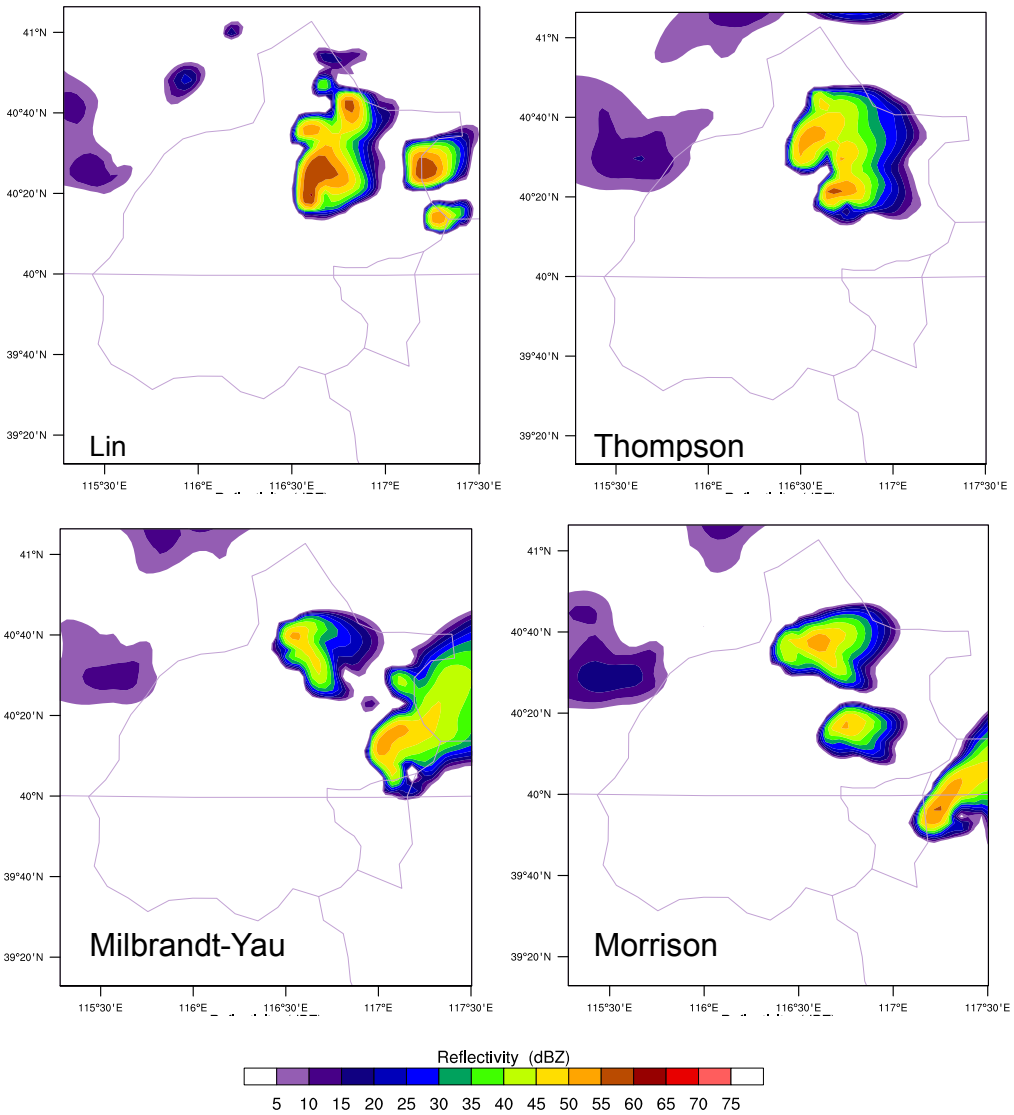

Fig. 3 Comparison of radar reflectivity at 10: 00 UTC on 31 May 2005 over Bei jing area from different microphysical schemes.

3.2 Comparison of rainfall rate

Figure 4 shows the pattern of simulated 24-h precipitation from 00:00 UTC on 31 May to 00:00 on 1 June 2005 using the four different microphysical schemes and available observations. In general, three schemes reproduce the precipitation pattern successfully compared with the observations. The two major intensive rainfall centers are predicted by the Lin, Thompson and Morrison schemes, but the Milbrand t-Yau scheme underestimates the rainfall rate as well as the preci pitation area. The simulations by Lin scheme has better agr eement with measurement s, although the precipitation amount is ov erestimated over the north and eastern area and is underestimated over southern part of Beijing. The major intensive centre of rainfall by Thompson and Morrison scheme appears to t he east and southeast of the measured region, respectively. Both two-moment schemes underestimate the precipitation in this

case, implying the importance of determining appropriate microphysical scheme to achieve comparable results with observations before detailed studies.

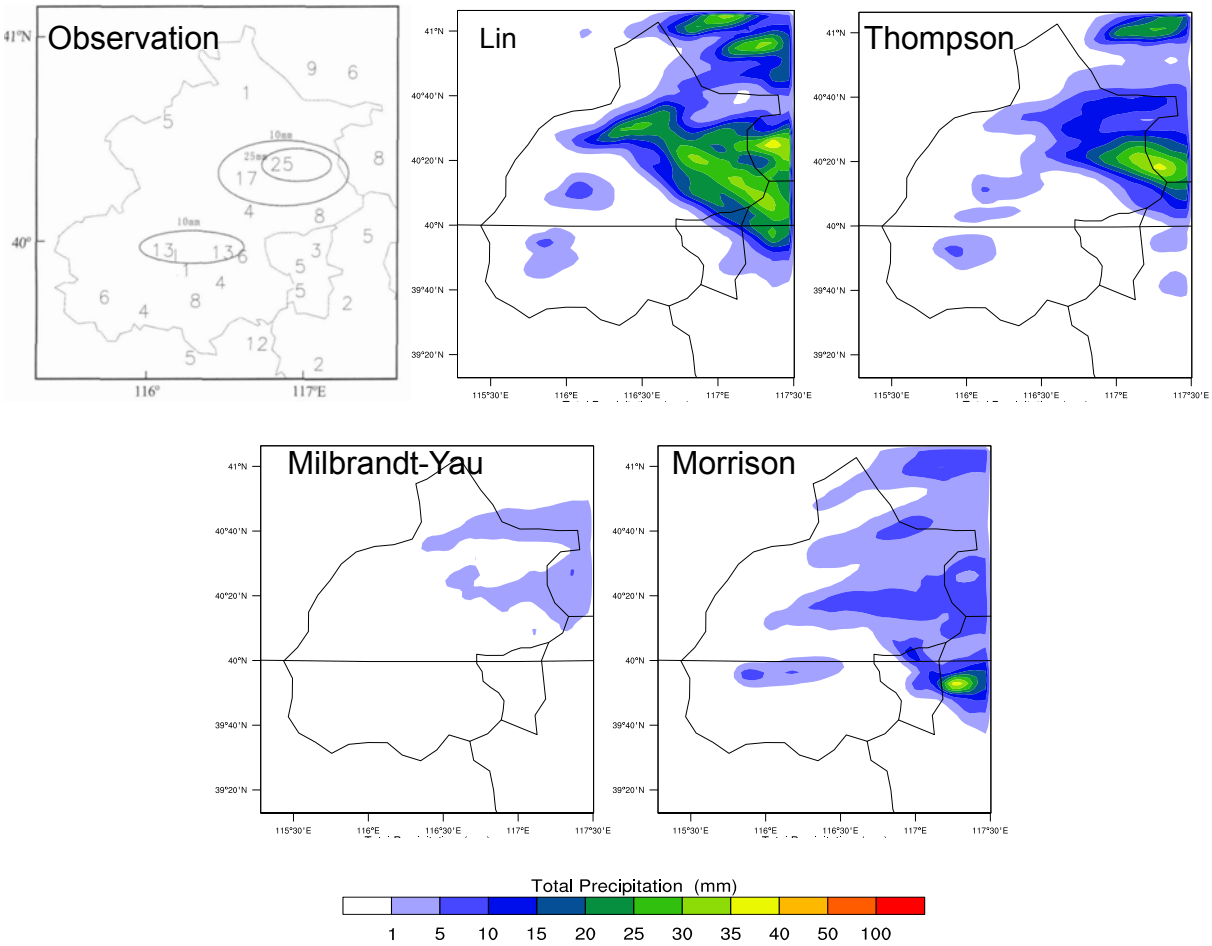

Fig. 4 Comparison of 24-h accumulated precipitation at Beijing area from 00:00 UTC, 31 May to 00:00, 1 June 2005 using different microphysical schemes with observations from Wang et al. (2009).

4. Summary

The effects of parameterization of cloud microphysics on precipitation for a deep convective system have been investigated using the WRF model. Different parameterization schemes for microphysical processes of cloud and precipitation included in the WRF model are tested. The results showed that the Lin and Thompson schemes could reproduce the precipitation pattern more consistent with the measurements than the other schemes, but both of these single-moment schemes overestimated the precipitation amount, especially for the Lin scheme. It is suggested that the microphysical schemes should be tested before the model is used for precipitation prediction for a specific region.

Acknowledgements:

This study was partially funded by the Public Meteorology Special Foundation of

MOST (Grant No. GYHY20070 6036), the National Natural Sciences Foundation of China (Grant No. 41030962), and the "Excellent Creative Research Team in Jiangsu Universities" program.

References

Khain, A. and B. Lynn, 2009: Simulation of a supercell storm in clean and dirty atmosphere using weather research and forecast model with spectral bin microphysics. *J. Geophys. Res.*, **114,** D19209.

Li, G., Y. Wang, K.-H. Lee, et al., 2009: Impacts of aerosols on the development and precipitation of a mesoscale squall line. *J. Geophys. Res.*, **114,** D17205.

Lin, Y.-L., R. D. Farley, and H. D. Orville, 1983: Bulk Parameterization of the Snow Field in a Cloud Model. *J. Appl. Meteorol.*, **22,** 1065-1092.

Lord, S. J., H. E. Willoughby, and J. M. Piotrowicz, 1984: Role of a Parameterized Ice-Phase Microphysics in an Axisymmetric, Nonhydrostatic Tropical Cyclone Model. *J. Atmos. Sci.*, **41,** 2836-2848.

Milbrandt, J. A. and M. K. Yau, 2005: A Multimoment Bulk Microphysics Parameterization. Part I: Analysis of the Role of the Spectral Shape Parameter. *J. Atmos. Sci.*, **62,** 3051-3064.

Morrison, H., G. Thompson, and V. Tatarskii, 2009: Impact of Cloud Microphysics on the Development of Trailing Stratiform Precipitation in a Simulated Squall Line: Comparison of One- and Two-Moment Schemes. *Mon. Wea. Rev.*, **137,** 991-1007.

Rutledge, S. A. and P. V. Hobbs, 1984: The Mesoscale and Microscale Structure and Organization of Clouds and Precipitation in Midlatitude Cyclones. XII: A Diagnostic Modeling Study of Precipitation Development in Narrow Cold-Frontal Rainbands. *J. Atmos. Sci.*, **41,** 2949-2972.

Tao, W.-K., J. Simpson, and M. McCumber, 1989: An Ice-Water Saturation Adjustment. *Mon. Wea. Rev.*, **117,** 231-235.

Thompson, G., P. R. Field, R. M. Rasmussen, et al., 2008: Explicit Forecasts of Winter Precipitation Using an Improved Bulk Microphysics Scheme. Part II: Implementation of a New Snow Parameterization. *Mon. Wea. Rev.*, **136,** 5095-5115.

Wang, X.-M, Q. Zhong, S.-Y. Han, 2009: A Numerical Case Study on the Evolution of Hail Cloud and the Three-Dimensional Structure of Supercell. *Plateau Meteorology* (in Chinese), **28**, 352-365.

Evaluation of Probabilistic Precipitation Forecast Using TIGGE data over Huaihe Basin

Linna ZHAO[1] Hao WU[1] Fuyou TIAN[1] Dan QI[1] Jingyue DI[1]
Qingyun DUAN[2] and Zhi WANG[1]

1. National Meteorological Center, China meteorological Center, P. R. China

2. College of Global change and Earth System, Beijing Normal University, P. R. China

zhaoln@cma.gov.cn

1. Introduction

Rainfall is one of the most important weather phenomena which could result in severe flood and huge economic loss. A timely and accurate quantitative precipitation forecast (QPF) is a primary goal of operational prediction and one of the most factor that affects the issuance of flood warning(Gourley and Vieux, 2005). Short-range, especially medium-range precipitation forecast, have been greatly improved by employing the ensemble prediction systems (Charba and Klein 1980; Charba et al. 2003). However, quantitative precipitation forecasts lose skill rapidly with range than forecast of any other surface elements (Sanders, 1986), such as the temperature forecasts. In order to improve a single ensemble prediction system (EPS), multi-model prediction system (MPS) and probabilistic prediction were developed with considering the characteristics of many EPS, i.e.. The simulation of initial uncertainties (Park et al, 2008; Johnson and Swinbank 2009). The THORPEX Interactive Grand Global Ensemble (TIGGE) program provides a very good opportunity for MPS, probabilistic precipitation, and flood with further research.

2. The data and the test catchment

The European Center for Medium-Range Weather Forecasts (ECMWF), the United States National Center for Environment Predictions (NCEP), and the China Meteorological Administration (CMA) multi- member 1-10 day' total precipitation forecasting with initial time is 0000GMT obtained from the TIGGE-CMA portal were used in this study. The Dapoling-Wangjiaba catchment of the upper Huaihe River with 19 rain gauges was taken as the test case. Three ensemble prediction systems (ECMWF, NCEP and CMA) multi-member 1-10 days' precipitation forecast from the TIGGE-CMA archiving center to be used. The test time lasts from 1 July to 6 August, 2008. Multi-model combination has more impact than calibration, so no quality control and bias correction are implemented for EPS and MMS. The equal weighted factor was arbitrarily imposed on the MMS with the assumption that all ensemble members are equal likely and ensemble size is irrelevant, not considering the forecasting skills of individual EPS.

3. Methodology and result analysis

The threat score (TS) method, Brier score method and Percentile precipitation method were applied to assess three EPSs and their grand EPS. The precipitation was divided into four categories with the consistency of operational forecasts at the

National Meteorological Center (NMC) of CMA as no rain, moderate rain and heavy rain for the threat score, bias score and the brier score assessment, but all intensities were taken into consideration with the percentile precipitation.

According to the results of threat score and bias score (Fig.1 and Fig.2), compare with the EC, the MPS has an equal or slightly better performance, meanwhile much better than CMA and NCEP. Maybe the number of ensemble members is the key to explain the MPS inclined to EC. What must be pointed out is that the little rain forecast of CMA gives the best threat scores with the lead time less than 6 days. But the false alarm rate of CMA is also higher than the others with all 10-day' little rain forecast. With the result of the threat score and bias score of CMA for the moderate rain and heavy rain, the CMA have a good performance on the little rain forecast at the price of the poor capacity on the heavy precipitation forecast.

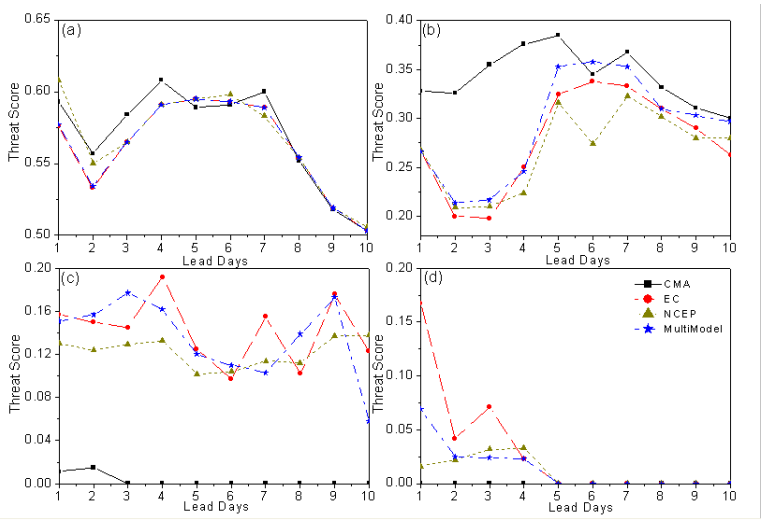

Fig. 1 Threat Scores of ensemble mean, CMA (black line with rectangles), EC (red dashed-circle line), NCEP (brown dotted-triangle line), and MPS (blue dashed-star line). (a)No Rain, (b) Little Rain (c) Moderate Rain (d) Heavy Rain

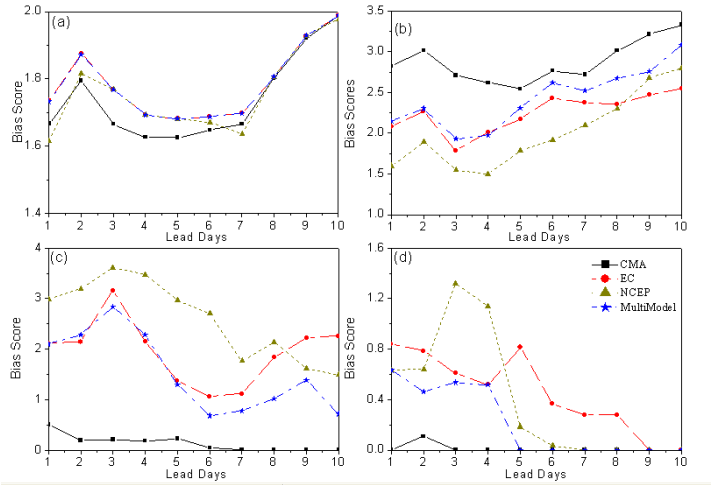

Fig. 2 Bias Scores of the ensemble mean, CMA (black line with rectangles), EC (red dashed-circle line), NCEP (brown dotted-triangle line), and MPS (blue dashed-star line). (a)No Rain, (b) Little Rain (c) Moderate Rain (d) Heavy Rain

It is can be seen from the results of Brier score (Fig.3), for little rain forecast, the MPS give the best performance, and the CMA does the worse which is just as the result of the threat score and bias score. The evaluation of brier score of moderate and heavy rain shows that some members in the three EPSs have the cap abilities to catch some extreme events within 10 days, and MPS increased the probabilistic skill of heavy precipitation prediction, though the capabilities is weakened evidently by the smoothing process of ensemble mean.

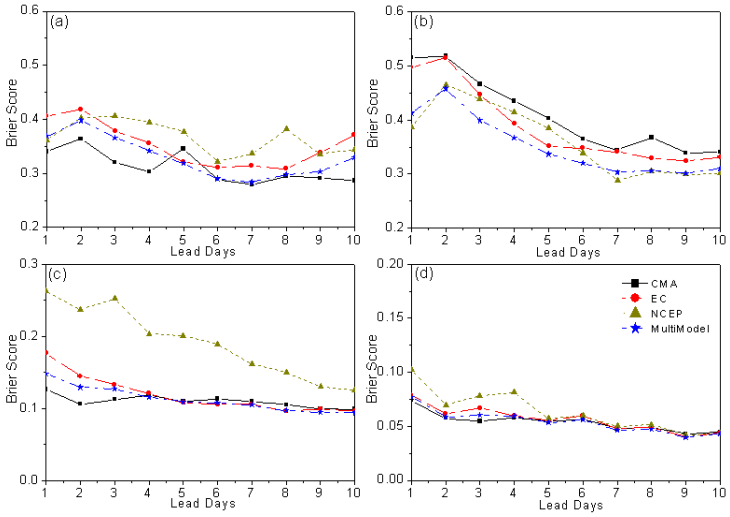

Fig. 4 Brier Scores of CMA (thick-solid black line with rectangles), EC (dashed red line with circles), NCEP (dotted brown line with triangles), and MPS (dashed blue line with stars). (a)No Rain, (b) Little Rain (c) Moderate Rain (d) Heavy Rain.

With Percentile precipitation method, the percentile precipitation has been used to reveal the result of probabilistic forecast intuitively (Fig.4). The observed precipitations were usually included by the 25th and 75th percentile precipitation with short time forecasts. The percentile precipitation perform well with temporal precipitation distribution, Meanwhile, the result of the percentile precipitation shows that the MPS include more probabilities than a single EPS for the daily area rainfall. For station precipitation, the analysis for an extreme rainfall event that happened on 23 July, 2008 displays that the precipitation tends to be underestimated as the lead time ranges up to 5 days, and the error suddenly increased in the 6-day' forecast. However, the MPS outperforms any of the three EPSs, which is improved in space distribution of precipitation and the intensity, but the result just could be only used as reference for forecasts longer than 5 days.

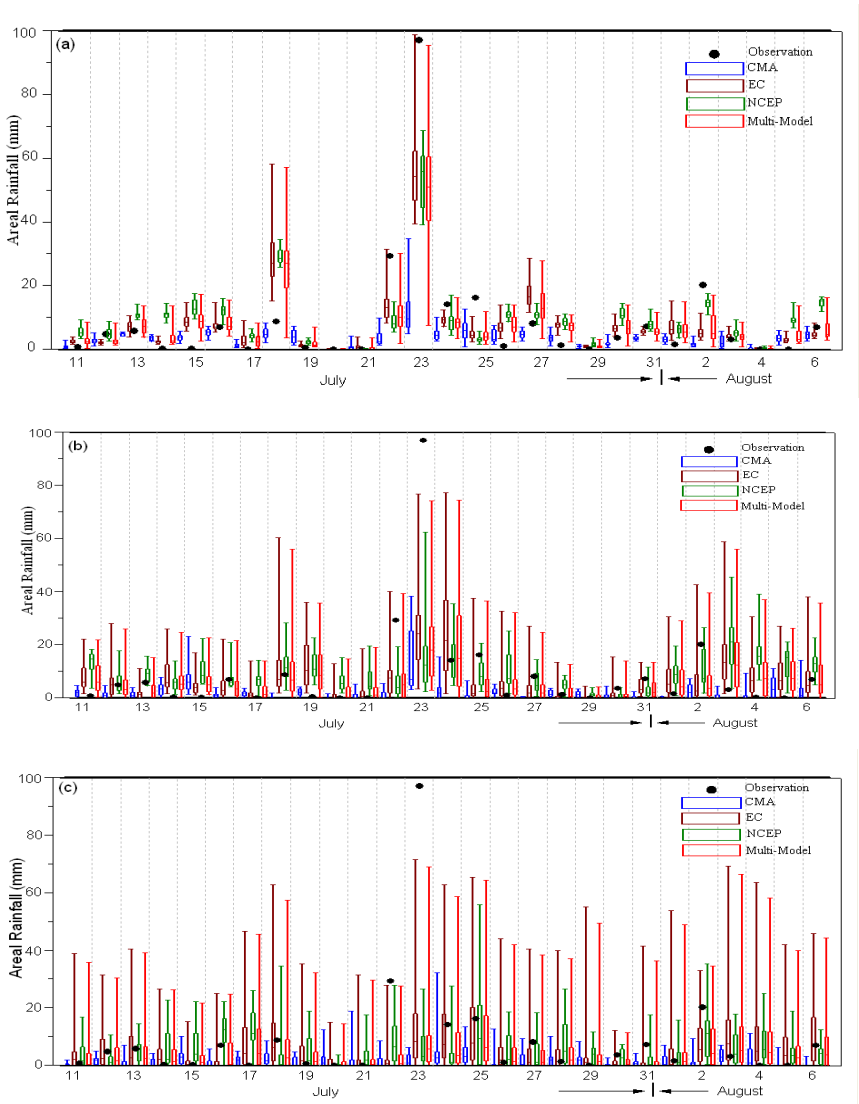

Fig. 4 Comparison of percentile areal-averaged-precipitation of CMA, NCEP, EC and MPS over Dapoling-Wangjiaba catchment for lead time of (a) 1 day, (b) 5 day, and (c) 10 day between 11 Jul and 6 Aug, 2008. （The five short lines in every box-and-whisker plot indicate the 5th, 25th, 50th, 75th, and 99th percentile precipitation, respectively）

4． Conclusion and outlook

With the developing of EPS and methodology of probabilistic forecast, and importantly our un derstanding of the scientific b ases of forecasting extreme precipit ation eve nts, providing 3-10 days' probabilit y flood forecast was being well developed. Meanwhile, based on the development of num erical prediction, the f easibility and ample sp ace of developing probability forecast have been well documented (Krzysztofowicz 2001, Thielen et al. 2009). Something we must point out is that, the bilinear interpolation method was implemented in this study, and the effect of topography was no t considered. In addition, Buizza and Palmer (199 8) and Verbunt et al. (2007) pointed out that precipitation usually affected by the total number of ensemble members, though not sure how many members are necessary. More work should be done about how to particularly set the weight of every single EPS.

Acknowledgements

This work was supported by the Research Fund for Commonweal Trades (Meteorology) (Grant number: GYHY200906007 and GYHY201006037).

References:

Buizza, R., and Palmer, T. N.: Impact of ensemble size on ensemble prediction. *Mon. Wea. Rev*., 126: 2503-2518, 1998.

Charba J. P., D. W. Reynolds, B. E. Mcdonald, and G. M. Carter, 2003: Comparative verification of recent quantitative precipitation forecasts in the National Weather Service: a simple approach for scoring forecast accuracy. *Wea. Forecasting*, 18:161-183.

Charba, J. P., and W. H. Klein, 1980: Skill in precipitation forecasting in the National Weather Service. *Bull. Amer. Meteor. Soc.* 61(12): 1546-1555.

Gourley, J., and B. E. Vieux, 2005: A method for evaluating the accuracy of quantitative precipitation estimates from a hydrologic modeling perspective. *J. Hydrometeor.* 6: 115-132.

Krzysztofowicz, R. 2001: The case for probabilistic forecasting in hydrology. *J. Hydrol.*, 249: 2-9.

Park, Y.-Y., R. Buizza, and M. Leutbecher, 2008: TIGGE: preliminary results on comparing and combining ensembles. *Quart. J. Roy. Meteor. Soc.* 134: 2029-2050.

Sanders, F. 1986; Trends in skill of Boston forecasts made at MIT 1966-84. Bull. Amer. Meteor. Soc., 67: 170-176.

Thielen, J., J. Bartholmes, M.-H. Ramos, and A. de Roo. 2009: The European Flood Alert System- Part1 : concept and development. *Hydrol. Earth Syst. Sci.*, 13: 125-140.

Toth Z., and E. Kalnay, 1997: Ensemble forecasting at NCEP and the breeding method. *Mon. Wea. Rev.*, 125, 3297-3319.

Verbunt, M., A. Walser, J. Gurtz, A. Montani, et al., 2007; Probabilistic flood forecasting with a limited-area ensemble prediction system: selected case studies. *J. Hydrometeor.*, 8: 897-909.

Impact of Different Boundary Layer Parameterization Schemes on the Numerical Simulation for a Rainstorm

ZHANG Bing[1] ZHONG Min[2]

(1.Wuhan Institute of heavy rain, CMA, Wuhan 430074, China;
2.Wuhan Central Meteorological Observatory, Wuhan 430074,China)

zhangbi6231@163.com

ABSTRACT

Planetary boundary layer(PBL) parameterization is an essential part of numerical weather prediction model. There have been many PBL schemes applied in all kinds of models, such as AREM, GRAPES, MM5, WRF and so on. There are several layers in boundary layer for all PBL schemes except for The Bulk boundary layer scheme in MM5. Therefore, the PBL scheme itself is a part of model's function. Each PBL scheme is different in its formulation of vertical mixing within the PBL and the surface fluxes, which in turn leads to the difference in upper free convection atmosphere. The main work and findings of this study are shown as follows:

GRAPES(Global/Regional Assimilation and Prediction System) is a new generation numerical model in China. The model version is GRAPESv3.0. It is used to simulate a heavy rain case with the same conditions except for the PBL parameterization schemes. Tests are conducted to determine the sensitivity of the simulation to the available PBL parameterization schemes, including the MRF scheme, MYJ scheme, YSU scheme and no PBL parameterization scheme.

Significant sensitivity is seen that the structure of meteorological fields and the precipitation vary greatly with different PBL schemes. The MRF boundary layer scheme produced the strongest storm while NO boundary layer scheme produced the weakest storm. Results suggest that accurate forecast of heavy rain is sensitive to the boundary layer parameterization scheme.

The schemes and model parameters are set in Table 1.

Table 1 the scheme and model parameters

item	schemes
dynamical process	Non-hydrostatic, full compressible atmospheric dynamics scheme
resolution Grid	Horizontal resolution 0.15 degree, vertical 31 levels
Grid number	Arakawa-C
model top	500*330
data	35000m
spatial interpolation	NCEP reanalysis data
Microphysics	bilinear interpolation
Cumulus	NCEP cloud5
Radiation	Kain-Fritsch
land surface	RRTM long wave and Dudhia short wave
PBL	OSU LSM
time step	no PBL parameterization scheme (test 1), MRF (test 2), MYJ (test 3), YSU (test 4)
lateral boundary	90s

time-dependent boundary condition

During the period of 8th-10th June 2008, a heavy rain occurred in Hubei Province. The GRAPES model version 3.0 is used to conduct investigation of numerical simulation for this case.

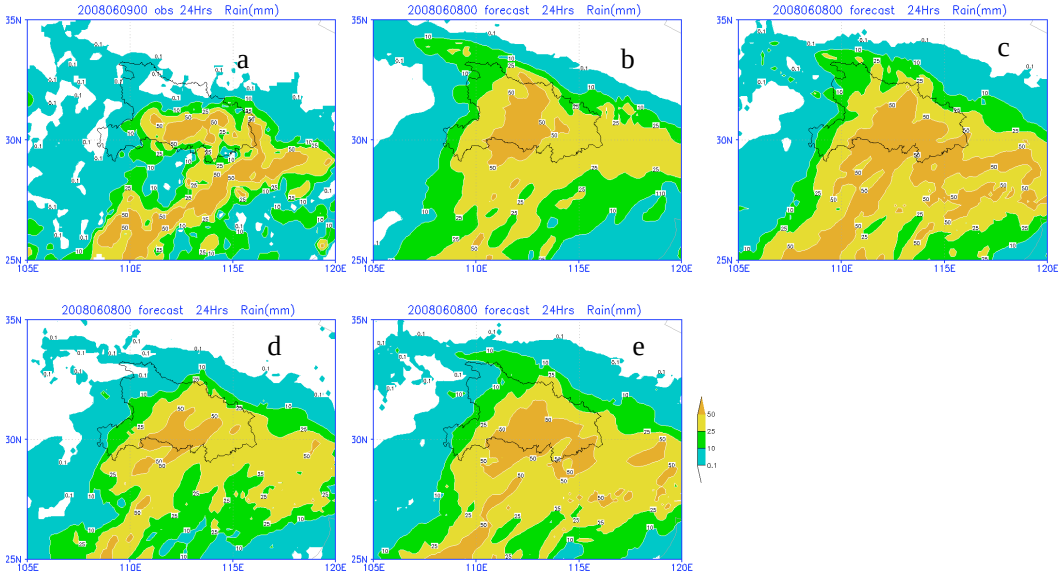

Figure1 observed rainfall distribution and simulated rainfall distribution (00-24hour). (a)observed rainfall,(b)simulated rainfall(test 1),(c)simulated rainfall(test 2),(d)simulated rainfall(test 3),(e)simulated rainfall(test 4)

4 PBL parameterization schemes are used to make 48 hour precipitation simulation. Figure 1 gives observed precipitation and test 1-4 simulated 24 hour precipitation chart. It shows that the distribution of the Hubei Province precipitation simulated by 4 tests are basically in harmony with the distribution of observed precipitation, but the direction of the rain belt simulated by test 1 (no PBL parameterization) has the deviation with observation, the simulate effects simulated by test 2-4 compared to test 1 good. The boundary layer parameterization scheme can improve the rainstorm forecasting, MRF scheme simulate the distribution of rainfall area closest observation data.

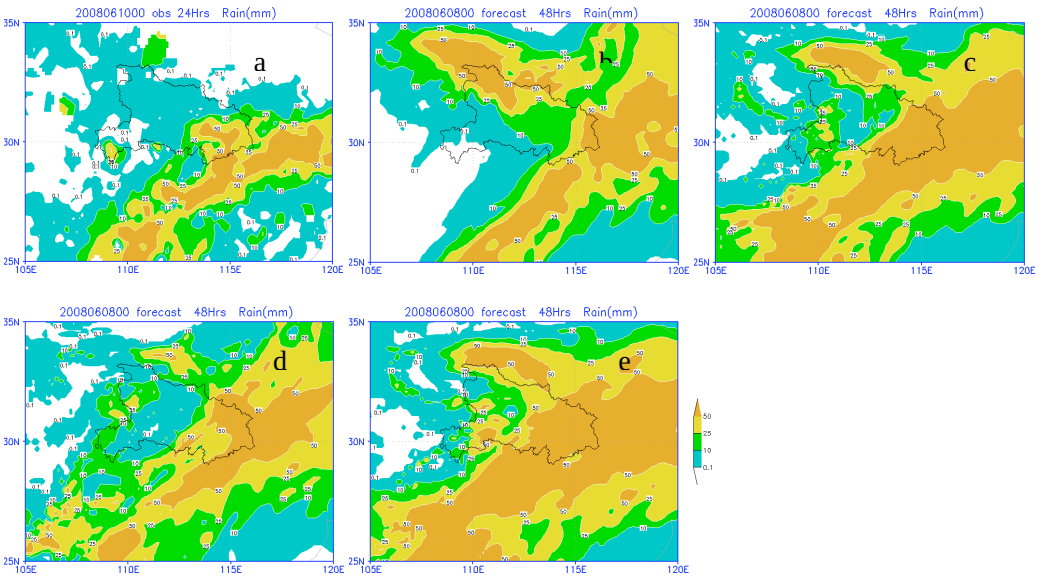

Figure1 observed rainfall distribution and simulated rainfall distribution (24-48hour).

(a)observed rainfall,(b)simulated rainfall(test 1),(c)simulated rainfall(test 2),(d)simulated rainfall(test 3),(e)simulated rainfall(test 4)

Figure 2 gives observed precipitation and test 1-4 simulated 24-48 hour precipitation chart. It shows that the precipitation area of east part of Hubei Province can be simulated by test 1-4, but the rain belt simulated by test 1(no PBL parameterization) moves east quickly, the distribution of the precipitation area simulated by MRF scheme is closest to observed data. To the northeast of Hubei Province, the false precipitation simulated by test are most, the precipitation simulated by MYJ scheme is closest to observed data , the precipitation simulated by test 2-4 are all better than test 1. To the northwest of Hubei Province, the test 1 Failed to report the precipitation, the precipitation simulated by MRF scheme is closest to observed data, next is the YSU scheme. Overall, in this precipitation process, the precipitation simulated by MRF scheme is the best and that of the test 1 is the worst.

The simulation was basically possessed of a capability to reproduce the genesis, development and evolution of the large-scale and meso-scale weather systems. Special analysis is made to see the impact of different boundary layer parameterization schemes on some factors which affect the heavy rainfall such as vertical velocity, divergence, vorticity, divergence of water vapor flux, θ_{se} field and so on. The simulated results revealed that the precipitation simulated by the model is sensitive to the boundary layer parameterization scheme. Different parameterization schemes have different influences on the maximum intensity of rainfall and the distribution of rain area. Suitable boundary layer parameterization scheme has obvious improvement on simulated results.

Key words: GRAPES， PBL parameterization, Numerical Simulation， Rainstorm

Reference

[1]Garrett, J .R . Sensitivity of climate simulations to land-surface and atmospheric boundary layer treatments-a review. J .Climate, 1993, 6:419-449.

[2]Xu LiRen, Zhao Ming. The influence of boundary layer parameterization schemes on meso-scale heavy rain system. Adv. Atmos. Sci., 2000, 17:458-472.

[3] Braun, S. A. and Tao W. K., Sensitivity of high-resolution simulations of hurricane Bob (1991) to planetary boundary layer parameterizations. Mon.Wea.Rev.2000, 128:3941-3961.

[4] Burk, S. D. and W. T. Thompson, A vertically nested regional numerical weather prediction model with second-order closure physics. Mon. Wea. Rev.,1989, 117:2305 -2324.

[5]Holtslag, A. A. M .and C. H. Moeng, Eddy diffusivity and counter gradient transport in the convective atmospheric boundary layer. J. Atmos. Sci., 1991,48:1690-1698.

The Dynamics and Energetics of Error-growth in Heavy Rainfall Prediction*

Zhang Li-Feng, Luo Yu
(Institute of Meteorology, PLA University of Science and Technology, Nanjing 211101, China)

Understanding the heavy rainfall predictability and the associated error growth dynamics is crucial to the enhancement of severe weather prediction, implementation of short-term ensemble forecast and the design of efficient data assimilation technique. Focusing on the forecast difference due to initial uncertainty, many investigations of meso-scale predictability validates the impact of moist convection on initial error growth (Zhang, 2003; Tan and Zhang, 2004; Zhang and Bei, 2007). Recent studies on the predictability of Mei-Yu front heavy precipitation in China also reveal that the significant error growth is associated with moist convection (Bei and Zhang, 2007; Liu and Tan, 2009) or diabatic latent heating (Luo and Zhang, 2010).

To explore the predictability of heavy rainfall and the key physical process affecting it, this essay focuses on the flood event of 12-13 June 2008 in Guang Xi Province in China. The difference between control- and perturbed-simulation in A REM (Advanced Regional Eta-Coordinate Numerical Heavy-Rain Prediction Model) is discussed to analyze the evolvement of error growth and study the error growth rate budget through its energetic form. The control simulation (CNTL) is initialized by NCEP $1^\circ \times 1^\circ$ reanalysis data while the perturbed simulation (Pert-2K) is performed through the addition of initial temperature perturbation (error).

The power spectrum of precipitation difference reveals that the precipitation with longer accumulated time is more predictable and thus indicates the difficulties faced for small-scale, short-period rainfall prediction. Generally, the forecast difference grows from localized patches to larger coverage. However, the detail of upscale error-growth differs in upper and lower troposphere. The significant error growth of lower level is confined in the vicinity of active moist convections (Fig.1a) and this proves the relation between rapid error growth and convective instability. In contrast, upper-level error growth presents larger coverage (Fig.1b), which is characterized by the error growth propagating from convective regions to jet stream and hence taking on further amplification. As the high jet stream region becomes another sensitive area of error growth, this implies the plausible impact of baroclinic instability on error growth.

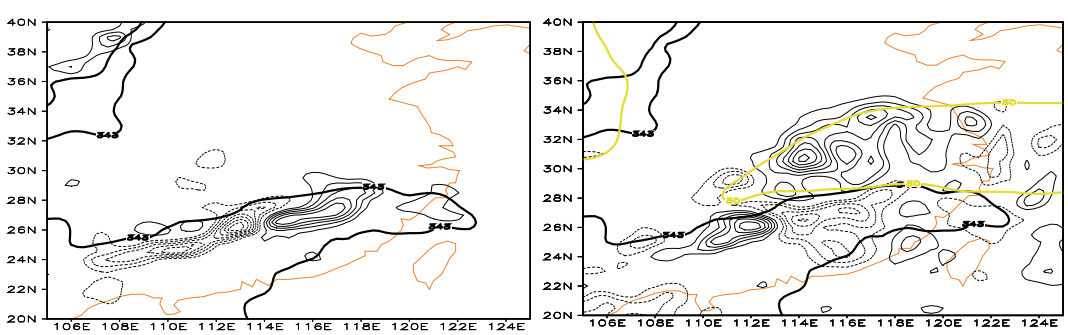

(a) (b)

Fig.1 The meridional wind difference at 24 h (thin lines for positive; short dashed lines for negative; interval is 2 m s^{-1}) between CNTL and Pert-2K over (a) 850 hPa and (b) 200 hPa

(thick dark line for $\theta_{se} = 343$ K at 850 hPa to define the convective region; thick yellow line for velocity of 30 m s^{-1} to define the high jet stream)

In terms of energetics, the heavy rainfall process can be described as a series of energy conservation. The condensation of water vapor causes the release of latent heat, thus the latent energy (LE) is converted into total potential energy (TPE) through latent heating (LHT). As the pressure gradient is changed due to the condensation warming, the kinetic energy (KE) must increases at the expense of TPE via the adiabatic cross-isobaric flow (KGEN) to regain the balance between wind field and pressure. Such energy budget modality indicates that TPE acts as the intermediary between LE and KE. LHT and KGEN reflect the main energy conservation process and these two terms are well correlated (Fig.2). Since the energy growth is mainly determined by LHT, the latent heating serves the energy source during the generation of precipitation.

In addition, through the examination of the error-energy budget, it is found that the dominant source terms for error growth are nonlinear velocity advection (ADVT) and difference in latent heating from convection (DLHT). These two terms present comparable magnitude during the entire integration (Fig.3). Particularly, DLHT is mainly responsible for the rapid error growth during the early stage (about the first 6 h). Therefore, the generation of precipitation and the error growth share the energy source—latent heating. Such negative role of latent heating due to moist convection indicates that the predictability of heavy rainfall is inherently limited.

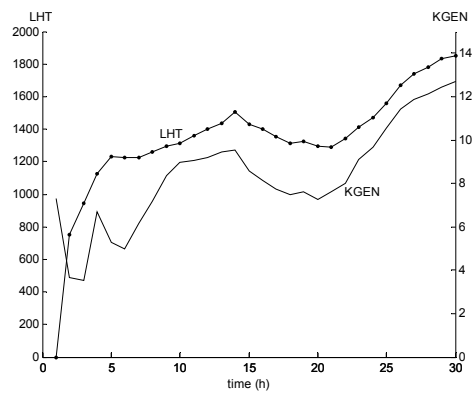

Fig.2 Time evolution of latent heating term (LHT) and kinetic energy generation term (KGEN) ($J\ s^{-1}\ m^{-2}$)

Based on the error-energy budget, the decomposition of nonlinear velocity advection term (ADVT) can explain the error growth near high jet stream where the latent heating is less important. The components of ADVT indicate that the error growth mostly depends on the background flow (UVBFG) and its evolution (Fig.4). A further decomposition of UVBFG into different terms associated with background horizontal shear (BHS) and vertical shear (BVS) shows that the horizontal shear of wind field mainly serves the error-energy source though, the intensifying vertical shear can cause drastic increase in ADVT and the associated error-energy growth. This further proves that the baroclinic instability is also an important mechanism for error growth.

As the terminology of instability is concerned, it is noted that the knowledge of instability theory is generally modulated by the amplification of perturbation within the basic state flow. Actually, the flow-dependent error growth in this essay can be well analogized to the perturbation-growth associated with instability mechanism (or dynamics). Therefore, the problem of predictability is closely related to the atmospheric stability. In this context, it can be concluded that the fast initial error growth due to instability within atmospheric flow contaminates the forecast and limits the predictability. Thus, the weather system growing from unstable flow regime has its intrinsic

predictability.

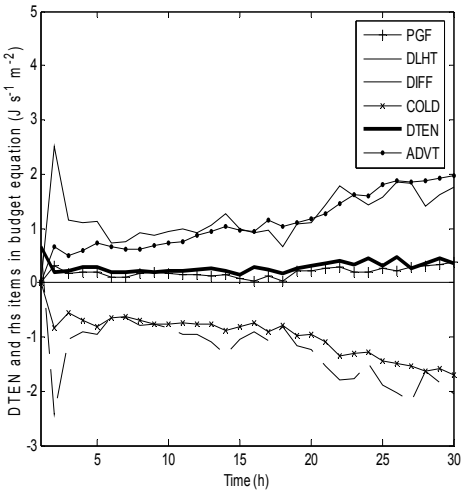

Fig.3 Time evolution of the error-energy tendency (DTEN) and each of its source/sink term.
(PGF: production of pressure gradient forcing;
COLD: production of adiabatic cooling;
DIFF: production of diffusion)

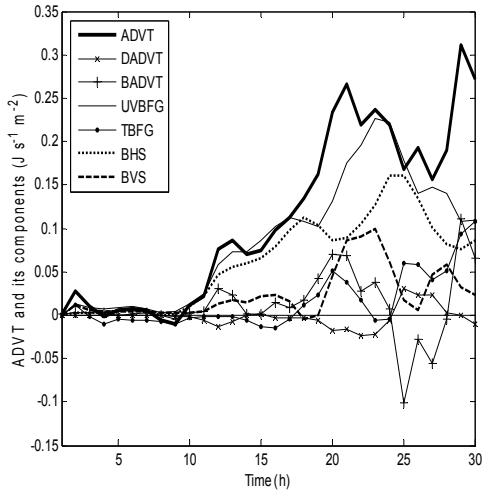

Fig.4 Time evolution of the ADVT near high jet stream and each of its components.
(DADVT: production of nonlinear interaction between perturbations or errors;
BADVT: term due to the propagation of erro r by background flow;
TBFG: production due to the background temperature gradient)

Therefore, the improvement of observation and data assimilation technique is essential to the fine precipitation prediction though, the intrin sic predictability of precip itation disrup ts the det erministic prediction. Thus an alternative is to develop the probabilistic or ensemble forecasting schemes.

*This research was supported by the National Natural Science Foundation of China (40975031)
Corresponding author: Zhang Li-Feng, (zhanglif@yeah.net)

Reference

Bei, N., and F. Zhang, 2007: Impacts of initial errors on predictability of heavy precipitation along the Mei-Yu front of China. Quart. J. Roy. Meteor. Soc., 133:83-99

Liu , J.Y., and Z.-M. Tan, 2009: Mesoscale predictability of mei-yu heavy rainfall. Adv. Atmos. Sci., 26(3): 438-450

Luo,Y., and L.-F. Zhang, 2010: A case study of the error growth evolution in a meiyu front heavy precipitation forecast and an analysis of the predictability. Acta Meteorologica Sinica, 68(3): 411-420

Tan, Z.-M., F. Zhang, R. Rotunno, and C. Snyder, 2004: Mesoscale predictability of moist baroclinic waves: Experiments with parameterized convection. J. Atmos. Sci., 61: 1794-1804

Zhang, F., 2003: Effect of moist convections on mesoscale predictability. J. Atmos. Sci., 60: 1173-1185

Zhang, F., N. Bei, 2007: Mesoscale predictability of moist baroclinic wave: Convection-permitting experiments and multistage error growth dynamics. J. Atmos. Sci., 64: 3579-3593

The Estimation of Rainstorm Forecast Skill along Yangtze Valley through Atmospheric "Strong Signal" Area Data Assimilation in Key Area on Tibetan Plateau

Shengjun Zhang[1)], Xiangde Xu[1)], Shiqiu Peng[2)]

[1)]*State Key Laboratory of Severe Weather , Chinese Academy of Meteorological Sciences , Beijing 100081 , China*

[2)]*Laboratory for Tropical Marine Environmental Dynamics, South China Sea Institute of Oceanology, Chinese Academy of Sciences, Guangzhou, China*

Key Words: Tibetan Plateau, TS Score, Rainfall forecast

1 Introduction

Tibetan Plateau has always been referred to as "roof of the world". It is the largest and highest plateau in the world. Because of its unique topographic feature, Tibetan Plateau (TP, briefly) plays an important and special role in the global atmospheric energy and hydrological cycles.

Some Research indicates that, as the largest and highest plateau in the world, TP has become an abnormal key area of water vapor transport with great triangle shape, which encompasses the abnormally remarkable warm and wet air-flow and the transport of water vapor coming from the southern Indian Ocean, South-China Sea, and the low-latitude pacific, effected by the dynamic- and heating influence. Furthermore, it has been documented that the key regions of occurrence of flooding and drought in the East Asia, particularly in the Yangtze River valley, present a great deal of sensitivity to the anomalies in the water vapor distribution in this great triangle region. Because water vapor converges and transports to the east, Tibetan Plateau serves not only as a water-vapor pump, but also acts as "a water storage and rechannel station".

Although TP accounts for nearly 1/4 of the total land area of China, meteorological observational and operational stations are scarce over this vast land. This problem has been causing uncertainty in the prediction of high-impact weather over the plateau and its downstream regions, especially in the Yangtze and Yellow river valleys and East Asian countries.

In order to improve the weather forecast skill, WWRP/WMO has put great effort to develop the observation technique in sensitive area and observation system. That is, for some high-impact weather to be forecasted, there exist corresponding sensitive area in its upstream regions, where, the observation will benefit the forecast quality. If such sensitive area can be found, and some useful observational factors can be defined, then the observation data are assimilated into the numerical model and, the prediction of high-impact weather in its downstream regions will be enhanced.

In 2008, basing on New Integrated Observational System over the Tibetan Plateau supported by the Chinese–Japanese joint international cooperation program, Peng Shiqiu, Xu Xiangde et al. put forward the concept of "key area" utilizing a north-south line of observational data from GPS and AWS stations on the east fringe of TP (Fig. 1), which has been used in the numerical simulation on the severe snow in south China in 2008. The results indicated the concept would benefit the numerical simulation on the severe snow in winter. But how about the use of the concept on the rainstorm forecast in summer? How about the effect?

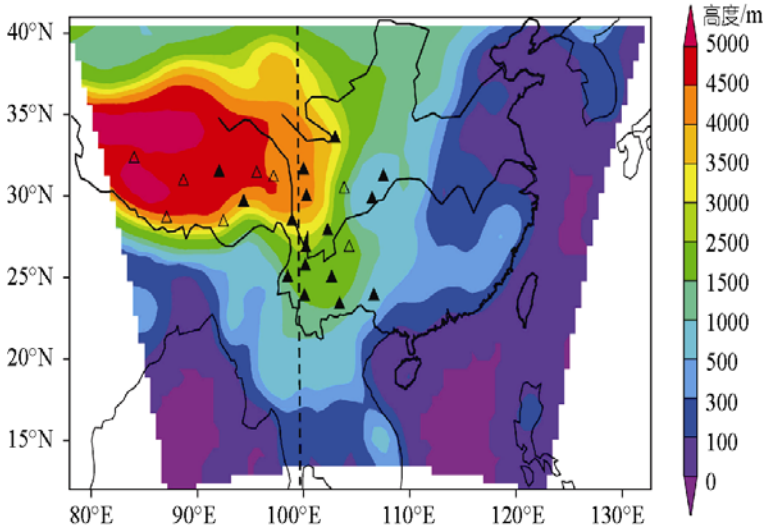

Fig. 1 The terrain height in simulation area and the distribution of AWS stations (solid triangles mean stations whose AWS data is assimilated into model, empty triangle are stations failed to pass the quality control, the dashed line denotes the "key area" with 7 stations in it)

2 Data and Methodology

In this research, according to the concept of "key area" acros s the south-north profile of eastern the TP, 24 AWS-data from the new generation of Integrated Meteorological Observation Network in JICA Project , which has passed th e quality control, were assi milated into the numerical model, to inve stigate its i mpact on m odel si mulation results. T wo rainfall case s, (0800UTC 8 th-0800UTC11th, Jun. 20 08, and 08 00UTC 28 th-0800UTC 1 th, Jul. 2009 separately), are elected as t he target cases. The NCEP forecast data is selected as the large-scale background f ield and t o a fford t he for ecast boundary . As a result, our focus will be on t he rainfall forec ast by assi milating AWS-data into th e firstguess fiel d. In the experi ment desig n, some key factors, including water vapor , surface te mperature, surface pre ssure et al., a re assimilated i nto the firstguess filed. In the meanwhile, in sensitive experi ments, the ef fect of different assi milation-window in the assi milation scheme on the forecast r esult is furt her discussed.

3 Results

3.1 Results in case 1 (0800UTC 28th, Jun.-0800UTC 1th, Jul. 2009)

According to the TS score of accumulated rainfall after 2 4h-, 48h- an d 72h num erical simulation (Fig. 2), the TS score for the moderate rain is almost the same whether the AWS-data were assimilated into the firstguess field or not. But for heavy rain, rainstorm, the TS score were improved sig nificantly on the whole. Furthermore, for dif ferent rainfall order and dif ferent assimilation-window, the rainfall forecast in sens itive experi ments with 7 A WS-data in "ke y area" as similated into the firstguess fi eld was be tter than the rainfall forecast in experime nts with 24 AWS-data assimilated into the firstguess field.

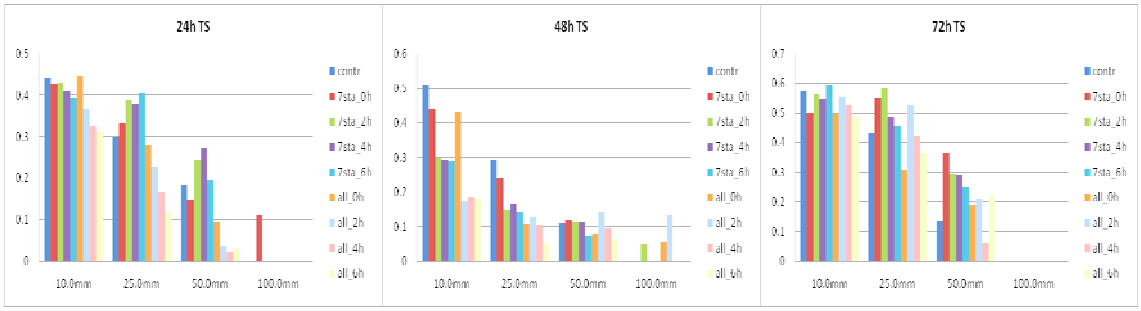

Fig. 2 TS Score of accumulated 24h rainfall after 24h forecast (a), 48h forecast (b) 72h forecast (c) (0h, 2h…denote different assimilation windows, 7s denotes 7 stations in key area, all for 24 stations)

Comparing with the real r ainfall observation (Fig. 3a), in con trolling experim ent without AWS-data were assimilated into the firstguess field, there is a remarkable distance in the pattern of the foreca sted rainfall (Fig. 3b). After 7 A WS-data in "ke y area" wer e assi milated into the firstguess field, the pattern of the forecasted rainfall was more close to the real observation (Fig. 3c).

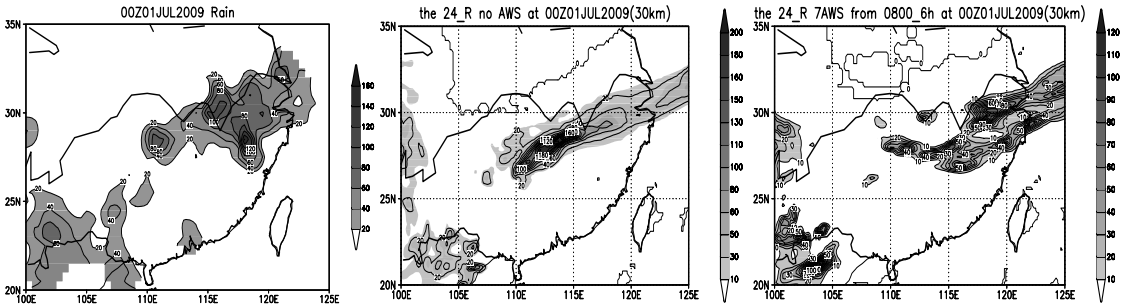

a observation b c ontrol experiment (no assimilation) c se nsitive experiment 6h assimilation windows and 7 station

Fig. 3 24h accumulated rainfall after72h forecast

3.2 Results in case 2 (0800UTC 8th-0800UTC11th, Jun. 2008)

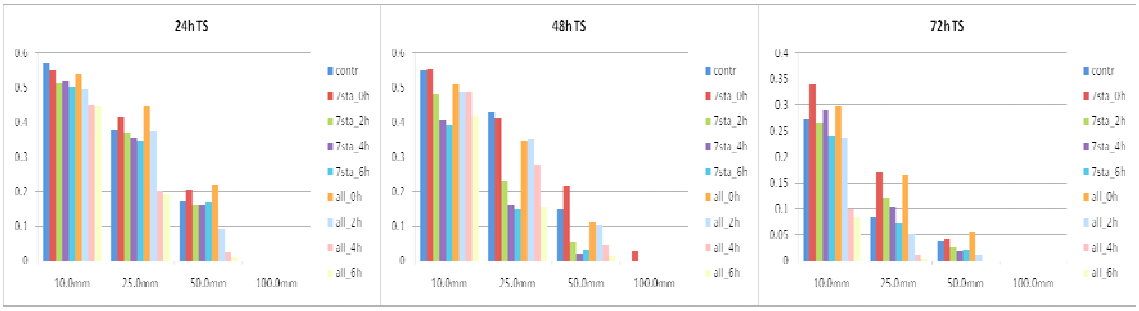

Fig. 4 the same as in Fig. 2, but for case 2

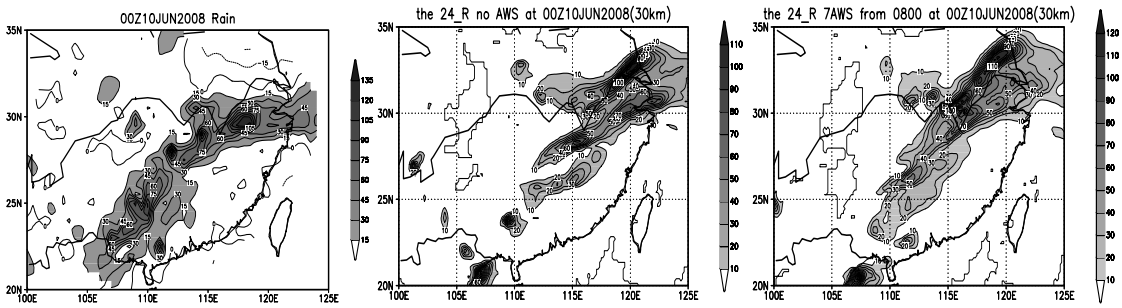

Fig. 5 the same as in Fig. 3, but for case 2

In case 2, for the TS score of accumulated rainfall after 24h-, 48h- and 72h- numerical integration and the forecasted rainfall, the same conclusion can be gotten as in case 1.

4 Conclusions

Comparing all results in different experiments, we can see that, the forecast result with the AWS data assimilated into the initial firstguess field, are better than result without AWS data in all two cases on the whole. Furthermore, for experiments, in which only the AWS data in "key area" are assimilated into the firstguess field, the forecast result, including the TS score, are better than those experiments with all AWS data are assimilated into the firstguess field. Especially for those rainstorm event, the TS score in experiment with only 7 AWS data are assimilated into the firstguess field, are improved remarkably. So the concept of "key area" not only benefits the simulation on severe snow in winter, but also helps to improve the rainstorm forecast in summer.

Study on the 3D Structure of Typhoon Krosa (0716) Rainband with Dual-Doppler Radar

Zhou Haiguang

State Key Laboratory of Severe Weather, Chinese Academy of Meteorological Science, zhg@cams.cma.gov.cn

The typhoon Krosa (0716) landed on the vi cinity region between Zhejiang province and Fujian province at 1530 LST 7 October 2007 for the third ti me. The spiral rainband produced a heavy rainfall in the south and middle region of Zhejiang province. An outer spiral rainband passed through the dual-Doppler radar observation domain composed by Ningbo and Zhoushan Doppler radar. Three dimensional wind fields were retrieved by the dual-Doppler radar volume scan data. The mesoscale structure of the spiral rainband was studied by the 3D wind. It shown that there were some strong reflectivity areas at the low level of the rainband. The inflow in the up stream of the rainband out side was weak. On the other hand, the inflow in the downstream of the rainband outside was strong. There was out flow in the inside of the rainband at the low level. In the vertical cross-section, t here was inflo w in the low level of the outside rainband. The inflow entered the rainband at low level (z<2km) from the outside rainband. On the other hand, there was outflow in the inner side of the rainband. These flows conve rged at the low level of the rainband center region. The t angential com ponent of the wind decr eased with height and the maximum wind region was at 2km height

Acknowledgements

This work was supported by the National Science Foundation of Chin a (grant 40605014) , and the science f oundation of st ate key Laboratory of Sever e Weather.

Research of Meso-scale Convective Systems over Jinan on 18 July 2007

ZHUO Hong[1, 2],ZHAO Ping[3],REN Jian[2],PU Zhangxu[2],and YANG Furong[2]
1. State Key Laboratory of Severe Weather, Chinese Academy of Meteorological Sciences, Beijing, China
2. Jinan Meteorological Bureau, Jinan , China
3. National Meteorological Information Centre, Beijing, China, zhaop@cma.gov.cn

1. Introduction

Meso-scale convective systems (MCSs) appear repeatedly in the same region often result in severe heavy rain. The first study of MCS focused on the Meso-scale convective complex (MCC, a large scale MCS), which was defined by Maddox (1980) based on satellite infrared Black Body Temperature (TBB)(Velasco et al,1987;Miller D,et al,1991;Tao et al,1998).After that, Scholars have revised the shape and scale (Augustine, et al,1988; Ma Yu,1997). Recently, the shape and scale of MCSs have been reclassified(Anderson，et al，1998；Jirak，et al，2003) and divided into four categories(Table 1): MCC, permanent elongated convective system(PECS), Meso-β-scale MCC (MβCCS) ,and Meso-β-scale PECS(MβECS).

Table 1. MCS definitions based upon analysis of IR satellite data (Jirak 2003)

MCS category	Size	Duration	Shape
MCC	Cold cloud region ≤-52℃ with area ≥50000km^2	Size definition met for ≥6h	Eccentricity≥0.7 at time of maximum extent
PECS			0.2≤eccentricity＜0.7 at time of maximum extent
MβCCS	Cold cloud region ≤-52℃ with area ≥30000km^2 and maximum size must be≥30000km^2	Size definition met for ≥3h	Eccentricity≥0.7 at time of maximum extent
MβECS			0.2≤eccentricity＜0.7 at time of maximum extent

A large PECS occurred on July 18, 2007 in North China. Figure 1 shows that Jinan city, the capital of Shandong province, was located in the heavy rainfall center, and the maximum 1h precipitation reached 151 mm.

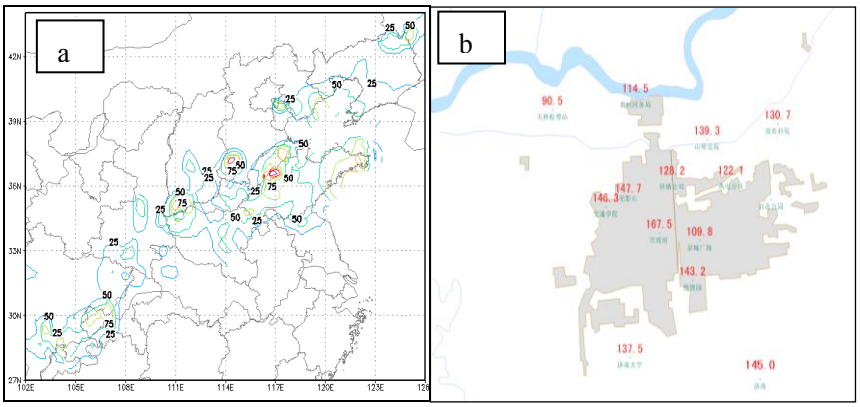

Fig.1 (a) Total precipitation (mm) from 08:00 BST on 18 July to 8:00 BST on 19 July, 2007; and (b) total precipitation (mm) from 17:00 BST to 20:00 BST on July 18, 2007 at Jinan automatic weather stations（the shaded areas indicate the Jinan urban area).

2. Data

The data include the conventional observations, FY-2 satellite infrared and visible cloud images, and the meso-scale automatic weather station data.

3. Background before the PECS formation

The east Asian trough presented near the mid-latitudes of Japan at 200 hPa, and less moved (Fig. 2a). A long wave trough situated from inner Mongolia to Xinjiang province. Between the two troughs was the power South Asia high. The upper-level westerly jet was located in the north of the South Asia high, and the maximum winds exceeded 48m/s , with obvious anti-cyclonic curvature(Fig.2a).Figure 2b gives the Geopotential height, temperature and wind fields at 850hPa. Obviously, the maximum wind speed of low-level jet that over 18m/s existed in south China. On the left of the low level jet was Shangdong province. From figure 2c, the lower southwest flow in the northwest side of subtropical high transported vapor to north China continuously. At this time, Jinan city was the center of strongest water vapor flux convergence zone. This weather situation caused a wide range of wet unstable energy region ($\theta se500-\theta se850<0$) in north China (Fig.2d). From T-LogP chart at 08:00BST (figure omitted), the humidity level was deep, and saturated layer extended from surface to 500hPa.Meanwhile, there was a significant warm, dry cover between 300 and 400hPa. Clockwise wind turning from southwest at bottom level to northwest at up level showed strong warm advection. The humidity level became thicker, but the lifting and free convection levels were lower at 14:00BST.These show that there were small negative buoyancy over Jinan city, and just a very little lift force could produce deep convection.

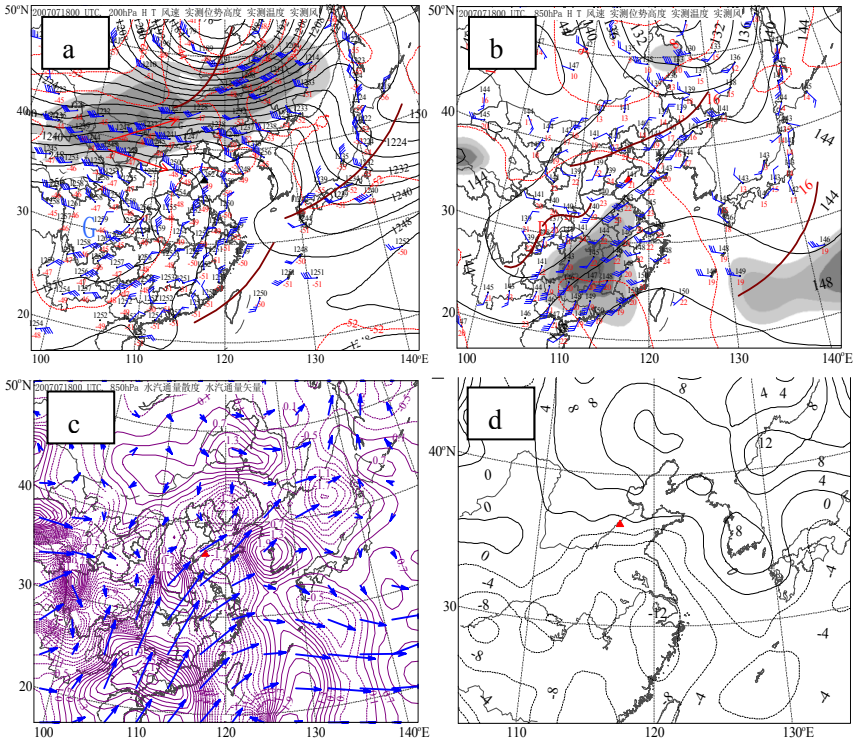

Fig.2 (a) Geopotential height (10gpm,thin solid lines), temperature (℃,thin dotted lines), and wind (m/s) fields at 200 hPa at 8:00 BST on 18 July 2007 (shaded areas are for ≥30m/s, and the pentagram indicates the position of Jinan City, long arrowheads denote the prevailing current directions), (b) same as (a) but for geopotential height, temperature, and wind fields at 850 hPa(shaded areas are for ≥12m/s), (c) same as (a) but for water vapor flux (vector) and its divergence(10-7g/hPa.cm^2.s), and (d) same as (a) but for the difference of pseudoequivalent potential temperature(K) between 500hPa and 850hPa

4. Trigger condition

It is quite evident from Fig. 3 that the PECS trigger had close relationship with the invasion of cold air from the northeast. The cold air behind the eastern cold front reached the Northeast Plain where the temperature was lower than other places, then returned to the southwest along the cold front, made temperature lower than before, and the wind discontinuity line between northwest and southwest became to northeast and southwest .This strong convergence strengthened updraft and vapor that the heavy rain needed. A string convective cloud clusters which were composed by A and Bγ-scale convective cells, developed behind the front. Two cloud tops might represent two separate updrafts.

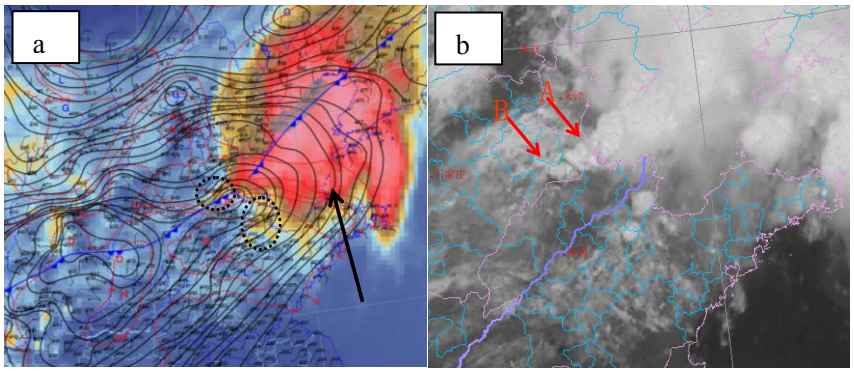

Fig.3 (a) surface pressure (hPa,solid contours), temperature(℃,dashed contours), wind(m/s) ,and infrared

satellite images at 12：00BST on 18 July 2007(arrow indicated the location of MCC，thick dashed lines indicated the locations of outflows); (b) for amplified FY-2C satellite visible cloud image at 12：00BST on 18 July 2007(arrow A and B indicated the location of convective cells).

5. Cloud characteristics

The PECS has been composed by 10 convective cells successively, and soon fromβorγ-scale became toα-scale with abundant moisture. When it developed in vigorously growing stage, the PECS contained five isolated convective cells with higher cloud tops. The initial convection occurred at 12:00BST and the cold cloud cover area of less than 221K developed into 50000 km^2 within 2 hours, and matured in the morning at 1:00BST,but disappeared rapidly at 6:00BST. From birth to die, the PECS have experienced 18 hours. In general, the PECS cold cloud cover area of less than 221K when it matured was much larger than ordinary MCC (figure omitted).

Two heavy precipitations over Jinan city and Shanghe, a county in north Jinan, were related to sudden cloud top strength when two clouds combined. The heavy precipitation over Shanghe was produced by a 191k cloud top when two independent clouds compound into a MCC, however, the heavy precipitation over Jinan happened when a 187k and another 189k cloud top merged into a stronger 183k cloud top in the same α-scale MCC(figure omitted).

At 15:30BST, when heavy precipitation began, a curved thin line of cumulus clouds generated in the windward side of Shanghe(fig.4a), in which included four small cloud tops. After half an hour, a convergence line formed between the cold air and warm atmosphere. Figure 4(b) shows that a mesoscale thunderstorm high appeared at 16:00BST, which east-west length was about 2 longitude distances and width was about 1/4 length (fig.4b). One hour later, the high expanded into high-pressure group, and its range increased from γ-scale toα-scale. At 19:00BST (figure omitted), the rear of thunderstorms formed a complete wake low. After the high pressure disappeared, the scope and intensity of the wake low have achieved the strongest peak (figure omitted).

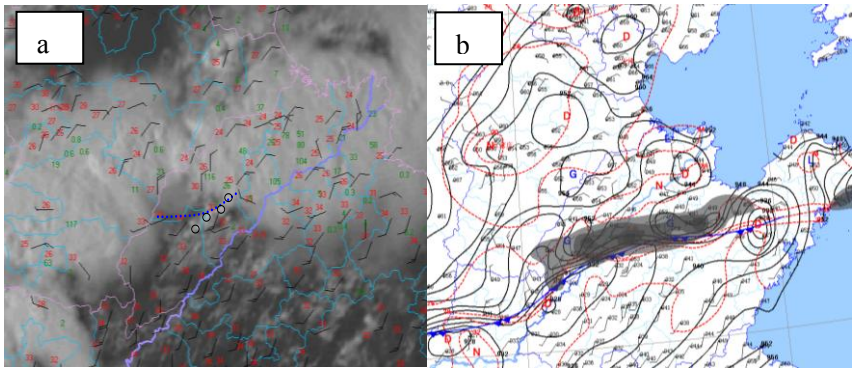

Fig.4 (a)FY-2 visible cloud image at 15：30BST on 18 July 2007 (black circle indicate the formation locations of convective cells and cloud tops. blue dotted line for convergence line) ;(b) surface pressure (hPa,solid contours, blue G and D for center of high and low pressure), temperature(℃,dashed contours, L、N for the center of cold and warm air), wind(m/s),and rain at16：00BST on 18 July 2007 (from shadow to dark areas is 10、25、50、75、100mm respectively）.

6. Conclusion

By using the conventional observations, the unconventional FY—2 satellite infrared and visible cloud images, and the meso-scale automatic weather station data, the formation and development process of a PECS were analyzed in North China on 18 July 2007. Results indicated that the PECS formation and development were associated with low-level cold air activities from Northeast China. The cold and the south-west wet warm air made stronger convergence to produce the PECS. Cloud images also indicated that the PECS was a long life meso-α-scale convective system, which has lived 18 hours from formation to termination. The PECS is successively composed by 10 convection cells. When two α-scale convective systems combined, the heavy rain over Shanghe produced. At the same time, a narrow cloud line (also is called outflow or gust front) that contained 4 γ-scale convective cells can be seen on the visible cloud images. The gust front corresponded with the narrow cloud line. Behind the cold front and the gust front, a γ-scale high pressure occurred, and the individual high pressure soon grows up to a α-scale high pressures, with rain happens between the cold front and the high pressures. The strongest heavy rain over Shanghe occurred when the mesohigh pressure appeared. Different from the suburb rain, the urban rain over Jinan generated when two different cloud tops in the same cloud merged into one stronger cloud top. The precipitation over Shanghe was produced by the main thunderstorm outflow from the PECS and warm atmosphere from the environment, and the heavy rain over Jinan might have some connection with two β-scale and one γ-scale convective cells in a multi-cells thunderstorm which was produced by main outflow and sub-outflow combining.

References

Maddox R A. 1980. Mesoscale Convective Complexes. Bull Amer.soc, 6(11):9-17 .

Velasco L,Fritsch J M. 1987.Mesoscale Convective Complexes in America. J Geophys Res,192：9591-9613.

Miller D，Fritsch J M. 1993 .Mesoscale Convective Complexes in theWestern in the Pacific region. Mon Wea Rev,121:2254-2263.

Tao Zuyu,Wang Hongqing,Wang Yu,et al. 1998.A Survey of Meso- α-scale Convective System over China during 1995. Acta Meteorologica Sinica(in Chinese), 56(2):166-177.

Augustion J A, and Cotton W R. 1988.The Precipitation Life Cycle of Mesoscale Convective over United States. Mon. Wea. Rev,,116:685-701.

Ma Yu,WANG Xu,and TAO Zuyu. 1997.Geographic Distribution and Life Cycle of Mesoscale Convective System in China and its Vicinity. Progess in Nature Sciece(in Chinese), 7(6):701-706.

C. J. Anderson , and Raymond W. Arritt. 1998. Mesoscale Convective Complexes and Persistent Elongated Convective Systems over the United States during 1992 and 1993.Monthly Weather Review,126(3)：578-599.

Jirak I L, Cotton W R, McAnelly R L.2003.Satellite and Radar Servey of Mesoscale Convective System Evelopment. Mon Wea Rev,131(10):2428-2449.